STRUCTURING HIGH-ORDER HARMONIC GENERATION WITH THE ANGULAR MOMENTUM OF LIGHT

Laura Rego Cabezas

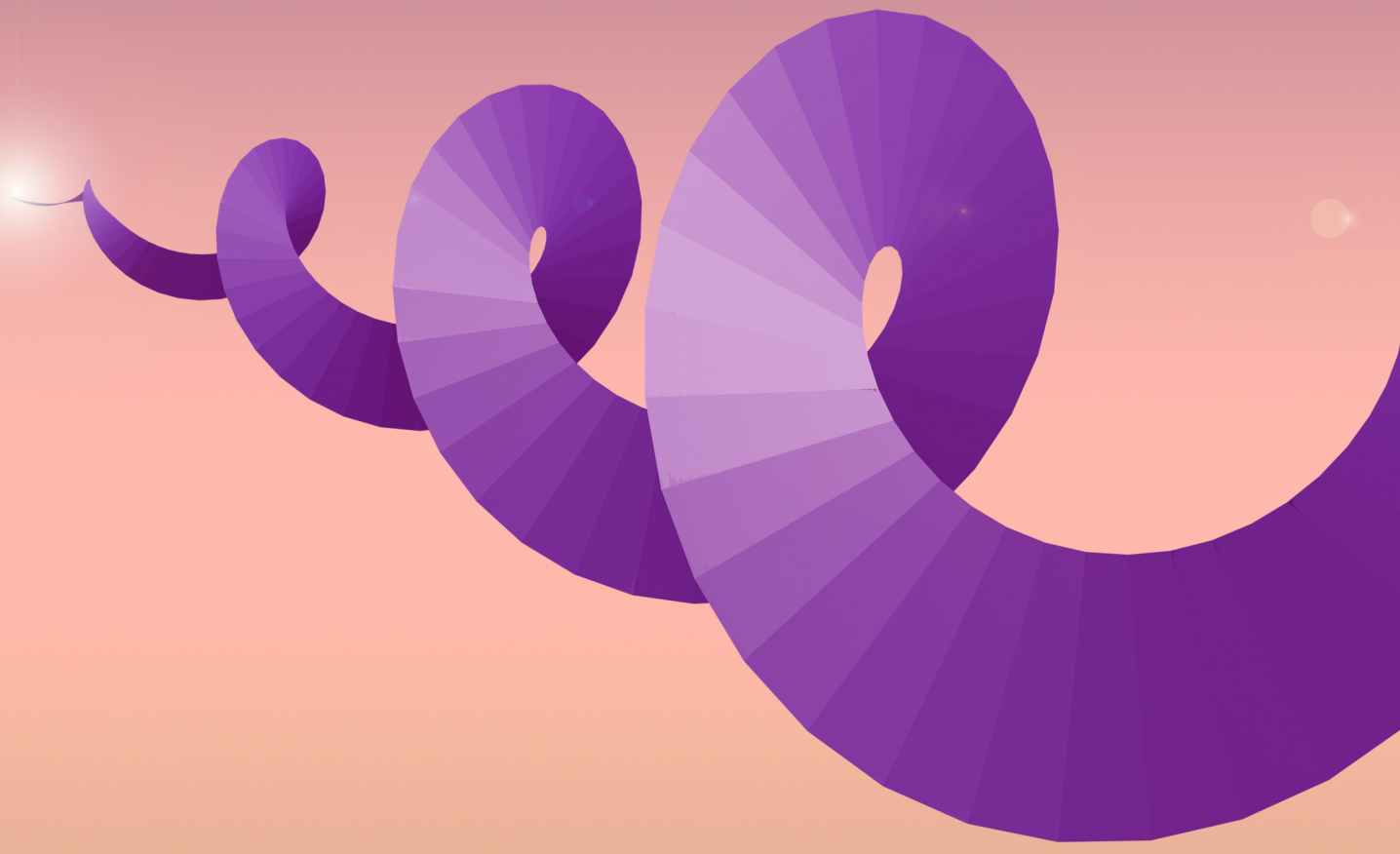

PhD Thesis

VNiVERSiDAD D SALAMANCA
CAMPUS DE EXCELENCIA INTERNACIONAL

LAURA REGO CABEZAS

STRUCTURING HIGH-ORDER HARMONIC GENERATION WITH THE ANGULAR MOMENTUM OF LIGHT

STRUCTURING HIGH-ORDER HARMONIC GENERATION WITH THE ANGULAR MOMENTUM OF LIGHT

LAURA REGO CABEZAS

VNiVERSiDAD D SALAMANCA

CAMPUS DE EXCELENCIA INTERNACIONAL

Departamento de Física Aplicada

Grupo de Investigación en Aplicaciones del Láser y Fotónica

A thesis submitted for the degree of

Doctor in Physics at Universidad de Salamanca

Supervised by Prof. Dr. Luis Plaja Rustein and Dr. Carlos Hernández García

Julio 2021

Esta tesis doctoral es un compendio de las siguientes publicaciones:

1. Dorney, K. M., Rego, L., Brooks, N. J., Román, J. S., Liao, C.-T., Ellis, J. L., Zusin, D., Gentry, C., Nguyen, Q. L., Shaw, J. M., Picón, A., Plaja, L., Kapteyn, H. C., Murnane, M. M. & Hernández-García, C. Controlling the polarization and vortex charge of attosecond high-harmonic beams via simultaneous spin–orbit momentum conservation. *Nature Photonics* **13,** 123–130. doi:10.1038/s41566-018-0304-3 (2019).

2. Rego, L., Dorney, K. M., Brooks, N. J., Nguyen, Q. L., Liao, C.-T., Román, J. S., Couch, D. E., Liu, A., Pisanty, E., Lewenstein, M., Plaja, L., Kapteyn, H. C., Murnane, M. M. & Hernández-García, C. Generation of extreme-ultraviolet beams with time-varying orbital angular momentum. *Science* **364,** eaaw9486. doi:10.1126/science.aaw9486 (2019).

3. Rego, L., Hernández-García, C., Picón, A. & Plaja, L. Site-specific tunnel-ionization in high harmonic generation in molecules. *New Journal of Physics* **22,** 043012. doi:10.1088/1367-2630/ab7dde (2020).

4. Rego, L., Román, J. S., Plaja, L. & Hernández-García, C. Trains of attosecond pulses structured with time-ordered polarization states. *Optics Letters* **45,** 5636. doi:10.1364/ol.404402 (2020).

5. Rego, L., Brooks, N. J., Nguyen, Q. L. D., Román, J. S., Binnie, I., Plaja, L., Kapteyn, H. C., Murnane, M. M. & Hernández-García, C. Necklace-structured high harmonic generation for low-divergence, soft X-ray harmonic combs with tunable line spacing. Submitted to Science Advances. arXiv: 2107.12669 [physics.optics] (2021).

VNiVERSiDAD D SALAMANCA

CAMPUS DE EXCELENCIA INTERNACIONAL

D. LUIS PLAJA RUSTEIN, Catedrático de Óptica y D. CARLOS HERNÁNDEZ GARCÍA, Investigador Ramón y Cajal, ambos del Departamento de Física Aplicada de la Universidad de Salamanca, CERTIFICAN:

Que la presente memoria,"Structuring high-order harmonic generation with the angular momentum of light / *Estructurando la generación de armónicos de orden alto con el momento angular de la luz*" ha sido realizada bajo su dirección en el Aréa de Óptica del Departamento de Física Aplicada de la Universidad de Salamanca por Dña. LAURA REGO CABEZAS y constituye su Tesis Doctoral para optar al grado de Doctora en Física con Mención Internacional.

En Salamanca, a 28 de julio de 2021

PLAJA RUSTEIN LUIS - 35084508D
lplaja@usal.es Universidad de Salamanca
2021.07.28 13:14:29 +02'00'

Fdo.: Luis Plaja Rustein

HERNANDEZ GARCIA CARLOS - 70879854H
Firmado digitalmente por HERNANDEZ GARCIA CARLOS - 70879854H
Fecha: 2021.07.28 13:08:17 +02'00'

Fdo.: Carlos Hernández García

Dedicado a mis padres, mi hermano
y mi abuela Vicenta.

ABSTRACT

Ultrashort laser pulses are a unique tool to explore the fastest dynamics in matter. Remarkably, the shortest laser pulses to date are produced from the non-linear frequency upconversion phenomenon of high-order harmonic generation (HHG), which results in the emission of pulses of attosecond durations. Importantly, such attosecond pulses can exhibit a very exciting property, the angular momentum, which presents two different forms, the spin angular momentum (SAM) and the orbital angular momentum (OAM), and that brings new scenarios for the light-matter interactions at the nanometric spatial and ultrashort temporal scales.

In this thesis work, we develop a compilation of schemes for the creation of high-order harmonics and attosecond pulses with novel angular momentum properties by structuring the HHG process through the characteristics of the driving beams. For that purpose, we first address the description of the fundamental physical mechanisms of HHG. In particular, we study the tunnel ionization in molecules, finding that it is site-specific—its rate depends on the position of the electronic wavefunction at the ion sites—, due to the extended nature of the molecules. This characteristic leaves important signatures in the HHG and photoelectron spectra. Therefore, we provide a recipe for implementing the site-specificity in the existing strong-field models.

Afterwards, we theoretically predict and describe the creation of extreme-ultraviolet (XUV) beams with novel angular momentum properties, which, in most of the cases, are experimentally generated and characterized by our collaborators from the Kapteyn-Murnane group in JILA, at the University of Colorado (USA) and from the group of Prof. M.-Ch. Chen at the Institute of Photonics Technologies of the Tsing Hua University (Taiwan). To begin with, we demonstrate the generation, for the first time, of light beams with time-varying OAM, a property which we denote as the self-torque of light. Importantly, self-torqued beams arise naturally in the XUV regime from HHG driven by two time-delayed infrared vortex beams. Under this configuration, the OAM of the high-order harmonics changes along time in the attosecond time-scale, being the amount of self-torque controlled through the temporal properties of the driving pulses. Thus, we believe that self-torqued beams can serve as unprecedented tools for laser-matter manipulation. In addition, we show how the OAM can serve as an instrument to manipulate the spectral and divergence properties of the high-order harmonics. By driving HHG with two vortex beams with properly selected OAM, we obtain high-order harmonic frequency

combs with tunable line-spacing and low divergence. Such control is particularly interesting for XUV/soft-X-ray spectroscopy and imaging.

Moreover, we present several schemes for the ellipticity control of the high-order harmonics and attosecond pulses. Using the non-collinear counter-rotating scheme, we extract the scaling of the ellipticity of the high-order harmonics with that of the driving beams' and we unveil the information about the non-perturbative dipole response hidden in that connection. Also, we show the generation of circularly polarized vortex beams from HHG driven by a bi-circular vortex field. Interestingly, by properly selecting the OAM of the driving field we can obtain either circularly polarized attosecond pulses, or high-order harmonics with low topological charge. Finally, we theoretically demonstrate the generation of attosecond pulse trains with time-ordered polarization states by combining two time-delayed bi-circular vortex driving fields. We believe that the generation of attosecond pulses with controlled ellipticity can be employed for the study of ultrafast spin dynamics in chiral molecules or magnetic materials.

RESUMEN

Los pulsos láser ultracortos son una herramienta única para explorar las dinámicas más rápidas de la materia. Sorprendentemente, los pulsos de láser más cortos obtenidos hasta la fecha se producen a partir del fenómeno no lineal de conversión de frecuencias de generación de armónicos de orden alto (HHG), que resulta en la emisión de pulsos con duraciones de attosegundo. Es importante destacar que estos pulsos de attosegundo pueden exhibir una propiedad muy interesante, el momento angular, que presenta dos formas diferentes, el momento angular de espín (SAM) y el momento angular orbital (OAM), y que abre nuevos escenarios para las interacciones luz-materia a escalas espaciales nanométricas y temporales ultracortas.

En esta tesis desarrollamos un conjunto de esquemas para la creación de armónicos de orden alto y pulsos de attosegundo con nuevas propiedades de momento angular mediante la estructuración del proceso de HHG a través de las características de los haces incidentes. Para ese propósito, primero abordamos la descripción de los mecanismos físicos fundamentales de la HHG. En particular, estudiamos la ionización túnel en moléculas, descubriendo que depende de la ubicación del electrón dentro de la molécula, debido a la naturaleza extendida de estas. Esta característica deja huellas importantes en los espectros de HHG y de fotoelectrones. Por lo tanto, hemos desarrollado una receta para implementar este fenómeno en los modelos de campos intensos existentes.

A continuación, predecimos y describimos teóricamente la generación de haces láser en el ultravioleta extremo (XUV) con nuevas

propiedades de momento angular que, en la mayoría de los casos, son también creadas y caracterizadas experimentalmente por nuestros colaboradores del grupo Kapteyn-Murnane en JILA, en la Universidad de Colorado (EE. UU.), y del grupo del Prof. M.-Ch. Chen del Instituto de Tecnologías Fotónicas de la Universidad Tsing Hua (Taiwán). Para empezar, demostramos la generación, por primera vez, de haces de luz con OAM variable en el tiempo, una propiedad que denominamos como el auto-torque de la luz. Es importante destacar que los haces con auto-torque surgen naturalmente en el régimen XUV cuando el campo incidente para la HHG está formado por dos vórtices infrarrojos retardados en el tiempo. Bajo esta configuración, el OAM de los armónicos de orden alto cambia a lo largo del tiempo en una escala de tiempo de attosegundos, siendo la cantidad de auto-torque controlada a través de las propiedades temporales de los pulsos incidentes. Por lo tanto, creemos que los haces con auto-torque pueden servir como nuevas herramientas para la manipulación láser-materia. Además, mostramos cómo el OAM puede servir como instrumento para manipular las propiedades espectrales y de divergencia de los armónicos de orden alto. Empleando dos vórtices con el contenido adecuado de OAM como pulsos incidentes, obtenemos peines de frecuencias de armónicos de orden alto con un espaciado entre líneas espectrales sintonizable y baja divergencia. Este control es particularmente interesante para espectroscopía y formación de imagen en el XUV o incluso en los rayos X blandos.

Además, presentamos varios esquemas para el control de la elipticidad de los pulsos de attosegundo y de los armónicos de orden alto. Utilizando la configuración no colineal contrarrotante, extraemos el escalado de la elipticidad de los armónicos de orden alto con la de los haces incidentes y desvelamos la información sobre la respuesta dipolar oculta en esa conexión. Además, mostramos la generación de vórtices polarizados circularmente a partir de la HHG usando un campo incidente bi-circular vorticial. Destacablemente, al seleccionar correctamente el OAM del campo incidente, podemos obtener, o bien pulsos de attosegundo polarizados circularmente, o bien armónicos de orden alto con baja carga topológica. Por último, demostramos teóricamente la generación de trenes de pulsos de attosegundo con estados de polarización ordenados temporalmente mediante la combinación de dos campos incidentes bi-circulares vorticiales retardados en el tiempo. Creemos que la generación de pulsos de attosegundo con elipticidad controlada se puede emplear para el estudio de la dinámica ultrarrápida de SAM en moléculas quirales o materiales magnéticos.

PUBLICATIONS

The main results included in this report have been published in the following research articles:

1. Dorney, K. M., Rego, L., Brooks, N. J., Román, J. S., Liao, C.-T., Ellis, J. L., Zusin, D., Gentry, C., Nguyen, Q. L., Shaw, J. M., Picón, A., Plaja, L., Kapteyn, H. C., Murnane, M. M. & Hernández-García, C. Controlling the polarization and vortex charge of attosecond high-harmonic beams via simultaneous spin–orbit momentum conservation. *Nature Photonics* **13,** 123–130. doi:10.1038/s41566-018-0304-3 (2019).
2. Rego, L., Dorney, K. M., Brooks, N. J., Nguyen, Q. L., Liao, C.-T., Román, J. S., Couch, D. E., Liu, A., Pisanty, E., Lewenstein, M., Plaja, L., Kapteyn, H. C., Murnane, M. M. & Hernández-García, C. Generation of extreme-ultraviolet beams with time-varying orbital angular momentum. *Science* **364,** eaaw9486. doi:10.1126/science.aaw9486 (2019).
3. Rego, L., Hernández-García, C., Picón, A. & Plaja, L. Site-specific tunnel-ionization in high harmonic generation in molecules. *New Journal of Physics* **22,** 043012. doi:10.1088/1367-2630/ab7dde (2020).
4. Rego, L., Román, J. S., Plaja, L. & Hernández-García, C. Trains of attosecond pulses structured with time-ordered polarization states. *Optics Letters* **45,** 5636. doi:10.1364/ol.404402 (2020).
5. Rego, L., Brooks, N. J., Nguyen, Q. L. D., Román, J. S., Binnie, I., Plaja, L., Kapteyn, H. C., Murnane, M. M. & Hernández-García, C. Necklace-structured high harmonic generation for low-divergence, soft X-ray harmonic combs with tunable line spacing. Submitted to Science Advances. arXiv: 2107.12669 [physics.optics] (2021).

The following additional publications are also part of this thesis work and are included in the Appendix:

1. Huang, P.-C., Hernández-García, C., Huang, J.-T., Huang, P.-Y., Lu, C.-H., Rego, L., Hickstein, D. D., Ellis, J. L., Jaron-Becker, A., Becker, A., Yang, S.-D., Durfee, C. G., Plaja, L., Kapteyn, H. C., Murnane, M. M., Kung, A. H. & Chen, M.-C. Polarization control of isolated high-harmonic pulses. *Nature Photonics* **12,** 349–354. doi:10.1038/s41566-018-0145-0 (2018).

2. Pisanty, E., Rego, L., Román, J. S., Picón, A., Dorney, K. M., Kapteyn, H. C., Murnane, M. M., Plaja, L., Lewenstein, M. & Hernández-García, C. Conservation of Torus-knot Angular Momentum in High-order Harmonic Generation. *Physical Review Letters* **122,** 203201. doi:10.1103/physrevlett.122.203201 (2019).

3. Chang, K.-Y., Huang, L.-C., Asaga, K., Tsai, M.-S., Rego, L., Huang, P.-C., Mashiko, H., Oguri, K., Hernández-García, C. & Chen, M.-C. High-order nonlinear dipole response characterized by extreme ultraviolet ellipsometry. *Optica* **8,** 484. doi:10.1364/optica.413531 (2021).

Furthermore, the following publications, which support the current thesis, were carried out before the predoctoral period:

1. Rego, L., Román, J. S., Picón, A., Plaja, L. & Hernández-García, C. Nonperturbative Twist in the Generation of Extreme-Ultraviolet Vortex Beams. *Phys. Rev. Lett.* **117,** 163202. doi:10.1103/PhysRevLett.117.163202 (16 2016).

2. Turpin, A., Rego, L., Picón, A., Román, J. S. & Hernández-García, C. Extreme Ultraviolet Fractional Orbital Angular Momentum Beams from High Harmonic Generation. *Scientific Reports* **7.** doi:10.1038/srep43888 (2017).

3. Rego, L., San Román, J., Plaja, L., Picón, A. & Hernández-García, C. *Ultrashort Extreme Ultraviolet Vortices* ISBN: 9789533070520. doi:10.5772/64908. arXiv: 0803973233 (2017).

4. Hernández-García, C., Rego, L., Román, J. S., Picón, A. & Plaja, L. Attosecond twisted beams from high-order harmonic generation driven by optical vortices. *High Power Laser Science and Engineering* **5.** doi:10.1017/hpl.2017.1 (2017).

5. Hernández-García, C., Vieira, J., Mendonça, J., Rego, L., Román, J. S., Plaja, L., Ribic, P., Gauthier, D. & Picón, A. Generation and Applications of Extreme-Ultraviolet Vortices. *Photonics* **4,** 28. doi:10.3390/photonics4020028 (2017).

During the thesis, it was realized a 3-month visit to the Department of Physics of Lund University (Sweden) to collaborate with the international research group leaded by Anne L'Huillier. In addition, the thesis resulted in 6 oral (2 in XII RNO 2018, CLEO/Europe 2019, Reunión Bienal RSEF 2019, CLEO/USA 2021, CLEO/Europe 2021) and 4 poster (PALM 2018, ICOAM 2019, Atomic Physics 2019, USTS 2019) contributions to national and international conferences.

There's real poetry in the real world.
Science is the poetry of reality.

— Richard Dawkins

ACKNOWLEDGMENTS

Doing a PhD is difficult, but it would have been completely impossible without the contribution and support of many people, who have illuminated the way in each of my steps and who have helped me in my professional, but also personal, development. Although nothing that I write will fully reflect my feeling of gratitude, I hope that at least an ultrashort flash is perceived.

First, I would like to thank Luis Plaja Rustein and Carlos Hernández García for their efforts as my PhD directors. Thank you for allowing me to learn so much from you and for all the work and dedication that you have put into this thesis. In general, I would like to thank all the members of the Grupo de Investigación en Aplicaciones del Láser y Fotónica of the University of Salamanca for having welcomed me so warmly, having taught me so much and having guided me during all these years. I have really enjoyed doing research with you. A special thank you to Enrique Conejero, Julio San Román, Javier Rodríguez and Ana García González for their unconditional help and for transmitting to me not only their enthusiasm for science but also their passion for teaching.

A big thank also to the Attogroup of the University of Lund, which I visited during 3 months. Thank you to the professors Anne L'Huillier, Cord Arnold and Marcus Dahlström for welcoming me so kindly, it has been an honor to have had the opportunity to investigate with you. I would also like to thank David Busto, Felipe Zapata, Chen Guo, and everyone else for their warm hospitality. I really enjoyed the visit, I learned a lot from you and I got infected with your excitement for science.

Additionally, during these years of as a PhD student, I have been had the fortune to have collaborated with various research groups, without which this thesis work would not have been possible. First, I would like to thank our experimental collaborators for their immense work and for the very fruitful scientific conversations: Margaret Murnane, Henry Kapteyn, Kevin Dorney, Quynh Nguyen, Nathan Brooks and all the other members of the Kapteyn-Murnane group in JILA (Boulder University); and Ming-Chang Chen and the other members of his group at the Institute of Photonics Technologies (Tsing Hua University). Thank you also to Emilio Pisanty and Maciej Lewenstein, for the enlightening theoretical discussions; to Antonio Picón, whose role was fundamental at the beginning of my thesis; and to Rocío Borrego and

David Ayuso, for their time and dedication in reading the manuscript of this thesis.

Now, I would like to thank my friends and companions on this tough, and at the same time satisfying, odyssey of learning and researching physics. A big thank you to Aurora and Roberto, my colleagues from the beginning of this path towards the PhD, for having supported and helped me whenever I needed it. I have fond memories of the basement and the conferences, but also of our adventures outside the University. Thank you also to Javier, Alba, Elena, Víctor and Miguel for the good times at the end of the weeks, which I hope will not end. Thank you to all the current and former members of the OSAL Student Chapter, because one of the most beautiful aspects of doing my PhD studies here, and which I will certainly miss a lot, is having the pleasure of doing outreach with you. I have learned a lot and I have enjoyed it infinitely. A big thank you also to my friends from the bachelor's and master's degrees: to Andrea, my good friend and companion in battle; to Jesus, because everything looks different after a good conversation; to Ángel, for motivating and supporting me from the beginning; and to Martín, Adriana, Paula, Pilar, Juan Miguel, Miguel Ángel, and all the others, for all the good times and for everything that I have learned from you.

On a more personal level, many people have formed an essential support network for me. To begin with, I am very grateful to my family. Thank you to my parents for providing me, since I was little, with the two main ingredients to become a scientist: to my mother, for teaching me the importance of perseverance and hard work; and to my father, for feeding and motivating my curiosity about the world around us. A big thank you also to my brother Marcos, for always supporting me, and to my cousins, my uncles, and my grandparents for all their affection. A special gratitude to my grandmother Vicenta: thanks to your sacrifice, I am here today. This thesis also belongs to my friends from Ponferrada, Ana, Elena, Irene, Marta, Paloma, Rebeca, Sandra, and Tamara, for their unconditional support and affection. You are my safety net and my second family. Thank you for making everything so much easier. Thank you also to Esther, for her contagious unstoppable strength. Thank you to Luisa, for teaching me so much and because without her help I would not have been able to get here. And finally, a big thank you to Ana, for always believing in me and being there whenever I need it.

Hay poesía en el mundo real.
La ciencia es la poesía de la realidad.

— Richard Dawkins

AGRADECIMIENTOS

Hacer un doctorado es difícil, pero hubiese sido completamente imposible sin la contribución y el apoyo de muchas personas, que han iluminado el camino a cada uno de mis pasos y que me han ayudado no solo en mi desarrollo profesional, sino también en el personal. Aunque nada de lo que escriba reflejará completamente mi sentimiento de gratitud, espero que al menos se perciba un pequeño destello.

En primer lugar, me gustaría agradecer a Luis Plaja Rustein y a Carlos Hernández García por su labor como mis directores de doctorado. Gracias por haberme permitido aprender tanto de vosotros y por todo el trabajo y dedicación que habéis puesto en esta tesis. En general, me gustaría agradecer a todos los miembros del Grupo de Investigación en Aplicaciones del Láser y Fotónica de la Universidad de Salamanca por haberme acogido tan amistosamente, haberme enseñado tanto y haberme guiado durante todos estos años. He disfrutado mucho investigando con vosotros. Un agradecimiento especial para Enrique Conejero, Julio San Román, Javier Rodríguez y Ana García González por su incondicional ayuda y por transmitirme no solo su entusiasmo por la ciencia, sino también su pasión por la enseñanza.

Debo dar las gracias también al Attogroup de la Universidad de Lund, donde realicé una estancia de 3 meses. Gracias a los profesores Anne L'Huillier, Cord Arnold y Marcus Dahlström por acogerme tan amablemente, ha sido un honor para mí haber tenido la oportunidad de investigar con vosotros. También agradezco a David Busto, Felipe Zapata, Chen Guo, y todos los demás su cálida hospitalidad. Disfruté mucho de la estancia, aprendí mucho con vosotros y me contagiasteis vuestro fervor por la ciencia.

Por otro lado, durante estos años de doctorado, he tenido la suerte de haber podido colaborar con varios grupos de investigación sin los cuales el trabajo de esta tesis no hubiese sido posible. En primer lugar, gracias a nuestros colaboradores experimentales por su inmenso trabajo y por las muy fructíferas conversaciones científicas: a Margaret Murnane, Henry Kapteyn, Kevin Dorney, Quynh Nguyen, Nathan Brooks y todos los demás componentes del grupo Kapteyn-Murnane de JILA (Universidad de Boulder); y a Ming-Chang Chen y los demás miembros de su grupo en el Instituto de Tecnologías Fotónicas (Universidad de Tsing Hua). Gracias también a Emilio Pisanty y Maciej Lewenstein, por las iluminadoras discusiones teóricas; a Antonio Picón, cuyo papel fue fundamental en los inicios de mi doctorado;

y a Rocío Borrego y David Ayuso, por su tiempo y dedicación al leer el manuscrito de esta tesis.

A continuación, me gustaría dar las gracias a mis amigos y acompañantes en esta dura, y a la vez satisfactoria, odisea que es aprender e investigar sobre física. A Aurora y Roberto, mis compañeros desde el principio en este camino hacia la tesis, por haberme apoyado y ayudado siempre que lo he necesitado. Guardo muy buenos recuerdos del sótano y las conferencias, pero también de nuestras aventuras fuera de la facultad. A Javier, Alba, Elena, Víctor y Miguel por los buenos momentos al final de la semanas, que espero que no acaben. A todos los miembros y exmiembros de la OSAL Student Chapter, porque una de las facetas más bonitas de hacer el doctorado aquí, y que sin duda echaré mucho de menos, es el haber tenido el placer de divulgar con vosotros. He aprendido mucho y lo he disfrutado infinitamente. Muchas gracias también a mis amigos de la carrera de física y el máster de láseres: a Andrea, mi buena amiga y compañera de batalla; a Jesús, porque todo se ve de otro color después de una buena charla; a Ángel, por motivarme y apoyarme desde el principio; y a Martín, Adriana, Paula, Pilar, Juanmi, Miguel Ángel, y todos los demás, por los números buenos momentos y por todo lo que he aprendido de vosotros.

En el plano más personal, muchas personas han formado una red de apoyo imprescindible para mí. Para empezar, muchas gracias a mi familia. A mis padres por proporcionarme desde pequeña los ingredientes principales para convertirme en una científica: a mi madre, por enseñarme importancia de la perseverancia y el trabajo duro; y a mi padre, por alimentar y motivar mi curiosidad por el mundo que nos rodea. Muchas gracias también a mi hermano Marcos, por apoyarme siempre, y a mis primos, mis tíos y mis abuelos por todo su cariño. Un agradecimiento especial a mi abuela Vicenta: gracias a tu sacrificio, estoy hoy yo aquí. Además, esta tesis también pertenece a mis amigas ponferradinas, Ana, Elena, Irene, Marta, Paloma, Rebeca, Sandra y Tamara, por su apoyo y cariño incondicionales. Sois mi red de seguridad y mi segunda familia. Gracias por hacerlo todo mucho más fácil. Gracias también a Esther, por contagiarme su fuerza imparable. A Luisa, por enseñarme tanto y porque sin su ayuda no hubiese podido llegar hasta aquí. Y, finalmente, muchas gracias a Ana, por creer siempre en mí y estar ahí para todo lo que necesito.

CONTENTS

LIST OF FIGURES

ACRONYMS

HHG high-order harmonic generation
XUV extreme-ultraviolet
SAM spin angular momentum
OAM orbital angular momentum
TDSE time-dependent Schrödinger equation
SFA strong field approximation
SAE single active electron approximation
TSM thin slab model
SFA+ strong field approximation plus
TFA time-frequency analysis
SDT-SFA site-dependent tunnelling strong field approximation
s-SFA standard strong field approximation
LCP left circular polarized
RCP right circular polarized
FWHM full-width half maximum

1 INTRODUCTION

Science allows us to build new knowledge about the world around us and, afterwards, to apply this information to develop new technologies that improve our well-being. This acquisition of novel insight often requires pushing the established limits towards unexplored scales. The examination of light is an excellent example of how the study of a particular physical phenomenon can modify our general understanding of Nature. It may be difficult to find any other phenomenon with such leading role in the build-up of the foundations of physics. Its investigation has led to the unification of laws in Nature, revealing hidden connections that have unveiled important paths to new knowledge. Just to mention a few examples, the incompatibility of the Maxwell equations and Galileo's relativity in the description of light gave rise to the unification of the two areas into special relativity; Young's experiment, demonstrating the wave behaviour of light, was essential for the discussion of the wave/particle nature of light and, therefore, for the flourish of quantum mechanics; and Feynman's description of the light-matter interaction at the most fundamental level gave rise to quantum electrodynamics.

Nowadays, the understanding of light, its properties, and its interaction with matter, is still a source of exciting information. Nevertheless, light can be also used as a tool to measure, or even trigger, different phenomena. One of the most notorious tools used to this purpose is the laser, widely used since its invention in 1960. Laser light is coherent—i.e. it possesses a spatio-temporal ordered phase—and it exhibits other exceptional characteristics, such as directionality and focusability. Most importantly, these properties can be precisely controlled to adjust laser light to different specific functions. Among them, laser light is a main a tool to investigate phenomena at the shortest time scales. New laser sources allow, nowadays, to access to the most fundamental mechanisms in atoms, molecules, or solid systems, which are governed by dynamic interactions that take place in the attosecond (10^{-18}s) timescale. Attosecond science, therefore, uses pulses of attosecond durations as ultrashort flashes of laser light to capture the ultrafast dynamics of the fundamental systems, an information that remains inaccessible with conventional light sources. Also, these pulses can be used to control or trigger such dynamics in matter.

Attosecond pulses can be routinely produced from the process of high-order harmonic generation (HHG) [1, 2]. In a nutshell, HHG is a well-established method to produce coherent high-frequency radiation in table-top experiments. It consists in the upconversion

of intense low-frequency (usually infrared) laser pulses into high-frequency radiation (up to X-rays), as a result of a highly non-linear, non-perturbative, light-matter interaction. Interestingly, HHG allows to obtain attosecond pulses right from the selection of the most energetic part of the harmonic spectrum, thanks to its phase-locked nature. In addition, one of the main merits of HHG is that it is a highly coherent process, so it is able to map properties of the driving field into the high-frequency radiation. As a consequence, some characteristics of the infrared laser are translated straightforwardly to the higher-frequency attosecond pulses. This later aspect prompts an exciting perspective for attosecond science: the possibility to structure attosecond pulses with angular momentum.

In mechanics, momentum is defined as a quantitative description of the motion of a body. The total mechanical momentum can be expressed as the composition of linear momentum, associated to the straight translation of the centre of mass, and the angular momentum, associated to rotations. The angular momentum of a rigid body can be also split into two parts: the orbital angular momentum (OAM), that describes the centre of mass orbiting around a focus, and the spin angular momentum (SAM), associated to the rotation of the body around itself.

Despite of being an electromagnetic wave, light also possesses momentum, and, remarkably, it can be transferred to matter. The first conjecture about the momentum of light was raised by Johannes Kepler in 1619, when he postulated that the pressure of the sunlight affected the orientation of the tails of the comets, which always pointed away from the Sun. Two centuries later, Maxwell equations described the phenomenon of radiation pressure, that, at the beginning of the 20th century, was experimentally measured [3, 4]. Promising recent technologies, such as laser cooling, are based on the transfer of momentum from light to matter. Interestingly, as in a rigid body, the angular momentum of light can also be split into SAM and OAM.

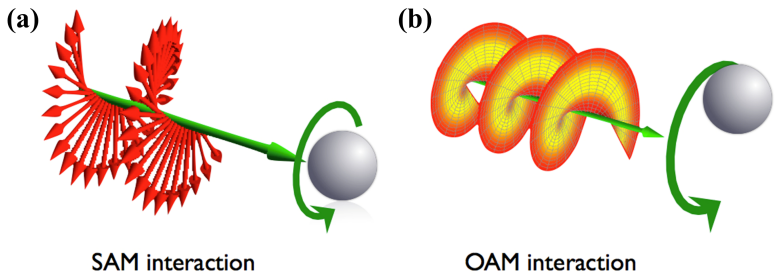

Figure 1: Differences between the SAM (a) and the OAM (b) of light and their interaction with a small particle. Figure by E-karimi - Own work, CC BY-SA 3.0.

The SAM of light is related to its polarization, as shown in figure 1a. Although polarization was first studied in natural light in 1669 using

birefringent materials, only centuries later, in 1909, it was associated to a manifestation of the angular momentum of light [5]. In 1936, it was discovered that, like light's linear momentum, SAM could also be transferred to matter [6]. As it is widely known, polarization has an important role in technology (as in the fabrication of liquid-crystal displays, glasses, etc), as well as in basic sciences, from chemistry to biology.

The OAM of light is, on the other side, a macroscopic property associated to vorticity. As a consequence, light beams carrying OAM are also known as vortex beams. One can imagine a vortex beam as a "light corkscrew", since its wavefront is twisted, forming an helical shape around its propagation axis, as depicted in figure 1b. Specifically, the OAM topological charge characterizes the azimuthal variation of the beam's phase in the transverse plane around a singularity. Importantly, while the SAM is limited to two values, $\pm\hbar$, where $\hbar$ is the reduced Planck constant, the OAM can exhibit an infinite number of discrete values in the form of integer multiples of $\hbar$. Furthermore, in contrast to SAM, the OAM of light was discovered much more recently, in 1992 [7], and it is not yet implemented in our day to day technology. Nevertheless, interesting applications have been already proposed. For example, vortex beams have been demonstrated to trap microparticles and to make them rotate, which offers exciting possibilities in the field of particle manipulation [8, 9]. In addition, they can be used to transfer information at a higher rate than conventional light [10]. Also, other interesting opportunities can be found in phase contrast [11] and super-resolution microscopies [12], or in quantum information [13, 14].

Objectives of this thesis and publications

The main aim of this thesis is to explore schemes to develop new ultrafast laser tools for applications of the angular momentum of light in attoscience. Such goal requires a precise description of the process of HHG, and a deep understanding of its characteristics. Particularly, the proposals within this thesis rely heavily in the above-mentioned mapping of the infrared driver characteristics to the harmonics, as one of the properties which is directly translated to the harmonics is the OAM. This thesis, therefore, contains a wide set of strategies to harvest the potential of HHG to structure high-frequency laser radiation and attosecond pulses.

We present theoretical developments, most of them supported by the experiments from our collaborators, that demonstrate the generation of coherent extreme-ultraviolet (XUV) light with on-demand combinations of angular momenta. Remarkably, some of the schemes allow us to control the ultrafast variation of the angular momenta. The incentive for generating high-frequency ultrashort pulses with particular polarization or vorticity configurations is the possibility to

interact with matter at the nanometric spatial and ultrashort temporal scales in an unprecedented manner—i.e. to interact with atoms, electrons, etc, at their natural scales. Thus, we believe that our results may boost the applications of angular momenta of light into ultrafast nanotechnology, opening a route with exciting novel perspectives.

This thesis report contains the main objectives and results presented in our publications:

1. *Reference* [15]. The fundamental aspects of HHG need to be addressed in order to accurately describe the characteristics of the emitted radiation. In this paper, we investigate the spectral traces of tunnel-ionization from molecular systems, an elemental feature of HHG. Our results show that the tunnel ionization is strongly affected by the specific location of the electronic wavepacket within the molecule, prior to ionization. This leaves a signature in the harmonic spectrum. Thus, we demonstrate that the standard picture of tunnel ionization in atoms needs to be modified to be applied to molecular systems. For this, we develop an extension of the molecular strong field approximation (SFA), the site-dependent tunnelling strong field approximation (SDT-SFA), which can serve as a guide for high-harmonic spectroscopy applications.

2. *Reference* [16]. We introduce a new class of light beams that possess a unique property, associated with the temporal variation of their OAM: the *self-torque* of light. We theoretically predict, and experimentally validate, that a self-torque can be imprinted onto XUV beams through HHG driven by two time-delayed infrared pulses with different OAM. The amount of self-torque can be controlled via the modification of the temporal characteristics of the driving field. Interestingly, the self-torque imprints an azimuthal frequency chirp onto the harmonics that enables its precise experimental characterization.

3. *Reference* [17]. We demonstrate that the combination of different OAM modes allows not only for the control of the OAM of the harmonics, but also for modifications in the spectral content and divergence properties of the HHG emission. By combining two infrared pulses with opposite and non-degenerate OAM content, creating a phased-necklace driving beam, we demonstrate theoretically and experimentally the generation of harmonic combs with tunable line spacing and low divergence.

4. *Reference* [18]. We show that the incorporation of the OAM in a bi-circular driving field enables the simultaneous control over the SAM and OAM of the attosecond pulses emitted from HHG. This scheme allows for the generation of circularly polarized

attosecond pulses with tailored OAM, as well as high-order harmonics with the same topological charge as the driving laser beam.

5. *Reference* [19]. We propose the generation of attosecond pulse trains with time-ordered polarization states through HHG driven by two time-delayed bi-circular vortex fields. Our theoretical simulations demonstrate that two spatially separated rings of harmonics are generated, each with polarization evolving temporally from left-circular to right-circular and vice versa. The proper choice of the driving pulses' properties allows for the custom control of the temporal evolution of the SAM of the pulses within the train.

Further work carried out during the PhD studies, which will be only briefly mentioned in this report, is:

1. *Reference* [20]. The non-collinear counter-rotating driving field allows for the generation of circularly polarized isolated attosecond pulses. We explore the dependence of the ellipticity of the harmonics with the ellipticity of the driving beams by contrasting theoretical and experimental results.

2. *Reference* [21]. Following a similar configuration than that in Ref. [20], the polarization is used as a degree of freedom to precisely quantify the complex dipole response of the HHG. We theoretically support this new experimental high-harmonic ellipsometry technique.

3. *Reference* [22]. The bi-circular vortex field from [18] can be described as a torus-knot field. The conservation of the torus-knot angular momentum allows for the derivation of simple rules for the angular momentum of the harmonics.

On the other hand, the particular methodological contributions of this thesis work to the results presented in the mentioned publications can be summarized as:

1. The development of a theoretical SFA model for the computation of HHG in molecules, including the side-dependent tunneling, and a numerical tool to extract information from the exact time-dependent Schrödinger equation (TDSE) calculations.

2. The extension of the thin slab model (TSM) to multiple configurations of the driving fields, such as non-collinear or time-delayed beams, studying the role of the different parameters of the driving pulses and of the HHG process itself.

3. The adjustment of the full-quantum SFA model including propagation, a tool previously developed by the group of the University of Salamanca, to simulate the new schemes for the generation of XUV/X-ray beams with angular momentum.

4. The extraction of simple mathematical laws that predict the properties of the harmonics, especially their OAM and SAM.

Organization of the thesis

This thesis is organized in three main topics. First, the investigation of the HHG fundamentals and, in particular, the description of the tunnel-ionization picture in molecules [15]. Second, the generation of high-order harmonics with novel OAM properties, including their implications on the spatial and spectral features of the XUV emission [16, 17]. Third, the production of attosecond pulses with new polarization properties from the so-called non-collinear counter-rotating driving field [20, 21] and the bi-circular vortex field [18, 19, 22].

Accordingly, in chapter 2, we will deal with the foundations of HHG and apply high-harmonic spectroscopy to explore tunnel ionization in molecules. We shall review the well-known theory of HHG, starting from the fundamentals of light-matter interactions and the numerical solution of the TDSE. Then we will approach the subject from the point of view of the SFA, and review the accuracy of the HHG description in this framework. Next, we shall derive the semiclassical description of the harmonic emission process. The chapter will finish with the application of this knowledge to the study of tunnelling, the first step in HHG, deriving insight on the role of the proximity of the electron to the potential barrier from our SDT-SFA model.

Chapter 3 will be devoted to the generation of XUV beams with new OAM structures. The chapter will begin with an introduction to the OAM of light. The following section will address the control of the OAM in HHG, and it will establish the implications of the combination of several OAM components to drive HHG. The next section will deal with the generation of harmonic beams with self-torque, a new kind of coherent beams in which the OAM varies linearly in time. Finally, we shall present our results on the modifications of the HHG spectrum through the OAM of the driving field.

Chapter 4 will explore the production of attosecond pulses with novel polarization states. The first section will introduce state-of-the-art of the polarization control in HHG. The next section will exploit the non-collinear counter-rotating driving field to monitor the ellipticity of the attosecond pulses and to extract the non-perturbative dipole response. The following section will analyse the possibility of harnessing the angular momentum conservation rules to introduce specific polarization states by combining the OAM and SAM of the driving field.

The last section will be committed to the generation of trains of pulses with time-ordered polarization states.

Finally, chapter 5 summarizes the main findings and perspectives of this thesis.

INTRODUCCIÓN

La ciencia nos permite construir nuevos conocimientos sobre el mundo que nos rodea y, posteriormente, aplicar esta información para desarrollar tecnologías que mejoren nuestro bienestar. Esta adquisición de nuevos datos a menudo requiere extender los límites establecidos hacia escalas inexploradas. La investigación de la luz es un ejemplo destacable de cómo el estudio de un fenómeno físico en particular puede modificar nuestra visión general de la naturaleza. Es difícil encontrar otro fenómeno con un papel tan importante en la construcción de los fundamentos de la física. Su comprensión ha llevado a la unificación de leyes de la naturaleza, revelando conexiones ocultas que han señalado caminos importantes hacia nuevos conocimientos. Solo por mencionar algunos ejemplos, la incompatibilidad de las ecuaciones de Maxwell y la relatividad de Galileo en la descripción de la luz llevó a la unificación de las dos áreas en relatividad especial; el experimento de Young, que demuestra la comportamiento ondulatorio de la luz, fue esencial para la discusión de la naturaleza ondulatoria/corpuscular de la luz y, por tanto, para el florecimiento de la mecánica cuántica; y la descripción de Feynman de la interacción luz-materia en el nivel más fundamental dio lugar a la electrodinámica cuántica.

Hoy en día, la comprensión de la luz, sus propiedades y su interacción con la materia, sigue siendo una atractiva fuente de información. Sin embargo, la luz también se puede utilizar como herramienta para medir, o incluso desencadenar, fenómenos físicos. Podría decirse que una de las herramientas más útiles para este propósito es el láser, inventado en 1960. La luz láser es coherente—es decir, posee una fase ordenada espaciotemporalmente—y además exhibe otras características excepcionales, como la direccionalidad y la capacidad de enfoque. Es importante destacar que estas propiedades se pueden controlar con precisión para ajustar la luz láser a diferentes funciones específicas. Entre ellas, la luz láser es una herramienta principal para investigar fenómenos en las escalas de tiempo más cortas. Las nuevas fuentes de luz láser permiten, en la actualidad, acceder a los mecanismos más fundamentales de los sistemas atómicos, moleculares o sólidos, que se rigen por interacciones dinámicas que tienen lugar en la escala de tiempo de los attosegundos (10^{-18}s). La ciencia del attosegundo, por lo tanto, utiliza pulsos de esta duración como destellos de luz ultracortos para capturar la dinámica ultrarrápida de sistemas físicos fundamentales, una información que permanece inaccesible con fuentes de luz convencionales. Además de para medir, estos pulsos de attosegundo se pueden utilizar para controlar o desencadenar esas dinámicas ultrarrápidas en la materia.

Los pulsos de attosegundo se producen de forma rutinaria a partir del proceso de generación de armónicos de orden alto (HHG) [1, 2]. En pocas palabras, la HHG es un método bien establecido para producir radiación coherente de alta frecuencia en experimentos "sobre mesa", es decir, que no requieren grandes instalaciones. Consiste en la conversión de pulsos láser intensos de baja frecuencia (usualmente infrarrojos) en radiación de alta frecuencia (actualmente hasta los rayos X), como resultado de una interacción luz-materia altamente no lineal y no perturbativa. El anclaje de fase de los armónicos inherente en la HHG permite obtener pulsos de attosegundo a partir de la selección de la parte más energética de los espectros. Además de esto, otro de los principales méritos de la HHG es que, al ser un proceso altamente coherente, es capaz de mapear las propiedades del campo incidente en la radiación de alta frecuencia. Como consecuencia, algunas características del láser infrarrojo se traducen directamente a los pulsos de attosegundos de alta frecuencia. Este último aspecto da lugar a una perspectiva emocionante para la ciencia del attosegundo: la posibilidad de estructurar pulsos de attosegundo con momento angular.

En mecánica, el momento se define como la descripción cuantitativa del movimiento de un cuerpo. El momento mecánico total se puede expresar como la composición del momento lineal, asociado a la traslación rectilínea del centro de masas, y el momento angular, asociado a las rotaciones. El momento angular de un cuerpo rígido puede a su vez dividirse en dos partes: el momento angular orbital (OAM), que describe la órbita del centro de masas alrededor de un foco, y el momento angular de spin (SAM), asociado a la rotación del cuerpo alrededor de sí mismo.

A pesar de ser una onda electromagnética, la luz también posee momento y, sorprendentemente, este puede transferirse a la materia. La primera conjetura sobre el momento de la luz fue planteada por Johannes Kepler en 1619, cuando postuló que la presión de la luz solar afectaba la orientación de las colas de los cometas, que siempre apuntan en dirección opuesta al Sol. Dos siglos más tarde, las ecuaciones de Maxwell proporcionaron una descripción cuantitativa del fenómeno de la presión de radiación, que, a principios del siglo XX, se midió experimentalmente [3, 4]. Prometedoras tecnologías recientes, como el enfriamiento por láser, se basan en la transferencia del momento de la luz a la materia.

El SAM de la luz se manifiesta como su polarización, tal y como se muestra en la figura 2a. Aunque la polarización se estudió por primera vez con luz natural en 1669 utilizando materiales birrefringentes, hasta siglos más tarde, en 1909, no se asoció con el SAM de la luz [5]. En 1936, se descubrió que, al igual que el momento lineal, el SAM podía transferirse a la materia [6]. Como es bien sabido, la polarización tiene un papel importante en la tecnología, como en la fabricación de

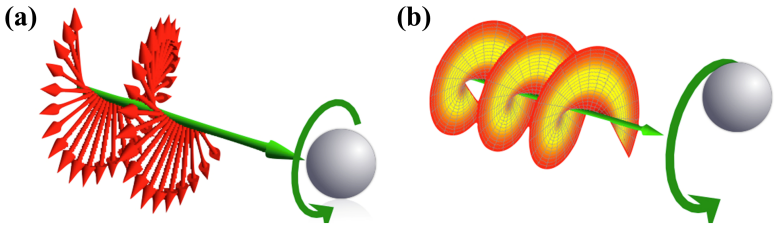

Figure 2: Diferencias entre el momento angular de spin (a) y el momento angular orbital (b) de la luz y su interacción con una partícula pequeña. Figura hecha por E-karimi - Own work, CC BY-SA 3.0.

pantallas de cristal líquido, gafas, etc., así como en las ciencias básicas, desde la química hasta la biología.

El OAM de la luz es, por otro lado, una propiedad macroscópica asociada a la vorticidad. Por lo tanto, los haces de luz que transportan OAM también se conocen como vórtices de luz. Uno puede imaginar la estructura de un vórtice de luz como un "sacacorchos", ya que su frente de onda se retuerce sobre sí mismo, exhibiendo una forma helicoidal alrededor de su eje de propagación, como se muestra en la figura 2b. La carga topológica de OAM describe la variación azimutal de la fase del haz en el plano transversal alrededor de una singularidad. Es importante destacar que, mientras que el SAM está limitado a dos valores, $\pm\hbar$, donde $\hbar$ es la constante de Planck reducida, el OAM puede exhibir un número infinito de valores en forma de múltiplos enteros de $\hbar$. Por otro lado, a diferencia del SAM, el OAM de la luz se descubrió recientemente, en 1992 [7], y aún no está implementado en nuestra tecnología del día a día. Sin embargo, ya se han propuesto aplicaciones muy interesantes. For ejemplo, se ha demostrado que los vórtices de luz pueden atrapar micropartículas y hacerlas rotar, lo que ofrece emocionantes posibilidades en el campo de la manipulación a esta escala [8, 9]. Además, se pueden utilizar para transferir información a una tasa mayor que con la luz convencional [10]. Asimismo, se pueden encontrar otras oportunidades ventajosas en microscopia de contraste de fase [11] y de alta definición [12], o en la información cuántica [13, 14].

Objetivos de esta tesis y publicaciones

El objetivo principal de esta tesis es explorar diferentes esquemas para desarrollar nuevas herramientas para aplicaciones del momento angular de la luz en la attociencia. Dicho objetivo requiere una descripción precisa del proceso de HHG y una comprensión profunda de sus características. En particular, las propuestas dentro de esta tesis se basan en gran medida en la posibilidad mencionada anteriormente de mapear las características del campo de infrarrojos en los armóni-

cos, ya que una de las propiedades que se traduce directamente a los armónicos es el OAM. Esta tesis, por lo tanto, está motivada por esta perspectiva y contiene un amplio conjunto de propuestas para aprovechar el potencial de la HHG para estructurar la radiación de alta frecuencia y los pulsos de attosegundo.

Presentamos desarrollos teóricos, la mayoría apoyados por los experimentos de nuestros colaboradores, que demuestran la generación de luz coherente de frecuencia en el rango del ultravioleta extremo (XUV) con combinaciones de momentos angulares deseadas. Cabe señalar que algunos de estos esquemas nos permiten controlar la evolución ultrarrápida del momento angular. El incentivo para generar pulsos ultracortos de alta frecuencia con una polarización o un estado de vorticidad particular es la posibilidad de interactuar con la materia a escalas espaciales nanométricas y escalas temporales ultracortas de una manera sin precedentes—es decir, interactuar con átomos, electrones, etc., en sus escalas naturales. Por lo tanto, creemos que nuestros resultados pueden impulsar las aplicaciones del momento angular de la luz en el ámbito de la nanotecnología ultrarrápida, abriendo una ruta con novedosas e interesantes perspectivas.

En esta tesis nos centramos en los principales objetivos y resultados presentados en las siguientes publicaciones:

1. *Referencia* [15]. Es necesario abordar los aspectos fundamentales de la HHG para describir con precisión las características de la radiación emitida. En este artículo, investigamos las trazas espectrales de la ionización túnel de sistemas moleculares, una característica fundamental de la HHG. Nuestros resultados muestran que la ionización túnel se ve fuertemente afectada por la ubicación específica del paquete de ondas electrónico dentro de una molécula, justo antes de la ionización. Esta dependencia deja una huella en el espectro de armónicos. Por lo tanto, demostramos que el panorama estándar de la ionización túnel en átomos debe modificarse para los sistemas moleculares. Para ello, desarrollamos una extensión de la aproximación de campo fuerte (SFA) molecular, la aproximación de campo fuerte con túnel dependiente de la ubicación (SDT-SFA), que puede servir como guía para aplicaciones de espectroscopia de armónicos de orden alto.

2. *Referencia* [16]. Introducimos una nueva clase de haces de luz que poseen una propiedad única asociada con la variación temporal de su OAM: el *auto-torque*. Predecimos teóricamente, y validamos experimentalmente, que el auto-torque puede imprimirse naturalmente en haces XUV a través de la HHG empleando como haces incidentes dos pulsos infrarrojos retardados en el tiempo y con diferente OAM. La cantidad de auto-torque se puede controlar modificando las características temporales del campo incidente.

Notablemente, el auto-torque imprime un desplazamiento de frecuencias azimutal en los armónicos que permite su caracterización experimental precisa.

3. *Referencia* [17]. Demostramos que la combinación de diferentes modos de OAM permite no solo el control del OAM de los armónicos, sino también modificaciones en el contenido espectral y las propiedades de divergencia de la emisión. Al combinar dos pulsos infrarrojos con contenido OAM opuesto y no degenerado, creando un campo incidente con forma de "collar de cuentas", demostramos teórica y experimentalmente la generación de peines de armónicos con espaciado sintonizable y baja divergencia.

4. *Referencia* [18]. Demostramos que la incorporación del OAM en un campo incidente bi-circular, permite el control simultáneo sobre el SAM y el OAM de los pulsos de attosegundos emitidos en la HHG. Este esquema permite la generación de pulsos de attosegundos polarizados circularmente con OAM a medida, así como armónicos de orden alto con la misma carga topológica que el haz incidente.

5. *Referencia* [19]. Proponemos la generación de trenes de pulsos de attosegundo con estados de polarización ordenados en el tiempo a través de la HHG, empleando como haces incidentes dos vórtices bi-circulares retardados en el tiempo. De esta manera, se generan dos anillos de armónicos separados espacialmente, cada uno con una elipticidad que evoluciona temporalmente de polarización circular levógira a polarización circular dextrógira y viceversa. La elección adecuada de las propiedades de los pulsos incidentes permite controlar la evolución temporal del SAM de los pulsos dentro del tren.

El trabajo adicional realizado durante los estudios de doctorado, pero solo mencionado brevemente en este informe, consiste en:

1. *Referencia* [20]. El campo de incidente contrarrotante no colineal permite la generación de pulsos de attosegundo aislados polarizados circularmente. Exploramos la dependencia de la elipticidad de los armónicos con la elipticidad de los haces incidentes contrastando los resultados teóricos y experimentales.

2. *Referencia* [21]. Siguiendo una configuración similar a la de [20], el grado de libertad de la polarización se usa para cuantificar con precisión la respuesta dipolar de la HHG. Apoyamos teóricamente esta nueva técnica experimental de elipsometría de armónicos de orden alto.

3. *Referencia* [22]. El campo bi-circular con OAM de [18] se puede describir como un campo de nudo toroidal. La conservación del

momento angular de nudo toroidal permite la derivación de reglas simples para el momento angular de los armónicos.

Por otro lado, las contribuciones metodológicas particulares de esta tesis a los resultados presentados en las publicaciones mencionadas se pueden resumir en:

1. El desarrollo de un modelo teórico de SFA para el cálculo de la HHG en moléculas, incluyendo el túnel dependiente de la ubicación, y de una herramienta numérica para extraer información de los cálculos exactos de la TDSE.

2. La extensión del modelo de lámina fina (TSM) a múltiples configuraciones de los haces incidentes, como esquemas no colineales o con retardados temporales, estudiando el papel de los diferentes parámetros de los pulsos incidentes y del propio proceso de HHG.

3. El ajuste del modelo de SFA cuántico incluyendo propagación (una herramienta previamente desarrollada por el grupo de la Universidad de Salamanca) para simular los nuevos esquemas para la generación de haces XUV o de rayos X con momento angular.

4. La extracción de leyes matemáticas simples que predigan las propiedades de los armónicos, especialmente su OAM y SAM.

Organización de la tesis

Esta tesis está organizada en tres temas principales. Primero, la investigación de los fundamentos de la HHG y, en particular, la descripción de la ionización túnel en moléculas [15]. En segundo lugar, la generación de armónicos de orden alto con propiedades de OAM novedosas, incluidas sus implicaciones en las características espaciales y espectrales de la emisión XUV [16, 17]. En tercer lugar, la producción de pulsos de attosegundos con nuevas propiedades de polarización a partir del campo contrarrotante no colineal [20, 21], y del campo bi-circular con OAM [18, 19, 22].

Por consiguiente, esta tesis se organiza de la siguiente manera. En el capítulo 2, trataremos los fundamentos de la HHG y aplicaremos la espectroscopia de armónicos de orden alto para explorar la ionización túnel en moléculas. Repasaremos la teoría conocida de la HHG, partiendo de los fundamentos de las interacciones materia-luz y la solución numérica de la ecuación de Schrödinger dependiente del tiempo (TDSE). Luego, abordaremos el tema desde el punto de vista de la SFA y revisaremos la precisión de la descripción de la HHG en este marco. A continuación, derivaremos la descripción semiclásica del proceso de emisión de armónicos. El capítulo terminará con la

aplicación de este conocimiento al estudio de la ionización túnel, el primer paso en la HHG, obteniendo información sobre el papel de la proximidad del electrón a la barrera de potencial según nuestro modelo SDT-SFA.

El capítulo 3 se dedicará a la generación de haces XUV con nuevas configuraciones de OAM. El capítulo comenzará con una introducción al OAM de la luz. La siguiente sección abordará el control del OAM en la HHG y establecerá las implicaciones de la combinación de varios componentes de OAM en el haz incidente. La siguiente sección se ocupará de la generación de un nuevo tipo de haz coherente en el que el OAM varía linealmente en el tiempo. Finalmente, presentaremos nuestros resultados sobre las modificaciones del espectro de la HHG a través del OAM del campo incidente.

El capítulo 4 explorará la producción de pulsos de attosegundo con nuevos estados de polarización. La primera sección introducirá el estado del arte del control de la polarización en HHG. La sección posterior explotará el campo contrarrotante no colineal para controlar la elipticidad de los pulsos de attosegundo y extraer la respuesta dipolar no perturbativa. La siguiente sección analizará la posibilidad de aprovechar las reglas de conservación del momento angular para introducir estados de polarización específicos mediante la combinación del OAM y el SAM del campo incidente. La última sección estará dedicada a la generación de trenes de pulsos con estados de polarización ordenados en el tiempo.

Finalmente, el capítulo 5 resume los principales hallazgos y perspectivas de esta tesis.

2 FUNDAMENTALS

In this chapter, we explain the fundamentals of HHG. To this aim, in section 2.1, we introduce the dynamics that governs HHG from the classical perspective, including the characteristics of the emitted radiation. In section 2.2, we describe the quantum and semiclassical approaches as well as the theoretical models for the harmonic emission. In section 2.3, we extend these models for the computation of HHG from macroscopic targets. The methods developed in these sections will provide us with a full description of the harmonic emission, from the microscopic to the macroscopic level. In section 2.4, we show an example of how the details of the spectral emission reveal fundamental aspects in the dynamics of matter. In particular, we have carried on a study on spectroscopic evidences of the modification of the tunnel-ionization probabilities with the distance of the electrons to the potential barrier. As a result, we shall demonstrate that tunnel ionization in extended systems, even in simple molecules, departs from the case of atoms. These modifications, that leave a clear signature in the high-harmonic spectra, can be observable in experiments of high-harmonic spectroscopy. Our publication on this subject [15] is included in the final section, 2.5.

2.1 INTRODUCTION TO HIGH-ORDER HARMONIC GENERATION

The investigation of ultrafast mechanisms in Nature benefits from the use of laser pulses with two characteristics: (i) ultrashort duration, to resolve in time the ultrafast dynamics, and (ii) high frequency, to access the nanometric scale avoiding the limit imposed by diffraction. Luckily, these two requirements can be fulfilled simultaneously, as ultrashort pulses must contain radiation spanning into the XUV or X-ray regimes in order to reach the attosecond timescale. For that reason, there has been an important scientific effort towards the development of coherent high-frequency light sources during the last three decades. Among these, HHG-based sources are remarkable, due to their outstanding degree of coherence, the exquisite control of their radiation properties, as well as their table-top configuration, making them available at laboratories worldwide.

Apart from its importance as a source of high-frequency ultrashort radiation, HHG is also widely used as a spectroscopy tool by itself. The HHG spectrum encodes signatures of the dynamics and the structure of the radiating materials [23–25]. Techniques of high-harmonic spectroscopy have been successful in retrieving information about the

molecular structure [26], nuclear dynamics [27], energy dispersion in solids [28], dynamics in strongly correlated systems [29], and orbital tomography [30].

2.1.1 *A non-perturbative phenomenon*

HHG is a highly non-linear and non-perturbative frequency upconversion process, that occurs when an intense laser is focused into a target. Targets are typically gas jets of noble atoms, although molecular gases, solids or liquids are also employed [31–36]. In general, the non-linear response of the medium's polarization density to a sufficiently intense electric field produces the emission of new frequencies. Conceptually, this non-linear response can be described using a Taylor series expansion of the polarization density vector P(t) in terms of the electric field E(t). In its scalar form it is expressed as:

$$P(t) = \epsilon_0 \left[\chi^{(1)} E(t) + \chi^{(2)} E^2(t) + \chi^{(3)} E^3(t) ... \right], \tag{1}$$

where the coefficients $\chi^{(n)}$ are the n^{th}-order susceptibilities of the medium and ϵ_0 is the vacuum permittivity constant. If the medium is centro-symmetrical, only the odd terms in the expansion are different from zero.

Non-linear optical phenomena require intense or moderately intense electromagnetic driving fields. Thus, although they were predicted in 1931 by Maria Goeppert-Mayer in her doctoral dissertation [37], their experimental demonstration was linked to the development of laser sources 30 years later, which provided light with enough intensity. Right after the laser invention, two-photon-excited fluorescence was detected in a europium-doped crystal [38] and, almost simultaneously, second-harmonic generation was also discovered [39]. Nowadays, non-linear laser-matter interactions are the basis of laser frequency conversion schemes.

Non-linear interactions at moderately high intensities are perturbative, which means that the intensity of subsequent harmonic orders decays exponentially. As a consequence, high frequencies exhibit extremely low conversion efficiencies. This behaviour can be understood in terms of the gradual decrease in the probability of composing an increasingly large number of photons into a single high-frequency one. On the other hand, if the driving laser is intense enough ($10^{13} - 10^{15}\, W/cm^2$), the force exerted by the laser field becomes comparable to the binding force of the electrons to matter, and the perturbative interpretation schematized in Eq. (1) is no longer valid. In fact, when the laser-matter interaction enters in this non-perturbative regime, the ionization rate increases and high-order harmonics emerge efficiently [40]. The development of intense lasers reached enough intensity to observe extreme non-linear optical phenomena during the 80's, and non-perturbative HHG from gas targets

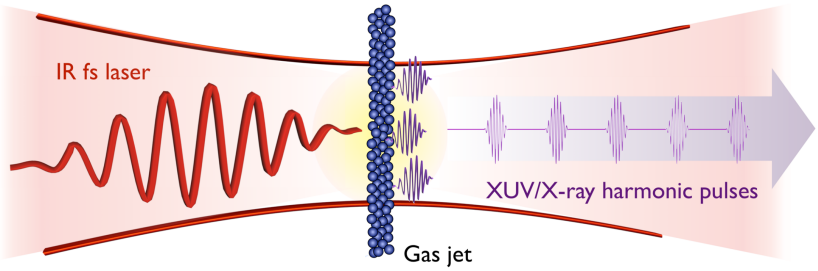

Figure 3: Scheme of HHG in a gas jet driven by an intense infrared (IR), femtosecond (fs) laser. From the non-perturbative, non-linear laser-matter interaction, high-order harmonics are emitted.

was first reported at the end of that decade [41, 42]. In figure 3, we show a basic scheme of HHG in a gas jet.

In contrast to the perturbative case, where the harmonics' efficiency decreases monotonously (see figure 4a), the non-perturbative HHG spectra present a *plateau* of harmonics, extending towards high frequencies with nearly constant intensity [43], as depicted schematically in figure 4b. This plateau ends abruptly at a cut-off frequency, after which the harmonic efficiency decays exponentially. As a result, HHG provides for efficient sources of coherent radiation extending from the XUV to the soft-X-rays [44, 45]. In addition, the phase-locked na-

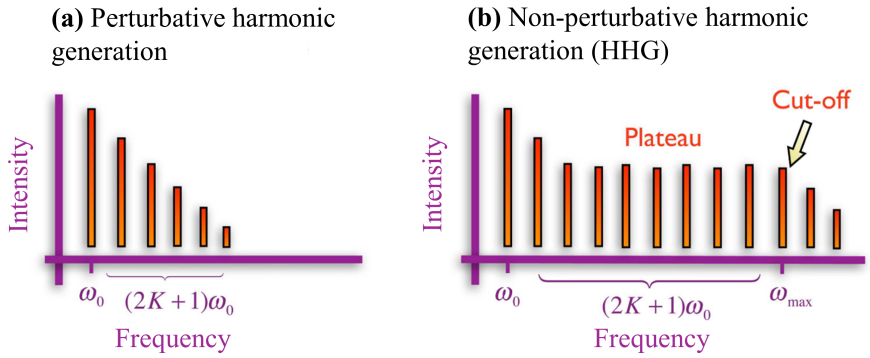

Figure 4: Scheme of the typical harmonic spectra in the perturbative (a) and non-perturbative (b) regimes. The intensity of the harmonics is shown in logarithmic scale. In both cases, odd-order harmonics of the fundamental frequency are emitted from centro-symmetrical systems. However, in the non-perturbative regime, corresponding to the HHG process, the spectrum presents a plateau of harmonics with similar intensity, that ends in the so-called cut-off frequency.

ture of the harmonics at the end of the spectral plateau, implies that, temporally, they are radiated in the form of pulses of attosecond duration. The generation of trains of attosecond pulses [46–48], or even isolated pulses [49, 50] is of great interest for ultrafast applications, as

pump-probe experiments to elucidate attosecond electron dynamics [51–53].

Nowadays, HHG can be driven in a wide variety of configurations. Along this thesis, we will primarily consider the standard scenario of atomic and molecular gas jet targets irradiated with femtosecond driving fields, with a central wavelength of 800 nm and about $10^{14} W/cm^2$ peak intensity.

2.1.2 *The microscopic description*

In atomic or molecular gases, HHG can be described semi-classically in terms of a three-step process [1, 2]: first, near the maxima of the driving field, an electronic wavepacket is tunnel-ionized from the parent atom; in a second step, the electronic wavepacket is accelerated and, after reversal of the sign of the electric field, it is redirected to the parent ion; finally, in a third step, upon recollision the electron's kinetic energy is released in the form of high-frequency radiation. To some extent, the atom-field system acts like a nanometric electron-ion collider, where the three steps finally result in a short pulse of high-frequency light emitted each half cycle of the driving field, as sketched in figure 5.

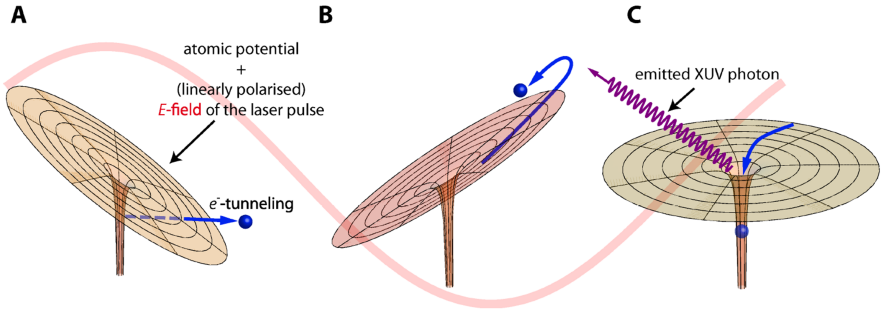

Figure 5: Scheme of the semi-classical three step description of HHG. The electron is first tunnel-ionized by the external electric field (A), then it is accelerated (B), and finally it recombines with its parent ion, emitting XUV radiation (C). Figure extracted from [54].

Let us now highlight some of the specific characteristics of the HHG process. First, it is important to note that the ionization must take place within the limits of the tunneling regime. This ensures the injection of a subcycle electron wavepacket in the continuum, which during recollision will emit an attosecond pulse. The tunneling condition implies that, for a given laser frequency, the amplitude of the field must be restricted to a certain range. This can be explained qualitatively using classical arguments. Let us consider the simple case of a classical electron in an atomic Coulombic potential, $V_C(\mathbf{r})$, distorted by the interaction with the external electric field, $E(t)$, linearly polarized

along the z coordinate. The distorted potential is given by $V_{eff}(\mathbf{r}, t) = V_C(\mathbf{r}) + eE(t)z$, where e is the elementary charge ($e = |e|$).

For an efficient HHG, the electric field must bend the atomic potential barrier sufficiently to ensure that the electron may tunnel-ionize before it changes its sign. Let us consider that, initially, the electron is placed at $z = 0$ with an energy equal to $-I_P$, I_P being the ionization potential, as shown schematically in figure 6. After ionization, a reasonable assumption consists in neglecting the Coulomb potential and considering that the electron is placed at the exit of the tunneling barrier, $z_0 = I_P/(eE_0)$, with a total energy of $-eE_0z_0$, where E_0 is the amplitude of the external electric field. Assuming that, while tunnel-

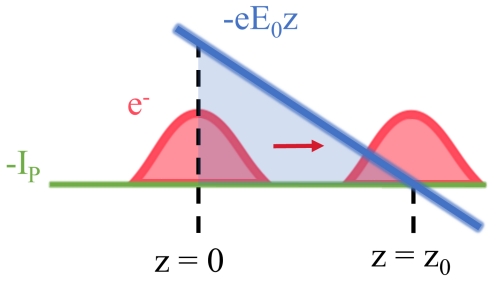

Figure 6: Scheme of the simplified tunnel ionization picture, where the Coulomb potential is neglected. The electronic wavepacket is initially placed at $z = 0$ with energy equal to $-I_P$ and, afterwards, it exists the barrier at $z_0 = I_P/(eE_0)$.

ing, the electron's kinetic energy equals the energy of the bound state $K = -I_P$, the velocity can be approximated as $v = \sqrt{2m_eK} = i\sqrt{2m_eI_P}$, where m_e is the electron mass. According to this picture, the estimated tunneling time would be:

$$\tau_t = \frac{z_0}{v} = -i\frac{\gamma}{2\omega_0}, \tag{2}$$

where ω_0 is the external field frequency and γ is the so-called *Keldysh parameter* [55]:

$$\gamma = \frac{\omega_0\sqrt{2m_eI_P}}{eE_0} = \sqrt{\frac{I_P}{2U_P}}, \tag{3}$$

$U_P = e^2E_0^2/(4m_e\omega_0^2)$ being the ponderomotive energy—the mean kinetic energy of the free electron oscillations during the interaction with the electromagnetic field. It is important to note that the complex value of the classical velocity and tunneling time reflect the inability of the classical picture to fully describe the quantum nature of tunneling. Expressing Eq. (2) in terms of the electric field's period, T, the relative tunneling time corresponds to $\frac{|\tau_t|}{T} = \frac{\gamma}{4\pi}$. Therefore, it can be considered that the electron would tunnel-ionize efficiently if the magnitude of the tunnel time is much smaller than half of the field

period, thus, if $\gamma < 1$. The main distinction between the tunneling and multiphoton regimes is, therefore, that in the former the electron's injection to the continuum takes place at the attosecond timescale, while in the later the electron is ionized over the whole laser period. The tunnel condition, $\gamma < 1$, holds for large field amplitudes and/or low frequencies, as it can be inferred from Eq. (3).

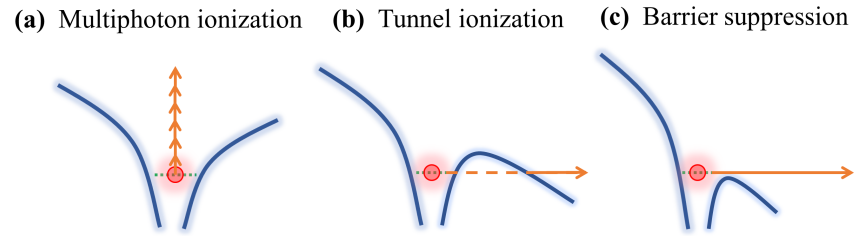

Figure 7: Schematic comparison between the multiphoton ionization (a), tunnel ionization (b), and barrier suppression (c) regimes.

In addition, the field amplitudes for tunnel ionization also have an upper limit, known as *barrier suppression* [56]. If the electric field is too intense, the top of the effective potential barrier lies below the electron's ground state energy, and the electronic wavepacket remains unbound during a longer temporal interval. As a consequence, both the harmonic generation's efficiency and the maximum energy of the photons emitted are reduced drastically [57]. The barrier suppression limit can be obtained calculating the position where the effective potential barrier is maximum:

$$\frac{\partial V_{eff}(\mathbf{r})}{\partial z} = 0 \rightarrow z_{max} = \sqrt{\frac{K_e e}{E_0}}, \tag{4}$$

where K_e is the Coulomb constant. Then, we apply the condition that the top of the barrier equals the electron's bound state energy. Thus, in order to avoid barrier suppression, the electric field amplitude must satisfy $E_0 < K_e e^3 I_p^2/4$. In figure 7, we show a simple scheme comparing the three described ionization regimes. For the most frequent configuration used in this thesis—a driving field with a central wavelength of 800 nm and an argon gas target—, the driving field's intensity is limited to a range from $1.3 \times 10^{14}\,W/cm^2$ to $2.6 \times 10^{14}\,W/cm^2$, approximately, to remain in the tunnel ionization regime.

Let us now address the excursion of the electron after ionization. Despite the quantum nature of the electronic wavepacket, the Ehrenfest theorem ensures the description of the mean free electron excursion in terms of classical trajectories [2, 58]. For this we assume the electron initially at $z = 0$ with zero velocity, as the maximum tunnel ionization probability corresponds to the electron released with zero kinetic

energy. Also, we will follow the dipole's approximation, neglecting the effect of the magnetic field and we will consider the external electric field as monochromatic and linearly polarized in the z direction: $E(t) = E_0 \sin(\omega_0 t)$. Then, Newton's equation for the free electron released at t_1 leads to the classical electronic dynamics:

$$\ddot{z}(t) = \frac{-eE_0}{m_e}\sin(\omega_0 t), \tag{5}$$

$$\dot{z}(t) = \frac{eE_0}{\omega_0 m_e}[\cos(\omega_0 t) - \cos(\omega_0 t_1)], \tag{6}$$

$$z(t) = \frac{eE_0}{\omega_0^2 m_e}[\sin(\omega_0 t) - \sin(\omega_0 t_1) - \omega_0(t - t_1)\cos(\omega_0 t_1)]. \tag{7}$$

Eqs. (6) and (7) show that the electron's trajectory is composed of a linear displacement together with a quiver motion at the frequency of the external field. Note that the trajectory followed by the electron

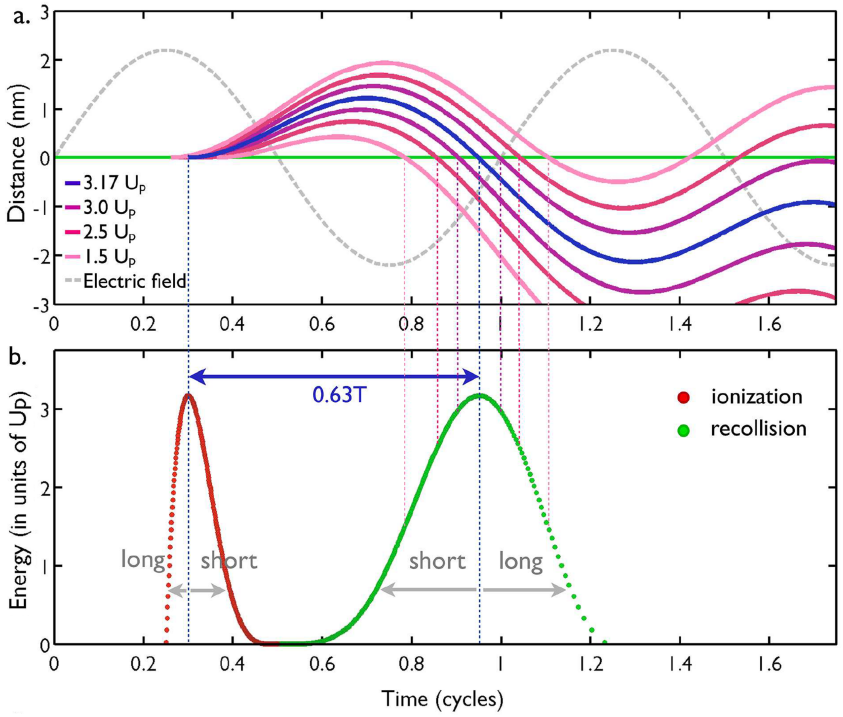

Figure 8: (a) Electronic trajectories calculated from the classical equations of motion. The grey-dashed line represents the electric field (in arbitrary units) and the green line indicates the nucleus position. Three pairs of short and long trajectories are represented for energies at recollision of $3.0\,U_P$ (purple), $2.5\,U_P$ (dark pink) and $1.5\,U_P$ (light pink), whereas the most energetic trajectory, corresponding to $3.17\,U_P$ at recollision, is represented in blue. (b) Returning kinetic energy of the electron at the instant of the first recollision. The green points represent the recollision time, whereas the red points indicate the ionization time. The blue arrow shows the excursion time for the most energetic trajectory. Figure extracted from [59].

strongly depends on the instant of ionization, t_1. Consequently, not

all the electron's paths return to the parent ion. Since the harmonics are radiated during recollisions, only the returning paths are relevant for HHG. We show in figure 8a a set of these returning paths. The slopes of the trajectories at recollision indicate the velocity of the electron and, therefore, its kinetic energy when returning to the ion, $K(t) = m_e \dot{z}^2(t)/2$. This recollision energy is depicted in figure 8b as a function of the ionization and recollision times.

Note from figure 8b that the most energetic trajectory exhibits a kinetic energy of $3.17\,U_P$ at the recollision. For the other cases, the same recollision energy—and, thus, the emission of a specific harmonic—can be reached by two different trajectories within each half cycle. Defining the excursion time as the elapsed time between the ionization and the recombination, the paths whose excursion time is less than that of the path of maximum recollision energy are called *short* trajectories, while those whose excursion time is longer are denoted as *long* trajectories. In both cases, the recollision energy is smaller the more the excursion time differs from the path of maximum energy.

2.1.3 *The harmonic emission.*

To illustrate the characteristics of the HHG spectra, we show in figure 9 the harmonic emission from a xenon gas jet, comparing the experimental measurement from [42] and the theoretical results from [60]. Interestingly, the classical description in the previous subsection allows also to infer the cut-off frequency of the harmonic spectral plateau. If the released electron exhibits a kinetic energy equal to K at rescattering and after recombination the electron's final energy is

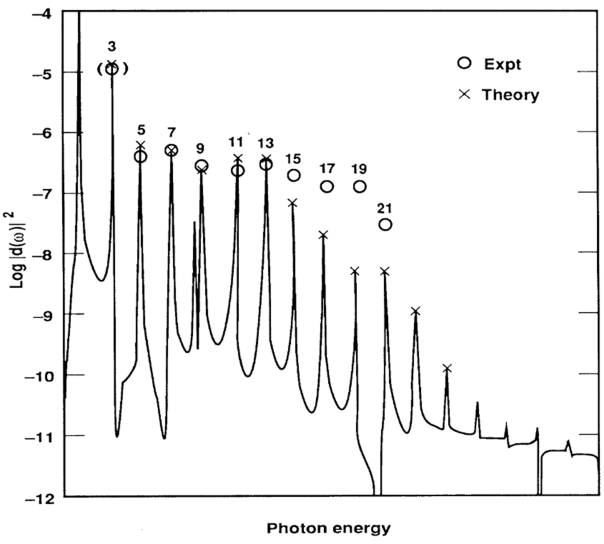

Figure 9: Sample of an experimental HHG spectrum from xenon compared with theoretical calculations. Figure extracted from [60].

the negative value of the ionization potential, $-I_P$, the energy of the emitted radiation corresponds to the total energy difference: $I_P + K$. Thus, the cut-off frequency, ω_c, associated to the maximum recollision energy, can be estimated as [2, 58]:

$$\hbar\omega_c = I_P + 3.17\, U_P. \tag{8}$$

Since the ponderomotive energy depends on the amplitude and the wavelength of the incident field as $U_P \propto E_0^2 \lambda_0^2$, higher harmonic frequencies can be generated extending the plateau's cut-off either by selecting targets with larger ionization potentials, or by employing driving lasers with higher intensities and/or longer driving wavelengths [44, 61, 62]. Note, however, that increasing the ionization potential decreases the probability of ionization, and therefore larger intensities would also be needed. Additionally, the quantum nature of the electron also plays an important role in the HHG efficiency, since, after ionization, the electronic wavefunction is dispersed during the electron's excursion and its probability density decreases accordingly. In other words, when driven by longer wavelengths, the electron spends more time in the continuum and, as a consequence, the probability of recombination will decrease, and the harmonic emission will be less efficient.

Another characteristic of the harmonic spectra, when radiated by centro-symmetric systems driven by multicycle pulses, is that only odd multiples of the driving frequency are present. This condition follows from the fact that in these systems the dipole response must follow the sign of the field and, therefore, it is an odd function with respect to it (see Eq. (1)). This symmetry rule can be broken, for example, either by considering non-symmetric targets, or by using electric fields with several frequency components, non-periodic oscillations or time-varying polarization [49, 63]. Also, for few-cycle laser pulses, the envelope of the electric field widens the harmonic peaks. In fact, if just one recollision event takes place along the pulse a so-called *supercontinuum* is obtained, i.e., a broad, nearly continuous harmonic spectrum. Such supercontinuum has applications as a light source for spectroscopy, and it can sustain single attosecond pulses [64].

Let us now discuss the temporal characteristics of the harmonic emission. Interestingly, the long and short electronic trajectories give rise to a different temporal ordering of the emitted harmonics. The underlying reason is the distribution of the recollision energies in time: the recollision energy increases with time for the short trajectories and decreases for the long ones, as it was shown in figure 8. Hence, the emission corresponding to short trajectories has a positive chirp, since the lower frequencies, corresponding to less energetic trajectories, are emitted earlier. On the contrary, long trajectories lead to a harmonic emission with negative chirp since higher frequencies are emitted before. This chirp is known as the *attochirp* and introduces a group

delay in the harmonic spectral phase [65]. The characterization of the *attochirp* allows to identify whether a particular radiation is associated mainly to short paths or to long paths.

Theoretically, the temporal characteristics of the harmonic emission can be studied retrieving the spectrogram from the harmonic signal. These spectrograms, that we denote as time-frequency analysis (TFA), are based on the Gabor transform. We obtain them from the computation of the Fourier Transform of selected spectral windows of the emitted spectrum. In figure 10, we present an example of the TFA of a harmonic emission, showing the spectral content of the radiation emitted at different instants of time. The difference between the contribution of the two types of electronic trajectories can be appreciated, where short trajectories exhibit a yield profile with a positive slope while the long ones exhibit a yield profile with a negative slope.

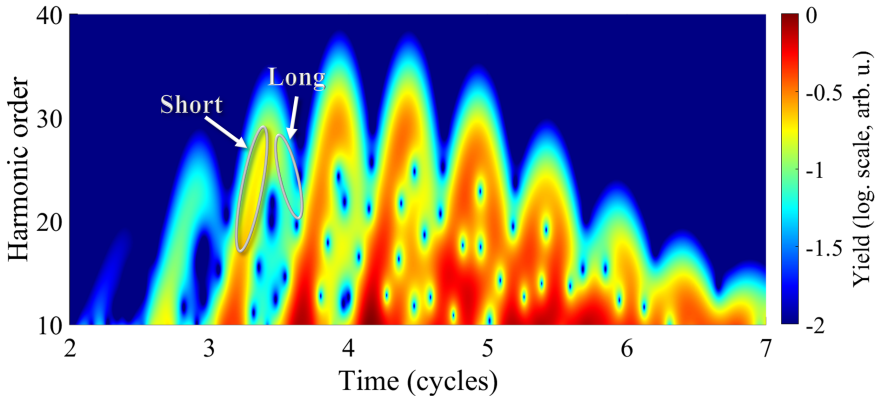

Figure 10: TFA of the HHG spectrum emitted from an argon atom interacting with a laser pulse of 800 nm wavelength, $1.53 \times 10^{14}\, W/cm^2$ peak intensity, $\sin^2$ envelope and duration of 8 cycles in total. The emission corresponding to short and long paths is identified by the positive and negative slopes of the yield distribution, respectively. The HHG signal has been obtained from our numerical simulations based on the TDSE using a $3.5\omega_0$ spectral window.

2.2 COMPUTATION OF HIGH-ORDER HARMONIC GENERATION

In this section, we explain in a nutshell the theoretical methods used in this thesis to reproduce and understand the characteristics of HHG. We will first present the strategy for the exact computation of HHG from the TDSE and, afterwards, we will use SFA-based models, that provide also a physical interpretation of the process.

2.2.1 *The time-dependent Schrödinger equation*

The interaction of quantum systems with classical laser fields is described by the TDSE, in Dirac's notation, as:

$$i\hbar\frac{\partial}{\partial t}|\psi(t)\rangle = H(t)\,|\psi(t)\rangle\,, \tag{9}$$

where $H(t)$ is the Hamiltonian of the interacting system and $\psi(t)$ is the electronic wavefunction. HHG in atoms and molecules can be well described in the so-called single active electron approximation (SAE), where $|\psi(t)\rangle$ is a single-electron ket. Additionally, we also consider the dipole approximation, where the electric field is assumed independent on the spatial coordinates. This approximation becomes reasonable when the laser wavelength ($\sim \mu m$) is much larger than the dimensions of the electronic wavefunction ($\sim nm$). Under these circumstances, the Hamiltonian exhibits the following form:

$$H(t) = \frac{p^2}{2m_e} + V_C(\mathbf{r}) + V_F(t), \tag{10}$$

where $V_F(t)$ is the field's interaction potential and $V_C(\mathbf{r})$ is the Coulombic potential.

Let us now select the *gauge* for the Hamiltonian. In the length gauge, the interaction potential is described as $V_F(t) = e\mathbf{r}\,\mathbf{E}(t)$ and $\mathbf{p}$ is the *kinetic momentum* operator. In the velocity gauge, the expression of the interaction potential is introduced by the relation of the kinetic momentum, $\mathbf{p}(t)$, with the *canonical momentum*, $\mathbf{P}$: $\mathbf{p}(t) = \mathbf{P} + (e/c)\mathbf{A}(t)$, where c is the speed of light in vacuum, and $\mathbf{A}(t)$ is the vector potential associated to the external electric field: $\mathbf{E}(t) = -(1/c)(\partial/\partial t)\mathbf{A}(t)$. The Hamiltonian, then, is written as:

$$\begin{aligned} H(t) &= \frac{[\mathbf{P} + (e/c)\mathbf{A}(t)]^2}{2m_e} + V_C(\mathbf{r}) \\ &= \frac{p^2}{2m_e} + V_C(\mathbf{r}) + \frac{e}{m_e c}\mathbf{A}(t)\cdot\mathbf{P} + \frac{e^2}{2m_e c^2}A^2(t). \end{aligned} \tag{11}$$

Thus, in the velocity gauge the interaction potential is written as $V_F(t) = \frac{e}{m_e c}\mathbf{A}(t)\cdot\mathbf{P} + \frac{e^2}{2m_e c^2}A^2(t)$. Note that the exact TDSE results are gauge invariant, so depending on the purpose of the calculations it is customary to select the most suitable gauge. For instance, the physical interpretation is generally more straightforward using the length gauge, but the velocity gauge is the best choice for numerical integrations involving ionized electrons. In this thesis, we employ the velocity gauge, as it will allow for simpler and faster calculations under the SFA.

The temporal evolution of the electronic wavepacket is computed by solving numerically Eq. (9) for the Hamiltonian described in Eq. (11). For this we use the *Crank-Nicolson* method [66], a well-known computational finite difference method used for the numerical resolution of

partial differential equations. The Crank-Nicolson scheme consists in a combination of the forward Euler method at the instant t with the backward Euler method at $t + \Delta t$. Applied to Eq. (9):

$$|\psi(t + \Delta t/2)\rangle \approx \left[1 - H(t)\frac{i\Delta t}{\hbar 2}\right]|\psi(t)\rangle\,, \tag{12}$$

$$|\psi(t + \Delta t/2)\rangle \approx \left[1 + H(t + \Delta t)\frac{i\Delta t}{\hbar 2}\right]|\psi(t + \Delta t)\rangle\,. \tag{13}$$

Thus, the expression for the numerical calculation of $|\psi(t + \Delta t)\rangle$ is found by combining Eqs. (12) and (13):

$$\left[1 + H(t + \Delta t)\frac{i\Delta t}{\hbar 2}\right]|\psi(t + \Delta t)\rangle = \left[1 - H(t)\frac{i\Delta t}{\hbar 2}\right]|\psi(t)\rangle\,. \tag{14}$$

Once we have integrated the TDSE, we compute the spectrum of the HHG emission. Since the nucleus position is fixed in the temporal scales of the interaction, the emitted radiation corresponds effectively to the electron's dipolar acceleration. The classical non-relativistic formula for the far-field radiation emitted by a moving charge is [67]:

$$\mathbf{E}(\mathbf{r}, t) = \frac{1}{c^2}\frac{\mathbf{n} \times \mathbf{n} \times \mathbf{a}(t')}{R_d}\bigg|_{t'=t-R_d/c}\,, \tag{15}$$

where $\mathbf{a}(t')$ is the electron acceleration at a advanced time t', and $\mathbf{n}$ is the unitary vector pointing from the electron to the detector, separated by a distance R_d. The instantaneous power radiated by the electron is calculated from Larmor's formula:

$$P(t) = \frac{2}{3}\frac{e^2}{c^3}|\mathbf{a}(t)|^2. \tag{16}$$

Consequently, we can express the spectral power as a function of the Fourier components of the acceleration:

$$P(\omega) = \frac{4}{3}\frac{e^2}{c^3}|\mathbf{a}(\omega)|^2. \tag{17}$$

Although Larmor's formula is derived for a classical charge, the acceleration can also be the result of a quantum-mechanical calculation. In this case, the instantaneous mean value of the acceleration can be written as the sum of the mean value and the quantum fluctuations:

$$\mathbf{a}(t) = \langle\hat{\mathbf{a}}(t)\rangle + \Delta\mathbf{a}(t). \tag{18}$$

However, by considering a set of identical emitting sources, $\mathbf{a}_j(t) = \langle\hat{\mathbf{a}}(t)\rangle + \Delta\mathbf{a}_j(t)$, the power radiated is

$$\begin{aligned} P(t) &\propto \left|\sum_{j=1}^{N}\langle\hat{\mathbf{a}}(t)\rangle + \Delta\mathbf{a}_j(t)\right|^2 \\ &= \sum_{i,j=1}^{N}\langle\hat{\mathbf{a}}(t)\rangle^2 + 2N\sum_{j=1}^{N}\langle\hat{\mathbf{a}}(t)\rangle\,\Delta\mathbf{a}_j(t) + \sum_{i,j=1}^{N}\Delta\mathbf{a}_i(t)\Delta\mathbf{a}_j(t) \\ &= N^2|\,\langle\hat{\mathbf{a}}(t)\rangle\,|^2 + \sum_{j=1}^{N}[\Delta\mathbf{a}_i(t)]^2, \end{aligned} \tag{19}$$

where N is the number of emitters, $\sum_{j=1}^{N} \langle \hat{\mathbf{a}}(t) \rangle \Delta \mathbf{a}_j(t) = 0$ and $\sum_{i,j=1}^{N} \Delta \mathbf{a}_i(t) \Delta \mathbf{a}_j(t) = \sum_{j=1}^{N} [\Delta \mathbf{a}_i(t)]^2$, being $\sum_{i \neq j}^{N} \Delta \mathbf{a}_j(t) \Delta \mathbf{a}_i(t) = 0$. It is important to note that $\sum_{j=1}^{N} [\Delta \mathbf{a}_i(t)]^2$ is an incoherent term (since it depends on the quantum fluctuations), while $N^2 |\langle \hat{\mathbf{a}}(t) \rangle|^2$ is the coherent, and therefore the relevant, term (the quadratic dependence on N is a signature of the coherency of the emission).

The acceleration mean's value is calculated by applying the Ehrenfest theorem to the mean value of the kinetic momentum $\mathbf{p}$:

$$\begin{aligned} \frac{d}{dt} \langle \hat{\mathbf{p}} \rangle &= \frac{1}{i\hbar} \langle [\hat{\mathbf{p}}, H] \rangle + \langle \frac{\partial \hat{\mathbf{p}}}{\partial t} \rangle \\ &= \frac{1}{i\hbar} \langle [\hat{\mathbf{P}}, H] \rangle + \frac{e}{c} \langle \frac{\partial \hat{\mathbf{A}}(t)}{\partial t} \rangle \\ &= -\langle \nabla V_C \rangle - e\mathbf{E}(t), \end{aligned} \tag{20}$$

where we have used the commutation property $[\hat{\mathbf{P}}, V_C] = -i\hbar \nabla V_C$. Thus, we obtain:

$$\langle \mathbf{a}(t) \rangle = \frac{1}{m_e} \langle \psi(t) | (-\nabla V_C) | \psi(t) \rangle - \frac{e}{m_e} \mathbf{E}(t). \tag{21}$$

Performing the Fourier transform of the mean acceleration, Eq. (21), we obtain the dipole acceleration spectrum, which is proportional to the spectral distribution of the harmonic field, as shown in Eq. (17). In figure 11, we show an example of the HHG spectrum emitted from an argon atom calculated using the exact integration of the TDSE.

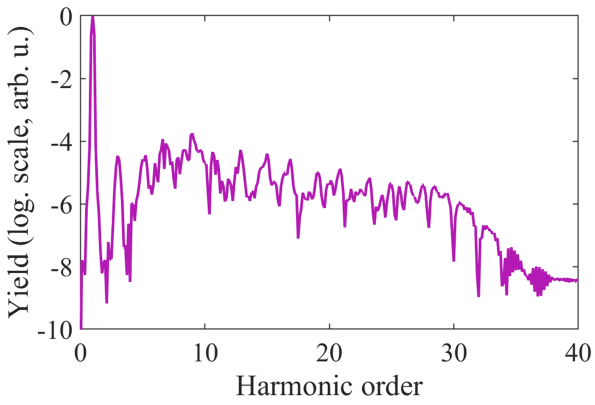

Figure 11: HHG spectrum emitted from an argon atom interacting with a laser pulse of 800 nm wavelength, $1.53 \times 10^{14}\, W/cm^2$ peak intensity and $\sin^2$ envelope with a duration of 8 cycles in total, obtained from the numerical integration of the TDSE. The TFA of this signal was shown in figure 10.

2.2.2 *The strong field approximation*

The exact solution of the TDSE is very demanding computationally for complex systems. Solving the 3-dimensional TDSE for a single atom or

molecule is only viable for systems with one or two electrons with the current computational means. In addition, in order to take into account the macroscopic effects—which are indispensable, for example, when working with beams with OAM—one must compute the emission of a large number of atoms. Therefore, the development of alternative models is crucial. Among them, the SFA [55, 68, 69] has been an extensively used approximation to investigate multi-photon ionization [57] and HHG [70, 71]. First, it reduces greatly the computational time, allowing to realize macroscopic calculations. Second, it facilitates the search for links between the harmonic spectral signatures and the structural properties of the radiating matter system, unveiling details that would be hidden in the exact TDSE calculations.

The SFA consists on neglecting the Coulomb potential in the electron's evolution after ionization. It has demonstrated to reproduce the main characteristics of the harmonic spectra in atoms [62, 72] and molecules [26, 73–77], and it has provided insight on electron and nuclear dynamics [25, 27, 78–80]. In this thesis, we have calculated most of our theoretical results using a non-semiclassical SFA model developed in our group [62], that has been previously validated by comparison against the TDSE results, and experiments.

Let us develop the mathematics for the computation of the HHG emission under the SFA. First, in order to compute the temporal evolution of the electronic wavefunction, $\psi(\mathbf{r}, t)$, from its initial state, $\psi(\mathbf{r}_i, t_i)$, we define the Green's function $G(\mathbf{r}, t; \mathbf{r}_i, t_i)$ as

$$\psi(\mathbf{r}, t) = i \int G(\mathbf{r}, t; \mathbf{r}_i, t_i)\psi(\mathbf{r}_i, t_i)d\mathbf{r}_i, \tag{22}$$

or, in Dirac's notation,

$$|\psi(t)\rangle = iG(t, t_i)\,|\psi(t_i)\rangle\,. \tag{23}$$

Then, it is convenient to follow the Lippmann-Schwinger procedure, where the Hamiltonian is separated into two components. In our case, the first component, whose eigenstates and eigenvalues must be known, is the atomic or molecular potential, $H_A = (1/2m)p^2 + V_C(\mathbf{r})$. The second component encompasses the remaining factors of the total Hamiltonian, Eq. (11), i.e. the interaction with the external electric field, $V_F(t)$. If we denote G_A as the Green's function associated to H_A, the evolution of the total Green's function can be formally written as

$$G(t, t_0) = G_A(t, t_0) + \frac{1}{\hbar}\int_{t_0}^{t} G(t, t_1)V_F(t_1)G_A(t_1, t_0)dt_1, \tag{24}$$

where, for convenience, we have omitted the spatial coordinates. The SFA is now applied by approximating the complete electron evolution, $G(t, t_1)$, by that of the electron interacting only with the field, $G_F(t, t_1)$, associated to the Hamiltonian $H_F = (1/2m)P^2 + V_F(t)$:

$$G(t, t_0) \approx G_A(t, t_0) + \frac{1}{\hbar}\int_{t_0}^{t} G_F(t, t_1)V_F(t_1)G_A(t_1, t_0)dt_1. \tag{25}$$

Physically, this equation can be interpreted as the combination of all possible stories followed by the electron. The first term corresponds to the evolution of the atomic electron without the influence of the external field. The second term corresponds to the summation over the stories of the atomic electron being released at time t_1 and evolving freely under the interaction with the field afterwards.

Now, the approximated Green's function, Eq. (25), can be employed to calculate the temporal evolution of the electronic wavefunction, $|\psi(t)\rangle$. Considering that the initial state is the atomic eigenstate, $|\phi_0\rangle$:

$$\begin{aligned} |\psi(t)\rangle &= iG_A(t,t_0)\,|\phi_0\rangle + \frac{i}{\hbar}\int_{t_0}^{t} G_F(t,t_1)V_F(t_1)G_A(t_1,t_0)\,|\phi_0\rangle\,dt_1 \\ &= |\phi_0(t)\rangle + |\delta\psi(t)\rangle\,, \end{aligned} \tag{26}$$

where $|\phi_0(t)\rangle = iG_A(t,t_0)\,|\phi_0\rangle$ is the wavefunction evolving solely under the influence of the Coulombic potential, while $|\delta\psi(t)\rangle$ is the released wavefunction, which results from the interaction with the external electric field. The evolution of an atomic electronic state is expressed as

$$|\phi_0(t)\rangle = iG_A(t,t_0)\,|\phi_0\rangle = e^{-i\epsilon_0(t-t_0)/\hbar}\,|\phi_0\rangle\,, \tag{27}$$

where ϵ_0 denotes its energy. On the other hand, to follow the procedure, we need the eigenstates of the free electron under the influence of an electromagnetic field. These are the so-called Volkov waves [81], $|\psi_{\mathbf{P}}(t)\rangle = e^{i\frac{1}{\hbar}S(\mathbf{P},t,t_1)}\,|\mathbf{P}\rangle$, where $|\mathbf{P}\rangle$ is an eigenstate of the canonical momentum operator, and $S(\mathbf{P},t,t_1)$ is frequently referred as the action of the free electron, calculated as

$$S(\mathbf{P},t,t_1) = -\frac{1}{2m_e}\int_{t_1}^{t} p^2(\tau)d\tau, \tag{28}$$

$p(\tau)$ being the kinetic momentum. Therefore, the Green's function corresponding to H_F can be written in terms of the Volkov states as

$$G_F(t,t_1) = -i\int e^{i\frac{1}{\hbar}S(\mathbf{P},t,t_1)}\,|\mathbf{P}\rangle\,\langle\mathbf{P}|\,d\mathbf{P}. \tag{29}$$

Combining Eqs. (26) to (29) we obtain

$$|\delta\psi(t)\rangle = \int \psi(\mathbf{P},t)\,|\mathbf{P}\rangle\,d\mathbf{P}, \tag{30}$$

where

$$\begin{aligned} \psi(\mathbf{P},t) &= -\frac{i}{\hbar}\int_{t_0}^{t} e^{i\frac{1}{\hbar}S(\mathbf{P},t,t_1)}e^{-i\frac{\epsilon_0}{\hbar}(t_1-t_0)} \\ &\times \langle\mathbf{P}|\,V_F(t_1)\,|\phi_0\rangle\,dt_1. \end{aligned} \tag{31}$$

Finally, a set of uncoupled differential equations, one for each momentum $\mathbf{P}$, is obtained by deriving in time Eq. (31):

$$\frac{d}{dt}\psi(\mathbf{P},t) = -\frac{i}{2m\hbar}p^2(t)\psi(\mathbf{P},t) - \frac{i}{\hbar}e^{-i\frac{\epsilon_0}{\hbar}(t-t_0)}\,\langle\mathbf{P}|\,V_F(t_1)\,|\phi_0\rangle\,. \tag{32}$$

Each of these equations can be integrated numerically using a standard Runge-Kutta algorithm.

Let us now compute the acceleration of the electronic wavepacket. By resorting to the decomposition in Eq. (26), the acceleration can be expressed as

$$\langle \mathbf{a}(t)\rangle = \langle \phi_0(t)|\,\mathbf{a}\,|\phi_0(t)\rangle + \langle \delta\psi(t)|\,\mathbf{a}\,|\delta\psi(t)\rangle + 2\Re\{\langle \phi_0(t)|\,\mathbf{a}\,|\delta\psi(t)\rangle\}, \quad (33)$$

where $\Re\{x\}$ denotes the real part of x. The first term in the right part of Eq. (33) is equal to $-\frac{e}{m_e}E(t)$, as $|\phi_0\rangle$ is an eigenstate with definite parity. On the other hand, the second term is the acceleration of the free electron, which is basically at the same frequency as the driving field. Therefore, the relevant contribution is the last term since it represents the acceleration of the dipole between the ionized electron and the ground state. Then, by applying the Ehrenfest theorem as described by Eq. (20), the SFA acceleration is:

$$\langle \mathbf{a}(t)\rangle = 2\Re\left\{\frac{1}{m_e}\langle \phi_0(t)|\,(-\nabla V_C)\,|\delta\psi(t)\rangle\right\} - \frac{e}{m_e}\mathbf{E}(t). \quad (34)$$

Combining Eqs. (31) and (34) we obtain the explicit expression of the acceleration:

$$\langle \mathbf{a}(t)\rangle = \int a(\mathbf{P},t)\,d\mathbf{P}, \quad (35)$$

where

$$\begin{aligned} a(\mathbf{P},t) &= 2\Re\left[\frac{1}{m_e}\langle \phi_0(t)|\,(-\nabla V_C)\,|\mathbf{P}\rangle\right. \\ &\times \left.\left\{-\frac{i}{\hbar}\int_{t_0}^{t} e^{i\frac{1}{\hbar}S(\mathbf{P},t,t_1)} e^{i\frac{\epsilon_0}{\hbar}(t-t_1)}\,\langle \mathbf{P}|\,V_F(t_1)\,|\phi_0\rangle\,dt_1\right\}\right]. \end{aligned} \quad (36)$$

It is worth noticing that some further refinements can improve the results from the SFA compared to those of the exact TDSE. First, SFA models fail in reproducing the quantitative amount of released electronic population. This can be corrected by modifying Eq. (36) as follows:

$$\langle \mathbf{P}|\,V_F(t_1)\,|\phi_0\rangle \to \langle \mathbf{P}|\,V_F(t_1)\frac{C_F}{r^n}\,|\phi_0\rangle\,, \quad (37)$$

where C_F is denoted as the Coulomb factor [82] $C_F = [4|\epsilon_0|/(eE_0)]^n$, and $n = [m_e Z^2 e^4/(2\hbar^2|\epsilon_0|)]^{1/2}$ is the effective quantum number of the atomic state (e.g. $n = 1$ for the fundamental state in the hydrogen atom), where Z is the ion charge. Other approaches include also Coulombic effects upon recombination, that result in a better description of the lower-order harmonics in the plateau [83], which are not a main concern in this thesis. Finally, the quantitative SFA results can be

improved by considering the influence of the external field on the fundamental state, in the so-called strong field approximation plus (SFA+), which we will explain in the following subsection.

An extended version of the SFA: the SFA+

The SFA+ correction consists in considering the instantaneous Stark shift of the bound state during the recollision [62, 84]. In the standard SFA we assumed that the part of the wavefunction that remained bound to the atom evolved as a bounded state without the influence of the external electric field. Under the SFA+ formalism, the recombination bound state, $\langle\phi_0(t)|$, is the combination of a *bare* state (field free) and a correction accounting for the field *dressing*, which is not present in the standard SFA. As a consequence, the dipole acceleration is composed of two contributions:

$$a(t) = a_b(t) + a_d(t) + \text{c.c.}, \tag{38}$$

where $a_b(t)$ corresponds to the acceleration of the *bare* state and $a_d(t)$ is the *dressing* correction. Thus, Eq. (35) is modified as:

$$a(t) = \int [a_b(\mathbf{P}, t) + a_d(\mathbf{P}, t)]d\mathbf{P} + \text{c.c.} \tag{39}$$

The *bare* term is calculated from the SFA while the *dressing* correction is calculated as:

$$a_d(\mathbf{P}, t) \approx -\left[1 + \frac{P^2/(2m\hbar^2) - \epsilon_0}{\Delta_s}\right] a_b(\mathbf{P}, t), \tag{40}$$

where Δ_s is the Stark displacement of the fundamental atomic state energy under the presence of the external electric field during the recollision time, which can be approximated [62] as:

$$\Delta_s \approx U_p + \frac{2\hbar}{\omega_0 \delta t_s}\sqrt{\frac{U_p}{m}}\frac{P_z}{\hbar}\sin(\omega_0\delta t_s)\frac{U_p}{2\omega_0\delta t_s}\sin(2\omega_0\delta t_s). \tag{41}$$

The factor P_z in Eq. (41) is a particular momentum of the bound state that can be estimated as:

$$\begin{aligned} P_z &= 2\sqrt{mU_p}\frac{\sin(\omega_0\delta t_s)}{\omega_0\delta t_s} \\ &\times \left[1 - \sqrt{1 - \frac{1}{6}\left(1 + \frac{\epsilon_0}{U_p} + \frac{\sin(2\omega_0\delta t_s)}{2\omega_0\delta t_s}\right)\left(\frac{\sin(\omega_0\delta t_s)}{\omega_0\delta t_s}\right)^{-2}}\right], \end{aligned} \tag{42}$$

where δt_s is the recollision time lapse. For the most energetic electrons, it can be approximated to:

$$\delta t_s \approx \frac{3\pi}{2\omega_0}\sqrt{\frac{|\epsilon_0|}{3.17\,U_p}}. \tag{43}$$

Finally, by combining Eqs. (38) and (40), the correction to the acceleration is obtained:

$$a(t) = -\int d\mathbf{P} \frac{P^2/(2m\hbar^2) - \epsilon_0}{\Delta_s} a_b(\mathbf{P}, t) + \text{c.c.} \tag{44}$$

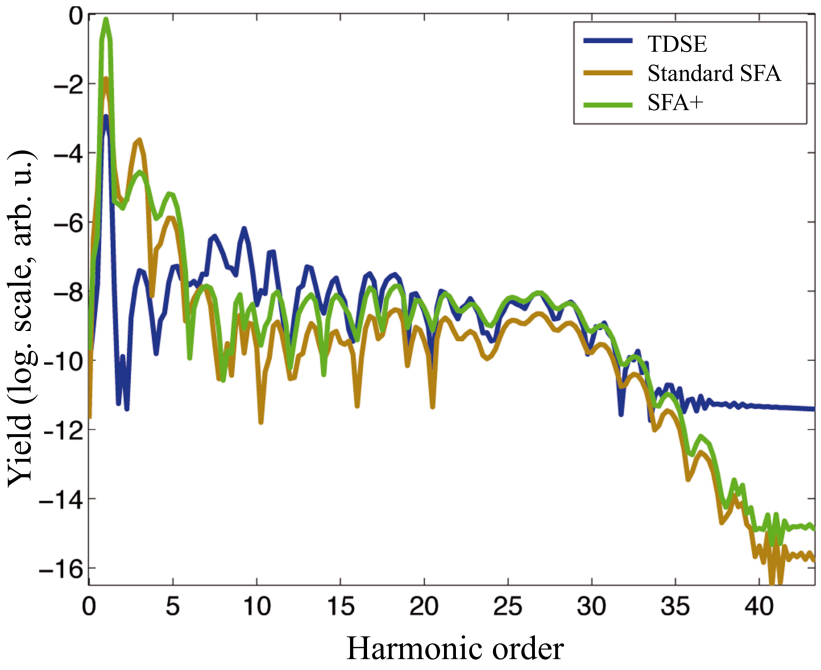

Figure 12: Comparison of the HHG spectra obtained using the SFA+ (green), the standard SFA (ochre) and the TDSE (blue) models. The target is an hydrogen atom and the laser field has a 800 nm wavelength, a $1.4 \times 10^{14} W/cm^2$ peak intensity and a $\sin^2$ envelope with a duration of 4-cycle pulse in total. The agreement with the TDSE calculations is improved by the SFA+, especially for the higher-order harmonics.

As a result of this correction, the quantitative comparison with the TDSE results improves, especially for the higher-order harmonics, as shown in figure 12. In addition, the scaling of the harmonic efficiency with the driving wavelength is correctly described [62].

2.2.3 *Semiclassical description: the saddle-point approximation*

The so-called saddle-point approximation applied to Eq. (36) provides for a semiclassical description of HHG in terms of electronic trajectories, bringing insight on the connection between the quantum and the classical descriptions of HHG explained in section 2.1. In principle, an infinite number of quantum paths contribute to HHG. Each quantum

path contributes with a phase factor equal to the real part of the action acquired by the electron following the respective path:

$$S(\mathbf{P}, t, t_1) = \int_{t_1}^{t} \left\{ \frac{[\mathbf{P} + \frac{e}{c}\mathbf{A}(t')]^2}{2m_e} \right\} dt'. \tag{45}$$

This action introduces very fast oscillations in the dipole phase. Then, only those momenta for which the action is stationary contribute effectively to the integrals for the total dipole acceleration in Eqs. (35) and (36).

Let us now define the electron's excursion time as $\tau = t - t_1$, and the frequency of each Fourier component of the dipole moment as ω. The stationary points are solutions of the saddle-point equations, obtained by equating the derivatives of $S(\mathbf{P}, t, \tau) - I_P\tau - \hbar\omega t$ with respect to $\mathbf{P}$, t and τ to zero [71]:

$$\tau\mathbf{P} + \frac{e}{c}\int_{t-\tau}^{t} \mathbf{A}(t')dt' = 0 \tag{46}$$

$$\frac{[\mathbf{P} + \frac{e}{c}\mathbf{A}(t)]^2}{2m_e} + I_P = \hbar\omega \tag{47}$$

$$\frac{[\mathbf{P} + \frac{e}{c}\mathbf{A}(t-\tau)]^2}{2m_e} + I_P = 0 \tag{48}$$

We denote the solutions of the saddle-point equations as $(\tau^{st}, t^{st}, \mathbf{P}^{st})$. The physical interpretation of this set of equations is the following: Eq. (46) is the time integration of the kinetic momentum equaled to zero, so it describes the return of the electron to its initial position after the excursion time τ; Eq. (47) reflects the energy conservation in the photon emission (the energy of the emitted photon is the energy difference between the electron's initial and final state); and Eq. (48) describes the energy conservation in the process of tunneling, at the ionization time $t_1^{st} = t^{st} - \tau^{st}$.

It is important to note that, since $I_P > 0$, Eq. (48) cannot be fulfilled within the real time domain. Thus, the solutions of the saddle-point equations for the ionization time are complex, in contrast to the real times considered in the classical trajectories in Eqs. (5), (6) and (7). Therefore, the quantum nature of the tunneling is revealed in the saddle-point solutions.

The imaginary part of the ionization time t_1^{st} is interpreted as the tunneling time of the under-barrier electron motion [85]—very much in the same sense that we have discussed in the classical description of tunneling in section 2.1.2—, whereas the real part of t_1^{st} is interpreted as the time when the electron exits the potential barrier. Interestingly, the definition of a complex ionization time leads to a correction to the classical cut-off law of Eq. (8) [70]:

$$\hbar\omega_c = F(I_P/U_P)I_P + 3.17\,U_P \tag{49}$$

where $F(I_P/U_p)$ is a function that takes values in the range between 1.24 and 1.32.

Many experimental efforts have been made in the recent years to determine the value of the tunneling time. Among them, the attoclock technique has allowed to experimentally measure the tunneling time of the electron with attosecond resolution. Although initial measurements reported vanishingly small tunneling times [86], finer experiments suggested the existence of a tunneling delay [87]. However, theoretical calculations have indicated that the tunneling time value is compatible with zero in the hydrogen atom, and that Coulombic effects can be responsible for the measured non-zero values [88].

2.2.4 *The dipole phase*

The phase of the high-order harmonics can be extracted from the solutions of the saddle-point Eqs. (46), (47) and (48). For a monochromatic driving field, it reads as [71]:

$$\Phi_q^r = \frac{1}{\hbar} S_q(\mathbf{P}^{st,r}, t^{st,r}, \tau^{st,r}) - \frac{1}{\hbar}\tau^{st,r} I_P \tau^{st,r} - q\omega_0 t_q^{st,r}, \tag{50}$$

where r denotes the type of trajectory, short or long and q is the harmonic order. The first term of Eq. (50) corresponds to the phase acquired by the electronic wavepacket during its excursion, also known as intrinsic phase [89]. Thus, it is the part of the harmonic phase that accounts for the non-perturbative response. Let us denote the non-perturbative dipole phase as ξ_q^r:

$$\xi_q^r = \frac{1}{\hbar} S_q(\mathbf{P}^{st,r}, t^{st,r}, \tau^{st,r}). \tag{51}$$

The second and third terms of Eq. (50) can be interpreted as time delays resulting from the mapping of the phase of the fundamental beam into the harmonics.

Interestingly, figure 13 shows that the dipole phase of the harmonics in the spectral plateau, varies approximately linearly with the driving beam intensity, a tendency that has been corroborated experimentally [90]. Importantly, this dependency of the dipole phase on the intensity is found in the non-perturbative term. Indeed, considering a monochromatic vector potential polarized along the z coordinate, $\mathbf{A}(t) = -(E_0\omega_0/c)\cos(\omega_0 t)\mathbf{e}_z$, ξ_q^r can be approximated as [71]:

$$\begin{aligned} \xi_q^r &\approx -\frac{1}{\hbar}\int_{t_1}^{t} \Big[\frac{p_z^2}{2m_e} + U_P - 2p_z\sqrt{\frac{U_P}{m_e}}\cos(\omega_0 t') \\ &+ U_P\cos(2\omega_0 t')\Big]dt' \approx -\frac{1}{\hbar}U_P\tau_q^{st,r} = \alpha_q^r I. \end{aligned} \tag{52}$$

Note that we have considered the following assumptions: (i) the approximated excursion time for short trajectories is $T/2$ while for the

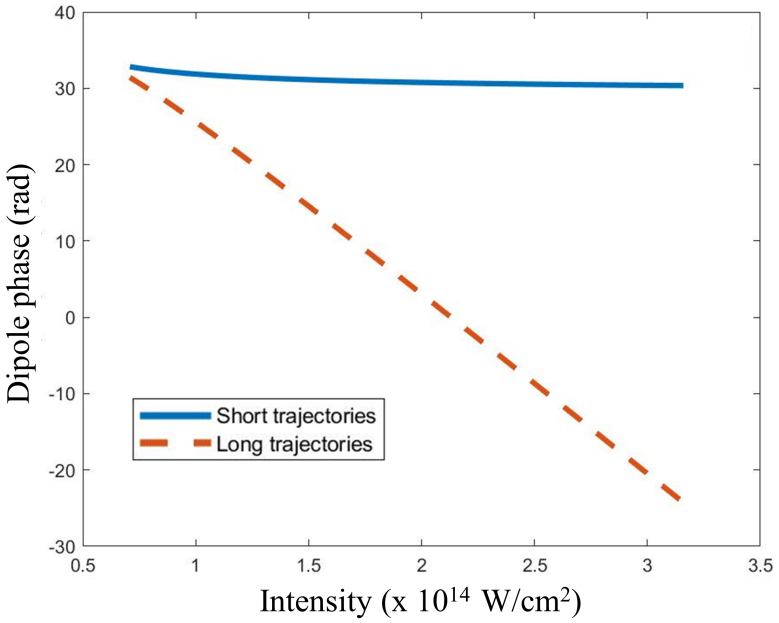

Figure 13: Variation of the dipole phase with the laser intensity. The dipole phase is calculated from the saddle-point equations for different driving field intensities for short (solid blue) and long (dashed orange) trajectories. In both cases, the dipole phase variation with intensity is approximately linear.

long ones it is T, and (ii) the tunnel ionization takes place at the field maximum, therefore, $p_z^{st} \approx 0$. Note that, in the final expression, I denotes the intensity of the laser field and α_q^r is a parameter dependent on the harmonic order, the laser field properties and the trajectory type. We will use this approximated description for the construction of our macroscopic model, the TSM (see subsection 2.3.3).

It is important to note that the parameter α_q^r can be extracted from the saddle-point equations but, alternatively, it can be calculated from the classical equations of motion: the dipole phase is obtained by integrating the curve of the emitted frequency along the return time, and then, α_q^r is calculated as the derivative of the dipole phase along the local intensity.

On the other hand, another method, developed by the Group of Prof. A. L'Huillier at the Attogroup at Lund University, provides a general analytical expression to calculate the dipole phase [48]. This method consists in approximating the classical curves as piecewise straight lines, as depicted in figure 14.

Then, the dipole phase is obtained by integrating these lines and, as a result, it has a parabolic shape:

$$\Phi_q^r(\rho, \phi, z_t) = \Phi_r(I_P) + t_{pr}(\omega_q - I_P) + \frac{2\gamma_r}{I(\rho, \phi, z_t)} \frac{(\omega_q - I_P)^2}{2}, \quad (53)$$

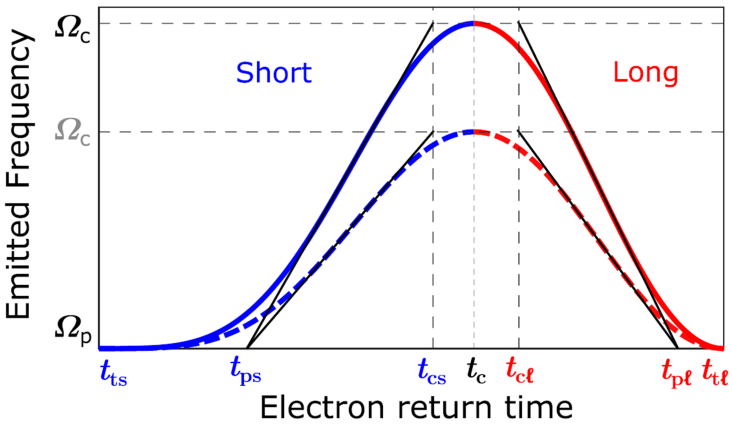

Figure 14: Harmonic frequency as a function of the recombination time for two different driving field intensities, calculated from the classical short (blue) and long (red) trajectories. The indicated return times are the following: $t_{ts,t\ell}$ are the return times for the short and long electron trajectories leading to the threshold frequency Ω_p (corresponding to I_P); t_c is the return time for the trajectory leading to the cut-off frequency Ω_c; t_{pr} and t_{cr} ($r = s, \ell$) are return times obtained by approximating $\Omega(t)$ as piecewise straight lines. Figure extracted from [91].

where $\Phi_r(I_P)$ is a constant, t_{pr} is the recombination time of the trajectory with an energy equal to I_P and γ_r is a parameter, calculated as $\gamma_r = (t_{cr} - t_{pr})\pi c^2 m_e/(3.17\alpha_{FS}\lambda^2)$, being α_{FS} the fine structure constant and t_{cr} the recombination time of the trajectory with an energy corresponding to the cut-off frequency. This method allows to compute the dipole phase in a very straightforward manner.

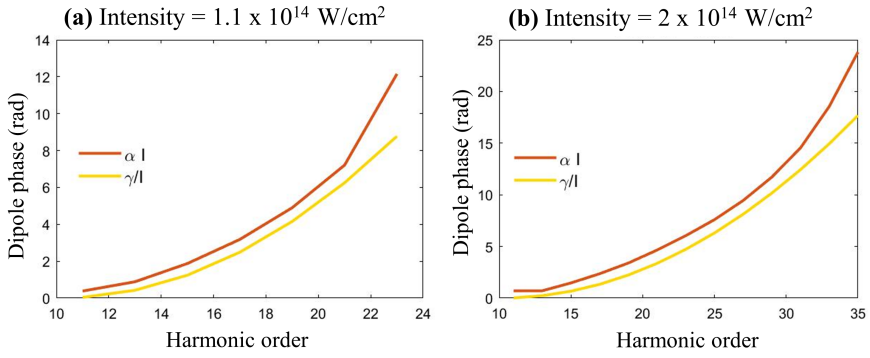

Figure 15: Dipole phase of the short trajectories calculated from the αI parametrization (red), where α is obtained from the classical classical equations of motion, and from Eq. (53) (yellow). The two models present very similar values of the dipole phase for the two different driving field peak intensities, except for an almost constant offset.

In figure 15, we show a comparison between two different dipole phase calculations: from the whole classical equations of motion parametrized as αI (red) and from Eq. (53) (yellow). In general, the α and γ parametrizations present very similar values of the dipole phase for the two driving field peak intensities, except for a small offset.

The role of the dipole phase

The dipole phase is a magnitude with a crucial role in multiple aspects of HHG. It depends on the harmonic order, the local phase and intensity of the driving field and the kind of trajectory—short or long—followed by the electron. Therefore, it is strongly related to the physics of the HHG process.

In addition, the dipole phase substantially influences the spectral and spatial distribution of the harmonic phase in the target and, as a consequence, it alters the pulse duration [65], spectrum [92], or wavefront [91, 93] of the attosecond pulses. Important spectral characteristics of the emitted radiation are described by the dipole phase, as its chirp and spectral bandwidth.

It is important to note that, since the femtosecond pulses used to drive HHG exhibit an intensity profile that varies along time, the dependency of the non-perturbative dipole phase on the intensity implies that the phase of the harmonics would be different at each recombination events. This introduces a negative chirp in each emitted harmonic, which has signatures in the total detected spectrum: the individual harmonics have a broader spectral content, where their higher frequencies are emitted at the beginning of the pulse, while their lower frequencies are emitted at the end [94]. This effect can be explained from the concept of instantaneous frequency: the derivative of the phase with respect to time. We denote as $\varphi'_q(t)$ the phase terms depending on time. The dipole phase introduces a time-dependent phase, $\alpha^r_q I(t)$, so the instantaneous frequency, ω_{inst}, is shifted from the central harmonic frequency, $\omega_q = q\omega_0$, by that term:

$$\varphi'_q(t) = \omega_q t + \alpha^r_q I(t) \rightarrow \omega_{inst} = \frac{\partial \varphi'_q(t)}{\partial t} = \omega_q + \alpha^r_q \frac{\partial I(t)}{\partial t}. \quad (54)$$

The variation in time of this frequency shift ($\frac{\partial^2 \varphi'_q(t)}{\partial t^2} = \alpha_q \frac{\partial^2 I(t)}{\partial t^2} < 0$) is the so-called *femtochirp*.

Furthermore, since the dipole phase corresponding to each kind of trajectory is different, the HHG spectrum can present signatures of the interference of the emission from the two different trajectories [95]. Thus, the HHG spectrum is modulated not only by the number of emissions but also by the interference between different quantum paths.

Finally, the dipole phase also strongly influences the divergence and focusing properties of the emission: the harmonic field corresponding

to the short trajectories is approximately collimated, while that from the long trajectories is very divergent [96].

It is worth noticing that the experimental characterization of the dipole phase is very challenging. Techniques such as the Reconstruction of Attosecond Bursts by Interference of Two-Photon Transition, also known as RABBITT, allow to extract the relative phase between different harmonics [47], but the measurement of the absolute phase remains complicated. The most commonly used strategies involve spectroscopic methods—based on the spectral modulation of HHG as a function of the driving laser intensity, resulting from the interference between short and long trajectories [95]—, and interferometric techniques—based on the use of two separated HHG sources interfering with each other [97].

2.3 MACROSCOPIC CALCULATIONS

Although the fundamental physics in HHG belongs to the microscopic level, this description alone is not sufficient to reproduce all the characteristics of the harmonic radiation from the macroscopic targets, i.e., as it is detected in an experiment. For this, the contributions of all the single emitters in the gas target must be added up coherently.

2.3.1 *Phase-matching effects*

For the nearly monochromatic field, of constant intensity profile, the phase of a specific harmonic at generation can be decomposed into three terms, see Eq. (50). Nonetheless, for the macroscopic perspective it is convenient to (i) neglect the global phase term $\frac{1}{\hbar} I_P \tau_q^{st,r}$ (since it does not depend on the local phase of the driving field) and (ii) rewrite the term $q\omega_0 t_q^{st,r}$ according to the perturbation theory: the total phase of the driving beam, $\Phi(\rho, \phi, z)$, is translated into the harmonics as $q\Phi(\rho, \phi, z)$. Hence, the phase of the harmonics can be generalized as:

$$\varphi_q^r(\rho, \phi, z) = q\Phi(\rho, \phi, z) + \alpha_q^r I(\rho, \phi, z). \tag{55}$$

Consequently, in macroscopic targets each elementary radiator emits harmonics according to the local configuration of the driving field. Therefore, the total emission will be the interfering superposition of the contributions of the elementary radiators [98, 99]. Thus, the optimal signal is obtained when the phases of these radiators are matched for constructive interference.

To understand better this phenomenon, let us consider the on-axis radiation from a one-dimensional target. The phase of the q-th order harmonic emitted at $z = z_0$ is denoted as $\varphi_q^r(z_0)$, and it propagates to a point z as $\varphi_q^r(z_0) + k_q(z - z_0)$. Since the phase of the harmonic generated at a point z is $\varphi_q^r(z)$, the phase difference between the propagating field and the generated one is $\Delta\varphi = \varphi_q^r(z) - \varphi_q^r(z_0) -$

$k_q(z-z_0)$. Then, according to Eq. (55), the phase-mismatch number corresponds to:

$$\Delta k_q^r = \frac{d\Delta\varphi_q^r}{dz} = \frac{d\varphi_q^r(z)}{dz} - k_q = qk_1 + \alpha_q^r \frac{dI(z)}{dz} - k_q, \tag{56}$$

where $k_1 = \frac{d\Phi}{dz}$ is the wavenumber of the driving field. The phase-mismatch number allows for the definition of the minimum distance between two atoms whose emitted radiation interferes destructively, i.e. the longitudinal coherence length, $L_{coh}^r = \pi/\Delta k_q^r$, as shown in figure 16. The optimal phase-matching condition is fulfilled if $\Delta k_q^r \approx 0$, and thus, $L_{coh}^r \approx \infty$.

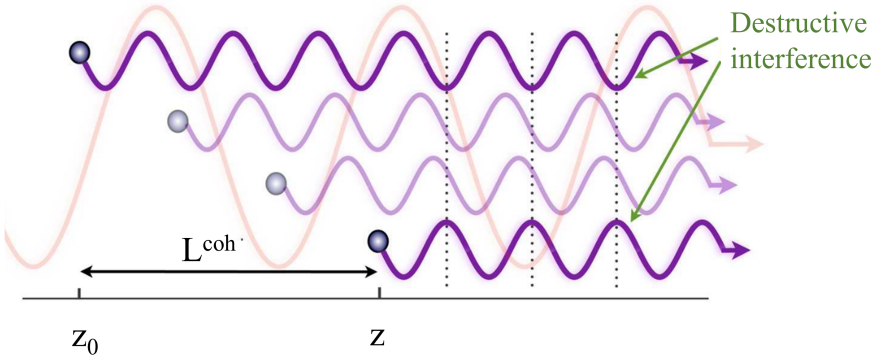

Figure 16: Scheme of the one-dimensional phase-matching of the harmonic radiation generated at different atomic positions. The coherence length corresponds to the separation of the two atoms whose emitted radiation interferes destructively. Modified version of a figure extracted from [59].

Typically, the phase-mismatch number is expressed in terms of four contributions:

$$\Delta k_q = \Delta k_q^{neutral} + \Delta k_q^{free} + \Delta k_q^{geom} + \Delta k_q^{dip}, \tag{57}$$

where the different terms refer to the phase mismatch due to the neutral atom dispersion ($\Delta k_q^{neutral}$), the dispersion due to the free electrons (Δk_q^{free}), the geometry of the fundamental field (Δk_q^{geom}) and the non-perturbative term of the dipole phase ($\Delta k_q^{dip,r}$), which depends on the quantum path r. Therefore, the optimal phase-matching condition can be pursued in different manners, depending on factors such as the gas geometry and pressure, or the laser focusing and intensity.

The effect of the neutral atom and free electron dispersion is more relevant for thicker gases at higher pressures. The neutral atom dispersion is induced by the bound-bound transitions in the gas atoms, while the free electron's mismatch is introduced by the inhomogeneous ionization caused by the driving field. Both effects produce a change on the gas refractive index, which affects the propagation of the pulse [59].

The spatial characteristics of the driving mode and harmonic beams, on the other hand, are responsible for the term Δk_q^{geom}. Typically, laser beams exhibit near Gaussian spatial profiles (see figure 17), that are described by:

$$\begin{aligned} E(\rho, z; k_0) &= E_0 \frac{w_0}{w(z)} \exp\left(-\frac{\rho^2}{w^2(z)}\right) \\ &\times \exp\left[ik_0 z + i\frac{k_0 \rho^2}{2R(z)} - i\Phi_G(z)\right], \end{aligned} \tag{58}$$

where $k_0 = 2\pi/\lambda_0$, $w(z) = w_0\sqrt{1+(z/z_R)^2}$ with w_0 being the waist of the beam and $z_R = k_0 w_0^2/2$ being the Rayleigh range, $R(z) = z\left[1+(z_R/z)^2\right]$ is the phase-front curvature radius and $\Phi_G(z) = \arctan(z/z_R)$ is the Gouy phase. The Gouy phase strongly depends on z and, thus, it constitutes a relevant source of phase-mismatch.

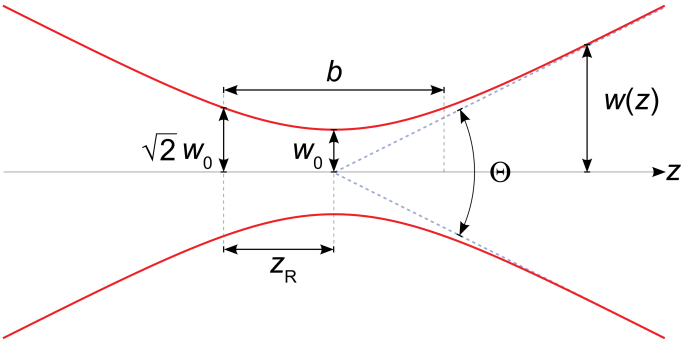

Figure 17: Scheme of the Gaussian beam width, $w(z)$, as a function of z where w_0 is the beam waist, b is the depth of focus, z_R is the Rayleigh range and Θ is the total angular spread. Figure by DrBob - Gaussianbeam.png, CC BY-SA 3.0.

In addition, the dependency of the non-perturbative dipole phase on the driving field's intensity, which changes along z, introduces an additional mismatch effect, $\Delta k_q^{dip,r} = \alpha_q^r \frac{dI(z)}{dz}$, which strongly depends on the type of trajectory.

Another important macroscopic effect connected with the non-perturbative dipole phase is the variation of the harmonic phase with the intensity profile along the transverse plane—also known as transverse phase-matching [100]. For thin gas jets and loose focusing geometries, the harmonic phase varies mainly due to the curvature of the driving beam's wavefront and the non-perturbative dipole phase variation associated with the intensity profile, es described by Eq. (55). The combination of these two effects determines the total variation of the harmonic phase along the transverse plane. Thus, the harmonic signal is strongly influenced by how the two effects match [59, 91]. For example, if the gas jet is placed before the laser focus, they can basically compensate each other, which optimizes the harmonic signal

[101]. This effect is depicted in figure 18, where we show the two phase contributions at different positions along the propagation axis of the incident Gaussian beam. At a certain z position, they can essentially compensate each other, which results in brighter, less divergent harmonics. It is important to note that as a result of the trend of the two phase contributions, different harmonics will focus at different positions [91].

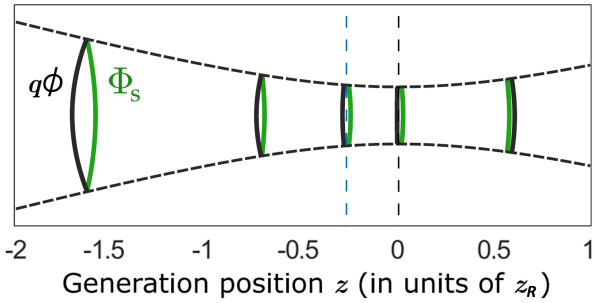

Figure 18: Representation of the two contributions to the harmonic wavefront, the mapping of the driving field (black) and the non-perturbative dipole phase (green), at different generation positions (z). The vertical thin dashed lines indicate the position where the two contributions compensate each other for the short trajectory (blue) and the driving beam focus (black). Modified version of a figure extracted from [91].

Finally, it is interesting to highlight the role of the dipole phase in the propagation of the harmonics, which can create chromatic aberrations [91], but also allows to optimize the HHG configuration to, for example, increase the intensity of the harmonic beam by reducing its divergence along propagation or to separate short and long trajectory contributions [102, 103].

2.3.2 *Computation of high-order harmonic generation from a macroscopic target*

Some of the calculations carried out in this thesis have been performed employing the propagation model described in [104]. This macroscopic model takes into account the phase-matching of the harmonics generated in the gas jet. Basically, first the emission of each elementary radiator, atom or molecule, is computed using full quantum SFA+ calculations—i.e., without performing the saddle-point approximation. Then, the electromagnetic propagator is obtained by solving the Maxwell equations for a point-like source in vacuum, assuming that the high-order harmonics are weakly perturbed by the neutrals' susceptibility (a reasonable assumption in partially ionized low-pressure

gases). For the j-th charge placed at the point $\mathbf{r}_j$ in the target, the contribution to the harmonic field in the far field is [67]:

$$\mathbf{E}_i^j(\mathbf{r}_d, t) = \frac{q_j}{c^2|\mathbf{r}_d - \mathbf{r}_j(0)|}\mathbf{s}_d \times \{\mathbf{s}_d \times \mathbf{a}_j[t - |\mathbf{r}_d - \mathbf{r}_j(0)|/c]\}, \tag{59}$$

where $\mathbf{a}_j$ is the charge's acceleration and $\mathbf{s}_d$ is the unitary vector pointing to a virtual detector located at $\mathbf{r}_d$, as depicted in figure 19.

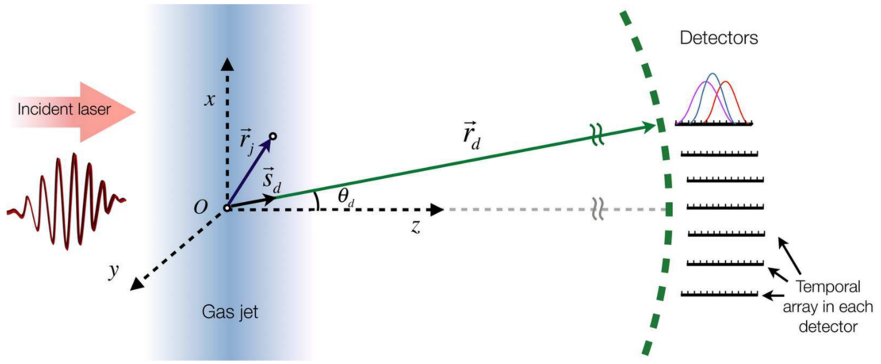

Figure 19: Scheme of the method to compute the propagation of the high-order harmonics. The target is discretized into elementary radiators, each placed at a coordinate $\mathbf{r}_j$. The radiation is detected at a distance $|\mathbf{r}_d|$ from the center of the target. At each far-field detector the field contributions emitted by the different radiators are added in a temporal array. Figure extracted from [59].

In addition, the absorption of the harmonics during their propagation through the gas is included in the model through Beer's law, though this is only relevant for thick, high-density targets, which are out of the scope of this thesis.

2.3.3 *The thin slab model*

Since the transverse phase-matching is the most important macroscopic effect for thin targets, we can picture the problem by considering and infinitely thin slab as the source of harmonic radiation [105–107].

The TSM has two main ingredients:

1. The harmonic emission of the elementary radiators is calculated using a simple expression reproducing the basic laws of HHG obtained from the TDSE and SFA.

2. The elementary radiators are assumed to be placed in a plane slab with zero thickness transverse to the propagation axis of the driving field. The far-field radiation is calculated propagating the harmonic field at the slab according to the Fraunhofer diffraction integral. The geometry and the corresponding spatial coordinates are represented in figure 20.

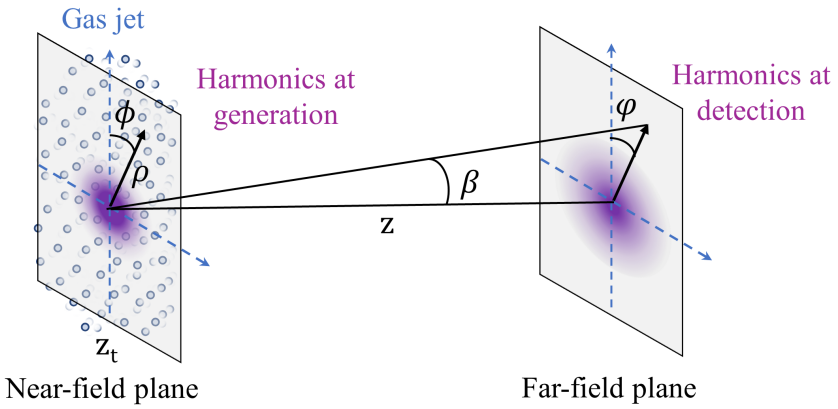

Figure 20: Scheme of the TSM coordinates for the near-field plane (ρ, ϕ) and the far-field plane (β, φ). The harmonics are generated in an infinitely thin gas jet placed at z_t and, afterwards, they propagate towards the far-field plane, placed at a distance z, where they are detected.

Let us now address the first point by deriving a simplified computation of the harmonic field from an elementary radiator. We denote the driving field at the slab as $U(\rho, \phi, z_t)$ and its phase as $\Phi(\rho, \phi, z_t)$. The amplitude and phase of the non-perturbative harmonics—those that conform the plateau—are calculated from the amplitude and phase of the driving field, following the general perturbative formulation, but extended to the non-perturbative case. First, in the perturbative case the amplitude of the q-th order harmonic is proportional to the q-th power of the driver's amplitude, $|U(\rho, \phi, z_t)|^q$. In contrast, in the non-perturbative case the amplitude scales with a lower power, $p < q$, which is approximately constant along the plateau, therefore, $|U(\rho, \phi, z_t)|^p$ [108]. Second, the non-perturbative dipole phase follows the parametrization in Eq. (55). Therefore, the harmonic emission placed at position (ρ, ϕ, z_t) of the gas slab can be expressed as

$$A^q(\rho, \phi) \propto |U(\rho, \phi, z_t)|^p e^{iq\Phi(\rho,\phi,z_t)} e^{i\alpha_q^r I(\rho,\phi,z_t)}. \tag{60}$$

Then, we compute the far-field emission from the thin layer using the Fraunhofer diffraction integral of the harmonic emission at the gas slab:

$$\begin{aligned} U^q(\varphi, \beta, z) &= -iq \frac{e^{i\frac{2\pi z}{\lambda_0}} e^{i\frac{\pi z \tan^2\varphi}{\lambda_0}}}{z\lambda_0} \int_0^\infty \int_0^{2\pi} A^q(\rho, \phi) \\ &\times e^{-i\frac{2\pi}{\lambda_0} q\rho(\sin\beta\tan\varphi\sin\phi + \cos\beta\tan\varphi\cos\phi)} \rho d\rho d\phi, \end{aligned} \tag{61}$$

where (φ, β, z) are the far-field coordinates, being β the divergence angle, φ the azimuth, and z the position of the detector, that must satisfy the Fresnel number's condition $N_F = \frac{q\rho^2}{z\lambda_0} \ll 1$ (see figure 20). It is worth noting that the non-perturbative nature of the HHG process

substantially influences the characteristics of the harmonics through both p and α_q^r.

The TSM has demonstrated to be a very useful tool to disentangle and simplify complex processes in macroscopic HHG [16, 20, 105, 106]. Note that, although we have presented it in its scalar form here, the TSM can be also expressed in a vector form, which has allowed us to apply it to more complex polarization distributions [20, 21]. The main advantages of the TSM are that (i) its numerical implementation is very simple and the calculations are very fast and not computationally demanding but, more importantly, (ii) it allows us to modify and, therefore, to study the role of the different non-perturbative parameters.

2.4 HIGH-ORDER HARMONIC SPECTROSCOPY OF TUNNEL IONIZATION IN MOLECULES

In this section, we shall present our theoretical approach to high-harmonic spectroscopy in small molecules. For that purpose, we will study the details of the tunnel ionization process in molecules. In particular, we will demonstrate that the electron localization in the molecule, i.e. its distance to the tunnel barrier, is a relevant aspect to take into account in the SFA to reproduce both the quantitative and qualitative structure of the harmonic spectrum calculated from the TDSE. For this, we introduce a reformulation of the molecular tunnel ionization in the SFA description of HHG that accounts for the inner spatial molecular structure. In the subsection 2.4.1, we present our theoretical model for molecular HHG, the SDT-SFA. Then, in the subsection 2.4.2, we show how the electron's position in the molecule affects the HHG spectrum and how this improves the agreement with the TDSE simulations. Further information about this work is presented in section 2.5, where we include our publication [15].

2.4.1 *The site-dependent tunneling theory*

The HHG spectrum encodes information of the molecular structure [26], as well as its nuclear [25] and electronic dynamics [78]. This information can be unraveled using high-harmonic spectroscopy and time-resolved attosecond spectroscopy techniques. Interestingly, the molecular orbital matrix elements are mapped into the HHG spectrum, which allows for the reconstruction of the molecular geometry and orbital structure. Therefore, the quality of the retrieval of the molecular features relies crucially in the fairness of the theoretical description used to model the HHG process.

The SFA has successfully demonstrated to reproduce the main characteristics of the harmonic spectra in molecules [30, 73, 76]. Nevertheless, its description of tunnel ionization, which constitutes a fundamental

first step in the process of HHG, is based in a rather strong assumption: the SFA neglects the actual shape of the potential barrier. As a consequence, it describes the ionization from each molecular site on an equal footing. However, the internal potential barriers are usually lower, or even absent, for most of the realistic potential shapes. Thus, part of the electron wavefunction is effectively separated from the edge of the tunnel ionization barrier.

In this section, we show that the tunnel ionization is affected by the extended nature of the molecular orbital, since the ionization probability depends on the electron's occupation of a specific molecular site. For this, we will consider as a target the hydrogen molecular ion, H_2^+, driven by a linearly polarized laser field oriented parallel to the molecular axis. The exact TDSE calculations are affordable for this simple case and they will serve as a benchmark for our results.

Standard molecular SFA

Let us derive the molecular SFA, which we will denote as standard strong field approximation (s-SFA) for distinction. The atomic SFA presented in section 2.2.2 is here extended to the H_2^+ molecule by incorporating two aspects: (i) the molecular orbital, and (ii) the energy shift of the maximum of the potential barrier.

The ground state of H_2^+ is a symmetric orbital that can be described in terms of atomic orbitals centered at the molecular ion sites, oriented along the z coordinate. Thus, the time-dependent molecular orbital can be expressed as:

$$\phi_0(\mathbf{r},t) = Ce^{-i\epsilon_0(t-t_0)/\hbar}\left[\chi_0\left(\mathbf{r}-\frac{R}{2}\mathbf{e}_z\right)+\chi_0\left(\mathbf{r}+\frac{R}{2}\mathbf{e}_z\right)\right], \tag{62}$$

where ϵ_0 is the ground state binding energy and $\chi_0(\mathbf{r})$ is a localized wavepacket, that we shall describe as a linear combination of Gaussian orbitals [109]. R is the internuclear distance, and C is the normalization factor. Applying the translation operator to the different molecular ion sites [110], Eq. (62) can be rewritten as

$$|\phi_0(t)\rangle = C\left(e^{-\frac{i}{\hbar}\hat{p}'_z(t)\frac{R}{2}}+e^{\frac{i}{\hbar}\hat{p}'_z(t)\frac{R}{2}}\right)|\chi_0(t)\rangle, \tag{63}$$

where $\mathbf{p}'(t)$ can be interpreted as the kinetic momentum of the recolliding electron, as seen from the bottom of the molecular potential well [26]. Thus, it is calculated as $p'_z(t) = \text{sign}\{p_z(t)\}\sqrt{p_z^2(t)+2m|\epsilon_0|}$, where $p_z(t)$ is the kinetic momentum of the recolliding electron right outside the molecular well.

The extension of the molecular potential displaces the tunnel barrier along the coordinate of the molecule axis, as depicted in figure 21. The dipole interaction $E\cdot z$ is therefore greater and the maximum of the height of the potential barrier decreases with respect to the atomic case.

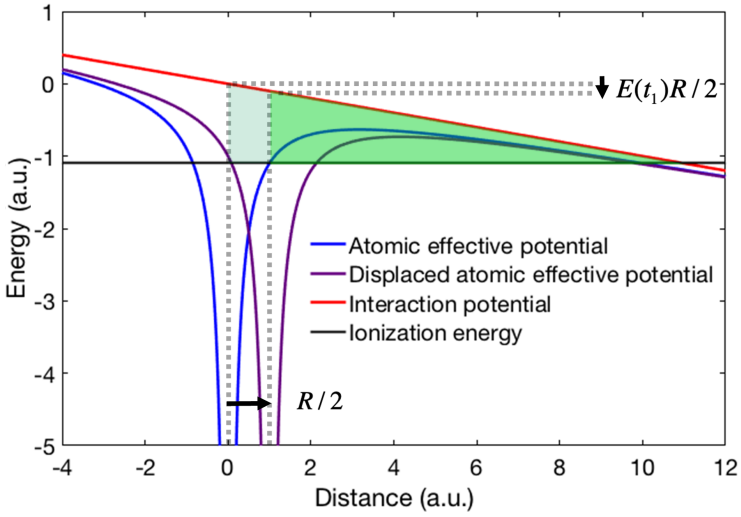

Figure 21: Scheme of the dipole energy shift of the potential barrier's maximum due to extended nature of the molecule. An atomic potential (blue) is displaced a distance $R/2$ from the origin (purple), while interacting with an external field (red). As a consequence of the displacement, the height of the barrier (green) seen by the electronic wavepacket (with ionization energy in black) is lowered in an amount of $E(t_1)R/2$.

The correction associated to the dipole energy shift of the barrier's maximum is incorporated into the transition matrix element as:

$$\eta(\mathbf{P}, t_1) = \left[\frac{W_{ADK}[\epsilon(R/2, t_1)]}{W_{ADK}(\epsilon_0)}\right]^{1/2} \langle \mathbf{P}|\frac{C_F}{r^n}|\chi_0\rangle. \tag{64}$$

where $\epsilon(R/2, t_1) = \epsilon_0 - e|E(t_1)|R/2$ is the ionization potential as seen from the top of the barrier at the ionization time t_1 and W_{ADK} is the Ammosov-Delone-Krainov ionization rate [85]. This later quantity is calculated as

$$\begin{aligned} w_{ADK}(\epsilon) &= \left(\frac{2e}{n^*}\right)^{2n^*} \frac{1}{2\pi n^*} \frac{(2\ell+1)(\ell+|m|)!}{2^{|m|}|m|!(\ell-|m|)!}|\epsilon| \left[\frac{3E_0}{\pi(2|\epsilon|)^{3/2}}\right]^{1/2} \\ &\times \left[\frac{2}{E_0}(2|\epsilon|)^{3/2}\right]^{2n^*-|m|-1} e^{-\left(\frac{2(2|\epsilon|)^{3/2}}{3E_0}\right)}, \end{aligned} \tag{65}$$

where e is the Euler number, m y ℓ are the quantum numbers of the considered state (both null in this case), and

$$n^*(\epsilon) = \frac{Ze^2}{\hbar}\sqrt{\frac{m_e}{2|\epsilon|}}, \tag{66}$$

Z being the charge of the ionic core ($Z = 2$ for H_2^+).

These two features lead to the following expression for the molecular dipole acceleration (i.e., the molecular version of Eqs. (35) and (36)):

$$\langle \mathbf{a}(t)\rangle = 2\Re\left[\int \frac{P^2/2m_e-\epsilon_0}{\Delta_s}\frac{1}{m_e}\langle\chi_0(t)|\left(-\nabla V_C\right)|\mathbf{P}\rangle\,|\mathcal{F}_s\left[p'_z(t)\right]|^2 \times \left\{-\frac{i}{\hbar}\int_{t_0}^{t} e^{i\frac{1}{\hbar}S(\mathbf{P},t,t_1)}e^{-i\frac{\epsilon_0}{\hbar}(t_1-t_0)}V_F(\mathbf{P},t_1)\eta(\mathbf{P},t_1)dt_1\right\}d\mathbf{P}\right], \tag{67}$$

where $(P^2/2m_e-\epsilon_0)/\Delta_s$ accounts for the SFA+ correction and we denote

$$\mathcal{F}_s[\mathbf{p}'(t)] = C\left[e^{\frac{i}{\hbar}p'_z(t)\frac{R}{2}}+e^{-\frac{i}{\hbar}p'_z(t)\frac{R}{2}}\right] \tag{68}$$

as the standard molecular form factor.

Site-dependent tunneling SFA

Eq. (67) indicates that the ionization probability from each localized wavepacket, $\chi_0(\mathbf{r}-R/2\mathbf{e}_z)$ and $\chi_0(\mathbf{r}+R/2\mathbf{e}_z)$, is equal at every instant of time. However, these wavefuncions are not separated by internal potential barriers. Thus, each of them is located at a different distance from the molecular potential barrier formed by the external field at the left or right side of the molecule. Let us compute the difference in ionzation probability caused by this distinct separation to the barrier—i.e., the site-specific ionization probability.

In figure 22a, we show a wavepacket centered at z_c, and placed at the left of a potential barrier $V(z)$ whose edges are denoted as z_b (left) and z_f (right). Such wavepacket exhibits a tunnel transmission rate of

$$P(z_c,z_b) = \frac{|\chi_0(z_f)|^2}{|\chi_0(z_c)|^2} = W_{WKB}\frac{|\chi_0(z_b)|^2}{|\chi_0(z_c)|^2}, \tag{69}$$

where W_{WKB} is the WKB rate of tunneling for a particle located at z_b [111],

$$W_{WKB} = e^{-\frac{2}{\hbar}\int_{z_b}^{z_f}\sqrt{2m[V(z')-\epsilon_0]}dz'}, \tag{70}$$

ϵ_0 being the energy of the wavepacket. Thus, Eq. (69) can be interpreted as the tunneling rate multiplied by the relative probability of the particle being at the edge of the barrier to that of being at the ion site. Importantly, therefore, the tunnel transmission rate of the wavepacket decreases with the distance from its ion site to the edge of the barrier, as the electron probability at the barrier's edge decreases accordingly.

Hence, we define a new quantity,

$$T(z_c,z_b) = \left[\frac{P(z_c,z_b)}{P(z_b,z_b)}\right]^{1/2} = \frac{|\chi_0(z_b)|}{|\chi_0(z_c)|}, \tag{71}$$

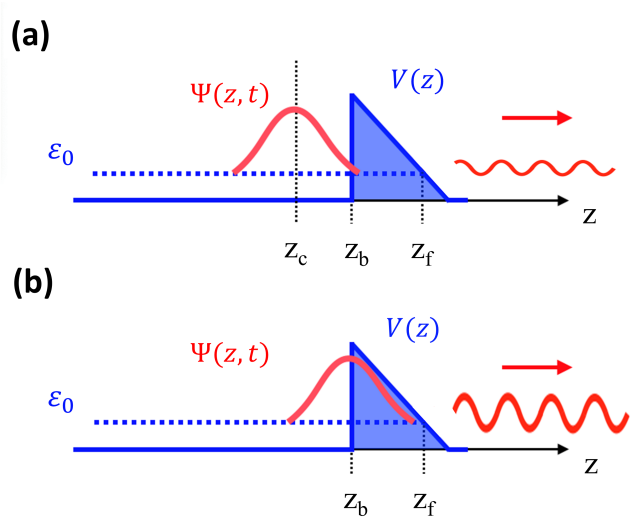

Figure 22: Scheme of the tunneling of the wavepacket $\Psi(z,t)$ (red), with energy ϵ_0 (dashed blue), through a potential barrier, $V(z)$ (solid blue), whose edges are placed at z_b and z_f. The tunneling of a distant wavepacket centered at z_c (a) exhibits a lower rate than that centered at the edge of the barrier (b).

that describes the ratio between the tunneling rates for an electron placed at the ion site z_c (figure 22a) and that for an electron located at the edge of the barrier (figure 22b).

Let us incorporate this site-specificity information into the standard molecular SFA theory for the H_2^+ molecule. In this case, the barrier's edge location, z_b, corresponds approximately to $-R/2$ for a positive field and to $R/2$ for a negative field. The molecular form factor described in Eq. (68) is now redefined as

$$\mathcal{F}^{\pm}_{SDT}\left[p'_z(t)\right] = T\left(-\frac{R}{2}, \pm\frac{R}{2}\right) e^{\frac{i}{\hbar}p'_z(t)\frac{R}{2}} + T\left(\frac{R}{2}, \pm\frac{R}{2}\right) e^{-\frac{i}{\hbar}p'_z(t)\frac{R}{2}}. \quad (72)$$

The positive index corresponds to ionization through a potential barrier located at the right side of the molecule, while the negative index corresponds to a barrier at the left.

Thus, the dipole acceleration described in Eq. (67) is modified by introducing the site-specific form factor:

$$\begin{aligned}\langle \mathbf{a}(t)\rangle \;=\; & 2\Re\left[\int \frac{P^2/2m_e - \epsilon_0}{\Delta_s}\frac{1}{m_e}\langle\chi_0(t)|\left(-\nabla V_C\right)|\mathbf{P}\rangle\,|\mathcal{F}_{SDT}\left[p'_z(t)\right]|^2\right. \\ & \left.\times\left\{-\frac{i}{\hbar}\int_{t_0}^{t} e^{i\frac{1}{\hbar}S(\mathbf{P},t,t_1)}e^{-i\frac{\epsilon_0}{\hbar}(t_1-t_0)}V_F(\mathbf{P},t_1)\eta(\mathbf{P},t_1)\,dt_1\right\}d\mathbf{P}\right],\end{aligned} \quad (73)$$

where we have employed the following property: $|\mathcal{F}_{SDT}|^2 = |\mathcal{F}^{+}_{SDT}|^2 = |\mathcal{F}^{-}_{SDT}|^2$. Thus, Eq. (73) expresses the computation of the dipole acceleration in our SDT-SFA model.

2.4.2 *Spectral analysis of tunnel ionization in extended targets*

Since tunnel ionization is the first step of HHG, it may be expected that the signatures of the site-dependent tunneling should be found in the HHG spectrum. Previous works have reported the so-called structural minimum in the HHG spectrum, whose position is a signature of the internuclear distance or the alignment of the molecule [26]. This minimum can be described as the result of the destructive interference between two radiating point sources located at the ion positions in the molecule. The destructive interference condition is calculated as:

$$R\cos\theta = (2m+1)\lambda/2, \tag{74}$$

where m is an integer, θ is the angle between the molecular axis and the laser polarization direction and λ is the wavelength of the emitted radiation. For our configuration ($R = 2$ a.u., $\theta = 0$), λ corresponds to the 21-st order harmonic. Note that this condition does not depend on the laser parameters, but exclusively on the molecule structural properties.

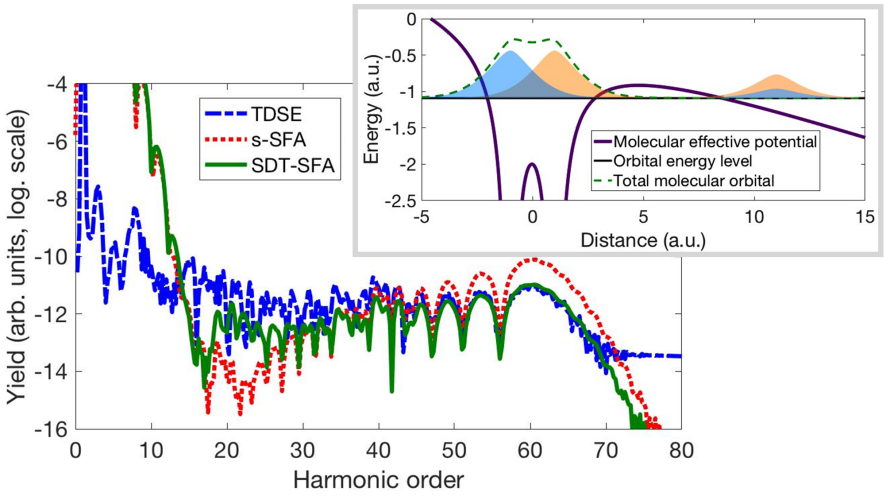

Figure 23: Comparison of the HHG spectra from H_2^+ calculated using the exact TDSE (dashed blue), the standard SFA (dotted red) and the SDT-SFA (solid green). The molecule is aligned along the polarization direction of the laser, which has a 800 nm wavelength, 4-cycles duration in total, $\sin^2$ envelope and 3.5×10^{14} W/cm^2 peak intensity. The inset shows a scheme of the molecular profile in the site-dependent tunnel-ionization picture: the atomic orbital placed next to the barrier exhibits a higher tunneling rate.

Interestingly, the exact TDSE calculations show that depth of this minimum is strongly attenuated when the molecule is at the equilibrium internuclear distance and it is placed parallel to the laser polarization [26, 112]. In contrast, the standard SFA calculations (see Eq. (67)) show a rather profound minimum [113]. However, our site-dependent correction significantly improves the comparison between

the TDSE and SFA results. In figure 23, we show that the SDT-SFA (green solid line) achieves a level of agreement with the TDSE (blue dashed line) simulations comparable to the atomic case. The laser parameters used in the simulations are $I_0 = 3.5 \times 10^{14}\, W/cm^2$ peak intensity, $\lambda_0 = 800\, nm$ wavelength and 4-cycles duration in total.

In order to discard rescattering effects as the origin of the discrepancy between the TDSE and the s-SFA, we also calculated the photoelectron spectra emitted from the H_2^+ molecule under the same conditions as in the HHG simulations. In figure 24, we show that the photoelectron spectrum from the s-SFA also exhibits deep structural minima, arising from the interference of the emission from the electronic wavepackets initially placed at each ion site. The demise of these minima in the TDSE photoelectron emission supports the tunnel ionization as a relevant effect.

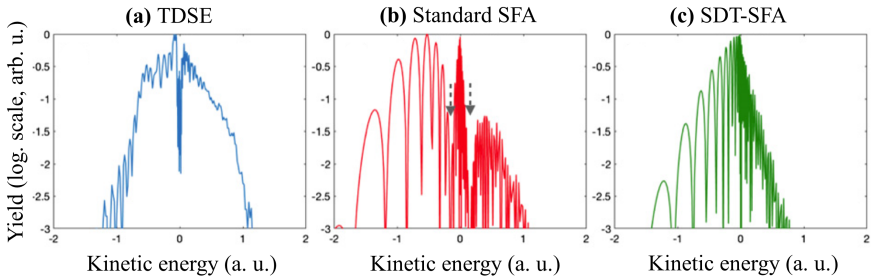

Figure 24: Photoelectron spectra from the H_2^+ molecule calculated using the TDSE (a), the standard SFA (b) and the SDT-SFA (c) models for the same laser parameters and molecular configuration as those of figure 23. The grey arrows in panel (b) indicate the presence of structural minima, which are not evidenced in the TDSE and SDT-SFA spectra. The sign in the kinetic energy axis indicates the direction—left (minus) or right (plus)—of the ionized wavepacket.

Interestingly, our macroscopic calculations show that the site-specificity tunneling signatures are not obscured by propagation effects [15]. Thus, we expect the implications of the site-specificity to be found in experimental HHG in molecules. Further results and information about the theoretical methods can be found in our publication [15], presented in section 2.5.1.

Let us finally remark that, in the following chapters of this thesis, we have considered atomic targets. The extension of these studies to molecular targets can be of great interest because, for example, their non-centro-symmetrical structure may affect the angular momentum properties of the emitted harmonics [33, 114]. Therefore, we believe that the extension of SFA models to molecular targets is of special interest for HHG studies involving SAM or OAM.

2.5 PUBLICATION

To conclude this chapter, we include the full text of the article where the site-specific molecular tunnel-ionization is developed under the title "Site-specific tunnel-ionization in high harmonic generation in molecules" [15], extending the information in section 2.4. According to the requirements of the University of Salamanca, we also incorporate an abstract in Spanish.

2.5.1 *Site-specific tunnel-ionization in high harmonic generation in molecules*

Resumen

Los pulsos láser ultracortos y coherentes nos permiten estudiar las dinámicas nucleares [25] y electrónicas [78], así como las estructuras moleculares [26], con la mejor resolución temporal y espacial hasta el momento. Uno de los procesos más relevantes inducidos por los pulsos láser ultracortos y coherentes es la generación de armónicos de orden alto (HHG), puesto que su espectro codifica información sobre la estructura y la dinámica del objeto en el que tiene lugar. Esta información se puede decodificar utilizando técnicas como la espectroscopia de armónicos altos, donde la calidad de la recuperación de las características moleculares se basa habitualmente en la exactitud de los modelos teóricos utilizados para describir el proceso de la HHG.

En este trabajo [15], exploramos una parte clave de la HHG: la ionización túnel. En particular, demostramos que el proceso de ionización túnel en moléculas se ve fuertemente afectado por el lugar específico que ocupa el paquete de ondas electrónico en la molécula antes de la ionización, debido a que la naturaleza extendida del potencial molecular implica que parte del orbital molecular está separado del borde de la barrera de ionización. Por lo tanto, encontramos que la descripción estándar de la ionización túnel debe modificarse para los sistemas moleculares.

Para recuperar la información sobre la ionización túnel contenida en el espectro armónicos de orden alto, hemos implementado numéricamente un modelo basado en la aproximación de campo fuerte (SFA). Nuestros resultados muestran que tanto los espectros de armónicos de orden alto como los de fotoelectrones indican que la tasa de ionización túnel es mayor para la parte del orbital molecular situada junto a la barrera potencial. Para tener en cuenta este efecto, hemos desarrollado una extensión de la SFA molecular estándar, la SFA con ionización túnel dependiente del sitio (SDT-SFA). Concretamente, introducimos un factor de forma molecular modificado en la SFA standard. Este factor de forma mejora significativamente la concordancia entre los modelos de SFA y los cálculos exactos obtenidos a partir de la ecuación de Schrödinger dependiente del tiempo, y, además, se puede calcular fácilmente, independientemente de la complejidad de la geometría molecular.

Finalmente, es importante destacar que este efecto distorsiona el mapeo de las características de los orbitales moleculares en el espectro de armónicos, por lo que es necesario tener en cuenta el grado de deformación debido a la ionización túnel dependiente de la posición para la correcta recuperación experimental de los orbitales moleculares.

New Journal of Physics
The open access journal at the forefront of physics

Deutsche Physikalische Gesellschaft DPG IOP Institute of Physics

PAPER • OPEN ACCESS

Site-specific tunnel-ionization in high harmonic generation in molecules

To cite this article: Laura Rego *et al* 2020 *New J. Phys.* **22** 043012

IOP Publishing New J. Phys. 22 (2020) 043012 https://doi.org/10.1088/1367-2630/ab7dde

New Journal of Physics
The open access journal at the forefront of physics

Deutsche Physikalische Gesellschaft DPG
IOP Institute of Physics

Published in partnership with: Deutsche Physikalische Gesellschaft and the Institute of Physics

OPEN ACCESS

RECEIVED
11 November 2019

REVISED
21 February 2020

ACCEPTED FOR PUBLICATION
9 March 2020

PUBLISHED
21 April 2020

PAPER

Site-specific tunnel-ionization in high harmonic generation in molecules

Laura Rego[1], **Carlos Hernández-García**[1], **Antonio Picón**[2] **and Luis Plaja**[1]

[1] Grupo de Investigación en Aplicaciones del Láser y Fotónica, Departamento de Física Aplicada, University of Salamanca, E-37008 Salamanca, Spain
[2] Departamento de Química, Universidad Autónoma de Madrid, Madrid, Spain

E-mail: laura.rego@usal.es

Keywords: high-harmonic spectroscopy, tunnel ionization, high harmonic generation in molecules, strong field approximation, ultrafast lasers, attosecond laser pulses, photoionization of molecules

Abstract

We demonstrate that the standard picture of strong-field tunnel-ionization from molecules should be reformulated. The extended nature of the molecular potential implies the separation of some of the molecular sites from the edge of the ionization barrier. We show that the dependence of the tunnel probability with the distance to the barrier is translated into the ionized wavepacket, modifying substantially the high-order harmonic emission. The introduction of the dependence of tunnel ionization with the molecular site significantly improves the theoretical description of high-order harmonic generation in molecules, which is used as a cornerstone in high-harmonic spectroscopy and attosecond imaging.

1. Introduction

High-order harmonic generation (HHG) is an extreme non-linear process induced by intense fields. In atomic or molecular gases, it can be described as a three-step process [1, 2]: first, near the maxima of the driving field's amplitude, an electronic wavepacket is tunnel-ionized from the parent atom; in the second step, the electronic wavepacket is accelerated and, after reversal of the sign of the electric field, it is redirected to the parent ion; finally, upon recollision, the electron's kinetic energy is emitted in the form of high-frequency radiation. The harmonic spectra encode information of the target structure and dynamics, that can be disentangled using high-harmonic spectroscopy (HHS) and time resolved attosecond spectroscopy techniques [3]. These procedures have been successful in retrieving the information from the HHG spectra about molecular structure [4–6], nuclear dynamics [7], molecular orbitals [8, 9], energy dispersion in solids [10], dynamics in strongly correlated systems [11], tunneling times [12], and orbital tomography [13–15].

The study of molecular systems interacting with strong laser fields has a main tool in computationally solving the time-dependent Schrödinger equation (TDSE). The detailed physics, however, is frequently hidden by the complexity of the processes involved. To this end, approximated models are needed to describe the problem in terms of fundamental physical mechanisms. Among them, those based in the strong-field approximation (SFA) [16–18] allow to establish a link between the harmonic spectral signatures and the structural details of the radiating matter system. The SFA has successfully demonstrated to reproduce the main characteristics of the harmonic spectra in atoms [19–21], and molecules [13, 22–26], and their electron and nuclear dynamics [7, 27–31].

A key ingredient in HHS is the mapping of the molecular orbital matrix elements into the harmonic spectrum and phase, as predicted from the SFA. This relation allows for the reconstruction of the molecular geometry, as well as the molecular orbital structure. The quality of the retrieval of the molecular features relies, therefore, on the fairness of the SFA in describing the HHG process. The first step of HHG is the tunnel ionization, which constitutes a fundamental process in strong-field interactions and has been extensively studied in atoms [16, 32–34] and extended to molecules [35–39] in the SFA. Notably, the SFA

neglects the shape of the molecular potential barrier at ionization, thus, describing the ionization from each molecular site on equal foot. However, for the actual potential shapes, the elimination of the ion potential barriers inside the molecule leads to extended molecular orbitals, where part of the electron wavefunction is effectively separated from the edge of the tunnel ionization barrier. Recently, Liu and Liu have suggested treating the ionization from each atomic site differently, though by considering different effective barrier widths [39]. Finally, Labeye *et al* have studied the implications of the internal molecular barrier in the semiclassical description of HHG from molecules [40].

In this work, we demonstrate that the standard tunnel ionization picture has to be revised in the molecular case. As we will show, the tunnel ionization probability is affected by the separation of part of the electronic wavefunction from the potential barrier, introducing a molecular-site specificity in the electron ionization. As tunnel ionization is a key ingredient in HHG, the signature of its site-specificity is evidenced in the details of the high-order harmonic and photoelectron spectra. The total ionization rates, as given by the molecular Ammosov–Delone–Krainov theory [35] and the weak-field asymptotic theory [37], are little affected. As a practical consequence, the orbital information encoded in the harmonic spectrum is substantially distorted from the prediction of the standard SFA models. We, however, show that the proper description of electron tunneling from molecular orbitals can be incorporated into these existing models with the introduction of a modified molecular form factor. The consequences of this study are two-fold: on the one side, it modifies the interpretation of the harmonic signal in HHS, since the retrieved orbital is not a raw image of the actual molecular wavefunction; on the other side, it demonstrates that the HHG spectrum shows well-resolved signatures of the tunnel-ionization site-specificity. Finally, our considerations lead to a derivation of a molecular SFA HHG model with quantitative accuracy.

The article is organized as follows. First, we describe our theoretical approach to the site-depending tunneling ionization and its incorporation in the strong field approximation formalism. Second, we present the results for HHG and photoelectrum spectra obtained from our model compared to those from the exact TDSE calculations, and finally we conclude.

2. Theoretical approach to site-dependent tunnel ionization in molecules

We consider as the subject of study the hydrogen molecular ion (H_2^+) in a linearly polarized laser field, since the exact TDSE calculations are affordable for this simple case [41]. The molecule is assumed to lie parallel to the polarization direction, a feasible scenario after using laser alignment techniques [42]. We also neglect nuclei dynamics, which is reasonable for time scales of few femtoseconds [43]. We consider an 800 nm wavelength laser pulse described as $E(t) = E_0 \sin^2\left(\pi t/\tau\right) \sin\left(\omega_0 t\right)$, ω_0 being the laser carrier frequency, $\tau = 10.67$ fs, which leads to 3.88 fs full-width at half maximum (FWHM) in intensity, and a peak intensity of 3.5×10^{14} W cm^{-2}. The Hamiltonian governing the interaction is

$$H\left(t, \mathbf{r}\right) = \frac{\mathbf{p}^2(t)}{2m} + V_{\mathrm{M}}(\mathbf{r}), \tag{1}$$

where m is the electron mass, and

$$V_{\mathrm{M}}\left(\mathbf{r}\right) = -\frac{q^2}{\sqrt{\rho^2 + (z + R/2)^2}} - \frac{q^2}{\sqrt{\rho^2 + (z - R/2)^2}} \tag{2}$$

is the Coulomb potential in cylindrical coordinates (q is the electron charge, and R is the internuclear distance). $\mathbf{p}$ is the kinetic momentum operator, $\mathbf{p} = -i\hbar\nabla - (q/c)A(t)\mathbf{e}_z$, $A(t)$ being the vector potential of the laser field, polarized in the z direction. As shown in appendix A, the ground-state of H_2^+ is a symmetric orbital that can be described in terms of atomic orbitals centered at the molecular ion sites, as

$$\phi_0(\mathbf{r}) = C\left[\chi_0\left(\mathbf{r} - \frac{R}{2}\mathbf{e}_z\right) + \chi_0\left(\mathbf{r} + \frac{R}{2}\mathbf{e}_z\right)\right], \tag{3}$$

where $\chi_0(\mathbf{r})$ is a localized wavepacket, described as a linear combination of Gaussian orbitals [44, 45], and C is the normalization factor. The harmonic spectrum is calculated from the Fourier transform of the mean dipole acceleration along the z axis, $a_z(t) = \langle \hat{a}_z \rangle = \langle -(1/m)\partial V_{\mathrm{M}}/\partial z \rangle$. The TDSE is integrated using the Crank–Nicholson algorithm in the finite differences scheme.

IOP Publishing New J. Phys. 22 (2020) 043012 L Rego et al

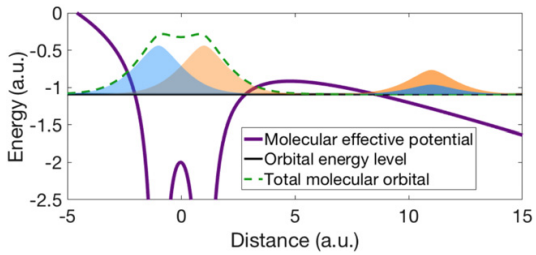

Figure 1. Scheme of the influence of the molecular profile in the site-dependent tunnel picture. The purple line shows the effective molecular potential (Coulombic potential deformed by the external field). The localized-atomic orbitals composing the groundstate and ionized wavefunctions are depicted in blue and orange. The total molecular orbital is indicated by the dashed green line.

Molecular HHG can be described using an extension of the atomic SFA models. We use the SFA + approach, which provides a quantitative accurate reproduction of the harmonic spectra in atoms [21]. The extension to molecules leads to the following expression for the dipole acceleration (see appendix A):

$$a_z(t) = -\frac{\mathrm{i}}{\hbar}\int_{\mathbf{P}} \alpha_+(\mathbf{P})\langle\chi_0|\hat{a}_z|\mathbf{P}\rangle|\mathcal{F}_s[\mathbf{p}'(t)]|^2 \times \int_{t_0}^{t} \mathrm{e}^{\mathrm{i}\frac{1}{\hbar}S(\mathbf{P},t,t_1)}\mathrm{e}^{-\mathrm{i}\frac{\epsilon_0}{\hbar}(t_1-t)}V_{\mathrm{F}}(\mathbf{P},t_1)\times\ \eta(\mathbf{P},t_1)\mathrm{d}t_1\mathrm{d}\mathbf{P}, \qquad (4)$$

where ϵ_0 is the bound state energy, $\eta(\mathbf{P}, t_1)$ is the transition matrix element (see equation (A15) in appendix A) and $\mathcal{F}_s[\mathbf{p}'(t)] = C\left[\mathrm{e}^{\frac{\mathrm{i}}{\hbar}p'_z(t)\frac{R}{2}} + \mathrm{e}^{-\frac{\mathrm{i}}{\hbar}p'_z(t)\frac{R}{2}}\right]$ is the molecular form factor, arising from the application of the translation operator to the different molecular ion sites [46]. $\mathbf{P}$ is the electron's canonical momentum, $S(\mathbf{P}, t, t_1)$ is the ionized electron's action, $|\mathbf{P}\rangle$ are free-electron wavefunctions [47] and $V_{\mathrm{F}}(\mathbf{P}, t) = -(q/mc)\mathbf{A}(t)\cdot\mathbf{P} + (q^2/2mc^2)A^2(t)$. We shall refer to equation (4) using the form factor $\mathcal{F}_s[\mathbf{p}'(t)]$ as the standard SFA (s-SFA). According to reference [4], $\mathbf{p}'$ is interpreted as the kinetic momentum of the recolliding electron, as seen from the bottom of the molecular potential well, i.e. $p'_z(t) = \mathrm{sign}\{p_z(t)\}\sqrt{p_z^2(t) + 2mI_P}$, $p_z(t)$ being the kinetic momentum of the recolliding electron outside the molecular well, and I_P being the bound-state ionization energy. This description has been validated by exact calculations using Coulomb–Volkov wavefunctions [48]. Finally, the term $\alpha_+(\mathbf{P}) = (P^2/2m - \epsilon_0)/\Delta_s$ in equation (4) is a prefactor necessary to describe the harmonic yield with quantitative accuracy [21], being Δ_s the ground-level Stark shift at the instant of recollision. As it is well-known, the form factor $\mathcal{F}_s[\mathbf{p}'(t)]$ in equation (4) is responsible for the interference pattern in the harmonic spectrum, dubbed as *structural minimum* [4].

2.1. Introduction of the site-depending tunneling

As pointed out above, a main assumption in SFA is to neglect the form of the Coulomb potential upon ionization and, therefore, it oversimplifies the nature of the tunnel barrier [33]. In figure 1 the molecular potential is depicted showing that the inner potential barrier is nonexistent. As a consequence, one of the wavepackets χ_0 in equation (3) is effectively separated from the outer tunneling barrier, reducing its ionization probability. According to the derivation in appendix B, the SFA description of molecular ionization should be modified to include this site-dependent tunnel probability. To incorporate it, we reformulate the decomposition of the molecular orbital, equation (3), as

$$\phi_0(\mathbf{r}) = C\left[T\left(\frac{R}{2},\pm\frac{R}{2}\right)\chi_0\left(\mathbf{r}-\frac{R}{2}\mathbf{e}_z\right) + T\left(-\frac{R}{2},\pm\frac{R}{2}\right)\chi_0\left(\mathbf{r}+\frac{R}{2}\mathbf{e}_z\right)\right], \qquad (5)$$

where $T(z_c, z_b)$ is the ratio between the tunnel amplitude probability of the wavepacket placed at the z_c molecular site, $P(z_c, z_b)^{1/2}$, to the amplitude probability near the z_b edge of the potential barrier, $P(z_b, z_b)^{1/2}$. The positive (negative) sign of z_b corresponds to ionization through a barrier located at the right (left) side of the molecule. According to appendix B,

$$T(z_c, z_b) = \left[\frac{P(z_c, z_b)}{P(z_b, z_b)}\right]^{1/2} = \frac{|\chi_0(z_b)|}{|\chi_0(z_c)|}. \qquad (6)$$

$T(z_c, z_b)$ in equation (5) modulates the SFA ionization, so that the wavepackets that are located further away from the barrier have less probability to be ionized, as depicted schematically in figure 1.

Thus, due to this different probability of tunneling, the wavepackets ionized from each molecular site have a different amplitude. The site-specific tunnel probability, $T(z_c, z_b)$, can be included in equation (4) redefining the s-SFA form factor, $\mathcal{F}_s$, as a new site-dependent tunneling (SDT) version. This new form factor not only accounts for the application of the translation operator but also for the consequences of site-dependent tunneling in the ionized wavepacket:

$$\mathcal{F}^{\pm}_{\mathrm{SDT}}\left[p'_z(t)\right] = C\left[T\left(-\frac{R}{2}, \pm\frac{R}{2}\right)\mathrm{e}^{\frac{\mathrm{i}}{\hbar}p'_z(t)\frac{R}{2}} + T\left(\frac{R}{2}, \pm\frac{R}{2}\right)\mathrm{e}^{-\frac{\mathrm{i}}{\hbar}p'_z(t)\frac{R}{2}}\right]. \tag{7}$$

Note, however, that the modulus of the $\mathcal{F}^{\pm}_{\mathrm{SDT}}$ form factor is the same regardless the position $\pm R/2$ of the barrier. We can, therefore, drop the superindices $(\pm)$ when substituting $\mathcal{F}_s$ by $\mathcal{F}_{\mathrm{SDT}}$ in equation (4). After this substitution, we shall refer to equation (4) as the site-dependent tunneling SFA (SDT-SFA).

The interpretation of the site-depending tunneling is probabilistic, as given in appendix B, right after equation (B6). Basically, equation (B5) is the compound probability of two independent events: (i) the particle being located at the edge of the barrier and (ii) the tunnel ionization of a particle in contact with the internal edge of the barrier. The final probability is the product of the probabilities these two events. The compound event appears intrinsically in the TDSE calculations, but it is not well described within the strong field approximation models, as they neglect the shape of the potential, and, therefore the information of the location of the inner edge of the tunneling barrier.

3. Signatures of the site-dependent tunnel-ionization in H_2^+

In this section, we show the comparison between the HHG spectra obtained from the TDSE, the standard SFA and the site-dependent tunneling SFA using the form factor F_{SDT} in equation (7). Second, we show the comparison of the HHG spectra calculated from the s-SFA, the SDT-SFA and the TDSE, for different laser parameters and different molecular internuclear distances, showing a much better agreement of SDT-SFA with the TDSE. Next, we extract F_{SDT} form factor directly from the TDSE calculation, and compare it with equation (7), showing that the TDSE results are consistent with our interpretation. Afterwards, we present results where macroscopic propagation in a molecular target is taken into account, demonstrating that the spectral signature of the site-dependent tunneling is resilient to propagation. Finally, we show the suitability of the SDT-SFA in the photoelectron spectrum emitted in H_2^+.

3.1. High harmonic spectra: single-molecule response

Figure 2(a) shows the quantitative comparison between the HHG spectrum obtained with the exact TDSE (blue), the s-SFA (red), and the SDT-SFA (green) as raw data (no rescaling is done). The spectra show the typical feature of non-perturbative harmonic generation: a *plateau* followed by a cut-off. The s-SFA shows a qualitative recovery of the harmonics close to the cut-off (though, one order of magnitude quantitative error), but a serious qualitative and quantitative departure (up to four orders of magnitude) in the *plateau*, most evident for harmonic orders below the 45th. These trends are also present in calculations for different laser parameters, as it will be shown below. In contrast, this clear departure is not found in HHG from atoms. To illustrate this, we show in figure 2(b) the same comparison as figure 2(a) but for the helium atom, with an ionization potential similar to H_2^+. The helium case corresponds to equation (4), replacing $\mathcal{F}_s[\mathbf{p}'(t)]$ by the atomic form factor, which is equal to one, and substituting the matrix elements and orbital energies accordingly. Figure 2(b) shows that the agreement between atomic SFA and TDSE is excellent even for harmonics well into the cutoff (in this case, for harmonic orders above the 30th). The departure of the SFA description for the lowest frequencies (below 30th harmonic in this case) is a known artifact of the strong field approximation. Thus, while the SFA offers an accurate description of HHG in atoms, it substantially fails to describe HHG in H_2^+. Such departure reveals that some relevant information is missing in the s-SFA formulation, equation (4).

The presence of the sharp minimum in the s-SFA spectra has been reported before [49, 50], and it corresponds to the molecular structural minimum mentioned above. For H_2^+ at equilibrium internuclear distance, interacting with an 800 nm-wavelength laser pulse, the structural minimum is centered at the 22nd harmonic, extending up to the 49th harmonic (as found when imposing the condition $\lambda_{\mathrm{dB}} = 4R/3$, where λ_{dB} is the deBroglie wavelength of the recombining electron). However, in contrast to the s-SFA results, the exact integration of the TDSE shown in figure 2(a) shows a weak trace of this interference. This attenuation of the structural minimum in H_2^+ at the equilibrium internuclear distance, parallel to the laser polarization, has been also evidenced in previous works [4, 6, 50]. On the other hand, it is also known that

IOP Publishing New J. Phys. 22 (2020) 043012 L Rego et al

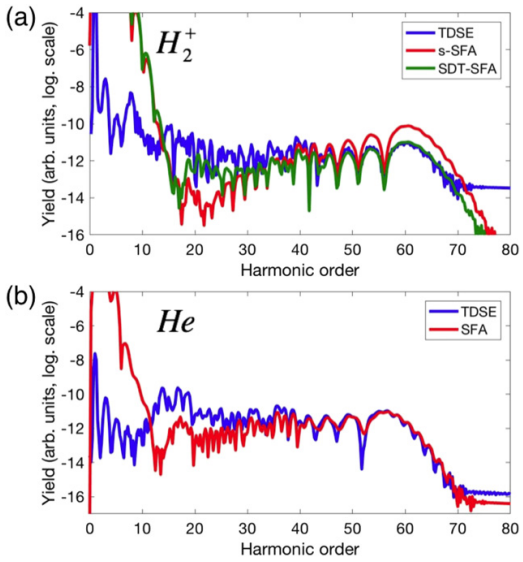

Figure 2. (a) HHG spectra of the H_2^+ molecule aligned along the polarization direction of the laser (800 nm, 3.88 fs FWHM, $I = 3.5 \times 10^{14}$ W cm^{-2}) for the equilibrium internuclear distance (1 Å). The SDT-SFA results (green) adjust to the exact TDSE (blue), while the standard s-SFA (red) exhibits a deep geometrical minimum at $q = 22$. (b) HHG spectra of the atom of helium for the same laser parameters. In the case of atoms, the SFA approach (red) gives an accurate quantitative reproduction of the exact TDSE (blue) for harmonics above 30th. Both panels show raw data since no rescaling has been done.

the minimum shows up for tilted molecular orientations [6, 25], where the projection of the molecular axis onto the field polarization results into an effective internuclear distance smaller than the equilibrium one. We will later show results of the TDSE for such case, where the structural minimum is clearly observed.

The comparisons of the results of SDT-SFA with s-SFA and the exact TDSE are shown in figure 2(a). In agreement with the TDSE, the SDT-SFA spectrum shows a weaker signature of the structural minimum. Remarkably, also the overall correspondence of SDT-SFA with the TDSE—both quantitative and qualitative—is substantially improved in comparison with the s-SFA. It should be reminded that the departure at the lowest part of the spectral *plateau* (harmonic orders <30th) is also found in the atomic case (figure 2(b)). As discussed before, it reflects a fundamental inaccuracy of the SFA approach, not connected to the atomic or molecular nature of the species.

We validate the SDT-SFA model for different laser parameters and internuclear distances. First, in figure 3 we present the HHG spectra considering different laser peak intensities and wavelengths. As a general conclusion, the SDT-SFA (green lines) reproduces very satisfactorily the exact TDSE results (blue lines).

On the other hand, tilted molecules present an effective internuclear distance smaller than the equilibrium one: $R_{\rm eff} = R_{\rm eq} \cos\theta$. Under such configurations the ratio of the tunnel probability of a distant wavepacket (equation (6)) increases, and the structural minimum shows up. Thus, we have chosen a smaller internuclear distance in order to study the capability of the SDT-SFA to reproduce the well-known structural minimum [4] in a configuration where it is evidenced. In figure 4 we present the HHG spectra and its corresponding time–frequency analysis for a different internuclear distance, $R = 0.6$Å, which would correspond to a rotation of $\theta = 53°$. The minimum appears in the TDSE spectrum at the harmonic order $q = 61$, approximately. While the standard SFA fails in predicting the minimum's depth, the SDT-SFA provides a better approach. Note that the time–frequency description of the SDT-SFA has also a better coincidence with the TDSE results. As pointed out before, the departures for harmonic orders below 30th are a consequence of the SFA, also present in the atomic case (figure 2(b)).

3.2. Extraction of the form factor from the harmonic spectra

A strong evidence of site-specificity in molecular tunnel ionization can be found directly from the exact TDSE using high-harmonic spectroscopy techniques to retrieve the form factor from the TDSE and compare it with our SDT proposal, equation (7). For that purpose, we follow the same philosophy used in tomographic studies and we compare the HHG molecular emission to that from an atom with similar

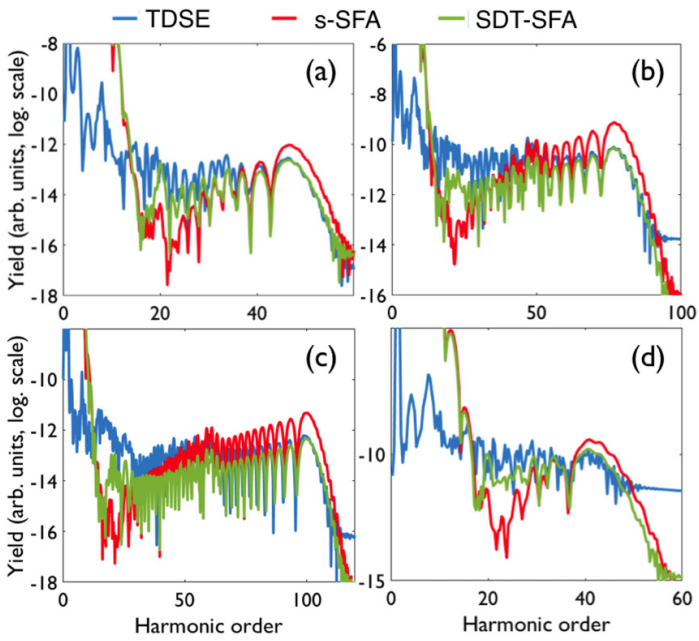

Figure 3. HHG spectra from the H_2^+ molecule at the internuclear distance of equilibrium, obtained through the exact TDSE (blue), s-SFA (red) and the SDT-SFA (green) for different laser peak intensities (3.88 fs FWHM, 800 nm): (a) $I = 2.19 \times 10^{14}$ W cm^{-2}, (b) $I = 4.92 \times 10^{14}$ W cm^{-2}, and different laser wavelengths (3.88 fs FWHM, $I = 3.42 \times 10^{14}$ W cm^{-2}): (c) 1220 nm, (d) 560 nm.

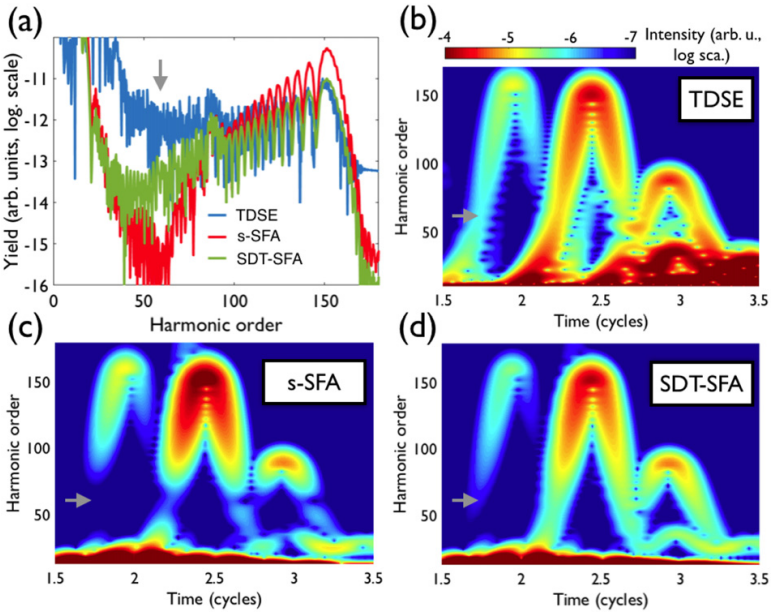

Figure 4. (a) HHG spectra from the H_2^+ molecule for a smaller internuclear distance ($R = 0.6$ Å, 800 nm, 3.88 fs FWHM, $I = 1.11 \times 10^{15}$ W cm^{-2}) for the exact TDSE (blue), the s-SFA (red) and the SDT-SFA (green). The time–frequency analysis of these spectra are shown at (b), (c) and (d), respectively. In this case the structural minimum (located at $q = 61$, as pointed out by the gray arrows) emerges in the TDSE but its depth is again in better agreement with the one of the SDT-SFA.

IOP Publishing New J. Phys. 22 (2020) 043012 L Rego et al

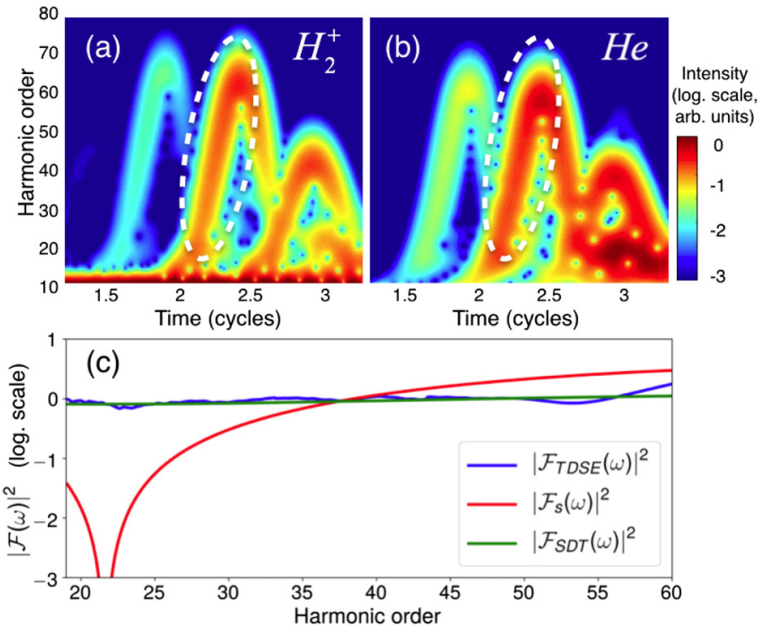

Figure 5. Time–frequency analysis of the HHG emission from the H_2^+ molecule (a) and the helium atom (b) for the same parameters as in figure 2(c) The form factor extracted from the TDSE calculations, $\mathcal{F}_{\rm TDSE}$, following equation (8) (blue) for the selected region within the white dashed lines in panels (a) and (b), is compared to the form factors from s-SFA, $\mathcal{F}_s$, (red) and SDT-SFA, $\mathcal{F}_{\rm SDT}$, (green).

ionization potential. Figures 5(a) and (b) show the time–frequency analysis corresponding to the TDSE harmonic spectra of figures 2(a) and (b), for H_2^+ and He respectively. These maps reveal that each harmonic in the *plateau* is emitted in a discrete series of bursts, corresponding to the rescattering of the different electron trajectories, the well-known short and long trajectories [19, 51]. We have selected the harmonic emission corresponding to a single rescattering event emitted from the short trajectories during a half-cycle of the driving field (as indicated with white dashed circles in figures 5(a) and (b)) and calculated the associated spectral amplitudes for both species: $a_{z,\rm He}(\omega)$ and $a_{z,H_2^+}(\omega)$. Then, the form factor can be retrieved as

$$|\mathcal{F}_{\rm TDSE}(\omega)|^2 \simeq a_{z,H_2^+}(\omega)/a_{z,\rm He}(\omega). \tag{8}$$

This assumption follows from the SFA saddle point method, which applied to the integrals in equation (4) leads to a simple identification of the harmonic spectral amplitudes and the quasiclassical electron trajectories [19]. After the saddle-point analysis, the Fourier transform of equation (4) can be cast into a simple expression [52]:

$$a_z(\omega) \propto \sum_{st} |\mathcal{F}_{\rm TDSE}(p'_{st})|^2\, \xi(\mathbf{P}_{st}, t_{st}, t_{1,st})\eta(\mathbf{P}_{st}), \tag{9}$$

where η includes the terms containing the electronic wavefunctions, χ_0, and ξ includes the remaining terms, except the form factor $\mathcal{F}_{\rm TDSE}$, which is to be determined from the TDSE. The summation in equation (9) extends over all saddle points, *st*, each representing a recolliding electron trajectory responsible of the harmonic emission at frequency $\omega = p'^2_{st}/2m\hbar$. Each rescattering corresponds to a term in the summation in equation (9), therefore, in selecting a single rescattering event from the TDSE time–frequency maps, we are isolating a single term in the summation. Thus, in this case, equation (8) follows directly from equation (9).

Figure 5(c) shows the comparison of the form factor extracted from the TDSE, $\mathcal{F}_{\rm TDSE}$, using equation (8), against the s-SFA form factor, $\mathcal{F}_s$, and the modified SDT-SFA version, $\mathcal{F}_{\rm SDT}$. The excellent agreement between $\mathcal{F}_{\rm SDT}$ and $\mathcal{F}_{\rm TDSE}$ strongly supports equation (7) and, therefore, our interpretation of distant tunneling as well as molecular site-dependent ionization. We note that evidences of the site-dependent ionization due to the distant tunneling may also be found implicity in photoionization studies where electron localization leads to an asymmetric molecular dissociation [53–55].

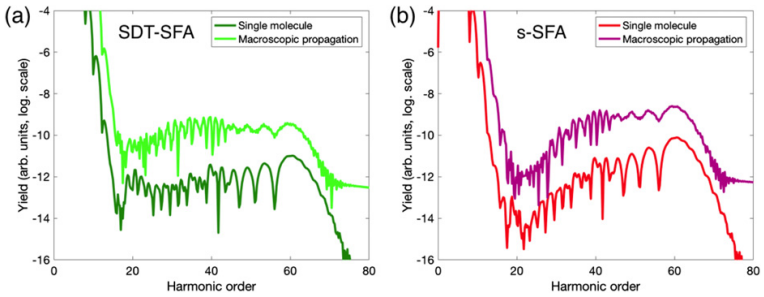

Figure 6. HHG spectra from macroscopic propagation calculated using the SDT-SFA (a) and s-SFA (b) for the same parameters as those of figure 2 qualitatively compared to the single-molecule case. The distinction between the two models survives upon propagation. For both cases, the relative yield between the spectra of the single-molecule and the macroscopic propagation is arbitrary.

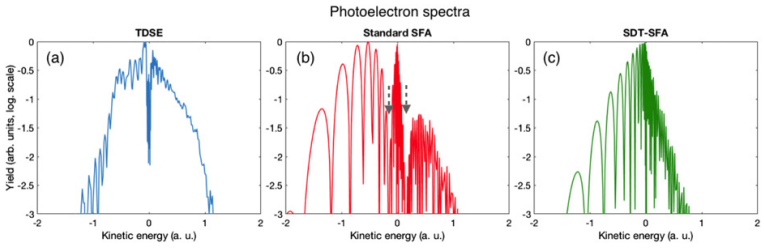

Figure 7. Photoelectron spectra from the H_2^+ molecule obtained using the TDSE (a), the standard SFA (b) and the SDT-SFA (c) models. The laser parameters and molecular configuration are the same as those of figure 2. The gray arrows in panel (b) indicate the presence of structural minima, which are not evidenced in the TDSE and SDT-SFA calculations. We have added a sign to the kinetic energy axis, according to the direction left (minus) or right (plus) of the ionized wavepacket.

3.3. Signature of the site-dependent tunnel-ionization in the propagated high-harmonic signal

We introduce the macroscopic picture in order to gain insight about the survival of the features of the single-molecule spectrum in an experimental situation. It is known that macrosocopic phase-matching can strongly influence the HHG spectrum measured in an experiment [56, 57]. In previous works, the experimental HHG spectrum has been used to retrieve the molecular orbital using tomographic techniques [13]. Therefore, it is important to know if the SDT features of the single-molecule HHG spectrum are also found in the macroscopic picture.

The macroscopic simulation of HHG in H_2^+ is based on the electromagnetic field propagator [58], in which we discretize the target (molecular gas jet) into elementary radiators. The dipole acceleration of each elementary source is computed using the SFA models described by equations (A21) and (B10). We assume that the harmonic radiation propagates with the vacuum phase velocity, which is a reasonable assumption for high-order harmonics. The low-density molecular gas jet, flowing along the perpendicular direction to the beam propagation is modelled as a Gaussian distribution of 200 μm at full width half maximum, and with a peak pressure of 5 torr. The driver field has a Gaussian profile with a beam waist at the focus position of 120 μm. All molecules are assumed to be oriented parallel to the polarization direction.

In figure 6, we show a qualitative comparison between the single-molecule and macroscopic HHG spectra for the SDT-SFA and the s-SFA models. The main features of the single-molecule spectrum calculated using both models are conserved in the macroscopic case and, although the shape of SDT-SFA spectra suffers modifications upon macroscopic propagation, it remains clearly distinct from the s-SFA results. Our results show that the main properties of the single-molecule HHG spectrum shown in figure 2 survive after macroscopic propagation.

3.4. Signatures of the site-dependent tunnel-ionization in the photoelectron spectra

In this section, we calculate the photoelectron spectra from the H_2^+ molecule along the z coordinate, $|\delta\Psi(P_z)|^2$, after the interaction with the pulse. In figure 7, we present the photoelectron spectra calculated from the TDSE (a), standard SFA (b) and SDT-SFA (c) models. We show that, while the SDT-SFA spectrum

IOP Publishing New J. Phys. 22 (2020) 043012 L Rego et al

exhibits a better agreement with the TDSE spectrum, the standard SFA spectrum presents two deep minima [59]. The origin of those minima is the interference of the ionization from each atomic orbital. The SDT-SFA, on the other hand, includes the side-dependency of the ionization, which sharply decreases the structural interference.

Note that, in order to obtain the photoelectron spectrum from the TDSE, we have filtered the fundamental state from the final wavefunction. As a result, an artificial minimum at the lowest kinetic energies appears in the spectrum.

4. Conclusions

In conclusion, we have demonstrated that the standard picture of tunnel ionization needs to be modified for the non-atomic case. Our exact computations of the TDSE in H_2^+ reveal that wavepacket portions located at the ion sites separated from the barrier ionize with lower probability. We propose a corrected molecular form factor to implement into the existing strong-field models. The new form factor agrees extremely well with the one extracted from the exact TDSE solution, and it improves both the HHG and photoelectron spectra. In addition, the signatures of the site-dependent tunneling are present in the HHG spectra for different laser parameters and molecular internuclear distances. We show that those spectral signatures are also present when the macroscopic phase-matching is taken into account. We believe that the implementation of the site-dependent corrections in the retrieval algorithms will improve substantially the accuracy of high-harmonic spectroscopy measurements, as well as tomographic orbital image reconstruction.

Acknowledgments

C H-G and L P acknowledge support from Junta de Castilla y León and European Union, FEDER (Project SA287P18), Spanish MICINN (FIS2016-75652 P). C H-G acknowledges Ministerio de Ciencia, Innovación y Universidades for a Ramón y Cajal contract (RYC-2017-22745), co-funded by the European Social Fund. L R acknowledges support from Ministerio de Educación, Cultura y Deporte (FPU16/02591). A P acknowledges support from Comunidad de Madrid through the TALENTO program with Reference No. 2017-T1/IND-5432. We thankfully acknowledge the computer resources at MareNostrum and the technical support provided by Barcelona Supercomputing Center
(FI-2019-1-0013).

Appendix A. Standard SFA description of molecular HHG

In this appendix, we present the standard (s-SFA) description of molecular high-order harmonic generation (HHG) within the strong-field approximation (SFA).

The interaction of a one-electron system with electromagnetic radiation, in the dipole approximation, is governed by the Hamiltonian

$$H(t) = \frac{p^2}{2m} + V_{\rm C}(\mathbf{r}) + V_{\rm F}(\mathbf{P}, t), \tag{A1}$$

where $V_{\rm C}(\mathbf{r})$ is the Coulombic potential and $V_{\rm F}(\mathbf{P}, t) = -(q/mc)\mathbf{A}(t)\cdot\mathbf{P} + (q^2/2mc^2)A^2(t)$, being $\mathbf{A}(t)$ the vector potential of the laser field, $\mathbf{P}$ the canonical momentum and m and q the mass and the charge of the electron, respectively.

The standard SFA approach is based in the assumption that, once ionized, the electron dynamics is governed by the field interaction, neglecting the effect of the ion Coulombic potential. The SFA propagator is written as [18]

$$G_{\rm SFA}(t, t_0) = G_0(t, t_0) + \frac{1}{\hbar}\int_{t_0}^{t} G_{\rm F}(t, t_1)V_{\rm F}(t_1)G_0(t_1, t_0)\mathrm{d}t_1, \tag{A2}$$

where G_0 is the propagator of the non-interacting Hamiltonian, $H_0 = \frac{p^2}{2m} + V_{\rm C}(\mathbf{r})$, and $G_{\rm F}$ is the propagator of the free electron in the electromagnetic field, described by $H_F(t) = \frac{p^2}{2m} + V_{\rm F}(t)$. Within SFA, the electron's wavefunction is given by $|\psi(t)\rangle = iG_{SFA}(t, t_0)|\phi_0\rangle$, with $|\phi_0\rangle$ an initial bound-state of the system. We can split the wavefunction into two terms, $|\psi(t)\rangle = |\phi_0(t)\rangle + |\delta\psi(t)\rangle$, with $|\phi_0(t)\rangle = iG_0(t, t_0)|\phi_0\rangle$ the bound electron evolving in the absence of the field, and

$$|\delta\psi(t)\rangle = \frac{\mathrm{i}}{\hbar}\int_{t_0}^{t} G_{\rm F}(t, t_1)V_{\rm F}(t_1)G_0(t_1, t_0)|\phi_0\rangle\mathrm{d}t_1 \tag{A3}$$

the electron in the continuum. Defining ϵ_0 as the bound-state energy, we have $G_0(t_1,t_0)|\phi_0\rangle = -\mathrm{i}\mathrm{e}^{-\mathrm{i}\epsilon_0(t_1-t_0)/\hbar}|\phi_0\rangle$. For the electron in the continuum, we resort to the Volkov basis [47]: $|\mathbf{P}(t)\rangle = \mathrm{e}^{\mathrm{i}\frac{1}{\hbar}S(\mathbf{P},t,t_0)}|\mathbf{P}\rangle$, with $S(\mathbf{P},t,t_0)$ is the action defined as $S(\mathbf{P},t,t_0) = -\frac{1}{2m}\int_{t_0}^{t} p^2(\tau)\mathrm{d}\tau$, with $\mathbf{p}(t) = \mathbf{P} - (q/c)\mathbf{A}(t)$, the kinetic momentum. Accordingly, the free electron propagator can be expressed in the Volkov basis as $G_\mathrm{F}(t,t_1) = -\mathrm{i}\int \mathrm{e}^{\mathrm{i}\frac{1}{\hbar}S(\mathbf{P},t,t_1)}|\mathbf{P}\rangle\langle\mathbf{P}|\mathrm{d}\mathbf{P}$. Using these definitions in (A3) the ionized electron wavefunction in momentum space reads as

$$\delta\psi(\mathbf{P},t) = \langle\mathbf{P}|\delta\psi(t)\rangle = -\frac{\mathrm{i}}{\hbar}\int_{t_0}^{t}\mathrm{e}^{\mathrm{i}\frac{1}{\hbar}S(\mathbf{P},t,t_1)}\mathrm{e}^{-\mathrm{i}\epsilon_0(t_1-t_0)/\hbar}V_\mathrm{F}(\mathbf{P},t_1)\eta(\mathbf{P})\mathrm{d}t_1, \tag{A4}$$

where $\eta(\mathbf{P})$ is the transition matrix element

$$\eta(\mathbf{P}) = \langle\mathbf{P}|\frac{C_\mathrm{F}}{r^n}|\phi_0\rangle, \tag{A5}$$

where the factor C_F/r^n is a Coulomb correction [33] that improves the quantitative accuracy of the SFA description [21, 60], with $C_\mathrm{F} = [4|\epsilon_0|/(|q|E_0)]^2$ and $n = \left(Zq^2/\hbar\right)\sqrt{m/2|\epsilon_0|}$, Z being the charge of the atomic or ionic core ($Z = 1$ for the hydrogen atom and $Z = 2$ for H_2^+).

The coherent radiation spectrum is proportional to the Fourier transform of the mean acceleration. Since we are interested only in high-harmonics, we compute the complex acceleration amplitude as [21]

$$\langle\mathbf{a}(t)\rangle = \int \frac{p^2/2m - \epsilon_0}{\Delta_s}\mathbf{a}(\mathbf{P},t)\mathrm{d}\mathbf{P}, \tag{A6}$$

with

$$\mathbf{a}(\mathbf{P},t) = (1/m)\langle\phi_0(t)|(-\nabla V_C)|\mathbf{P}\rangle\delta\psi(\mathbf{P},t) \tag{A7}$$

being the contribution of each Volkov wave to the total acceleration. The prefactor of the integrand in (A6) accounts for the boundstate dressing at the instant of recollision, necessary to describe the harmonic yield with quantitative accuracy, ϵ_0 being the energy of the bound orbital and Δ_s the Stark shift at the instant of recollision [21, 61]. This formulation has been previously applied to atoms successfully, and an example is shown in figure 2(b).

Let us now introduce the extension of this SFA description to molecules, named as standard SFA (s-SFA) in this paper. We describe the molecular hydrogen ion ground state as a linear combination of atomic orbitals (LCAO), with two centers at $\pm R/2$, $R = 2$ a.u being the internuclear distance. The LCAO are described with a 6-311G Pople basis, and determined from a variational calculation. For the case of H_2^+ we have three basis in each molecular site, $\mathbf{R}_i$ defined as

$$\begin{aligned}
\Phi_{1s}(\mathbf{r}) &= 0.025\,4938\,g_s(33.865\,0000,\mathbf{r}) + 0.190\,3730\,g_s(5.094\,7900,\mathbf{r}) + 0.852\,1610\,g_s(1.158\,7900,\mathbf{r})\\
\Phi_{2s}(\mathbf{r}) &= 1.000\,0000\,g_s(0.325\,8400,\mathbf{r})\\
\Phi_{3s}(\mathbf{r}) &= 1.000\,0000\,g_s(0.102\,7410,\mathbf{r})
\end{aligned} \tag{A8}$$

being $g_s(\alpha,\mathbf{r}) = (2\alpha/\pi)^{3/4}\mathrm{e}^{-\alpha r^2}$. By using Hartree–Fock, the molecular orbital for the ground state is found to be:

$$\phi_0(\mathbf{r},t=0) = C\left[\chi_0\left(\mathbf{r} - \frac{R}{2}\mathbf{e}_z\right) + \chi_0\left(\mathbf{r} + \frac{R}{2}\mathbf{e}_z\right)\right], \tag{A9}$$

where C is the normalization factor and

$$\chi_0(\mathbf{r}) = 0.1937\ \Phi_{1s}(r) + 0.3990\ \Phi_{2s}(r) + 0.0484\ \Phi_{3s}(r). \tag{A10}$$

Thus, the time-dependent molecular orbital can be expressed as

$$\phi_0(\mathbf{r},t) = C\mathrm{e}^{-\mathrm{i}\epsilon_0(t-t_0)/\hbar}\left[\chi_0\left(\mathbf{r} - \frac{R}{2}\mathbf{e}_z\right) + \chi_0\left(\mathbf{r} + \frac{R}{2}\mathbf{e}_z\right)\right] \rightarrow |\phi_0(t)\rangle = C\left(\mathrm{e}^{-\frac{\mathrm{i}}{\hbar}\hat{p}_z'(t)\frac{R}{2}} + \mathrm{e}^{\frac{\mathrm{i}}{\hbar}\hat{p}_z'(t)\frac{R}{2}}\right)|\chi_0(t)\rangle, \tag{A11}$$

where $|\chi_0(t)\rangle = \mathrm{e}^{-\mathrm{i}\epsilon_0(t-t_0)/\hbar}|\chi_0\rangle$ and the binding energy is calculated to be $\epsilon_0 = -29.65$ eV (-1.09 a.u.). Consequently, the ionized wavefunction can be written as

$$|\delta\Psi(t)\rangle = C\left(\mathrm{e}^{-\frac{\mathrm{i}}{\hbar}\hat{p}_z'(t)\frac{R}{2}} + \mathrm{e}^{\frac{\mathrm{i}}{\hbar}\hat{p}_z'(t)\frac{R}{2}}\right)|\delta\psi(t)\rangle, \tag{A12}$$

IOP Publishing New J. Phys. 22 (2020) 043012 L Rego et al

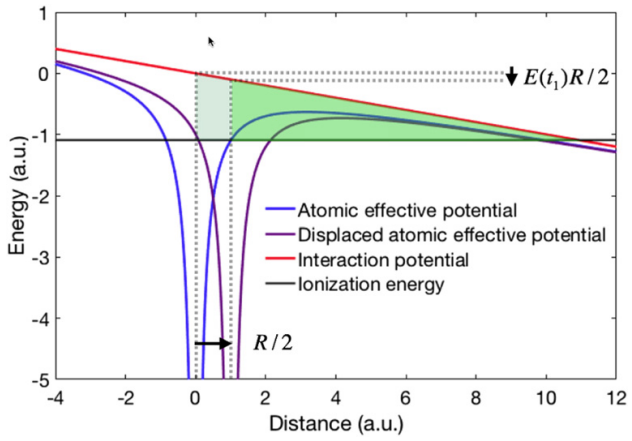

Figure 8. Scheme of the dipole energy shift of the potential barrier's maximum due to the molecular configuration. An atomic potential (blue) is displaced $R/2$ from the origin (purple) under the presence of an external field (red). As a consequence, the height of the potential barrier (green) seen by the electronic wavepacket (whose ionization potential is depicted in black) decreases in an amount of $E(t_1)R/2$.

where $\hat{p}'_z(t)$ is the projection of the kinetic momentum operator, as seen from the molecular well (see below). The expression for $|\delta\psi(t)\rangle$ in equation (A4) should be corrected to take into account the dipole energy shift of the barrier's maximum, as the molecule is an extended object. For a symmetric aligned molecule of length R, the change in the barrier height affects the ionization probability by a fraction $W_{\rm ADK}[\epsilon(R/2,t_1)]/W_{\rm ADK}(\epsilon_0)$, where $\epsilon(R/2,t_1)=\epsilon_0-q|\mathbf{E}(t_1)|R/2$ is the ionization potential as seen from the top of the barrier at the ionization time t_1 (see figure 8). $W_{\rm ADK}$ is the Ammosov–Delone–Krainov the ionization rate [34]

$$W_{\rm ADK}(\epsilon)=\left(\frac{2e}{n^*}\right)^{2n^*}\frac{1}{2\pi n^*}\frac{(2\ell+1)(\ell+|m|)!}{2^{|m|}|m|!(\ell-|m|)!}|\epsilon|\left[\frac{3E_0}{\pi(2|\epsilon|)^{3/2}}\right]^{1/2}\times\left[\frac{2}{E_0}(2|\epsilon|)^{3/2}\right]^{2n^*-|m|-1}\mathrm{e}^{-\left(\frac{2(2|\epsilon|)^{3/2}}{3E_0}\right)}, \tag{A13}$$

where e is the Euler number, m and ℓ are the quantum numbers of the atomic orbital, E_0 is the amplitude of the electric field and

$$n^*(\epsilon)=\frac{Zq^2}{\hbar}\sqrt{\frac{m}{2|\epsilon|}}. \tag{A14}$$

We implement this correction including the probability ratio into the bound-to-continuum amplitude probability, thus, redefining η in equation (A4) as

$$\eta(\mathbf{P},t_1)=\left[\frac{W_{\rm ADK}[\epsilon(R/2,t_1)]}{W_{\rm ADK}(\epsilon_0)}\right]^{1/2}\langle\mathbf{P}|\frac{C_{\rm F}}{r^n}|\chi_0\rangle, \tag{A15}$$

where R is the equilibrium internuclear distance ($R=1.055\,\text{Å}=2$ a.u.).

Equations (A7), (A11) and (A12), lead to the following expression for the dipole acceleration for the H_2^+ molecule,

$$\mathbf{a}(\mathbf{P},t)=\frac{C^2}{m}\langle\chi_0(t)|\left(\mathrm{e}^{\frac{\mathrm{i}}{\hbar}\hat{p}'_z(t)\frac{R}{2}}+\mathrm{e}^{-\frac{\mathrm{i}}{\hbar}\hat{p}'_z(t)\frac{R}{2}}\right)(-\nabla V_{\rm M})|\mathbf{P}\rangle\langle\mathbf{P}|\left(\mathrm{e}^{-\frac{\mathrm{i}}{\hbar}\hat{p}'_z(t)\frac{R}{2}}+\mathrm{e}^{\frac{\mathrm{i}}{\hbar}\hat{p}'_z(t)\frac{R}{2}}\right)|\delta\psi(t)\rangle, \tag{A16}$$

$V_{\rm M}$ where is the Coulomb molecular potential. For H_2^+, $V_{\rm M}$ can be written as a superposition of the hydrogen potential at the ionic sites, $V_{\rm M}(\mathbf{r})=V_{\rm C}\left(\mathbf{r}-\frac{R}{2}\mathbf{e}_z\right)+V_{\rm C}\left(\mathbf{r}+\frac{R}{2}\mathbf{e}_z\right)$. The dipole acceleration $\mathbf{a}(\mathbf{P},t)$, therefore, results from the added contributions of eight different physical paths (see figure 9). Naming $\{\alpha,\beta,\gamma\}$ the sign of the displacements ($+1$ for right and -1 for left) of the recombination wavefunction $\chi_0(\mathbf{r}-\alpha R/2)$, the rescattering potential $V_{\rm C}\left(\mathbf{r}-\beta R/2\right)$, and the ionizing wavefunction $\chi_0(\mathbf{r}-\gamma R/2)$, respectively, we rewrite (A16) as the sum over the different paths $\mathbf{a}(\mathbf{P},t)=\sum_{\alpha,\beta,\gamma}\mathbf{a}^{\alpha,\beta,\gamma}(\mathbf{P},t)$, where

$$\mathbf{a}^{\alpha\beta\gamma}(\mathbf{P},t)=\frac{C^2}{m}\langle\chi_0(t)|\left\{\mathrm{e}^{\frac{\mathrm{i}}{\hbar}\hat{p}'_z\alpha\frac{R}{2}}\left[-\nabla V_{\rm C}\left(\mathbf{r}-\beta\frac{R}{2}\mathbf{e}_z\right)\right]|\mathbf{P}\rangle\langle\mathbf{P}|\mathrm{e}^{-\frac{\mathrm{i}}{\hbar}\hat{p}'_z\gamma\frac{R}{2}}\right\}|\delta\psi(t)\rangle. \tag{A17}$$

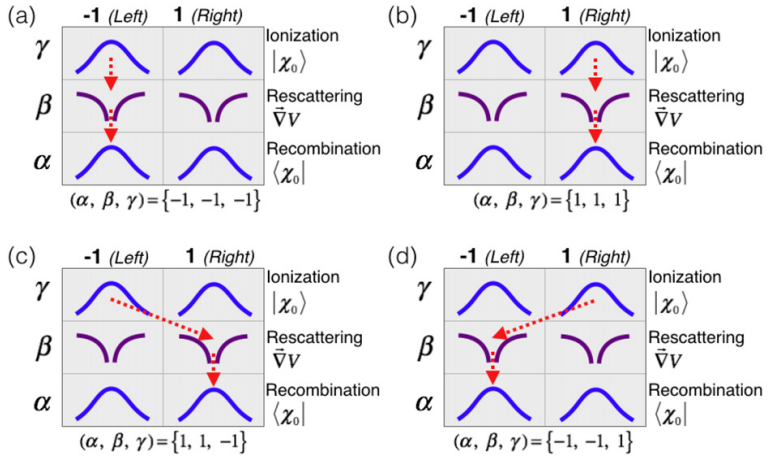

Figure 9. Scheme of the main different paths followed by the electronic wavepacket contributing to the HHG spectrum. The atomic orbitals are depicted in blue and the scattering with the Coulombic potential is depicted in purple. The γ index refers to the atomic orbital from which the electronic wavepacket is ionized, the β index refers to the atomic potential responsible of the rescattering and the α index refers to the atomic orbital where the wavepacket recombines. The four main paths (a), (b), (c) and (d), are represented by the red arrows.

Our calculations show that the main contributions come from terms with $\alpha = \beta$, meaning that the scattering on a potential site is most probably followed by a recombination to the same site's bound wavefunction. Thus, using

$$-\nabla V_{\mathrm{C}}\left(\mathbf{r}-\beta\frac{R}{2}\mathbf{e}_z\right) = \mathrm{e}^{-\frac{\mathrm{i}}{\hbar}\hat{p}'_z\beta\frac{R}{2}}\left(-\nabla V_{\mathrm{C}}(\mathbf{r})\right)\mathrm{e}^{\frac{\mathrm{i}}{\hbar}\hat{p}'_z\beta\frac{R}{2}} \tag{A18}$$

we can approximate equation (A17) to

$$\mathbf{a}^{\beta\gamma}(\mathbf{P},t) \simeq \frac{C^2}{m}\langle\chi_0(t)|\left[-\nabla V_{\mathrm{C}}(\mathbf{r})\right]|\mathbf{P}\rangle\mathrm{e}^{\frac{\mathrm{i}}{\hbar}p'_z(\beta-\gamma)\frac{R}{2}}\langle\mathbf{P}|\delta\psi(t)\rangle. \tag{A19}$$

For a free electron $\mathbf{p}'(t) = \mathbf{p}(t) = \mathbf{P} - (q/c)\mathbf{A}(t)$, with $\mathbf{A}(t)$ the electromagnetic vector potential. In molecules, however, $\mathbf{p}'(t)$ describes the kinetic momentum of the free electron at the instant of recombination, t, as seen from the molecular sites, so it includes the acceleration by the potential well, i.e. $(1/2m)p'^2(t) = (1/2m)p^2(t) + I_P$, I_P being the molecular ionization potential. Therefore $p'_z(t) = \mathrm{sign}\{p_z(t)\}\sqrt{p^2(t) + 2mI_P}$ [48]. This correction to the free electron's kinetic momentum is found necessary to recover the correct position of the molecular structural minimum in the harmonic spectrum [4]. Summing over all the relevant paths, the acceleration $\mathbf{a}(\mathbf{P},t)$ can be written as

$$\mathbf{a}(\mathbf{P},t) = \frac{1}{m}|\mathcal{F}_s\left[p'_z(t)\right]|^2\langle\chi_0(t)|(-\nabla V_{\mathrm{C}})|\mathbf{P}\rangle\delta\psi(\mathbf{P},t), \tag{A20}$$

where $\mathcal{F}_s\left[p'_z(t)\right] = C(\mathrm{e}^{\frac{\mathrm{i}}{\hbar}p'_z(t)\frac{R}{2}} + \mathrm{e}^{-\frac{\mathrm{i}}{\hbar}p'_z(t)\frac{R}{2}})$ is the molecular form-factor. Substituting in equation (A6), we finally obtain the total acceleration

$$\langle\mathbf{a}(t)\rangle = \int\frac{p^2/2m-\epsilon_0}{\Delta_s}\frac{1}{m}\langle\chi_0(t)|(-\nabla V_{\mathrm{C}})|\mathbf{P}\rangle|\mathcal{F}_s\left[p'_z(t)\right]|^2 \times\left\{-\frac{\mathrm{i}}{\hbar}\int_{t_0}^{t}\mathrm{e}^{\mathrm{i}\frac{1}{\hbar}S(\mathbf{P},t,t_1)}\mathrm{e}^{-\mathrm{i}\frac{\epsilon_0}{\hbar}(t_1-t_0)}V_{\mathrm{F}}(\mathbf{P},t_1)\eta(\mathbf{P},t_1)\mathrm{d}t_1\right\}\mathrm{d}\mathbf{P}. \tag{A21}$$

Appendix B. Tunnel of a distant wavepacket

In this appendix, we compute the tunnel probability of a wavepacket located at a finite distance from the barrier's edge. In a description using localized atomic orbitals (LAO), the molecular orbital is decomposed into a basis of wavepackets, each centered at a different ion site. In molecules at equilibrium nuclear distances, these localized wavefunctions are generally not separated by internal potential barriers, therefore

IOP Publishing New J. Phys. 22 (2020) 043012 L Rego et al

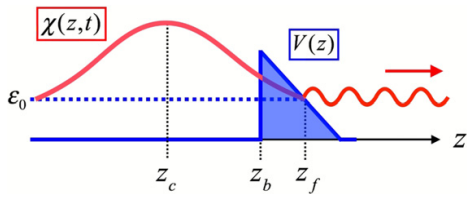

Figure 10. Scheme of the tunneling of a distant wavepacket. The wavefunction $\chi(z,t)$ (red) is centered at z_c and its energy is ϵ_0, while the blue triangle is the potential barrier $V(z)$ whose edges are placed at z_b and z_f.

dwelling in a multi-ion Coulomb potential well. The presence of a strong field modulates the molecular potential, forming an external potential barrier, that separates the bound orbitals from the continuum. The extended nature of the molecular well, therefore, results in some of the LAO positioned at finite, non zero, distances from the edge of the barrier (see figure 1 in the main text).

Let us consider a stationary wavepacket with energy ϵ_0 centered at the coordinate z_c, at the left of a potential barrier $V(z)$. The barrier's edges z_b and z_f are defined so that $V(z) = 0$ if $z < z_b$, and $V(z) > \epsilon_0$ if $z_b < z < z_f$ (see figure 10).

We express the wavepacket as a planewave decomposition, $\chi(z,t) = \mathrm{e}^{-\mathrm{i}\epsilon_0 t/\hbar}\chi_0(z)$, with

$$\chi_0(z) = \int_{-\infty}^{\infty} \tilde{g}(p)\mathrm{e}^{\mathrm{i}S(p,z)/\hbar}\mathrm{e}^{\mathrm{i}p(z-z_c)/\hbar}\mathrm{d}p \simeq \int_{-\infty}^{\infty} \tilde{g}(p)\mathrm{e}^{\mathrm{i}S_{\mathrm{WKB}}(z)/\hbar}\mathrm{e}^{-\mathrm{i}pz_c/\hbar}\mathrm{d}p, \tag{B1}$$

where we have defined $S_{\mathrm{WKB}}(z) = \int_{-\infty}^{z}\sqrt{2m\left[\epsilon - V(z')\right]}\mathrm{d}z'$ as the semiclassical approximation ($\hbar \to 0$) to the planewave phase $S(p,z) + pz$, according to the 0th-order WKB approximation [62]. Note that it is crucial to preserve the localized nature of the wavepacket, therefore the 0th order WKB approximation is used at the level of the individual planewaves composing it, rather that to the total wavefunction. We can rewrite equation (B1) as

$$\chi(z,t) = \mathrm{e}^{-\mathrm{i}\epsilon_0 t/\hbar}\mathrm{e}^{\mathrm{i}S_{\mathrm{WKB}}(z)/\hbar}\int_{-\infty}^{\infty}\tilde{g}(p)\mathrm{e}^{-\mathrm{i}pz_c/\hbar}\mathrm{d}p. \tag{B2}$$

Defining $S_{\mathrm{WKB}}(z_b)$ as the semiclassical approximation to $S(p,z_b) + pz_b$, equation (B2) can be approximated by

$$\chi_0(z) \simeq \mathrm{e}^{\mathrm{i}\left[S_{\mathrm{WKB}}(z) - S_{\mathrm{WKB}}(z_b)\right]/\hbar}\int_{-\infty}^{\infty}\tilde{g}(p)\mathrm{e}^{\mathrm{i}S(p,z_b)}\mathrm{e}^{\mathrm{i}p(z_b-z_c)/\hbar}\mathrm{d}p \tag{B3}$$

$$= \mathrm{e}^{\mathrm{i}\left[S_{\mathrm{WKB}}(z) - S_{\mathrm{WKB}}(z_b)\right]/\hbar}\chi_0(z_b). \tag{B4}$$

The tunnel transmission probability of the particle located at the wavepacket's mean position z_c, is therefore given by

$$P(z_c,z_b) = \frac{|\chi_0(z_f)|^2}{|\chi_0(z_c)|^2} = W_{\mathrm{WKB}}\frac{|\chi_0(z_b)|^2}{|\chi_0(z_c)|^2}, \tag{B5}$$

where W_{WKB} corresponds to the WKB probability of tunneling of a particle located at the left edge of the barrier [62],

$$W_{\mathrm{WKB}} = \mathrm{e}^{-\frac{2}{\hbar}\int_{z_b}^{z_f}\sqrt{2m\left[V(z')-\epsilon_0\right]}\mathrm{d}z'}. \tag{B6}$$

Therefore, equation (B5) can be interpreted as the probability of tunneling times the probability of the particle being near the edge of the barrier. The quotient in equation (B5) shows that the tunnel probability is reduced when the wavepacket's center is at a distance $z_b - z_c$ from the edge of the barrier. We define the ratio of the tunnel amplitude probability of a distant wavepacket to the amplitude probability of the particle being at the barrier's edge is given by

$$T(z_c,z_b) = \left[\frac{P(z_c,z_b)}{P(z_b,z_b)}\right]^{1/2} = \frac{|\chi_0(z_b)|}{|\chi_0(z_c)|}. \tag{B7}$$

In the case of the H_2^+ molecule, the wavepackets χ_0 are atomic orbitals localized at the molecular ion sites, $z_c = \pm R/2$, where R is the internuclear distance. The coordinate of the barrier's edge, z_b, corresponds approximately to $-R/2$ ($R/2$) for a positive (negative) field amplitude. To introduce the site-dependent probabilities in the SFA formalism it is sufficient to redefine the molecular form factor, $\mathcal{F}_s\left[p_z'(t)\right]$, in the

s-SFA formula (A21) as

$$\mathcal{F}^{\pm}_{\rm SDT}\left[p'_z(t)\right] = T\left(-\frac{R}{2}, \pm\frac{R}{2}\right) e^{\frac{i}{\hbar}p'_z(t)\frac{R}{2}} + T\left(\frac{R}{2}, \pm\frac{R}{2}\right) e^{-\frac{i}{\hbar}p'_z(t)\frac{R}{2}}, \tag{B8}$$

where the positive (negative) index corresponds to ionization through a barrier at the right (left) side of the molecule. Note however that the modulus of the form factor is the same, regardless the right/left position of the barrier, and therefore we can drop the superindex,

$$|\mathcal{F}_{\rm SDT}\left[p'_z(t)\right]|^2 = |\mathcal{F}^{+}_{\rm SDT}\left[p'_z(t)\right]|^2 = |\mathcal{F}^{-}_{\rm SDT}\left[p'_z(t)\right]|^2. \tag{B9}$$

Therefore equation (A21) finally becomes

$$\begin{aligned}\langle \mathbf{a}(t)\rangle = \int \frac{p'/2m - \epsilon_0}{\Delta_s}\frac{1}{m}\langle\chi_0|(-\nabla V_{\rm C})|\mathbf{P}\rangle|\mathcal{F}_{\rm SDT}\left[p'_z(t)\right]|^2 e^{i\frac{\epsilon_0}{\hbar}(t-t_0)} \\ \times\left\{-\frac{i}{\hbar}\int_{t_0}^{t} e^{i\frac{1}{\hbar}S(\mathbf{P},t,t_1)} e^{-i\frac{\epsilon_0}{\hbar}(t_1-t_0)} V_{\rm F}(\mathbf{P},t_1)\langle\mathbf{P}|\frac{C_{\rm F}}{r^n}|\chi_0\rangle dt_1\right\} d\mathbf{P}.\end{aligned} \tag{B10}$$

The new form factor, $\mathcal{F}_{\rm SDT}$, defines the difference between the standard SFA (s-SFA) and the site-dependent-tunneling SFA (SDT-SFA) proposed in this work.

ORCID iDs

Laura Rego https://orcid.org/0000-0002-7214-7402
Carlos Hernández-García https://orcid.org/0000-0002-6153-2647
Antonio Picón https://orcid.org/0000-0002-6142-3440
Luis Plaja https://orcid.org/0000-0001-8709-7295

References

[1] Corkum P B 1993 Plasma perspective on strong field multiphoton ionization *Phys. Rev. Lett.* **71** 1994
[2] Schafer K J, Yang B, DiMauro L F and Kulander K C 1993 Above threshold ionization beyond the high harmonic cutoff *Phys. Rev. Lett.* **70** 1599
[3] Peng P, Marceau C and Villeneuve D 2019 Attosecond imaging of molecules using high harmonic spectroscopy *Nat. Rev. Phys.* **1** 144
[4] Lein M, Hay N, Velotta R, Marangos J P and Knight P L 2002 Interference effects in high-order harmonic generation with molecules *Phys. Rev.* A **66** 023805
[5] Lein M, Hay N, Velotta R, Marangos J P and Knight P L 2002 Role of the intramolecular phase in high-harmonic generation *Phys. Rev. Lett.* **88** 183903
[6] Lein M, Corso P P, Marangos J P and Knight P L 2003 Orientation dependence of high-order harmonic generation in molecules *Phys. Rev.* A **67** 023819
[7] Baker S *et al* 2008 Dynamic two-center interference in high-order harmonic generation from molecules with attosecond nuclear motion *Phys. Rev. Lett.* **101** 053901
[8] Haessler S *et al* 2010 Attosecond imaging of molecular electronic wavepackets *Nat. Phys.* **6** 200206
[9] Yun H, Lee K-M, Sung J H, Kim K T, Kim H T and Nam C H 2015 Resolving multiple molecular orbitals using two-dimensional high-harmonic spectroscopy *Phys. Rev. Lett.* **114** 153901
[10] Luu T T, Garg M, Kruchinin S Y, Moulet A, Hassan M T and Goulielmakis E 2015 Extreme ultraviolet high-harmonic spectroscopy of solids *Nature* **521** 498
[11] Silva R E F, Blinov I V, Rubtsov A N, Smirnova O and Ivanov M 2018 High-harmonic spectroscopy of ultrafast many-body dynamics in strongly correlated systems *Nat. Photon.* **12** 266
[12] Landsman A S, Weger M, Maurer J, Boge R, Ludwig A, Heuser S, Cirelli C, Gallmann L and Keller U 2014 Ultrafast resolution of tunneling delay time *Optica* **1** 343–9
[13] Itatani J, Levesque J, Zeidler D, Niikura H, Pépin H, Kieffer J C, Corkum P B and Villeneuve D M 2004 Tomographic imaging of molecular orbitals *Nature* **432** 867871
[14] Patchkovskii S, Zhao Z, Brabec T and Villeneuve D M 2006 High harmonic generation and molecular orbital tomography in multielectron systems: Beyond the single-active-electron approximation *Phys. Rev. Lett.* **97** 123003
[15] Ciriolo A G, Devetta M, Faccialà D, Geetha P P, Pusala A, Vozzi C and Stagira S 2018 Molecular orbital tomography based on high-order harmonic generation: principles and perspectives *Advances in the Application of Lasers in Materials Science* ed P M Ossi (Berlin: Springer) 274 pp 191–216
[16] Keldysh L V 1965 Ionization in the field of a strong electromagnetic wave *Zh. Eksp. Teor. Fiz.* **20** 1307
[17] Faisal F H M 1973 Multiple absorption of laser photons by atoms *J. Phys. B: At. Mol. Phys.* **6** L89
[18] Reiss H R 1980 Effect of an intense electromagnetic field on a weakly bound system *Phys. Rev.* A **22** 1786
[19] Lewenstein M, Balcou P, Ivanov M Y, L'Huillier A and Corkum P B 1994 Theory of high-harmonic generation by low-frequency laser fields *Phys. Rev.* A **49** 2117
[20] Salières P *et al* 2001 Feynman's path-integral approach for intense-laser-atom interactions *Science* **292** 902
[21] Pérez-Hernández J A, Roso L and Plaja L 2009 Harmonic generation beyond the strong-field approximation: the physics behind the short-wave-infrared scaling laws *Opt. Express* **17** 9891

[22] Chirilă C C and Lein M 2006 Strong-field approximation for harmonic generation in diatomic molecules *Phys. Rev.* A **73** 023410
[23] Zhou X X, Tong X M, Zhao Z X and Lin C D 2005 Alignment dependence of high-order harmonic generation from and molecules in intense laser fields *Phys. Rev.* A **72** 033412
[24] Zimmermann B, Lein M and Rost J M 2005 Analysis of recombination in high-order harmonic generation in molecules *Phys. Rev.* A **71** 033401
[25] Lagmago Kamta G and Bandrauk A D 2005 Three-dimensional time-profile analysis of high-order harmonic generation in molecules: Nuclear interferences in H_2^+ *Phys. Rev.* A **71** 053407
[26] Vozzi C, Negro M, Calegari F, Sansone G, Nisoli M, De Silvestri S and Stagira S 2011 Generalized molecular orbital tomography *Nat. Phys.* **7** 822
[27] Miller M R, Jarón-Becker A and Becker A 2016 High-harmonic spectroscopy of laser-driven nonadiabatic electron dynamics in the hydrogen molecular ion *Phys. Rev.* A **93** 013406
[28] Smirnova O, Mairesse Y, Patchkovskii S, Dudovich N, Villeneuve D, Corkum P and Yu M 2009 Ivanov, High harmonic interferometry of multi-electron dynamics in molecules *Nature* **460** 972–7
[29] Baker S, Robinson J S, Haworth C A, Teng H, Smith R A, Chirilă C C, Lein M, Tisch J W G and Marangos J P 2006 Probing proton dynamics in molecules on an attosecond time scale *Science* **312** 424–7
[30] Wagner N, Wuest A, Christov I, Popmintchev T, Zhou X, Murnane M and Kapteyn H 2006 Monitoring molecular dynamics using coherent electrons from high harmonic generation *Proc. Natl Acad. Sci. USA* **103** 13279
[31] Blaga C I, Xu J, DiChiara A D, Sistrunk E, Zhang K, Agostini P, Miller T A, DiMauro L F and Lin C D 2012 Imaging ultrafast molecular dynamics with laser-induced electron diffraction *Nature* **483** 194197
[32] Perelomov A M, Popov V S and Terentev M V 1966 Ionization of atoms in an alternating electric field *Zh. Eksp. Teor. Fiz.* **50** 1393
[33] Krainov V P 1997 Ionization rates and energy and angular distributions at the barrier-suppression ionization of complex atoms and atomic ions *J. Opt. Soc. Am. B.* **14** 425–31
[34] Ammosov M V, Delone N B and Krainov V P 1986 Tunnel ionization of complex atoms and of atomic ions in an alternating electromagnetic fiel *Zh. Eksp. Teor. Fiz.* **91**
[35] Tong X M, Zhao Z X and Lin C D 2002 Theory of molecular tunneling ionization *Phys. Rev.* A **66** 033402
[36] Muth-Böhm J, Becker A and Faisal F H M 2000 Suppressed molecular ionization for a class of diatomics in intense femtosecond laser fields *Phys. Rev. Lett.* **85** 2280
[37] Tolstikhin O I, Morishita T and Madsen L B 2011 Theory of tunneling ionization of molecules: weak-field asymptotics including dipole effects *Phys. Rev.* A **84** 053423
[38] Murray R, Spanner M, Patchkovskii S and Ivanov M Y 2011 Tunnel ionization of molecules and orbital imaging *Phys. Rev. Lett.* **106** 173001
[39] Liu M and Liu Y 2016 Application of the partial-Fourier-transform approach for tunnel ionization of molecules *Phys. Rev.* A **93** 043426
[40] Labeye M, Risoud F, Lévêque C, Caillat J, Maquet A, Shaaran T, Salières P and Taïeb R 2019 Dynamical distortions of structural signatures in molecular high-order harmonic spectroscopy *Phys. Rev.* A **99** 013412
[41] Zuo T, Chelkowski S and Bandrauk A D 1993 Harmonic generation by the H_2^+ molecular ion in intense laser fields *Phys. Rev.* A **48** 3837
[42] Hay N, Velotta R, Lein M, de Nalda R, Heesel E, Castillejo M and Marangos J P 2002 High-order harmonic generation in laser-aligned molecules *Phys. Rev.* A **65** 053805
[43] Lara-Astiaso M, Silva R E F, Gubaydullin A, Rivière P, Meier C and Martín F 2016 Enhancing high-order harmonic generation in light molecules by using chirped pulses *Phys. Rev. Lett.* **117** 093003
[44] Hehre W J, Stewart R F and Pople J A 1969 self-consistent molecular-orbital methods. I. use of gaussian expansions of Slater-type atomic orbitals *J. Chem. Phys.* **51** 2657
[45] Palke W E and Lipscomb W N 1966 Molecular SCF Calculations on CH_4, C_2H_2, C_2H_4, C_2H_6, BH_3, B_2H_6, NH_3, and HCN *J. Am. Chem. Soc.* **88** 2384–93
[46] Smirnova O, Spanner M and Ivanov M 2007 Anatomy of strong field ionization II: to dress or not to dress? *J. Mod. Opt.* **54** 1019–38
[47] Volkov D M 1935 Concerning a class of solution of the Dirac equation *Z. Phys.* **94** 250–60
[48] Ciappina M F, Chirilă C C and Lein M 2007 Influence of Coulomb continuum wave functions in the description of high-order harmonic generation with H_2^+ *Phys. Rev.* A **75** 043405
[49] Suárez N, Chacón A, Pérez-Hernández J A, Biegert J, Lewenstein M and Ciappina M F 2017 High-order-harmonic generation in atomic and molecular systems *Phys. Rev.* A **95** 033415
[50] Anh-Thu. L, Della Picca R, Fainstein P D, Telnov D A, Lein M and Lin C D 2008 Theory of high-order harmonic generation from molecules by intense laser pulses *J. Phys. B: At. Mol. Opt. Phys.* **41** 081002
[51] Zaïr A *et al* 2008 Quantum path interferences in high-order harmonic generation *Phys. Rev. Lett.* **100** 143902
[52] Lewenstein M, Salières P and L'Huillier A 1995 Phase of the atomic polarization in high-harmonic generation *Phys. Rev.* A **52** 4747
[53] Kling M F *et al* 2006 Control of electron localization in molecular dissociation *Science* **312** 246
[54] He F, Ruiz C and Becker A 2007 Control of electron excitation and localization in the dissociation of H_2^+ and its isotopes using two sequential ultrashort laser pulses *Phys. Rev. Lett.* **99** 083002
[55] Sansone G *et al* 2010 Electron localization following attosecond molecular photoionization *Nature* **465** 763
[56] Gaarde M B, Tate J L and Schafer K J 2008 Macroscopic aspects of attosecond pulse generation *J. Phys. B: At. Mol. Opt. Phys.* **41** 13
[57] Rundquist A, Durfee C, Chang Z, Herne C, Kapteyn H and Murnane M 1998 Phase-matched generation of coherent soft x-rays *Science* **280** 14121415
[58] Hernández-García C, Pérez-Hernández J A, Ramos J, Jarque E C, Roso L and Plaja L 2010 High-order harmonic propagation in gases within the discrete dipole approximation *Phys. Rev.* A **82** 033432
[59] Suárez N, Chacón A, Ciappina M F, Wolter B, Biegert J and Lewenstein M 2016 Above-threshold ionization and laser-induced electron diffraction in diatomic molecules *Phys. Rev.* A **94** 043423
[60] Becker A, Plaja L, Moreno P, Nurhuda M and Faisal F H M 2001 Total ionization rates and ion yields of atoms at nonperturbative laser intensities *Phys. Rev.* A **64** 023408
[61] Pérez-Hernández J A, Ramos J, Roso L and Plaja L 2010 Harmonic generation beyond the strong-field approximation: phase and temporal description *Laser Phys.* **20** 1044–50
[62] Schiff L I 1949 *Quantum Mechanics* (New York: McGraw-Hill)

3

HIGH-ORDER HARMONICS WITH NOVEL ORBITAL ANGULAR MOMENTUM PROPERTIES

The generation of OAM beams in the XUV and X-ray spectral regimes is motivated by the possibility of extending the current applications of vortex beams to the nanometric scale, especially in microscopy and spectroscopy [115–119]. In this chapter, we will explore different schemes to structure HHG with driving vortex beams for the generation of XUV harmonics with novel OAM and spatial properties. First, in section 3.1, we shall present the fundamentals of the OAM of light. In section 3.2, we will show the generation of XUV vortex fields from HHG, considering also the combination of several infrared vortices as the driving beam, providing a richer and more complex scenario. Then, in section 3.3, we will demonstrate the generation of XUV beams with time-varying OAM, which we have denoted as *self-torqued* beams. Afterwards, in section 3.4, we shall present how by properly selecting the OAM of two driving vortex beams, we have an unprecedented control of the frequency spacing of the HHG spectrum and the divergence of the harmonic emission. Finally, in section 3.5, we include our publications [16, 17], as additional information on the topics discussed in sections 3.3 and 3.4.

3.1 INTRODUCTION TO THE ORBITAL ANGULAR MOMENTUM OF LIGHT

In chapter 1, we introduced light beams carrying OAM, also known as vortex beams, which present a twisted phase and donut-like intensity profiles around the phase point-singularity. Vortex beams are typically produced in the optical and infrared regimes using spiral-phase plates [120], q-plates [121], or holographic techniques [122]. Additionally, the different OAM modes can be efficiently sorted [123, 124]. However, these optical elements become highly inefficient for imprinting OAM to XUV or X-ray light [125], because they are nearly transparent in those frequency regimes. As alternatives, XUV or X-ray beams carrying OAM can be generated via HHG or particle accelerators [118, 126]. In this thesis we will focus in this former method.

The spatial structure of the vortex beams follows from the solution of the paraxial wave equation, imposing cylindrical symmetry [127].

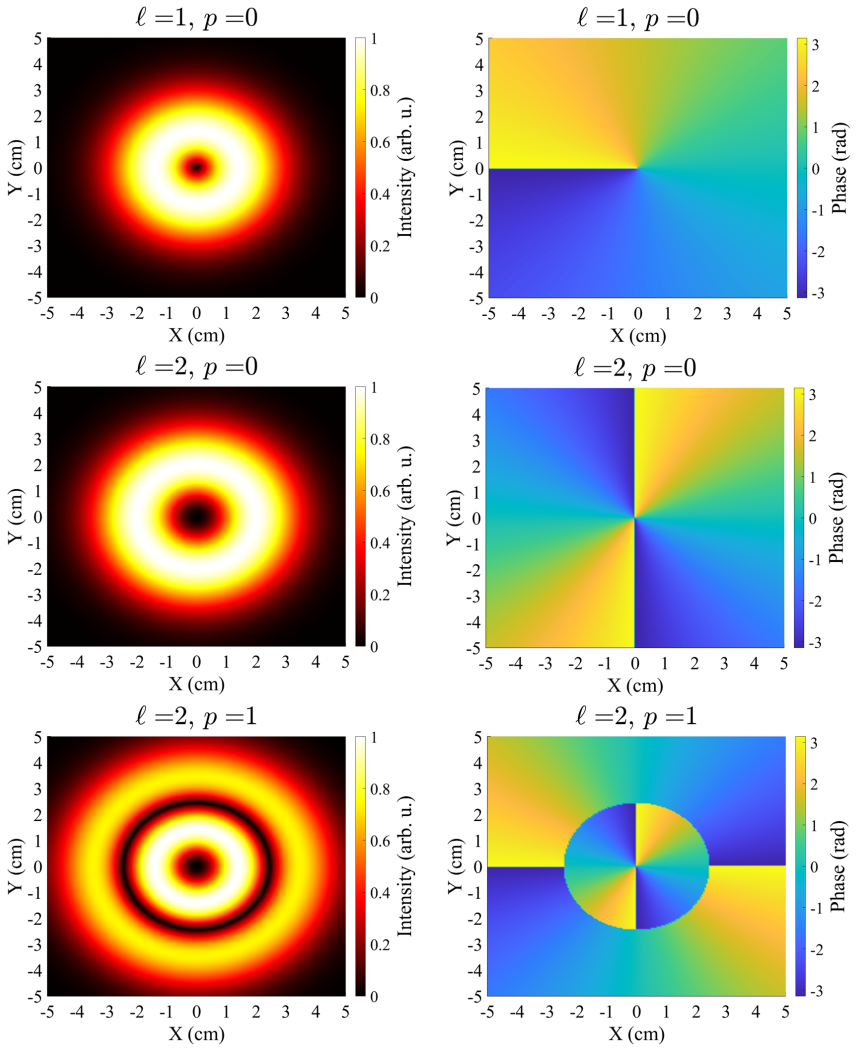

Figure 25: Representation of different Laguerre-Gauss modes at the focal plane for a beam waist of $w_0 = 2\,\mathrm{cm}$. The transverse intensity profiles (left column) exhibit ring shapes whose radii increase with ℓ. The number of non-axial radial nodes is determined by p, while the transverse phase rotation along the azimuthal coordinate is dictated by ℓ (right column).

They are represented as Laguerre-Gaussian modes propagating in the z-direction and with transverse coordinates ρ (radius) and ϕ (azimuth):

$$\begin{aligned} LG_{\ell,p}(\rho,\phi,z;k_0) &= E_0 \frac{w_0}{w(z)} \left(\frac{\sqrt{2}\rho}{w(z)}\right)^{|\ell|} L_p^{|\ell|}\left(\frac{2\rho^2}{w^2(z)}\right) \\ &\times \exp\left(-\frac{\rho^2}{w^2(z)}\right) \exp\left[i\ell\phi + i\frac{k_0\rho^2}{2R(z)} + i\Phi_G(z)\right], \end{aligned} \tag{75}$$

where $k_0 = 2\pi/\lambda_0$ (λ_0 is the wavelength of the beam), w_0 is the beam waist, $w(z) = w_0\sqrt{1+(z/z_R)^2}$ where $z_R = k_0 w_0^2/2$ is the Rayleigh range, $R(z) = z\left[1+(z_R/z)^2\right]$ is the phase-front radius, $\Phi_G(z) =$

$-(2p+|\ell|+1)\arctan(z/z_R)$ is the Gouy phase, and $L_p^{|\ell|}(x)$ is the associated Laguerre polynomial. The index $\ell = 0, \pm1, \pm2, \ldots$ corresponds to the topological charge—which describes the number of 2π phase shifts along the azimuthal coordinate—while the index $p = 0, 1, 2, \ldots$ is the number of non-axial radial nodes of the mode. Note that the OAM associated to a topological charge ℓ is $\hbar\ell$. In figure 25, we show some examples of the intensity and phase transverse profiles at $z = 0$ corresponding to different Laguerre-Gauss modes.

3.2 GENERATION OF EXTREME-ULTRAVIOLET VORTEX BEAMS

Our strategy for the generation of high-frequency vortex beams arises from the mapping capability of the HHG process, where some of the OAM properties of the driving vortices are translated to the harmonic field. In particular, as a general rule, the harmonics generated by a vortex beam are "born" as vortex beams.

3.2.1 *Single-mode harmonic vortex beams*

The first experimental generation of XUV vortex beams by driving HHG with an infrared vortex beam was carried out in 2012 [128]. This first demonstration reported that the harmonics were emitted with the same topological charge as that of the driving vortex beam ($\ell = 1$). Shortly after it was predicted theoretically [129], and later confirmed experimentally [130, 131], that harmonic vortices should exhibit an OAM whose topological charge follows the simple conservation rule:

$$\ell_q = q\ell_{IR}, \tag{76}$$

where ℓ_{IR} is the charge of the driving beam. This law is easily understood in terms of photon composition rules: the conservation of energy, $\omega_q = q\omega_0$, suggests that q photons are converted into a single one and, consequently, Eq. (76) must be satisfied for the conservation of the total OAM.

In figure 26, we show the intensity, phase and OAM content of the 21-st order harmonic, proving Eq. (76). It is important to note that the OAM content of the harmonics is extracted by performing the Fourier transform of the harmonic field along the azimuthal coordinate, since the azimuthal coordinate and ℓ are conjugate variables, and integrating along the divergence angle. This provides us with an OAM spectrum that represents the intensity of each of the OAM components in a beam.

Interestingly, Eq. (76) can also be extracted from the phase of the harmonics (see section 2.3). Since the harmonics exhibit a phase term equal to q times the phase of the driving field, the q^{th} harmonic order will exhibit a phase term that depends on the azimuthal coordinate ϕ as $q\ell_{IR}\phi$, which implies an OAM of $\ell_q = q\ell_{IR}$.

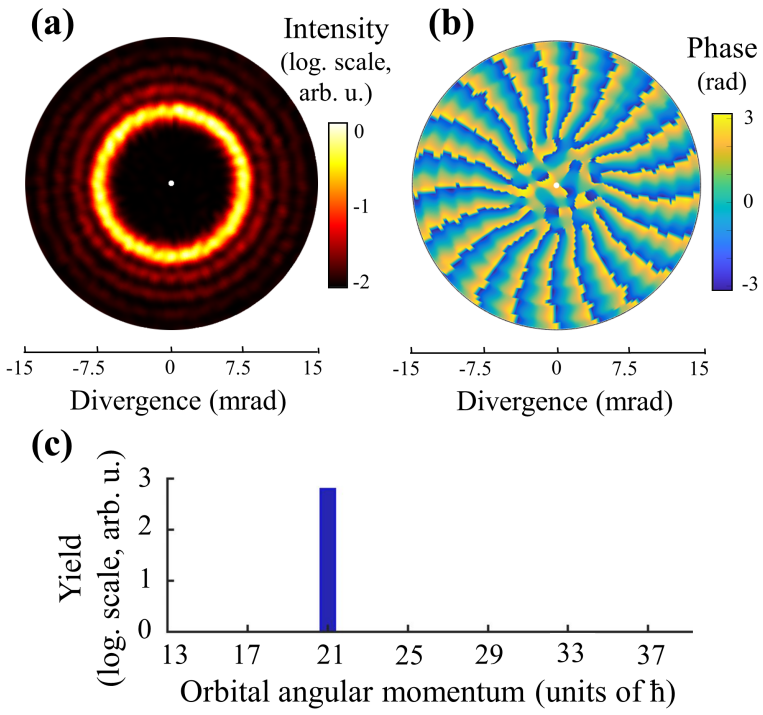

Figure 26: Generation of the 21-st order harmonic vortex beam by an infrared driving beam ($\ell = 1$, $\lambda_0 = 800\,nm$, $w_0 = 30\,\mu m$ and peak intensity $I_0 = 1.4 \times 10^{14}\,W/cm^2$). The far-field harmonic transverse intensity (a) and phase (b) profiles are obtained from full-quantum SFA simulations including propagation. The OAM spectrum (c), that confirms Eq. (76), is computed by performing the Fourier transform of the harmonic field along the azimuthal coordinate. Figure adapted from [129].

Note that, for a single-mode vortex, the non-perturbative dipole phase does not affect the OAM conversion of the resulting harmonics, as the intensity profile of the driving beam is constant along the azimuthal coordinate. However, when HHG is driven by a combination of vortex modes, it becomes relevant [106], as we will explain in section 3.2.2. In contrast, the non-perturbative dipole phase has an important role in the radial structure of the XUV harmonic vortices, since the radial variation of the intensity modifies the quantum path interferences. In fact, the result of the coherent addition of the contributions of the short and long trajectories is also greatly influenced by the relative position of the target with respect to the beam focus, in analogy to the case of a Gaussian beam mentioned in section 2.3.1. As a result, it is even possible to spatially separate the two contributions in rings with different divergences [105, 107]. It is interesting to note that, theoretically, the contribution from short and long trajectories can be disentangled using the TSM. For example, in figure 27, we show the results of the 19-th order harmonic generated by a driving beam with $\ell = 1$. The intensity profile is composed of a brighter ring which

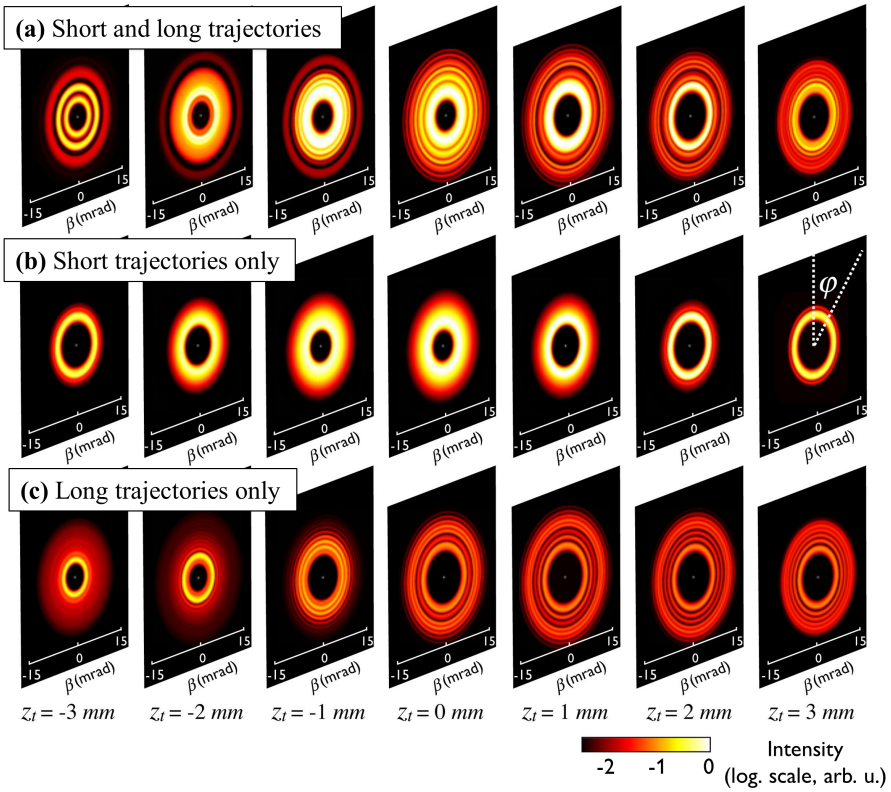

Figure 27: Intensity profiles of the 19-th order harmonic generated by an infrared driving beam ($\ell = 1$, $\lambda_0 = 800\,nm$, $w_0 = 30\,\mu m$, $z_R = 3.5\,mm$ and peak intensity $I_0 = 1.4 \times 10^{14}\,W/cm^2$) as a function of the gas jet position with respect to the beam focus (z_t), obtained using the TSM. The total emission is composed of short and long trajectory contributions (a), where the short trajectories present a bright single ring (b) and long ones show several weaker rings (c). The two contributions are essentially spatially separated at $z_t = -3\,mm$.

originates from the short trajectories, and several weaker rings that originate from the long ones. The combination of the two contributions results in different interference patterns for different gas jet positions with respect to the driving beam focus.

Finally, it is worth to conclude this subsection by mentioning other additional properties of harmonic vortex beams analyzed during the last few years. For example, it turns out that the OAM of the XUV vortex beams can be controlled by combining two non-collinear driving beams [132, 133]. In addition, XUV beams with fractional OAM can be obtained using conical refraction driving beams [134]. Also, it has been demonstrated that the radial index of the Laguerre-Gaussian beams is affected by the HHG process [135]. Lastly, let us mention that single-mode XUV vortex beams can also be generated using schemes involving solid targets [136] or underdense plasmas [137].

3.2.2 *Multi-mode harmonic vortex beams*

In this subsection, we introduce the possibility of generating XUV harmonic vortices with multiple OAM contributions. Such harmonic beams are obtained when HHG is driven by a combination of two infrared vortex beams with the same frequency and linear polarization, but different topological charges [106].

Before analyzing the properties of these harmonic beams, we shall derive the OAM selection rules that govern this scenario. Let us consider the total driving field as the superposition of two vortex beams with spatial complex amplitudes $U_1(\rho)e^{i\ell_1\phi}$ and $U_2(\rho)e^{i\ell_2\phi}$ at $z = 0$, where the gas jet is placed. We shall consider that both vortex beams exhibit the same peak intensity and their waists are selected so their rings of maximum intensity overlap at $\rho = \rho_{max}$: $U_2(\rho_{max}) = U_1(\rho_{max}) = U_0$. Thus, the driving field's complex amplitude at $\rho = \rho_{max}$ can be written as

$$\begin{aligned} U(\phi) &= U_0\left(e^{i\ell_1\phi} + e^{i\ell_2\phi}\right) \\ &= 2U_0\cos\left(\frac{\ell_1-\ell_2}{2}\phi\right)e^{i\frac{\ell_1+\ell_2}{2}\phi} \\ &= \left|2U_0\cos\left(\frac{\ell_1-\ell_2}{2}\phi\right)\right|e^{i\frac{\ell_1+\ell_2}{2}\phi}\mathrm{Sign}\left\{\cos\left(\frac{\ell_1-\ell_2}{2}\phi\right)\right\}. \end{aligned} \tag{77}$$

According to the TSM description presented in section 2.3.3, the harmonic field associated to the r (short or long) quantum path can be expressed as:

$$A_q^r(\phi) = \left[2U_0\cos\left(\frac{\ell_1-\ell_2}{2}\phi\right)\right]^p e^{i\,q\frac{\ell_1+\ell_2}{2}\phi}e^{i\alpha_q^r I_0\cos^2\left(\frac{\ell_1-\ell_2}{2}\phi\right)}, \tag{78}$$

where we have considered that the sign of the cosine factor fulfills $\mathrm{Sign}\left\{\cos\left(\frac{\ell_1-\ell_2}{2}\phi\right)^{q-p}\right\} = 1$—because q is an odd integer and $p \approx 3$—and $I_0 = 4U_0^2$. Let us now extract the OAM contributions from each factor in Eq. (78). The second term is the most relevant because it describes the most intense OAM contribution, which is also at the center of the OAM distribution. Note that it is a perturbative phase term, which contributes to the OAM content as $q(\ell_1+\ell_2)/2$. The other two factors, on the other hand, can be interpreted as scattering terms that redistribute the OAM, describing photon annihilation channels different from that of the main contribution—i.e. the absorption of more ℓ_1 photons at the expense of ℓ_2 photons, or vice versa. In partic-

ular, the first factor, which describes the amplitude modulation, can be expressed as a binomial distribution:

$$\begin{aligned}\left[2U_0\cos\left(\frac{\ell_1-\ell_2}{2}\phi\right)\right]^p &= U_0^p\left(e^{i\frac{\ell_1-\ell_2}{2}\phi}+e^{i\frac{\ell_2-\ell_1}{2}\phi}\right)^p \\ &= U_0^p\sum_{j=0}^{p}\binom{p}{j}e^{ij\frac{\ell_1-\ell_2}{2}\phi}e^{i(p-j)\frac{\ell_2-\ell_1}{2}\phi} \\ &= U_0^p\sum_{j=0}^{p}\binom{p}{j}e^{i\ell_1(j-\frac{p}{2})\phi}e^{i\ell_2(\frac{p}{2}-j)\phi}.\end{aligned} \tag{79}$$

Thus, this contribution to the OAM content of the q-th order harmonic field is $\ell_1(j-p/2)+\ell_2(p/2-j)$, where j ranges from zero to p. On the other hand, the third factor in Eq. (78) derives from the non-perturbative dipole phase. Its contribution to the OAM content can be calculated by expanding it in a series of OAM components:

$$e^{i\alpha_q^r I_0\cos^2\left(\frac{\ell_1-\ell_2}{2}\phi\right)} = e^{i\alpha_q^r I_0/2}\sum_m i^m J_m[\alpha_q^r I_0/2]e^{im(\ell_2-\ell_1)\phi}, \tag{80}$$

where the amplitudes of the Bessel functions decay drastically for $|m|>\alpha_q^r I_0/2$. Therefore, the contribution of this term to the OAM of the q-th order harmonic is equal to $m(\ell_2-\ell_1)$, m being an integer number limited by the quantity $\alpha_q^r I_0/2$. Thus, it is an OAM scattering term, analogous to that of Eq. (79), describing the absorption of m units of ℓ_2 photons at the expenses of m units of ℓ_1 photons, so the effect of both scattering terms is to broad the OAM distribution. Note, however, that the contribution of Eq. (80) depends on the driving field intensity and OAM content, as well as on the harmonic order and the quantum path. Remarkably, as $\alpha_q^{short}<\alpha_q^{long}$, the OAM spectrum of the long trajectories contribution is broader than that of the short trajectories.

Therefore, using Eqs. (79) and (80) in (78), the OAM content of the q-th order harmonic is

$$\begin{aligned}\ell_q &= (j-p/2)\ell_1+(p/2-j)\ell_2+q(\ell_1+\ell_2)/2+m(\ell_2-\ell_1) \\ &= (j-p/2+q/2)\ell_1+(p/2-j+q/2)\ell_2+m(\ell_2-\ell_1),\end{aligned} \tag{81}$$

with $j\in(0,p)$ and $|m|<\alpha_q^r I_0/2$. Let us rewrite this expression in a more compact form by introducing the quantity $n=p/2-j+q/2$. Thus, finally, the OAM of the q-th order harmonic generated by a combination of two Laguerre-Gauss modes with ℓ_1 and ℓ_2 is given by

$$\ell_q=(q-n)\ell_1+n\ell_2+m(\ell_2-\ell_1). \tag{82}$$

Interestingly, the term $(q-n)\ell_1+n\ell_2$ can be understood in perturbative arguments as different OAM channels distinguished by the

number n that lead to the generation of the same harmonic, where n represents the number of photons absorbed from the infrared vortex beam ℓ_2 and $q-n$ is the remaining number of photons, which are absorbed from the infrared vortex beam ℓ_1. Note, however, that the efficiency associated to each channel n is related to the non-perturbative nature of the process through the power $p < q$, being the relevant contributions limited to a range from $(q-p)/2$ to $(q+p)/2$. On the other hand, the term $m(\ell_2 - \ell_1)$ is a purely non-perturbative contribution leading to a redistribution of the OAM around the main values.

The prediction from Eq. (82) is confirmed by our numerical simulations of HHG driven by multi-mode vortex beams using the TSM as well as the full-quantum SFA, including propagation, models described in section 2.3. We consider a driving field composed of two Laguerre-Gauss modes with topological charges of $\ell_1 = 1$ and $\ell_2 = 2$, and waists of $w_1 = 30\,\mu m$ and $w_2 = 21.4\,\mu m$, respectively, so their rings of maximum intensity overlap at $\rho = 30/\sqrt{2}\,\mu m$. Their wavelength is $\lambda_0 = 800\,nm$, and the total peak intensity is $1.4 \times 10^{14}\,W/cm^2$. In figure 28a, we show a scheme of the TSM configuration for the generation XUV harmonic vortices from an argon gas jet under these conditions. The transverse intensity and phase profiles of each vortex beam that interfere to compose the total driving field, which exhibits a *crescent* shape, are shown in figure 28b.

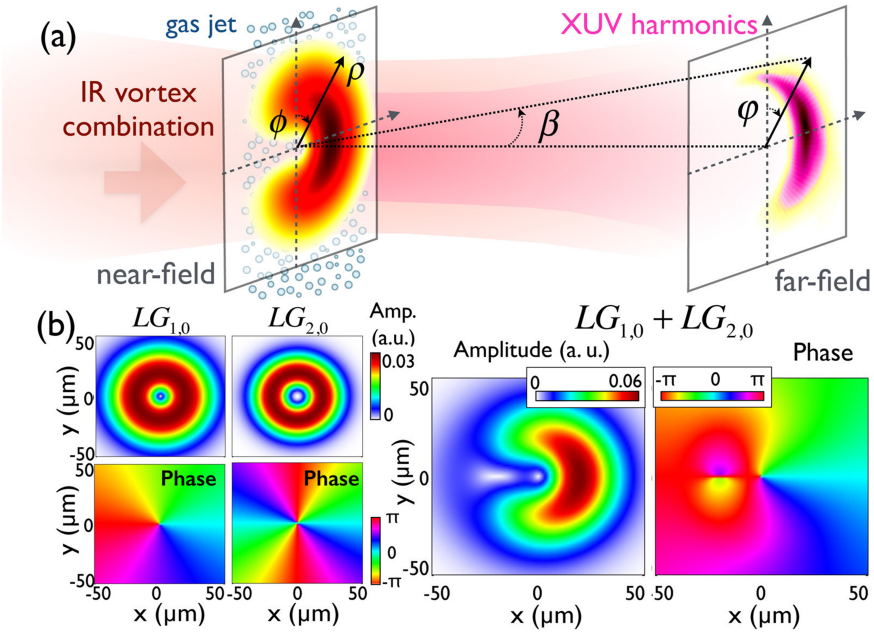

Figure 28: (a) Scheme of HHG driven by a combination of two vortex beams. (b) The driving beam is composed of two Laguerre-Gauss modes with $\ell_1 = 1$ and $\ell_2 = 2$, respectively (left panel). The combination of the two modes results in an intensity profile with a *crescent* shape (right panel).

Our results predict that the presence of a combination of OAM in the driving field implies that each harmonic does not exhibit a single OAM component (as it was shown in figure 26c), but a broader OAM spectrum. Importantly, the TSM allows us to distinguish the different perturbative and non-perturbative contributions, as presented in figure 29 for the 21-st order harmonic. Panel (a) shows the topological charge without the influence of the non-perturbative dipole phase in the perturbative ($p = q$) and non-perturbative ($p < q$) regimes; panels (b) and (c) represent the decomposition of the OAM in several channels discerned by the value of n; and, finally, panel (d) shows the total ℓ_{21} content, in good agreement with Eq. (82).

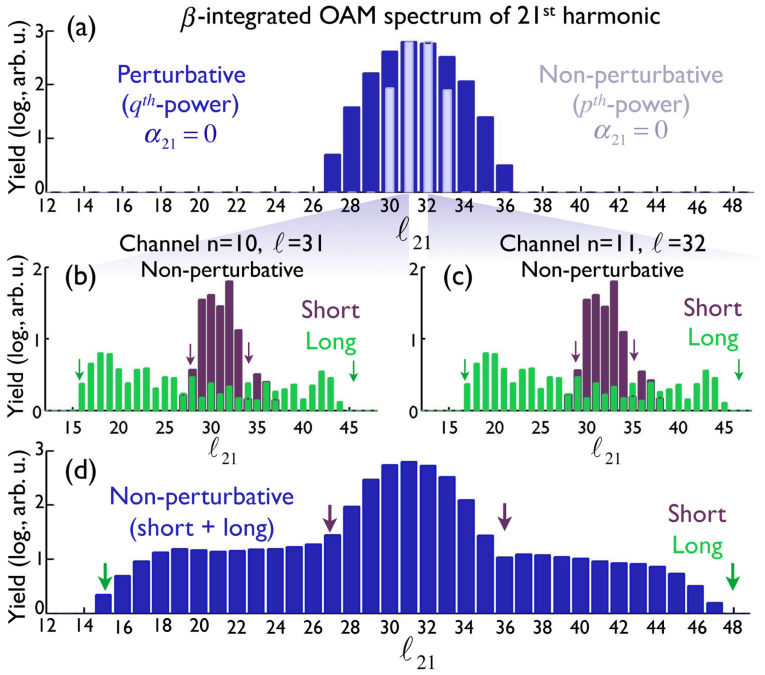

Figure 29: Spatially integrated OAM spectrum of the 21-st order harmonic vortex, obtained with the TSM using (a) the perturbative q-th power (dark blue) and the non-perturbative p-th power (light blue) without non-perturbative dipole phase ($\alpha_{21} = 0$); (b), (c) the non-perturbative scenario for the channels $n = 10$ and $n = 11$, respectively, from the short (purple) and long (green) trajectories contributions; and (d) all the non-perturbative channel contributions. The arrows indicate the OAM interval predicted by Eq. (82) for the short (purple) and long (green) trajectory contributions. The driving beams parameters are described in the text.

It is important to note that the comparison of panels (a) and (d) reveals that the non-perturbative nature of the HHG process modifies the OAM content under this configuration. In contrast to the single-vortex driving field, where the OAM conservation rule can be explained from perturbation theory, the combination of several vortex driving beams brings a new scenario. On the one side, the p-th scaling power is smaller than the q-th's, which narrows the width of the main OAM

channels, by limiting the n values in Eq. (82), compared to that the one expected for the perturbative case ($p = q$). On the other side, the intensity pattern of the combined driving field presents now modulations along the azimuthal coordinate, which result in a further redistribution of the harmonic's OAM content through the non-perturbative phase term (third term in Eq. (82)). Thus, although the non-perturbative exponent $p < q$ narrows the harmonic OAM distribution, the intensity dependent dipole phase introduces the opposite effect: it extends the extremes of the OAM distribution. As expected from Eq. (82), this latter contribution has an especially relevant role for long trajectories.

Interestingly, as a collateral result, our simulations also show that the OAM spectrum of the harmonics is a sensitive probe the presence of OAM impurities in the driving vortex beam in an experiment. Our publication with the results, mathematical derivations, and additional information about this work are can be found in [106].

3.3 TIME-VARYING ORBITAL ANGULAR MOMENTUM

An interesting aspect of the configuration presented in the previous section is that the most intense OAM contribution in Eq. (82) is $\ell_q = q(\ell_1 + \ell_2)/2$. However, this condition is only satisfied if both driving vortex beams have the same peak intensity, which was the case considered through that section. In a more general case, the OAM content of the harmonics will depend on the amplitude ratio between the two driving vortex beams. Thus, by changing their relative amplitude, the main OAM channel of the harmonics can be tuned. This finding paved for us the route towards the study of the generation of harmonics exhibiting time-varying OAM.

In this section, therefore, we introduce a new class of light beams that possess a unique property associated with a temporal variation of their OAM: the self-torque of light. As we will demonstrate, such beams naturally emerge from HHG driven by two time-delayed infrared vortex beams carrying different OAM. Under this configuration, the high-order harmonics exhibit a time-dependent OAM, and, thus, we define the self-torque of light as:

$$\hbar\xi = \hbar\frac{d\ell(t)}{dt}, \tag{83}$$

where $\hbar\ell(t)$ describes the inherent OAM variation along a light pulse.

It is important to note that the self-torque does not refer to the ability of light to exert photo-mechanical torques by transferring its OAM [138, 139]. On the contrary, the time-dependent OAM is an inherent property of the light beam propagating in free space, without the interaction with any external agent. Remarkably, a self-torque can also be found in other physical systems that can self-induce a temporal variation of their angular momentum. However, up to now it has not been

realized that light could possess self-torque. Although trains of non-overlapping pulses with different OAM have been reported [140], there is no evidence of pulses with time-dependent OAM in any spectral regime, previous to this thesis.

3.3.1 *Derivation of the self-torque of light*

Let us calculate the OAM of the XUV beams generated from two time-delayed infrared vortex beams, following a similar procedure to that described in section 3.2.2. Since in this case the two driving vortex beams do not completely overlap in time, Eq. (77) should be modified as

$$U(\phi,t) = U_1(t)e^{i\ell_1\phi} + U_2(t)e^{i\ell_2\phi}. \tag{84}$$

Now, we rewrite this equation by defining the quantity $U_0(t) = U_1(t) + U_2(t)$ and the ratio $\eta(t) = U_2(t)/U_0(t)$:

$$\begin{aligned} U(\phi,t) &= U_0(t)\left[(1-\eta(t))e^{i\ell_1\phi} + \eta(t)e^{i\ell_2\phi}\right] \\ &= U_0(t)e^{i(\ell_1+\ell_2)\phi/2} \\ &\times \left[\cos\frac{(\ell_1-\ell_2)\phi}{2} + i\big(1-2\eta(t)\big)\sin\frac{(\ell_1-\ell_2)\phi}{2}\right]. \end{aligned} \tag{85}$$

We can extract the phase of this expression by factorizing the driving field as $U(\phi,t) = |U(\phi,t)|^{i\varphi(\phi,t)}$, where

$$\begin{aligned} \varphi(\phi,t) &= \arctan\left\{[1-2\eta(t)]\tan\frac{(\ell_1-\ell_2)\phi}{2}\right\} + \frac{(\ell_1+\ell_2)\phi}{2} \\ &\approx [1-2\eta(t)]\frac{(\ell_1-\ell_2)\phi}{2} + \frac{(\ell_1+\ell_2)\phi}{2} \\ &= \{[1-\eta(t)]\ell_1 + \eta(t)\ell_2\}\phi, \end{aligned} \tag{86}$$

considering that $\eta(t)$ evolves approximately linearly in time.

For the calculation of the q-th order harmonic field, we resort to the TSM description (see section 2.3.3):

$$\begin{aligned} A_q(\phi,t) &= |U(\phi,t)|^p e^{iq\varphi(\phi,t)} = \left[|U(\phi,t)|e^{i\varphi(\phi,t)}\right]^p e^{i(q-p)\varphi(\phi,t)} \\ &= U^p(\phi,t)e^{i(q-p)\varphi(\phi,t)}. \end{aligned} \tag{87}$$

Note that, in contrast to Eq. (60), the effects of the non-perturbative term of the dipole phase are now not included, because we restrict our calculation to the main OAM components.

We now insert the driving field's expression from Eq. (85) into Eq. (87) and we expand the binomial expression to the p-th power:

$$\begin{aligned} A_q(\phi,t) &= U_0(t)^p\left[(1-\bar\eta(t))e^{i\ell_1\phi} + \bar\eta(t)e^{i\ell_2\phi}\right]^p e^{i(q-p)\varphi(\phi,t)} \\ &= U_0(t)^p\Big[\sum_{j=0}^{p}\binom{p}{j}(1-\bar\eta(t))^j e^{ij\ell_1\phi}\bar\eta(t)^{(p-j)}e^{i(p-j)\ell_2\phi}\Big] \\ &\times e^{i(q-p)\varphi(\phi,t)}. \end{aligned} \tag{88}$$

Note that $\bar{\eta}(t)$ is the average of $\eta(t)$ over the short-trajectories excursion time (approximately half a cycle). Then, we include the expression of the phase $\varphi(\phi,t)$ from Eq. (86) to obtain the harmonic field:

$$\begin{aligned} A_q(\phi,t) &= U_0(t)^p\Big[\sum_{j=0}^{p}\binom{p}{j}(1-\bar{\eta}(t))^j e^{ij\ell_1\phi}\bar{\eta}(t)^{(p-j)}e^{i(p-j)\ell_2\phi}\Big] \\ &\times\ e^{i(q-p)\{[1-\bar{\eta}(t)]\ell_1+\bar{\eta}(t)\ell_2\}\phi}. \end{aligned} \tag{89}$$

We extract the OAM from this expression by considering two separated terms: the sum over j and the last exponential term. The former term can be understood as the statistical binomial distribution of selecting a total of p photons by combining photons of two different kinds, ℓ_1 and ℓ_2, assuming that each ℓ_1 photon joins with a probability $P_{\ell_1} = 1-\bar{\eta}(t)$ and each ℓ_2 photon with a probability $P_{\ell_2} = \bar{\eta}(t)$. Let us calculate its mean OAM as:

$$\begin{aligned} \langle \ell_q(t)\rangle &= \sum_{j=0}^{p}\binom{p}{j}P_{\ell_1}^{j}P_{\ell_2}^{(p-j)}[j\ell_1+(p-j)\ell_2] \\ &= (\ell_1-\ell_2)\sum_{j=0}^{p}\binom{p}{j}P_{\ell_1}^{j}P_{\ell_2}^{(p-j)}j + p\ell_2\sum_{j=0}^{p}\binom{p}{j}P_{\ell_1}^{j}P_{\ell_2}^{(p-j)} \\ &= p\{[1-\bar{\eta}(t)]\ell_1+\bar{\eta}(t)\ell_2\}. \end{aligned} \tag{90}$$

where we have used the following relations: $\sum_{j=0}^{p}\binom{p}{j}P_{\ell_1}^{j}P_{\ell_2}^{(p-j)} = 1$ and $\sum_{j=0}^{p}\binom{p}{j}P_{\ell_1}^{j}P_{\ell_2}^{(p-j)}j = pP_{\ell_1}$. Thus, the total mean OAM from Eq. (89) is calculated as:

$$\begin{aligned} \bar{\ell}_q(t) &= \langle \ell_q(t)\rangle + (q-p)\{[1-\bar{\eta}(t)]\ell_1+\bar{\eta}(t)\ell_2\} \\ &= q\{[1-\bar{\eta}(t)]\ell_1+\bar{\eta}(t)\ell_2\}. \end{aligned} \tag{91}$$

Finally, by including Eq. (91) in Eq. (83) we obtain the self-torque of the emitted harmonics:

$$\hbar\xi_q = \frac{\hbar d\bar{\ell}_q(t)}{dt} = \hbar q(\ell_2-\ell_1)\frac{d\bar{\eta}(t)}{dt} \approx \hbar q(\ell_2-\ell_1)/\tau_d. \tag{92}$$

where τ_d is the time delay between the two infrared driving vortex beams. The approximation $\frac{d\bar{\eta}(t)}{dt} \approx 1/\tau_d$ is a reasonable assumption under the condition $\tau_d \approx t_{FWHM}$, where t_{FWHM} is the full-width half maximum (FWHM) of the duration of each of the infrared vortex pulses. Indeed, this is the optimal time delay for the generation of the self-torqued XUV beams, since in this case all the OAM states are generated with similar efficiency (see section 3.5.1).

Eq. (92) shows that the HHG process imprints a *continuous* temporal OAM variation into the XUV beams. In addition, the self-torque depends not only on the harmonic order, but also on the driving beams OAM and temporal properties, which allows us to control the amount of self-torque of each harmonic beam.

Lastly, the instantaneous width of the OAM distribution is calculated as:

$$\sigma_{\ell_q} = \sqrt{\langle \ell_q^2(t)\rangle - [\langle \ell_q(t)\rangle]^2} = |\ell_2 - \ell_1|\sqrt{p\bar{\eta}[1-\bar{\eta}(t)]}, \tag{93}$$

as demonstrated in the Supplemental information of [16]. Note that the non-perturbative nature of HHG ($p < q$) strongly reduces the value of σ_{ℓ_q}. In the perturbative case ($p = q$), the uncertainty on the OAM would be larger and the self-torque would be ill-defined. Thus, HHG allows to obtain well-defined values of self-torque.

3.3.2 *Main results*

In figure 30a, we show the scheme for the generation of self-torqued XUV beams, where two time-delayed driving vortex beams with ℓ_1 and ℓ_2, respectively, are directed into an argon gas jet. In figure 30b, on the other hand, we present the numerical results from our full-quantum SFA model including propagation (see section 2.3.2). The OAM of the selected harmonic (the 17-th order) varies along time, presenting all the intermediate OAM states. The green curves represent the predictions from Eqs. (91) and (93), which are in good agreement with the quantum simulations.

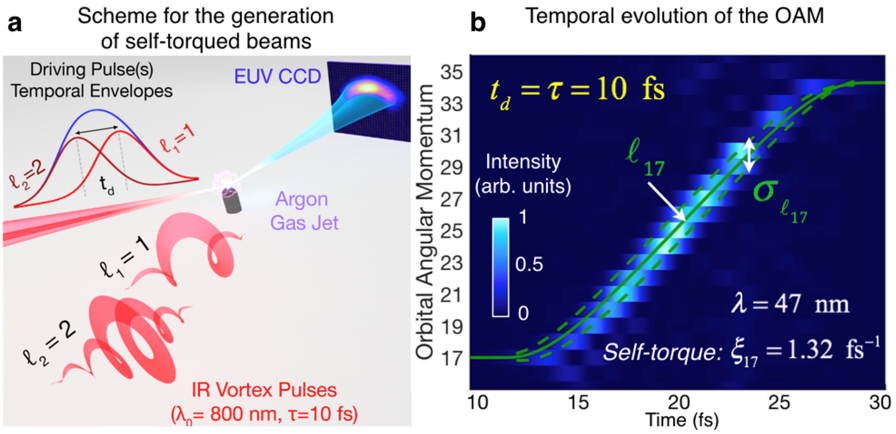

Figure 30: (a) Scheme for the creation of self-torqued XUV pulses via HHG driven by two infrared vortex beams carrying ℓ_1 and ℓ_2, respectively, and with a variable time delay, t_d. (b) Time-varying OAM of the 17-th order harmonic when HHG is driven by 10 fs FWHM drivers delayed by 10 fs. The color background shows the full-quantum simulations results, whereas ℓ_{17} (solid green lines) is the mean OAM, whose slope is the self-torque ($\xi_{17} = 1.32\,fs^{-1}$), and $\sigma_{\ell_{17}}$ is the width of the OAM content (dashed-green lines), calculated from Eqs. (91) and (93), respectively.

Interestingly, a relevant property of self-torqued beams is that they present an azimuthal frequency chirp because the temporal variation of the OAM introduces a time-dependent phase in the harmonics. The

harmonic instantaneous frequency, which is calculated as the time derivative of the total harmonic phase, $\Phi_q(\phi, t)$, is:

$$\omega_q^{inst}(\phi) = \frac{d\Phi_q(\phi,t)}{dt} = \omega_q + \frac{d\ell_q(t)}{dt}\phi = \omega_q + \xi_q\phi \tag{94}$$

Therefore, the harmonic frequency-chirp along the azimuthal coordinate is equal to the amount of self-torque of each individual harmonic. Luckily, this unequivocal relation between the self-torque and the azimuthal frequency chirp allows us to quantify the self-torque of the XUV beams by an experimental measurement of the azimuthal distribution of the HHG spectrum.

The experimental production and measurement of the self-torqued beams has been carried out by our collaborators from the Kapteyn-Murnane group in JILA, at the University of Colorado, in Boulder (USA). The details of the experimental methods can be found in section 3.5.1. In figure 31, we present the comparison between the theoretical and the experimental results of the azimuthal frequency chirp of the harmonics induced by the self-torque, where the driving pulses parameters were chosen to mimic the experimental ones ($\tau = 52\,fs$, $\tau_d = 50.4\,fs$, $I_0 = 1.4\times10^{14}\,W/cm^2$, $\lambda_0 = 800\,nm$, $w_1 = 30\,\mu m$, $w_2 = 21.4\,\mu m$). Note that the self-torque of each harmonic order is different, as predicted by Eq. (92).

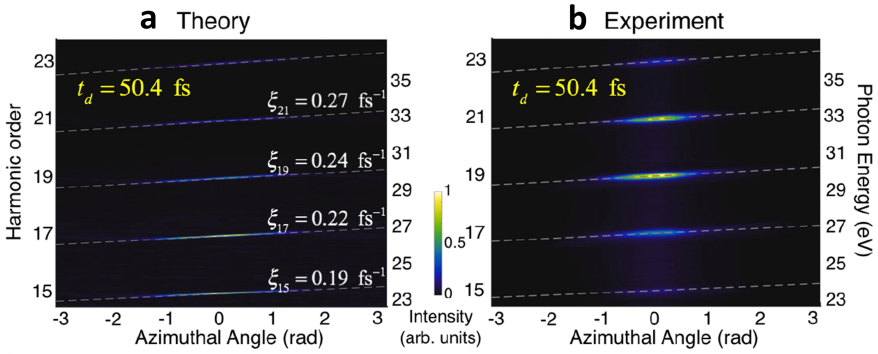

Figure 31: Theoretical (a) and experimental (b) spatial HHG spectrum along the azimuthal coordinate. The self-torque of light imprints an azimuthal frequency chirp, which is different for each harmonic, as indicated by the grey dashed lines, obtained from Eq. (94), whose slope is displayed in panel (a). The driving pulses parameters were chosen to mimic the experimental ones ($t_{FWHM} = 52\,fs$, $\tau_d = 50.4\,fs$, $I_0 = 1.4\times10^{14}\,W/cm^2$, $\lambda_0 = 800\,nm$, $w_1 = 30\,\mu m$, $w_2 = 21.4\,\mu m$).

Additionally, we demonstrate our control over the self-torque value by varying the time delay in figure 32, where the self-torque increases almost linearly with the time delay. The excellent agreement between our theory and experiments confirms the creation of XUV self-torqued beams.

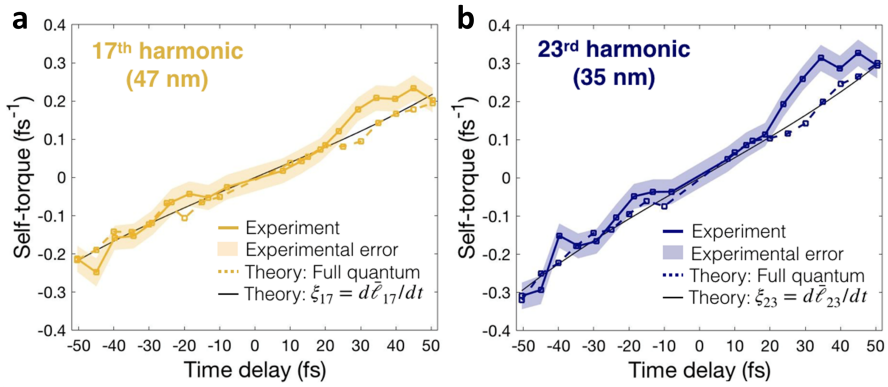

Figure 32: Simulated (dashed line) and experimental (solid line) self-torque versus the time delay between the two infrared drivers for the 17-th (a) and 23-rd (b) order harmonics. The black line indicates the theoretical prediction by Eq. (92) and the shaded region depicts the experimental uncertainty in the retrieved self-torque. The simulation parameters are the same as those of figure 31, but considering a wide range of time delays.

In conclusion, we have demonstrated the generation and characterization of self-torqued XUV beams. Our work not only presents and confirms an inherently new property of light beams, but also offers a path for the study of systems with time-varying OAM. Noticeably, a subsequent work has reported the generation of optical pulses with time-varying OAM from time-modulated metasurfaces [141], and it has also been recently proposed the generation of ultrafast self-torqued beams by a superposition of multiple tailored vortex pulses [142]. Finally, we believe that thanks to their ultrafast nature, XUV self-torqued beams can be extraordinary tools for laser-matter manipulation on attosecond time and nanometric spatial scales.

Further information and results of this work can be found in our publication [16], included in section 3.5.1.

3.4 HARMONIC COMBS WITH TUNABLE LINE-SPACING

Up to now we have studied how we can control the OAM properties of the high-order harmonics via the OAM of the driving beam. In this section, we will demonstrate that the temporal and spectral properties of the high-order harmonics can also be controlled by properly selecting the OAM of the driving field. Note that, usually, the frequency content emitted from HHG is controlled by changing the wavelength of the driving laser or by using frequency-selective optics or monochromators. However, the manipulation of the frequency of the XUV beams emitted from HHG is still challenging and demands very efficient monochromators in the XUV and soft-X-ray regions.

In particular, here we will demonstrate how we can generate harmonic combs with tunable line-spacing, by taking advantage of the OAM selection rules and therefore imprinting the desired frequency line-spacing directly onto the HHG light. Remarkably, we also demonstrate that such harmonic combs exhibit lower divergence than standard Gaussian-driven harmonics. Our experimental collaborators have corroborated such frequency control in the XUV regime. Note, moreover, that our theoretical simulations predict that such control can be extended towards soft-X-ray frequencies.

3.4.1 *Physical mechanisms behind the harmonic line-spacing control via the orbital angular momentum of the driving beams*

As shown in figure 33a, typically, the HHG radiation consists of bursts emitted every half cycle of the driving field, thus with a time delay of $\Delta\tau = T/2$ (T being the driving field period). Accordingly, the harmonic comb spacing is $\Delta\omega = 2\pi/\Delta\tau = \pi/T = 2\omega_0$. Interestingly, the line spacing would be customized by modifying the number of bursts per cycle of the incident field, as shown in figure 33b. This possibility is difficult to achieve microscopically, but it turns to be feasible from the macroscopic perspective. For that purpose, we consider a driving beam composed of two infrared linearly polarized vortex beams carrying $\ell_1 = |\ell_1|$ and $\ell_2 = -|\ell_2|$, respectively, with $|\ell_1| < |\ell_2|$, and with no time delay between them. Such driving beam has a transverse distribution that can be interpreted as a phased necklace, as schematically depicted in figure 33c. Thus, upon HHG, the gas target behaves as a phased antenna array of $N = |\ell_1| + |\ell_2|$ lobes, where each lobe's harmonic emission takes place at a delayed time determined by the relative phase shift, as it is demonstrated in our publication [17], included in section 3.5.2. The minimum phase shift between different lobes is given by

$$\Delta\varphi_{min} = \frac{\pi}{\xi_1 + \xi_2}, \tag{95}$$

where $\xi_i = L_{l.c.m}/|\ell_i|$, $L_{l.c.m}$ being the least common multiple of $|\ell_1|$ and $|\ell_2|$. Thus, the time delay between two successive emissions is

$$\Delta\tau = \frac{\Delta\varphi_{min}}{\omega_0} = \frac{T}{2(\xi_1 + \xi_2)}. \tag{96}$$

Let us now focus on the harmonic radiation that is detected on axis. The on-axis harmonic yield at the far-field is the result of the coherent addition of the emission from all the lobes. Since the optical path from each of the lobes to the axis is the same, $\Delta\tau$ is also the time delay between the harmonic bursts detected at the on-axis far-field. Therefore, in such case, the harmonic line spacing is:

$$\Delta\omega = 2(\xi_1 + \xi_2)\omega_0, \tag{97}$$

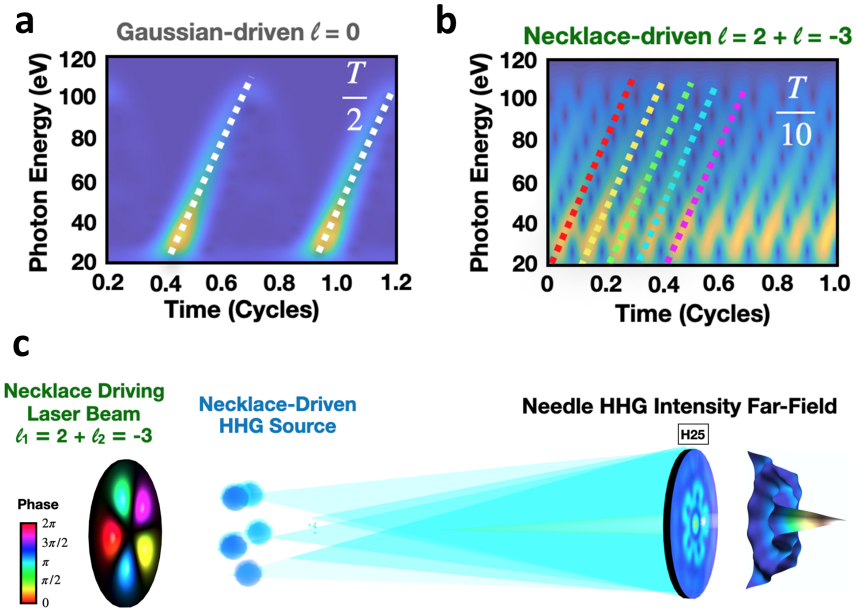

Figure 33: (a) TFA of the harmonic emission calculated on-axis corresponding to HHG in helium driven by a standard Gaussian beam ($\lambda_0 = 800\,nm$). (b) Same as (a) but using a phased-necklace driving beam. The radiation bursts exhibit a higher cadence. (c) Scheme of the generation of high-order harmonic combs via HHG driven by a phased-necklace beam. Two infrared linearly polarized vortex beams carrying $\ell_1 = 2$ and $\ell_2 = -3$ are combined forming a phased-necklace beam, where the phase colors correspond to those of the dashed lines in panel (b). The harmonic emission interferes in the far-field to create a strong low-divergence on-axis yield (represented for the 25-th order harmonic in the figure), whose spectrum is a frequency comb with a spacing that depends on the OAM of the driving fields.

and only the harmonic orders satisfying

$$q = (2m+1)(\xi_1 + \xi_2), \tag{98}$$

will be emitted, where m is an integer number. Taking into account that, due to inversion symmetry, the harmonic orders must be odd, Eq. (98) is restricted to the OAM combinations of the driving beam that result in odd values for $\xi_1 + \xi_2$.

From the OAM point of view, note that the on-axis detected yield corresponds to harmonics with $\ell_q = 0$. However, the harmonics that present an on-axis yield also exhibit an off-axis weaker emission, corresponding to additional non-zero OAM components, that can be calculated using Eq. (82). On the other hand, the harmonics that do not fulfil Eq. (98) are detected completely off-axis, which means that they solely exhibit non-zero OAM values. In addition, note that we have found that the on-axis yield can be optimized by properly selecting the amplitude ratio between the $|\ell_1|$ and $-|\ell_2|$ components

(see section 3.5.2). It is also worth mentioning that, although the generation of necklace-shaped high-order harmonics have been very recently proposed theoretically [143], here we demonstrate, for the first time, the important implications on the frequency content and divergence of the harmonic combs.

3.4.2 *Main results*

In figure 34, we show the results of our full-quantum SFA simulations including propagation (see section 2.3.2) corresponding to HHG in a helium gas jet. In contrast to the standard Gaussian-driven HHG spectra (grey solid lines), the line spacing is modified when HHG is driven by the phased necklace beam. In the inset of the figure, we represent the predicted line-spacing depending on the OAM components of the driving field given by Eq. (97).

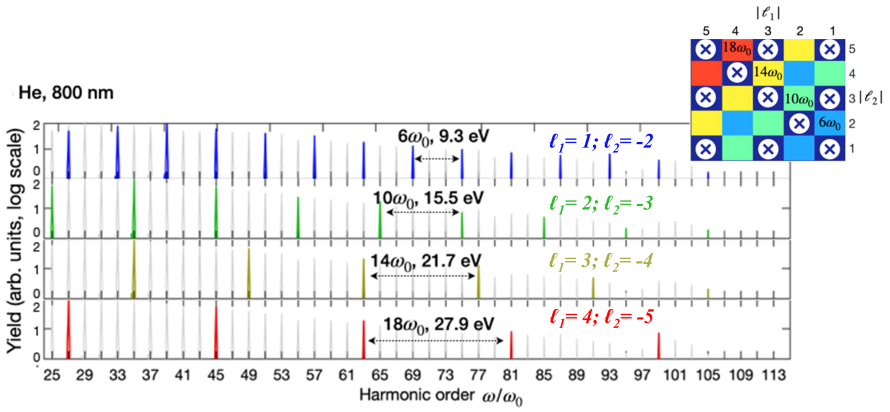

Figure 34: XUV harmonic combs with tunable line spacing. Simulated on-axis spectra of HHG in helium ($\lambda_0 = 800\,nm$) for different OAM combinations in the driving beam: $\ell_1 = 1, \ell_2 = -2$ (blue); $\ell_1 = 2, \ell_2 = -3$ (green); $\ell_1 = 3, \ell_2 = -4$ (yellow); and $\ell_1 = 4, \ell_2 = -5$ (red). The laser pulses exhibit a total peak intensity of $6.9 \times 10^{14}\,W/cm^2$ and are modeled with a trapezoidal envelope with 26.7 fs of constant amplitude. The harmonic line-spacing is compared to that from a standard Gaussian-driving beam (grey lines). The inset shows a scheme of the line-spacing predicted by Eq. (97) depending on the OAM content of the driving field, which is in good agreement with the results from the simulations. The color scale represents the line spacing, being $6\omega_0$ (blue), $10\omega_0$ (green), $14\omega_0$ (yellow) and $18\omega_0$ (red).

Another relevant characteristic of the on-axis yield is its low divergence compared to that in HHG driven by a Gaussian beam, showing a needle-like intensity profile. By selecting the $\ell_q = 0$ component, the FWHM divergence angle of the intensity distribution is calculated using the Fraunhofer integral as:

$$\Delta\beta_q^{FWHM} = 2.25\frac{\lambda_0}{2\pi q R} \tag{99}$$

where R is the radius of maximum intensity of the necklace driving beam (see section 3.5.2). Notably, the divergence decreases with the harmonic order, in contrast to the case of Gaussian-driven harmonics, where it generally increases [91, 93]. In figure 35, we compare the divergence of the harmonics from a standard Gaussian-driving beam and the on-axis yield from our phased-necklace beam. Our numerical simulations show the decrease of the divergence in the latter case, in accordance with the prediction from Eq. (99).

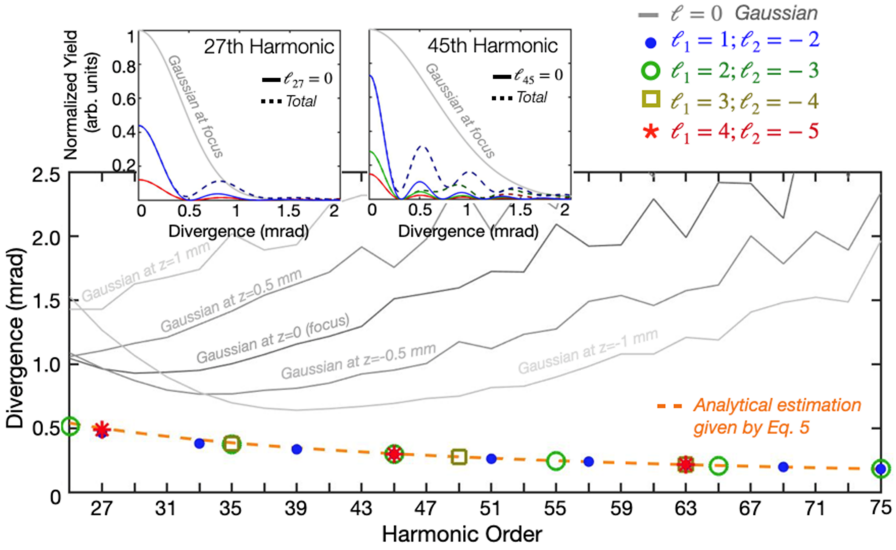

Figure 35: Simulation results of the FWHM divergence of the high-order harmonics for different OAM driving combinations—in good agreement with the estimation given by Eq. (99) (orange dashed line)—and for a Gaussian driving beam where the gas jet is placed at different positions relative to the focus. The top insets show the divergence profile of the 27th and 45th harmonics (the solid lines represent the $\ell_q = 0$ contribution while dashed ones indicate the total) and for the Gaussian beam, when the gas jet is placed at the focus. The simulation parameters are those of figure 34.

Finally, the experimental validation of the predicted harmonic combs, performed by our colleagues from the Kapteyn-Murnane group in JILA, at the University of Colorado in Boulder, is presented in figure 36. The good agreement between the theoretical and experimental results confirms the generation of XUV harmonic combs with controlled line-spacing and low divergence. Note that the efficiency of the harmonics generated from the necklace-shaped driving beam is similar to that of the standard Gaussian-driven case.

Interestingly, these harmonic combs with tunable line-spacing and low divergence can be extended towards the X-ray regime by using driving beams with longer wavelengths, allowing for the generation of structured X-ray light for probing and imaging the fastest correlated charge and spin dynamics in molecules, nanoparticles and materials.

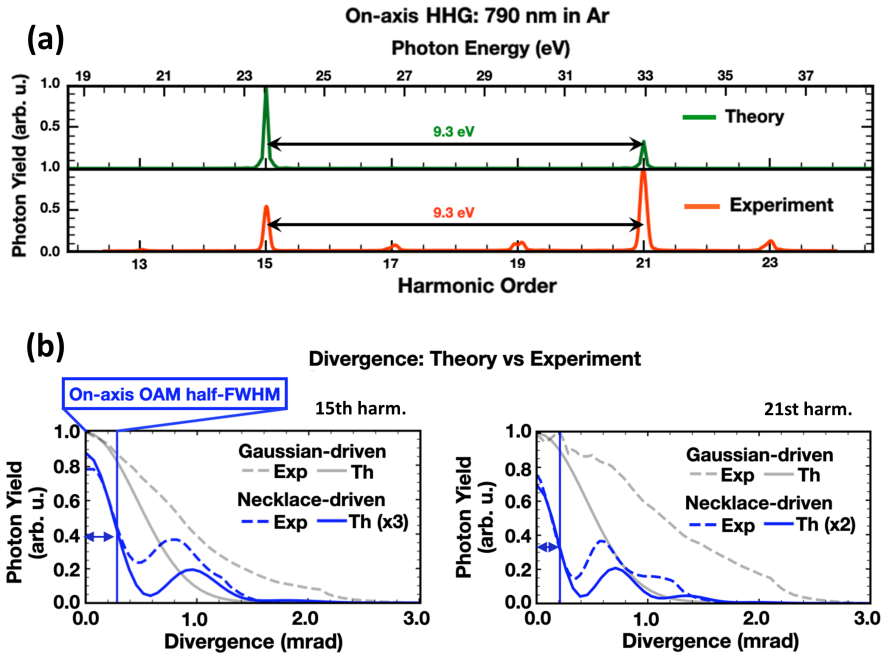

Figure 36: Experimental confirmation of the generation of XUV harmonic combs with tunable line-spacing and low divergence. (a) Theoretical (green) and experimental (orange) high-order harmonic combs detected on axis, emitted from an argon gas jet driven by a phased-necklace beam carrying $\ell_1 = 1$ and $\ell_2 = -2$ and with wavelength $\lambda_0 = 790\,\mathrm{nm}$. (b) Divergence of the 15-th (left) and 21-st (right) order harmonics in the phased-necklace-driven case (blue) compared to the equivalent Gaussian (grey) from the simulations (solid lines) and experimental (dashed lines) results. The vertical blue line indicates half of the FWHM of the divergence of the on-axis yield.

Further information and results about this work can be found in [17], included in section 3.5.2.

3.5 PUBLICATIONS

In this section, we include the full text of the two articles explained in sections 3.3 and 3.4 about structuring HHG with the OAM of the driving beams. The first one, included in section 3.5.1, details the methods and results corresponding to the generation of self-torqued beams, under the title "Generation of extreme-ultraviolet beams with time-varying orbital angular momentum" [16]. The second one, included in section 3.5.2, contains the full information and results about the generation of frequency combs with controlled line-spacing via the OAM, which has been submitted for publication under the title "Necklace-structured high harmonic generation for low-divergence, soft-X-ray harmonic combs with tunable line spacing" [17]. In order to comply with the

regulations of the University of Salamanca, before each article we include an abstract in Spanish.

3.5.1 *Generation of extreme-ultraviolet beams with time-varying orbital angular momentum*

Resumen

Los haces de luz que poseen momento angular orbital (OAM) [7], también conocidos como vórtices de luz, son muy prometedores en cuanto a aplicaciones en muchos campos, como comunicaciones ópticas, microscopía, óptica cuántica, información cuántica o manipulación de micropartículas [144]. En este trabajo presentamos una nueva clase de haces de luz que poseen una propiedad única asociada con una variación temporal de su OAM: el auto-torque de la luz [16], una característica que hasta ahora no se había ni propuesto ni demostrado en ningún régimen espectral. Concretamente, definimos el auto-torque de la luz como la derivada del OAM respecto al tiempo, en analogía con los sistemas mecánicos que se autoinducen una variación de su momento angular.

En este trabajo, predecimos teóricamente y validamos experimentalmente la producción de haces de frecuencia ultravioleta extrema (XUV) con auto-torque a través del proceso no lineal extremo de generación de armónicos de orden alto (HHG). Al incidir con dos pulsos infrarrojos retardados en el tiempo con diferente OAM sobre un chorro de gas, los pulsos de frecuencia XUV que surgen del proceso de HHG tienen un OAM que varía en el tiempo. Esta distribución de OAM es continua (donde están presentes todos los componentes de OAM intermedios) y varía en una escala de tiempos de attosegundos.

Por otro lado, el auto-torque de la luz imprime un ordenado de frecuencias a lo largo de la coordenada azimutal en el plano transversal a su propagación, lo cual permite medir su magnitud de manera precisa. El excelente acuerdo entre nuestras simulaciones y la caracterización experimental (llevada a cabo por nuestros colaboradores del grupo Kapteyn-Murnane en JILA en la Universidad de Colorado) confirma la creación de haces de frecuencia XUV con auto-torque. Además, es importante destacar que las propiedades de los pulsos incidentes (duración y retardo en el tiempo) proporcionan un control exquisito sobre la cantidad de auto-torque impreso en un pulso de luz.

Finalmente, esta nueva clase de haces puede servir como una nueva herramienta para obtener imágenes de excitaciones magnéticas y topológicas, para provocar la excitación selectiva de materia cuántica o para la nanomanipulación en escalas de tiempo y longitud sin precedentes.

RESEARCH ARTICLE SUMMARY

ULTRAFAST OPTICS

Generation of extreme-ultraviolet beams with time-varying orbital angular momentum

Laura Rego*†, Kevin M. Dorney*†, Nathan J. Brooks, Quynh L. Nguyen, Chen-Ting Liao, Julio San Román, David E. Couch, Allison Liu, Emilio Pisanty, Maciej Lewenstein, Luis Plaja, Henry C. Kapteyn, Margaret M. Murnane, Carlos Hernández-García

INTRODUCTION: Light beams carry both energy and momentum, which can exert a small but detectable pressure on objects they illuminate. In 1992, it was realized that light can also possess orbital angular momentum (OAM) when the spatial shape of the beam of light rotates (or twists) around its own axis. Although not visible to the naked eye, the presence of OAM can be revealed when the light beam interacts with matter. OAM beams are enabling new applications in optical communications, microscopy, quantum optics, and microparticle manipulation. To date, however, all OAM beams—also known as vortex beams—have been static; that is, the OAM does not vary in time. Here we introduce and experimentally validate a new property of light beams, manifested as a time-varying OAM along the light pulse; we term this property the self-torque of light.

RATIONALE: Although self-torque is found in diverse physical systems (e.g., electrodynamics and general relativity), to date it was not realized that light could possess such a property, where no external forces are involved. Self-torque is an inherent property of light, distinguished from the mechanical torque exerted on matter by static-OAM beams. Extreme-ultraviolet (EUV) self-torqued beams naturally arise when the extreme nonlinear process of high harmonic generation (HHG) is driven by two ultrafast laser pulses with different OAM and time delayed with respect to each other. HHG imprints a time-varying OAM along the EUV pulses, where all subsequent OAM components are physically present. In the future, this new class of dynamic-OAM beams could be used for manipulating the fastest magnetic, topological, molecular, and quantum excitations at the nanoscale.

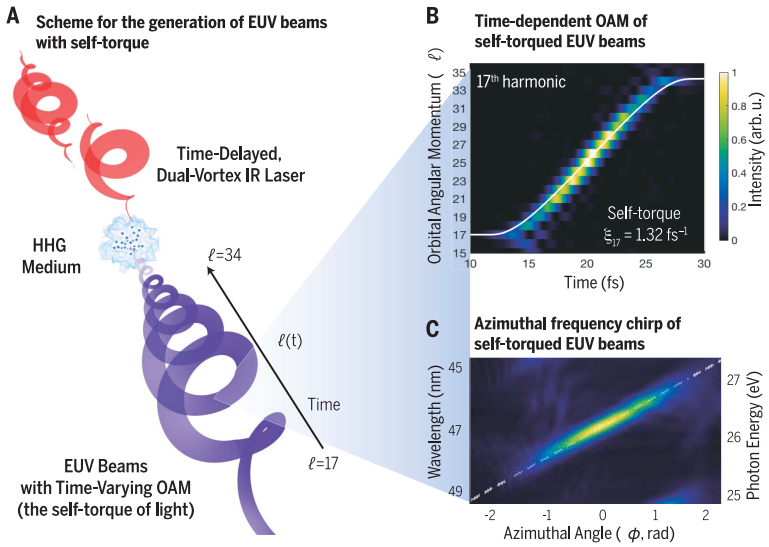

Generation of EUV beams with self-torque. (**A**) Two time-delayed, femtosecond infrared (IR) pulses with different OAM are focused into a gas target to produce self-torqued EUV beams through HHG. The distinctive signature of self-torqued beams is their time-dependent OAM, as shown in (**B**) for the 17th harmonic (47 nm, with self-torque ξ_{17} = 1.32 fs^{-1}). (**C**) The self-torque imprints an azimuthal frequency chirp, which enables its experimental measurement.

RESULTS: Self-torqued beams are naturally produced by HHG, a process in which an ultrafast laser pulse is coherently upconverted into the EUV and x-ray regions of the spectrum. By driving the HHG process with two time-delayed, infrared vortex pulses possessing different OAM, ℓ_1 and ℓ_2, the generated high harmonics emerge as EUV beams with a self-torque, $\hbar\xi_q \simeq \hbar q(\ell_2 - \ell_1)/t_d$, that depends on the properties of the driving fields—that is, their OAM content and their relative time delay (t_d)—and on the harmonic order (q). Notably, the self-torque of light also manifests as a frequency chirp along their azimuthal coordinate, which enables its experimental characterization. This ultrafast, continuous, temporal OAM variation that spans from $q\ell_1$ to $q\ell_2$ is much smaller than the driving laser pulse duration and changes on femtosecond (10^{-15} s) and even subfemtosecond time scales for high values of self-torque. The presence of self-torque in the experimentally generated EUV beams is confirmed by measuring their azimuthal frequency chirp, which is controlled by adjusting the time delay between the driving pulses. In addition, if driven by few-cycle pulses, the large amount of frequency chirp results in a supercontinuum EUV spectrum.

CONCLUSION: We have theoretically predicted and experimentally generated light beams with a new property that we call the self-torque of light, where the OAM content varies extremely rapidly in time, along the pulse itself. This inherent property of light opens additional routes for creating structured light beams. In addition, because the OAM value is changing on femtosecond time scales, at wavelengths much shorter than those of visible light, self-torqued HHG beams can be extraordinary tools for laser-matter manipulation on attosecond time and nanometer spatial scales. ■

ON OUR WEBSITE

Read the full article at http://dx.doi.org/10.1126/science.aaw9486

The list of author affiliations is available in the full article online.
***Corresponding author. Email: laura.rego@usal.es (L.R.); kevin.dorney@colorado.edu (K.M.D.)**
†These authors contributed equally to this work.
Cite this article as L. Rego *et al.*, *Science* 364, eaaw9486 (2019). DOI: 10.1126/science.aaw9486

RESEARCH

RESEARCH ARTICLE

ULTRAFAST OPTICS

Generation of extreme-ultraviolet beams with time-varying orbital angular momentum

Laura Rego[1]*†, Kevin M. Dorney[2]*†, Nathan J. Brooks[2], Quynh L. Nguyen[2], Chen-Ting Liao[2], Julio San Román[1], David E. Couch[2], Allison Liu[2], Emilio Pisanty[3], Maciej Lewenstein[3,4], Luis Plaja[1], Henry C. Kapteyn[2,5], Margaret M. Murnane[2], Carlos Hernández-García[1]

Light fields carrying orbital angular momentum (OAM) provide powerful capabilities for applications in optical communications, microscopy, quantum optics, and microparticle manipulation. We introduce a property of light beams, manifested as a temporal OAM variation along a pulse: the self-torque of light. Although self-torque is found in diverse physical systems (i.e., electrodynamics and general relativity), it was not realized that light could possess such a property. We demonstrate that extreme-ultraviolet self-torqued beams arise in high-harmonic generation driven by time-delayed pulses with different OAM. We monitor the self-torque of extreme-ultraviolet beams through their azimuthal frequency chirp. This class of dynamic-OAM beams provides the ability for controlling magnetic, topological, and quantum excitations and for manipulating molecules and nanostructures on their natural time and length scales.

Structured light is critical for a host of applications in imaging and spectroscopy, as well as for enhancing our ability to optically manipulate macro- to nanoscale objects such as particles, molecules, atoms, and electrons. The distinctive phase and intensity properties of structured light beams achieved by exploiting the angular momentum of light have garnered renewed interest in optical manipulation and control (*1*). One of the most relevant structured light beams are those carrying orbital angular momentum (OAM), also known as vortex beams (*2*). The OAM of light manifests from a spatially dependent wavefront rotation of the light beam, which is characterized by the phase winding number, or topological charge, ℓ. OAM beams have been harnessed for applications in diverse fields (*3*) such as laser communication (*4*, *5*), phase-contrast (*6*, *7*) and superresolution microscopy (*8*), kinematic micromanipulation (*9*), quantum information (*10*), and lithography (*10*). Spurred by these exciting technologies, a paralleled interest in the ability to control and manipulate the OAM of ultrafast light pulses has also emerged, resulting in numerous techniques that can imprint OAM directly onto an arbitrary waveform. Diffractive and refractive optics (e.g., q-plates, spiral-phase plates, and holographic techniques) (*11*–*13*) can impart OAM onto waves from radio, to optical, and even x-ray (*14*) frequencies, and recent advances in high harmonic generation (HHG) have produced attosecond extreme-ultraviolet (EUV) pulses with designer OAM (*15*–*28*).

One of the most exciting capabilities enabled by OAM beams is their ability to exert photomechanical torques (*2*, *29*, *30*). Whereas the linear momentum of light can be employed to control and manipulate microscopic objects via the gradient and scattering forces associated with its intensity profile, optically induced torque manifests from angular momentum transfer between an object and a light field. This enables fundamental capabilities in advanced classical and quantum optical control and manipulation techniques, such as optical tweezers, lattices, and centrifuges (*9*, *31*–*34*), allowing for the realization of molecular and micromechanical rotors, single-particle trafficking, and fundamental studies of atomic motion in liquids and Bose-Einstein condensates (*35*, *36*).

We theoretically predict and experimentally validate the generation of light beams that carry time-dependent OAM, thus presenting a self-torque. This inherent property of structured light, the self-torque, $\hbar\xi$, is defined as $\hbar\xi = \hbar d\ell(t)/dt$, where $\hbar\ell(t)$ is the time-dependent OAM content of the light pulse. After being generated, the time-dependent OAM remains as a structural property of the light beam propagating in free space, where no interaction with external agents is present. Thus, the term self-torque refers to the inherent angular acceleration of the light beam, in an analogy with other physical systems that possess a self-induced time variation of the angular momentum—such as the radiation reaction of charged particles (*37*) or gravitational self-fields (*38*). Although OAM is well understood as a spatial property of light beams, to date, light pulses with time-dependent OAM have not been proposed or observed. We demonstrate that the self-torque arises as a necessary consequence of angular momentum conservation during the extreme nonlinear optical process of HHG. In HHG, the interaction of an intense field with an atom or molecule leads to the ionization of an electronic wave packet, which acquires energy from the laser field before being driven back to its parent ion, emitting a high-frequency photon upon recollision (*39*, *40*). The emitted harmonic radiation can extend from the EUV to the soft x-ray regime if the emissions from many atoms add together in phase (*41*–*44*). The resulting comb of fully coherent harmonics of the driving field in turn yields trains of phase-locked attosecond pulses (*45*, *46*).

Self-torqued light beams naturally emerge when HHG is driven by two time-delayed infrared (IR) pulses that differ by one unit of OAM (Fig. 1). The dynamical process of HHG makes it possible to imprint a continuous time-varying OAM, where all OAM components are present—thus creating self-torqued EUV beams. Intuitively, these exotic pulses can be understood as being composed of time-ordered photons carrying consecutively increasing OAM.

The self-torque of light translates to an azimuthal frequency chirp (i.e., a spectral shift along the azimuthal coordinate) on the radiation emission—and vice versa, which allows us to quantify the self-torque by an experimental measurement of the azimuthal frequency chirp. In addition, the degree of self-torque of EUV harmonic beams can be precisely controlled through the time delay and pulse duration of the driving, IR laser pulses. The generation of light beams with self-torque opens up a route for the investigation of systems with time-varying OAM that spontaneously appear in nature (*47*) as macroscopic dynamical vortices or—owing to the high frequency of the beams—microscopic ultrafast systems. For example, because short-wavelength light can capture the fastest dynamics in materials (*48*, *49*), self-torqued EUV beams can be expected to be used for imaging magnetic and topological excitations, launching selective and chiral excitation of quantum matter (*50*), imprinting OAM centrifuges (*32*), switching superpositions of adiabatic charge migration in aromatic or biological molecules (*51*, *52*), or manipulating the OAM dichroism of nanostructures (*53*) on attosecond time scales.

Theory underlying the self-torque of light

To create light beams with self-torque, we drive the HHG process with two linearly polarized IR

[1]Grupo de Investigación en Aplicaciones del Láser y Fotónica, Departamento de Física Aplicada, University of Salamanca, Salamanca E-37008, Spain. [2]JILA, Department of Physics, University of Colorado and NIST, Boulder, CO 80309, USA. [3]ICFO, Institut de Ciencies Fotoniques, The Barcelona Institute of Science and Technology, Av. Carl Friedrich Gauss 3, 08860 Castelldefels (Barcelona), Spain. [4]ICREA, Pg. Lluís Companys 23, 08010 Barcelona, Spain. [5]Kapteyn-Murnane Laboratories Inc. (KMLabs Inc.), 4775 Walnut Street no. 102, Boulder, CO 80301, USA.
***Corresponding author. Email: laura.rego@usal.es (L.R.); kevin.dorney@colorado.edu (K.M.D.)**
†These authors contributed equally to this work.

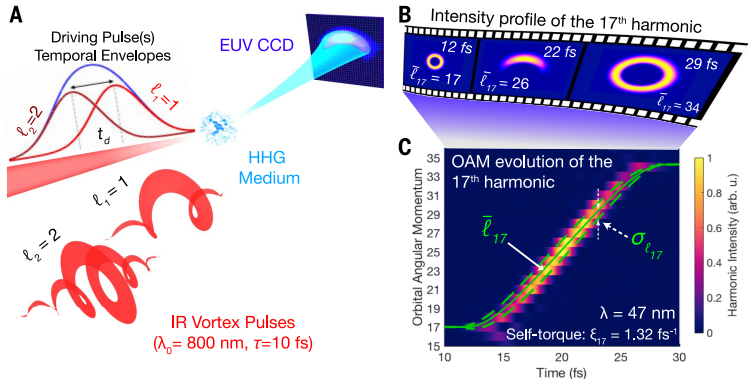

Fig. 1. Generation of EUV beams with self-torque. (**A**) Two time-delayed, collinear IR pulses with the same wavelength (800 nm), but different OAM values, are focused into an argon gas target (HHG medium) to produce harmonic beams with self-torque. The spatial profile of the complete, time-integrated, HHG beam from full quantum simulations is shown on the EUV CCD. (**B**) Predicted evolution of the intensity profile of the 17th harmonic at three instants in time during the emission process. (**C**) Temporal evolution of the OAM of the 17th harmonic, for two driving pulses with the same duration $\tau = 10$ fs, at a relative time delay of $t_d = \tau$. The average OAM, $\bar{\ell}_{17}$ (solid green), and the width of the OAM distribution, $\sigma_{\ell_{17}}$ (distance between the solid and dashed-green lines), are obtained from Eqs. 2 and 3. The self-torque associated with this pulse, $\xi_{17} = 1.32$ fs^{-1}, is obtained from the slope of the smooth and continuous time-dependent OAM.

pulses exhibiting the same frequency content (centered at $\omega_0 = 2\pi c/\lambda_0$), but with different OAM, ℓ_1 and ℓ_2, where $|\ell_1 - \ell_2| = 1$. The two laser pulses are separated by a variable time delay, t_d, which is on the order of the individual pulse widths (Fig. 1A) [see also supplementary text section S1 in (*54*)]. These two collinear IR vortex beams are then focused into an atomic gas target, such that the transverse intensity distribution of the two drivers exhibits maximum overlap. We model the HHG process using full quantum simulations in the strong-field approximation (SFA) that include propagation via the electromagnetic field propagator (*55*), a method that was used in several previous calculations of HHG involving structured pulses (*16*, *18*, *20*, *21*, *26*, *28*, *44*, *56*). We consider the driving vortex pulses possessing ℓ_1 and ℓ_2, described by a $\sin^2$ envelope with τ = 10 fs full width at half-maximum (FWHM) in intensity, centered at λ_0 = 800 nm, and delayed by $t_d = \tau$ = 10 fs (see materials and methods for further details). Figure 1A shows a schematic of the temporal envelopes of each pulse (red), as well as their superposition (blue). Figure 1C shows the time-dependent OAM of the 17th harmonic obtained from our simulations (color scale), whereas in Fig. 1B the spatial intensity distribution of the 17th harmonic is sketched at three instants of time during the emission process. To extract the temporal variation of the OAM, we first select the HHG spectrum in the frequency range $(q-1)\omega_0$ to $(q+1)\omega_0$ (where q is the harmonic order to explore, being q = 17 in Fig. 1), and then we perform a Fourier transform along the azimuthal coordinate (*20*) at each time instant along the harmonic pulse. Notably, the temporal variation of the OAM is monotonic and continuous, spanning over an entire octave of consecutive topological charges—i.e., it includes all OAM components from $q\ell_1 = 17$ to $q\ell_2 = 34$.

The nature of self-torqued beams can be understood through a simple theoretical analysis. Previous works in OAM-HHG have demonstrated that an IR vortex beam can be coherently converted into high-frequency vortex beams (*15*–*28*). When HHG is driven by a single, linearly polarized, IR vortex beam with integer topological charge, ℓ_1, the OAM of the qth-order harmonic follows a simple scaling rule, $\ell_q = q\ell_1$ (*16*, *17*). This scaling reflects the nature of OAM conservation in HHG, where q IR-photons combine to produce the qth-order harmonic. If HHG is driven by the combination of two collinear and temporally overlapped IR vortices with different OAM, ℓ_1 and ℓ_2, each harmonic order will span over a wide OAM spectrum, given by $\ell_q = n_1\ell_1 + n_2\ell_2$ (*20*), where n_1 and n_2 are the number of photons absorbed from each driver ($n_1 + n_2 = q$, whose total must be odd due to parity restrictions). Each channel, (n_1, n_2), is weighted according to a binomial distribution, associated with the different combinations of absorbing n_1 photons with ℓ_1 and n_2 photons with ℓ_2. The effect of the harmonic intrinsic phase in the OAM spectrum, also explored in (*20*), is second order, and negligible for the results presented here.

In this work, we consider the HHG fields that can be produced by two IR laser vortex pulses separated by some time delay. The superposition of the delayed envelopes turns into a temporal dependence in the relative weights of the driving fields—thus introducing time as an additional parameter. To show how this influences the OAM structure of the EUV harmonics, we consider two time-delayed, collinear, linearly polarized, IR driving pulses with different OAM, ℓ_1 and ℓ_2. We denote, in cylindrical coordinates (ρ, ϕ, z), the complex amplitudes of the driving fields at the focus position (z = 0) as $U_1(\rho, \phi, t)$ and $U_2(\rho, \phi, t)$. For simplicity, we consider the field amplitudes at the ring of maximum intensity at the target—where the HHG efficiency is highest—and the resulting field can be written as $U(\phi, t) = U_0(t)\{[1-\eta(t)]e^{i\ell_1\phi} + \eta(t)e^{i\ell_2\phi}\}$, where $U_0(t) = U_1(t) + U_2(t)$ and $\eta(t) = U_2(t)/U_0(t)$ is the relative amplitude of the second beam. According to the strong-field description of HHG, the amplitude of the qth-order harmonic, $A_q(\phi, t)$, scales nonperturbatively with that of the driving laser, with an exponent $p < q$ [$p \simeq 4$ for our laser parameters (*20*)], whereas the qth-order harmonic phase is considered to be q times that of the driver (see supplementary text section S1 for the complete derivation); thus

$$A_q(\phi, t) \propto U_0^p(t) \times \left[\sum_{r=0}^{p} \binom{p}{r} (1-\bar{\eta}(t))^r e^{ir\ell_1\phi} \bar{\eta}^{(p-r)}(t) e^{i(p-r)\ell_2\phi}\right] \times e^{i(q-p)[(1-\bar{\eta}(t))\ell_1 + \bar{\eta}(t)\ell_2]\phi} \quad (1)$$

where r is an integer and $\bar{\eta}(t)$ is the average of $\eta(t)$ over the time it takes the ionized electron to complete the rescattering trajectory that contributes to the generation of a particular harmonic. For this average, we have considered the so-called short trajectories (*57*, *58*), whose excursion time can be approximated to half a cycle. The contribution of long trajectories to the OAM content is two orders of magnitude weaker than that of the short ones (*20*). The summation in Eq. 1 is carried over p different OAM channels, each weighted by a binomial distribution in accordance with the combinatory nature of the HHG up-conversion process. Parity conservation in HHG demands that the total number of photons absorbed from each driving field, $n_1 + n_2$, must be odd, which implies that to generate all intermediate OAM states between $q\ell_1$ and $q\ell_2$, the OAM of the drivers must differ by one unit, i.e., $|\ell_1 - \ell_2|$ =1. The mean OAM of the qth-order harmonic at any instant of time along the harmonic pulse is given by [see (*54*)]

$$\bar{\ell}_q(t) = q\left[(1-\bar{\eta}(t))\ell_1 + \bar{\eta}(t)\ell_2\right] \quad (2)$$

and the width of the OAM distribution is

$$\sigma_{\ell_q} = |\ell_2 - \ell_1|\sqrt{p\bar{\eta}(t)\left(1-\bar{\eta}(t)\right)} \quad (3)$$

In analogy with mechanical systems, we characterize the time-varying OAM spectrum of the qth-order harmonic via the self-torque

$$\xi_q = d\bar{\ell}_q(t)/dt \quad (4)$$

As the OAM of light is defined as $\hbar\ell$, the self-torque is given by $\hbar\xi$. For simplicity we factor

out $\hbar$ and denote the self-torque by ξ, in units of fs^{-1}. It is worth mentioning that σ_{ℓ_q} depends weakly on the harmonic order, as the parameter p remains almost constant along the nonperturbative spectral plateau. The nonperturbative nature of the HHG process reduces the number of available channels to generate the qth-order harmonic from q (perturbative) to $p \sim 4$ (nonperturbative). As typically $p << q$, $\bar{\ell}_q(t)$ appears as a well-defined quantity whose relative error, $\sigma_{\ell_q}/\bar{\ell}_q$, decreases as the harmonic order increases. Thus, $\bar{\ell}_q(t)$ approaches the classical behavior, i.e., its relative uncertainty tends to 0 in the limit of large harmonic orders, converging to perfectly defined intermediate OAM states.

In Fig. 1C, we show the temporal evolution of the mean OAM of the 17th harmonic, $\bar{\ell}_{17}$ (solid-green line), and its OAM width, $\sigma_{\ell_{17}}$ (dashed-green lines). In this case, where $t_d = \tau$, we can approximate the self-torque as constant over the OAM span:

$$\xi_q \sim q(\ell_2 - \ell_1)/t_d \tag{5}$$

which provides a straightforward route for controlling the self-torque through the OAM of the driving pulses and their temporal properties. The example shown in Fig. 1C corresponds to a self-torque of $\xi_{17} = 1.32\ fs^{-1}$, which implies an attosecond variation of the OAM. Equation 5 is valid only if $t_d \simeq \tau$, and if this condition is relaxed, the self-torque must be calculated from the definition given by Eq. 4. Actually, $t_d = \tau$ is a particularly interesting case, as it corresponds to the time delay where the weight of all intermediate OAM states is more uniform over all the OAM span (see fig. S1 for the time-dependent OAM for different time delays, showing a consistently excellent agreement between the full quantum simulations and the OAM content predicted by Eqs. 2 and 3).

It is important to stress that even though the mean OAM value at each instant of time may be a noninteger, the nature of self-torqued beams is different from that of the well-known fractional OAM beams (*21*, *59*–*61*). In particular, the mere superposition of two time-delayed vortex beams—carrying $\ell_i = q\ell_1$ and $\ell_f = q\ell_2$ units of OAM, respectively—does not contain a self-torque. Although it does lead to a temporal variation of the average OAM similar to that in Eq. 2, it does not contain physical intermediate OAM states, i.e., photons with OAM other than ℓ_i and ℓ_f. Self-torqued beams, by contrast, contain all intermediate OAM states, which are time-ordered along the pulse (see Fig. 1C).

In addition, the width of the instantaneous OAM distribution of self-torqued beams (Eq. 3) is much narrower than that of the mere superposition of two time-delayed OAM beams—which in the case of $\ell_i = q\ \ell_1$ and $\ell_f = q\ \ell_2$ is $\sigma_{\ell_q} = q|\ell_2 - \ell_1|\ \sqrt{\eta(t)(1-\eta(t))}$. This is a result of the nonperturbative behavior of HHG, which enables the creation of well-defined intermediate OAM states in a self-torqued beam. In Movie 1 (and in figs. S3 and S4) we further evidence the distinctions in the temporal evolution of the OAM content and phase and intensity profiles between self-torqued beams and the mere superposition of two time-delayed OAM beams. In the latter case, the phase and intensity profiles remain q-fold symmetric, whereas in self-torqued beams, the q-fold symmetry is broken. This breakdown in rotational symmetry is manifested in both the intensity distribution and the corresponding phase profiles of the self-torqued beams. Whereas the intensity distribution exhibits a characteristic "crescent" shape due to the coherent combination of vortex beams with subsequent OAM charges ($\ell_i + \ell_{i+1}$, as previously shown in Fig. 1), the associated phase profiles show the continuous appearance of new vortex singularities along a single row. In other words, a self-torqued beam can be understood as a topological structure where new vortices emerge one at a time.

It is of paramount relevance to evidence the physical nature of the self-torqued beams by temporally characterizing the intermediate OAM states, $\ell_q(t_k)$, with $q\ell_1 < \ell_q(t_k) < q\ell_2$. Assuming a beam with constant self-toque ξ_q, the component of the qth-order harmonic carrying an OAM of $\ell_q(t_k)$ will appear at the time $t_k = \frac{\ell_q(t_k) - q\ell_1}{\xi_q}$ after the peak amplitude of the first driving pulse, exhibiting a temporal width, according to Eq. 3, of $\Delta t_k = \frac{\sigma_{\ell_q}}{\xi_q} = \tau\frac{\sqrt{p\bar{\eta}(1-\bar{\eta})}}{q} \ll \tau$. Therefore, a self-torqued pulse can be thought of as a pulse with a time-dependent OAM, with a temporal OAM variation much smaller than the width of the driving pulses, reaching the attosecond time scale for sufficiently high values of self-torques. This allows us to stress the difference between self-torqued beams and a train of nonoverlapping pulses with different OAM (*62*). Finally, in analogy to polarization gating techniques (*63*), self-torqued EUV beams open the possibility of subfemtosecond OAM-gating techniques, providing a high degree of temporal control over laser-matter interactions involving OAM.

The azimuthal frequency chirp of self-torqued beams

A direct consequence of self-torque is the presence of an azimuthal frequency chirp in the light beam. As the phase term associated with a time-dependent OAM is given by $\ell_q(t)\phi$, the instantaneous frequency of the qth-order harmonic—given by the temporal variation of the harmonic phase, $\varphi_q(t,\ \phi)$—is shifted by the self-torque as

$$\omega_q(t,\phi) = \frac{d\varphi_q(t,\phi)}{dt} = \omega_q + \frac{d\ell_q(t)}{dt}\phi \approx \omega_q + \xi_q\phi \tag{6}$$

Therefore, the harmonics experience an azimuthal frequency chirp whose slope is the self-torque. Although $\omega_q(t,\phi)$ in Eq. 6 is a continuous function of $\phi(-\pi \le \phi < \pi)$, the null intensity region in the crescent profile of the beam (see inset in Fig. 2A) avoids the frequency discontinuity. However, further studies on this region of "structured darkness" (*61*) could be beneficial for a thorough fundamental understanding of self-torqued beams.

We present in Fig. 2 the HHG spectrum along the azimuthal coordinate obtained in our full quantum simulations for driving pulses of $\tau =$ 10 fs and time delays of (A) $t_d = \tau = 10$ fs and (B) $t_d = -\tau = -10$ fs, respectively. The intensity crescent shape of the whole HHG beam is shown in the inset of Fig. 2A. Both spectra reflect the presence of an azimuthal chirp that depends on the harmonic order, and thus, an associated self-torque, whose sign depends on t_d. The full quantum simulations are in perfect agreement with the analytical estimation given by Eq. 6 (gray

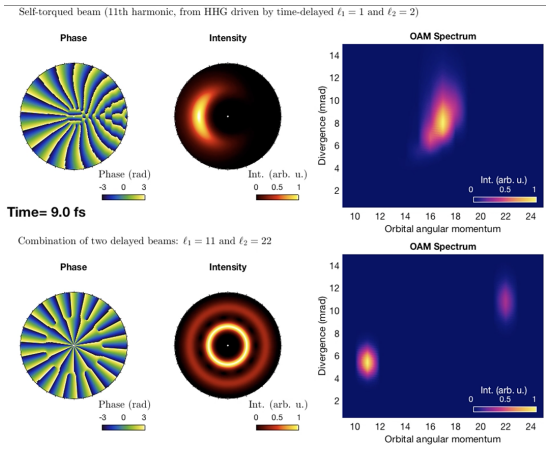

Movie 1. Comparison between the temporal evolution of phase, intensity, and OAM content of self-torqued beams and two delayed vortex beams. Temporal evolution of the phase (left column), intensity (central column), and OAM distribution along the divergence (right column) of a self-torqued beam (top) and a combination of two time-delayed vortex beams. The self-torqued beam (top) corresponds to the 11th harmonic generated through HHG ($\ell_1 = 1$, $\ell_2 = 2$, $\tau = 10$ fs, $t_d = 10$ fs, $\lambda_1 = \lambda_2 = 800$ nm) calculated using the thin slab model (see supplementary text section S2), whereas the vortex combination (bottom) corresponds to two time-delayed vortex beams ($\ell_1 = 11$, $\ell_2 = 22$, $\tau = 10$ fs, $t_d = 10$ fs, $\lambda_1 = \lambda_2 = 800$ nm).

dashed lines). This result shows that the spectral bandwidth of the harmonics can be precisely controlled via the temporal and OAM properties of the driving pulses. Moreover, it provides a direct, experimentally measurable parameter to extract the self-torque, without measuring the OAM of each harmonic at each instant of time with subfemtosecond resolution, which is currently unfeasible. This reasoning implies that a beam with azimuthal frequency chirp would also exhibit self-torque. Up to now, however, HHG beams have only been driven either by spatially chirped pulses [such as the so-called "attosecond lighthouse" technique (*64*, *65*)], or angularly chirped pulses through simultaneous spatial and temporal focusing, which (in theory) yield spatially chirped harmonics (*66*). However, to the best of our knowledge, azimuthal chirp—and thus, self-torque—has not been imprinted into EUV harmonics or in any other spectral regime.

Experimental confirmation of the self-torque of EUV beams

Light beams possessing a self-torque were experimentally generated by driving the HHG process in argon gas using two collinear, IR vortex beams with topological charges $\ell_1 = 1$ and $\ell_2 = 2$ that are derived from a high-power, ultrafast regenerative amplifier (Fig. 3A). Briefly (see materials and methods for full details), the two vortex beams are spatiotemporally overlapped to yield a mixed OAM driving mode, which is then directed onto a supersonic expansion of argon gas to generate self-torqued EUV beams (q = 13 to 23, ~20 to 36 eV). The presence of self-torque in the emitted high harmonics is confirmed by using a cylindrical mirror–flat-grating EUV spectrometer that serves to transform the self-torque-induced azimuthal chirp into a spatial chirp, which is then spectrally resolved as the (1D) focusing harmonic beam is dispersed (Fig. 3B). This simultaneous mapping of the azimuthal frequency chirp and high-harmonic comb to the same spectral axis is achieved by aligning the intensity crescent of the EUV beam [see materials and methods and (*54*)] such that its intensity-weighted center of mass (COM) is orthogonal to the mutually parallel focusing and dispersion axes of the EUV spectrometer. In this configuration, the azimuthal frequency chirp is mapped to a linear spatial chirp by the cylindrical mirror, and this resulting spatial chirp in each harmonic is then resolved by the grating. The resulting spatial-spectral distribution is then imaged via a high–pixel density, EUV charge-coupled device (CCD) camera, which allows for the simultaneous measurement of the azimuthal angular extent of the self-torqued beams (*54*) and the induced azimuthal frequency chirp with a high precision. High-resolution HHG spectra are collected as a function of time delay between the driving pulses by scanning the relative time delay between the two beams in two-cycle increments (i.e., 5.272 fs), which ensures that the HHG beam remains aligned to the spectrometer at each experimentally sampled time delay. Such exquisite control (fig. S6) allows us to simultaneously measure both the self-torque-induced frequency chirp of the HHG beams and the azimuthal angular range over a large range of relative time delays.

Figure 4 shows the comparison between experimental and theoretical results. Panels (A) and (B) show the experimental and theoretical spatial profile of the high harmonic beams, respectively. The crescent shape of the measured spatial profile already gives a clear indication of the presence of all intermediate OAM contributions from $q\ell_1$ to $q\ell_2$, and thus, of the creation of self-torqued beams. Panels (C) to (F) show

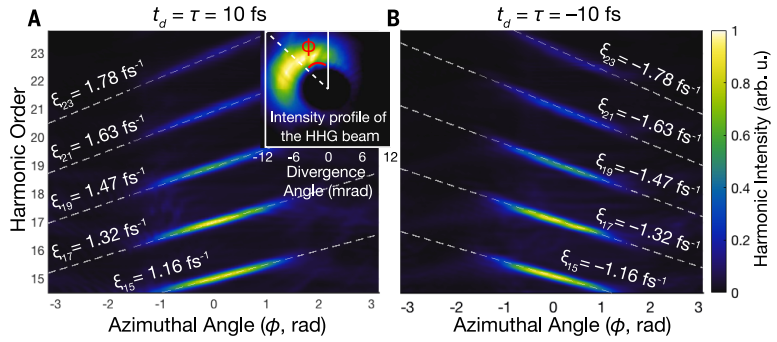

Fig. 2. Azimuthal frequency chirp of self-torqued beams. Simulated spatial HHG spectrum along the azimuthal coordinate (ϕ) when the time delay between the driving pulses is (**A**) 10 fs and (**B**) −10 fs. The self-torque of light imprints an azimuthal frequency chirp, which is different for each harmonic, as indicated by the gray dashed lines (obtained from Eq. 6). The azimuthal frequency chirp serves as a direct measurement of the self-torque of each harmonic beam. The inset of (A) shows the intensity profile of the HHG beam, as well as the definition of the azimuth, ϕ.

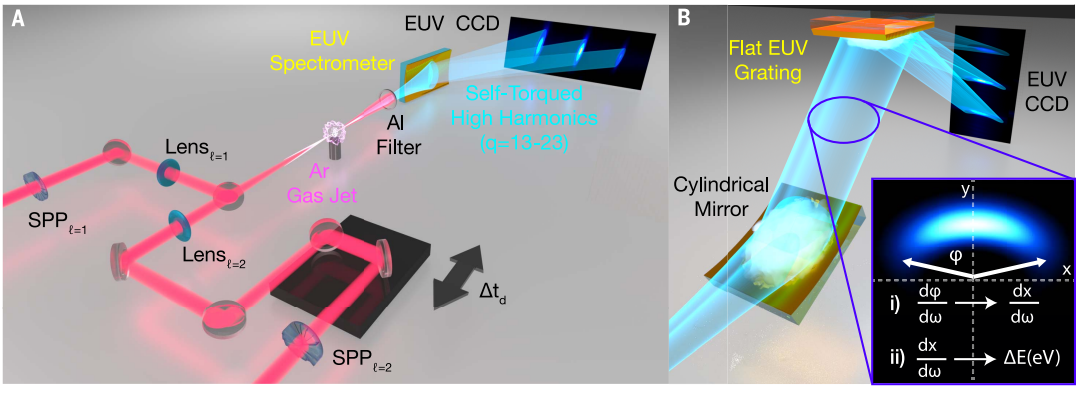

Fig. 3. Experimental scheme for generating and measuring light beams with a self-torque. (**A**) Two time-delayed, collinear IR pulses with the same wavelength (790 nm), but different OAM values, are focused into an argon gas target to produce harmonic beams with self-torque. (**B**) An EUV spectrometer, composed of a cylindrical mirror and flat-grating pair, collapses the HHG beam in the vertical dimension (lab frame y axis), while preserving spatial information, and thus the azimuthal extent in the transverse dimension (lab frame x axis). (Lower-right inset) The cylindrical mirror effectively maps the azimuthal frequency chirp into a spatial chirp along the lab frame x axis (i), which is then dispersed by the grating (ii).

the azimuthal chirp of the high harmonics for time delays of t_d = 50.4 (C and D) and −50.4 fs (E and F), respectively. The different slope of the azimuthal chirp, and the excellent agreement with the analytical theory given by Eq. 6 (gray dashed lines), and the full quantum simulations, confirm the presence of self-torque in the retrieved harmonic beams. Driving pulses of $\tau = 52$ fs have been used in our full quantum simulations to mimic the experimental parameters.

In Fig. 5, we plot the experimental (solid lines) and theoretical (dashed lines) self-torques obtained for the 17th (A), 19th (B), 21st (C), and 23rd (D) harmonics as a function of the time delay between the IR drivers, for the same parameters as in Fig. 4. As the time delay is varied, so too is the degree of azimuthal frequency chirp across the entire harmonic spectrum (according to Eqs. 2 and 6), verifying the dynamical build-up of OAM in the self-torqued beams. The self-torque is extracted from the measured azimuthal spectral shift (see Fig. 4F) and the azimuthal extent of the HHG beam [see (*54*) for details], using Eq. 6. The excellent agreement and, especially, the overall trend, unequivocally demonstrate the presence of a temporally evolving OAM content and, thus, a self-torque, in all the EUV harmonics generated.

Self-torque versus time duration and EUV supercontinuum generation

EUV beams with self-torque can be generated and controlled via the properties of the driving IR vortex beams, with optimal self-torque produced when the laser pulse separation is equal to their duration (i.e., $t_d = \tau$), where all intermediate OAM contributions appear with a similar weight (fig. S1). To illustrate this concept, Fig. 6A shows the simulated self-torque obtained for different IR driving pulse durations.

In particular, if driven by few-cycle pulses, the self-torque—and thus the azimuthal chirp—is high, with large amounts of OAM building up on an attosecond time scale (Fig. 6B, where $\tau = 4$ fs). If the torque is high enough, the harmonic frequency comb sweeps along the azimuth, encapsulating all the intermediate frequencies between the teeth of the harmonic comb. Thus, the frequency chirp of time-dependent OAM beams not only is useful to measure the self-torque but also represents an approach to obtain an EUV supercontinuum, as shown in the right inset of Fig. 6B. This allows for the creation of a very precise, azimuthally tunable frequency comb in the EUV and a supercontinuum spectrum that is complementary, yet distinct, from that of other approaches (*67*–*69*).

Conclusions

We have demonstrated that light beams with time-dependent OAM can be created, thus carrying optical self-torque. This property spans the applications of structured light beams (*1*) by adding a new degree of freedom, the self-torque, and thus introducing a new route to control light-matter interactions. In particular, ultrafast, short-wavelength, high harmonic beams with

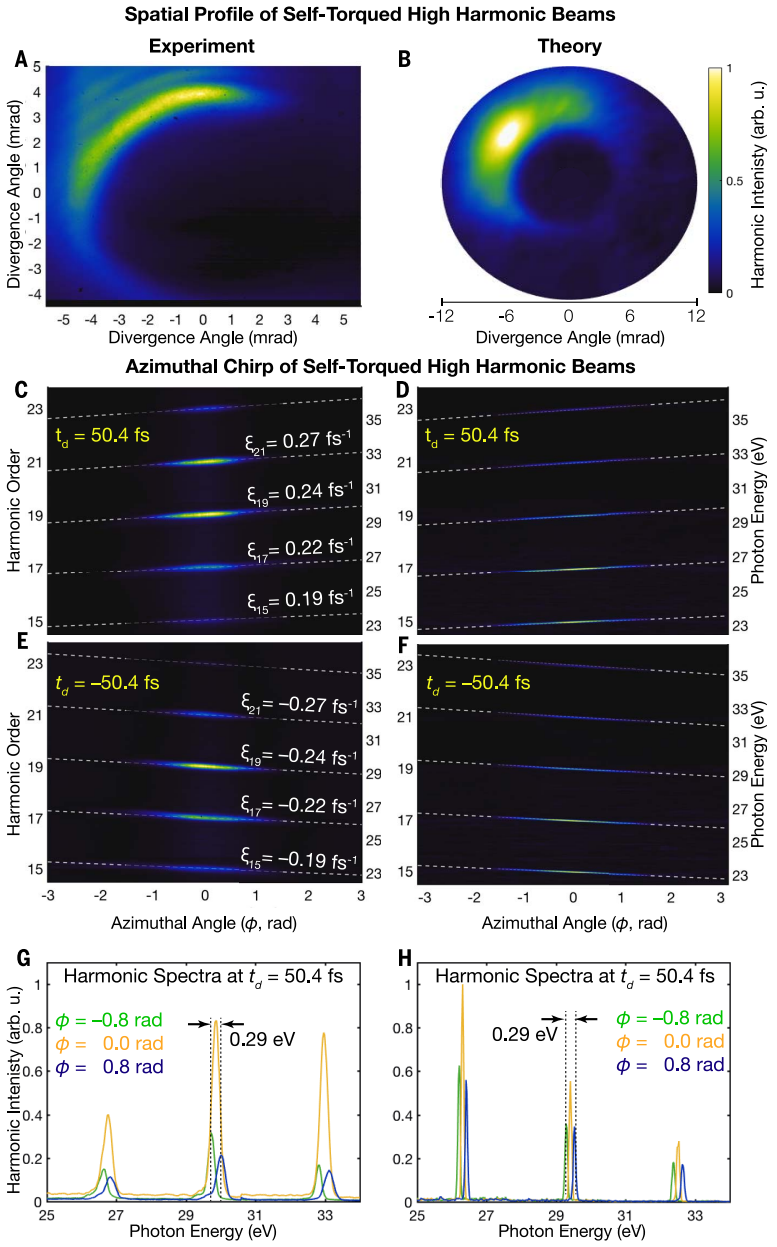

Fig. 4. Azimuthal frequency chirp and experimental measurement of the self-torque of EUV beams. (**A** and **B**) Experimental and theoretical spatial intensities of the HHG beams, after passing through an Al filter, comprising harmonics q = 13 to 23. (**C** to **F**) Spatial HHG spectrum along the azimuthal coordinate (ϕ) from experiment [(C) and (E)] and quantum simulations [(D) and (F)], when the time delay between the driving pulses is [(C) and (D)] 50.4 fs and [(E) and (F)] −50.4 fs. The self-torque of light imprints an azimuthal frequency chirp, which is different for each harmonic, as indicated by the gray dashed lines (obtained from Eq. 6). (**G** and **H**) Theoretical and experimental harmonic lineouts obtained at ϕ = −0.8 rad (green), ϕ = 0.0 rad (yellow), and ϕ = 0.8 rad (blue) for t_d = 50.4 fs. The azimuthal frequency chirp serves as a direct measurement of the self-torque of each harmonic beam. Differences in mode size of the theoretical and experimental EUV beam are due to slight differences in the fundamental beam mode sizes (see materials and methods).

self-torque can be naturally produced by taking advantage of the conservation laws inherent to extreme nonlinear optics. This capability can yield distinctively structured light beams that can deliver optical torque on the natural time and length scales of charge and spin ordering, e.g., femtosecond and nanometer. Finally, the self-torque of light imprints an azimuthal frequency chirp, which allows a way to experimentally measure and control it. Moreover, if the self-torque is high enough, the harmonic frequency comb sweeps smoothly along the azimuth, and if integrated, a high-frequency supercontinuum is obtained, thus presenting exciting perspectives in EUV and ultrafast spectroscopies of angular momentum dynamics.

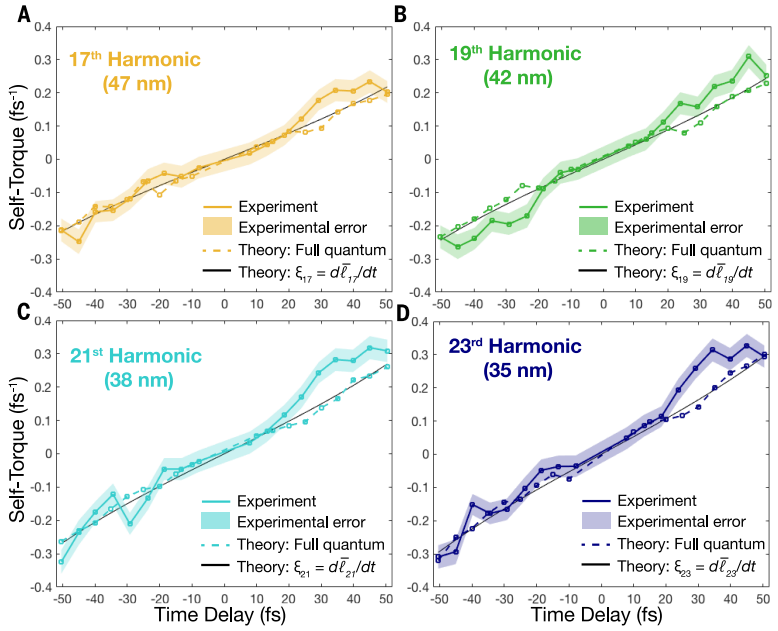

Fig. 5. Experimental confirmation of the self-torque of light in EUV beams. Self-torques obtained as a function of the time delay between the IR laser drivers for the 17th (**A**), 19th (**B**), 21st (**C**), and 23rd (**D**) harmonics. The experimental data are shown in solid-color lines, the results from full quantum simulations in dashed lines, and the analytical estimation given by Eq. 2 in solid black lines. The shaded regions depict the experimental uncertainty in the retrieved self-torque for each harmonic order, which themselves comprise the standard "one sigma" deviation of the measured self-torque (i.e., 68% of the measured self-torque values will fall within this uncertainty range).

Materials and methods

Theoretical approach for full quantum simulations describing the self-torque of OAM high harmonic beams

To calculate the HHG driven by two time-delayed OAM pulses, we use a theoretical method that computes both the full quantum single-atom HHG response and subsequent propagation (*55*). The propagation is based on the electromagnetic field propagator, in which we discretize the target (gas jet) into elementary radiators (*55*). The dipole acceleration of each elementary source is computed using the full quantum SFA, instead of solving directly the time-dependent Schrödinger equation, yielding a performance gain in computational time when computing HHG over the entire target (*55*). At the microscopic single-atom level, and for the parameters considered in this work, the spatial phase of the electric field can be well approximated as homogeneous in the vicinity of the atom where the wave packet dynamics take place. We assume that the harmonic radiation propagates with the vacuum phase velocity, which is a reasonable assumption for high-order harmonics. Propagation effects in the fundamental field, such as the production of free charges, the refractive index of the neutrals, and the group velocity walk-off, as well as absorption in the propagation of the harmonics, are taken into account. Although we account for the time-dependent nonlinear phase shifts in the driving fields, nonlinear spatial effects are not taken into account. We consider two vortex beams with $\ell_1 = 1$ and $\ell_2 = 2$, whose spatial structure is represented by a Laguerre-Gaussian beam [see

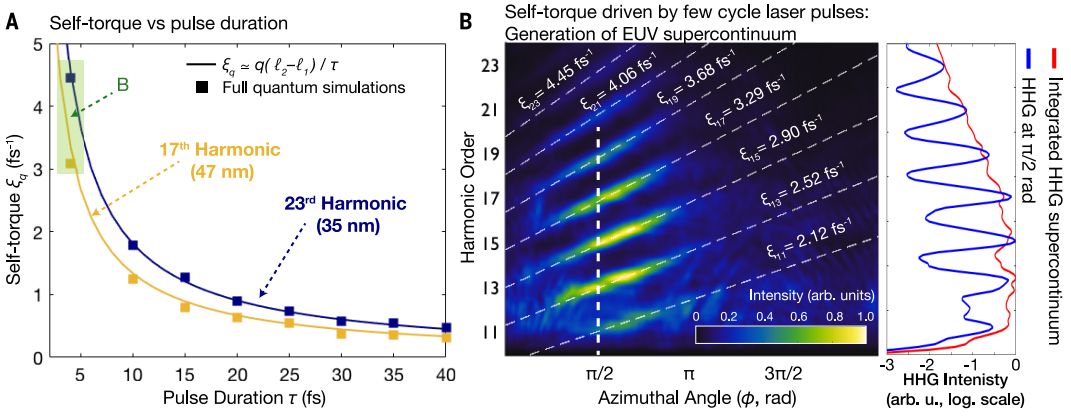

Fig. 6. Manifestation of self-torque for EUV supercontinuum generation. (**A**) Self-torque as a function of pulse duration for the 17th and 23rd harmonics, for time delays equal to their pulse duration. Solid lines are calculated from Eq. 2, and the squares correspond to results from full quantum simulations. (**B**) Spatiospectral HHG distributions when driven by two 800-nm, 4-fs pulses with ℓ_1=1 and ℓ_2=2, delayed by 4 fs with respect to each other. The optical self-torque imprints an azimuthal frequency chirp, which is different for each harmonic order, as indicated by the gray dashed lines (obtained from Eqs. 5 and 6). The right panel shows the HHG yield at $\pi/2$ rad (blue line, and white vertical dashed line in B) and the spatially integrated supercontinuum (red line).

eq. S13 in (*54*)]. The laser pulses are modeled with a $\sin^2$ envelope whose FWHM in intensity is τ, and centered at 800 nm in wavelength. The amplitudes of the two fields are chosen to obtain the same peak intensity (1.4×10^{14} W/cm^2) at focus for each driver at the radii of maximum superposition (i.e., the brightest intensity rings overlap spatially). The driving beam waists are chosen to overlap at the focal plane (being $w_1 = 30.0\,\mu$m for ℓ_1, and $w_2 = w_1/\sqrt{2} = 21.4\,\mu$m for ℓ_2) where a 10-μm-wide Ar gas jet flows along the direction perpendicular to the beam propagation, with a peak pressure of 667 Pa (5 torr). The low thickness of the gas jet is due to computational time limitations; however, on the basis of our previous results of OAM-HHG (*18*), we do not foresee any fundamental deviation when considering thicker gas jets closer to the experimental jet used in this work (a diameter of 150 μm).

Experimental setup for the generation and characterization of self-torqued EUV beams

The generation of self-torqued high-harmonics is achieved by impinging a pair of collinear, linearly polarized, nondegenerate IR-vortex beams onto a supersonic expansion of argon gas. The IR vortex beams (with topological charges of $\ell_1 = 1, \ell_2 = 2$) are derived from a high-power, ultrafast regenerative amplifier (790 nm, 40 fs, 9 mJ, 1 kHz, KMLabs Wyvern HE). The near full output of the amplifier is sent into a frequency-degenerate Mach-Zehndertype interferometer, which separates and later recombines the two driving pulses to form the dual-vortex IR driver. In each spatially separated arm of the interferometer, a combination of half-waveplates, faceted spiral phase plates (16 steps per phase ramp, HoloOr), and independent focusing lenses result in each beam possessing linear polarization, nondegenerate topological charges, and similarly sized intensity rings at focus. Independent irises in each beam path allow for fine tuning of the transverse mode size at focus and are used to match the size of the maximum-intensity ring for each driver. Using this strategy, the two driving beams possessed a full diameter of the intensity of ~65 μm—corresponding to waists sizes of w_{ℓ_1} ≈45 μm and $w_{\ell_2} \approx 33$ μm (*70*). The driving laser modes themselves, both individually and combined, are characterized by a modified Gerchberg-Saxton phase retrieval algorithm, which solves for the phase of a propagating light beam and allows extraction of the OAM content of the IR vortices (see supplementary text section S4), thus ensuring high-quality vortex beams for driving the HHG process (movie S1). This modified Gerchberg-Saxton method acquires and retrieves OAM content much faster than our previous characterization method using ptychography (*71*), but it is limited to nonmultiplexed (i.e., single-color) beams. A high-precision, high-accuracy, and high-repeatability delay stage (Newport, XMS-160S) is used to control the relative time delay between the two driving pulses, with subfemtosecond precision. The pulses are recombined at the output of the interferometer using a low-dispersion beam-splitter and then directed onto the supersonic expansion of argon gas in a vacuum chamber. We take extreme care to ensure that the two arms experience similar dispersion by using the same thickness and design of optics in each arm of the interferometer, which helps to reduce effects from carrier-to-envelope phase variation in the separate beam paths, while also ensuring similar pulse widths. Finally, the use of a frequency-degenerate Mach-Zehnder interferometer results in a 50% intensity loss of each driver when combined at the interferometer's exit; however, this configuration proved ideal to minimize pulse dispersion, while also allowing for independent control of the polarization and topological charge of the driving beams.

Self-torqued high harmonics are generated via the HHG up-conversion process, then dispersed in 1D via a cylindrical mirror–flat-grating EUV spectrometer and finally collected by a CCD camera (Andor Newton 940). A 200-nm-thick aluminum filter blocks the residual driving light before entering the spectrometer—while passing harmonics over its transmission range, ~17 to 72 eV—and all harmonic spectra are corrected for the transmission of the EUV beamline. To align the resulting HHG crescent to the spectrometer, we exploit the natural physics of time-delayed OAM beams. When two vortex beams with $\ell_1 = 1$ and $\ell_2 = 2$ are superposed, such that their amplitudes and intensity rings are equal, the resulting intensity distribution exhibits a characteristic crescent shape. The azimuthal orientation of the COM of the intensity crescent can be controlled via a relative phase delay between the two single-mode OAM drivers, such that a full-cycle phase delay (i.e., 2.635 fs for the 790-nm pulses used here) returns the intensity crescent to its initial position. By carefully adjusting the time delay between the two single-mode IR vortex beams, we can control the alignment of the intensity crescent of the driving beam [see (*54*)], and so to the resulting crescent-shaped harmonic beam (because, to first order, the HHG beam profile mimics the intensity distribution of the driving beam). Once the harmonic beam is aligned to the spectrometer, the relative phase delay between the driving beams is scanned in two-cycle increments (i.e., 5.272 fs), which ensures that the HHG beam remains aligned to the spectrometer at each experimentally sampled time delay. Such exquisite control (see fig. S6) allows us to simultaneously measure both the self-torque-induced frequency chirp of the HHG beam and the azimuthal angular range (see supplementary text section S7) with a high resolution.

REFERENCES AND NOTES

1. H. Rubinsztein-Dunlop *et al.*, Roadmap on structured light. *J. Opt.* **19**, 013001 (2017). doi: 10.1088/2040-8978/19/1/013001
2. L. Allen, M. W. Beijersbergen, R. J. C. Spreeuw, J. P. Woerdman, Orbital angular momentum of light and the transformation of Laguerre-Gaussian laser modes. *Phys. Rev. A* **45**, 8185–8189 (1992). doi: 10.1103/PhysRevA.45.8185; pmid: 9906912
3. A. M. Yao, M. J. Padgett, Orbital angular momentum: Origins, behavior and applications. *Adv. Opt. Photonics* **3**, 161–204 (2011). doi: 10.1364/AOP.3.000161
4. A. E. Willner *et al.*, Optical communication using orbital angular momentum beams. *Adv. Opt. Photonics* **7**, 66–106 (2015). doi: 10.1364/AOP.7.000066
5. A. Trichili *et al.*, Optical communication beyond orbital angular momentum. *Sci. Rep.* **6**, 27674 (2016). doi: 10.1038/srep27674; pmid: 27283799
6. S. Fürhapter, A. Jesacher, S. Bernet, M. Ritsch-Marte, Spiral phase contrast imaging in microscopy. *Opt. Express* **13**, 689–694 (2005). doi: 10.1364/OPEX.13.000689; pmid: 19494929
7. M. A. Lauterbach, M. Guillon, A. Soltani, V. Emiliani, STED microscope with spiral phase contrast. *Sci. Rep.* **3**, 2050 (2013). doi: 10.1038/srep02050; pmid: 23787399
8. G. Vicidomini, P. Bianchini, A. Diaspro, STED super-resolved microscopy. *Nat. Methods* **15**, 173–182 (2018). doi: 10.1038/nmeth.4593; pmid: 29377014
9. M. Padgett, R. Bowman, Tweezers with a twist. *Nat. Photonics* **5**, 343–348 (2011). doi: 10.1038/nphoton.2011.81
10. J. P. Torres, L. Torner, *Twisted Photons: Applications of Light with Orbital Angular Momentum*. (Bristol: Wiley-VCH, 2011).
11. L. Marrucci, C. Manzo, D. Paparo, Optical spin-to-orbital angular momentum conversion in inhomogeneous anisotropic media. *Phys. Rev. Lett.* **96**, 163905 (2006). doi: 10.1103/PhysRevLett.96.163905; pmid: 16712234
12. M. W. Beijersbergen, R. P. C. Coerwinkel, M. Kristensen, J. P. Woerdman, Helical-wavefront laser beams produced with a spiral phase plate. *Opt. Commun.* **112**, 321–327 (1994). doi: 10.1016/0030-4018(94)90638-6
13. J. Atencia, M.-V. Collados, M. Quintanilla, J. Marín-Sáez, Í. J. Sola, Holographic optical element to generate achromatic vortices. *Opt. Express* **21**, 21056–21061 (2013). doi: 10.1364/OE.21.021056; pmid: 24103978
14. J. C. T. Lee, S. J. Alexander, S. D. Kevan, S. Roy, B. J. McMorran, Laguerre-Gauss and Hermite-Gauss soft x-ray states generated using diffractive optics. *Nat. Photonics* **13**, 205–209 (2019). doi: 10.1038/s41566-018-0328-8
15. M. Zürch, C. Kern, P. Hansinger, A. Dreischuh, C. Spielmann, Strong-field physics with singular light beams. *Nat. Phys.* **8**, 743–746 (2012). doi: 10.1038/nphys2397
16. C. Hernández-García, A. Picón, J. San Román, L. Plaja, Attosecond extreme ultraviolet vortices from high-order harmonic generation. *Phys. Rev. Lett.* **111**, 083602 (2013). doi: 10.1103/PhysRevLett.111.083602; pmid: 24010438
17. G. Gariepy *et al.*, Creating high-harmonic beams with controlled orbital angular momentum. *Phys. Rev. Lett.* **113**, 153901 (2014). doi: 10.1103/PhysRevLett.113.153901; pmid: 25375710
18. C. Hernández-García, J. San Román, L. Plaja, A. Picón, Quantum-path signatures in attosecond helical beams driven by optical vortices. *New J. Phys.* **17**, 093029 (2015). doi: 10.1088/1367-2630/17/9/093029
19. R. Géneaux *et al.*, Synthesis and characterization of attosecond light vortices in the extreme ultraviolet. *Nat. Commun.* **7**, 12583 (2016). doi: 10.1038/ncomms12583; pmid: 27573787
20. L. Rego, J. San Román, A. Picón, L. Plaja, C. Hernández-García, Nonperturbative twist in the generation of extreme-ultraviolet vortex beams. *Phys. Rev. Lett.* **117**, 163202 (2016). doi: 10.1103/PhysRevLett.117.163202; pmid: 27792355
21. A. Turpin, L. Rego, A. Picón, J. San Román, C. Hernández-García, Extreme ultraviolet fractional orbital angular momentum beams from high harmonic generation. *Sci. Rep.* **7**, 43888 (2017). doi: 10.1038/srep43888; pmid: 28281655
22. F. Kong *et al.*, Controlling the orbital angular momentum of high harmonic vortices. *Nat. Commun.* **8**, 14970 (2017). doi: 10.1038/ncomms14970; pmid: 28378823
23. D. Gauthier *et al.*, Tunable orbital angular momentum in high-harmonic generation. *Nat. Commun.* **8**, 14971 (2017). doi: 10.1038/ncomms14971; pmid: 28378741
24. C. Hernández-García, A twist in coherent X-rays. *Nat. Phys.* **13**, 327–329 (2017). doi: 10.1038/nphys4088
25. R. Géneaux *et al.*, Radial index of Laguerre-Gaussian modes in high-order-harmonic generation. *Phys. Rev. A* **95**, 051801 (2017). doi: 10.1103/PhysRevA.95.051801
26. K. M. Dorney *et al.*, Controlling the polarization and vortex charge of attosecond high-harmonic beams via simultaneous spin-orbit momentum conservation. *Nat. Photonics* **13**, 123–130 (2019). doi: 10.1038/s41566-018-0304-3
27. W. Paufler, B. Böning, S. Fritzsche, Tailored orbital angular momentum in high-order harmonic generation with bicircular Laguerre-Gaussian beams. *Phys. Rev. A* **98**, 011401 (2018). doi: 10.1103/PhysRevA.98.011401
28. E. Pisanty *et al.*, Conservation of torus-knot angular momentum in high-order harmonic generation. *Phys. Rev. Lett.*

122, 203201 (2019). doi: 10.1103/PhysRevLett.122.203201; pmid: 31172784
29. M. Babiker, W. L. Power, L. Allen, Light-induced torque on moving atoms. *Phys. Rev. Lett.* **73**, 1239–1242 (1994). doi: 10.1103/PhysRevLett.73.1239; pmid: 10057660
30. H. He, M. E. Friese, N. R. Heckenberg, H. Rubinsztein-Dunlop, Direct observation of transfer of angular momentum to absorptive particles from a laser beam with a phase singularity. *Phys. Rev. Lett.* **75**, 826–829 (1995). doi: 10.1103/PhysRevLett.75.826; pmid: 10060128
31. A. T. O'Neil, M. J. Padgett, Three-dimensional optical confinement of micron-sized metal particles and the decoupling of the spin and orbital angular momentum within an optical spanner. *Opt. Commun.* **185**, 139–143 (2000). doi: 10.1016/S0030-4018(00)00989-5
32. D. M. Villeneuve *et al*., Forced molecular rotation in an optical centrifuge. *Phys. Rev. Lett.* **85**, 542–545 (2000). doi: 10.1103/PhysRevLett.85.542; pmid: 10991335
33. D. G. Grier, A revolution in optical manipulation. *Nature* **424**, 810–816 (2003). pmid: 12917694
34. M. E. J. Friese, H. Rubinsztein-Dunlop, J. Gold, P. Hagberg, D. Hanstorp, Optically driven micromachine elements. *Appl. Phys. Lett.* **78**, 547–549 (2001). doi: 10.1063/1.1339995
35. E. M. Wright, J. Arlt, K. Dholakia, Toroidal optical dipole traps for atomic Bose-Einstein condensates using Laguerre-Gaussian beams. *Phys. Rev. A* **63**, 013608 (2000). doi: 10.1103/PhysRevA.63.013608
36. A. Turpin *et al*., Blue-detuned optical ring trap for Bose-Einstein condensates based on conical refraction. *Opt. Express* **23**, 1638–1650 (2015). doi: 10.1364/OE.23.001638; pmid: 25835921
37. A. F. Rañada, L. Vázquez, On the self-torque on an extended classical charged particle. *J. Phys. Math. Gen.* **17**, 2011–2016 (1984). doi: 10.1088/0305-4470/17/10/013
38. S. R. Dolan *et al*., Gravitational self-torque and spin precession in compact binaries. *Phys. Rev. D Part. Fields Gravit. Cosmol.* **89**, 064011 (2014). doi: 10.1103/PhysRevD.89.064011
39. K. J. Schafer, B. Yang, L. F. DiMauro, K. C. Kulander, Above threshold ionization beyond the high harmonic cutoff. *Phys. Rev. Lett.* **70**, 1599–1602 (1993). doi: 10.1103/PhysRevLett.70.1599; pmid: 10053336
40. P. B. Corkum, Plasma perspective on strong field multiphoton ionization. *Phys. Rev. Lett.* **71**, 1994–1997 (1993). doi: 10.1103/PhysRevLett.71.1994; pmid: 10054556
41. A. Rundquist *et al*., Phase-matched generation of coherent soft x-rays. *Science* **280**, 1412–1415 (1998). doi: 10.1126/science.280.5368.1412; pmid: 9603725
42. R. A. Bartels *et al*., Generation of spatially coherent light at extreme ultraviolet wavelengths. *Science* **297**, 376–378 (2002). doi: 10.1126/science.1071718; pmid: 12130779
43. T. Popmintchev *et al*., Bright coherent ultrahigh harmonics in the keV x-ray regime from mid-infrared femtosecond lasers. *Science* **336**, 1287–1291 (2012). doi: 10.1126/science.1218497; pmid: 22679093
44. T. Fan *et al*., Bright circularly polarized soft X-ray high harmonics for X-ray magnetic circular dichroism. *Proc. Natl. Acad. Sci. U.S.A.* **112**, 14206–14211 (2015). doi: 10.1073/pnas.1519666112; pmid: 26534992
45. P. M. Paul *et al*., Observation of a train of attosecond pulses from high harmonic generation. *Science* **292**, 1689–1692 (2001). doi: 10.1126/science.1059413; pmid: 11387467
46. M. Hentschel *et al*., Attosecond metrology. *Nature* **414**, 509–513 (2001). doi: 10.1038/35107000; pmid: 11734845
47. B. Rodenburg *et al*., Influence of atmospheric turbulence on states of light carrying orbital angular momentum. *Opt. Lett.* **37**, 3735–3737 (2012). doi: 10.1364/OL.37.003735; pmid: 22941007
48. C. Chen *et al*., Distinguishing attosecond electron-electron scattering and screening in transition metals. *Proc. Natl. Acad. Sci. U.S.A.* **114**, E5300–E5307 (2017). doi: 10.1073/pnas.1706466114; pmid: 28630331
49. P. Tengdin *et al*., Critical behavior within 20 fs drives the out-of-equilibrium laser-induced magnetic phase transition in nickel. *Sci. Adv.* **4**, eaap9744 (2018). doi: 10.1126/sciadv.aap9744; pmid: 29511738
50. A. Picón *et al*., Transferring orbital and spin angular momenta of light to atoms. *New J. Phys.* **12**, 083053 (2010). doi: 10.1088/1367-2630/12/8/083053
51. F. Calegari *et al*., Charge migration induced by attosecond pulses in bio-relevant molecules. *J. Phys. B At. Mol. Opt. Phys.* **49**, 142001 (2016). doi: 10.1088/0953-4075/49/14/142001
52. G. Hermann *et al*., Attosecond angular flux of partial charges on the carbon atoms of benzene in non-aromatic excited state. *Chem. Phys. Lett.* **683**, 553–558 (2017). doi: 10.1016/j.cplett.2017.01.030
53. R. M. Kerber, J. M. Fitzgerald, S. S. Oh, D. E. Reiter, O. Hess, Orbital angular momentum dichroism in nanoantennas. *Commun. Phys.* **1**, 87 (2018). doi: 10.1038/s42005-018-0088-2
54. See supplementary materials.
55. C. Hernández-García *et al*., High-order harmonic propagation in gases within the discrete dipole approximation. *Phys. Rev. A* **82**, 033432 (2010). doi: 10.1103/PhysRevA.82.033432
56. C. Hernández-García *et al*., Extreme ultraviolet vector beams driven by infrared lasers. *Optica* **4**, 520 (2017). doi: 10.1364/OPTICA.4.000520
57. M. Lewenstein, P. Balcou, M. Y. Ivanov, A. L'Huillier, P. B. Corkum, Theory of high-harmonic generation by low-frequency laser fields. *Phys. Rev. A* **49**, 2117–2132 (1994). doi: 10.1103/PhysRevA.49.2117; pmid: 9910464
58. A. Zaïr *et al*., Quantum path interferences in high-order harmonic generation. *Phys. Rev. Lett.* **100**, 143902 (2008). doi: 10.1103/PhysRevLett.100.143902; pmid: 18518033
59. M. V. Berry, Optical vortices evolving from helicoidal integer and fractional phase steps. *J. Opt. A, Pure Appl. Opt.* **6**, 259–268 (2004). doi: 10.1088/1464-4258/6/2/018
60. J. Leach, E. Yao, M. Padgett, Observation of the vortex structure of non-integer vortex beam. *New J. Phys.* **6**, 71 (2004). doi: 10.1088/1367-2630/6/1/071
61. S. N. Alperin, M. E. Siemens, Angular Momentum of Topologically Structured Darkness. *Phys. Rev. Lett.* **119**, 203902 (2017). doi: 10.1103/PhysRevLett.119.203902; pmid: 29219346
62. E. Karimi, L. Marrucci, C. de Lisio, E. Santamato, Time-division multiplexing of the orbital angular momentum of light. *Opt. Lett.* **37**, 127–129 (2012). doi: 10.1364/OL.37.000127; pmid: 22854442
63. I. J. Sola *et al*., Controlling attosecond electron dynamics by phase-stabilized polarization gating. *Nat. Phys.* **2**, 319–322 (2006). doi: 10.1038/nphys281
64. H. Vincenti, F. Quéré, Attosecond lighthouses: How to use spatiotemporally coupled light fields to generate isolated attosecond pulses. *Phys. Rev. Lett.* **108**, 113904 (2012). doi: 10.1103/PhysRevLett.108.113904; pmid: 22540475
65. J. A. Wheeler *et al*., Attosecond lighthouses from plasma mirrors. *Nat. Photonics* **6**, 829–833 (2012). doi: 10.1038/nphoton.2012.284
66. C. Hernández-García, A. Jaron-Becker, D. D. Hickstein, A. Becker, C. G. Durfee, High-order-harmonic generation driven by pulses with angular spatial chirp. *Phys. Rev. A (Coll. Park)* **93**, 023825 (2016). doi: 10.1103/PhysRevA.93.023825
67. I. P. Christov, M. M. Murnane, H. C. Kapteyn, High-harmonic generation of attosecond pulses in the "single cycle" regime. *Phys. Rev. Lett.* **78**, 1251–1254 (1997). doi: 10.1103/PhysRevLett.78.1251
68. M. Chini, K. Zhao, Z. Chang, The generation, characterization and applications of broadband isolated attosecond pulses. *Nat. Photonics* **8**, 178–186 (2014). doi: 10.1038/nphoton.2013.362
69. W. Holgado *et al*., Continuous spectra in high-harmonic generation driven by multicycle laser pulses. *Phys. Rev. A* **93**, 013816 (2016). doi: 10.1103/PhysRevA.93.013816
70. J. Zhang, S.-J. Huang, F.-Q. Zhu, W. Shao, M.-S. Chen, Dimensional properties of Laguerre-Gaussian vortex beams. *Appl. Opt.* **56**, 3556–3561 (2017). doi: 10.1364/AO.56.003556; pmid: 28430234
71. Y. Esashi *et al*., Ptychographic amplitude and phase reconstruction of bichromatic vortex beams. *Opt. Express* **26**, 34007–34015 (2018). doi: 10.1364/OE.26.034007; pmid: 30650831

ACKNOWLEDGMENTS

Funding: C.H.-G., J.S.R., and L.P. acknowledge support from Junta de Castilla y León (SA046U16), Ministerio de Economía y Competitividad (FIS2016-75652-P), FEDER funds, and Ministerio de Ciencia, Innovación y Universidades (Eq. C2018-0041 17-P). L.R. acknowledges support from Ministerio de Educación, Cultura y Deporte (FPU16/02591). C.H.-G. acknowledges support from a 2017 Leonardo Grant for Researchers and Cultural Creators, BBVA Foundation, and Ministerio de Ciencia, Innovación y Universidades for a Ramón y Cajal contract (RYC-2017-22745), cofunded by the European Social Fund. H.K. and M.M. acknowledge support from the Department of Energy BES Award no. DE-FG02-99ER14982 for the experimental implementation, the DARPA TEE Program Award. no. D18AC00017 for the new experimental characterization methods developed, as well as a MURI grant from the Air Force Office of Scientific Research under Award no. FA9550-16-1-0121 for the theory. Q.L.N. acknowledges support from National Science Foundation Graduate Research Fellowships (grant no. DGE-1144083). N.J.B. and D.C. acknowledge support from National Science Foundation Graduate Research Fellowships (grant no. DGE-1650115). E.P. acknowledges Cellex-ICFO-MPQ fellowship funding; E.P. and M.L. acknowledge the Spanish Ministry MINECO (National Plan 15 Grant: FISICATEAMO no. FIS2016-79508-P, SEVERO OCHOA no. SEV-2015-0522, FPI), European Social Fund, Fundació Cellex, Generalitat de Catalunya (AGAUR grant no. 2017 SGR 1341 and CERCA/Program), ERC AdG OSYRIS, EU FETPRO QUIC, and the National Science Centre, Poland-Symfonia grant no. 2016/20/W/ST4/00314. We acknowledge the computer resources at MareNostrum and the technical support provided by Barcelona Supercomputing Center (RES-AECT-2014-2-0085). This research made use of the high-performance computing resources of the Castilla y León Supercomputing Center (SCAYLE, www.scayle.es/), financed by the European Regional Development Fund (ERDF). **Author contributions:** L.R., J.S.R, L.P., and C.H.-G. conceived the idea of self-torqued beams. K.M.D., L.R., H.C.K., M.M.M., and C.H.-G. designed the experiment. K.M.D., N.J.B., Q.L.N., C.-T.L., D.E.C., and A.L. conducted the experiment. K.M.D. and N.J.B. analyzed the experimental data. L.R., J.S.R., L.P., E.P., and C.H.-G. performed the theoretical simulations and analyzed the resulting data. C.H.-G., L.P., M.L., M.M.M., and H.C.K. supervised the theoretical simulations, experimental work, and developed the facilities and measurement capabilities. L.R., K.M.D., J.S.R., M.M.M., L.P., and C.H.-G. wrote and prepared the manuscript. All authors provided constructive improvements and feedback to this work. **Competing interests:** M.M.M. and H.C.K. have a financial interest in KMLabs. All other authors declare no competing financial interests. **Data and materials availability:** All data needed to evaluate the conclusions in the paper are present in the paper or the supplementary materials.

SUPPLEMENTARY MATERIALS

science.sciencemag.org/content/364/6447/eaaw9486/suppl/DC1
Supplementary Text
Figs. S1 to S8
References (72–79)
Movie S1

8 February 2019; accepted 3 May 2019
10.1126/science.aaw9486

Science

Generation of extreme-ultraviolet beams with time-varying orbital angular momentum

Laura Rego, Kevin M. Dorney, Nathan J. Brooks, Quynh L. Nguyen, Chen-Ting Liao, Julio San Román, David E. Couch, Allison Liu, Emilio Pisanty, Maciej Lewenstein, Luis Plaja, Henry C. Kapteyn, Margaret M. Murnane and Carlos Hernández-García

Science **364** (6447), eaaw9486.
DOI: 10.1126/science.aaw9486

Pulses with a twist and torque

Structured light beams can serve as vortex beams carrying optical angular momentum and have been used to enhance optical communications and imaging. Rego *et al.* generated dynamic vortex pulses by interfering two incident time-delayed vortex beams with different orbital angular momenta through the process of high harmonic generation. A controlled time delay between the pulses allowed the high harmonic extreme-ultraviolet vortex beam to exhibit a time-dependent angular momentum, called self-torque. Such dynamic vortex pulses could potentially be used to manipulate nanostructures and atoms on ultrafast time scales.

Science, this issue p. eaaw9486

3.5.2 *Necklace-structured high harmonic generation for low-divergence, soft-X-ray harmonic combs with tunable line spacing*

Resumen

Las nuevas fuentes de luz de rayos X coherentes son fundamentales para el avance de la nanotecnología, ya que permiten descubrir nueva física fundamental, así como manipular las propiedades electrónicas, magnéticas y de transporte de los materiales. Entre ellas, la generación de armónicos de orden alto (HHG) proporciona capacidades únicas para controlar las propiedades de la luz de longitud de onda corta como la duración del pulso, la polarización, la amplitud y la fase.

En este trabajo [17], demostramos teórica y experimentalmente una técnica para controlar el contenido espectral y la divergencia de los pulsos de luz emitidos en la HHG, cuyas frecuencias están en el rango del ultravioleta extremo o incluso en los rayos X blandos. Para ello, combinamos dos pulsos infrarrojos con contenido de momento angular orbital (OAM) opuesto y no degenerado para crear un haz infrarrojo cuyo perfil transversal tiene forma de "collar de cuentas" con fase. Este haz incide sobre un chorro de gas dando lugar al proceso de HHG en el cual se emiten peines de frecuencias de armónicos de orden alto cuyo espaciado podemos regular. Concretamente, la conservación del OAM nos permite ajustar el espaciado entre líneas de los peines de armónicos de orden alto. Además, la emisión de la HHG en eje tiene una divergencia muy baja, por debajo de la obtenida cuando se utilizan haces incidentes Gaussianos, y que disminuye aún más con el orden armónico.

Este trabajo proporciona un nuevo grado de libertad para el diseño de peines de armónicos, particularmente en el régimen de rayos X, donde las opciones disponibles son muy limitadas. En particular, estos haces de armónicos pueden dar lugar a sondas más sensibles para estudiar las dinámicas de carga y espín ultrarrápidas en moléculas, nanopartículas y materiales.

Necklace-structured high harmonic generation for low-divergence, soft X-ray harmonic combs with tunable line spacing

Laura Rego[1]†, Nathan J. Brooks[2]†, Quynh L. D. Nguyen[2*], Julio San Román[1], Iona Binnie[2], Luis Plaja[1], Henry C. Kapteyn[2], Margaret M. Murnane[2], Carlos Hernández-García[1]

[1]Grupo de Investigación en Aplicaciones del Láser y Fotónica, Departamento de Física Aplicada, University of Salamanca, Salamanca E-37008, Spain

[2]JILA - Department of Physics, University of Colorado and NIST, Boulder, Colorado 80309, USA

†These authors contributed equally to this work.

[*]Corresponding Authors: Quynh.L.Nguyen@colorado.edu

Abstract

The extreme nonlinear optical process of high-harmonic generation (HHG) makes it possible to map the properties of a laser beam onto a radiating electron wavefunction, and in turn, onto the emitted x-ray light. Bright HHG beams typically emerge from a longitudinal phased distribution of atomic-scale quantum antennae. Here, we form a transverse necklace-shaped phased array of HHG emitters, where orbital angular momentum conservation allows us to tune the line spacing and divergence properties of extreme-ultraviolet and soft X-ray high harmonic combs. The on-axis HHG emission has extremely low divergence, well below that obtained when using Gaussian driving beams, which further decreases with harmonic order. This work provides a new degree of freedom for the design of harmonic combs – particularly in the soft X-ray regime, where very limited options are available. Such harmonic beams can enable more sensitive probes of the fastest correlated charge and spin dynamics in molecules, nanoparticles and materials.

Introduction

A new generation of coherent x-ray sources are opening up a new understanding of the fastest coupled charge, spin and phonon interactions and transport in materials (1-5). X-ray sources such as free electron lasers (6, 7) and high-harmonic generation (HHG) (8-14) can produce coherent light from the extreme-ultraviolet (EUV) to the soft X-ray (SXR) region. Moreover, in the case of HHG sources, they are perfectly synchronized to the driving laser, to sub-femtosecond precision, and present high temporal coherence. In HHG, an atom undergoes strong field ionization in an intense femtosecond laser field. The liberated electron is then accelerated in the laser field before recombining with the parent ion, which results in the emission of higher-order harmonics. In the microscopic quantum picture, the driving laser creates a nanoscale dipole antenna in each atom, which radiates high harmonics of the fundamental laser field. This short wavelength radiation can be manipulated at the single atom level or at the macroscopic phase-matching level by structuring the intensity, frequency content, polarization and orbital angular momentum (OAM) of the driving laser field (15-21).

Currently, control of the frequency content of the HHG light source – a key property for many advanced applications – is gained by changing the wavelength of the driving laser or by using frequency-selective optics or monochromators. By tuning the driving laser wavelength from the mid- and near-infrared to the ultraviolet, the HHG spectrum can be tuned from a bright coherent supercontinuum to a set of narrow-band (22, 23). Bright high-order harmonics extending into the keV region, well beyond the water window, can be obtained by using mid-infrared driving fields (22, 24-30). Narrow spectral peaks into the SXR region can be achieved by driving harmonics with UV lasers, although the low ponderomotive energy ($\sim\lambda^2$) necessitates the use of extremely high laser intensities (23). The manipulation of the frequency and the divergence of these HHG beams is still challenging and demands very efficient monochromators and good focusing optics in the EUV and SXR regions. An appealing alternative is to instead imprint the desired properties directly onto the HHG light, by tailoring the driving laser and taking advantage of selection rules. Recent

works have demonstrated the relevance of non-perturbative dynamics underlying HHG in rephasing the wavefront to achieve good divergence profiles (31, 32), which can lead to focusing of harmonic beams without additional optics. However, it is still not possible to achieve general/full control over the frequency content and divergence properties of HHG radiation, to tailor the HHG illumination for applications.

The emerging field of ultrafast structured light is providing exciting techniques for enhancing laser-matter interactions for applications (33). In particular, exploitation of the OAM is opening up unexpected avenues for controlling the properties of high-harmonic fields as they are being generated. OAM manifests itself as a variation of the beam's spatial phase along its transverse profile, and it is characterized by its topological charge, ℓ, or number of 2π phase twists along the azimuthal coordinate (34, 35). Since the first experiments in 2012 (36), OAM-driven HHG has proven to be a powerful tool for shaping the spatial properties of higher order harmonics—including the topological charge, intensity distribution (37-42), and polarization properties (20, 43). OAM can also be used to control the temporal shape of HHG—through the generation of helical attosecond pulses (37,39) or high harmonics with an OAM that increases during the pulse, which is a unique capability of HHG light (21). Although the ability to control the temporal shape implies an ability to also control the spectral shape, to date OAM has not been yet exploited to tailor the spectral content in HHG.

In this work, we are able to control the spectral and divergence properties of HHG by driving it with optimally phased necklace laser beams – a class of ring-shaped beams with azimuthally modulated amplitude and phase, resulting from the interference of multiple OAM modes. Our theoretical and experimental results show that by driving HHG with these structured beams, we generate a transverse phased array of HHG sources which emit a bright and adjustable harmonic comb along the optical axis. OAM selection rules and transverse phase-matching conditions allow us to tune the spectral spacing and divergence properties of these harmonics. Significantly, the on-axis HHG emission has extremely low divergence, which is not only lower than that obtained with

standard Gaussian beams, but the scaling behavior with the harmonic order is also reversed — such that higher-order harmonics exhibit progressively lower divergences (see Fig. 1). Our simulations demonstrate that these properties extend into the water window SXR regime, when driven by mid-IR necklace beams. This work provides a new degree of freedom for the design of harmonic combs – particularly in the SXR regime, where very limited options are available.

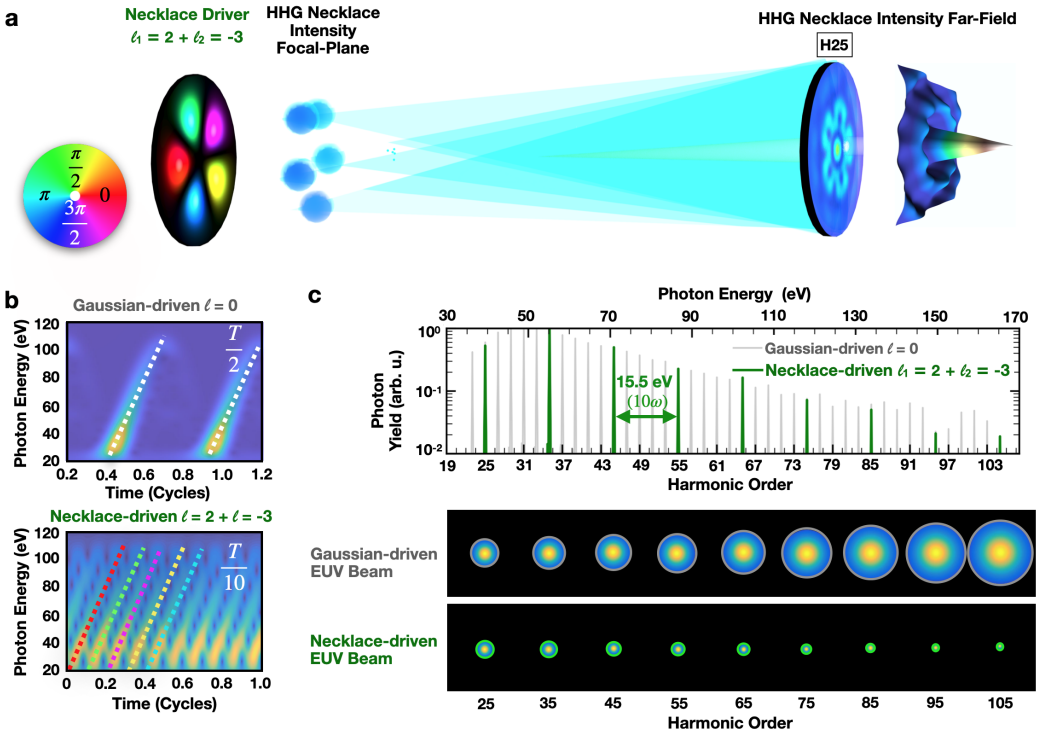

Figure 1 | Tunable, low-divergence high harmonic combs via necklace-driven HHG. a Two linearly polarized vortex beams carrying OAM of $\ell_1=2$ and $\ell_2=-3$ are overlapped to create a necklace-structured intensity and phase profile, and focused into He/Ar gas to drive HHG. The intensity lobes at the necklace focal plane represent a phased array of EUV/SXR emitters which interfere on-axis to form a comb of harmonics with a spacing dependent on the OAM of the driving fields. The harmonic intensity profile shows a strong emission on-axis (detailed in the figure for the 25th harmonic). **b** Time-frequency analysis of the simulated on-axis harmonic comb for Gaussian and necklace ($\ell_1=2$, $\ell_2=-3$) driven HHG in He at 800 nm. The dashed-color lines indicate the corresponding phase from panel **a** for each emission event. **c** HHG spectrum for the case of necklace-driven and Gaussian-driven HHG simulated in panel **b**. The harmonic spacing, $\Delta\omega=10\omega_0$, (15.5 eV), in the necklace-driven on-axis HHG spectrum is a result of OAM conservation, and is tunable by varying the OAM content of the driving laser (upper panel). The on-axis harmonics are emitted with a divergence which is significantly reduced compared to that of Gaussian-driven HHG, and decreases with increasing harmonic order (bottom panel).

Tailoring the high-harmonic line spacing through necklace-driven HHG

Necklace beams can be generated and maintained through self-focusing in nonlinear media (44, 45), or by creating them utilizing either spatial light modulators (46) or specially tailored diffractive optical elements (47, 48). Here, we form necklace beams with a distinctive phase structure by spatiotemporally overlapping two femtosecond laser pulses with identical duration, wavelength, and polarization, but opposite and non-degenerate OAM ($\ell_1=|\ell_1|$, $\ell_2=-|\ell_2|$). The composite electric field exhibits a modulated intensity necklace structure, with evenly-spaced lobes of similar amplitude arranged at a constant distance from the optical axis, and with a relative phase shift between neighboring lobes. Figure 1a shows the intensity-modulated phase profile at the focus resulting from the superposition of two vortex beams with $\ell_1=2$, $\ell_2=-3$, as well as the far-field spatial intensity distribution of a given harmonic order (the 25th). Remarkably, even though the driving field contains a singularity and hence has zero intensity at all points along the optical axis, we observe numerically and experimentally that a subset of harmonic orders develops a bright on-axis maximum upon propagation. We further find that by using different combinations of OAM beams to synthesize the necklace driver, this subset can be varied, allowing us to tune the line spacing of the harmonic comb emitted on the optical axis without altering the driving laser wavelength.

This surprising result can be understood by viewing the combined dual-vortex source as an EUV/SXR phased antenna array. The composition of OAM beams creates a necklace-structured electric field containing $N = |\ell_1| + |\ell_2|$ lobes equidistant from the optical axis/origin, where the relative phase offset of the fundamental field across the n^{th} lobe is constant and equal to $(2\pi n|\ell_1|)/(|\ell_1| + |\ell_2|)$ (see Supplemental Material). Treating each lobe as a radiator of the q^{th} order harmonic which is coherent with the driving laser, the total field at a point $\overrightarrow{r_f}$ away from the source plane is the sum of fields propagated from all the lobes in the necklace, and can be approximated by

$$E_q(\vec{r_f}, t) \propto \sum_{n=0}^{N-1} e^{i(q\omega_0 t + qk_0 d_n + 2\pi n \frac{q|\ell_1|}{|\ell_1|+|\ell_2|})} \quad [1]$$

The second phase term qk_0d_n describes the phase accumulated by the q^{th} harmonic propagating a distance $d_n = |\vec{r_f} - \overrightarrow{r_{0,n}}|$ from the n^{th} lobe to the observation point. Let us now consider the harmonic emission that is emitted on-axis. For all points lying along the optical axis, these $d_n = d$ are equal. Thus, the propagation amounts to a constant phase shift (independent of n), which we can omit without loss of generality. The final phase term can be simplified by reordering the terms in the summation, yielding (see Supplemental Material)

$$E_q(\vec{r}_{on-axis}, t) \propto e^{iq\omega_0 t} \sum_{n=0}^{N-1} e^{i2\pi n \frac{q}{\xi_1+\xi_2}} \quad [2]$$

where we have introduced $\xi_1 = L_{lcm}/|\ell_1|$ and $\xi_2 = L_{lcm}/|\ell_2|$, L_{lcm} being the least common multiple of $|\ell_1|$ and $|\ell_2|$. From the above equation, we can observe that for harmonics where the quantity $q/(\xi_1 + \xi_2)$ is an integer, the emission from all lobes arrives in phase, resulting in a maximum on axis, while for all other harmonics the contributions sum to zero. In other words, for certain harmonic orders, the necklace emitters are transversely phase-matched by the high-harmonic upconversion process to interfere constructively on the optical axis. Taking into account the additional constraint that q must be odd due to inversion symmetry results in an HHG comb with line spacing equal to

$$\Delta\omega = 2(\xi_1 + \xi_2)\omega_0 \quad [3].$$

The temporal counterpart of this modified line spacing manifests in the periodicity of harmonic emission recorded on the optical axis. In Fig. 1b we perform a time-frequency analysis of the on-axis harmonic signal extracted from our simulation results in He at 800 nm (see theoretical methods below). We compare the harmonic emission driven by a standard Gaussian beam against that driven by a necklace beam with OAM content ℓ_1=2, ℓ_2=-3. For the Gaussian driving beam, harmonics are emitted every half period of the driving field, showing a periodicity of $\Delta t = T_0/2$ (where $T_0 = 2\pi/\omega_0$ is the optical cycle associated to the central frequency of the driving field), which

physically corresponds to the cadence of the ionization-rescattering mechanism leading to HHG. This structure corresponds to a harmonic frequency comb composed of odd harmonics, with spacing $\Delta\omega=2\omega_0$ (see Fig. 1c). However, for the combined $\ell_1=2$, $\ell_2=-3$ OAM driving field, harmonic events are observed on-axis 10 times—i.e. $2(\xi_1+\xi_2)$—per period of the driving frequency, reflecting the coherent addition of the 5—$\xi_1+\xi_2$—unique HHG emitters in the necklace. As a consequence, the on-axis harmonic emission shows a periodicity of $\Delta t=T_0/10$ — $\Delta t=T_0/2(\xi_1+\xi_2)$—corresponding to a harmonic frequency comb with the line spacing given by Eq. (3). We emphasize that this is accomplished without altering the wavelength of the driving laser nor the microscopic dynamics. The spectral changes arise purely as a result of the macroscopic arrangement of the phased emitters.

A deeper understanding of the modified harmonic comb spacing can be gained by invoking the selection rules resulting from OAM conservation. HHG driven by two spatiotemporally overlapped OAM pulses leads to the generation of a comb of harmonics with several, non-trivial, OAM contributions (40). In particular, neglecting the intrinsic or dipole phase contributions (40), the q-th order harmonic order has allowed OAM channels given by $\ell_q=n\ell_1+(q-n)\ell_2$, where n is a positive integer representing the number of photons of the ℓ_1 driver. If we apply this conservation rule to our scheme where the two drivers have opposite, non-degenerate OAM, i.e. $\ell_1=|\ell_1|$ and $\ell_2=-|\ell_2|$, we can readily observe that high-order harmonics emitted on-axis, i.e. with $\ell_q=0$, are generated if $n|\ell_1|=(q-n)|\ell_2|$. In order to extract the allowed harmonics that fulfill this condition, and thus the content of the harmonic comb emitted on-axis, we again denote L_{lcm} as the least common multiple of $|\ell_1|$ and $|\ell_2|$, which fulfills $\eta L_{lcm}=n|\ell_1|=(q-n)|\ell_2|$, η being an integer. Retaining the definitions of ξ_1 and ξ_2, the harmonic orders emitted with $\ell_q=0$ must fulfill $q=\eta(\xi_1+\xi_2)$. Taking into account that q must be odd due to the inversion symmetry, η must be odd, and the high-order harmonics that are emitted on-axis are

$$\omega_q=(2m+1)(\xi_1+\xi_2)\omega_0, \qquad [4]$$

where $m=0,1,2\ldots$, again leading to the line spacing rule given by Eq. (3).

The line spacing Δω, is shown in Fig. 2a. in terms of $|\ell_1|$ and $|\ell_2|$. We see that the appearance of on-axis harmonics with modified spectral spacing is a necessary consequence of a fundamental conservation law for OAM in HHG, as the OAM content of the driver determines which harmonic wavelengths have an allowed ℓ_q=0 channel. This interpretation naturally implies that the intensity ratio between the driving beams can be chosen to optimize the ℓ_q=0 (on axis) contribution (see Supplemental Material). Note that those harmonics that are not emitted on-axis possess non-zero OAM, and though they are present in the HHG beam, they present a singularity at the center.

To verify these predictions, we performed full quantum HHG simulations including propagation using the electromagnetic field propagator (49) (see Methods), a method that was used in several previous calculations of HHG involving OAM (20, 21, 37, 40, 43). In Figs. 2b and 2c we present the on-axis HHG spectra driven in He with 800 nm and 2 μm wavelength driving fields, respectively, and for different drivers' OAM combinations: ℓ_1=1, ℓ_2=-2 (blue); ℓ_1=2, ℓ_2=-3 (green); ℓ_1=3, ℓ_2=-4 (yellow); and ℓ_1=4, ℓ_2=-5 (red). In Fig. 2b we also show the spectra obtained with a standard Gaussian beam driver (grey). The simulation results clearly show the versatility of this technique to modify the frequency content of the harmonic combs, whose line spacing can be properly varied through the choice of the drivers' OAM, from $2\omega_0$ to $18\omega_0$ for the cases presented in Fig. 2.

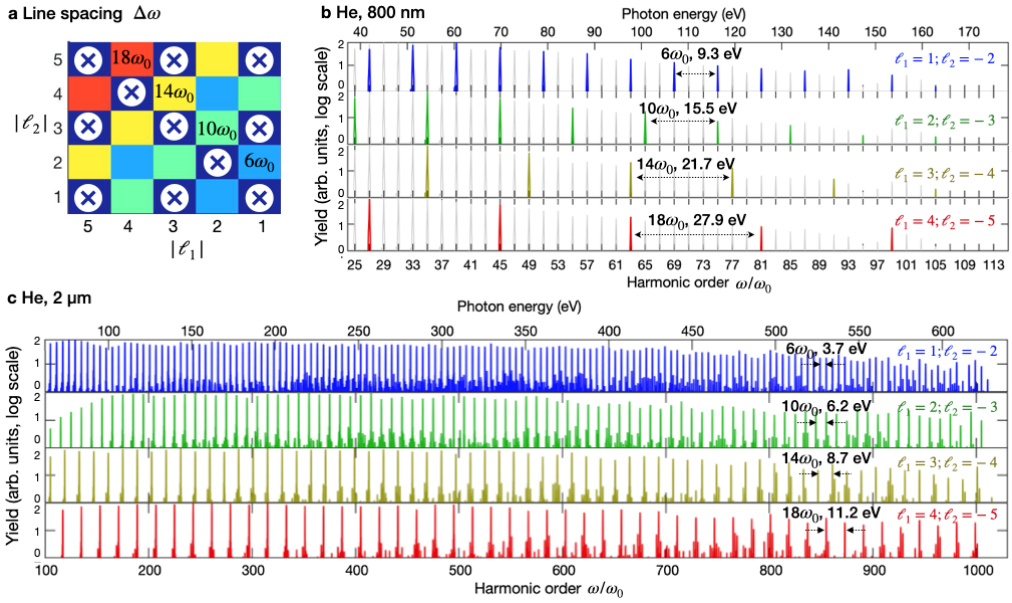

Figure 2 | Harmonic frequency combs with tunable line spacing controllable through the drivers' OAM content. **a** Representation of the line spacing allowed by the selection rules for different values of $|\ell_1|$ and $|\ell_2|$. The color scale represents the line spacing, being $6\omega_0$ (blue), $10\omega_0$ (green), $14\omega_0$ (yellow) and $18\omega_0$ (red). **b, c** Simulation results of the high harmonic spectra obtained in He for **b** 800 nm and **c** 2 µm wavelength drivers respectively, for the driver's OAM combinations: ℓ_1=1, ℓ_2=-2 (blue); ℓ_1=2, ℓ_2=-3 (green); ℓ_1=3, ℓ_2=-4 (yellow); and ℓ_1=4, ℓ_2=-5 (red). The line spacing corresponds to that predicted in panel **a**. The driving beam waists of the different OAM modes are chosen to overlap at the radius ($30/\sqrt{2}$ µm) of maximum intensity (6.9×10^{14} W/cm^2 for 800 nm, and 5×10^{14} W/cm^2 for 2 µm) at the focal plane. The laser pulses are modeled with a trapezoidal envelope with 26.7 fs of constant amplitude.

By using mid-infrared drivers, this technique can be exploited to customize harmonic combs extending into the SXR—as depicted in Fig. 2c, where photon energies of up to 640 eV are reached using 2 µm wavelength. This is particularly promising in a regime where, driven by long-wavelength Gaussian beams, neighboring harmonic orders tend to merge into a near or true supercontinuum (22, 23), necessitating the use of lossy dispersive optics for spectroscopic applications. In contrast, these simulation results demonstrate that, using necklace-driven HHG, the discrete and tunable peak structure can be preserved up to the SXR when driven by mid-IR wavelengths. Note that the intensity ratio between the two driving pulses has been adjusted independently for each OAM combination, in order to optimize the ℓ_q=0 contribution (see Supplemental Material). In addition, the driving beam waists of the different OAM modes are chosen so their rings of maximum intensity overlap at $\rho_1=30/\sqrt{2}=21.21$ µm at the focal plane (see

Methods), corresponding to the ring of maximum intensity of a vortex beam with ℓ=1 with w_0=30 μm, used as a reference.

To experimentally confirm the predicted spectral properties of this unique EUV light source, we use a Mach-Zehnder interferometer to synthesize the necklace-structured driver from two OAM laser beams with identical wavelength λ=790 nm and distinct topological charges of ℓ_1=1, ℓ_2=-2 (see Methods). The component beams are overlapped in time and space, and focused into an argon gas jet to drive HHG. The spectrum and shape of the emitted harmonics are then analyzed via a 2D imaging spectrometer consisting of a toroidal mirror and flat grating. As the on-axis HHG beam component is predicted to develop through propagation away from the source, we place an EUV charge-coupled device (CCD) camera slightly behind the focal plane of the toroidal mirror. The measured spatio-spectral images thus simultaneously record the harmonic photon energies and individual far field spatial profiles.

The measured spatial intensity profile of each of the high-order harmonics presents a structure with a symmetry similar to that of the driving necklace beam, in agreement with the results from our theoretical simulations (see Fig. 3). In this OAM combination, the predicted line spacing of the on-axis harmonic comb is $\Delta\omega=6\omega_0$, (9.5 eV) and the highest measurable harmonic orders allowed by the selection rule given by Eq. (2) are the 15th (23.5 eV) and the 21st (33.0 eV). This is supported by the intensity profiles shown in Fig. 3, where the central bright spot in the 15th and the 21st harmonics indicates a strong on-axis (ℓ=0) component. In contrast, all other observed harmonic orders exhibit a central null, i.e., they only possess non-zero OAM contributions which lead to off-axis emission profiles. In order to confirm that these features indeed constitute the predicted harmonic combs with on-demand line spacing, we insert a small circular aperture into the HHG beam prior to the spectrometer. We observe that the harmonics with on-axis components are cleanly transmitted through the aperture, while other harmonic orders are strongly suppressed. In the Supplemental Material, experimental results for another phased-necklace driver (ℓ_1=2, ℓ_2=-

3) further support the predicted line spacing of the on-axis harmonic combs.

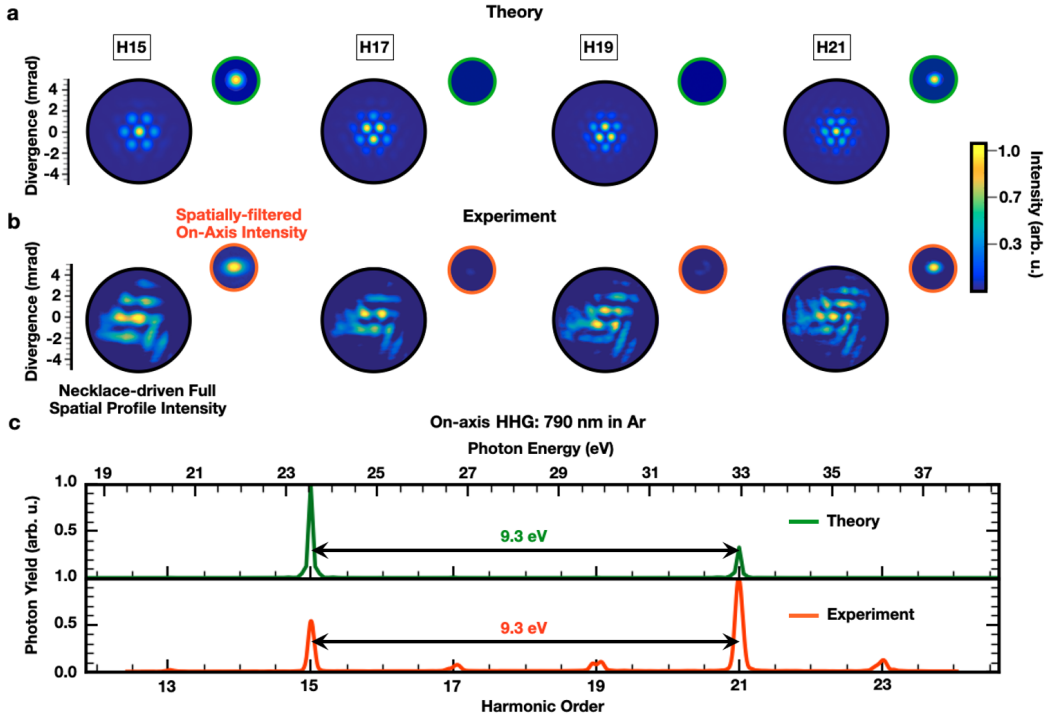

Figure 3 | Experimental and theoretical high harmonic combs in Ar gas using a pair of 790-nm OAM driving lasers with opposite parity (ℓ_1 = 1 and ℓ_2 = −2). The intensity spatial structure for the 15th (H15) to 21st (H21) harmonics are shown for **a** theory and **b** experiment. On-axis emission is allowed for H15 and H21 as a result of OAM selection rules and transverse phase matching conditions. Thus, the on-axis component is transmitted for H15 and H21, while H17 and H19 are blocked (insets in **a** & **b**). **c** Simulated (top) and experimental (bottom) HHG spectra of necklace-driven on-axis emission. By measuring the spectrum along a line in the dispersion plane which intersects the optical axis for all orders, we find that the line spacing of the transmitted harmonics, $\Delta\omega=6\omega_0$, (9.5 eV), is consistent with that predicted by OAM conservation laws. Small HHG signals experimentally observed at other harmonic orders are due to leak-through of the components carrying higher topological charges, and could be further suppressed by using a smaller aperture. The difference in the ratio H15/H21 is due to slightly different cutoff energies between simulation and experiment.

Generation of low-divergence high-order harmonics via necklace-driven HHG

In addition to their spectral content, the divergence of the high harmonic combs is also crucial for applications in x-ray spectroscopy and imaging. In our scheme, the on-axis harmonics with on-demand line spacing are generated with a remarkably low divergence, compared to that obtained from standard Gaussian driving laser beams. This is a consequence of the generation mechanism, in which the on-axis beam, not present in the source plane, arises from the constructive interference

of multiple phased-shifted radiators arranged with circular symmetry about the optical axis. Figure 4a shows the simulation results of the spatial intensity profile (top) and OAM content (bottom) of the 27th harmonic generated in He at 800 nm for two different OAM combinations: ℓ_1=1, ℓ_2=-2 (left) and ℓ_1=4, ℓ_2=-5 (right). It can be observed that most of the harmonic intensity is contained near the beam axis, corresponding to the ℓ_{27}=0 contribution. This is a result of the intensity ratio of the component OAM beams, which has been selected to optimize the channel for on-axis harmonic emission (see Supplemental), such that the surrounding OAM contributions are naturally suppressed (see OAM spectra in the bottom-panels of Fig. 4a). This needle-like beam naturally separates from the driving laser, which has zero on-axis intensity, and can be easily isolated through a pinhole for direct use in an experiment.

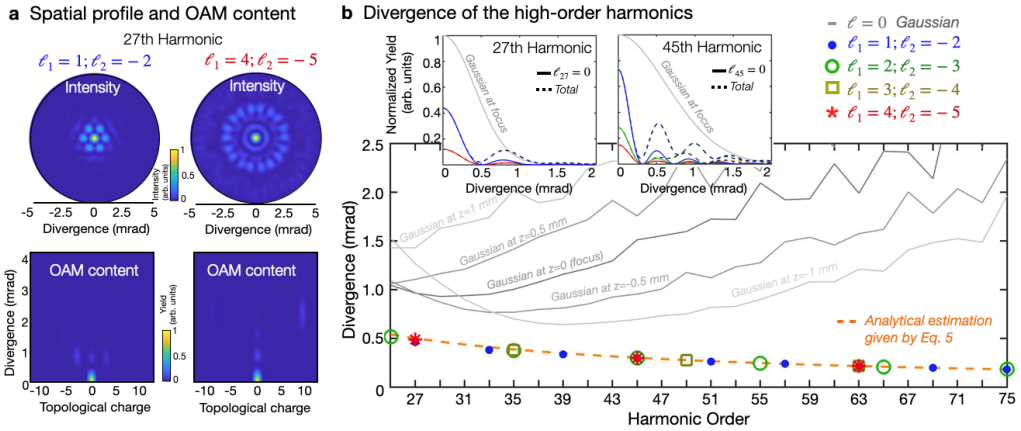

Figure 4 | Low divergence of the OAM-driven harmonic frequency combs. a Simulation results of the spatial intensity profile (top) and OAM content (bottom) of the 27th harmonic generated in He for ℓ_1=1, ℓ_2=-2 (left) and ℓ_1=4, ℓ_2=-5 (right) driving fields. The OAM spectra are obtained from the azimuthal Fourier transform at each divergence angle. **b** Simulation results of the Full width at half maximum (FWHM) divergence of the high-order harmonics for different OAM driving combinations (color dots)—with the gas jet placed at the focus position—, and for a Gaussian driving beam where the gas jet is placed at different positions relative to the focus. The orange dashed line indicates the estimation given by Eq. (5). The top insets show the divergence profile of two sample harmonics (27th and 45th) for different OAM driving combinations (showing the ℓ_q=0 contribution in solid and the total one in dashed line) and for a Gaussian beam where the gas jet is placed at the focus position. Simulation parameters correspond to those of Fig. 2b.

In order to show the low divergence of the ℓ_q=0 harmonic beam, we present in Fig. 4b the divergence of the high-order harmonics driven by the opposite non-degenerate OAM combination (corresponding to those of Fig. 2b), compared to that of the harmonics driven by a Gaussian beam.

We have chosen a beam waist of 30 μm for the Gaussian beam, as a reasonable comparison against the OAM combination scheme, where the necklace ring presents a radius of 30/√2 μm. The insets show the divergence profile of two sample harmonics (27th and 45th) driven by different drivers' OAM combinations (the solid lines show the ℓ=0 contribution of each harmonic, whereas the dashed lines show the sum of all the OAM contributions), and by a Gaussian beam. Note that the intensity yield of the on-axis emission is comparable to the yield obtained with a Gaussian beam. The bottom panel shows the divergence calculated as the full width at half maximum (FWHM) for different drivers' OAM combinations (dots and dashed lines) —with the gas jet placed at the focus position—and for a Gaussian beam placed at different positions relative to the gas jet (solid grey lines).

It is worth noticing that Gaussian-driven high-order harmonics, counterintuitively, exhibit a divergence that in general increases with the harmonic order (31, 32). In such cases, the divergence of the central intensity peak of the q-th-harmonic scales as $\beta_q \sim \lambda_q/D_q$, D_q being the size of the near-field target area in which the driving field is intense enough to generate that particular harmonic. The fact that D_q decreases with the harmonic order faster than λ_q results in an increasing divergence with the harmonic order, as can be observed in Fig. 4b. Remarkably, due to the use of an optimized OAM-driving laser combination, we are able to reverse this behavior. When considering the opposite non-degenerate OAM driving field, the divergence of the ℓ_q=0 intensity peak of the q-th-harmonic scales as

$$\Delta\beta_q^{FWHM} = 2.25\frac{\lambda_0}{2\pi qR} \quad [5]$$

R being the radius of the necklace driving structure (see Supplemental Material). The result is that higher-order harmonics can be generated with progressively lower divergence, as R is constant for all harmonic orders. Note also that this behavior does not depend on the choice of ℓ_1 and ℓ_2, but on the size of the resulting necklace structure, which, for the cases presented in Fig. 4b, presents the same size. As a consequence, similar driving schemes without OAM, such as a Gaussian-necklace

driver or a continuous-ring driver, would also result in on-axis high-order harmonics with progressively lower divergence. Note however that our phased-necklace driver is composed on a combination of Laguerre-Gaussian modes, whose propagation behaviour is regular, and which allow us to control the on-axis harmonic content as described in the previous section.

We experimentally validate the predicted divergence behavior of the HHG frequency combs for Ar at 790 nm in Fig. 5. Taking an angular integration centered about the optical axis for the necklace-driven HHG, and considering the imaging condition of the spectrometer, we measure the divergence of the on-axis, Bessel-like lobe. We then compare these divergence values to those obtained with an equivalent Gaussian driver. In order to make as direct a comparison as possible, we match the beam waist parameter (lens focal length), focal position, gas pressure, and peak intensity between the two cases, resulting in HHG spectra with similar spectral envelopes and cutoff photon energies.

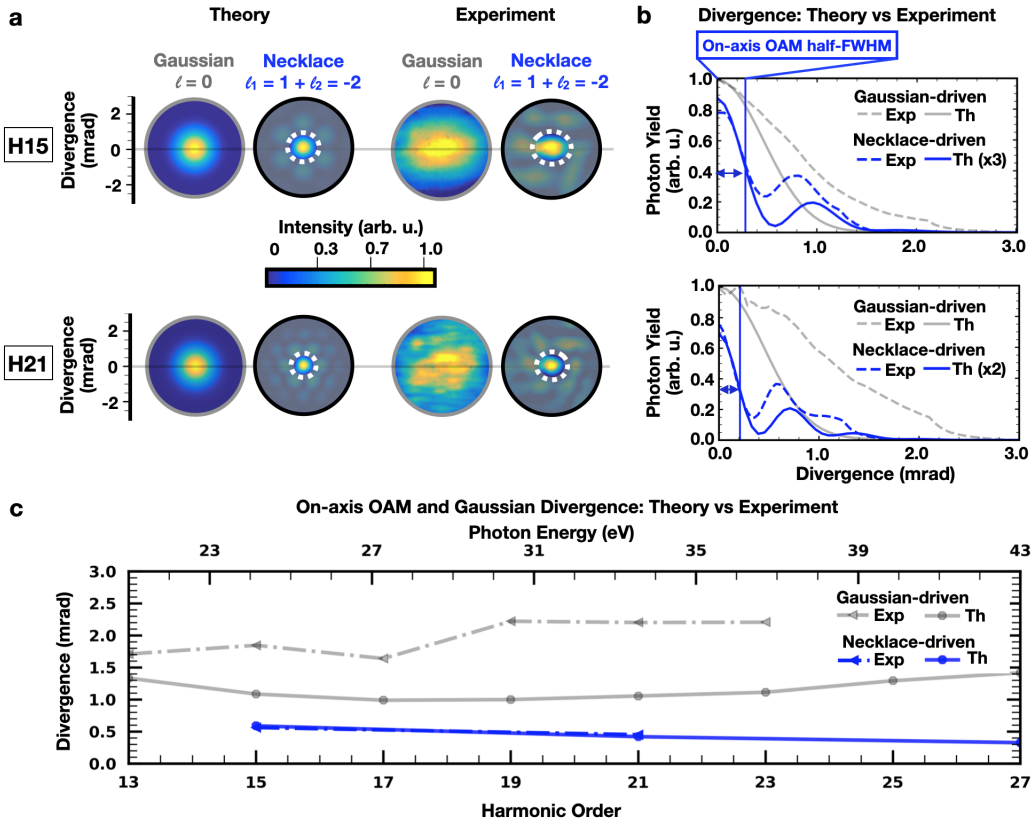

Figure 5 | Ar-driven harmonic divergences. a Theoretical (Th.) and experimental (Exp.) comparison of the intensity spatial profiles for the 790-nm Gaussian-driven and necklace-driven ($\ell_1 = 1$ and $\ell_2 = -2$) in Ar gas. The white dashed circles indicate the on-axis emission of the 15th (H15) and 21st (H21) for both theory and experiment. We applied an angular integration radially to these profiles to extract the divergences. **b** Angularly integrated radial profiles for H15 and H21 for the on-axis emission, necklace-driven case compared to the equivalent Gaussian. The vertical blue line and double-headed arrow indicate half of the full width at half maximum (FWHM) of the dual-vortex, necklace-driven profile. The intensities of the theoretically predicted on-axis divergence are rescaled for H15 and H21, respectively, to match the intensities of the experimental profiles. **c** Theoretical (Eq. 5) and measured FWHM for necklace-driven on-axis emission profile indicate a decrease in the divergence with increasing harmonic order. This is in contrast to Gaussian-driven HHG, where divergence increases at higher harmonic orders.

From these spectra, we make several observations. First, it is clear that the central lobe of the necklace-driven harmonics with on-axis components has a significantly lower divergence than that achievable with the equivalent Gaussian driver. Furthermore, we observe a clear decrease in the divergence of the 21st harmonic relative to the 15th harmonic, whereas the Gaussian harmonics, as expected, actually increase in divergence over the same energy range. Both the divergence values and trend quantitatively agree with our simulations, as well as the prediction given by Eq. (5). Finally, we note that both our numerical and experimental results show that the on-axis harmonics

are nearly equal in peak brightness to their Gaussian counterparts, indicating that the frequency selectivity and low divergence achieved in this scheme do not come at the cost of reduced flux at those frequencies. Note that the brightness of the on-axis harmonics can be controlled through the intensity ratio between the drivers (see Supplemental Material).

Discussion

Our results present a significant advance for applications that require highly coherent EUV/SXR beams with customizable properties. By changing only the OAM content and radius of the necklace driving field, one can adjust on-demand the line spacing and divergence behavior of the emitted high-harmonic combs in order to tailor the light source for a particular application. Necklace-driven HHG thus enables dramatic control over the HHG spectra without altering the wavelength of the driving laser. The spectral control instead arises as a result of OAM conservation and macroscopic transverse phase-matching conditions—the microscopic HHG physics remains unchanged, thus avoiding tradeoffs in cutoff energy or conversion efficiency. The ability to adjust the spacing between harmonic orders enhances the flexibility of HHG light sources for a variety of applications, particularly in the SXR region, when driven by mid-IR lasers.

In addition to the potential advantages of the unique spectral properties, the needle-like divergence behavior of the harmonics generated in our scheme may enable a simplification of selected imaging and spectroscopy experiments by removing the need for either refocusing optics or methods to eliminate the driving laser beam. Instead, the on-axis contribution of the OAM harmonics could be selected through a pinhole spatial filter, transmitting the full on-axis EUV/SXR flux while blocking the driving laser. This is particularly true at shorter wavelengths due to the unique divergence scaling – since the divergence decreases monotonically with increasing photon energy. This result is especially relevant for HHG driven by mid-infrared lasers, where harmonics up to the 1000^{th} can be obtained (see Fig. 2c), for a 2 μm driving laser, extending well into the SXR region. We do not foresee any fundamental restriction to applying this technique

to even longer driving wavelengths (22, 50), making it possible to tailor very high-order discrete harmonics with extremely low divergence.

Conclusion

In conclusion, we have presented a new technique for the generation of EUV and SXR harmonic combs with a line spacing that is controlled through the OAM makeup of infrared necklace driving laser beams. The emitted harmonics exhibit remarkably low divergence which further decreases with the harmonic order, in contrast to standard HHG driven by a Gaussian beam. Our theoretical simulations are corroborated by our experimental results, which demonstrate both the frequency control and divergence behaviour of the generated harmonic combs. Our work will facilitate a variety of applications which require high beam quality and spectroscopic precision, such as tabletop SXR-ARPES or resonant magnetic scattering. The ability to adjust and maintain separation between adjacent harmonic orders is also likely to be beneficial for hyperspectral coherent diffractive imaging techniques (51, 52), particularly in the SXR region. The low divergence and high beam quality enable these experiments to be carried out with simplified setups and enhanced flux throughput. Thus, we believe necklace-driven HHG will become a powerful tool for tabletop EUV/SXR spectroscopy and imaging, as well as measurements of ultrafast charge and spin dynamics at the nanoscale.

Methods

Theoretical simulations of HHG driven by a combination of OAM beams. We use a theoretical method that computes both the full quantum single-atom HHG response and subsequent propagation (49), thus taking into account phase-matching of the high-order harmonics generated in the gas jet. On one hand, the quantum single-atom response is reproduced by calculating the dipole acceleration through the full quantum extended strong field approximation—without performing the saddle-point approximation—, which presents an excellent qualitative and quantitative agreement against the time dependent Schrödinger equation. Such approximation allows us to achieve substantial computational time gain when computing macroscopic HHG over the entire gas jet. On the other hand, harmonic propagation and phase-matching is computed through the electromagnetic field propagator (49). We discretize the target (gas jet) into elementary

radiators, assuming that the emitted harmonic radiation propagates with the vacuum phase velocity. In the present simulations, we have assumed an infinitely thin gas jet, flowing along the perpendicular direction to the beam propagation, with a peak pressure of 667 Pa (5 torr). We note that such 2D assumption for the gas target—performed due to computational time limitations— is a reasonable assumption for low density gas jets, based on previous theoretical and experimental results (20, 21). Thus, we do not foresee fundamental deviations if thicker gas jets, closer to the experimental one (150 μm in diameter) are considered.

The spatial structure of the driving beams is represented as a Laguerre-Gaussian beam propagating in the z-direction, with wavelength $\lambda_0, (k_0 = 2\pi/\lambda_0),$ given by

$$LG_{\ell,p}\,(\rho,\theta,z;k_0) = E_0\,\frac{w_0}{w(z)}\left(\frac{\sqrt{2}\rho}{w(z)}\right)^{|\ell|} L_p^{|\ell|}\left(\frac{2\rho^2}{w^2(z)}\right)$$

$$\times \exp\left[-\frac{\rho^2}{w^2(z)}\right]\exp\left[i\ell\theta + i\,\frac{k_0\rho^2}{2R(z)} + i\phi_G(z)\right] \qquad [2],$$

where $w(z) = w_0\sqrt{1+(z/z_0)^2}$ is the beam waist (w_0 being the beam waist at focus and $z_0 = \pi w_0^2/\lambda_0$ the Rayleigh range), $R(z) = z[1+(z_0/z)^2]$ is the phase-front radius, $\phi_G(z) = -(2p+|\ell|+1)\arctan(z/z_0)$ is the Gouy phase, and $L_p^{|\ell|}(x)$ are the associated Laguerre polynomials. ℓ =0,±1, ,±2,… and p=0,1,2…correspond to the topological charge and the number of nonaxial radial nodes of the mode, respectively. In this work we will not consider beams with radial nodes, and thus p=0. The driving beam waists (w_0) of the different ℓ modes are chosen to overlap at the focal plane, which corresponds to w_0, $w_0/\sqrt{2}$, $w_0/\sqrt{3}$, $w_0/2$ and $w_0/\sqrt{5}$ for ℓ =±1,±2, ±3, ±4, ±5 respectively. In particular, we have considered w_0 =30 μm. Finally, the laser pulses are modeled with a trapezoidal envelope. In the simulations performed in Ar and He with 800 nm central wavelength, the envelope consists of three cycles of $\sin^2$ turn-on, ten cycles of constant amplitude—26.7 fs—, and three cycles of $\sin^2$ turn-off. In the simulations performed in He with 2 μm central wavelength, the pulse duration is reduced due to computational time restrictions, and the envelope consists of two cycles of $\sin^2$ turn-on, four cycles of constant amplitude—26.7 fs—, and two cycles of $\sin^2$ turn-off. The amplitudes (E_0) of the driving pulses are chosen to obtain a maximum peak intensity at focus at the radii of maximum superposition ($w_0/\sqrt{2}$) of 1.7×10^{14} W/cm^2 for Ar, 6.9×10^{14} W/cm^2 for He at 800 nm, and 5×10^{14} W/cm^2 for He at 2 μm. Note that the intensity ratio for each LG combination has been chosen to optimize the harmonic radiation emitted around the beam axis (see Supplemental Material).

Experimental generation. Necklace-beam driven high-harmonics are generated by focusing a pair of collinear, linearly polarized IR-vortex beams (with topological charges of $\ell_1=1$, $\ell_2=-2$) into a supersonic expansion of argon gas. The dual-vortex driver is synthesized from the output of a

high-power, ultrafast regenerative amplifier (790 nm, 40 fs, 8 mJ, 1 kHz, KMLabs Wyvern HE) passed through a frequency degenerate Mach-Zehnder interferometer. In each arm of the interferometer, independent spiral phase plates (16 steps per phase ramp, HoloOr), and focusing lenses (f_1=40cm, f_2=30cm) result in each beam possessing identical (linear) polarization, distinct topological charges, and similarly sized spatial profiles at focus. Independent irises allow for fine tuning of the transverse mode size at the focal plane, and are used to overlap the maximum-intensity ring of the two component beams. The ring of maximum intensity of the two driving beams was matched at a radius of ~32 μm (see Supplemental Material). Half-waveplate/polarizer pairs are used to independently adjust the pulse energy in each arm in order to optimize the on-axis intensity. For the data presented in this manuscript, the pulse energies are set to E_1=480μJ and E_2=290μJ. The combined necklace driver is characterized by a modified Gerchberg-Saxton phase retrieval algorithm, which solves for the spatial phase of the composite electric field and allows confirmation of the desired OAM content of the driving IR field, while additionally confirming the high stability of the interferometer setup (see Supplemental). The two component pulses experience approximately equal dispersion throughout each arm of the interferometer, and are confirmed through FROG measurements to have equal pulse widths $\tau \approx 57$ fs. A high-precision, high-stability translation stage (Newport, XMS-160S) is used to synchronize the two pulses in time. The beams are recombined at the output of the interferometer and focused into the supersonic expansion of argon from a circular gas jet (150μm diameter). The generated high harmonics, which range in photon energy from 20-35 eV, are transmitted through a 200-nm-thick aluminum filter (Luxel), which serves to block the residual IR driver. A removable circular pinhole (200 μm diameter) is placed on the optical axis at a distance of 60cm from the generation region, in order to spatially filter for the on-axis frequency comb. The transmitted harmonics are subsequently focused by a toroidal mirror (f_{eff} = 27cm) and dispersed by a plane ruled EUV grating (1200 grooves/mm, Richardson) at an incidence angle $\boldsymbol{\theta_{inc} \approx 45°}$. The high incidence angle is chosen to balance the dispersion and imaging quality of the spectrometer. An EUV CCD camera (Andor Newton 940) is placed behind the toroidal focal plane so as to image the far field (20 cm from the gas jet) of the dispersed harmonics with a magnification of 1.67. These parameters are used to calculate the divergence of the produced harmonics. A 100nm titanium filter (Lebow) with an absorption edge prior to the 21st harmonic (33 eV) is used to verify the photon energies of the harmonics exhibiting on-axis intensity.

Data Availability

The datasets and analysis routines utilized to prepare the data presented in this manuscript are available, free of charge, from the corresponding author under reasonable request.

References

[1] J. Miao, T. Ishikawa, I. K. Robinson & M. Murnane. Beyond crystallography: Diffractive imaging using coherent X-ray light sources. *Science* **348**, 530-535 (2015).

[2] Z. Tao, C. Chen, T. Szilvasi, M. Keller, M. Manos, H. Kapteyn, M. Murnane. Direct time-domain observation of attosecond final-state lifetimes in photoemission from solids. *Science* **353**, 62–67 (2016).

[3] J. A. Van Bokhoven & C. Lamberti. *X-Ray Absorption and X-Ray Emission Spectroscopy: Theory and Applications* (John Wiley & Sons: New York, 2016).

[4] Y. Pertot, S. Cédric, M. Matthews, A. Chauvet, M. Huppert, V. Svoboda, A. von Conta, A. Tehlar, D. Baykusheva, J-P Wolf, H. J. Wörner. Time-resolved X-ray absorption spectroscopy with a water window high-harmonic source. *Science* **55**, 264-267 (2017).

[5] Y. Zhang, X. Shi, W. You, Z. Tao, Y. Zhong, F. C. Kabeer, P. Maldonado, P. M. Oppeneer, M. Bauer, K. Rossnagel, H. Kapteyn, M. Murnane. Coherent modulation of the electron temperature and electron-phonon couplings in a 2D material. *PNAS* **117**, 8788-8793 (2020).

[6] P. Emma, R. Akre, J. Arthur, R. Bionta, C. Bostedt, J. Bozek, A. Brachmann, P. Bucksbaum, R. Coffee, F.-J. Decker, Y. Ding, D. Dowell, S. Edstrom, A. Fisher, J. Frisch, S. Gilevich, J. Hastings, G. Hays, Ph. Hering, Z. Huang, R. Iverson, H. Loos, M. Messerschmidt, A. Miahnahri, S. Moeller, H.-D. Nuhn, G. Pile, D. Ratner, J. Rzepiela, D. Schultz, T. Smith, P. Stefan, H. Tompkins, J. Turner, J. Welch, W. White, J. Wu, G. Yocky and J. Galayda. First lasing and operation of an ångstrom-wavelength free-electron laser. *Nat. Photonics* **4**, 641–647 (2010).

[7] T. Ishikawa, H. Aoyagi, T. Asaka, Y. Asano, N. Azumi, T. Bizen, H. Ego, K. Fukami, T. Fukui, Y. Furukawa, S. Goto, H. Hanaki, T. Hara, T. Hasegawa, T. Hatsui, A. Higashiva, T. Hirono, N. Hosoda, M. Ishii, t. Inagaki, Y. Inubushi, T. Itoga, Y. Joti, M. Kago, T. Kameshima, H. Kimura, Y. Kirihara, G. Kiyomochi, T. Kobayashi, C. Kondo, T. Kudo, H. Maesaka, X. M. Maréchal, T. Masuda, S. Matsubara, T. Matsushita, S. Matsui, M. Nagasono, N. Nariyama, H. Ohashi, T. Ohata, T. Ohshima, S. Ono, Y. Otake, C. Saji, T. Sakurai, T. Sato, K. Sawada, T. Seike, K. Shirasawa, T. Sugimoto, S. Suzuki, S. Takahashi, H. Takebe, K. Taheshita, K. Tamasaku, H. Tanaka, R. Tanaka, T. Tanaka, T. Togashi, K. Togawa, A. Tokuhisa, H. Tomizawa, K. Tono, S. Wu, M. Yabashi, M. Yamaga, A. Yamashita, K. Yanagida, C. Zhang, T. Shintake, H. Kitamura & N. Kumagai. A compact X-ray free-electron laser emitting in the sub-ångström region. *Nat. Photonics* **6**, 540–544 (2012).

[8] A. McPherson, G. Gibson, H. Jara, U. Johann, T. S. Luk, I. A. McIntyre, K. Boyer, C. K. Rhodes. Studies of multiphoton production of vacuum-ultraviolet radiation in the rare gases. *J. Opt. Soc. Am. B* **4,** 595 (1997).

[9] M. Ferray, A. L'Huillier, X. F. Li, L. A. Lompre, G. Mainfray, C. Manus. Multiple-harmonic conversion of 1064-nm radiation in the rare gases. *J. Phys. B* **21,** L31 (1998).

[10] A. Rundquist, C. G. Durfee III, Z. Chang, C. Herne, S. Backus, M. M. Murnane, H. C. Kapteyn. Phase-matched generation of coherent soft X-rays. *Science*, **280**, 5368, pp. 1412-1415 (1998).

[11] R. A. Bartels, A. Paul, H. Green, H. C. Kapteyn, M. M. Murnane, S. Backus, I. P. Christov, Y. Liu, A. Attwood, C. Jacobsen. Generation of spatially coherent light at extreme ultraviolet wavelengths. *Science* **297**, 5580, pp. 376-378 (2002).

[12] P. Agostini & L. F. DiMauro. The physics of attosecond light pulses. *Rep. Prog. Phys.* **67** 813–855 (2004).

[13] T. Popmintchev, M.-C. Chen, P. Arpin, M. M. Murnane, H. C. Kapteyn. The attosecond nonlinear optics of bright coherent X-ray generation. *Nat. Photonics* **4** (12), 822–832 (2010).

[14] F. Calegari, G. Sansone, S. Stagira, C. Vozzi & M. Nisoli. Advances in attosecond science. *J. Phys. B* **49**, 062001 (2016).

[15] H. Eichmann, A. Egbert, S. Nolte, C. Momma, B. Wellegehausen, W. Becker, S. Long, J. K. McIver, "Polarization-dependent high-order two-color mixing," *Phys. Rev. A* **51**, R3414–R3417 (1995).

[16] Z. Chang, A. Rundquist, H. Wang, H. Kapteyn, M. M. Murnane. Temporal phase control of soft-X-ray harmonic emission. *Phys. Rev. A Rapid Communications* **58**, R30 (1998).

[17] R. Bartels, S. Backus, E. Zeek, L. Misoguti, G. Vdovin, I. P. Christov, M. M. Murnane, H. C. Kapteyn. Shaped-pulse optimization of coherent emission of high-harmonic soft X-rays. *Nature* **406**, 6792, 164-166 (2000).

[18] T. Fan, P. Grychtol, T. Knut, C. Hernández-García, D. D. Hickstein, D. Zusin, C. Gentry, F. J. Dollar, C. A. Mancuso, C. W. Hogle, O. Kfir, D. Legut, K. Carva, J. L. Ellis, K. M. Dorney, C.

Chen, O. G. Shpyrko, E. E. Fullerton, O. Cohen, P. M. Oppeneer, Dejan B. Milošević, A. Becker, A. Jaroń-Becker, T. Popmintchev, M. M. Murnane, H. C. Kapteyn et al. Bright circularly polarized soft X-ray high harmonics for x-ray magnetic circular dichroism. *PNAS* **112**, 14206–14211 (2015).

[19] D. D. Hickstein, F. J. Dollar, P. Grychtol, J. L. Ellis, R. Knut, C. Hernández-García, D. Zusin, C. Gentry, J. M. Shaw, T. Fan, K. M. Dorney, A. Becker, A. Jaroń-Becker, H. C. Kapteyn, M. M. Murnane, C. G. Durfee. Non-collinear generation of angularly isolated circularly polarized high harmonics. *Nat. Photonics* **9**, 743–750 (2015).

[20] K. M. Dorney, L. Rego, N. J. Brooks, J. San Román, C-T Liao, J. L. Ellis, D. Zusin, C. Gentry, Q. L. Nguyen, J. M. Shaw, A. Picón, L. Plaja, H. C. Kapteyn, M. M. Murnane, C. Hernández-García. Controlling the polarization and vortex charge of attosecond high-harmonic beams via simultaneous spin-orbit momentum conservation. *Nat. Photonics* **13**, 123-130 (2019).

[21] L. Rego, K. M. Dorney, N. J. Brooks, Q. L. Nguyen, C.-T. Liao, J. San Román, D. E. Couch, A. Liu, E. Pisanty, M. Lewenstein, L. Plaja, H. C. Kapteyn, M. M. Murnane, C. Hernández-García. Generation of extreme-ultraviolet beams with time-varying orbital angular momentum. *Science* **364**, eaaw9486 (2019).

[22] T. Popmintchev, M.-C. Chen, D. Popmintchev, P. Arpin, S. Brown, S. Ališauskas, G. Andriukaitis, T. Balčiunas, O. D. Mücke, A. Pugzlys, A. Baltuška, B. Shim, S. E. Schrauth, A. Gaeta, C. Hernández-García, L. Plaja, A. Becker, A. Jaroń-Becker, M. M. Murnane, H. C. Kapteyn. Bright coherent ultrahigh harmonics in the keV X-ray regime from mid-infrared femtosecond lasers. *Science* **336,** 1287 (2012).

[23] D. Popmintchev, C. Hernández-García, F. Dollar, C. Mancuso, J. A. Pérez-Hernández, M.-C. Chen, A. Hankla, X. Gao, B. Shim, A. L. Gaeta, M. Tarazkar, D. A. Romanov, R. J. Levis, J. A. Gaffney, M. Foord, S. B. Libby, A. Jaron-Becker, A. Becker, L. Plaja, M. M. Murnane, H. C. Kapteyn, T. Popmintchev. Ultraviolet surprise: Efficient soft x-ray high-harmonic generation in multiply-ionized plasmas. *Science* **350**, 6265, 1225-1231 (2015).

[24] Z. Chang, A. Rundquist, H. Wang, M. M. Murnane, H. C. Kapteyn. Generation of coherent X-rays at 2.7nm using high harmonic generation. *Phys. Rev. Lett.* **79**, 2967 (1997).

[25] Ch. Spielmann, N. H. Burnett, S. Sartania, R. Koppitsch, M. Schnürer, C. Kan, M. Lenzner, P. Wobrauschek, F. Krausz. Generation of coherent X-rays in the water window using 5-femtosecond laser pulses. *Science* **278**, 661–664 (1997).

[26] E. J. Takahashi, T. Kanai, K. L. Ishikawa, Y. Nabekawa, K. Midorikawa. Coherent water window X ray by phase-matched high-order harmonic generation in neutral media. *Phys. Rev. Lett.* **101**, 253901 (2008).

[27] M.-C. Chen, P. Arpin, T. Popmintchev, M. Gerrity, B. Zhang, M. Seaberg, D. Popmintchev, M. M. Murnane, and H. C. Kapteyn. Bright, coherent, ultrafast soft X-ray harmonics spanning the water window from a tabletop light source. *Phys. Rev. Lett.* **105**, 173901 (2010)

[28] S. M. Teichmann, F. Silva, S. L. Cousin, M. Hemmer, J. Biegert. 0.5-keV Soft X-ray attosecond continua. *Nat. Commun.* **7**, 11493 (2016).

[29] A. S. Johnson, D. R. Austin, D. A. Wood, C. Brahms, A. Gregory, K. B. Holzner, S. Jarosch, E. W. Larsen, S. Parker, C. S. Strüber, P. Ye, John W. G. Tisch, Jon P. Marangos. High-flux soft X-ray harmonic generation from ionization-shaped few-cycle laser pulses. *Sci. Adv.* **4**, eaar3761 (2018).

[30] J. Schötz, B. Förg, W. Schweinberger, I. Liontos, H. A. Masood, A. M. Kamal, C. Jakubeit, N. G. Kling, T. Paasch-Colberg, S. Biswas, M. Högner, I. Pupeza, M. Alharbi, A. M. Azzeer, M. F. Kling. Phase-matching for generation of isolated attosecond XUV and soft-X-ray pulses with few-cycle drivers. *Phys. Rev. X* **10**, 041011 (2020).

[31] H. Wikmark, C. Guo, J. Vogelsang, P. W. Smorenburg, H. Coudert-Alteirac, J. Lahl, J. Peschel, P. Rudawski, H. Dacasa, S. Carlström, S. Maclot, M. B. Gaarde, P. Johnsson, C. L. Arnold, A. L'Huillier. Spatiotemporal coupling of attosecond pulses. *PNAS* **116**, 4779-4787 (2019).

[32] L. Quintard, V. Strelkov, J. Vabek, O. Hort, A. Dubrouil, D. Descamps, F. Burgy, C. Péjot, E. Mével, F. Catoire, E. Constant. Optics-less focusing of XUV high-order harmonics. *Adv. Sci.* **5**, eaau7175 (2019).

[33] H. Rubinsztein-Dunlop, A. Forbes, M. V. Berry, M. R. Dennis, D. L. Andrews, M. Mansuripur, C. Denz, C. Alpmann, P. Banzer, T. Bauer, E. Karimi, L. Marrucci, M. Padgett, M. Ritsch-Marte, N. M. Litchinitser, N. P. Bigelow, C. Rosales-Guzmán, A. Belmonte, J. P. Torres, T. W. Neely, M. Baker, R. Gordon, A. B. Stilgoe, J. Romero, A. G. White, R. Fickler, A. E. Willner, G. Xie, B. McMorran, A. M. Weiner. Roadmap on structured light. *J. Opt.* **19**, 013001 (2017).

[34] R. A. Beth. Mechanical detection and measurement of the angular momentum of light. *Phys.*

Rev. **50,** 115-125 (1936).

[35] A. Allen, M. W. Beijersbergen, R. J. C. Spreeuw, J. P. Woerdman. Orbital angular momentum of light the transformation of Laguerre-Gaussian laser modes. *Phys. Rev. A* **45,** 8185-8189 (1992).

[36] M. Zürch, C. Kern, P. Hansinger, A. Dreischuh, Ch. Spielmann. Strong-field physics with singular light beams. *Nat. Phys*. **8**, 743 (2012).

[37] C. Hernández-García, A. Picón, J. San Román, L. Plaja. Attosecond extreme ultraviolet vortices from high-order harmonic generation. *Phys. Rev. Lett.* **111**, 083602 (2013).

[38] G. Gariepy, J. Leach, K. T. Kim, T. J. Hammond, E. Frumker, R. W. Boyd, P. B. Corkum. Creating high-harmonic beams with controlled orbital angular momentum. *Phys. Rev. Lett.* **113**, 153901 (2014).

[39] R. Géneaux, A. Camper, T. Auguste, O. Gobert, J. Caillat, R. Taïeb, T. Ruchon. Synthesis and characterization of attosecond light vortices in the extreme ultraviolet. *Nat. Commun.* **7**, 12583 (2016).

[40] L. Rego, J. San Román, A. Picón, L. Plaja, C. Hernández-García. Nonperturbative twist in the generation of extreme-ultraviolet vortex beams. *Phys. Rev. Lett.* **117,** 163202 (2016).

[41] F. Kong, C. Zhang, F. Bouchard, Z. Li, G. G. Brown, D. H. Ko, T. J. Hammond, L. Arissian, R. W. Boyd, E. Karimi, P. B. Corkum. Controlling the orbital angular momentum of high harmonic vortices. *Nat. Commun*. **8,** 14970 (2017).

[42] D. Gauthier, P. Rebernik Ribic, G. Adhikary, A. Camper, C. Chappuis, R. Cucini, L. F. DiMauro, G. Dovillaire, F. Frassetto, R. Géneaux, P. Miotti, L. Poletto, B. Ressel, C. Spezzani, M. Stupar, T. Ruchon, G. De Ninno. Tunable orbital angular momentum in high-harmonic generation. *Nat. Commun.* **8,** 14971 (2017).

[43] L. Rego, J. San Román, L. Plaja, C. Hernández-García. Trains of attosecond pulses structured with time-ordered polarization states. *Opt. Lett.* **45**, 5636 (2020).

[44] M. Soljačić, S. Sears, M. Segev. Self-trapping of "necklace" beams in self-focusing Kerr media. *Phys. Rev. Lett*. **81**, 4851 (1998).

[45] W. Walasik, S. Z. Silahli, N. M. Litchinitser. Dynamics of necklace beams in nonlinear

colloidal suspensions. *Scientific Reports* **7**, 11709 (2017).

[46] L. Zhu & J. Wang. Arbitrary manipulation of spatial amplitude and phase using phase-only spatial light modulators. *Sci. Rep.* **4**, 7441 (2014).

[47] T. D. Grow, A. A. Ishaaya, L. T. Vuong & A. L. Gaeta. Collapse and stability of necklace beams in Kerr media. *Phys. Rev. Lett*. **99**, 133902 (2007).

[48] J. C. T. Lee, S. J. Alexander, S. D. Kevan, S. Roy & M. J. McMorran. Laguerre-Gauss and Hermite-Gauss soft X-ray states generated using diffractive optics. *Nat. Photon*ics **13**, 205-209 (2019).

[49] C. Hernández-García, C. J. A. Pérez-Hernández, J. Ramos, E. Conejero Jarque, L. Roso, and L. Plaja. High-order harmonic propagation in gases within the discrete dipole approximation. *Phys. Rev. A*. **82**, 0033432 (2010).

[50] C. Hernández-García, J. A. Pérez-Hernández, T. Popmintchev, M. M. Murnane, H. C. Kapteyn, A. Jaron-Becker, A. Becker, and L. Plaja. Zeptosecond high harmonic keV X-ray waveforms driven by midinfrared laser pulses. *Phys. Rev. Lett.* **111**, 2, 033002 (2013).

[51] D. J. Batey, D. Claus & J. M. Rodenburg. Information multiplexing in ptychography. *Ultramicroscopy* **138**, 13–21 (2014).

[52] B. Zhang, D. F. Gardner, M. H. Seaberg, E. R. Shanblatt, C. L. Porter, R. Karl, C. A. Mancuso, H. C. Kapteyn, M. M. Murnane, D. E. Adams. Ptychographic hyperspectral spectromicroscopy with an extreme ultraviolet high harmonic comb. *Opt. Express* **24,** 16 (2016).

[53] M. Abramowitz & I. A. Stegun. *Handbook of Mathematical Functions with Formulas, Graphs and Mathematical Tables* (New York: Dover, 1965).

[54] R. W. Gerchberg & W. O. Saxton. A practical algorithm for the determination of phase from image and diffraction plane pictures. *Optik* **35**, 237-246 (1972).

[55] S. Fu, S. Zhang, T. Wang & C. Gao. Pre-turbulence compensation of orbital angular momentum beams based on a probe and the Gerchberg-Saxton algorithm. *Opt. Lett*. **41**, 3185–3188 (2016).

[56] H. Chang, X.-L. Yin, X.-Z. Cui, Z.-C. Zhang, J.-X. Ma, G.-H. Wu, L.-J. Zhang, X.-J. Xin. Adaptive optics compensation of orbital angular momentum beams with a modified Gerchberg-Saxton-based phase retrieval algorithm. *Opt. Commun*. **405**, 271–275 (2017).

Acknowledgments

J.S.R., L.P. and C.H.-G. acknowledge support Ministerio de Ciencia e Innovación (FIS2016-75652-P and PID2019-106910GB-I00). This project has received funding from the European Research Council (ERC) under the European Union's Horizon 2020 research and innovation program (Grant Agreement No. 851201). J.S.R., L.P. and C.H.-G. also acknowledge support from Junta de Castilla y León FEDER funds (Project No. SA287P18). L. R. acknowledges support from Ministerio de Educación, Cultura y Deporte (FPU16/02591). C.H.-G. acknowledges Ministerio de Ciencia, Innovación, y Universidades for a Ramón y Cajal contract (RYC-2017-22745), co-funded by the European Social Fund. L.R., J.S.R., L.P. and C.H.-G thankfully acknowledge the computer resources at MareNostrum and the technical support provided by Barcelona Supercomputing Center (FI-2020-3-0013). The JILA team graciously acknowledges support from the Department of Energy BES Award No. DE-FG02-99ER14982 for the experimental implementation, a MURI grant from the Air Force Office of Scientific Research under Award No. FA9550-16-1-0121 for the mid-infrared laser soft X-ray research, and a National Science Foundation Physics Frontier Center grant PHY-1734006 for theory. N.J.B. acknowledges support from National Science Foundation Graduate Research Fellowships (grant no. DGE-1650115). Q.L.D.N. acknowledges support from National Science Foundation Graduate Research Fellowships (grant no. DGE-1144083).

Author contributions

L.R., J.S.R., L.P., and C.H.-G. performed the theoretical simulations and analyzed the resulting data. N.J.B. and Q.L.D.N. designed and constructed the experiment. N.J.B., Q.L.D.N., and I.B. collected and analyzed experimental data. C.H.-G., L.P., M.M.M., and H.C.K. supervised the theoretical simulations, experimental work, and developed the facilities and measurement capabilities. L.R., N.J.B., Q.L.D.N., J.S.R., M.M.M., L.P., and C.H.-G. wrote and prepared the manuscript. All authors provided constructive improvements and feedback to this work.

Competing interests

M.M.M. and H.C.K. have a financial interest in KMLabs. The other authors declare no competing financial interests.

4

ATTOSECOND PULSES WITH NOVEL POLARIZATION STATES

Controlling the SAM or polarization state of XUV/X-ray pulses opens the route to new exciting capabilities. For example, ultrafast chiral light beams, such as circularly polarized beams, are particularly important in the study of chiral molecules, making it possible to discriminate between enantiomers and to resolve their dynamics [145–147]. However, although the generation and characterization of light beams with certain polarization states can be routinely performed in the visible or longer wavelength regimes using polarizers, it becomes much more challenging in the XUV/X-ray regimes, where standard polarizers are highly inefficient.

In the last decade, high-frequency beams with controlled polarization have been generated using different set-ups, as accelerator based light sources, such as synchrotrons or X-ray free electron lasers, and HHG. On the one hand, the former techniques have demonstrated to provide bright X-ray pulses with controlled polarization [148], with minimum durations of tens of femtoseconds [149]. On the other hand, several works have demonstrated that proper configurations of HHG allow for the generation of high-order harmonics and attosecond pulses with controlled polarization in table-top set-ups. The generation of XUV beams with novel polarization states through HHG often follows a similar strategy to that of XUV vortex beams: the incident infrared laser beam is designed to transmit certain SAM properties to the high-order harmonics. However, in contrast to the case of OAM, it turns our that a single circularly polarized driving beam does not lead to the generation of circularly polarized harmonics. Thus, more complex strategies have been developed in the past years to circumvent this problem.

In this chapter, we show different HHG schemes for the control of the polarization of high-order harmonics and attosecond pulses. First, in section 4.1, we summarize the main state-of-the-art strategies for polarization control in HHG. Then, in section 4.2, we introduce the non-collinear counter-rotating scheme, as a configuration in which the ellipticity of the harmonics can be tuned. Interestingly, we demonstrate that this capability can be used to characterize the non-perturbative dipole response during HHG. In section 4.3, we employ the bi-circular vortex field for the generation of attosecond pulses with simultaneously controlled SAM and OAM. In section 4.4, we propose a scheme for the generation of attosecond pulse trains with time-ordered polarization states from HHG driven by two time-delayed bi-circular vortex

fields. Finally, in section 4.5, we include the full text of our publications [18, 19], as additional information on the topics discussed in sections 4.3 and 4.4.

4.1 STATE-OF-THE-ART OF POLARIZATION CONTROL IN HIGH-ORDER HARMONIC GENERATION

HHG is typically driven by linearly polarized lasers, which constrains the electron dynamics to a one dimension. As a consequence, the emitted harmonics are also linearly polarized. Generating high-order harmonics with high ellipticity is not straightforward, since the efficiency of HHG decreases greatly with the ellipticity of the driving field, as shown in figure 37. The reason of this decrease is that, for increasing ellipticities of the driving field the electronic wavepacket is driven far away from its parent ion, which diminishes its recollision probability [150–152]. A first approach to convert the linear polarization of the harmonics into circular polarization consists in using multiple reflections on surfaces with different complex reflectivities for the S and P polarization [153]. However, this method is also very inefficient.

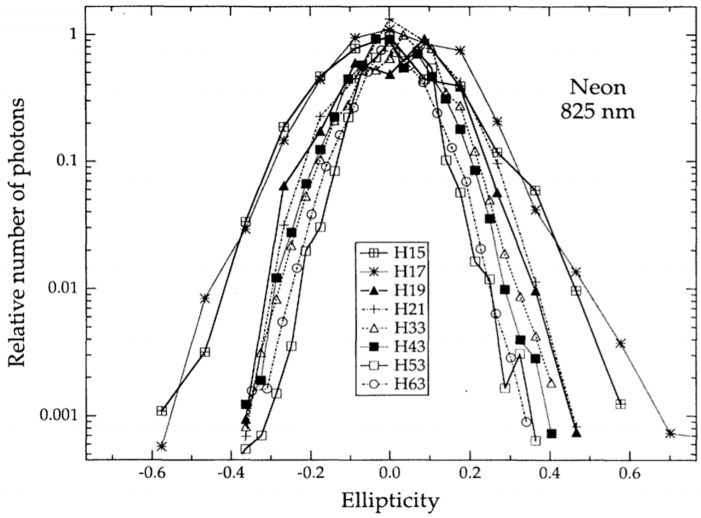

Figure 37: High-order harmonics produced in neon as a function of the ellipticity of the driving field (for a peak intensity of 10^{15} W/cm^2 and wavelength of 825 nm). The number of photons corresponding to each harmonic is normalized. Figure extracted from [150].

Luckily, several schemes have been developed in the last decades to circumvent this problem, either by structuring the driving field or by selecting different targets. Elliptically polarized high-order harmonics have been produced employing strategies based on the use of non-symmetric targets—such as molecules or solids—[33, 114, 154], resonant HHG of an elliptical laser pulse [155] or combinations of linearly polarized drivers with different frequencies [156, 157]. Also, the

use of two HHG sources can provide harmonics with spatially varying ellipticity [158, 159]. On the other hand, purely circularly polarized harmonics can be generated from schemes based on non-collinear counter-rotating driving beams with the same color [20, 160, 161] and two-color, counter-rotating, circularly polarized laser fields (the so-called bi-circular driving) [162–167]. These two last methods, however, differ in the characteristics of the generated attosecond pulses. On the one side, the non-collinear counter-rotating driving produces circularly polarized attosecond pulses, since the left circular polarized (LCP) and right circular polarized (RCP) harmonics are spatially separated in the far-field. On the other side, in the bi-circular scheme the RCP and LCP harmonics spatially overlap and, as a result, the attosecond pulses are linearly polarized. Nevertheless, the bi-circular field provides harmonics with brightness and energies comparable to single-color linearly polarized HHG, so in this thesis we approach these two schemes. First, we show how to exploit the ellipticity control and how to retrieve information about the dipole response using the non-collinear counter-rotating driving field (section 4.2). Second, we study how to modify the bi-circular HHG scheme to generate circularly polarized attosecond pulses (section 4.3). Finally, since all the mentioned strategies provide attosecond pulse trains with approximately constant ellipticity along the train, we also propose a method for the generation of trains of pulses with consecutive, time-ordered, polarization states using the bi-circular driving field (section 4.4).

4.2 THE NON-COLLINEAR COUNTER-ROTATING SCHEME

This scheme is based on a convenient combination of the HHG emission at different points in the target, by using a driving field whose macroscopic structure presents a non-homogeneous polarization in the transverse plane. To do so, two circularly polarized counter-rotating laser beams are arranged in a non-collinear configuration, as shown in figure 38a [160]. Let us consider the non-collinear angle as the angle between the propagation axis of each beam and the horizontal axis. In the target plane, the combination of the two circularly polarized driving beams results in linear polarization, which allows for the efficient generation of linearly polarized harmonics. However, the tilt angle of the local polarization of the driving field rotates along the horizontal axis, due to the different temporal delay between the two drivers at different spatial positions. Thus, at the target plane, the harmonics are generated linearly polarized, but with a spatially varying tilt angle, as shown in figure 38c. Importantly, the propagation direction of each harmonic follows from the addition of the driving pulse wavevectors, leading to two off-axis harmonic beams, as depicted in figure 38b.

In the far-field, the harmonic radiation results from the coherent superposition of the linearly polarized harmonics generated at differ-

ent positions in the target plane. The rotation of the polarization tilt at the target, together with the different propagation distance from each local emitter to the detector—which introduces a temporal delay between the different rotated linear polarization components—, results in a circularly polarized harmonic signal in the far-field. Thus, the

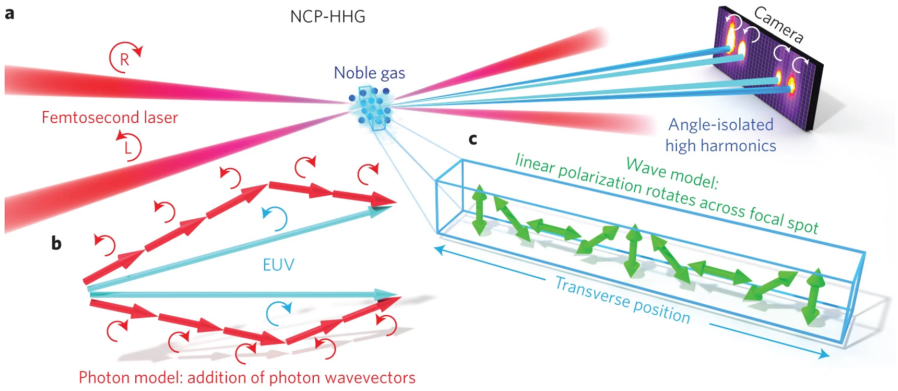

Figure 38: (a) Scheme of HHG driven by a non-collinear counter-rotating beam. Two counter-rotating circularly polarized femtosecond laser pulses are focused into the gas to produce both RCP and LCP XUV beams. (b) The propagation direction of each harmonic follows the simple vector addition of the wavevectors of the driving pulse. (c) The driving field in the target plane exhibits linear polarization rotating as a function of the transverse position, which is translated to the harmonics. In the far-field the coherent addition of the rotating polarization results in circular polarization. Figure extracted from [160].

spatial distribution of the harmonics in the far field consists in two XUV beams exhibiting circular polarization and opposite helicity.

Note that within each XUV beam, the individual harmonics are detected at a slightly different position along the horizontal coordinate. This can be understood in terms of the linear momentum conservation, taking into account that each harmonic is generated from the absorption of a different number of photons from each driving beam (see figure 38b). On the other hand, since all the harmonics within each beam exhibit the same helicity, the composition of the harmonic signal corresponds to circularly polarized attosecond pulses.

It is worth mentioning that, under this configuration, the efficiency of the attosecond pulses is limited by three different constrains: the transverse temporal walk-off, the driving field's overlapping area within the target, and the overlap of the harmonics in the far field. These two latter aspects can be optimized by using smaller non-collinear angles, while, on the other hand, it has been demonstrated theoretically that the effect of the spatial walk-off can be reduced by introducing an angular chirp in the driving beams [161].

4.2.1 *Ellipticity control*

Here we demonstrate the possibility of the generation of isolated attosecond pulses with controlled polarization states using the non-collinear counter-rotating scheme. The detailed information about this work can be found in our publication [20], included in the Appendix A.1. The experiments were carried out by our collaborators in the group of Prof. M.-Ch. Chen at the Institute of Photonics Technologies of the National Tsing Hua University (Taiwan).

The isolated attosecond pulses with tunable ellipticity are obtained by using few-cycle infrared counter-rotating driving fields, as schematically depicted in figure 39. A time delay between the driving pulses allows to reduce the number of attosecond pulses, similar to a polarization-gating technique [161]. Interestingly, by simultaneously modifying the ellipticity of the two driving pulses (both always exhibiting the same absolute ellipticity but with opposite helicity), we can control the amplitude and phase of the distribution of the linearly polarized harmonic emissions at the focal plane. As a consequence, we can modify the polarization state of the XUV beams—and, thus, that of the attosecond pulses—, from circular through elliptical to linear polarization, without a loss of conversion efficiency.

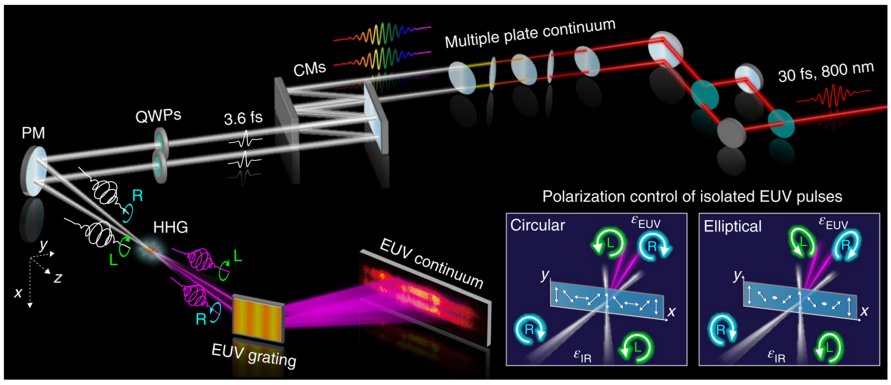

Figure 39: Representation of the experimental set-up for generating isolated high-order harmonic pulses using a non-collinear counter-rotating few-cycle driving field. The driving pulses have a duration of 3.6 fs each and the time delay between them is 1.8 fs ($\lambda_0 = 800\,nm$). The ellipticity of the harmonics is controlled through the ellipticity of the individual driving pulses. CM, chirped mirror; QWP, quarter-wave plate; PM, off-axis parabolic mirror. The insets show the polarization of the driving field at the focal plane.

The experimental and theoretical results from our macroscopic SFA and TSM models (explained in section 2.3) allow us to extract the harmonic's ellipticity and tilt angle as a function of the driving fields' ellipticity, as shown in figure 40a. Interestingly, the TSM results show that the non-perturbative characteristics of the HHG—i.e. the non-perturbative dipole phase and the amplitude scaling power—,

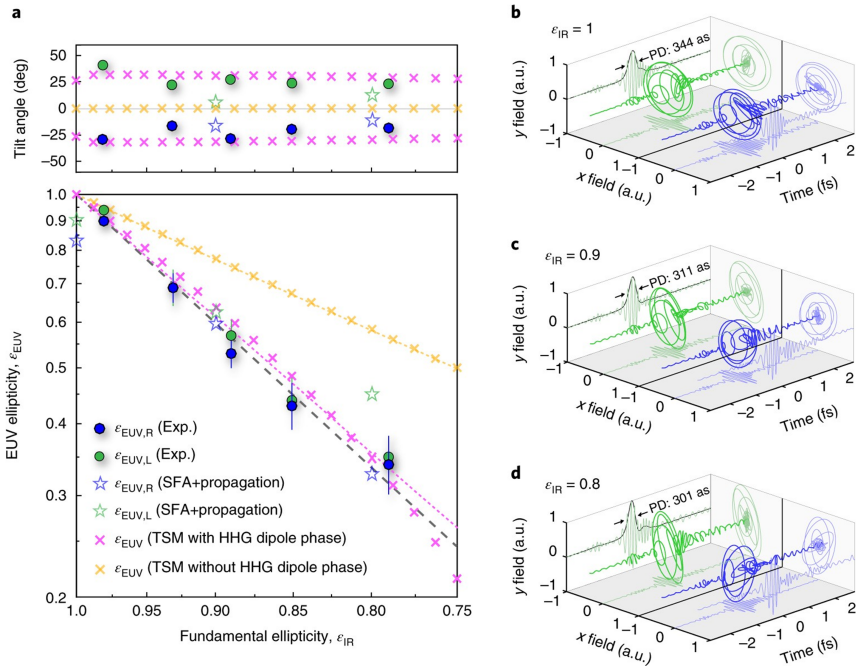

Figure 40: (a) Tilt angle—with respect to the driving beams' polarization major axis—(top) and ellipticity (bottom) of the XUV beams as a function of the driving beams' ellipticity obtained from the experimental measurements (blue circles for RCP harmonics and green circles for LCP harmonics), our SFA model including propagation (blue stars for RCP harmonics and green stars for LCP harmonics), and our TSM model (pink crosses including the non-perturbative dipole phase and orange crosses neglecting it). (b)–(d) Temporal evolution of the RCP (blue) and LCP (green) attosecond pulses computed for different driving beams' ellipticities: 1.0 (b), 0.9 (c), and 0.8 (d).

play a crucial role in the resulting harmonic ellipticity. The reason for this is that the total driving field at the focal plane exhibits a spatially varying intensity with modulations along the horizontal axis for non-circularly polarized driving fields, which is translated into the spatial distribution of the dipole phase and amplitude. In particular, the non-perturbative parameters determine the dependency of the harmonic field with the local intensity, thus shaping the harmonic near field structure and, ultimately, dictating the far-field ellipticity of the harmonics. Our numerical simulations show that, under the configuration depicted in figure 39, isolated attosecond pulses with controlled polarization are generated, as presented in figures 40b-d.

4.2.2 *Characterization of the non-perturbative dipole response*

As mentioned in section 2.2.4, the experimental characterization of the non-perturbative response, especially of the dipole phase, is very challenging. In this subsection, we present a scheme for the charac-

terization of the non-perturbative response in HHG by measuring the harmonic polarization state in the non-collinear geometry. We have already seen in figure 40a the crucial role of the non-perturbative dipole phase to determine the harmonic ellipticity (see the comparison between the pink and orange crosses, where the dipole phase is and is not included in the TSM calculations, respectively). Now we have developed an ellipsometry technique that fully resolves the polarization state—helicity, ellipticity, tilt angle, and degree of polarization—for each high-harmonic order, simultaneously. These experiments have been also carried out by our collaborators from the group of Prof. M.-Ch. Chen at the Institute of Photonics Technologies of the National Tsing Hua University (Taiwan). Further details about this work can be found in our publication [21], included in the Appendix A.2.

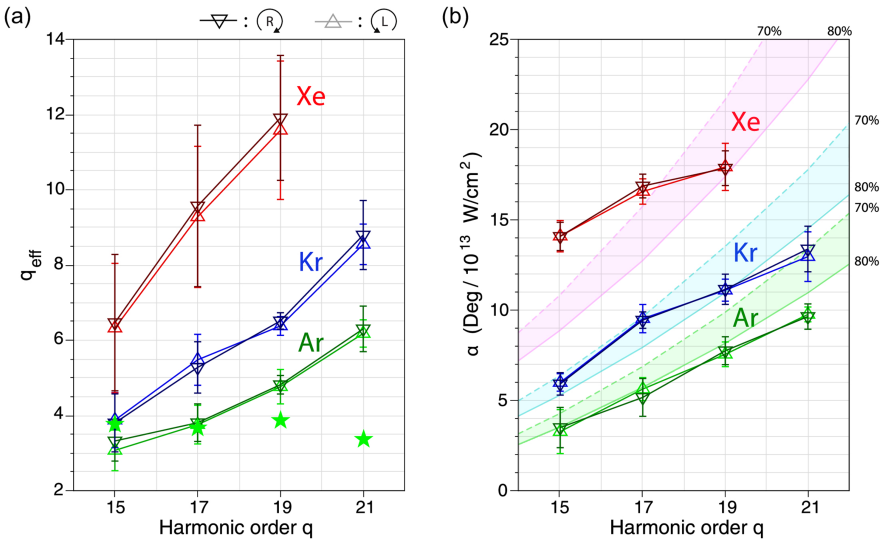

Figure 41: Dipole response information extracted from high harmonic ellipsometry for three different gas species: argon (green), krypton (blue), and xenon (red). (a) Power scaling (which we have previously denoted as p) as a function of the harmonic order. The green stars represent the calculated scaling power in argon obtained from SFA calculations. (b) α_q coefficient corresponding to short trajectories as a function of the harmonic order. The light strips indicate the calculations from a semiclassical model [98] for the 70% and 80% of the experimental average peak intensity. The use of a reduced intensity in our simulations is attributed to inhomogeneities at the experimental focus.

Our results show that the ellipticity of the harmonics, ϵ_{XUV}, scales with the driving fields' ellipticity, ϵ_{IR}, as $\epsilon_{XUV} \propto \epsilon_{IR}^{\sigma}$, where σ varies with the harmonic order and the gaseous species. The ellipsometric retrieval reveals that σ depends on the amplitude scaling power, p, and the dipole phase coefficient, α_q^r (see section 2.2.4), which change substantially with the harmonic order and the atomic element.

Let us briefly explain how the ellipsometry technique works. First, the ellipticity and tilt angle of each harmonic is experimentally measured as a function of the driving fields' ellipticity. From these measurements, we calculate the amplitude ratio and the phase difference between the two linearly polarized orthogonal components of the harmonic electric field. Finally, a genetic algorithm is used to find the non-perturbative parameters that lead to the far-field harmonics. In this later step, we use the TSM to obtain the harmonic near-field—which is described as a function of the known driving field and the unknown non-perturbative parameters—and then to compute the far-field harmonics (as indicated by Eqs. (60) and (61)). Note that the retrieved scaling parameter p and dipole phase coefficient α_q^r show good agreement with the classical results, as shown in figure 41 for short trajectories and three different gas species.

4.3 SIMULTANEOUS CONTROL OF ORBITAL AND SPIN ANGULAR MOMENTUM

In this section, we shall present a different method for the control of the polarization state of the attosecond pulses. We will show that, interestingly, the SAM and OAM of the high-order harmonics can be simultaneously controlled by driving HHG with a bi-circular vortex field. We will demonstrate, theoretically and experimentally, that this ability allows for an unprecedented control over the OAM and over the divergence of the XUV beams. As a result, by properly selecting the OAM of the driving field we can control the polarization state of the attosecond pulses, from linear to circular, or we can generate circularly polarized XUV beams with the same OAM content as the driving beam. Such structured beams can serve as an alternative tool for the study of novel ultrafast phenomena of spin/charge dynamics in magnetic materials or chiral molecular systems, as well as of spatially resolved circular dichroism, or even skyrmionic spectroscopy.

4.3.1 *The standard bi-circular driving*

Let us first explain the characteristics of the standard bi-circular driving. The bi-circular field was theoretically proposed in the 90's to generate circularly polarized harmonics [162, 163]. However, this was not experimentally realized until 2014 [165, 166]. This technique consists in the combination of two collinear beams with different frequencies and counter-rotating circular polarization. Since they have different frequencies, their combination results in a complex Lissajous polarization structure [164]. Typically, the bi-circular field consists in a fundamental frequency and its second harmonic, and the resulting structure corresponds to a trefoil shape, as shown in figure 42.

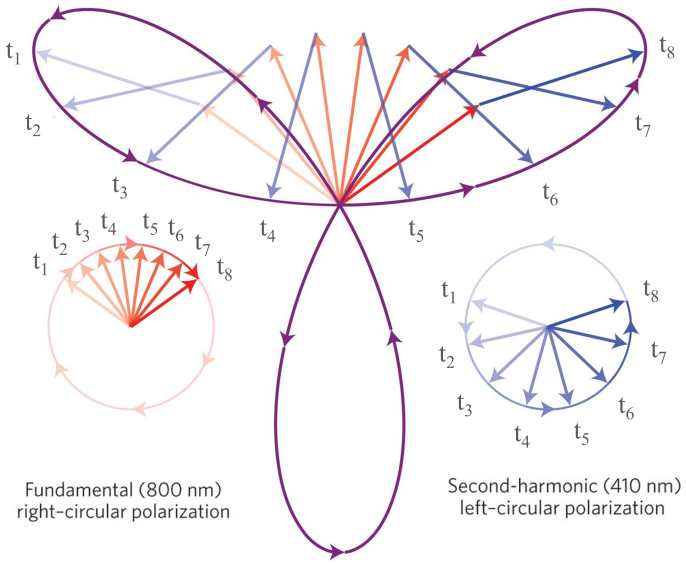

Figure 42: The bi-circular field: combination of a RCP infrared driver (red arrows) with its LCP second harmonic (blue arrows) at equal intensities, which results in a trefoil-shaped electric field (purple curve). Modified version of a figure extracted from [168].

Under such configuration, the electronic wavepacket follows a trajectory that is not restricted to one dimension but, remarkably, it still recollides efficiently with the parent ion. It is important to note that, in contrast to the non-collinear counter-rotating scheme discussed in the previous section, in the bi-circular scheme the physics that leads to the generation of circularly polarized harmonics resides at the microscopic level: the electric field has a complex polarization structure at each point of the target that results in the local emission of circularly polarized harmonics. Interestingly, since the field is dichromatic, the emitted spectrum is not composed of odd harmonics as in regular HHG. Besides, as the electric field exhibits a different symmetry, it drives three recombination events within a fundamental field period, and the polarization direction of the harmonics is rotated 120 degrees between successive emissions.

The energy selection rules in this case can be more easily described in terms of the number of driving photons that are annihilated in the HHG process. Let us consider a bi-circular field with frequencies ω_1 and $\omega_2 = 2\omega_1$, and with σ_1 and σ_2 the spin of each frequency component ($\sigma_2 = -\sigma_1$, since they have opposite helicity). Note that $\sigma = 1$ corresponds to right-circular polarization, while $\sigma = -1$ corresponds to left-circular polarization. The energy conservation for a particular harmonic satisfies:

$$\omega_q = q\omega_1 = n_1\omega_1 + n_2\omega_2 \tag{100}$$

where n_1 and n_2 are integer numbers representing the number of photons annihilated from each driver. On the other hand, SAM conservation,

$$\sigma_q = n_1\sigma_1 + n_2\sigma_2 = \pm 1, \tag{101}$$

results in the following condition:

$$n_2 = n_1 - \sigma_q\sigma_1. \tag{102}$$

Thus, the photon composition of Eq. (100) is restricted to:

$$\omega_q = n_1(\omega_1 + \omega_2) - \sigma_q\sigma_1\omega_2 = (3n_1 - 2\sigma_q\sigma_1)\omega_1, \tag{103}$$

where $\sigma_q\sigma_1 = \pm 1$.

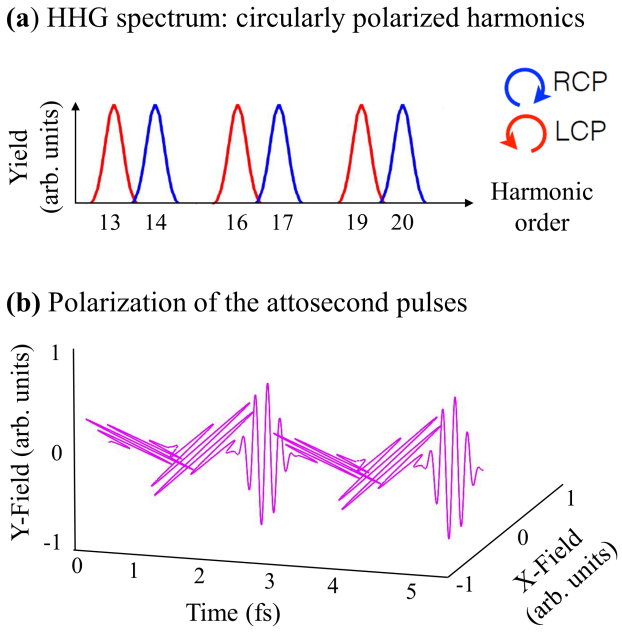

Figure 43: (a) Representation of the HHG spectrum when driven by a bicircular field ($\omega_2 = 2\omega_1, \sigma_1 = -1, \sigma_2 = 1$). It is composed of pairs of RCP and LCP high-order harmonics separated by a missing one. (b) Under this configuration, the attosecond pulses exhibit linear polarization, with a tilt-angle rotation of 120 degrees from pulse to pulse.

As a result, the HHG spectrum consists of pairs of harmonics with opposite circular polarization states, separated by a missing harmonic, as represented in figure 43a. The absence of each third harmonic can be used as an indicator of the degree of circularity of the harmonics. Conversely, the ellipticity of the harmonics can be manipulated by varying the driving fields' ellipticity [165], while small variations of the attosecond pulses polarization can be achieved by changing and intensity ratio between the driving fields [169].

Finally, figure 43b shows that the attosecond pulses, which result from the spectral integration over harmonics with opposite circular polarization, exhibit linear polarization, with a tilt-angle rotation of 120 degrees from burst to burst [170].

4.3.2 *Generation of harmonics with spin and orbital angular momentum*

In contrast to the non-collinear scheme explained in section 4.2, where the efficiency of the harmonics is limited by the macroscopic configuration, the bi-circular field allows for the generation of bright circularly polarized harmonics [166]. Yet, each attosecond pulse is linearly polarized. In this subsection, we introduce OAM into the bi-circular scheme, aiming for the possibility of producing attosecond pulses with circular polarization states. The experiments have been carried out by our collaborators in the Kapteyn-Murnane group in JILA, at the University of Colorado in Boulder (USA). The details of the experimental methods and further information about this work can be found in our publication [18], included in section 4.5.1.

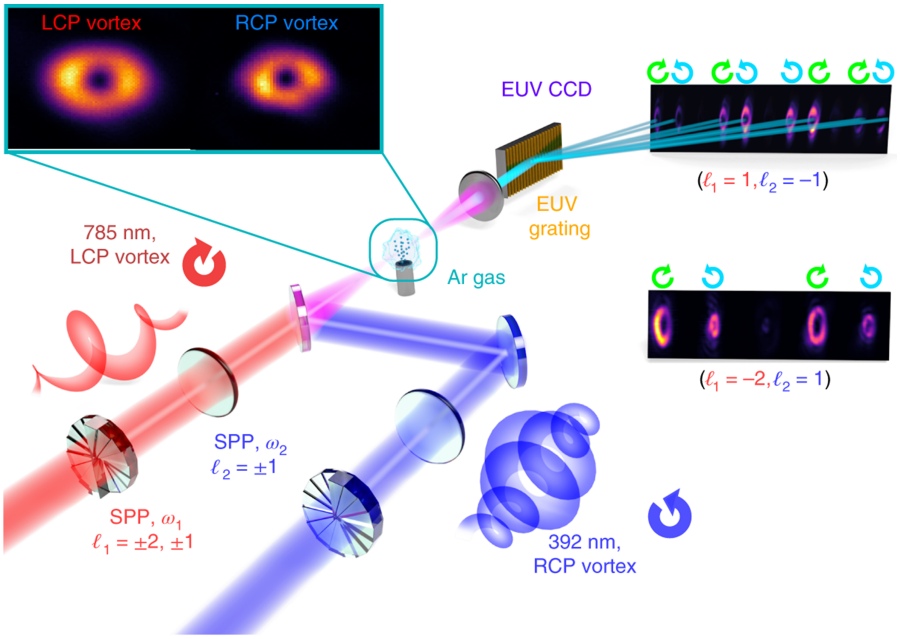

Figure 44: Scheme of HHG driven by a bi-circular vortex field. In the experiment, circularly polarized beams of opposite helicity are passed through spiral phase plates (SPPs) producing circularly polarized vortex beams (top-left inset). The XUV beams emitted from an argon gas jet are collected via a cylindrical mirror-grating pair (EUV grating) and into a XUV camera (EUV CCD). The panels at the detectors (right) show the experimental harmonics obtained for two different OAM configurations of the driving beams: $\ell_1 = 1, \ell_2 = -1$ (up-right panel), and $\ell_1 = -2, \ell_2 = 1$ (down-right panel).

In figure 44, we show a scheme of HHG driven by a bi-circular vortex field. Here, both driving beams conforming the bi-circular field exhibit OAM content, ℓ_1 and ℓ_2, respectively. As in the standard bi-circular field, the resulting HHG spectrum is composed of pairs of circularly polarized harmonics with opposite helicity. However, the high-order harmonics are now also vortex beams. Notably, the choice of ℓ_1 and ℓ_2 determines the OAM content of the harmonics and, as result, their spatial properties.

Let us now derive the selection rules for the OAM of the harmonics. In this case, the general OAM conservation rule, Eq. (82), is expressed as:

$$\ell_q = n_1\ell_1 + n_2\ell_2, \tag{104}$$

where n_1 and n_2 are the number of photons annihilated from each of the driving beams. Note that the non-perturbative dipole phase contributions in Eq. (82) are not present in Eq. (104) because in this case the driving field's intensity distribution does not present an azimuthal variation. Applying the SAM and energy conservation rules in Eqs. (103) and (102), n_1 and n_2 are rewritten as:

$$n_1 = \frac{1}{3}(q + 2\sigma_q\sigma_1), \tag{105}$$

$$n_2 = \frac{1}{3}(q - \sigma_q\sigma_1). \tag{106}$$

Thus, combining Eqs. (104), (105), and (106), we obtain the selection rule for the OAM of the harmonics which, importantly, depends on their particular SAM:

$$\ell_q = \frac{q + \sigma_q\sigma_1}{3}(\ell_1 + \ell_2) - \sigma_q\sigma_1\ell_2. \tag{107}$$

Note that, in contrast to the more general OAM rule—Eq. (104)—where each harmonic exhibits a broad OAM content corresponding to the different (n_1, n_2) absorption channels, in the bi-circular case—Eq. (107)—the OAM of each harmonic is restricted to one single allowed value due to the SAM conservation. Thus, the SAM and OAM of the harmonics generated from the bi-circular vortex driving are inherently entwined.

An interesting particular case is the driver's OAM combination satisfying $\ell_1 = -\ell_2$, since Eq. (107) is reduced to $\ell_q = -\sigma_q\sigma_1\ell_2$. In this case, the harmonics are generated with the same OAM as the driving field. In particular, the RCP harmonics exhibit the same OAM as the RCP component of the driving field, while the LCP harmonics exhibit the same OAM as the LCP component. To illustrate this effect, in figure 45 we show the results for the generation of harmonics with $\ell_q = \pm 1$ from the bi-circular vortex driving beam carrying $\ell_1 = 1$ and $\ell_2 = -1$ ($\lambda_1 = 800\,nm, \omega_2 = 2\omega_1, \sigma_1 = -1, \sigma_2 = 1$). Note again that the absence of each third harmonic is an indication of an almost perfect

circular polarization in the pairs of counter-rotating harmonics. In addition, the good agreement between the theoretical (figure 45a) and the experimental (figure 45b) beam profiles proves the restriction of the OAM of the harmonics by the SAM conservation rules, in Eq. (107). Moreover, the uniform intensity profile of the harmonics discards any

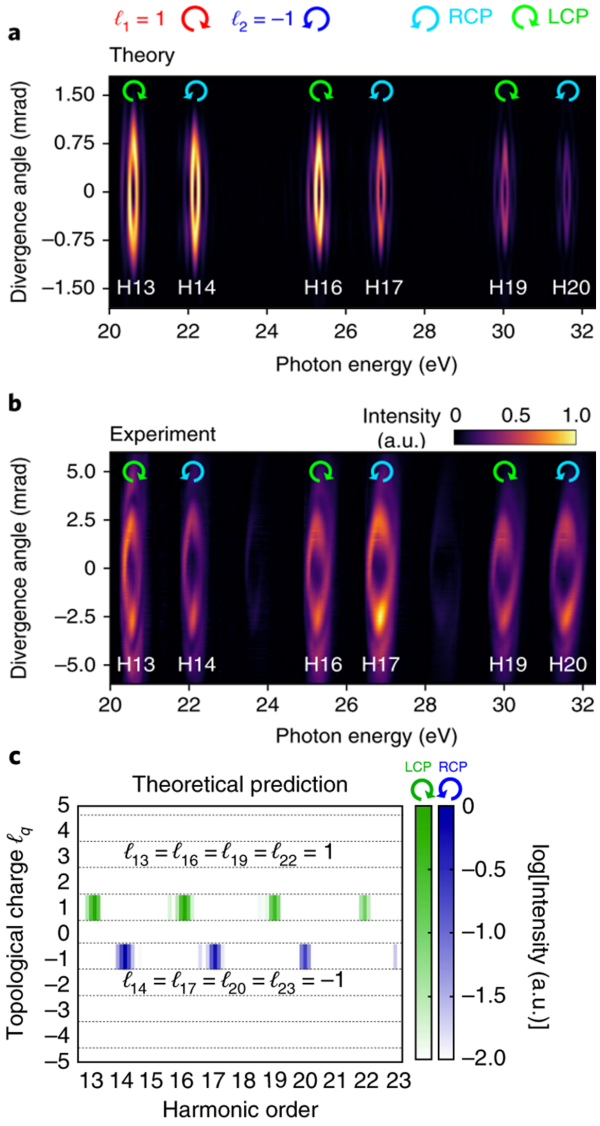

Figure 45: Simulated (a) and experimental (b) circularly polarized high-harmonic vortex beams with low OAM charge generated by a degenerate, complementary bi-circular field ($\ell_1 = 1, \ell_2 = -1$). (c) The full-quantum theoretical simulations show that the OAM of each harmonic is the same as that of the driving pulse with its same helicity. The driving pulses used in the quantum simulations mimic the experimental field with the following parameters: wavelengths of $\lambda_1 = 800\,nm$ and $\lambda_2 = 400\,nm$, respectively, waists of $w_1 = w_2 = 30\,\mu m$, trapezoidal envelopes with 16 fs of constant amplitude and a total peak intensity of $I_0 = 2 \times 10^{14}\,W/cm^2$.

possibility of a superposition of different OAM values, ensuring that the harmonics are pure vortices.

It is also important to stress that, while the high-order harmonics from vortex drivers are typically produced with high OAM values, following Eq. (76), the bi-circular scheme allows to obtain high-order harmonics with low OAM. The generation of XUV beams with low OAM is interesting for the simplification of their light-matter interactions and detection geometries. To date, such beams have been previously demonstrated using non-collinear schemes [132, 133], while, here, we have demonstrated their generation from a collinear configuration (see figure 45c).

4.3.3 *Attosecond pulses with customized polarization states.*

Remarkably, our control over the OAM of the harmonics allows us also to manipulate the divergence of the RCP and LCP harmonics separately and, as a result, the polarization state of the resulting attosecond pulses. Let us calculate the divergence of the harmonics using a simplified version of the TSM (see section 2.3.3), where we approximate the intensity profile of the driving vortex field to an infinitely thin ring at the radius of maximum intensity. Under these circumstances, the far-field distribution of the q-th order harmonic as a function of the divergence angle, β, satisfies [18]:

$$U_q(\beta) \propto J_{|\ell_q|}\Big(\frac{2\pi}{\lambda_1} q r_{max} \tan(\beta)\Big), \tag{108}$$

where $J_n(x)$ is the Bessel function of order n and r_{max} is the radius of the driving field's ring. Importantly, for given values of r_{max} and λ_1, the maximum of the Bessel function is proportional to the ratio $|\ell_q|/q$. Hence, the relation between the order and the argument of the Bessel function unequivocally determines the divergence of the harmonic.

In the typical single-mode OAM driving case, where the OAM scales linearly with the harmonic order (see Eq. (76) in section 3.2.1), the divergence of the harmonics is proportional to $|\ell_q|/q = |\ell_{IR}|$, and, thus, all the harmonics exhibit a similar ring diameter [129, 131]. In contrast, Eq. (107) shows that, in the bi-circular vortex driving scenario, $|\ell_q|$ follows a more involved rule. The divergence of each harmonic is now proportional to:

$$\frac{|\ell_q|}{q} = \Big|\frac{1}{3}(\ell_1+\ell_2) + \frac{\sigma_q\sigma_1(2\ell_1-\ell_2)}{3q}\Big|. \tag{109}$$

This expression allows us to obtain the difference in divergence between the RCP and LCP harmonics (see 4.5.1 and [18]):

$$\Delta\beta \propto \frac{|\ell_q|}{q} - \frac{|\ell_{q-1}|}{q-1} \propto (\ell_2 - 2\ell_1)\frac{|\ell_1+\ell_2|}{\ell_1+\ell_2} \tag{110}$$

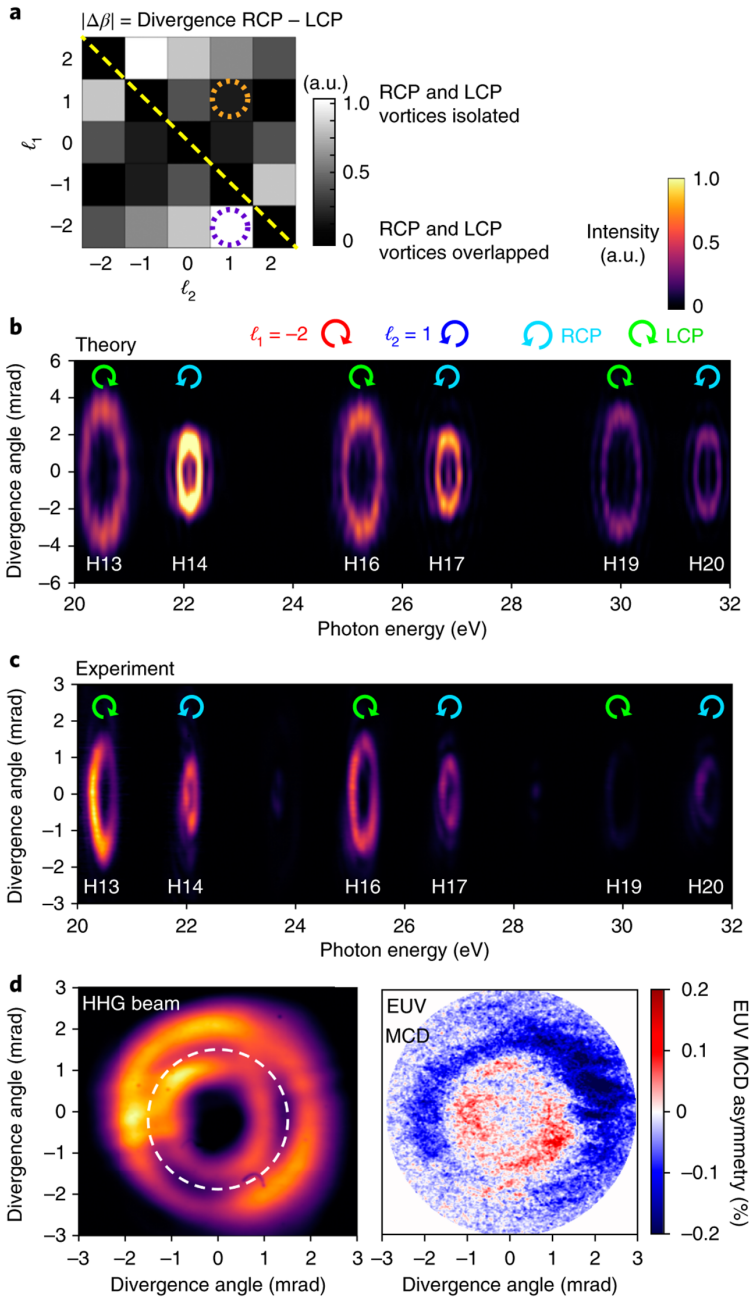

Figure 46: (a) Theoretical estimation of the divergence difference between the RCP and LCP harmonics as a function of the OAM of the bi-circular vortex field. (b) Theoretical high-order harmonics from HHG driven by a bi-circular vortex field carrying $\ell_1 = -2, \ell_2 = 1$. The LCP and RCP vortices exhibit significantly different divergence. (c) Experimental high-order harmonics for the same configuration as in (b). (d) The far-field HHG beam (left) presents a dual intensity ring structure where the inner ring is RCP and the outer ring is LCP, as confirmed by a spatially resolved XUV magnetic circular dichroism measurement (right). The driving field parameters are the same as those in figure 45 but with $w_1 = 21.4\,\mu m$.

In figure 46a, we depict the value of $\Delta\beta$ for different combinations of ℓ_1 and ℓ_2. Notably, by properly selecting the OAM of the driving beams, the RCP and LCP harmonics can be spatially separated. In figure 46b, we show the results from the theoretical simulations using our full-quantum SFA model including propagation for HHG in an argon gas jet (see section 2.3.2), for the $\ell_1 = -2, \ell_2 = 1$ combination. The LCP harmonics exhibit a larger divergence than the RCP harmonics because their OAM is higher. These results are confirmed by the experimental measurements, shown in figure 46c, where RCP and LCP harmonics present a clear spatial separation. Indeed, the total XUV beam exhibits two distinct rings (see the left panel of figure 46d), the inner ring presenting right circular polarization and the outer ring presenting left circular polarization, as confirmed by the measurement of spatially resolved XUV magnetic circular dichroism (see the right panel of figure 46d).

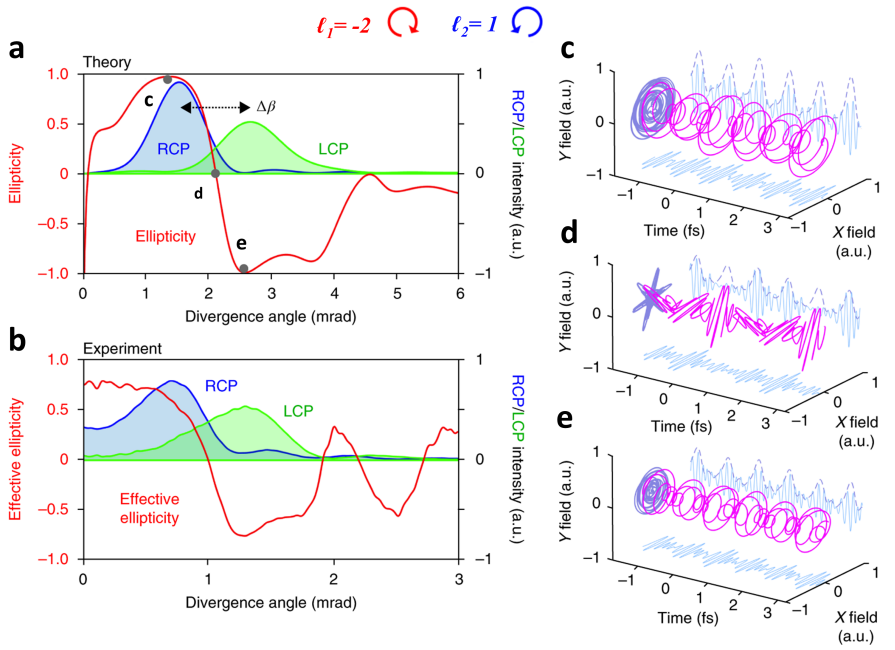

Figure 47: Theoretical (a) and experimental (b) spectral integration of the harmonic signal as a function of the divergence angle for the configuration of figure 46. The total RCP (blue) and LCP (green) beams are separated, introducing a spatially varying ellipticity (red), which results in a spatial variation of the polarization of the attosecond pulses trains from RCP (c, 1.4 mrad), to linear (d, 2.1 mrad), to LCP (e, 2.6 mrad).

The spatial isolation between the RCP and LCP harmonics has an important consequence: the attosecond pulses associated to each ring are circularly polarized. In figure 47a, we show our theoretical simulations of the total yield of the RCP and LCP harmonics along the divergence, as well as the spectrally integrated ellipticity. Figure 47b,

on the other hand, presents its experimental confirmation. Finally, by performing the Fourier transform of the theoretical harmonic emission, we obtain the attosecond pulse trains at different divergence angles, with polarization states that range from right-circular (47c), to linear (47d), and, lastly, to left-circular (47e).

4.3.4 *The torus-knot conservation law*

In this final subsection, we show that the conservation rules for the SAM and OAM in the HHG driven by the bi-circular vortex field can be derived resorting to the symmetries of the driving field, a work in collaboration with our colleagues from the group of Prof. M. Lewenstein at ICFO in Barcelona (Spain) [22]. In other words, we will show how the individual symmetries associated with these conservation laws can be composed to create new non-trivial ones.

In figure 48, we present a scheme of the bi-circular vortex field where the rotation symmetry of the trefoil polarization structure is evidenced: a displacement along the azimuthal coordinate implies a rotation of the polarization structure. Thus, the bi-circular vortex

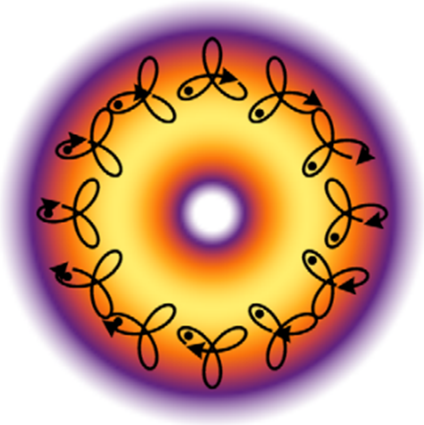

Figure 48: Torus-knot beam from the combination of an infrared RCP beam and its LCP second harmonic, both carrying $\ell = 1$. Tracking one lobe over an azimuthal loop around the beam axis (black dots) produces a 120° rotation, as well as a time delay within each trefoil (arrows).

field has the topology of a torus-knot: the trefoil tips trace out a knotted curve embedded on the surface of a torus [171]. Therefore, it is invariant under coordinated rotations, which combine a rotation of the spatial dependence by an angle θ with a rotation of the polarization by a fraction of that angle $\gamma\theta$, where γ is the coordination parameter. The generator of this coordinated rotation is the torus-knot angular momentum [171], defined as:

$$j_\gamma = \ell + \gamma\sigma, \tag{111}$$

thus, linking the SAM and OAM of the driving field through the γ parameter. If we consider that $\sigma_1 = 1$ and $\sigma_2 = -1$, the two frequency components of the driving field exhibit a torus-knot angular momentum of $j_\gamma^{(1)} = \ell_1 + \gamma$ and $j_\gamma^{(2)} = \ell_2 - \gamma$, respectively, where $\gamma = (\ell_2 - 2\ell_1)/3$ [22].

Importantly, for centro-symmetric targets, the topology of the driving field is transmitted to the harmonic emission, and, as a consequence, the generator of the coordinated rotation is conserved. Indeed, we have demonstrated that the torus-knot angular momentum is conserved in HHG [22], following a simple linear scaling law,

$$j_\gamma^{(q)} = q j_\gamma^{(1)}, \tag{112}$$

analogous to the OAM scaling for pure vortices (Eq. (76) in section 3.2.1).

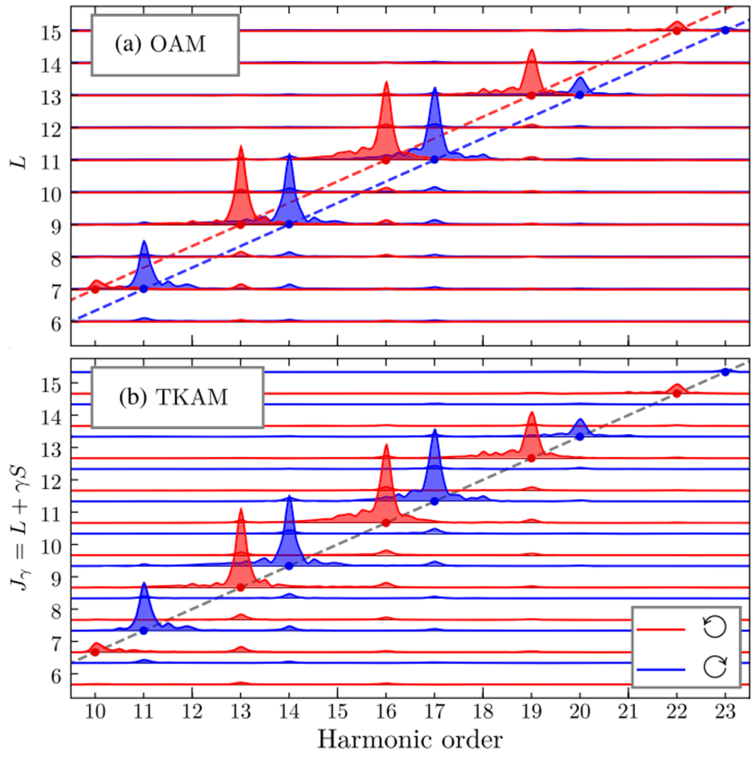

Figure 49: Simulated RCP (red) and LCP (blue) high-order harmonics from HHG driven by a bi-circular vortex beam ($\ell_1 = \ell_2 = 1$, $\sigma_1 = 1$, $\sigma_2 = -1$, so $\gamma = -1/3$). We compare the OAM (a) and torus-knot angular momentum, TKAM (b) as a function of the harmonic order. Note that the torus-knot angular momentum spectrum is equal to the OAM charge shifted by γ times the individual harmonic SAM. The conservation of the torus-knot angular momentum is demonstrated by the linear trend (dashed grey line) in (b).

This conservation law is demonstrated in figure 49, where we compare the OAM and the torus-knot angular momentum of the harmonics

obtained from our numerical simulations. We show that the torus-knot angular momentum scales linearly with the harmonic order.

Therefore, while the OAM selection rule can be explained using a photon-composition approach, as explained in section 4.3.2, the spectrum scales linearly with $j_\gamma^{(q)}$, therefore it can be understood easier via the torus-knot angular momentum conservation law. Further information about this work can be found in our publication [22], included in the Appendix A.3.

4.4 EVOLUTION OF THE POLARIZATION STATE ALONG THE ATTOSECOND PULSE TRAIN

In this section, we introduce a technique that allows to produce trains of attosecond pulses with a progressive variation of their ellipticity. These time-ordered polarization structures are generated by driving HHG with two time-delayed bi-circular vortex fields. Similarly to the time-ordered OAM [16] presented in section 3.3, this structured light beam adds a new degree of freedom, the time-ordered polarization, to the existing techniques for ultrafast control and measurement. For example, trains of attosecond pulses with sequential ellipticity offer a new stroboscopic utensil for the study of ultrafast dynamics in chiral systems, pump-probe experiments with polarization-varying states, or time-dependent polarization X-ray magnetic circular dichroism.

4.4.1 *Scheme for the generation of attosecond pulse trains with time-ordered ellipticities*

In section 4.3.3, we showed that the bi-circular vortex field allows us not only to generate circularly polarized harmonic vortex beams, but also to control the polarization state of the attosecond pulse trains by properly selecting the OAM of the driving beams [18]. This configuration allows the spatial separation of the high-order harmonics with opposite helicity in the far-field into a double ring profile, as shown in figure 50a, where the difference in divergence between the LCP and RCP harmonics is given by Eq. (110). In particular, from that expression we can infer that the divergence separation between RCP and LCP harmonics is maximized if

$$\ell_2 = -\ell_1 \pm 1, \tag{113}$$

being ℓ_1 as high as possible (it is usually limited by the experimental conditions). If we consider the following driving field parameters: $\lambda_1 = 800\,\mathrm{nm}, \omega_2 = 2\omega_1, \sigma_1 = -1, \sigma_2 = 1$, Eq. (110) shows that, if $|\ell_1| > |\ell_2|$, the far-field outer ring corresponds to the LCP harmonics. On the contrary, if $|\ell_2| > |\ell_1|$, the outer ring corresponds to the RCP harmonics. Thus, the OAM content of the driving field determines the helicity of each of the harmonic rings.

From the temporal point of view, the attosecond pulse trains with LCP or RCP states are obtained by selecting the high-order harmonics at each of the rings. For the following, it is important to note that the polarization state along the attosecond pulse trains is time-independent in this case. Thus, the ellipticity remains as a constant variable along the attosecond pulse trains. To the best of our knowledge, this is also the case in the rest of techniques involving the generation of attosecond pulses with controlled polarization. Note, however, that a recent work has reported that high-order harmonics generated from ultrashort bi-circular driving fields present a polarization state that slightly changes along the course of the harmonic pulse [172].

Here we present a technique to generate trains of attosecond pulses presenting a time-ordered SAM. The temporal progression is introduced by driving HHG with two time-delayed bi-circular vortex beams with different OAM content. Let us denote each of the bi-circular vortex beams as A and B. The most convenient choice of OAM satisfies Eq. (113) for each of the driving beams, together with $\ell_1^B = -\ell_2^A$

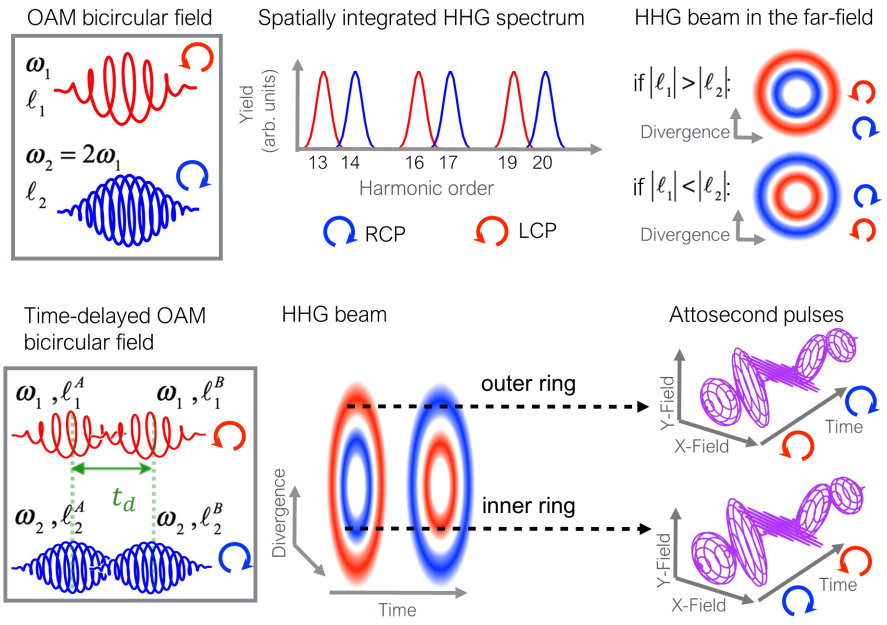

Figure 50: (a) Scheme of HHG driven by a bi-circular vortex field (with ω_1, ℓ_1, LCP and $\omega_2 = 2\omega_1$, ℓ_2, RCP). The HHG spectrum is composed of pairs of circularly polarized harmonics with opposite helicity, which can be separated in divergence in the far-field by properly selecting the OAM combination in the driving field. (b) Generation scheme of attosecond pulse trains with time-ordered polarization states. In this case, the driving beam is composed of two time-delayed bi-circular vortex fields, A and B, where, for this example, we have chosen $|\ell_1^A| > |\ell_2^A|$ and $|\ell_1^B| < |\ell_2^B|$. As a consequence, in the outer (inner) ring, the polarization of the attosecond pulses, changes monotonously from pulse to pulse.

and $\ell_2^B = -\ell_1^A$. Under this configuration, the harmonics produced by the beam B diverge as two separated rings with the opposite helicity than the corresponding rings generated by the driving A, as depicted schematically in figure 50b. The temporal delay between the two bi-circular vortex beams, t_d, causes the temporal variation of the ellipticity of the harmonics, from LCP to RCP in the outer ring, and vice versa in the inner ring. As a consequence, the attosecond pulse trains at each ring exhibit a gradual change in the polarization state from pulse to pulse.

4.4.2 *Results from the numerical simulations*

We have performed simulations of HHG in an argon gas jet using our full-quantum SFA model including propagation (see section 2.3.2). In figure 51, we present the results of the simulations when considering $\ell_1^A = 3, \ell_2^A = -2, \ell_1^B = 2, \ell_2^B = -3$ and a duration of each driver of $\tau = 7.7$ fs in FWHM in intensity. The time delay between beams A and

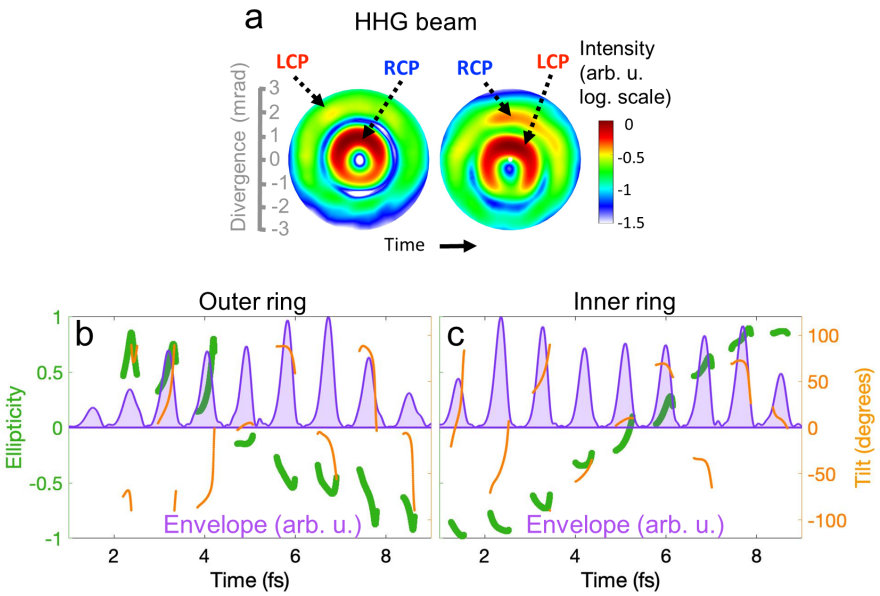

Figure 51: (a) Total intensity profile corresponding to the XUV beam obtained with two time-delayed bi-circular vortex field carrying $\ell_1^A = 3, \ell_2^A = -2$ and $\ell_1^B = 2, \ell_2^B = -3$, respectively, at two different instants of time: at the beginning of the second driving pulse (left) and at the end of the first driving pulse (right). (b)-(c) Envelope (purple), ellipticity (green), and tilt angle (orange) of the attosecond pulse trains as a function of time corresponding to the outer (b) and inner (c) rings. We model the driving pulses with a $\sin^2$ envelope ($\tau = t_d = 7.7$ fs FWHM), with central wavelengths of $\lambda_1 = 800\,nm$ and $\lambda_2 = 400\,nm$, waists of $w = 30\,\mu m$ for $\ell = \pm 2$ and $w = 24.54\,\mu m$ for $\ell = \pm 3$, and a peak intensity of $1.4 \times 10^{14}\,W/cm^2$ each.

B is chosen to be the same as the width of the pulses, $t_d = \tau$, which

is the optimal in order to obtain a smooth and constant variation of the ellipticity along the train (in analogy to the optimal generation of the time-varying OAM [16]). In figure 51a, we show that the spectrally integrated HHG beam exhibits two isolated rings, where the helicity is exchanged along time.

The polarization state of the attosecond pulse trains can be described by the time-dependent Stokes parameters [173]. From these, we calculate the time-dependent ellipticity as

$$\epsilon(t) = \tan\left[0.5 \arctan\left(S_3(t)/\sqrt{S_2^2(t) + S_1^2(t)}\right)\right]. \tag{114}$$

For the complete characterization of the polarization state we also compute the time-dependent tilt angle of the ellipse's major axis, calculated as

$$\theta(t) = 0.5 \arctan\left[S_2(t)/S_1(t)\right]. \tag{115}$$

The temporal evolution of the ellipticity and tilt angle along the

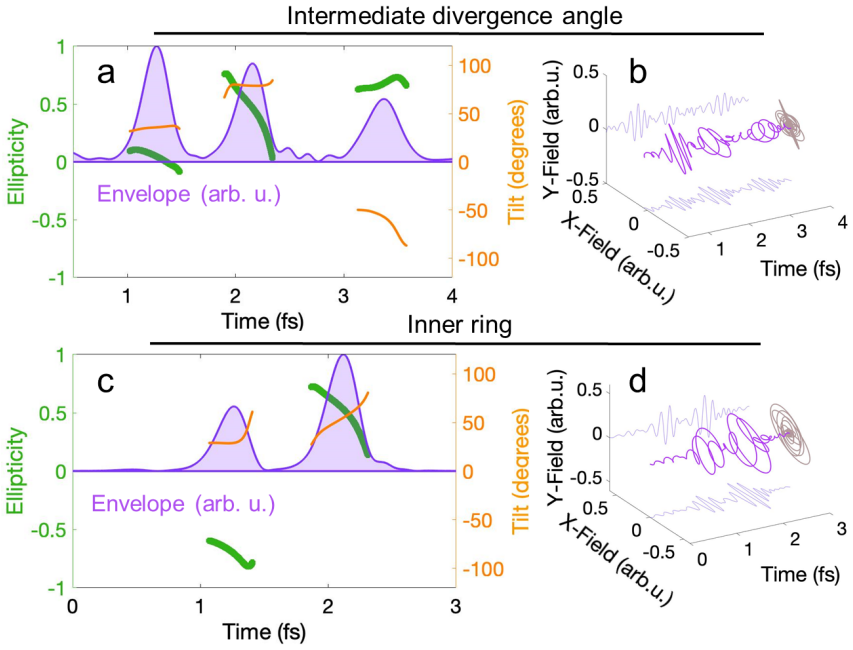

Figure 52: Envelope (purple), ellipticity (green) and tilt angle (orange) of the attosecond pulse trains obtained using two time-delayed few-cycle bi-circular vortex driving beams, carrying $\ell_1^A = 2, \ell_2^A = -1$ and $\ell_1^B = 1, \ell_2^B = -2$, respectively, corresponding to the intermediate divergence angle (a) and the inner ring (c). In panels (b) and (d) we show the respective temporal evolutions of the electric field. The driving pulses' parameters are the same as those in figure 51 but with $\tau = t_d = 1.9\,\text{fs}$ FWHM and waists of $w = 30\,\mu\text{m}$ for $\ell = \pm 1$ and $w = 21.4\,\mu\text{m}$ for $\ell = \pm 2$.

attosecond pulse train is shown in the lower panels for the outer (figure 51b) and inner (figure 51c) rings, respectively. Note that in

these rings the ellipticity decreases (outer ring) or increases (inner ring) almost linearly along the pulse train.

In addition, our simulations show that the ultrafast evolution of the polarization state along the pulse train can be controlled via the OAM, pulse duration, and time delay of the driving fields. In figure 52, we present our numerical simulations for a different OAM combination, $\ell_1^A = 2, \ell_2^A = -1, \ell_1^B = 1, \ell_2^B = -2$, and shorter driving beams, $\tau = t_d = 1.9$ fs (FWHM), for the inner ring and the divergence angle between the two rings. The intermediate divergence angle illustrates the possibility of obtaining a polarization evolution from linear to highly elliptical. Note also that the variation of the ellipticity is faster, since we are using shorter driving pulses.

Further information and results of this work can be found in our publication [19] included in section 4.5.2.

4.5 PUBLICATIONS

To finalize this chapter, we include the full text of the two articles explained in sections 4.3 and 4.4. The first one, included in section 4.5.1, details the methods and results from the bi-circular vortex driving, under the title "Controlling the polarization and vortex charge of attosecond high-harmonic beams via simultaneous spin–orbit momentum conservation" [18]. The second one, included in section 4.5.2, addresses the generation of time-ordered polarization states, under the title "Trains of attosecond pulses structured with time-ordered polarization states" [19]. Before each article we include an abstract in Spanish.

4.5.1 *Controlling the polarization and vortex charge of attosecond high-harmonic beams via simultaneous spin–orbit momentum conservation*

Resumen

Los pulsos ultracortos con momento angular abren la puerta a interesantes posibilidades de control de la respuesta electrónica primaria en la materia. Este momento angular se presenta en dos formas diferentes: el momento angular de espín (SAM) [6], relacionado con la polarización, y el momento angular orbital (OAM) [7], asociado a la vorticidad del perfil espacial de la fase del haz. Si bien el momento angular se puede transferir de forma rutinaria a haces visibles/infrarrojos, esta transferencia no es trivial en los regímenes de rayos X y ultravioleta extremo (XUV). Afortunadamente, la generación de armónicos de orden alto (HHG) ha emergido como un mecanismo robusto para imprimir OAM y SAM en el régimen XUV, mediante la conversión no lineal de frecuencias de un pulso láser incidente infrarrojo. Este método proporciona pulsos de attosegundo estructurados con propiedades de momento angular controladas.

Basándonos en el proceso de HHG, en esta publicación [18], presentamos, por primera vez, la generación de haces XUV coherentes y pulsos de attosegundo con control total y simultáneo tanto de su OAM como de su SAM. Para ello, utilizamos como haz incidente un campo dicromático, contrarrotante y con OAM (conocido como campo bi-circular vorticial). Nuestros resultados teóricos, apoyados por los experimentos de nuestros colaboradores, muestran que la conservación simultánea del OAM y del SAM introduce un acoplamiento entre ellos, de manera que el OAM de los armónicos está restringido por su SAM. Como consecuencia, seleccionando apropiadamente el OAM y el SAM del campo incidente, podemos controlar la divergencia de los vórtices armónicos polarizados circularmente. Gracias a ello, podemos generar vórtices XUV con polarización circular pura levógira o dextrógira espacialmente aislados, lo cual nos permite controlar la polarización de los pulsos de attosegundo emitidos, de lineal a circular. Además, podemos producir vórtices XUV con carga de OAM alta o baja. Este aspecto es destacable ya que en esquemas colineales se esperaba que la carga topológica aumentara siempre con el orden armónico, pero, con este método podemos producir armónicos de orden alto polarizados circularmente con la misma carga topológica que el campo incidente.

Finalmente, estos haces pueden extenderse al rango de los rayos X, posibilitando interesantes aplicaciones en manipulación de moléculas quirales o materiales espintrónicos, así como en microscopía o formación de imagen.

nature photonics

ARTICLES

https://doi.org/10.1038/s41566-018-0304-3

Controlling the polarization and vortex charge of attosecond high-harmonic beams via simultaneous spin–orbit momentum conservation

Kevin M. Dorney[1*], Laura Rego[2], Nathan J. Brooks[1], Julio San Román[2], Chen-Ting Liao[1], Jennifer L. Ellis[1], Dmitriy Zusin[1], Christian Gentry[1], Quynh L. Nguyen[1], Justin M. Shaw[3], Antonio Picón[2,4], Luis Plaja[2], Henry C. Kapteyn[1], Margaret M. Murnane[1] and Carlos Hernández-García[2*]

Optical interactions are governed by both spin and angular momentum conservation laws, which serve as a tool for controlling light–matter interactions or elucidating electron dynamics and structure of complex systems. Here, we uncover a form of simultaneous spin and orbital angular momentum conservation and show, theoretically and experimentally, that this phenomenon allows for unprecedented control over the divergence and polarization of extreme-ultraviolet vortex beams. High harmonics with spin and orbital angular momenta are produced, opening a novel regime of angular momentum conservation that allows for manipulation of the polarization of attosecond pulses—from linear to circular—and for the generation of circularly polarized vortices with tailored orbital angular momentum, including harmonic vortices with the same topological charge as the driving laser beam. Our work paves the way to ultrafast studies of chiral systems using high-harmonic beams with designer spin and orbital angular momentum.

Since the pioneering studies of Beth[1] and Allen et al.[2], it has been well known that propagating light waves, under the paraxial approximation, can possess two distinct forms of angular momenta—spin and orbital angular momentum (SAM and OAM, respectively). Although similar in nature, the distinction between the SAM and OAM of light is straightforward when one considers an interaction picture: the SAM of light is mediated through anisotropic interactions, whereas the OAM of light is associated with inhomogeneity in a physical system[3]. This powerful decoupling allows for the independent manipulation and measurement of either the SAM or OAM of a single light field[4–6], and enables many applications[7], including optical sensing and communication[8], molecular detection[9], kinematic micromanipulation[10] and photonic momentum control[11].

Initially, applications exploiting optical SAM or OAM interactions were largely limited to macroscopic systems using visible light. These limitations stemmed from the challenges in producing and controlling coherent, short-wavelength light beyond the ultraviolet (UV). Fortunately, recent advances in high-harmonic generation (HHG) have bridged this photonic gap, allowing for the straightforward generation of coherent, subfemtosecond radiation in the extreme UV (EUV), with controllable SAM or OAM properties[12–27]. These advanced light sources have opened up the possibility of monitoring and manipulating the SAM and OAM of light–matter interactions on the atomic scale, with the potential of extending quantum optical/logical metrologies, optical manipulation and chiral spectroscopies to the nanometre spatial and subfemtosecond temporal scales.

Fundamentally, these exciting capabilities are enabled by the quantum physics of the high-harmonic upconversion process[28,29]. In HHG, an electron wavepacket in an atomic, molecular or material system is liberated by an intense laser field, which then accelerates the free electron wavepacket. The oscillatory nature of the laser field can drive the wavepacket back to the parent ion and, on recollision, the acquired kinetic energy is released in the form of high-order harmonics, which can span deep into the EUV and soft X-ray spectral regions[30–34]. It is this field-driven nature of HHG that provides an opportunity for mapping the properties of near-infrared laser light, in particular SAM and OAM, to short-wavelength radiation. Indeed, recent experimental demonstrations of independent control of SAM[13,18,35,36] or OAM[21,24,37] in the EUV via HHG have propelled the topic of optical angular momentum control and measurement to the forefront of attosecond science.

Here, we present a significant advance in producing EUV beams with designer angular momenta (that is, helicity and twist) by generating high-order harmonics—and attosecond pulses—possessing controllable spin and orbital angular momenta. By driving the HHG process with a bichromatic, counter-rotating vortex beam (that is, a bicircular vortex beam), we uncover and subsequently harness, a novel form of simultaneous SAM–OAM momentum conservation. We exploit this simultaneous conservation to produce spatially isolated vortex beams of opposite SAM through proper selection of the angular momenta of the bicircular vortex driver, which allows us to control the polarization state of attosecond EUV vortex beams in the time domain; from linear to purely circularly polarized. This unique SAM–OAM control also makes it possible to generate highly elliptically polarized high-harmonic OAM beams with controllable topological charge. In particular, apart from generating highly charged vortex beams with designer OAM, we generate harmonic beams of highly circular polarization with the same, low, topological

[1]JILA - Department of Physics, University of Colorado and NIST, Boulder, CO, USA. [2]Grupo de Investigación en Aplicaciones del Láser y Fotónica, Departamento de Física Aplicada, University of Salamanca, Salamanca, Spain. [3]Quantum Electromagnetics Division, National Institute of Standards and Technology, Boulder, CO, USA. [4]Present address: Departamento de Química, Universidad Autónoma de Madrid, Madrid, Spain. *e-mail: kevin.dorney@colorado.edu; carloshergar@usal.es

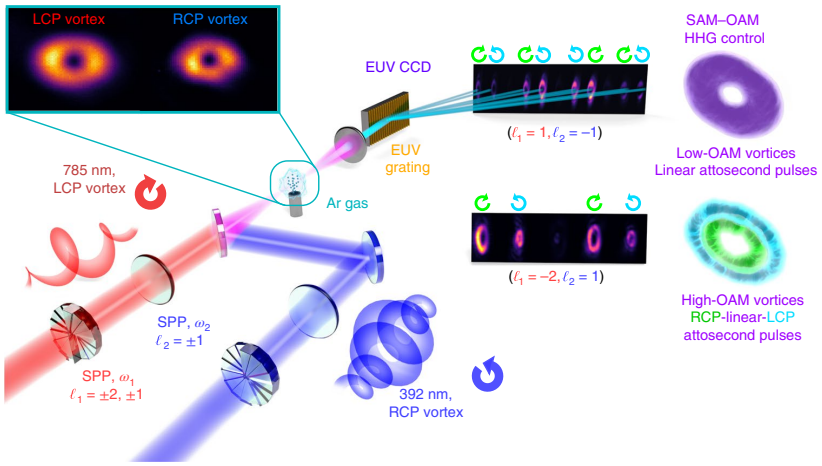

Fig. 1 | Bicircular HHG in the presence of simultaneous SAM–OAM conservation (SAM–OAM HHG). a, In the experiment, circularly polarized beams of opposite helicity are passed through independent spiral phase plates (SPPs) producing high-purity circularly polarized OAM vortex beams (top-left inset). These beams are spatiotemporally overlapped in a supersonic expansion of Ar gas, yielding a bicircular SAM–OAM vortex beam that drives the HHG process. The SAM–OAM EUV beams are collected via a cylindrical mirror-grating pair (cylindrical mirror omitted for clarity) and an EUV camera. The detectors show experimental EUV OAM beam profiles collected in the far field, ~8 cm beyond the flat-field focal plane of the spectrometer. In this scheme, the detectors show experimental SAM–OAM HHG for both complementary ($\ell_1 = 1, \ell_2 = -1$) and non-degenerate ($\ell_1 = -2, \ell_2 = 1$) configurations of the bicircular vortex driver. When driven with complementary OAM beams, OAM harmonics are generated with a low OAM charge, equal to the components of the bicircular vortex (top-right inset). If a non-degenerate vortex driver is employed for the SAM–OAM HHG process, EUV vortices of high-OAM charge and opposite helicity exhibit significantly different OAM charges, which results in RCP and LCP harmonics being spatially separated in the far field (bottom-right inset).

charge—equal to the co-rotating component of the bicircular vortex driving laser field. Our work opens a route to perform ultrafast studies of angular momentum exchange and interactions at EUV/X-ray wavelengths, with the potential for nanometre spatial and sub-femtosecond temporal resolution.

Results

Generation of high-harmonic beams with SAM and OAM. The generation of SAM–OAM EUV vortex beams is depicted in Fig. 1. A bichromatic Mach–Zehnder interferometer is used to produce two collinear, vortex laser beams with opposite helicities derived from the fundamental (frequency ω_1, spin $\sigma_1 = -1$, left-circular polarization, LCP, and topological charge ℓ_1) and frequency-doubled ($\omega_2 = 2\omega_1$, $\sigma_1 = +1$, right-circular polarization, RCP, ℓ_2) output of an ultrafast Ti:sapphire amplifier (see Methods and Supplementary Section 1). These beams are then combined, spatially and temporally, to yield a bicircular vortex beam that drives HHG in a supersonic expansion of Ar gas. The emitted harmonics are collected via an EUV spectrometer consisting of a cylindrical mirror-flat grating spectrometer and an EUV charge coupled device (CCD) camera (see Methods). As a reference for these experiments, we have performed full quantum HHG simulations including propagation using the electromagnetic field propagator[38], a method that was used in several previous calculations of HHG involving either SAM[17,18,32,35,39,40] or OAM[20,23,26,27,41] (see Methods and Supplementary Section 2).

As a first demonstration of this novel, simultaneous SAM–OAM conservation in HHG, we drive the SAM–OAM HHG process with a bicircular vortex laser field with $\ell_1 = 1$ and $\ell_2 = 1$. In this configuration, a high-harmonic spectrum consisting of doublets of EUV vortex beams is generated, where the harmonics in each doublet possess the same topological charge, but opposite helicities (Fig. 2a,b). Most notably, the strong suppression of every third harmonic order confirms that the same SAM conservation rules are upheld in SAM–OAM HHG as in traditional bicircular HHG[42,43]. SAM conservation, $\sigma_q = n_1\sigma_1 + n_2\sigma_2$, together with the parity constraints, implies that the number of photons absorbed from each of the drivers (n_1, n_2) to generate the qth order harmonic must differ by one: $n_2 = n_1 - \sigma_q\sigma_1$. Taking into account photon energy conservation, $q\omega_1 = n_1\omega_1 + n_2\omega_2$, the resulting HHG spectrum consists of pairs of adjacent harmonics with opposite circular polarization, and a third, missing harmonic, whose suppression indicates a high circularity of the SAM–OAM EUV beams. This is confirmed by EUV magnetic circular dichroism (EUV MCD) measurements on an $Fe_{0.75}Co_{0.25}$ film (Fig. 2d and Methods). Unfortunately, a quantitative value of the harmonic ellipticity cannot be obtained at this time, as MCD-derived ellipticities require a comparison with existing synchrotron data and such experimental data does not exist for this energy range. However, a comparison with extrapolated synchrotron data from resonant MCD measurements of Fe films[15] allows us to confirm that the SAM–OAM HHG harmonics are highly elliptically polarized. In short, the strong non-resonant EUV MCD signal, suppression of spin-forbidden harmonic orders, and the excellent agreement with the theoretical simulations verifies the near-circular polarization of the SAM–OAM EUV vortex beams (see below). We note that depolarization effects are unlikely in this geometry, as the MCD sample is placed far from the generating region, yet a strong MCD signal is still observed.

The simultaneous conservation of SAM and parity in SAM–OAM HHG also restricts the allowed OAM values for each harmonic[44]. If both beams are linearly polarized, the topological charge of the qth order harmonic driven by a bichromatic laser field is given by a simple OAM conservation rule $\ell_q = n_1\ell_1 + n_2\ell_2$ (ref. [23]). Each harmonic can, therefore, exhibit several OAM contributions depending on the number of photons absorbed from each driver[23]. Note that non-perturbative OAM contributions[23] do not appear in our SAM–OAM HHG scheme since the intensity distribution at

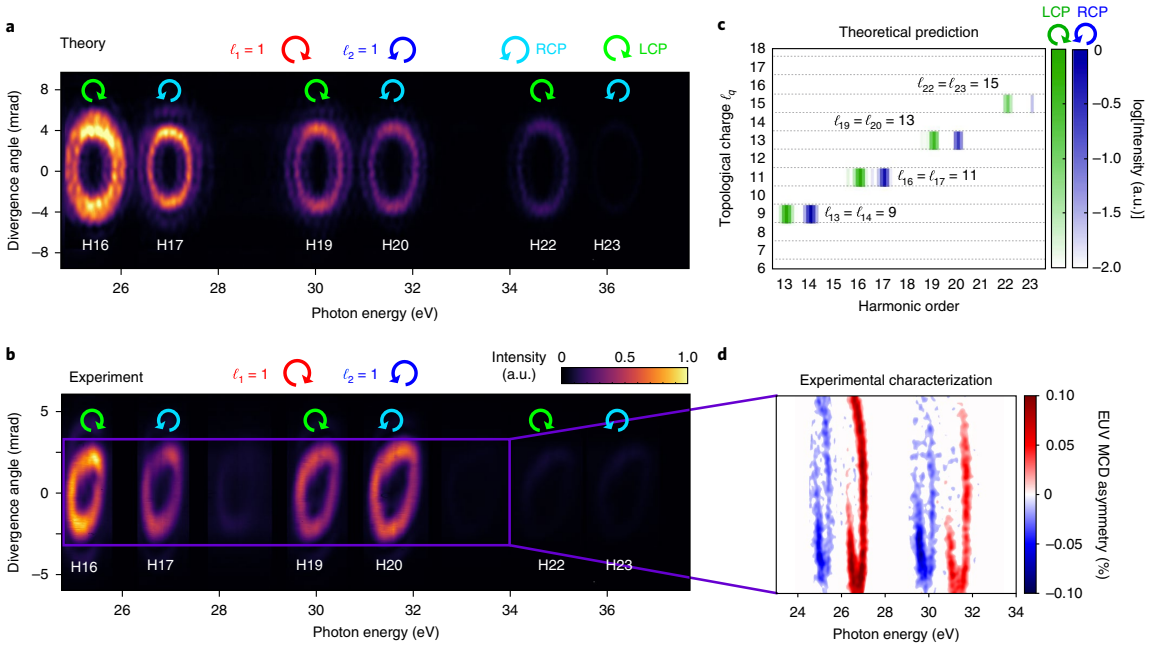

Fig. 2 | Experimental generation and theoretical confirmation of SAM–OAM EUV vortices in the presence of simultaneous SAM–OAM conservation. **a**, Full quantum simulation results showing spectrally dispersed SAM–OAM harmonics driven by a bicircular vortex driving beam ($\sigma_1 = -1$, $\sigma_2 = +1$, $\ell_1 = 1$, $\ell_2 = 1$). **b**, Spatio-spectral measurement of SAM–OAM EUV vortex beams produced via HHG from the same configuration of the bicircular driver, exhibiting a clean mode with a clear singularity on axis, a single bright intensity ring and strong suppression of every spin-forbidden (that is, every third) harmonic order. Further calculations (not shown) indicate that the different divergences between the theory (**a**) and experimental (**b**) results are due to slightly different driving-beam waists. **c**, Calculated topological charge of the LCP (green) and RCP (blue) harmonic vortices confirms that the presence of simultaneous SAM–OAM conservation results in neighbouring harmonics possessing a similar OAM spectrum. The OAM is calculated through a Fourier transform along the azimuthal coordinate for each RCP and LCP frequency component. **d**, EUV MCD measurement of a 20-nm-thick $Fe_{0.75}Co_{0.25}$ film confirms the near-circular polarization of the generated SAM–OAM EUV vortices. Note that inhomogeneity in the EUV MCD signal for each harmonic is the result of slight pointing fluctuations and changes in the sample structure for the different magnetizations of the $Fe_{0.75}Co_{0.25}$ film.

focus does not vary azimuthally, as also observed in non-collinear bichromatic OAM HHG[24,25]. However, combining the above-mentioned SAM and OAM conservation rules in bicircular SAM–OAM HHG, the topological charge of the qth order harmonic satisfies

$$\ell_q = \frac{q + 2\sigma_q\sigma_1}{3}(\ell_1 + \ell_2) - \sigma_q\sigma_1\ell_2 \quad (1)$$

where SAM conservation restricts ℓ_q to a single value. The products $\sigma_{2,1}\ell_{1,2}$ show that the SAM and OAM of the bicircular vortex driver are inherently entwined via the HHG process, which connects the SAM and OAM of the harmonics to those of the driving beams. This manifests as an entirely new form of simultaneous conservation of SAM and OAM, where the OAM (ℓ_q) and SAM (σ_q) of each harmonic vortex can be controlled via the interplay of the SAM (σ_1, σ_2) and the OAM (ℓ_1, ℓ_2) of the drivers. At this point we would like to remark that the SAM and OAM of the harmonics are controlled via simultaneous conservation of these quantities during the HHG process, and that SAM and OAM are not converted from one another as in more traditional SAM–OAM coupling observed in subwavelength and non-paraxial optical regimes[45].

The effects of simultaneous SAM–OAM conservation are readily evident by comparing the theoretical (Fig. 2a) and experimental (Fig. 2b) SAM–OAM EUV spectra. In such a configuration, ($\ell_1 = \ell_2 = 1$), the OAM conservation rule, equation (1), reads as $\ell_q = (2q + \sigma_q\sigma_1)/3$. This implies that each pair of adjacent harmonics exhibits the same OAM, as can be seen in Fig. 2c, where the OAM is calculated by performing a Fourier transform along the azimuthal coordinate for each frequency component[23]. This method of determining the OAM content is ideally suited for arbitrary, structured beams possessing OAM as it does not rely on decomposition into a particular basis set and is thus more general than methods employing modal decomposition. We note that each harmonic in the SAM–OAM EUV spectrum has a uniform azimuthal intensity profile and little radial mode character, indicating similar modal content between the experimental and theoretical SAM–OAM HHG. Moreover, the excellent agreement of the beam profiles between the experiment and theory also suggests a highly elliptical polarization of the harmonics; if depolarization effects were present, the SAM-dependent OAM selection rules would be relaxed, leading to a superposition of topological charges in each harmonic and consequently nonuniform SAM–OAM HHG beam profiles[23]. Although the OAM of the experimental harmonics was not measured in this work, the points mentioned above strongly suggest a similar modal content as that obtained in the theoretical spectra. Taken together, the generated SAM–OAM EUV vortex beams possess both a high modal purity as well as near-circular polarization.

Polarization control of attosecond EUV pulses through simultaneous SAM–OAM conservation. In the past decade, there has been an explosion of interest in controlling the spin polarization of attosecond EUV waveforms, as full polarization control would allow for

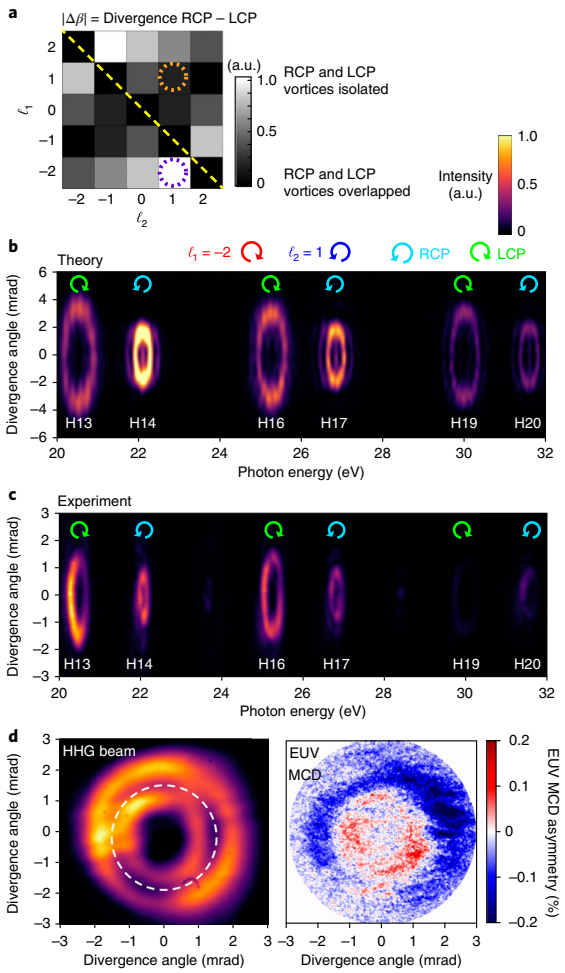

Fig. 3 | Separation of EUV high-harmonic vortex beams with opposite circularities through the OAM of the bicircular vortex driver. a, Theoretical estimation for the divergence difference between the RCP and LCP harmonics ($|\Delta\beta|$) as a function of the OAM of the constituents of the bicircular vortex field. The dashed circles correspond to configurations of the bicircular vortex drive used to generate the experimental SAM–OAM EUV harmonics (orange dashed circle shows OAM case with $\ell_1 = \ell_2 = 1$ in Fig. 2, purple dashed circle shows OAM case with $\ell_1 = -2$, $\ell_2 = 1$, and yellow dashed line shows the case for opposite OAMs of the driving fields, see main text for details). **b**, A full quantum simulation, including propagation, shows that when SAM–OAM HHG is driven with a bicircular OAM driver of $\ell_1 = -2$, $\ell_2 = 1$, the RCP and LCP vortices exhibit significantly different divergence, resulting in spatially separated RCP and LCP beams in the far field. Further calculations (not shown) indicate that differences in the theoretical and experimental spectra are due to slightly different driving beam parameters. **c**, A spatio-spectral measurement of SAM–OAM EUV harmonics under the same configuration of the bicircular vortex driver as in **b**, which confirms the OAM-dependent divergence control afforded by SAM–OAM HHG. **d**, This control results in a dual intensity ring structure in the far field of the HHG beams (left, dashed circle highlights the intensity null between the vortices), where the inner, RCP beam is entirely contained by the LCP vortex beam, as confirmed by a spatially resolved EUV MCD measurement (right). The inhomogeneity observed in the EUV MCD-retrieved beam profiles is the result of slight fluctuations in beam pointing, microstructuring of the MCD sample, and attenuation of low-intensity regions of the beam.

the possibility of custom-tailored harmonic beams for attosecond, nanometric chiral spectroscopies and metrologies. As such, a wide variety of experimental[12–18,32,35,36,40] and theoretical[41,46–48] schemes have been investigated to control the SAM of EUV high harmonics. Here we show that the interplay of SAM–OAM conservation inherent to SAM–OAM HHG opens a route to control the polarization of attosecond pulses.

In traditional bicircular HHG driven by collinear pulses with a Gaussian spatial profile, RCP and LCP harmonics spatially overlap in the far field, yielding attosecond bursts with a rotating, linear polarization in the time domain[39,43,46,48,49]. This is largely the result of the similar propagation properties between RCP and LCP harmonics, as the divergence of a light field does not typically depend on its SAM. Fortunately, recent advances in bicircular HHG have shown that elliptically polarized attosecond pulse trains (APTs)[35,36], spatially isolated APTs[15] and isolated attosecond pulses[18] of opposite helicity can be generated and the ellipticity can be fully tuned by the parameters of the visible driving lasers. Although elegant, these methodologies are only capable of controlling either the SAM or the divergence of the EUV harmonics, instead of both simultaneously. However, the simultaneous conservation of SAM and OAM in bicircular SAM–OAM HHG, together with the OAM-dependent divergence inherent to vortex beams, allow us to circumvent these limitations and simultaneously control the divergence of EUV light and the polarization of the underlying APTs.

To show the power of this concept, we consider HHG driven by a single-mode OAM driver. It is known that the divergence of a harmonic beam decreases with the harmonic order, while the divergence of a vortex beam increases with its topological charge. Therefore, for a single-mode OAM driver, the simple OAM conservation rule, $\ell_q = q\ell_1$, results in a HHG spectrum where all harmonics are emitted with a similar divergence[20–22,41]. In the case of bicircular SAM–OAM HHG, the restricted selection rules resulting from the mixing of SAM and OAM can be exploited to control the divergence of the harmonics and, for example, to yield spatially isolated vortex beams of pure RCP and LCP polarization, something that is not possible with either linear OAM HHG or collinear, bicircular HHG with Gaussian drivers. This point is illustrated below, where we employ a simple theoretical analysis based on Fraunhofer diffraction that predicts the divergence difference between the RCP and LCP harmonics ($\Delta\beta$) as a function of the OAMs of the bicircular vortex driver (see Supplementary Section 4) as

$$\Delta\beta \propto (\ell_1 - 2\ell_2)\frac{|\ell_1 + \ell_2|}{\ell_1 + \ell_2} \qquad (2)$$

where $\Delta\beta = 0$ if $\ell_1 + \ell_2 = 0$, and we are assuming $\omega_2/\omega_1 = 2$. In Fig. 3a, we plot the relative values of $|\Delta\beta|$ as a function of ℓ_1 and ℓ_2. The divergence difference between RCP and LCP harmonics depends strongly on the choice of ℓ_1 and ℓ_2, and as a general trend, the greatest differences in divergence correspond to large differences in the OAMs of the drivers. Thus, it is the OAM-dependent divergence, combined with the simultaneous angular momentum selection rules induced by the bicircular OAM driver, that gives control over the spatial distribution of RCP and LCP harmonics in the EUV vortex beam, and as a consequence, over the polarization of the attosecond pulses.

To further illustrate this point, we return to the case of $\ell_1 = \ell_2 = 1$, presented in Fig. 2 (orange dashed circle in Fig. 3a). The RCP and LCP vortices exhibit similar divergences and thus spatially overlap, yielding linearly polarized APTs in the time domain. However, closer inspection of the divergence analysis shows that spatial separation of RCP and LCP components of the EUV beams is achieved when the OAMs of the drivers are complementary, but different in magnitude. To demonstrate this unique capability, we drive the

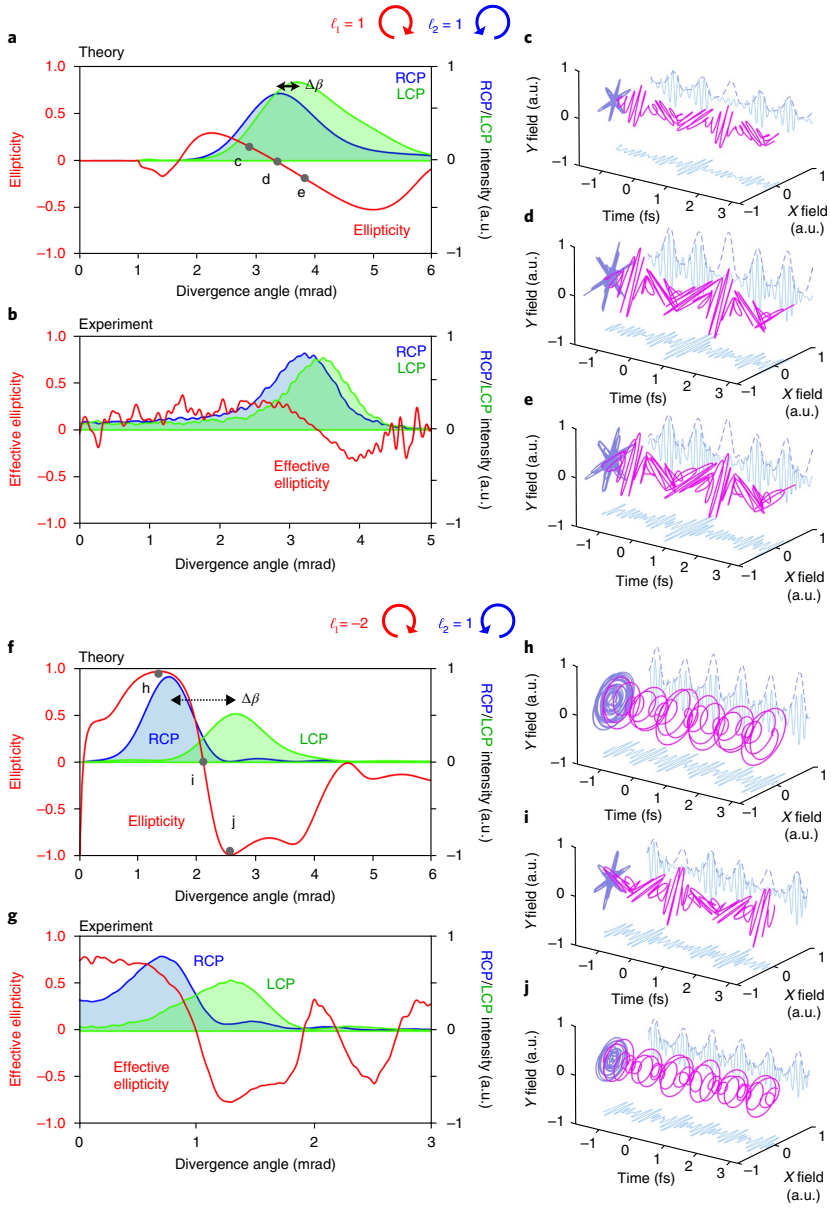

Fig. 4 | Control over the OAMs of the bicircular driver yields full control of the polarization state of APTs in SAM–OAM HHG. a–e, Spectrally integrated intensities of RCP (blue) and LCP (green) harmonics (from the 13th to the 23rd) for a degenerate bicircular vortex ($\ell_1 = \ell_2 = 1$) confirm that SAM–OAM high harmonics possess similar divergences and thus overlap spatially in the far field (theory (**a**) and experiment (**b**)), resulting in predominately linearly polarized APTs across the EUV vortex beam profile, as shown in the simulated temporal evolution detected at 2.7 (**c**), 3.3 (**d**) and 3.7 (**e**) mrad (magenta lines show full APT, while the blue and purple lines show component projections in the *XT*, *YT* and *XY* planes, respectively). **f–j**, When SAM–OAM HHG is driven with a non-degenerate bicircular vortex beam ($\ell_1 = -2$, $\ell_2 = 1$), the RCP and LCP harmonics exhibit significantly different divergences, which results in the spatial separation of RCP and LCP vortices in the far field (theory (**f**) and experiment (**g**)). The combined theoretical and experimental results confirm the degree of divergence control via simultaneous spin–orbit conservation in the HHG process, which results in a spatial evolution of the polarization of the APTs from RCP (**h**, 1.4 mrad), to linear (**i**, 2.1 mrad), to LCP (**j**, 2.6 mrad).

HHG process with a non-degenerate, complementary, bicircular OAM driver ($\ell_1 = -2, \ell_2 = 1$, purple dashed circle in Fig. 3a). The theoretical and experimental SAM–OAM HHG spectra (Fig. 3b,c) clearly confirm the ramifications of SAM–OAM conservation on controlling the divergence of the EUV vortices; RCP vortex harmonics are entirely contained by their LCP counterparts, resulting

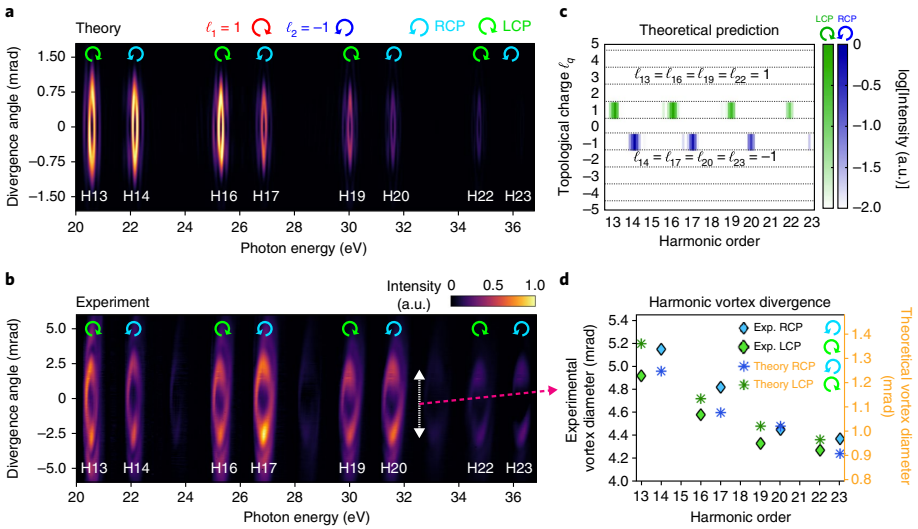

Fig. 5 | Circularly polarized high-harmonic vortex beams with equal, low-charge OAM. a,**b**, Simulated (**a**) and experimental (**b**) high-harmonic spectra of the EUV OAM beams driven by a degenerate, complementary bicircular field ($\ell_1 = 1, \ell_2 = -1$), exhibiting pairs of high harmonics of alternating helicity. The decrease in divergence of the harmonics as a function of energy, combined with the localized singularity indicate that each harmonic has a similar, low topological charge. **c**,**d**, Theoretical OAM content of the LCP (green) and RCP (blue) HHG projections, which shows that all harmonics with the same SAM present the same OAM as the driver with that SAM. The manifestation of the low topological charge of the EUV harmonics results in a decrease of the angular diameter of the beams as a function of energy, as clearly demonstrated in **d**, where experimental (theoretical) results are shown by diamonds (asterisks). Further calculations (not shown) indicate that the different divergences between the theory and experimental results are due to slightly different driving beam parameters (that is, size of beam waist and the exact location of beam waists), which also results in a low-intensity secondary intensity ring in the experimental spectra.

in a double-ring structure in the far field (Fig. 3d, left). The near-circular polarization of the double-ring vortex beam is confirmed by EUV MCD measurements, which reveal two distinct intensity rings of opposite helicity (Fig. 3d, right).

The effects of the OAM-dependent divergence control in SAM–OAM HHG—and thus the OAM-based control over the polarization of the attosecond pulses—can be more clearly demonstrated by performing a spectral integration across the SAM–OAM HHG spectra. Returning to a degenerate configuration of the driving field ($\ell_1 = 1, \ell_2 = 1$), the RCP and LCP harmonics both exhibit similar divergences, as well as comparable spectral intensities (Fig. 4a,b). If we define the ellipticity of the attosecond pulses as $\varepsilon = (I_{RCP} - I_{LCP}) / (I_{RCP} + I_{LCP})$, where I_{RCP} and I_{LCP} are the intensities of the RCP and LCP harmonics, the spatial overlap of the RCP and LCP components of the theoretical SAM–OAM HHG spectrum results in attosecond pulses with predominate linear polarization in the time domain (Fig. 4c–e). Given the excellent agreement between the theoretical and experimental spectra and spectrally integrated signals, it is highly likely that the experimental harmonics possess similar ellipticities, and thus we expect a similar polarization of the experimental APTs. However, our experimental and theoretical SAM–OAM HHG spectra show that this symmetry can be broken by employing a complementary, non-degenerate vortex driver (for example, $\ell_1 = -2, \ell_2 = 1$). In this configuration, the oppositely polarized vortex beams experience large enough divergences to be spatially isolated (Fig. 4f,g). As such, the ellipticity of the attosecond pulses evolves all the way from near right circular ($\varepsilon \approx 1$), to linear ($\varepsilon = 0$), to near left circular ($\varepsilon \approx -1$) across the EUV beam profile (Fig. 4h–j). Therefore, by properly modifying the OAM of the driving fields, we can spatially control the ellipticity of the attosecond pulses and this degree of control becomes even greater as the difference in OAM of the bicircular driver increases, where pure circular attosecond pulses ($\varepsilon = \pm 1$) can be obtained (see Supplementary Section 4).

High-harmonic vortices with circular polarization and identical low-charge OAM. Since the first experiments of HHG driven by OAM beams[19], there has been significant interest in controlling the OAM content of the high harmonics, as well as generating harmonic vortices with a low topological charge[24,25]. Such a desire is rather pragmatic: many OAM light–matter interactions depend on the topological charge of the optical vortex beam, and lower topological charges inherently lead to less complex interactions and detection geometries. Unfortunately, the simple OAM conservation law governing HHG driven by single OAM beams, $\ell_q = q\ell_1$, implies that high-order harmonic OAM beams emerge with highly charged OAM[20–23,39,50]. Recently, this limitation was overcome by employing a non-collinear scheme[24,25], resulting in linearly polarized EUV vortex beams with low OAM charge. Here we demonstrate that the simultaneous conservation of SAM and OAM in bicircular SAM–OAM HHG can yield high harmonics not only with high topological charge (as shown in the previous sections), but also with the same OAM as the driving field, without the complications induced by a non-collinear geometry.

When the OAM of the drivers fulfil $\ell_1 = -\ell_2$, equation (1) transforms into $\ell_q = -\sigma_q \sigma_1 \ell_2$, which indicates that all RCP (LCP) harmonics exhibit the same topological charge as the RCP (LCP) driving field (see Supplementary Section 4). This implies that the divergence decreases linearly with the harmonic order and that RCP and LCP harmonics exhibit similar divergence ($\Delta\beta \approx 0$, yellow dashed line in Fig. 3a). As a final demonstration of the control afforded by the conservation rules in SAM–OAM HHG, in Fig. 5a,b we present the

theoretical and experimental HHG spectra generated by a bicircular driver of complementary topological charge ($\ell_1 = 1, \ell_2 = -1$). Most notably, the divergence decreases with the harmonic order, which is a clear indication of the equal OAM of the harmonics, as shorter-wavelength harmonics have a lower divergence given the same topological charge. This fact is further corroborated by considering the highly circular polarization of the EUV beams. If the harmonics were not circularly polarized, the lack of SAM conservation would result in the generation of highly divergent, highly charged OAM HHG beams, as implied by the simple OAM conservation rule $\ell_q = n_1\ell_1 + n_2\ell_2$(ref. [23]). However, our SAM–OAM HHG scheme demands SAM conservation, which results in LCP harmonics emitted with $\ell_{LCP} = \ell_1 = 1$, and RCP harmonics with $\ell_{RCP} = \ell_2 = -1$ (Fig. 5c). The physical manifestation of this effect is a decrease in the angular diameter of the SAM–OAM harmonics as a function of harmonic energy, which is captured in both experiment and theory (Fig. 5d). Although the angular divergence of the experimental harmonics within each doublet show an opposite behaviour with respect to the theoretical spectra (a result of slight differences in beam parameters between the experiment and simulations), the general trend is clearly observed. Taken together, our observations demonstrate the power of SAM–OAM HHG for complete control of the angular momentum of attosecond, structured EUV beams carrying OAM.

Discussion

Despite the fact that many light–matter interactions can possess independent SAM and OAM conservation laws, the simultaneous conservation of both quantities has rarely been utilized to control the light–matter interaction, particularly in HHG. Here, we have shown that the simultaneous SAM–OAM conservation in highly nonlinear and intense field interactions can be used as a powerful tool for controlling the upconversion process, and producing HHG beams with designer SAM and OAM. By constructing a bicircular vortex driving beam with varying topological charges of the constituent waveforms, we showed that SAM–OAM HHG entwines the angular momentum conservation rules, yielding unprecedented and exquisite control of the SAM, OAM and the divergence of EUV light fields.

To demonstrate the potential of the simultaneous SAM–OAM conservation in this regime, we experimentally demonstrated three distinct mixing cases where (1) circularly polarized high-harmonic vortex beams are generated with a similar divergence, and thus similar propagation properties regardless of spin polarization or photon energy; (2) spatially isolated harmonic vortex beams are produced, allowing spatial tuning of the polarization of attosecond pulses—linear, elliptical or pure RCP/LCP—which enables spatially resolved dichroism measurements or isolation of an EUV vortex beam of pure RCP or LCP polarization; and (3) EUV harmonic vortex beams with topological charge equal to, and thus controlled by, the OAM of the driving lasers. These results significantly extend the degree of the control over short-wavelength radiation via manipulation of visible driving lasers. Perhaps most importantly, our results demonstrate the simultaneous optical spin–orbit angular momentum conservation as a gateway to an entirely new set of applications and fundamental investigations. These exciting applications are enabled by the short wavelength of high harmonics, which allows these designer SAM–OAM beams to be focused to scale lengths comparable to nanostructured and molecular systems, facilitating new nanometric spectroscopies and opportunities for nanoscale optical manipulation. Aside from these capabilities, we also add a degree of freedom, the OAM, to the recent experiments that uncovered ultrafast spin/charge dynamics in magnetic materials[51–54] and the ultrafast study of chiral molecular systems[9,55]. One could also envision the possibility for skyrmionic spectroscopies[56,57], or for taking advantage of SAM–OAM selection rules in photoionization/photoemission experiments[58,59], all of which do not necessarily demand nanometre-scale focusing conditions. Finally, circularly polarized short-wavelength OAM beams also open up new scenarios in spatially resolved circular dichroism spectroscopies (as demonstrated in this work), and even the possibility of performing SAM and/or OAM dichroism X-ray absorption measurements, which allows for decoupling the effects of orbital and spin contributions to energy transport[60].

Note added in proof: We note that while this work was under review, a theoretical work[44] was published describing the selection rules in SAM–OAM HHG.

Online content

Any methods, additional references, Nature Research reporting summaries, source data, statements of data availability and associated accession codes are available at https://doi.org/10.1038/s41566-018-0304-3.

Received: 29 May 2018; Accepted: 25 October 2018;
Published online: 10 December 2018

References

1. Beth, R. A. Mechanical detection and measurement of the angular momentum of light. *Phys. Rev.* **50**, 115–125 (1936).
2. Allen, L., Beijersbergen, M. W., Spreeuw, R. J. C. & Woerdman, J. P. Orbital angular momentum of light the transformation of Laguerre-Gaussian laser modes. *Phys. Rev. A* **45**, 8185–8189 (1992).
3. Yao, A. M. & Padgett, M. J. Orbital angular momentum: origins, behavior and applications. *Adv. Opt. Photon.* **3**, 161–204 (2011).
4. Calvo, G. et al. Measuring the complete transverse spatial mode spectrum of a wave field. *Phys. Rev. Lett.* **100**, 173902 (2008).
5. Ballantine, K. E., Donegan, J. F. & Eastham, P. R. There are many ways to spin a photon: half-quantization of a total optical angular momentum. *Sci. Adv.* **2**, e1501748 (2016).
6. Cardano, F. & Marrucci, L. Spin-orbit photonics. *Nat. Photon.* **9**, 776–778 (2015).
7. Willner, A. E. et al. Optical communication using orbital angular momentum beams. *Adv. Opt. Photon.* **7**, 66–106 (2015).
8. Torres, J. P. & Torner, L. *Twisted Photons: Applications of Light with Orbital Angular Momentum* (Wiley-VCH, Bristol, 2011).
9. Beaulieu, S. et al. Photoexcitation circular dichroism in chiral molecules. *Nat. Phys.* **14**, 484–489 (2018).
10. Padgett, M. & Bowman, R. Tweezers with a twist. *Nat. Photon.* **5**, 343–348 (2011).
11. Marrucci, L., Manzo, C. & Paparo, D. Optical spin-to-orbital angular momentum conversion in inhomogeneous anisotropic media. *Phys. Rev. Lett.* **96**, 163905 (2006).
12. Eichmann, H. et al. Polarization-dependent high-order two-color mixing. *Phys. Rev. A* **51**, R3414 (1995).
13. Fleischer, A., Kfir, O., Diskin, T., Sidorenko, P. & Cohen, O. Spin angular momentum and tunable polarization in high-harmonic generation. *Nat. Photon.* **8**, 543–549 (2014).
14. Ferré, A. et al. A table-top ultraviolet light source in the extreme ultraviolet for circular dichroism experiments. *Nat. Photon.* **9**, 93–98 (2015).
15. Hickstein, D. D. et al. Non-collinear generation of angularly isolated circularly polarized high harmonics. *Nat. Photon.* **9**, 743–750 (2015).
16. Lambert, G. et al. Towards enabling femtosecond helicity-dependent spectroscopy with high-harmonic sources. *Nat. Commun.* **6**, 6167 (2015).
17. Ellis, J. L. et al. High harmonics with spatially varying ellipticity. *Optica* **5**, 479–485 (2018).
18. Huang, P.-C. et al. Polarization control of isolated high-harmonic pulses. *Nat. Photon.* **12**, 349–354 (2018).
19. Zürch, M. et al. Strong-field physics with singular light beams. *Nat. Phys.* **8**, 743–746 (2012).
20. Hernández-García, C. et al. Attosecond extreme ultraviolet vortices from high-order harmonic generation. *Phys. Rev. Lett.* **111**, 083602 (2013).
21. Gariepy, G. et al. Creating high-harmonic beams with controlled orbital angular momentum. *Phys. Rev. Lett.* **113**, 153901 (2014).
22. Géneaux, R. et al. Synthesis and characterization of attosecond light vortices in the extreme ultraviolet. *Nat. Commun.* **7**, 12583 (2016).
23. Rego, L., San Román, J., Picón, A., Plaja, L. & Hernández-García, C. Nonperturbative twist in the generation of extreme-ultraviolet vortex beams. *Phys. Rev. Lett.* **117**, 163202 (2016).
24. Kong, F. et al. Controlling the orbital angular momentum of high harmonic vortices. *Nat. Commun.* **8**, 14970 (2017).
25. Gauthier, D. et al. Tunable orbital angular momentum in high-harmonic generation. *Nat. Commun.* **8**, 14971 (2017).

26. Turpin, A., Rego, L., Picon, L., Roman, J. S. & Hernandez-Garcia, C. Extreme ultraviolet fractional orbital angular momentum beams from high harmonic generation. *Sci. Rep.* **7**, 43888 (2017).
27. Hernández-García, C. et al. Extreme ultraviolet vector beams driven by infrared lasers. *Optica* **4**, 520–526 (2017).
28. Schafer, K. J., Yang, B., DiMauro, L. F. & Kulander, K. C. Above threshold ionization beyond the high harmonic cutoff. *Phys. Rev. Lett.* **70**, 1599–1602 (1993).
29. Corkum, P. B. Plasma perspective on strong-field multiphoton ionization. *Phys. Rev. Lett.* **71**, 1994–1997 (1993).
30. McPherson, A. et al. Studies of multiphoton production of vacuum-ultraviolet radiation in the rare gases. *J. Opt. Soc. Am. B* **4**, 595 (1997).
31. Ferray, M. et al. Multiple-harmonic conversion of 1064-nm radiation in the rare gases. *J. Phys. B* **21**, L31–L35 (1998).
32. Fan, T. et al. Bright circularly polarized soft X-ray high harmonics for X-ray magnetic circular dichroism. *Proc. Natl Acad. Sci. USA* **111**, 14206–14211 (2015).
33. Rundquist, A. et al. Phase matching of soft X-ray harmonic emission in hollow-core fibers. *Science* **280**, 1412–1415 (1998).
34. Popmintchev, T. et al. Bright coherent ultrahigh harmonics in the keV X-ray regime from mid-infrared femtosecond lasers. *Science* **336**, 1287–1291 (2012).
35. Dorney, K. M. et al. Helicity-selective enhancement and polarization control of attosecond high-harmonic waveforms driven by bichromatic circularly polarized laser fields. *Phys. Rev. Lett.* **119**, 063201 (2017).
36. Jiménez-Galán, Á. et al. Control of attosecond light polarization in two-color bicircular fields. *Phys. Rev. A* **97**, 023409 (2018).
37. Hernández-García, C. A twist in coherent X-rays. *Nat. Phys.* **13**, 327–329 (2017).
38. Hernández-García, C. et al. High-order harmonic propagation in gases within the discrete dipole approximation. *Phys. Rev. A* **82**, 033432 (2010).
39. Chen, C. et al. Tomographic reconstruction of circularly polarized high-harmonic fields: 3D attosecond metrology. *Sci. Adv.* **2**, e1501333 (2016).
40. Hernández-García, C. et al. Schemes for generation of isolated attosecond pulses of pure circular polarization. *Phys. Rev. A* **93**, 043855 (2016).
41. Hernández-García, C., San Román, J., Plaja, L. & Picón, A. Quantum-path signatures in attosecond helical beams driven by optical vortices. *New J. Phys.* **17**, 093029 (2015).
42. Alon, O. E., Averbukh, V. & Moisevev, N. Selection rules for the high harmonic generation spectra. *Phys. Rev. Lett.* **80**, 3743–3746 (1998).
43. Pisanty, E., Sukiasyan, S. & Ivanov, M. Spin conservation in high-order harmonic generation using bicircular fields. *Phys. Rev. A* **90**, 043829 (2014).
44. Paufler, W., Böning, B. & Fritzsche, S. Tailored orbital angular momentum in high-order harmonic generation with bicircular Laguerre-Gaussian beams. *Phys. Rev. A* **98**, 011401(R) (2018).
45. Bliokh, K. Y., Rodríguez-Fortuño, F. J., Nori, F. & Zayats, A. V. Spin-orbit interactions of light. *Nat. Photon.* **9**, 796–808 (2015).
46. Milošević, D. B., Becker, W. & Kopold, R. Generation of circularly polarized high-order harmonics by two-color coplanar field mixing. *Phys. Rev. A* **61**, 063403 (2000).
47. Medišauskas, L., Wragg, J., van der Hart, H. & Ivanov, M. Y. Generating elliptically polarized attosecond pulses using bichromatic counterrotating circularly polarized laser fields. *Phys. Rev. Lett.* **115**, 153001 (2015).
48. Milošević, D. B. Generation of elliptically polarized attosecond pulse trains. *Opt. Lett.* **40**, 2381–2384 (2015).
49. Milošević, D. B. & Becker, W. Attosecond pulse trains with unusual nonlinear polarization. *Phys. Rev. A* **62**, 011403(R) (2000).
50. Sanson, F. et al. Hartmann wavefront sensor characterization of a high charge vortex beam in the XUV spectral range. *Opt. Lett.* **43**, 2780–2783 (2018).
51. Beaurepaire, E., Merle, J.-C., Daunois, A. & Bigot, J.-Y. Ultrafast spin dynamics in ferromagnetic nickel. *Phys. Rev. Lett.* **76**, 4250–4253 (1996).
52. Boeglin, C. et al. Distinguishing the ultrafast dynamics of spin and orbital moments in solids. *Nature* **465**, 458–461 (2010).
53. Chen, C. et al. Distinguishing attosecond electron–electron scattering and screening in transition metals. *Proc. Natl Acad. Sci. USA* **114**, E5300–E5307 (2017).
54. Tengdin, P. et al. Critical behavior within 20 fs drives the out-of-equilibrium laser-induced magnetic phase transition in nickel. *Sci. Adv.* **4**, 9744 (2018).
55. Cireasa, R. et al. Probing molecular chirality on a sub-femtosecond timescale. *Nat. Phys.* **11**, 654–658 (2015).
56. Fujita, H. & Sato, M. Ultrafast generation of skyrmionics defects with vortex beams: printing laser profiles on magnets. *Phys. Rev. B* **95**, 054421 (2017).
57. van Veenendaal, M. Interaction between X-ray and magnetic vortices. *Phys. Rev. B* **92**, 245116 (2015).
58. Picón, A. et al. Transferring orbital and spin angular momenta of light to atoms. *New J. Phys.* **12**, 083053 (2010).
59. Eckart, S. et al. Ultrafast preparation and detection of ring currents in single atoms. *Nat. Phys.* **14**, 701–704 (2018).
60. van Veenendaal, M. & McNulty, I. Prediction of strong dichroism induced by X rays carrying orbital angular momentum. *Phys. Rev. Lett.* **98**, 157401 (2007).

Acknowledgements

The authors are thankful for useful and productive conversations with E. Pisanty, C. Durfee, D. Hickstein, S. Alperin and M. Siemens. H.C.K. and M.M.M. graciously acknowledge support from the Department of Energy BES Award No. DE-FG02–99ER14982 for the experimental implementation, as well as a MURI grant from the Air Force Office of Scientific Research under Award No. FA9550–16–1–0121 for the theory. J.L.E., N.J.B. and Q.L.N. acknowledge support from National Science Foundation Graduate Research Fellowships (Grant No. DGE-1144083). C.H.-G., J.S.R. and L.P. acknowledge support from Junta de Castilla y León (SA046U16) and Ministerio de Economía y Competitividad (FIS2013–44174-P, FIS2016–75652-P). C.H.-G. acknowledges support from a 2017 Leonardo Grant for Researchers and Cultural Creators, BBVA Foundation. L.R. acknowledges support from Ministerio de Educación, Cultura y Deporte (FPU16/02591). A.P. acknowledges support from the Marie Sklodowska-Curie Grant, Agreement No. 702565. We thankfully acknowledge the computer resources at MareNostrum and the technical support provided by Barcelona Supercomputing Center (RES-AECT-2014–2–0085). This research made use of the high-performance computingresources of the Castilla y León Supercomputing Center (SCAYLE, www.scayle.es),financed by the European Regional Development Fund (ERDF). Certain commercial instruments are identified to specify the experimental study adequately. This does not imply endorsement by the National Institute of Standards and Technology (NIST) or that the instruments are the best available for the purpose.

Author contributions

C.H.-G., K.M.D., M.M.M., H.C.K., L.R. and L.P. conceived and designed the SAM–OAM HHG experiment. K.M.D., N.J.B., C.-T.L., J.L.E. and Q.L.N. conducted the experiment. K.M.D. analysed the experimental data. C.H.-G., L.R., J.S.R., A.P. and L.P. performed the theoretical simulations and analysed the resulting data. J.M.S. prepared the EUV MCD sample. C.H.-G., L.P., M.M.M. and H.C.K. supervised the theoretical simulations and experimental work and developed the required facilities and measurement capabilities. C.H.-G., K.M.D., L.R., J.S.R., M.M.M. and L.P. wrote and prepared the manuscript, to which all authors provided constructive improvements and feedback.

Competing interests

M.M.M. and H.C.K. have a interest in KMLabs. The other authors declare no competing interests.

Additional information

Supplementary information is available for this paper at https://doi.org/10.1038/s41566-018-0304-3.

Reprints and permissions information is available at www.nature.com/reprints.

Correspondence and requests for materials should be addressed to K.M.D. or C.H.

Methods

Experimental generation of SAM–OAM high-harmonic vortices. To generate EUV SAM–OAM vortex beams, we utilized a modified version of the collinear, bichromatic scheme typically used in bicircular HHG. The full output of a regenerative Ti:sapphire amplifier (785 nm, 9 mJ, 1 kHz, KMLabs Wyvern HE) is passed into a Mach–Zhender-type interferometer with a branching ratio of 70/30. The more intense of the two arms contains a 200-μm-thick beta-barium borate crystal, which generates the second harmonic field at ~392 nm. Achromatic waveplates ($\lambda/2$ and $\lambda/4$) are placed in each arm to independently control the polarization of each component, resulting in LCP (785 nm, ω_1, $\sigma_1=-1$) and RCP (392 nm, ω_2, $\sigma_2=+1$) beams. A multifaceted spiral phase plate (SPP, HoloOr, 16-steps per phase wrap) is placed in each arm of the interferometer to control the topological charge of the visible vortex wavefront, and different SPPs and their orientations are utilized to generate vortex beams with charges of $\ell_1=\pm1$, ±2 and $\ell_2=\pm1$. The purity of the vortex mode and the relative sign of the OAM of each beam is characterized by a combination of a beam profiling camera and a cylindrical lens (see Supplementary Section 1). The two arms are then recombined via a dichroic mirror and spatiotemporal overlap is achieved via a delay stage and independent convex lenses in each arm; generating a bicircular, vortex driving beam. In the experiment, and also in the theoretical simulations (see below), the input beam parameters are carefully adjusted so that the ring of maximum intensity of each driver is spatially overlapped just before the gas jet (see Supplementary Section 1). The combined focus of the bicircular driver is placed just before the exit of a supersonic expansion of Ar gas to drive the HHG process. The generated high harmonics are collected via a 1D + 1D (spatio-spectral) spectrometer consisting of a gold-coated cylindrical mirror and a flat grating. The resulting spectrum is recorded with an EUV CCD array (Andor, Newton) at either the flat-field focal plane of the spectrometer (spectral measurements), or at a far field, ~8 cm beyond this focal plane (EUV vortex profile measurements), which measure both the spectrum and spatial mode of the SAM–OAM harmonics, respectfully.

EUV MCD measurements of SAM–OAM HHG ellipticity. One of the most straightforward ways to determine the helicity of EUV radiation is by exploiting the dichroic absorption of different helicities of light in a suitable chiral material. In this work, we employed EUV MCD measurements to quantify the relative helicity of high harmonics in our SAM–OAM HHG spectra. In EUV MCD, the transmission of RCP and LCP light is slightly different depending on the magnetic moment of a uniformly magnetized film, and the relative (and sometimes absolute) degree of polarization can be determined by measuring the absorption spectrum under different macroscopic magnetizations of the thin magnetic film. In this work, a 20-nm-thick $Fe_{0.75}Co_{0.25}$ alloy film (capped with a double bilayer consisting of 3 nm each of Cu/Ta) was deposited onto a 200 nm Al metal foil and served as the magnetic sample for the EUV MCD measurements. The MCD asymmetry was measured by applying a moderate magnetic field (~15 mT) to the film from an external electromagnet. The film was then oriented at 45° with respect to the SAM–OAM beam propagation direction to maximize the MCD effect in this geometry. For the spectrally dispersed measurements in Fig. 2, the absorption spectrum of the $Fe_{0.75}Co_{0.25}$ film was recorded for 10 s, then the magnetization of the film was switched via the electromagnet, and another absorption spectrum was recorded for another 10 s. This procedure was repeated for 90 paired measurements, giving a total exposure time of 30 min. For the spatially resolved EUV MCD measurements, a total of 120 absorption spectra were taken for each magnetization direction, yielding a total exposure time of 40 min.

Full quantum SAM–OAM HHG simulations including propagation. To simulate bicircular SAM–OAM HHG, we employed a theoretical method that computes both the full quantum single-atom HHG response and subsequent propagation[38]. The propagation is based on the electromagnetic field propagator, in which we discretize the target (gas jet) into elementary radiators[38]. The dipole acceleration of each elementary source is computed using the full quantum strong field approximation, instead of solving directly the time-dependent Schrödinger equation, yielding a performance gain in computational time when computing HHG over the entire target[38]. We assume that the harmonic radiation propagates with the vacuum phase velocity, which is a reasonable assumption for high-order harmonics. Propagation effects in the fundamental field, such as the production of free charges, the refractive index of the neutrals, the group velocity walk-off, as well as absorption in the propagation of the harmonics, are taken into account. Note that although we account for the time-dependent nonlinear phase shifts in the driving fields, nonlinear spatial effects are not taken into account. The spatial structure of the vortex beams considered in our simulations is represented as a Laguerre–Gaussian beam propagating in the z direction (see Supplementary Section 1 for further details). The laser pulses are modelled with a trapezoidal envelope with two cycles of linear turn-on, six cycles of constant amplitude—16 fs—and two cycles of linear turn-off (in cycles of the ω_1 field, of 800 nm in wavelength). The amplitudes (E_0) of the two fields—ω_1 of 800 nm and ω_2 of 400 nm in wavelength—are chosen to obtain the same peak intensity at focus for each driver at the radii of maximum superposition (that is, the brightest intensity rings overlap spatially), yielding a total intensity of 2×10^{14} W cm^{-2}. The driving-beam waists are chosen to overlap at the focal plane and the beam waists for the different cases $\ell=\pm1$, $w_0=30$ μm, for $\ell=\pm2$, $w_0=21.4$ μm and for $\ell=\pm4$, $w_0=15$ μm (see Supplementary Section 4). The gas jet, flowing along the perpendicular direction to the beam propagation is modelled as a Gaussian distribution of 10 μm at full width half maximum, and with a peak pressure of 667 Pa (5 torr). The low thickness of the gas jet is due to computational time limitations; however, based on our previous results of OAM HHG[39], we do not foresee any fundamental deviation when considering thicker gas jets closer to the experimental jet employed in this work (a diameter of 150 μm).

Data availability

The datasets and analysis routines utilized to prepare the data presented in this manuscript are available, free of charge, from the corresponding authors under reasonable request.

4.5.2 *Trains of attosecond pulses structured with time-ordered polarization states*

Resumen

Los pulsos de attosegundo de frecuencia en el ultravioleta extremo (XUV), que se generan de forma rutinaria mediante la generación de armónicos de orden alto (HHG) a partir de pulsos láser infrarrojos incidentes, sirven como herramientas para capturar las dinámicas más rápidas de la materia. Uno de los objetivos principales al respecto en las últimas décadas, ha sido la generación de pulsos de attosegundo estructurados, siendo ampliamente explorada la manipulación de su momento angular de espín (SAM), o polarización [165, 166]. En particular, se han generado experimentalmente pulsos de attosegundo polarizados circularmente, usando un campo dicromático contrarrotante con momento angular orbital (OAM) como campo incidente [18]. Sin embargo, hasta donde sabemos, el control de la secuencia de estados de polarización a lo largo del tren de pulsos de attosegundo ha permanecido inexplorado.

En este trabajo presentamos una técnica que permite producir trenes de pulsos de attosegundo con una variación progresiva de su elipticidad [19]. El estado de polarización de los pulsos de attosegundos cambia de pulso a pulso de manera ordenada, evolucionando, por ejemplo, de polarización circular levógira a polarización circular dextrógira, o viceversa. Estos trenes de pulsos de attosegundo estructurados se generan utilizando como campo incidente dos pulsos contrarrotantes dicromáticos retardados en el tiempo con un contenido de OAM apropiado. Además, nuestras simulaciones muestran que la evolución ultrarrápida del estado de polarización a lo largo del tren se puede controlar mediante el OAM, la duración y el retardo temporal de los pulsos incidentes.

De manera similar a la reciente introducción del OAM ordenado en el tiempo [16], esta fuente de luz estructurada en el XUV introduce un nuevo grado de libertad, la polarización ordenada en el tiempo, a las técnicas existentes para la medición y el control ultrarrápido en la nanoescala. Por ejemplo, estos trenes de pulsos de attosegundo con elipticidad secuencial ofrecen una nueva herramienta estroboscópica para el estudio de la dinámica ultrarrápida en sistemas quirales, experimentos de bombeo-prueba (*pump-probe*) con estados de polarización variable o dicroísmo circular magnético de polarización dependiente del tiempo.

5636 Vol. 45, No. 20 / 15 October 2020 / Optics Letters Letter

Optics Letters

Trains of attosecond pulses structured with time-ordered polarization states

LAURA REGO,* JULIO SAN ROMÁN, LUIS PLAJA, AND CARLOS HERNÁNDEZ-GARCÍA

Grupo de Investigación en Aplicaciones del Láser y Fotónica, Departamento de Física Aplicada, University of Salamanca, E-37008 Salamanca, Spain
**Corresponding author: laura.rego@usal.es*

Received 17 August 2020; revised 4 September 2020; accepted 5 September 2020; posted 8 September 2020 (Doc. ID 404402); published 6 October 2020

Ultrafast laser pulses generated at the attosecond timescale represent a unique tool to explore the fastest dynamics in matter. An accurate control of their properties, such as polarization, is fundamental to shape three-dimensional laser-driven dynamics. We introduce a technique to generate attosecond pulse trains whose polarization state varies from pulse to pulse. This is accomplished by driving high-harmonic generation with two time-delayed bichromatic counter-rotating fields with proper orbital angular momentum (OAM) content. Our simulations show that the evolution of the polarization state along the train can be controlled via OAM, pulse duration, and time delay of the driving fields. We, thus, introduce an additional control into structured attosecond pulses that provides an alternative route to explore ultrafast dynamics with potential applications in chiral and magnetic materials.

https://doi.org/10.1364/OL.404402

The most fundamental mechanisms in atoms, molecules, or solid systems are governed by dynamic interactions occurring at the attosecond timescale. The quest of obtaining light pulses at such short timescales, in order to drive, prove, and observe such dynamics, has driven the scientific community's efforts towards the development of coherent high-frequency light sources during the last two decades. As a consequence of the uncertainty principle, ultrashort pulses must contain coherent radiation spanning into the extreme-ultraviolet (XUV) or x-ray regimes in order to reach the sub-femtosecond timescale. While recently it has been shown that high-energy sub-femtosecond pulses can be obtained from free-electron lasers, highly coherent light bursts emitted at the attosecond timescale can be obtained through high-order harmonic generation (HHG). Shortly after the first demonstration of the comb of high-order harmonics driven by intense lasers [1,2], Farkas and Tóth theoretically forewarned of their characteristic sub-femtosecond duration [3]. Since its experimental confirmation by several groups in the early 2000s [4,5], HHG stands as the most robust tool not only to generate pulses down to few tens of attoseconds, but also to gain control on the properties of XUV radiation with unprecedented accuracy. Attosecond pulse trains provide extraordinary possibilities as quantum stroboscopes [6] for the time-control electron dynamics and the imaging of the electron's quantum state.

The success of HHG to produce attosecond pulses resides in its extraordinary coherence. At the microscopic level, the process is well understood from a semiclassical approach [7]. First, the driving laser field ionizes an electronic wavepacket, which is subsequently steered away from its parent ion. When the driving field reverses its sign, the wavepacket is driven back to the parent ion. Upon recombination, the kinetic energy acquired during the wavepacket excursion is released as high-order harmonics of the driving laser. This sub-femtosecond process is repeated at each half-cycle of the driving pulse, thus leading to the generation of a train of attosecond pulses.

One of the properties of HHG attosecond pulses whose control has been elusive for many years is spin angular momentum (SAM), associated with polarization. The generation of high harmonics and attosecond pulses with different polarization states is of great interest as a tool to probe the fastest spin dynamics in materials, and to uncover fundamental understanding on spin scattering and transport on attosecond timescales. Until recently, the dynamics leading to HHG were restricted along the direction of the linear polarization of the driving field, thus limiting the harmonic photons to linearly polarized states. If driven elliptically, the recombination probability diminishes, drastically reducing the yield of the high-order harmonic emission [8]. Fortunately, different techniques have recently exploited the extremely coherent nature of HHG to generate high-order harmonics—and attosecond pulses—with polarization states from linear to circular [9]. The use of non-symmetric targets, such as molecules or solids [10,11], or the use of proper combinations of linearly polarized drivers with different frequencies [12] enable the generation of elliptically polarized harmonics. Other approaches made use of proper macroscopic configurations, such as the use of non-collinear counter-rotating driving beams with the same color [13]—which allowed for the production of circularly polarized attosecond pulses for the first time [14,15]—or the combination of two HHG sources [16,17].

The first technique that allowed the generation of circularly polarized high-order harmonics used a driving field composed of two-color, counter-rotating, circularly polarized laser fields—the so-called bi-circular driver [18–20], which can present

Letter Vol. 45, No. 20 / 15 October 2020 / Optics Letters 5637

high ionization and recombination rates [21]. This technique stands nowadays as an efficient method to generate circularly polarized harmonics with brightness and energies comparable to single-color linearly polarized HHG [22,23]. The primary spectral feature of bi-circular HHG is the generation of pairs of circularly polarized harmonics with opposite helicity—right circular (RCP) and left-circular (LCP)—due to SAM conservation. The generation of both LCP and RCP harmonics from bi-circular HHG driving results in the emission of linearly polarized attosecond trains of pulses, where the polarization tilt angle rotates from pulse to pulse.

Recently, the introduction of orbital angular momentum (OAM) in the driving pulses, has allowed us to not only to generate circularly polarized harmonic vortex beams, but also to control the polarization of the attosecond pulse trains in the bi-circular scheme [24]. However, up to now, SAM—or the polarization state— has been introduced at the attosecond timescale as a time-independent variable. To the best of our knowledge, there is no proposal—nor experimental demonstration— yet to produce attosecond pulse trains with controlled, well resolved, time-ordered polarization. We note, however, that some recent works have reported the generation of high harmonics whose polarization state slightly changes along the course of the pulse as a result of the highly nonlinear nature of HHG [11,25].

In this Letter, we introduce a technique to generate trains of attosecond pulses with different—and controlled—polarization states from pulse to pulse, thus presenting time-ordered SAM along the pulse train. The control knob lies on the proper choice of the combination of two time-delayed bi-circular driving fields, with different OAM content. Very recently, HHG has been proven to introduce time-dependent OAM into a light beam, denoted as self-torque [26]. In this work, we demonstrate that driving HHG with two time-delayed bi-circular vortex beams with properly chosen OAM content results in trains of attosecond pulses of the SAM state changing sequentially from pulse to pulse. Similar schemes that make use of time-delayed pulses with different SAM, instead of OAM, are now widely used, such as the polarization gating technique [27].

It is already known that introducing OAM in bi-circular driving results in high-order harmonics with opposite helicity, that can be spatially separated in the far-field into a double ring profile [24], as we schematically illustrate in Fig. 1(a). If we consider an OAM bi-circular field composed of two pulses with fundamental (ω_1) and doubled frequency ($\omega_2 = 2\omega_1$), counter-rotating ($\sigma_1 = -1$ LCP, $\sigma_2 = 1$ RCP) and with topological charge—or OAM content—of ℓ_1 and ℓ_2, respectively, the difference in divergence in the far-field between the LCP and RCP harmonics is given by $\Delta\beta \propto (2\ell_1 - \ell_2)|\ell_1 + \ell_2|/(\ell_1 + \ell_2)$ [24]. As a general trend, the spatial separation between the LCP and RCP harmonic rings increases for larger differences between ℓ_1 and ℓ_2, if ℓ_1 and ℓ_2 have opposite signs. The outer (inner) ring—with larger (smaller) divergence— exhibits the same helicity as that of the driving pulse with higher (lower) $|\ell|$. For the convention adopted in this work, if $|\ell_1| > |\ell_2|$, the far-field outer ring is composed of LCP harmonics, whereas if $\ell_2| > |\ell_1|$, it is composed of RCP harmonics, as illustrated in Fig. 1(a). From the temporal point of view, by selecting the high-order harmonics emitted at each of the rings, attosecond pulse trains with LCP or RCP states are generated with a time-independent polarization state.

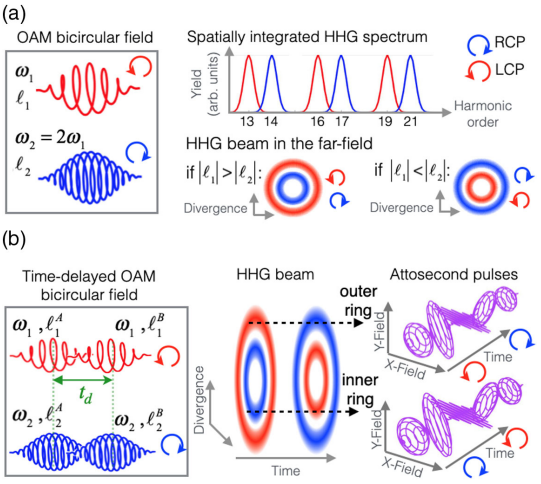

Fig. 1. (a) Scheme of polarization control of HHG driven by an OAM bi-circular field (ω_1, ℓ_1, LCP; $2\omega_1$, ℓ_2, RCP). The HHG spectrum is composed of pairs of circularly polarized harmonics with opposite helicity, separated in divergence in the far-field. (b) Generation scheme of trains of attosecond pulses with time-ordered polarization states. In this case, HHG is driven by two time-delayed OAM bi-circular fields, A and B, where, for this example, we have chosen $|\ell_1^A| > |\ell_2^A|$ and $|\ell_1^B| < |\ell_2^B|$. As a consequence, in the outer (inner) ring, the polarization of the harmonics—and the attosecond pulses—varies continuously in time from LCP (RCP) to RCP (LCP), as shown schematically in the right panel.

In order to introduce a temporal dependency into the polarization state of the attosecond pulses within the train, we drive HHG with a combination of two time-delayed OAM bi-circular beams with opposite topological charges [see Fig. 1(b)]. If we denote each of the OAM bi-circular beams as A and B, we require an OAM combination of $|\ell_1^A| = |\ell_2^B|$ and $|\ell_1^B| = |\ell_2^A|$, maintaining ℓ_1 and ℓ_2 with opposite signs, as mentioned before. The temporal delay between the two OAM bi-circular beams, t_d, causes the emitted high-order harmonics in each of the rings to evolve from LCP (RCP) to RCP (LCP), as depicted schematically in Fig. 1(b). For this figure, we have selected $|\ell_1^A| > |\ell_2^A|$ and $|\ell_1^B| < |\ell_2^B|$, and, thus, the polarization state of the emitted attosecond pulse trains will evolve from LCP (RCP) to RCP (LCP) at the outer (inner) harmonic ring. The pace of SAM changes can be controlled through the OAM of the driving pulses and their temporal properties (pulse duration and time delay).

We have performed simulations of macroscopic HHG in an argon gas jet, including propagation. Our calculations combine the strong-field approximation with the electromagnetic-field propagator [28]. This theoretical approach successfully describes the macroscopic HHG in several configurations involving SAM and/or OAM [13–16,24,26]. We model the driving pulses with a $\sin^2$ envelope, with central wavelengths of 800 nm (400 nm) for the ω_1 ($2\omega_1$) driver and a peak intensity of 1.4×10^{14} W/cm^2 each. The spatial structure of the laser beams is represented as a Laguerre–Gaussian beam propagating in the z direction, with topological charge ℓ and radial nodes index p. The beam waist, w_0, of each laser beam is chosen so

5638 Vol. 45, No. 20 / 15 October 2020 / Optics Letters Letter

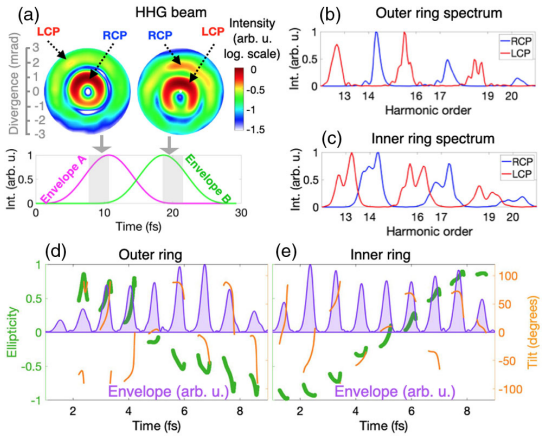

Fig. 2. (a) Spatial intensity profile of the HHG beam obtained with an OAM bi-circular field with $\ell_1^A = 3$, $\ell_2^A = -2$ (and, thus, $\ell_1^B = 2$, $\ell_2^B = -3$). The helicity of the inner and outer rings changes along time. In panels (b) and (c), we show the HHG spectrum of the outer and inner rings, whereas in panels (d) and (e) we show the corresponding attosecond pulse train envelopes (purple), ellipticity (green), and tilt angle (orange).

that the different OAM modes overlap at the rings of maximum intensity.

In Fig. 2, we present the results of the simulations when considering $\ell_1^A = 3$, $\ell_2^A = -2$ (and thus $\ell_1^B = 2$, $\ell_2^B = -3$), all of them with $p = 0$. The pulse duration of each driver is 7.7 fs in full width at half-maximum (FWHM) in intensity, and the temporal delay between the A and B drivers is $t_d = 7.7$ fs. The waist of the driving beams, w_0, is 30 μm for $\ell = \pm 2$ and 24.54 μm for $\ell = \pm 3$. Looking at the spatial intensity profile of the HHG beam in Fig. 2(a), integrated over harmonic orders above the 10th, we distinguish two spatial rings. In Figs. 2(b) and 2(c), we show the far-field HHG spectrum of the outer ring (detected at 1.6 mrad) and that at the inner ring (detected at 0.6 mrad), respectively. In both HHG spectra, we can already distinguish the pairs of LCP (red line) and RCP (blue line) harmonics, a well-known result of SAM conservation in HHG driven by the bi-circular field [22]. Note that we observe a frequency shift in the harmonics, which is induced by the pulse envelope through the time-dependent variation of the intrinsic phase. Computing the inverse Fourier transform of the HHG spectra above the 10th harmonic order, we can retrieve the attosecond pulse trains shown in purple in Figs. 2(d) and 2(e), for the outer and inner rings, respectively. The polarization state of the attosecond pulse trains can be monitored through the temporal evolution of the Stokes parameters [29]. The time-dependent ellipticity can be thus described as $\epsilon(t) = \tan\left[0.5 \arctan(S_3(t)/\sqrt{S_1^2(t) + S_2^2(t)})\right]$, while the time-dependent tilt angle is $\theta(t) = 0.5 \arctan[S_2(t)/S_1(t)]$.

In Figs. 2(d) and 2(e), we show the time-dependent ellipticity, $\epsilon(t)$, in green and the time-dependent tilt, $\theta(t)$, in orange for the outer and inner rings, together with the attosecond pulse train envelope in purple—which corresponds to the Stokes parameter $S_0(t)$. We can see how the polarization state of the attosecond pulses evolves from LCP (RCP) to RCP (LCP) along the train for the outer (inner) spatial ring. The tilt angle exhibits a rotation from pulse to pulse and also within each individual pulse. When driven by a single bichromatic counter-rotating field, the tilt angle is known to rotate 120 deg from pulse to pulse. In contrast, in this scenario, the rotation is more complicated due to the overlap of the two time-delayed fields. The structure of the trains remains almost invariant within a divergence angle width of 0.5 mrad, approximately. Finally, we note that the time-dependent degree of polarization, defined as $P(t) = \sqrt{S_1^2(t) + S_2^2(t) + S_3^2(t)}/S_0(t)$, is constant and equal to one for all of the cases presented in this work, as expected from the coherence of the HHG process.

To have a better insight into the origin of the temporal structure of the attosecond pulse trains, we present in Fig. 3 the time-frequency analysis for the two cases depicted in Fig. 2. At the outer ring (left column), the LCP harmonics dominate at the front part of the pulse train, whereas RCP harmonics dominate at the rear part of the pulse. This behavior is reversed at the inner ring (right column). Note that the temporal delay between the OAM bi-circular drivers A and B is chosen to be equal to the FWHM of the driving pulses in order to obtain a homogeneous and linear variation of the ellipticity over time. A different choice of the time delay can be used to customize the temporal variation of the ellipticity of the attosecond pulse train. Analogously, the choice of the driving pulse lengths, and their OAM, allows for a custom control of the time-dependent polarization structure of the attosecond pulse train. To show the versatility of this technique, we have performed simulations with few-cycle driving laser pulses and a different OAM combination. In Fig. 4, we present the simulation results when considering Laguerre–Gauss beams with $\ell_1^A = 2$, $\ell_2^A = -1$ (and, thus, $\ell_1^B = 1$, $\ell_2^B = -2$), all of them with $p = 0$. The driving pulse length is 1.9 fs FWHM, and the temporal delay between the A and B drivers is $t_d = 1.9$ fs. The waist of the driving beams is $w_0 = 30$ μm for $\ell = \pm 1$ and $w_0 = 21.4$ μm for $\ell = \pm 2$. Now, the number of attosecond pulses in the train is reduced—as expected—, and, thus, the variation rate of the ellipticity in time increases. In this case, we present the attosecond pulse train emitted at an intermediate divergence angle (detected at 1.7 mrad) in order to illustrate the possibility of obtaining a polarization evolution from linear to highly elliptical, in contrast to the elliptical-to-elliptical polarization variation in the outer and inner rings. On the other hand, the

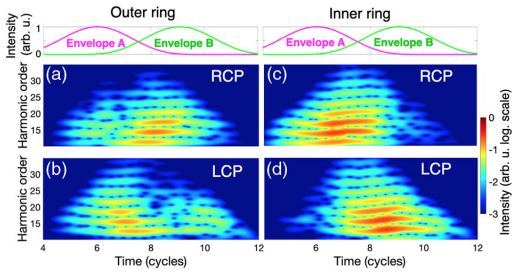

Fig. 3. Time-frequency analysis for RCP (first row) and LCP (second row) projections of the harmonic emission at the outer (left column) and inner (right column) rings, depicted in Fig. 2. The outer (inner) ring LCP (RCP) harmonics precede temporally the RCP (LCP) ones. The spectral width of the Gaussian mask used to perform the time-frequency analysis is ω_1.

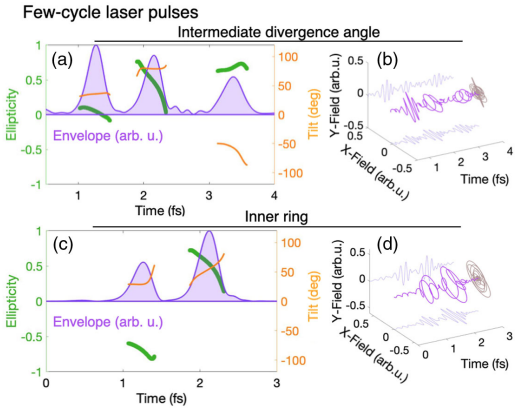

Fig. 4. Attosecond pulses—envelope (purple), ellipticity (green), and tilt angle (orange)—obtained with a few-cycle OAM bi-circular field with $\ell_1^A = 2$, $\ell_2^A = -1$ (and, thus, $\ell_1^B = 1$, $\ell_2^B = -2$) for an intermediate divergence angle (top) and inner ring (bottom) emission. The two-dimensional (2D) evolution of the attosecond electric fields is depicted in the right column.

inner ring consists of two elliptically polarized attosecond pulses with opposite helicities (detected at 1 mrad).

In conclusion, we have presented a scheme for the generation of attosecond pulse trains with time-ordered polarization states. By driving HHG with two time-delayed OAM bi-circular drivers, two spatially separated rings of harmonics are generated, each with polarization evolving from LCP to RCP and vice versa. The proper choice of the OAM, pulse length, and time delay of the driving pulses allows for custom control over the temporal evolution of the SAM of the pulses within the train.

We, thus, introduce a novel structured ultrafast light source by adding a new degree of freedom, time-ordered SAM, or polarization into the quantum stroboscope scheme. Similarly, time-ordered OAM—or self-torque—was introduced recently into the family of structured light beams thanks to HHG [26]. By adding this temporal dependency into the SAM of attosecond EUV beams, this work opens the route towards new probing scenarios—such as the study of ultrafast dynamics in chiral systems, pump–probe experiments with polarization varying states, or time-dependent polarization x-ray magnetic circular dichroism—that provide an alternative route to probe the ultrafast dynamics of matter systems at the nanoscale.

Funding. Junta de Castilla y León (SA287P18); FEDER funds; Ministerio de Ciencia, Innovación y Universidades (FIS2016-75652-P, RYC-2017-22745, PID2019-106910GB-I00); Ministerio de Educación, Cultura y Deporte (FPU16/02591); European Research Council (ERC) (851201); Barcelona Supercomputing Center (FI-2019-1-0013).

Disclosures. The authors declare no conflicts of interest.

REFERENCES

1. A. McPherson, G. Gibson, H. Jara, U. Johann, T. S. Luk, I. A. McIntyre, K. Boyer, and C. K. Rhodes, J. Opt. Soc. Am. B **4**, 595 (1987).
2. M. Ferray, A. L'Huillier, X. F. Li, L. A. Lompre, G. Mainfray, and C. Manus, J. Phys. B **21**, L31 (1988).
3. G. Farkas and C. Tóth, Phys. Lett. A **168**, 447 (1992).
4. P. M. Paul, E. S. Toma, P. Breger, G. Mullot, F. Augé, P. Balcou, H. G. Muller, and P. Agostini, Science **292**, 1689 (2001).
5. M. Hentschel, R. Kienberger, C. Spielmann, G. A. Reider, N. Milosevic, T. Brabec, P. Corkum, U. Heinzmann, M. Drescher, and F. Krausz, Nature **414**, 509 (2001).
6. J. Mauritsson, P. Johnsson, E. Mansten, M. Swoboda, T. Ruchon, A. L'Huillier, and K. J. Schafer, Phys. Rev. Lett. **100**, 073003 (2008).
7. K. J. Schafer, B. Yang, L. F. DiMauro, and K. C. Kulander, Phys. Rev. Lett. **70**, 1599 (1993).
8. P. Dietrich, N. H. Burnett, M. Ivanov, and P. B. Corkum, Phys. Rev. A **50**, R3585 (1994).
9. P. Huang, C. Hernández-García, J. Huang, P. Huang, L. Rego, C. Lu, S. Yang, L. Plaja, A. H. Kung, and M. Chen, IEEE J. Sel. Top. Quantum Electron. **25**, 1 (2019).
10. A. Ferré, C. Handschin, M. Dumergue, F. Burgy, A. Comby, D. Descamps, B. Fabre, G. A. Garcia, R. Géneaux, L. Merceron, E. Mével, L. Nahon, S. Petit, B. Pons, D. Staedter, S. Weber, T. Ruchon, V. Blanchet, and Y. Mairesse, Nat. Photonics **9**, 93 (2015).
11. Ó. Zurrón-Cifuentes, R. Boyero-García, C. Hernández-García, A. Picón, and L. Plaja, Opt. Express **27**, 7776 (2019).
12. G. Lambert, B. Vodungbo, J. Gautier, B. Mahieu, V. Malka, S. Sebban, P. Zeitoun, J. Luning, J. Perron, A. Andreev, S. Stremoukhov, F. Ardana-Lamas, A. Dax, C. P. Hauri, A. Sardinha, and M. Fajardo, Nat. Commun. **6**, 6167 (2015).
13. D. D. Hickstein, F. J. Dollar, P. Grychtol, J. L. Ellis, R. Knut, C. Hernandez-Garcia, D. Zusin, C. Gentry, J. M. Shaw, T. Fan, K. M. Dorney, A. Becker, A. Jaron-Becker, H. C. Kapteyn, M. M. Murnane, and C. G. Durfee, Nat. Photonics **9**, 743 (2015).
14. C. Hernández-García, C. G. Durfee, D. D. Hickstein, T. Popmintchev, A. Meier, M. M. Murnane, H. C. Kapteyn, I. J. Sola, A. Jaron-Becker, and A. Becker, Phys. Rev. A **93**, 043855 (2016).
15. P.-C. Huang, C. Hernández-García, J.-T. Huang, P.-Y. Huang, C.-H. Lu, L. Rego, D. D. Hickstein, J. L. Ellis, A. Jaron-Becker, A. Becker, S.-D. Yang, C. G. Durfee, L. Plaja, H. C. Kapteyn, M. M. Murnane, A. H. Kung, and M.-C. Chen, Nat. Photonics **12**, 349 (2018).
16. J. L. Ellis, K. M. Dorney, D. D. Hickstein, N. J. Brooks, C. Gentry, C. Hernández-García, D. Zusin, J. M. Shaw, Q. L. Nguyen, C. A. Mancuso, G. S. Matthijs Jansen, S. Witte, H. C. Kapteyn, and M. M. Murnane, Optica **5**, 479 (2018).
17. D. Azoury, O. Kneller, M. Krüger, B. D. Bruner, O. Cohen, Y. Mairesse, and N. Dudovich, Nat. Photonics **13**, 198 (2019).
18. H. Eichmann, A. Egbert, S. Nolte, C. Momma, B. Wellegehausen, W. Becker, S. Long, and J. K. McIver, Phys. Rev. A **51**, R3414 (1995).
19. S. Long, W. Becker, and J. K. McIver, Phys. Rev. A **52**, 2262 (1995).
20. D. B. Milošević, W. Becker, and R. Kopold, Phys. Rev. A **61**, 063403 (2000).
21. A. D. Bandrauk, J. Guo, and K. J. Yuan, J. Opt. **19**, 124016 (2017).
22. A. Fleischer, O. Kfir, T. Diskin, P. Sidorenko, and O. Cohen, Nat. Photonics **8**, 543 (2014).
23. O. Kfir, P. Grychtol, E. Turgut, R. Knut, D. Zusin, D. Popmintchev, T. Popmintchev, H. Nembach, J. M. Shaw, A. Fleischer, H. Kapteyn, M. Murnane, and O. Cohen, Nat. Photonics **9**, 99 (2015).
24. K. M. Dorney, L. Rego, N. J. Brooks, J. San Román, C.-T. Liao, J. L. Ellis, D. Zusin, C. Gentry, Q. L. Nguyen, J. M. Shaw, A. Picón, L. Plaja, H. C. Kapteyn, M. M. Murnane, and C. Hernández-García, Nat. Photonics **13**, 123 (2018).
25. L. Barreau, K. Veyrinas, V. Gruson, S. J. Weber, T. Auguste, J.-F. Hergott, F. Lepetit, B. Carré, J.-C. Houver, D. Dowek, and P. Salières, Nat. Commun. **9**, 4727 (2018).
26. L. Rego, K. M. Dorney, N. J. Brooks, Q. L. Nguyen, C.-T. Liao, J. San Román, D. E. Couch, A. Liu, E. Pisanty, M. Lewenstein, L. Plaja, H. C. Kapteyn, M. M. Murnane, and C. Hernández-García, Science **364**, eaaw9486 (2019).
27. I. J. Sola, E. Mével, L. Elouga, E. Constant, V. Strelkov, L. Poletto, P. Villoresi, E. Benedetti, J. P. Caumes, S. Stagira, C. Vozzi, G. Sansone, and M. Nisoli, Nat. Phys. **2**, 319 (2006).
28. C. Hernández-García, J. A. Pérez-Hernández, J. Ramos, E. C. Jarque, L. Roso, and L. Plaja, Phys. Rev. A **82**, 033432 (2010).
29. W. H. McMaster, Am. J. Phys. **22**, 351 (1954).

5 CONCLUSIONS

This thesis presents a collection of schemes for the generation high-order harmonics and attosecond pulses with novel angular momentum properties by structuring HHG through the characteristics of the driving beams. Additionally, we have studied the fundamentals of HHG and, in particular, the tunnel-ionization. From our research work we can derive the following main conclusions:

1. The tunnel ionization in molecules is site-specific: the ionization rate deeply depends on the position of the electronic wavefunction at the ion sites, decreasing with its distance to the edge of the molecular potential barrier. Importantly, both the HHG and photoelectron spectra present signatures of the site-dependent tunnel ionization, since it distorts the mapping of the molecular orbitals into the ionized electron.

2. XUV beams with ultrafast-time-varying OAM are produced from HHG driven by two time-delayed vortex beams. The OAM content of the high-order harmonics is well-defined and varies continuously and extremely rapidly in time along the beam itself, a quality that, to the best of our knowledge, has not been reported in any spectral regime. Noticeably, this novel property, that we denote as self-torque, imprints an azimuthal frequency chirp on the high-order harmonics, which allows for its experimental measurement. The amount of self-torque can be controlled by modifying the temporal properties—duration and time delay—of the driving fields.

3. High-order harmonic combs with tunable spectral line-spacing can be obtained from HHG driven by a phased-necklace driving beam, which is composed by two vortex beams. Remarkably, the OAM content of the phased-necklace driving beam determines the line-spacing of the XUV/soft-X-ray frequency combs. Additionally, such combs exhibit a low divergence, which decreases with the harmonic order, in contrast to that of the high-order harmonics generated from HHG driven by a standard Gaussian beam.

4. Isolated attosecond pulses with controlled ellipticity can be generated from HHG driven by a non-collinear counter-rotating field. Such control is achieved by properly modifying the ellipticity of the driving pulses. Noticeably, the scaling of the ellipticity of the high-order harmonics with that of the driving beams is strongly

influenced by the non-perturbative dipole response. We introduce an ellipsometry technique to retrieve the non-perturbative amplitude scaling power and dipole phase from experimental polarization measurements.

5. Circularly polarized XUV vortex beams are generated from HHG driven by a bi-circular vortex field. The simultaneous conservation of SAM and OAM entwines both quantities, and, as a result, the OAM of the harmonics depends on its particular SAM. Interestingly, this allows for the generation of XUV beams with unprecedented properties by properly selecting the OAM content of the driving field: (i) RCP and LCP high-order harmonics can be spatially separated, so circularly polarized attosecond pulses are synthesized, and (ii) high-order harmonics can be generated with the same topological charge than that of the driving beams. Additionally, the selection rules that govern this configuration can be described as the conservation of the torus-knot angular momentum in HHG.

6. Attosecond pulse trains with time-ordered polarization states from pulse to pulse can be generated from HHG driven by two time-delayed bi-circular fields carrying properly selected OAM. The evolution of the ellipticity along the attosecond pulse train is controlled through the driving field temporal properties and OAM.

From the methodological point of view, the novel tools developed in this thesis are the following:

1. We have incorporated the site-dependent tunnelling into the SFA by introducing a modified molecular form factor. Our SDT-SFA model improves substantially the agreement between the standard molecular SFA models and the exact TDSE calculations.

2. We have developed a numerical tool for the extraction of the molecular form factor from the TFA of the HHG emission for the confirmation of the site-dependent tunnel-ionization.

3. We have extended the TSM to new configurations: (i) the combination of several time-delayed vortex driving beams for the generation of XUV self-torqued beams; (ii) the non-collinear counter-rotating scheme for the generation of isolated attosecond pulses with controlled ellipticity and the non-perturbative dipole response characterization; and (iii) the bi-circular vortex driving field for the generation of circularly polarized attosecond pulses with OAM, as well as time-ordered polarization states along the attosecond pulse train.

In conclusion, in this thesis we have presented several strategies for structuring HHG with the angular momentum of light, a topic

at the forefront of the ultrafast research. As a first step, we have investigated the description of the fundamental characteristics and physical mechanisms of HHG. In this sense, we believe that we have contributed to a better understanding of tunnel ionization, providing the procedural implementation in the present modelling framework, which could be applied to high-harmonic spectroscopy techniques. In the future, our SDT-SFA model could be extended to the study of HHG in larger molecules and/or using structured driving beams.

Then, as the main contribution of this thesis, we have demonstrated the generation of XUV beams with novel angular momentum properties, which could serve henceforth as tools for laser-matter manipulation on attosecond time and nanometric spatial scales. In particular, in contrast to the static-OAM light-based technologies, our work opens a new regime of dynamic-OAM light-based optical control, that could potentially be used to image magnetic and topological excitations with time-dependent OAM, to launch selective excitation of quantum matter, or to manipulate molecules and nanostructures on their natural time and length scales. Furthermore, we have demonstrated that driving beams with proper OAM content can also be employed for the control of the spectral and spatial properties of the high-order harmonics, providing diverse frequency combs for tabletop XUV/soft-X-ray spectroscopy and imaging.

Finally, the generation of attosecond pulses with controlled ellipticity can serve to study chiral molecules or magnetic materials. Particularly, we foresee that the experimental generation of attosecond pulse trains with time-ordered polarization states could be an interesting future step towards the study of time-dependent chirality or polarization X-ray magnetic circular dichroism.

CONCLUSIONES

Esta tesis presenta una colección de esquemas para la generación de armónicos de orden alto y pulsos de attosegundo con nuevas propiedades de momento angular mediante la estructuración del proceso de HHG a través de las características de los haces incidentes. Además, hemos estudiado los fundamentos de la HHG y, en particular, la ionización túnel. De nuestro trabajo de investigación podemos derivar las siguientes conclusiones principales:

1. La ionización túnel en las moléculas es dependiente de la ubicación de los electrones en ellas: la tasa de ionización depende en gran medida de la posición de la función de onda electrónica en los iones, disminuyendo con su distancia al borde de la barrera de potencial molecular. Es importante destacar que tanto los espectros de HHG como los de fotoelectrones presentan huellas de la ionización túnel dependiente de la ubicación, ya que esta distorsiona el mapeo de los orbitales moleculares en el electrón ionizado.

2. Obtenemos haces XUV con un OAM que varía ultrarrápidamente en el tiempo a partir de la HHG usando como campo incidente dos vórtices retardados en el tiempo. El contenido de OAM de los armónicos de orden alto está bien definido y varía de forma continua y extremadamente rápida en el tiempo a lo largo del haz, una cualidad que, hasta donde sabemos, no ha sido descrita anteriormente en ningún régimen espectral. Cabe destacar que esta nueva propiedad, que denominamos auto-torque, imprime un ordenamiento de frecuencias azimutal en los armónicos de orden alto, lo cual permite su medición experimental. La cantidad de auto-torque se puede controlar modificando las propiedades temporales (duración y retardo) de los pulsos incidentes.

3. Generamos peines de armónicos de orden alto con espaciado espectral sintonizable a partir de la HHG usando como campo incidente un haz tipo "collar de cuentas" con fase, que se construye a partir de la combinación de dos vórtices de luz. Sorprendentemente, el contenido de OAM del haz incidente determina el espaciado entre líneas de los peines de alta frecuencia. Además, estos haces exhiben una divergencia baja, que disminuye con el orden armónico, en contraste con la de los armónicos de orden alto generados a partir de HHG usando un haz Gaussiano estándar.

4. Demostramos la generación de pulsos de attosegundo aislados con elipticidad controlada a partir de la HHG usando un campo

contrarrotante no colineal. Dicho control se logra modificando adecuadamente la elipticidad de los pulsos incidentes. Cabe destacar que el escalado de la elipticidad de los armónicos de orden alto con la de los haces incidentes está fuertemente influenciado por la respuesta dipolar no perturbativa. Por tanto, tanto la potencia de escalado de la amplitud como la fase dipolar no perturbativas pueden recuperarse a partir de mediciones experimentales de polarización.

5. Obtenemos vórtices XUV polarizados circularmente a partir de la HHG usando un campo bi-circular con OAM como haz incidente. La conservación simultánea del SAM y el OAM entrelaza ambas cantidades y, como resultado, el OAM de los armónicos depende de su SAM particular. Destacablemente, esto permite la generación de haces XUV con propiedades sin precedentes, seleccionando apropiadamente el contenido de OAM del campo incidente: (i) los armónicos de orden alto con polarización dextrógira y levógira pueden ser separados espacialmente, lo que lleva a la generación de pulsos de attosegundo polarizados circularmente, y (ii) se pueden generar armónicos de orden alto con la misma carga topológica que la de los haces incidentes. Además, las reglas de selección que gobiernan esta configuración se pueden describir como la conservación del momento angular de nudo toroidal en la HHG.

6. Proponemos la generación de trenes de pulsos de attosegundo con estados de polarización ordenados en el tiempo de pulso a pulso a partir de la HHG usando como haz incidente dos campos bi-circulares retardados en el tiempo con un OAM seleccionado adecuadamente. La evolución de la elipticidad a lo largo del tren de pulsos de attosegundo se controla mediante las propiedades temporales y el OAM del campo incidente.

Desde el punto de vista metodológico, las nuevas herramientas desarrolladas en esta tesis son las siguientes:

1. Hemos incorporado el efecto de la ionización tunel dependiente de la ubicación del electrón en la SFA mediante la modificación del factor de forma molecular. Nuestro modelo de SDT-SFA mejora substancialmente el acuerdo entre los modelos moleculares de la SFA estándar y los cálculos de la TDSE exactos.

2. Hemos desarrollado una herramienta numérica para la extracción del factor de forma molecular a partir del análisis espectro-temporal de la emisión de la HHG, que hemos utilizado para la confirmación de nuestro modelo de la ionización túnel dependiente de la ubicación electrónica.

3. Hemos extendido el TSM a nuevas configuraciones: (i) la combinación de varios vórtices retardados en el tiempo para la generación de haces XUV con auto-torque; (ii) el esquema no colineal contrarrotante para la generación de pulsos de attosegundo aislados con elipticidad controlada y para la caracterización de la respuesta dipolar no perturbativa; y (iii) el campo bi-circular vorticial para la generación de pulsos de attosegundo polarizados circularmente y con OAM, así como para la propuesta de trenes de pulsos con estados de polarización ordenados en el tiempo.

En conclusión, en esta tesis hemos presentado varias estrategias para estructurar la HHG con el momento angular de la luz, un tema a la vanguardia de la investigación ultrarrápida. Como primer paso, hemos investigado la descripción de las características fundamentales y los mecanismos físicos de la HHG. En este sentido, creemos que hemos contribuido a una mejor comprensión de la ionización túnel, proporcionando la implementación del procedimiento en el marco de los modelos actuales, lo cual podría aplicarse a estudios de espectroscopia de harmónicos altos. Además, en el futuro, nuestro modelo de SDT-SFA podría extenderse a moléculas más grandes, y también hacia el estudio de HHG haciendo incidir haces estructurados en moléculas.

A continuación, como principal contribución de esta tesis, hemos demostrado la generación de haces XUV con nuevas propiedades de momento angular, que podrían servir de ahora en adelante como herramientas para la manipulación láser-materia en escalas espaciales nanométricas y de tiempo de attosegundos. En particular, en contraste con las tecnologías basadas en el control de la luz con OAM estático, nuestro trabajo abre un nuevo régimen de control óptico basado en la luz con OAM dinámico. Esta característica podría potencialmente usarse para obtener imágenes de excitaciones magnéticas y topológicas con OAM dependiente del tiempo, iniciar la excitación selectiva de materia cuántica o manipular moléculas y nanoestructuras en sus escalas naturales de tiempo y longitud. Además, hemos demostrado que los haces incidentes con el contenido adecuado de OAM también se pueden emplear para el control de las propiedades espectrales y espaciales de los armónicos de orden alto, proporcionando diversos peines de frecuencia para espectroscopia y formación de imágenes con rayos X.

Finalmente, la generación de pulsos de attosegundo con elipticidad controlada puede servir para el estudio de moléculas quirales o materiales magnéticos. En particular, prevemos que la generación experimental de trenes de pulsos de attosegundo con estados de polarización ordenados en el tiempo podría ser un paso futuro hacia el estudio de la quiralidad dependiente del tiempo o del dicroísmo magnético de rayos X de polarización circular.

A

APPENDIX: ADDITIONAL PUBLICATIONS

In this appendix, we compile the full texts of the three articles that are part of the work carried out in this thesis but were not included in section 4.5. We first present two publications led by our experimental collaborators from the group of Prof. M.-Ch. Chen at the Institute of Photonics Technologies of the National Tsin Hua University (Taiwan), using the non-collinear counter-rotating driving field. In section A.1, we include the publication about the generation of attosecond pulses with monitored ellipticity, under the title "Polarization control of isolated high-harmonic pulses" [20], which was briefly explained in section 4.2.1. In section A.2, we present our article regarding the extraction of information of the dipole phase response from an ellipsometry technique, under the title "High-order nonlinear dipole response characterized by extreme ultraviolet ellipsometry" [21], mentioned in section 4.2.2. Finally, in section A.3, we include our publication regarding the torus-knot angular momentum in HHG, a work leaded by our collaborators from the group of Prof. M. Lewenstein at ICFO in Barcelona (Spain), under the title "Conservation of Torus-knot Angular Momentum in High-order Harmonic Generation" [22], which was briefly discussed in section 4.3.4.

A.1 POLARIZATION CONTROL OF ISOLATED HIGH-HARMONIC PULSES

nature photonics

ARTICLES

https://doi.org/10.1038/s41566-018-0145-0

Polarization control of isolated high-harmonic pulses

Pei-Chi Huang[1,2*], Carlos Hernández-García[3], Jen-Ting Huang[1], Po-Yao Huang[1], Chih-Hsuan Lu[1,2], Laura Rego[3], Daniel D. Hickstein[4], Jennifer L. Ellis[4], Agnieszka Jaron-Becker[4], Andreas Becker[4], Shang-Da Yang[1], Charles G. Durfee[5], Luis Plaja[3], Henry C. Kapteyn[4], Margaret M. Murnane[4], A. H. Kung[1,2] and Ming-Chang Chen[1,6*]

High-harmonic generation driven by femtosecond lasers makes it possible to capture the fastest dynamics in molecules and materials. However, thus far, the shortest isolated attosecond pulses have only been produced with linear polarization, which limits the range of physics that can be explored. Here, we demonstrate robust polarization control of isolated extreme-ultraviolet pulses by exploiting non-collinear high-harmonic generation driven by two counter-rotating few-cycle laser beams. The circularly polarized supercontinuum is produced at a central photon energy of 33 eV with a transform limit of 190 as and a predicted linear chirp of 330 as. By adjusting the ellipticity of the two counter-rotating driving pulses simultaneously, we control the polarization state of isolated extreme-ultraviolet pulses—from circular through elliptical to linear polarization—without sacrificing conversion efficiency. Access to the purely circularly polarized supercontinuum, combined with full helicity and ellipticity control, paves the way towards attosecond metrology of circular dichroism.

Ultrafast extreme-ultraviolet (EUV) and soft X-ray beams carrying spin angular momentum are used in many different fields of science due to their ability to temporally investigate the structural, electronic and magnetic properties of materials. For example, ultrafast circularly polarized beams are particularly important in the study of chiral molecules, making it possible to discriminate between enantiomers and resolve their dynamics. Bright ultrafast beams with adjustable polarization have recently been produced using both free-electron laser (FEL) facilities[1–4] and tabletop high-harmonic generation (HHG) set-ups[5–9]. Several schemes to generate circularly polarized beams have been implemented at X-ray FELs, including converting linearly polarized beams to circularly polarized beams using a phase retarder, or by using special undulators to precisely control the motion of electrons, and thus the polarization of the emitted radiation. FEL X-ray pulses are emitted with pulse durations as short as tens of femtoseconds[10]. However, although FEL radiation is well known for its brightness, the high cost of such large-scale facilities results in limited access.

A tabletop alternative to FELs is the extreme nonlinear optical process of HHG, where infrared light from a femtosecond laser can be coherently upconverted to produce fully coherent beams in the EUV and soft X-ray regimes with sub-femtosecond or attosecond pulse durations. HHG is a non-perturbative process that has both microscopic and macroscopic character. Microscopically, an atom is first ionized by the driving field, then the electronic wave packet is accelerated and finally driven back to recollide with the parent ion[11,12]. In this last step, the kinetic energy acquired from the laser field is released as high-frequency harmonics of the fundamental laser. Macroscopically, the phase relationship between harmonics radiated from different atoms in the target becomes crucial for determining both the efficiency and the spatio-temporal properties of the emitted coherent radiation[13–17].

Although tremendous progress has been made in generating and using linearly polarized high-harmonic beams, until recently it was not possible to directly generate bright circularly polarized HHG pulses. This is because when HHG is driven by a linearly polarized laser, the ionized electronic wave packet accelerates on a linear trajectory and therefore easily recollides with the parent ion. In contrast, with circularly polarized driving lasers (or elliptically polarized lasers with large ellipticity), the probability of electron recollision is strongly suppressed and therefore no harmonics are emitted[18,19]. Alternatively, EUV waveplates could be used to convert linearly polarized harmonics to circular polarization; however, this is extremely inefficient and is restricted to narrow bandwidths[20].

Recent work has demonstrated the synthesis of bright circularly polarized high-harmonic attosecond pulse trains by modifying the microscopic physics of HHG through the combination of collinear counter-rotating beams with different frequencies and macroscopic phase matching[5,6,8,9,21]. More recently, by using non-collinear counter-rotating circularly polarized driving lasers for HHG (NCP-HHGs), circularly polarized trains of attosecond pulses were experimentally generated that emerge as angularly separated beams[22]. Furthermore, numerical simulations suggest that isolated attosecond bursts of circularly polarized light can be generated in NCP-HHG, provided that the driving laser pulse duration is reduced to the few-cycle regime[23].

Here we experimentally generate circularly polarized high-harmonic EUV supercontinua, spanning photon energies from 20 to 45 eV, and thus supporting 190 as (transform-limited) isolated pulses. As discussed in more detail in the following, although the single isolated high-harmonic burst is predicted to be linearly chirped to ~330 as, it represents, to our knowledge, the broadest coherent circularly polarized supercontinuum generated so far. This experiment is realized by the use of few-cycle pulses synthesized from compressed multiple thin-plate supercontinua

[1]Institute of Photonics Technologies, National Tsing Hua University, Hsinchu, Taiwan. [2]Institute of Atomic and Molecular Sciences, Academica Sinica, Taipei, Taiwan. [3]Grupo de Investigación en Aplicaciones del Láser y Fotónica, Departamento de Física Aplicada, University of Salamanca, Salamanca, Spain. [4]JILA – Department of Physics, University of Colorado and NIST, Boulder, CO, USA. [5]Department of Physics, Colorado School of Mines, Golden, CO, USA. [6]Department of Physics, National Tsing Hua University, Hsinchu, Taiwan. *e-mail: l9xas9966514@gmail.com; mingchang@mx.nthu.edu.tw

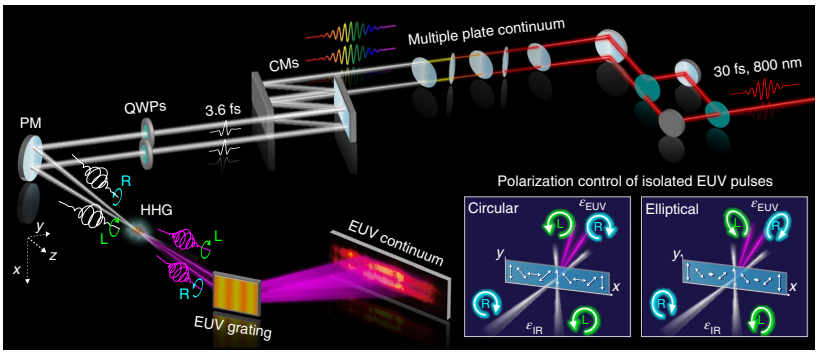

Fig. 1 | Set-up for generating arbitrarily polarized isolated high-harmonic pulses using few-cycle driving lasers. Controlling the ellipticity of the driving lasers results in coherent control of the amplitude and phase of the linearly polarized HHG fields at the focal plane, resulting in polarization control of the HHG beams in the far field. CM, chirped mirror; QWP, quarter-wave plate: PM, off-axis parabolic mirror. Insets: electric field distributions at the focal plane.

(MPContinua)[24]. The unique scalability of the MPContinuum technique enables the realization of almost identical near-single-cycle driving pulses without using split mirrors or a second compressor set-up. To characterize the isolated circularly polarized high-harmonic pulses, the pulse temporal contrast is characterized using an EUV Fourier-transform field autocorrelation, which is a reliable technique to distinguish an isolated EUV pulse from a train of such pulses[25]. Most importantly, we show that this work provides the first polarization control of isolated high-harmonic pulses. We smoothly control the ellipticity of isolated EUV pulses, from linear through elliptical to circular polarization, while retaining the conversion efficiency. Remarkably, the polarization control is based on the non-perturbative nature of HHG, as we unequivocally demonstrate that the polarization state of the isolated EUV pulses depends strongly on the quantum trajectory followed in the HHG process. The polarization state of the isolated high-harmonic pulses is fully analysed with a rigorous and reliable polarimeter composed of two rotatable sets of triple-reflection polarization analysers, which unambiguously determine their ellipticity (the ratio of the minor axis to the major axis of elliptically polarized light), helicity (left-handed or right-handed circular polarization) and degree of polarization (the energy portion of pulses that is polarized). The generation and characterization of arbitrarily polarized high-harmonic pulses represents a major breakthrough in attosecond science, enabling the real-time measurement of energy and angular momentum transfer in magnetic materials and the symmetry-dependent characteristics of chiral molecules.

Polarization control of isolated high-harmonic pulses

To control the ellipticity of high-harmonic EUV pulses ε_{EUV}, two identical elliptically polarized few-cycle fundamental laser beams with equal ellipticity ε_{IR} (but opposite helicity) were prepared and focused into a gas jet in a non-collinear geometry (Fig. 1). These two electric fields can be written as

$$\begin{aligned} E_{IR,R}(x,t-D) &= \frac{e^{-i(+kz\cos\theta+kx\sin\theta)}}{\sqrt{1+\varepsilon_{IR}^2}}[\varepsilon_{IR}\hat{x}+i\hat{y}] \\ &\quad e^{-2\ln 2\left(\frac{t-D}{\tau}\right)^2+i\omega(t-D)+i\Phi_{CEP}} \\ E_{IR,L}(x,t) &= \frac{e^{-i(+kz\cos\theta-kx\sin\theta)}}{\sqrt{1+\varepsilon_{IR}^2}}[\varepsilon_{IR}\hat{x}-i\hat{y}] \\ &\quad e^{-2\ln 2\left(\frac{t}{\tau}\right)^2+i\omega t+i\Phi_{CEP}} \end{aligned} \quad (1)$$

where $E_{IR,R}$ ($E_{IR,L}$) represents right-handed (left-handed) elliptically polarized infrared (IR) light, $k=2\pi/\lambda_{IR}$ is the fundamental wavevector, λ_{IR} is the wavelength of the driving laser, θ is the half-crossing angle between the two fundamental laser beams, x and z are the transverse and longitudinal distances away from the centre of the focal plane, respectively, τ is the full-width at half-maximum (FWHM) pulse duration, D is the delay between these two Gaussian-shaped electric fields, ω is the angular frequency of the driving laser, and Φ_{CEP} is the carrier-envelope phase of the fundamental pulses.

At the focal plane ($z=0$) and for perfect temporal overlap ($D=0$), the electric field E_{focus} becomes

$$\begin{aligned} E_{focus}(x,t) &= E_{IR,R}(x,t)+E_{IR,L}(x,t) \\ &= \frac{2}{\sqrt{(1+\varepsilon_{IR}^2)}}[\varepsilon_{IR}\cos(kx\sin\theta)\hat{x}+\sin(kx\sin\theta)\hat{y}] \\ &\quad e^{-2\ln 2(t/\tau)^2+i\omega t+i\Phi_{CEP}} \end{aligned} \quad (2)$$

Therefore, E-field vectors are created on the focal plane rotating across the transverse direction $\hat{x}$ with a period of $2\pi/(k\sin\theta)$. For any specific position x, the local E-field oscillates linearly, which is ideal for efficient single-atom HHG. In the far-field, the high-harmonic field distribution and vector varying with time can be numerically calculated with the 'thin slab model' (TSM)[26,27], a semiclassical method based on Fraunhofer diffraction (see Supplementary Section 2 for details). The diffraction integral of the linearly polarized oscillating high-harmonic field distributed along $\hat{x}$ (Fig. 1) results in two elliptically polarized EUV beams. Because both the amplitude and phase of HHG on the focal plane are coherently scaled and spatially imprinted by the driving IR field, ε_{EUV} can be well controlled by ε_{IR}, forming the ellipticity scaling as $\varepsilon_{EUV} \propto \varepsilon_{IR}^{4.5} - \varepsilon_{IR}^{4.8}$, as discussed in more detail in the section 'Complete polarization control of isolated EUV pulses'.

Isolated, circularly polarized EUV pulses

The output of a Ti:sapphire amplifier (30 fs, 1 kHz, 480 μJ) was split into two beams using a slightly misaligned Mach–Zehnder interferometer (Fig. 1). Both linearly polarized laser beams were focused into an array of individual thin quartz plates of 50 μm thickness to coherently broaden the pulse bandwidth (Supplementary Section 1 and ref. [24]). The resulting MPContinua were simultaneously compressed using the same chirped mirrors to ~3.6 fs (1.3 cycles), as confirmed by polarization gating cross-correlation frequency-resolved optical gating[28]. The NCP-HHG was implemented by inserting quarter

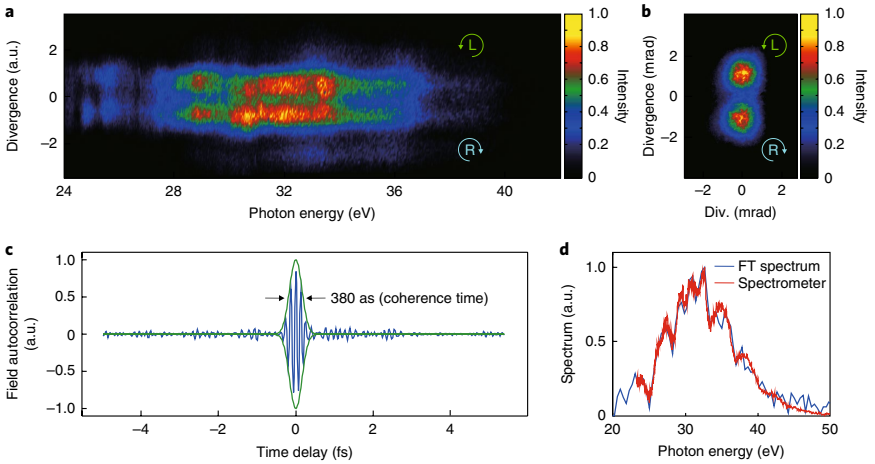

Fig. 2 | Experimental demonstration and characterization of circularly polarized EUV HHG supercontinua. a, Upper and lower spectra are left- and right-circularly polarized HHG supercontinua with $\varepsilon_{EUV,L} = 0.93$ and $\varepsilon_{EUV,R} = 0.9$. **b**, Beam profiles. Their normalized intensity scales are represented in the colour bar. **c**, Experimental field autocorrelation trace of circularly polarized HHG pulses (Supplementary Video 1). **d**, Circularly polarized EUV spectrum measured by a grating-dispersed spectrometer (red), compared with the Fourier transform of the field autocorrelation trace (blue).

waveplates into the two laser beams to produce counter-rotating polarization states. The two laser beams were then focused in a crossed-beam geometry onto a continuous-flow Ar gas jet placed in a vacuum chamber. The half-crossing angle was ~17 mrad, and the pulse energies were ~70 μJ. Two 200 nm Al filters were used to reject the residual laser light, and the HHG output was spectrally dispersed using an EUV spectrometer, calibrated to better than 0.3 eV resolution. When both driving pulses overlapped in time and space, a continuous high-harmonic spectrum was observed (Fig. 2), because both driving pulses are near single cycles. To optimize the EUV continuum, the two counter-rotating driving pulses were delayed with respect to each other, to narrow the linear-polarization temporal-gating window and thus obtain an isolated high-harmonic pulse[23,29] (Supplementary Section 3). Figure 2a presents the spatially resolved high-harmonic supercontinua for a relative time delay of 1.8 fs. The two HHG spectra with right and left circular polarization obtained with the NCP-HHG technique are clearly distinguishable. The generated photon flux of each beam is $\sim 3 \times 10^7$ counts per second over the whole EUV spectrum. Note that low-order harmonics below 24 eV are mainly reabsorbed in the Ar generating medium.

To measure the temporal coherence and to distinguish the generation of an isolated EUV pulse from a train of pulses, we implemented a Fourier-transform field autocorrelation, as has previously been done for linearly polarized pulses[25]. One of the circularly polarized EUV beams was spatially selected and sent to a split mirror, separating the beam into two halves. A piezo actuator controlled the relative time delay between the two halves of the beam with sub-nanometre resolution. The resulting interference pattern was measured by an EUV charge-coupled device (CCD) as a function of time delay, providing the autocorrelation trace of the HHG beam (Supplementary Video 1). The HHG autocorrelation trace in Fig. 2c shows that the main EUV pulse has a high-amplitude contrast compared to the adjacent pulses and a coherence length of 380 as. Although the carrier-envelope phase (Φ_{CEP}) of IR pulses was not stabilized in our experiment, our simulation results demonstrate that isolated high-harmonic pulses are still generated by controlling the linear-polarization temporal-gating window (Supplementary Section 3). Figure 2d shows a comparison between the spectrum extracted from a Fourier transform of the field autocorrelation trace and that experimentally measured by the grating-based spectrometer. The consistency between the two spectra indicates that all circularly polarized EUV light has been successfully delivered and spatially overlapped at one focal spot, which is an essential criterion for circularly polarized attosecond pulse generation. The observed bandwidth supports 190 as transform-limited pulses, while our theoretical simulations predict that isolated chirped pulses of 330 as are produced (Fig. 4 and Supplementary Fig. 4). It is worth noting that using a field autocorrelator, we can clearly show that the supercontinuum corresponds to an isolated pulse, while the good spectrum and beam observed indicate high temporal and spatial coherence of the circularly polarized pulses.

Complete polarization control of isolated EUV pulses

Furthermore, by adjusting the ellipticity ε_{IR} of the two counter-rotating driving pulses, we demonstrate full control of ellipticity of isolated high-harmonic EUV pulses, while keeping the high-harmonic beam quality and conversion efficiency (Fig. 3, Supplementary Fig. 8 and Supplementary Table 1). To maintain linearly polarized *E*-fields at the focal plane, as shown in equation (2) and Fig. 1, we prepared two counter-rotating driving pulses with identical elliptical polarization $\varepsilon_{IR,R} = \varepsilon_{IR,L} = \varepsilon_{IR}$. The resulted polarization state of the right-handed and left-handed EUV pulses, $\varepsilon_{EUV,R}$ and $\varepsilon_{EUV,L}$, were measured separately by one reflection polarimeter consisting of two independent rotatable sets of triple-reflection polarizers, with the first set acting as the phase shifter and the second acting as a linear-polarization analyzer as shown in Fig. 3a[30]. Such a polarimeter unambiguously determines the ellipticity and helicity of the EUV pulses, as well as discriminating between unpolarized and polarized light by retrieving the Stokes parameters (Supplementary Section 7). While those two polarizer sets are set in the same rotating angle ($\alpha = \beta$), the polarimeter becomes a great EUV polarization analyser with an extinction ratio of ~80:1. Figure 3c shows the angularly resolved intensity of the high-harmonic pulses recorded under different orientations of the analyser axis, together with a table showing the ellipticity of the high-harmonic pulses retrieved by the polarimeter. It is worth mentioning that we experimentally observed almost identical ellipticity and tilt over the entire HHG spectra, clearly indicating that full polarization control of a very broad bandwidth of several tens of electronvolts is straightforward with the NCP-HHG geometry (Supplementary Section 8).

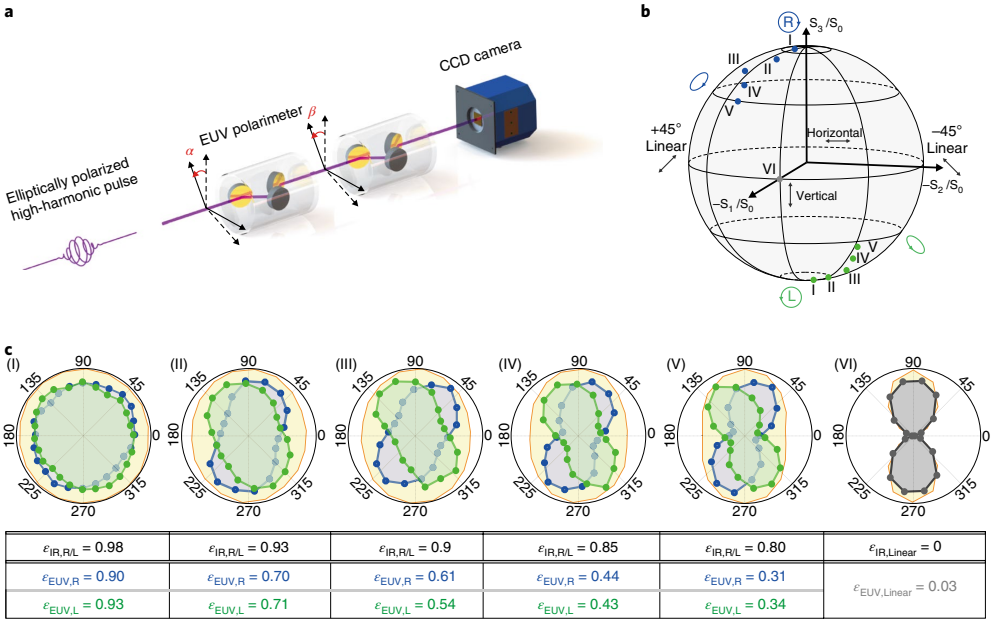

$\varepsilon_{IR,R/L}$ = 0.98	$\varepsilon_{IR,R/L}$ = 0.93	$\varepsilon_{IR,R/L}$ = 0.9	$\varepsilon_{IR,R/L}$ = 0.85	$\varepsilon_{IR,R/L}$ = 0.80	$\varepsilon_{IR,Linear}$ = 0
$\varepsilon_{EUV,R}$ = 0.90	$\varepsilon_{EUV,R}$ = 0.70	$\varepsilon_{EUV,R}$ = 0.61	$\varepsilon_{EUV,R}$ = 0.44	$\varepsilon_{EUV,R}$ = 0.31	$\varepsilon_{EUV,Linear}$ = 0.03
$\varepsilon_{EUV,L}$ = 0.93	$\varepsilon_{EUV,L}$ = 0.71	$\varepsilon_{EUV,L}$ = 0.54	$\varepsilon_{EUV,L}$ = 0.43	$\varepsilon_{EUV,L}$ = 0.34	

Fig. 3 | Full polarization control of isolated high-harmonic pulses. a, Schematic of the EUV polarimeter used to characterize the polarization state of isolated high-harmonic pulses, where α and β are the rotating angles of the two mirror sets, respectively. **b**, Several polarization states, Stokes parameters (S_1/S_0, S_2/S_0, S_3/S_0), have been generated, characterized and marked on the Poincaré surface. **c**, The polarization states of the input IR (orange lines) and output EUV (blue and green dots) are measured by one IR and one EUV polarization analyser, respectively, and are depicted in the polar plots. The table gives the ellipticity relation between ε_{IR} and ε_{EUV}. For comparison, linear high-harmonic pulses driven by a linearly polarized fundamental were also measured (grey dots in inset VI).

To verify the working principle behind this method, we performed numerical simulations of the NCP-HHG technique using two theoretical methods: (1) calculations of HHG including propagation, using a combination of the fully quantum strong-field approximation (SFA) and the electromagnetic field propagator[31]; and (2) a semiclassical HHG approximation, the TSM, based on Fraunhofer diffraction[26,27]. Figure 4a presents $\varepsilon_{EUV,R/L}$ versus ε_{IR} for experimental (dots), quantum SFA theory (stars) and TSM results with (pink crosses), and without (yellow crosses) the dipole harmonic phase. We see that the ellipticity scaling obtained by SFA with propagation ($\varepsilon_{EUV} \propto \varepsilon_{IR}^{4.5}$) or the TSM ($\varepsilon_{EUV} \propto \varepsilon_{IR}^{4.6}$) agrees well with that observed in the experiments ($\varepsilon_{EUV} \propto \varepsilon_{IR}^{4.8}$). The excellent agreement allows us to obtain a very straightforward ellipticity control that contrasts with all other approaches for polarization control of high-harmonic pulses so far, which are restricted to narrow bandwidths, low yields or cannot support isolated attosecond pulses[5–9,20,32–35]. Here, the quantum SFA simulations including propagation were performed using the 3.6 fs driving field as characterized in the experiment, applying a time delay between the non-collinear pulses of $D = +1.8$ fs (+0.7 cycles of IR). The ε_{EUV} is calculated for the far-field harmonic signal detected at ±1.0 mrad, integrating over a 1 mrad spatial window, mimicking the experiment (for more details of the simulation parameters see Supplementary Section 2).

The experimental results also show that the orientations of the two counter-rotating high-harmonic beams are mirror-symmetrically tilted with respect to the major axis of the fundamental beams (Fig. 3c). Figure 4a presents the scaling of the tilt angle versus ε_{IR} for experiments (dots) and quantum SFA theory (stars). To gain insight into the scalings of the ellipticity and tilt angle, we performed semiclassical simulations using the TSM. One of the advantages of the TSM is that it allows us to identify the role of the intensity-dependent dipole harmonic phase, which is the phase acquired by the electronic wave packet in the microscopic HHG process. In Fig. 4a, the TSM results are plotted including (pink crosses) and deliberately neglecting (yellow crosses) the dipole harmonic phase. The present results correspond to a photon energy of 33 eV, which is the central energy of the harmonic pulses, integrated over a 1 mrad window in the far-field, centred at ±1.0 mrad (for more details about the TSM calculations see Supplementary Section 2). Our TSM simulations unequivocally show (1) the relevance of the dipole phase in the ellipticity scaling, and (2) that the tilt is induced mainly by the intensity-dependent dipole phase of HHG. Thus, both the ellipticity and tilt angle of the harmonic pulses depend strongly on the quantum trajectory followed in the HHG process. According to equation (2), when the driving fields are elliptically polarized ($\varepsilon_{IR} < 1$) at the focal plane, not only does the direction of the linearly polarized E-field rotate, but there is also a field-amplitude modulation with a period of $2\pi/(k\sin\theta)$ along the transverse $\hat{x}$ direction. Because the dipole harmonic phase depends on the field intensity, such amplitude modulation induces an additional dipole phase modulation along the $\hat{x}$ direction. In short, the field-amplitude modulation on the focal plane actually induces an additional phase shift between the far-field $\hat{x}$ and $\hat{y}$ harmonic-field components, modifying the EUV ellipticity and rotating the major axis of the high-harmonic pulses.

Finally, Figure 4b–d presents numerical simulations of the time evolution of the high-harmonic pulses obtained for $\varepsilon_{IR} = 1.0$ (Fig. 4b), $\varepsilon_{IR} = 0.9$ (Fig. 4c) and $\varepsilon_{IR} = 0.8$ (Fig. 4d), for right-handed (blue) and left-handed (green) helicities, with a time delay of $D = +0.7$ cycles of IR. These results were obtained with our quantum simulations (SFA and propagation) using the 3.6 fs driving field as characterized in the experiment, and a time-gating delay of 1.8 fs. As can be observed, isolated attosecond pulses with controlled ellipticity are obtained. Note

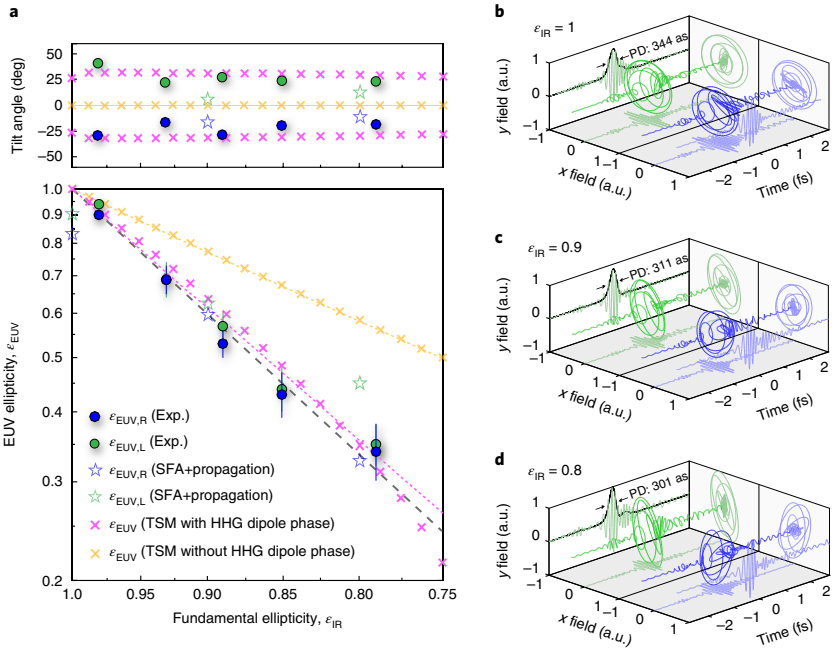

Fig. 4 | Ellipticity and tilt angle scaling of isolated high-harmonic pulses. a, Top: relative tilt angle of the major axis between the EUV pulses and the driving laser versus ε_{IR}. Bottom: log–log plot of the observed relation between ε_{EUV} and ε_{IR} (data were obtained from the result in Fig. 3c and Supplementary Table 1; the error bars represent the standard deviation (thin vertical lines), extracted from 5 individual polarization analyses). The ellipticity scaling can be approximated as $\varepsilon_{EUV} \propto \varepsilon_{IR}^{4.8}$ (black dashed line), in excellent agreement with the scaling of the TSM, including the HHG dipole phase (pink short dashed line), $\varepsilon_{EUV} \propto \varepsilon_{IR}^{4.6}$. **b**–**d**, Time evolution of the high-harmonic attosecond pulses obtained using ε_{IR} = 1.0 (**b**), ε_{IR} = 0.9 (**c**) and ε_{IR} = 0.8 (**d**) for the right-handed (blue) and left-handed (green) helicities detected at ±1 mrad, respectively. Black lines show the temporal intensity profiles and pulse durations (PDs) of 344, 311 and 301 as, respectively.

that each panel is normalized to the same quantity, so the upconversion efficiencies are similar for each ε_{IR}, agreeing well with our experimental observations (Supplementary Table 1). The simulations also indicate that, for each ε_{IR}, the pulse durations of resultant circularly or elliptically polarized attosecond pulses are very similar and linearly chirped to approximately 330 as because of the attochirp; however, these could be compressed to near their transform limit of ~190 as using chirped multilayer mirrors or metal-foil filters[36].

In summary, we demonstrate a robust polarization control scheme of isolated high-harmonic EUV pulses by exploiting non-collinear HHG driven by two counter-rotating few-cycle laser beams. The circularly polarized supercontinuum is produced in the photon energy range from 20 eV to 45 eV, with a high >0.90 degree of ellipticity. The isolation and temporal coherence of high-harmonic bursts was measured by EUV interferometry, and the polarization state of the pulses was characterized with an EUV polarimeter. Our simulation results provide clear insight into the three-dimensional electric field vector on attosecond timescales, revealing a pulse duration of ~330 as. Furthermore, by adjusting the ellipticity of the two counter-rotating driving pulses simultaneously, we achieve full control of the polarization state of high-harmonic pulses from circular through elliptical to linear polarization, while retaining the conversion efficiency. We unequivocally identify that the non-perturbative dipole phase of HHG is essential in the ellipticity and tilt angle scaling of HHG pulses, obtaining an ellipticity scaling rule of $\varepsilon_{EUV} \propto \varepsilon_{IR}^{4.5} - \varepsilon_{IR}^{4.8}$. This new technique presents an accessible and reliable route for the generation of isolated arbitrarily polarized attosecond EUV pulses. Because of the importance of this new capability for ultrafast dynamics in angular momentum transfer in atoms, chiral molecules, and 2D and magnetic materials[37–49], where very fast dynamics are known to occur and are not currently understood, our work represents an experimental breakthrough with several new aspects and impacts. This work can therefore motivate future work on methods to fully characterize the three-dimensional electric-field vector on attosecond timescales, which is currently a great challenge.

Data availability. The data that support the plots within this paper and other findings of this study are available from the corresponding author upon reasonable request.

Received: 9 November 2017; Accepted: 8 March 2018;
Published online: 23 April 2018

References

1. Spezzani, C. et al. Coherent light with tunable polarization from single-pass free-electron lasers. *Phys. Rev. Lett.* **107**, 084801 (2011).
2. Suzuki, M., Inubushi, Y., Yabashi, M. & Ishikawa, T. Polarization control of an X-ray free-electron laser with a diamond phase retarder. *J. Synchrot. Radiat.* **21**, 466–472 (2014).
3. Lutman, A. A. et al. Polarization control in an X-ray free-electron laser. *Nat. Photon.* **10**, 468–472 (2016).
4. Allaria, E. et al. Control of the polarization of a vacuum-ultraviolet, high-gain, free-electron laser. *Phys. Rev. X* **4**, 041040 (2014).
5. Eichmann, H., Egbert, A., Nolte, S., Momma, C. & Wellegehausen, B. Polarization-dependent high-order two-color mixing. *Phys. Rev. A* **51**, R3414–R3417 (1995).
6. Fleischer, A., Kfir, O., Diskin, T., Sidorenko, P. & Cohen, O. Spin angular momentum and tunable polarization in high-harmonic generation. *Nat. Photon.* **8**, 543–549 (2014).

7. Ferré, A. et al. A table-top ultrashort light source in the extreme ultraviolet for circular dichroism experiments. *Nat. Photon.* **9**, 93–98 (2015).
8. Kfir, O. et al. Generation of bright phase-matched circularly-polarized extreme ultraviolet high harmonics. *Nat. Photon.* **9**, 99–105 (2015).
9. Fan, T. et al. Bright circularly polarized soft X-ray high harmonics for X-ray magnetic circular dichroism. *Proc. Natl Acad. Sci. USA* **112**, 14206–14211 (2015).
10. Ribic, P. R. & Margaritondo, G. Status and prospects of X-ray free-electron lasers (X-FELs): a simple presentation. *J. Phys. D* **45**, 213001 (2012).
11. Schafer, K. J., Yang, B., DiMauro, L. F. & Kulander, K. C. Above threshold ionization beyond the high harmonic cutoff. *Phys. Rev. Lett.* **70**, 1599–1602 (1993).
12. Corkum, P. B. Plasma perspective on strong-field multiphoton ionization. *Phys. Rev. Lett.* **71**, 1994–1997 (1993).
13. Balcou, P., Salieres, P., L'Huillier, A. & Lewenstein, M. Generalized phase-matching conditions for high harmonics: the role of field-gradient forces. *Phys. Rev. A* **55**, 3204–3210 (1997).
14. Rundquist, A. et al. Phase-matched generation of coherent soft X-rays. *Science* **280**, 1412–1415 (1998).
15. Gaarde, M. B., Tate, J. L. & Schafer, K. J. Macroscopic aspects of attosecond pulse generation. *J. Phys. B* **41**, 132001 (2008).
16. Arpin, P., Murnane, M. M. & Kapteyn, H. C. Quasi-phase-matching of momentum and energy in nonlinear optical processes. *Nat. Photon.* **4**, 571–575 (2010).
17. Sun, H.-W. et al. Extended phase matching of high harmonic generation by plasma-induced defocusing. *Optica* **4**, 976–981 (2017).
18. Dietrich, P., Burnett, N. H., Ivanov, M. & Corkum, P. B. High-harmonic generation and correlated two-electron multiphoton ionization with elliptically polarized light. *Phys. Rev. A* **50**, R3585–R3588 (1994).
19. Weihe, F. A. et al. Polarization of high-intensity high-harmonic generation. *Phys. Rev. A* **51**, R3433–R3436 (1995).
20. Vodungbo, B. et al. Polarization control of high order harmonics in the EUV photon energy range. *Opt. Express* **19**, 4346–4356 (2011).
21. Medišauskas, L., Wragg, J., van der Hart, H. & Ivanov, M. Y. Generating isolated elliptically polarized attosecond pulses using bichromatic counterrotating circularly polarized laser fields. *Phys. Rev. Lett.* **115**, 153001 (2015).
22. Hickstein, D. D. et al. Non-collinear generation of angularly isolated circularly polarized high harmonics. *Nat. Photon.* **9**, 743–750 (2015).
23. Hernandez-Garcia, C. et al. Schemes for generation of isolated attosecond pulses of pure circular polarization. *Phys. Rev. A* **93**, 043855 (2016).
24. Lu, C.-H. et al. Generation of intense supercontinuum in condensed media. *Optica* **1**, 400–406 (2014).
25. Chen, M.-C. et al. Generation of bright isolated attosecond soft X-ray pulses driven by multicycle midinfrared lasers. *Proc. Natl Acad. Sci. USA* **111**, E2361–E2367 (2014).
26. Hernández-García, C., San Román, J., Plaja, L. & Picón, A. Quantum-path signatures in attosecond helical beams driven by optical vortices. *New. J. Phys.* **17**, 093029 (2015).
27. Rego, L., San Román, J., Picón, A., Plaja, L. & Hernández-García, C. Nonperturbative twist in the generation of extreme-ultraviolet vortex beams. *Phys. Rev. Lett.* **117**, 163202 (2016).
28. Trebino, R. et al. Measuring ultrashort laser pulses in the time-frequency domain using frequency-resolved optical gating. *Rev. Sci. Instrum.* **68**, 3277–3295 (1997).
29. Heyl, C. M. et al. Noncollinear optical gating. *New. J. Phys.* **16**, 052001 (2014).
30. Koide, T. et al. Elliptical-polarization analyses of synchrotron radiation in the 5–80-eV region with a reflection polarimeter. *Nucl. Instrum. Methods Phys. Rec. Sect. A* **308**, 635–644 (1991).
31. Hernández-García, C. et al. High-order harmonic propagation in gases within the discrete dipole approximation. *Phys. Rev. A* **82**, 033432 (2010).
32. Xie, X. et al. Internal momentum state mapping using high harmonic radiation. *Phys. Rev. Lett.* **101**, 033901 (2008).
33. Zhou, X. et al. Elliptically polarized high-order harmonic emission from molecules in linearly polarized laser fields. *Phys. Rev. Lett.* **102**, 073902 (2009).
34. Fleischer, A., Sidorenko, P. & Cohen, O. Generation of high-order harmonics with controllable elliptical polarization. *Opt. Lett.* **38**, 223–225 (2013).
35. Dorney, K. M. et al. Helicity-selective enhancement and polarization control of attosecond high harmonic waveforms driven by bichromatic circularly polarized laser fields. *Phys. Rev. Lett.* **119**, 063201 (2017).
36. Chini, M., Zhao, K. & Chang, Z. The generation, characterization and applications of broadband isolated attosecond pulses. *Nat. Photon.* **8**, 178–186 (2014).
37. Stöhr, J. et al. Element-specific magnetic microscopy with circularly polarized X-rays. *Science* **259**, 658–661 (1993).
38. Boeglin, C. et al. Distinguishing the ultrafast dynamics of spin and orbital moments in solids. *Nature* **465**, 458–461 (2010).
39. Meyer-Ilse, J., Akimov, D. & Dietzek, B. Recent advances in ultrafast time-resolved chirality measurements: perspective and outlook. *Laser Photon. Rev.* **7**, 495–505 (2013).
40. Graves, C. E. Nanoscale spin reversal by non-local angular momentum transfer following ultrafast laser excitation in ferrimagnetic GdFeCo. *Nat. Mater.* **12**, 293–298 (2013).
41. Chefdeville, S. et al. Direct determination of absolute molecular stereochemistry in gas phase by Coulomb explosion imaging. *Science* **341**, 1094–1096 (2013).
42. Bigot, J.-Y., Vomir, M. & Beaurepaire, E. Coherent ultrafast magnetism induced by femtosecond laser pulses. *Nat. Phys.* **5**, 515–520 (2009).
43. Mangot, L. et al. Broadband transient dichroism spectroscopy in chiral molecules. *Opt. Lett.* **35**, 381–383 (2010).
44. Janssen, M. H. & Powis, I. Detecting chirality in molecules by imaging photoelectron circular dichroism. *Phys. Chem. Chem. Phys.* **16**, 856–871 (2014).
45. Cireasa, R. et al. Probing molecular chirality on a sub-femtosecond timescale. *Nat. Phys.* **11**, 654–658 (2015).
46. Tao, Z. et al. Direct time-domain observation of attosecond final-state lifetimes in photoemission from solids. *Science* **353**, 62–67 (2016).
47. Fidler, A. F., Singh, V. P., Long, P. D., Dahlberg, P. D. & Engel, G. S. Dynamic localization of electronic excitation in photosynthetic complexes revealed with chiral two-dimensional spectroscopy. *Nat. Commun.* **5**, 3286 (2017).
48. Chen, C. et al. Distinguishing attosecond electron–electron scattering and screening in transition metals. *Proc. Natl Acad. Sci. USA* **114**, E5300–E5307 (2017).
49. Beaulieu, S. et al. Probing ultrafast dynamics of chiral molecules using time-resolved photoelectron circular dichroism. *Faraday Discuss.* **194**, 325–348 (2016).

Acknowledgements

The experimental work was carried out at National Tsing Hua University, Institute of Photonics Technologies, supported by the Ministry of Science and Technology, Taiwan (grants 105-2112-M-007-030-MY3, 105-2112-M-001-030 and 104-2112-M-007-012-MY3). The concept of isolated circularly polarized attosecond pulses was developed by C.H.-G., D.D.H., M.M.M., C.G.D., H.C.K., A.B. and A.J.-B.. C.H.-G. acknowledges support from the Marie Curie International Outgoing Fellowship within the EU Seventh Framework Programme for Research and Technological Development (2007–2013), under Research Executive Agency grant agreement no. 328334. C.H.-G. and L.P. acknowledge support from Junta de Castilla y León (SA046U16) and the Ministerio de Economía y Competitividad (FIS2013-44174-P, FIS2016-75652-P). C.H.-G. acknowledges support from a 2017 Leonardo Grant for Researchers and Cultural Creators (BBVA Foundation). M.M.M. and H.C.K. acknowledge support from the Department of Energy Basic Energy Sciences (award no. DE-FG02-99ER14982) for the concepts and experimental set-up. For part of the theory, A.B., A.J.-B., C.G.D., M.M.M. and H.C.K. acknowledge support from a Multidisciplinary University Research Initiatives grant from the Air Force Office of Scientific Research (award no. FA9550-16-1-0121). A.J.-B. also acknowledges support from the US National Science Foundation (grant no. PHY-1734006). This work utilized the Janus supercomputer, which is supported by the US National Science Foundation (grant no. CNS-0821794) and the University of Colorado, Boulder. This research made use of the high-performance computing resources of the Castilla y León Supercomputing Center (SCAYLE, www.scayle.es), financed by the European Regional Development Fund (ERDF). J.L.E. acknowledges support from the National Science Foundation Graduate Research Fellowship (DGE-1144083). L.R. acknowledges support from the Ministerio de Educación, Cultura y Deporte (FPU16/02591).

Author contributions

P.-C.H., J.-T.H., P.-Y.H., C.-H.L., D.D.H., J.L.E., C.G.D., H.C.K., M.M.M., A.H.K. and M.-C.C. designed the experiment with circularly polarized isolated high-harmonic pulses. P.-C.H., J.-T.H., P.-Y.H., S.-D.Y., A.H.K. and M.-C.C. proposed the full polarization control of HHG and designed the EUV polarimeter. P.-C.H., J.-T.H., P.-Y.H., C.-H.L. and M.-C.C. performed the experiments. C.H.-G., A.B. and A.J.-B. performed the theoretical simulations on circularly polarized isolated attosecond pulses. C.H.-G., L.R. and L.P. worked on the theoretical methods and simulations of the full polarization control of HHG. P.-C.H., C.H.-G., J.-T.H., P.-Y.H., L.R., L.P. and M.-C.C. analysed data. P.-C.H., C.H.-G., L.P., M.M.M. and M.-C.C. wrote the manuscript, to which all authors suggested improvement.

Competing interests

The authors declare no competing interests.

Additional information

Supplementary information is available for this paper at https://doi.org/10.1038/s41566-018-0145-0.

Reprints and permissions information is available at www.nature.com/reprints.

Correspondence and requests for materials should be addressed to P.-C.H. or M.-C.C.

Publisher's note: Springer Nature remains neutral with regard to jurisdictional claims in published maps and institutional affiliations.

A.2 HIGH-ORDER NONLINEAR DIPOLE RESPONSE CHARACTERIZED BY EXTREME ULTRAVIOLET ELLIPSOMETRY

484 Vol. 8, No. 4 / April 2021 / Optica Research Article

optica

High-order nonlinear dipole response characterized by extreme ultraviolet ellipsometry

KUANG-YU CHANG,[1] LONG-CHENG HUANG,[1] KOJI ASAGA,[2,3] MING-SHIAN TSAI,[1] LAURA REGO,[4] PEI-CHI HUANG,[1] HIROKI MASHIKO,[2] KATSUYA OGURI,[2] CARLOS HERNÁNDEZ-GARCÍA,[4] AND MING-CHANG CHEN[1,5,6,*]

[1]Institute of Photonics Technologies, National Tsing Hua University, Hsinchu, Taiwan
[2]NTT Basic Research Laboratories, 3-1 Morinosato Wakamiya, Atsugi, Kanagawa 243-0198, Japan
[3]Department of Electronic Engineering, Tokyo Denki University, 5 Senju-Asahi-cho, Adachi-ku, Tokyo 120-8551, Japan
[4]Grupo de Investigación en Aplicaciones del Láser y Fotónica, Departamento de Física Aplicada, University of Salamanca, Salamanca, Spain
[5]Department of Physics, National Tsing Hua University, Hsinchu, Taiwan
[6]Frontier Research Center on Fundamental and Applied Sciences of Matters, National Tsing Hua University, Hsinchu, Taiwan
*Corresponding author: mingchang@mx.nthu.edu.tw

Received 28 October 2020; revised 3 February 2021; accepted 5 February 2021 (Doc. ID 413531); published 6 April 2021

Polarization engineering and characterization of coherent high-frequency radiation are essential to investigate and control the symmetry properties of light–matter interaction phenomena at their most fundamental scales. This work demonstrates that polarization control and characterization of high-harmonic generation provides an excellent ellipsometry tool that can fully retrieve both the amplitude and phase of a strong-field-driven dipole response. The polarization control of high-harmonic generation is realized by a transient nonlinear dipole grating coherently induced by two noncollinear counterrotating laser fields. By adjusting the ellipticity of the two driving pulses simultaneously, the polarization state of every high-harmonic order can be tuned from linear to highly elliptical, and it is fully characterized through an energy-resolved extreme ultraviolet polarimeter. From the analysis of the polarization state, the ellipsometry indicated that both the amplitude and phase of the high-harmonic dipole scale rapidly with the driving laser field for higher-order harmonics, and, especially, for gases with a small ionization potential. Our experimental results were corroborated by theoretical simulations. Our findings revealed a novel high-harmonic ellipsometry technique that can be used for the next generation of high-harmonic spectroscopy and attosecond metrology studies because of its ability to provide single-digit attosecond accuracy. Our work also paves the way to precisely quantify the strong-field dynamics of fundamental processes associated with the transfer of energy and angular momentum between electron/spin systems and the symmetry-dependent properties of molecules and materials.

https://doi.org/10.1364/OPTICA.413531

1. INTRODUCTION

High-order harmonic generation (HHG), first observed in 1987 [1], describes a frequency upconversion technique in which an intense driving laser is focused into an atomic, molecular, or solid target. As a result of the laser–matter interaction, harmonic frequencies of the driving laser are emitted at the attosecond time scale. HHG in atomic gases can be intuitively understood as a sequence of three steps [2,3]: (i) tunnel ionization of the target, creating an electronic wave packet in the continuum; (ii) acceleration of the electronic wave packet by the strong laser field; and (iii) recombination of the electronic wave packet with the parent ion, with the emission of an attosecond burst of extreme ultraviolet (EUV) coherent light. At the core of the HHG process is the coherent nature of the electronic wave-packet dynamics driven by the intense laser field [4], able to produce a highly coherent beam of high-frequency harmonics of the fundamental field. HHG thus provides a tabletop ultrashort source of EUV/x-ray radiation emitted at the attosecond time scale, which has enabled a wide range of applications, such as for studying ultrafast molecular dissociation [5], for characterizing nanoscale heat flow [6], for following element-specific dynamics in magnetic materials [7,8], and for high-resolution coherent imaging [9,10]. Moreover, HHG can also be driven in molecular or solid targets, in which the emitted EUV radiation encodes unique information about the electronic and geometric arrangements of the radiating molecules or solid systems. This gives rise to self-probing schemes that allow the performance of molecular tomography [11,12], chirality assignment [13–15], and retrieval of the electronic band structure in solids [16].

Remarkably, the quantum wave-packet dynamics leave a unique signature in the phase of the emitted HHG radiation, the so-called dipole phase [17], which influences the wavefront

Research Article Vol. 8, No. 4 / April 2021 / Optica 485

[18,19], spectrum [20], and pulse duration of the emitted attosecond radiation [21]. Intriguingly, the dipole phase is sensitive to the laser field, enabling applications of direct E-field reconstruction [22,23] and light-assisted phase-matching of HHG [24,25]. As a consequence, precise measurements can extract quantitative information about the absolute dipole response—both amplitude and phase—that is essential to explain the quantum dynamics of the HHG process and to advance attosecond science.

Currently, the characterization of the high-harmonic dipole response has followed two main approaches: spectroscopy and interferometry. Spectroscopic methods are based on the spectral modulation of HHG as a function of the driving laser intensity, attributed to the interference between short- and long-quantum paths [26–28]. However, a strong quantum path dependence of the spectrum and wavefront might affect the fringe visibility [29,30]. Thus, the spectral phase information is not fully retrieved from the measured HHG spectra. Interferometric techniques make use of two separate HHG sources interfering with each other, but this approach is also challenging because undesirable mechanical vibrations strongly influence the stability of the fringes [31]. Furthermore, one must devote extreme attention to avoid nonlinear effects in the transmission elements (e.g., the beam splitter, polarizer, wave plate, and vacuum window) when designing the interferometer because any laser-induced change of the refraction index can unbalance two interferometric arms, resulting in a fringe shift [32]. For instance, when two driving fields pass through the same fused-silica window (of thickness 1 mm), a 1 μJ energy difference between them is enough to induce an effective path difference of 2 nm (corresponding to a temporal shift of ≈6.6 as in time) because of the self-phase-modulation effect (assuming a beam size of diameter 1 mm and a pulse duration of 30 fs). Additionally, in HHG experiments, one must account for the macroscopic phase-matching picture, in which the radiation emitted from many—trillions of—single emitters at the target are coherently combined. The differences in the properties of emission radiated at each single atom, which depend strongly on the driving beam mode, might hinder the investigation of the quantum wave-packet dynamics. Thus, extracting accurate information about the dipole response taking place in each emitter remains challenging.

Very recently, we found that the high-order harmonic (HH) dipole phase is a key element that enables the polarization control of attosecond pulses in noncollinear HHG geometry [33]. These results, which provide a unique control rule over the ellipticity of EUV radiation, also establish a strong link between the HH dipole phase and HH polarization, motivating the use of ellipsometry as a novel technique to characterize the HH dipole response. In the late 19th century, Drude first used the phase shift induced between mutually perpendicular components of polarized light to measure the film thickness, which could be considered the birth of ellipsometry. Currently, ellipsometry is one of the most precise and accurate measurement tools and has been widely used in diverse applications such as thin-film characterization, surface molecular imaging, ion-sensing engineering, and integrated circuit technology [34,35]. However, its application in the EUV regime is challenging because of absorption limitations.

In this work, we introduce HH ellipsometry to unveil the complicated dipole dynamics of HHG through the polarization properties of EUV harmonics. Our findings reveal that the single-atom response in HHG, dominated by the short-quantum path, is the primary mechanism behind polarization control when the driving field is arranged in a noncollinear geometry. This allows us to circumvent the macroscopic picture and to use HH ellipsometry to quantify both the amplitude and phase of the HH dipole, tailored by the fundamental driving field. By adding a diffraction element into our EUV polarimeter [see Fig. 1(a) and Supplement 1, Section 1], we can fully resolve the polarization state (the helicity, ellipticity, tilt angle, and degree of polarization) for every high-harmonic order simultaneously. To the best of our knowledge, this is the first all-optical energy-resolved EUV polarimeter in the EUV field, differing from previously published EUV polarimeter and polarizer work—in which only monochromatic light was measured [33,35,36] or only an upper bound of the ellipticity was provided without knowing the helicity [37,38], and molecular polarimetry [39,40]—which requires a detailed knowledge of the light–molecule interaction.

We show that the polarization control scaling rule found in [33] ($\varepsilon_{\mathrm{EUV}} \propto \varepsilon_{\mathrm{IR}}^{\sigma}$, where $\varepsilon_{\mathrm{EUV}}$ and $\varepsilon_{\mathrm{IR}}$ are the ellipticity of the EUV high-harmonics and infrared (IR) driving field, respectively, and σ is the ellipticity scaling coefficient) depends on not only the harmonic order but also the gaseous species. The ellipticity scaling coefficient σ becomes much larger for higher-order harmonics, especially in atoms of a large atomic number (Z) with a small ionization potential. Ellipsometry retrieval quantitatively shows that the polarization control scaling depends on the effective order of nonlinearity of the high-order harmonics (q_{eff}) and on the intensity-dependent dipole phase coefficient (α), which varies substantially with harmonic order and atomic elements. Remarkably, this study also shows that the power scaling of HHG is highly influenced by the dipole phase. The variation of the dipole phase induced by any inhomogeneity in the driving laser considerably limits the attainable EUV flux and harmonic order. The homogeneity of the driving field becomes essential to achieve high HHG brightness and to extend harmonic energies toward higher frequencies.

2. EXPERIMENTAL RESULTS OF HIGH-HARMONIC ELLIPSOMETRY

We performed HHG in Ar, Kr, and Xe using 35 fs Ti:Sapphire laser pulses arranged in a noncollinear geometry (see Methods and Supplement 1, Section 2). To control the polarization of the HH pulses, two elliptically polarized fundamental beams of the same ellipticity, but opposite helicity, were noncollinearly focused into a gas jet, as shown in Fig. 1(a).

We optimized the HHG in the same spectral range in Ar, Kr, and Xe to directly compare their HH dipole response; Supplement 1 Fig. S3 shows their harmonic spectra. Figure 2 and Supplement 1 Fig. S4 show the HH ellipsometry experimental measurements, including the helicity, ellipticity ($\varepsilon_{\mathrm{EUV}}$), tilt angle ($\tau$), and degree of polarization of the EUV harmonics driven by fundamental fields with varied ellipticities ($\varepsilon_{\mathrm{IR}}$). Our results showed the two counter-rotating HH beams to be mirror symmetrically tilted with respect to the major axis of the fundamental beams (y direction), in agreement with the rotational symmetry property of noble gas atoms. Both τ and $\varepsilon_{\mathrm{EUV}}$ of each harmonic order were scaled disparately, depending on the gaseous species. The complete harmonic-order-dependent ellipticity scaling could be approximated as power relations, as shown in Table 1. When $\varepsilon_{\mathrm{IR}}$ decreased, $\varepsilon_{\mathrm{EUV}}$ decreased more rapidly for higher-order harmonics, especially in high-Z atoms. Higher-order harmonics exhibited a larger tilt-angle τ in

Research Article Vol. 8, No. 4 / April 2021 / Optica 486

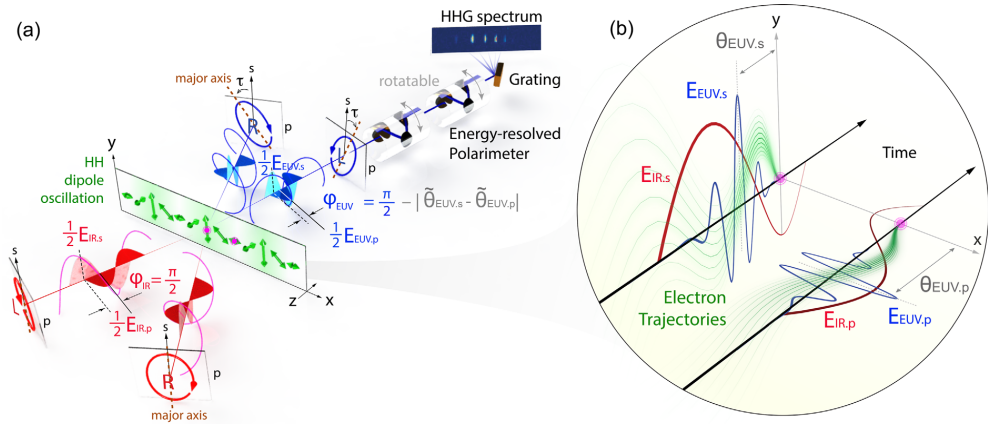

Fig. 1. HH ellipsometry technique is based on interferometry between $E_{\mathrm{EUV}\cdot p}$ and $E_{\mathrm{EUV}\cdot s}$. One can obtain the ratio of intensities and phase shift between $E_{\mathrm{EUV}\cdot p}$ and $E_{\mathrm{EUV}\cdot s}$ from the tilt-angle τ and ellipticity $\varepsilon_{\mathrm{EUV}}$ of the resultant HHG polarization. (a) Two elliptically polarized fundamental beams of the same ellipticity ($E_{\mathrm{IR}\cdot p}/E_{\mathrm{IR}\cdot s} = \varepsilon_{\mathrm{IR}}$) but opposite helicity are focused into a gas jet noncollinearly. The major axis (brown dashed line) points toward the y (or s) direction. In the focal plane, two fundamentals interferingly form local E-field vectors, rotating across direction x. Each location with linearly oscillating polarization acts as a HH local dipole oscillation (green vectors), which, when superposed, constitute a pair of elliptically polarized EUV beams in the far field. An energy-resolved polarimeter is developed to measure the ellipticity $\varepsilon_{\mathrm{EUV}}$ and tilt angle τ with respect to direction y (or s) of the harmonic emissions. (b) Microscopically, high harmonics are generated through ionization, acceleration, and recombination. Both the amplitude and phase of HHG on the focal plane are coherently scaled and spatially imprinted by the driving IR vectors. We highlight only two positions—marked in magenta—in which the dipole is driven by peaks of two perpendicular fundamentals, $E_{\mathrm{IR}\cdot p}$ and $E_{\mathrm{IR}\cdot s}$ (red lines). $E_{\mathrm{EUV}\cdot p/s}$ (blue lines) and $\theta_{\mathrm{EUV}\cdot p/s}$ present the amplitude and phase response of the dipole driven by $E_{\mathrm{IR}\cdot p/s}$; $\tilde{\theta}_{\mathrm{EUV}\cdot p/s}$ presents the phase shift in the far field from the coherent sum of all HH vectors projected to the p and s polarizations, respectively.

Table 1. Ellipticity Relation between $\varepsilon_{\mathrm{EUV}}$ and $\varepsilon_{\mathrm{IR}}$, Extracted from Fig. 2(b)

Gas	23.3 eV $\varepsilon_{15\mathrm{th}}$	26.4 eV $\varepsilon_{17\mathrm{th}}$	29.5 eV $\varepsilon_{19\mathrm{th}}$	32.6 eV $\varepsilon_{21\mathrm{st}}$
Ar	$\propto \varepsilon_{\mathrm{IR}}^{2.2}$	$\propto \varepsilon_{\mathrm{IR}}^{2.8}$	$\propto \varepsilon_{\mathrm{IR}}^{4.0}$	$\propto \varepsilon_{\mathrm{IR}}^{5.8}$
Kr	$\propto \varepsilon_{\mathrm{IR}}^{2.5}$	$\propto \varepsilon_{\mathrm{IR}}^{4.0}$	$\propto \varepsilon_{\mathrm{IR}}^{5.3}$	$\propto \varepsilon_{\mathrm{IR}}^{8.3}$
Xe	$\propto \varepsilon_{\mathrm{IR}}^{5.3}$	$\propto \varepsilon_{\mathrm{IR}}^{10.2}$	$\propto \varepsilon_{\mathrm{IR}}^{13.5}$	

Ar and Kr than in Xe, the reason being that there was a much more rapid amplitude decrease in the x direction in Xe. All these phenomena are associated with the harmonic dipole response—that is, the amplitude and phase of the high-order harmonics scale with the laser field—as explained in detail in the discussion section.

To disentangle the microscopic and macroscopic nature of the HH ellipsometry results, we performed two additional experiments. First, we measured the HH yield as a function of the backing pressure, as shown in Supplement 1, Section 4 and Fig. S6. The results clearly show that the yield of every order of HHG in Ar, Kr, and Xe exhibited a quadratic dependence on pressure, indicating that plasma effects did not influence the propagation of the driving fields. Second, we showed that the polarization state of the high-order harmonics did not depend on the backing pressure of the gas jet (Supplement 1 Fig. S7). Accordingly, we concluded that the polarization control in the noncollinear geometry was not related to the propagation of the IR effect in the generating medium; the single-atom response itself was thus responsible for shaping the polarization properties of the high-order harmonics. In the following section, we reveal the relationship between the polarization scaling of HHG and its complex dipole response.

3. RETRIEVAL OF HIGH-HARMONIC DIPOLE RESPONSE FROM ELLIPSOMETRY

Straightforwardly, ellipsometry can determine the sign of the HH phase change using the tilt direction. In Fig. 2(a), all orientations of the right-handed circularly polarized harmonics tilt counterclockwise with respect to the major axis of the fundamental beams (y direction), whereas the left-handed circularly polarized harmonics tilt clockwise. This effect can be explained in terms of the weight of the s and p components of the local E-field at the focal plane, as depicted in Fig. 1(b). If $E_{\mathrm{IR}\cdot s}$ is stronger than $E_{\mathrm{IR}\cdot p}$, the induced dipole phase advance (negative sign) of $\theta_{\mathrm{EUV}\cdot s} - \theta_{\mathrm{EUV}\cdot p}$ on the focal plane makes $\varphi_{\mathrm{EUV}} = \pi/2 - |\tilde{\theta}_{\mathrm{EUV}\cdot s} - \tilde{\theta}_{\mathrm{EUV}\cdot p}| < \pi/2$, resulting in a positive tilt angle τ in the far field, as defined and marked in Fig. 1(a).

To retrieve quantitative information of the atomic dipole response from an HH ellipsometry measurement, we applied the thin-slab model (TSM), based on strong-field assumptions about the nature of the produced harmonics, which are known to provide satisfactorily qualitative results for HHG in a thin gas-jet configuration [18,19,41–43] (also described in Supplement 1, Sections 6–7). The local q order HH emission in the x and y directions at time t can be described by

$$E_{\mathrm{EUV}\cdot x}(x, y, 0, t) \propto I_{\mathrm{IR}}(x, y, t)^{\frac{q_{\mathrm{eff}}}{2}} e^{i[q\omega_{\mathrm{IR}}t - I_{\mathrm{IR}}(x,y,t)\alpha]} \times \frac{E_{\mathrm{IR}\cdot x}(x, y, 0, t)}{\sqrt{I_{\mathrm{IR}}(x, y, t)}}\hat{x}, \quad (1)$$

$$E_{\mathrm{EUV}\cdot y}(x,y,0,t) \propto I_{\mathrm{IR}}(x,y,t)^{\frac{q_{\mathrm{eff}}}{2}} e^{i[q\omega_{\mathrm{IR}}t - I_{\mathrm{IR}}(x,y,t)\alpha]} \times \frac{E_{\mathrm{IR}\cdot y}(x,y,0,t)}{\sqrt{I_{\mathrm{IR}}(x,y,t)}}\hat{y}, \quad (2)$$

where ω_{IR} is the IR angular frequency, $E_{\mathrm{IR}\cdot x}(x,y,0,t)$ and $E_{\mathrm{IR}\cdot y}(x,y,0,t)$ represent structured IR in the focal plane toward the x and y directions, respectively, and $I_{\mathrm{IR}}(x,y,t) \propto |E_{\mathrm{IR}\cdot x}(x,y,0,t)|^2 + |E_{\mathrm{IR}\cdot y}(x,y,0,t)|^2$ represents the local intensity (details are presented in the Methods section). Equations (1) and (2) are based on the dipole response of the q-order harmonic as a function of the laser field having the form $E_{\mathrm{EUV}}(I_{\mathrm{IR}}) \propto A_q(I_{\mathrm{IR}})\exp[i\theta_q(I_{\mathrm{IR}})]$, which can be well approximated as $E_{\mathrm{EUV}}(I_{\mathrm{IR}}) \propto I_{\mathrm{IR}}^{q_{\mathrm{eff}}/2}\exp[-iI_{\mathrm{IR}}\alpha]$, where $A_q(I_{\mathrm{IR}}) \cong I_{\mathrm{IR}}^{q_{\mathrm{eff}}/2}$ is the amplitude of the q-order harmonic, q_{eff} is an effective order of nonlinearity, and $\theta_q(I_{\mathrm{IR}}) \cong -I_{\mathrm{IR}}\alpha$ is the phase of the q-order harmonic. The phase shift is approximately proportional to the local intensity and has been theoretically and experimentally validated [17,23,31]. The leading negative sign indicates that an increased driving intensity advances the HHG phase, which agrees with the tilt angle direction observed in Fig. 2. The coefficient α depends strongly on the quantum path followed by the electronic wave packet during the HHG process—that is, the type (short or long), peak intensity and frequency of the driving field, harmonic order, and gaseous species. We noted that the HHG emission was dominated by the short-quantum path contribution in this study of polarization control, as discussed in Supplement 1, Section 7.

The state of polarization of high-order harmonics in the far field was obtained through the coherent sum of Eqs. (1) and (2) for s and p polarizations at the focal plane, based on the Huygens–Fresnel principle [41,42,44,45], which results in two main diffraction EUV beams. The polarization characteristics of the helicity, ellipticity $\varepsilon_{\mathrm{EUV}}$, and tilt angle τ are determined by how the EUV vector [sum of Eqs. (1) and (2)] rotates as a function of time t. Consequently, the microscopic parameters q_{eff} and α can be directly extracted through the measured EUV ellipticity $\varepsilon_{\mathrm{EUV}}$ and tilt angle τ. Using two-dimensional range queries for the minimum deviations (see Supplement 1 Section 5, Figs. S9 and S10), the effective scaling parameters in amplitude and phase, q_{eff} and α, were obtained by fitting all observations of $\varepsilon_{\mathrm{EUV}}$ and τ from Fig. 2. The statistics of all retrieved q_{eff} and α are shown in Fig. 3. It should be emphasized that all polarization measurements of HHG were extracted to have a similar characterization response in q_{eff} and α in the same HH target, validating our TSM-based retrieval model.

4. DISCUSSION

Our polarization control scheme differs significantly from those in the literature, in which interferometry of two-color counterrotating beams [40,47] or two attosecond pulses [48,49] were applied. The resulting polarization provided by these two approaches—characterized by $\varepsilon_{\mathrm{EUV}}$ and τ—can be extremely sensitive to a delay between the two arms of the interferometer. The degree p of the HHG polarization can also deteriorate due to the instability of the interferometer. Compared to the two-color counterrotating

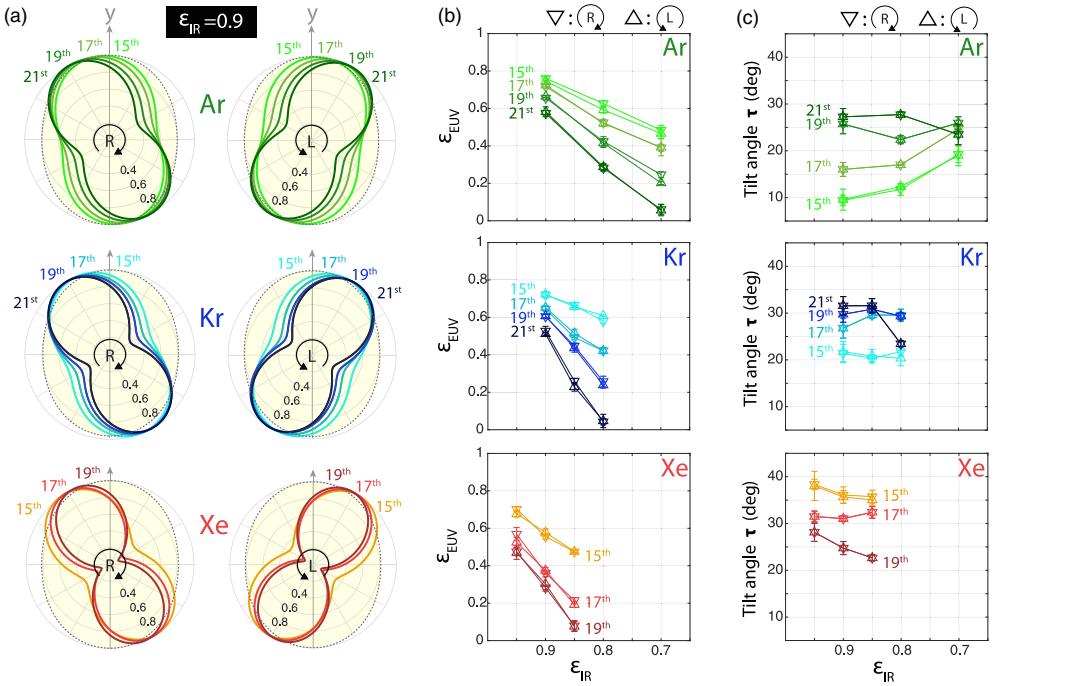

Fig. 2. Polarization scaling of HHG in Ar, Kr, and Xe. (a) The experimentally observed polarization states of HHG EUV (green lines for Ar, blue lines for Kr, and red lines for Xe) when driven by $\varepsilon_{\mathrm{IR}} = 0.9$ IR (yellow area with blask dashes) are depicted in the polar plots. Outputs (b) $\varepsilon_{\mathrm{EUV}}$ and (c) τ versus varied $\varepsilon_{\mathrm{IR}}$. The color gradient shows varied harmonic order q. The uncertainties (standard deviation) are derived from five individual measurements.

Research Article Vol. 8, No. 4 / April 2021 / Optica 488

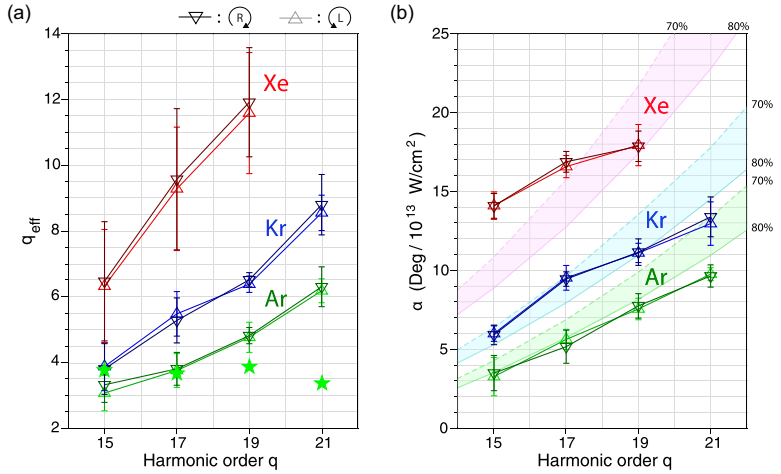

Fig. 3. Dipole response information extracted from HH ellipsometry. (a) Power scaling, q_{eff} versus harmonic order q, extracted from Ar (green), Kr (blue), and Xe (red). Green stars represent the calculated q_{eff} in Ar obtained from quantum strong-field approximation (SFA) theory, as described in [42] and Supplement 1, Section 6. This calculation uses a peak intensity, 1.2×10^{14} W/cm^2, less than the 2.8×10^{14} W/cm^2 applied in HH ellipsometry. (b) Phase-intensity slope α versus harmonic order q. Light strips mark α calculated from the semiclassical model (as indicated in [46]), using intensities 70% and 80% of their average peak intensities. The use of a reduced intensity in our simulations is attributed to nonuniformities at the experimental focus, and to remain in the tunneling regime.

scheme [40], in which p ranges from 0.4 to 0.85, and τ is unstable, we observed a high degree of polarization p in a range between 0.8 and 1 (see Supplement 1 Fig. S4). With no locking system for active stabilization of the path between two IR beams, the uncertainty of τ was only ≈1.5°, as shown in Fig. 2(c), indicating that the timing jitter between $E_{\text{EUV}\cdot s}$ and $E_{\text{EUV}\cdot p}$ was ≈3 as. Such excellent stability arises because our scheme is based on a transient polarization grating induced by two driving fields. Calculations show that the phase fluctuation between the two arms could easily alter the IR interference on the focal plane, but barely alter ε_{EUV} and τ of the EUV beams in the far field. Hence, our interferometry performs as an inline interferometer [32], in which the instability between two arms is negligible. The observed fluctuation is likely attributed to the power instability ≈1% of the driving laser as both the amplitude and phase of the HHG are coupled with the IR intensity.

Further insight was obtained by comparison with a semiclassical calculation [46,50]. The electronic dynamics in the three-step model can be approximated by integrating the classical equations of motion given by Newton's law. In the tunneling regime, one can assume that the ionization depends on only the instantaneous value of the electromagnetic field; immediately after ionization, the electron is located at the coordinate origin with zero velocity. Another assumption of this model is that the dynamics subsequent to ionization correspond to a classical free electron in the electromagnetic field, thus neglecting the influence of the Coulomb potential. Figure 4 shows the recollision kinetic energy of the electrons as a function of ionization time t_i (brown curves) and recollision time t_r (black curves). The phase of the harmonic emission depends not only on the phase of the fundamental field, but also on the particular quantum path followed by the electron. Our calculations reveal that HHG phase θ_{EUV} exhibits a piecewise-linear dependence on the electron excursion time $t_r - t_i$; the phase difference $|\theta_{\text{EUV}\cdot p} - \theta_{\text{EUV}\cdot s}|$ is approximately linearly proportional to the intensity difference, $\Delta I_{\text{IR}} = I_{\text{IR}\cdot s} - I_{\text{IR}\cdot p}$, in agreement with our ellipsometry observations in Supplement 1 Fig. S11.

Figure 3 shows that α increases as a function of the harmonic order q. This is understandable because the quantum path that requires a greater kinetic energy would ionize earlier at t_i and recombine later at t_r, as shown in Fig. 4. In such a case, a greater value of the quantum phase accumulates in the process of ionization, acceleration, and recombination. Moreover, for the same

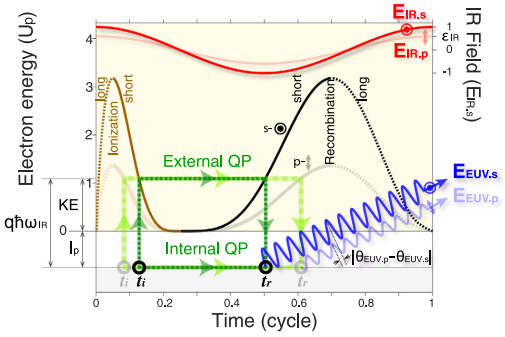

Fig. 4. Comparison of quantum paths of HHG in s and p polarizations. Output HH energy $q\hbar\omega_{\text{IR}}$ is the sum of ionization potential I_p and kinetic energy (KE) gained from the driving IR field (red lines). KE just before recombination is depicted as a function of time of ionization t_i (brown curves) and recombination t_r (black curves) with a semiclassical calculation. The driving IR field is normalized to the field amplitude in s-polarization $E_{\text{IR}\cdot s}$. Since $E_{\text{IR}\cdot p}$ (light red line) is weak with less pondermotive energy (Up), to keep the same output energy $q\hbar\omega_{\text{IR}}$—i.e., to obtain the same KE—an electron takes a longer excursion time in the continuum with an earlier t_i and a later t_r. As a result, there is a phase lag in $E_{\text{EUV}\cdot p}$ (light blue line) with respect to $E_{\text{EUV}\cdot s}$ (blue line) because more quantum phase is accumulated through the interference (green lines) between the external and internal quantum paths (QP).

harmonic order q, a larger α is also observed in a noble gas of large Z—the reason being that output energy $q\hbar\omega_{\mathrm{IR}}$ is the sum of ionization energy I_p overcome by the laser pulse and the kinetic energy gained from the electric force of the following field. Because I_p is smaller in a noble gas of large Z, more kinetic energy is required to maintain the same output energy $q\hbar\omega_{\mathrm{IR}}$. Electrons thus undergo a longer excursion period in the continuum, resulting in a larger HHG phase. The HHG phase dependent on I_p has also been observed in other findings in a mixed gas [51], and in 2-as pulse interference [52].

The semiclassical three-step model can also obtain α through an action integral over the electron trajectory [46], but such a calculation is based on a single-atom picture. For HHG driven with a Gaussian focus, many single emitters are excited with varied intensities. The interference effect should be considered when performing a coherent sum over all emitters. Two α curves using 70% and 80% of the average peak intensities are calculated and shown in Fig. 3(b) (their average peak intensities, $(I_{\mathrm{IR}\text{-}s} + I_{\mathrm{IR}\text{-}p})/2$, are listed in Supplement 1, Table S1). In Ar, α extracted from ellipsometry measurements shows quantitatively good agreement with that obtained from a semiclassical calculation, which indicates that the experimental α could be accurately estimated using 80% of the average peak intensity. Interestingly, in Kr and Xe, the slope of α obtained from ellipsometry measurements was flatter than that derived from a semiclassical calculation. Such a discrepancy between the theory and experimental results can be understood to be due to a strong variation in the beam size of HHG versus harmonic order in gases with a small ionization potential, as q_{eff} varies significantly [see Fig. 3(a)]. When HHG is driven with a Gaussian beam, higher-order harmonics with a larger q_{eff} tend to be generated nearer the center of the focus, at which the intensity is greater on average. Consequently, α should become smaller, as discussed in the preceding paragraph.

Moreover, Fig. 3(a) clearly shows that q_{eff} becomes larger in a large-Z gas. This phenomenon could be due to the tunnel ionization yield, as the single-atom yield of HHG is proportional to the ionization probability. A comparison of the ionization fraction of Ar, Kr, and Xe using the Ammosov–Delone–Krainov ionization model can be found as a function of time for a 35 fs duration pulse [53]. In a gas with a smaller ionization potential, there is a more rapid change in the fraction of ionization due to the variation of fundamental pulses—which implies that atoms with a small ionization potential have a large effective order of nonlinearity q_{eff}. Generally, a large quantum phase shift between the s and p polarization tends to enlarge the tilt angle τ, but in Xe, a much more rapid amplitude drop in p polarization leads to a small tilt-angle τ in higher-order harmonics, contrary to the τ behavior in Ar and Kr, as shown in Fig. 2. In short, q_{eff} also influences the tilt angle τ. HH ellipsometry can thus decouple and quantify the scaling of amplitude and phase with an accuracy of a few attoseconds, which differs markedly from other HH spectroscopic techniques [15,26–28,31,53]–55.

Finally, our HH ellipsometry results were validated using an alternative HHG experiment driven by a linearly polarized IR beam. Figure 5 shows a comparison of the HHG yield as a function of the driving laser intensity in Ar, Kr, and Xe. In Ar, the flux of all harmonics grew exponentially under a small IR intensity, whereas it saturated at a large intensity because of the depletion of neutral atoms, limiting the amplitude of single-atom emission. In Kr, the flux scaling of the low-order harmonics behaved similarly

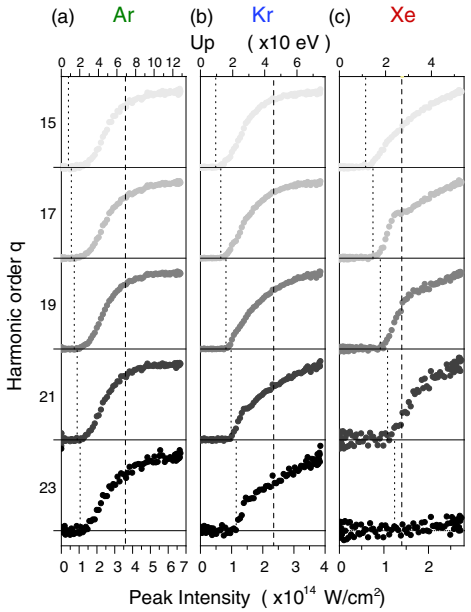

Fig. 5. Comparison of HHG yield as a function of driving laser intensity in (a) Ar, (b) Kr, and (c) Xe. The harmonic with a large phase-intensity slope α, observed in Fig. 3, also behaves more weakly and grows almost linearly with IR intensity because of the strong EUV phase variation induced by the transverse and longitudinal inhomogeneity of the IR beam. Dotted lines indicate the minimum peak intensity to generate the q-order harmonic. Dashed lines mark the peak intensity of 3.6×10^{14}, 2.35×10^{14}, and 1.4×10^{14} W/cm^2 for Ar, Kr, and Xe, respectively, that produces 50% ionization after a 35-fs IR laser field based on the Ammosov–Delone–Krainov ionization model [53].

to that in Ar, whereas the growth of the higher-order harmonics decreased gradually, becoming linearly proportional to the driving laser intensity in harmonic order 23. Such linear growth behavior occurred more significantly in Xe, for which—by comparison to the same harmonic order—the power scaling became more linear in large Z atoms in every order. It should be noted that all observed power scalings in these three gases exhibited no dependence on the backing pressure, indicating no propagation effect of IR that might have influenced the HH yield. Remarkably, these results agreed well with α, observed from the HH ellipsometry. The harmonic with a large phase-intensity slope α, as shown in Fig. 3(b), behaved much more weakly, growing almost linearly with the IR intensity. The power scaling of HHG became limited by a strong EUV phase variation induced by the intensity inhomogeneity of the driving IR in higher-order harmonics and in a gas with a small ionization potential, especially when $\alpha > 10$ deg./(10^{13} W/cm^2). It should also be emphasized that the power scaling of the single-atom response (q_{eff}) cannot be directly extracted from this yield-growth measurement, since it cannot correctly retrieve the single-atom response of HHG. Lastly, it is also interesting to note that, despite the phase of each HHG emitter varying widely in Xe, we still observed a large degree of polarization, $p \cong 0.9$, based on the polarimeter measurement, indicating that the wavefront of HHG was still stable and coherent.

5. CONCLUSIONS

We demonstrated that polarization control and characterization of HHG in a noncollinear geometry provides an excellent ellipsometry tool able to unveil the quantum dynamics of HH samples under intense laser fields. Our polarization control scheme was based on a transient polarization grating induced by two fundamental fields, being insensitive to the path fluctuation between the two arms of the driving fields and demonstrating excellent stability and single-digit attosecond accuracy. HH ellipsometry can measure two parameters—the ratio of intensities and phase difference information—compared with the single parameter of regular HH spectroscopic techniques, that is, only intensity without phase. Both the amplitude and phase of the HH dipole were precisely characterized using HH ellipsometry, carrying detailed information about the evolution of an ionized electronic wave packet. This study also clearly demonstrated how the amplitude and phase of the nonperturbative HH dipole influenced the power scaling of HHG and the achievable HH energy. Prospective future applications of HH ellipsometry should allow us to precisely quantify quantum dynamics, ultrafast chirality changes, and circular dichroism in HHG samples, as well as to enable critical comparisons with theory. This work also motivates future work to drive HH ellipsometry with structured light having tailored angular momentum and chiral properties [43,56], in which the most rapid transfer of energy and angular momentum in atoms, chiral molecules, 2D, and magnetic materials can be quantitatively resolved.

6. METHODS

A. Polarization Control of HHG in a Noncollinear Geometry

The pulse energies of the two IR arms were carefully tuned to be identical—that is, 130, 120, and 100 μJ for the Ar, Kr, and Xe gas jets, respectively. The average peak intensity of the crossing beam on the focal plane, $(I_{\mathrm{IR}\cdot s}+I_{\mathrm{IR}\cdot p})/2$, was estimated to be 2.82×10^{14}, 2.6×10^{14}, and 2.16×10^{14} W/cm^2, respectively (details of driving IR fields are shown in Supplement 1, Table S1). The tilt angle of the major axes of the driving pulses was carefully aligned toward the y direction. Each driving electric field thus consisted of two perpendicular components with an amplitude ratio and ellipticity $E_{\mathrm{IR}\cdot p}/E_{\mathrm{IR}\cdot s}=\varepsilon_{\mathrm{IR}}$, and phase shift $\varphi_{\mathrm{IR}}=\pi/2$. At the focal plane, the combination of the two noncollinear driving fields resulted in local linearly polarized E-field vectors, of which the direction rotated along the x axis. Each local linearly polarized IR field produced linearly polarized HH emission in the near field, which, upon propagation into the far field, led to a pair of elliptically polarized EUV beams. The ellipticity $\varepsilon_{\mathrm{EUV}}$ of the HH pulses—that is, the ratio of the minor axis with respect to the major axis of elliptically polarized light, and tilt angle τ of the major axis with respect to the y direction—were controlled with the fundamental ellipticity $\varepsilon_{\mathrm{IR}}$, while maintaining a good beam profile (Supplement 1, Section S3), as well as an upconversion efficiency.

B. Structured IR Light on the Focal Plane

We consider two identical elliptically polarized IR driving beams with equal ellipticity but opposite helicity [see Fig. 1(a)], given by

$$E_{\mathrm{IR}\cdot R}(x,y,z,t)=E_0\frac{-i\varepsilon_{\mathrm{IR}}\hat{p}+\hat{s}}{\sqrt{1+{\varepsilon_{\mathrm{IR}}}^2}}\times\exp\left[-ikz\cos\xi+ikx\sin\xi+i\omega_{\mathrm{IR}}t\right], \tag{3}$$

$$E_{\mathrm{IR}\cdot L}(x,y,z,t)=E_0\frac{i\varepsilon_{\mathrm{IR}}\hat{p}+\hat{s}}{\sqrt{1+{\varepsilon_{\mathrm{IR}}}^2}}\times\exp\left[-ikz\cos\xi-ikx\sin\xi+i\omega_{\mathrm{IR}}t\right], \tag{4}$$

where $E_{\mathrm{IR}\cdot R}$ ($E_{\mathrm{IR}\cdot L}$) represents the right-handed (left-handed) elliptically polarized IR field, E_0 is the field amplitude, $k=2\pi/\lambda_{\mathrm{IR}}$ is the fundamental wave vector, λ_{IR} is the wavelength of the driving laser, ω_{IR} is the IR angular frequency, and ξ is the half-crossing angle between the two fundamental laser beams. As the noncollinear angle is small in the experiment ($\xi=20.9$ mrad), $\hat{y}=\hat{s}$ and $\hat{x}=\hat{p}\cos(\xi)\cong\hat{p}$, considering a Gaussian intensity distribution (with beam waist ω_0), the electric field at the focal plane ($z=0$) can be written as

$$\begin{aligned}E_{\mathrm{focus}}(x,y,0,t)&\propto E_{\mathrm{IR}\cdot R}(x,y,0,t)+E_{\mathrm{IR}\cdot L}(x,y,0,t)\\&=2E_0\frac{e^{-\left(\frac{x^2+y^2}{\omega_0^2}\right)+i\omega_{\mathrm{IR}}t}}{\sqrt{(1+{\varepsilon_{\mathrm{IR}}}^2)}}\\&\quad\times\left[\varepsilon_{\mathrm{IR}}\sin(kx\sin\xi)\hat{x}+\cos(kx\sin\xi)\hat{y}\right]\\&=E_{\mathrm{IR}\cdot x}(x,y,0,t)\hat{x}+E_{\mathrm{IR}\cdot y}(x,y,0,t)\hat{y},\end{aligned} \tag{5}$$

in which

$$E_{\mathrm{IR}\cdot x}(x,y,0,t)=2E_0\frac{\varepsilon_{\mathrm{IR}}\sin(kx\sin\xi)}{\sqrt{(1+\varepsilon_{\mathrm{IR}}^2)}}e^{-\left(\frac{x^2+y^2}{\omega_0^2}\right)+i\omega_{\mathrm{IR}}t}, \tag{6}$$

and

$$E_{\mathrm{IR}\cdot y}(x,y,0,t)=2E_0\frac{\cos(kx\sin\xi)}{\sqrt{(1+\varepsilon_{\mathrm{IR}}^2)}}e^{-\left(\frac{x^2+y^2}{\omega_0^2}\right)+i\omega_{\mathrm{IR}}t}. \tag{7}$$

One calculated snapshot of the IR E-field vector distribution is shown in Supplement 1 Fig. S8. For the retrieval, the IR laser amplitude E_0, focal beam waist ω_0, half-crossing angle ξ, and ellipticity $\varepsilon_{\mathrm{IR}}$ were calibrated experimentally, and then used as an input for Eqs. (1) and (2).

Funding. Ministry of Science and Technology (109-2634-F-007-023, 109-2636-M-007-008); Ministry of Education; Japan Society for the Promotion of Science KAKENHI (JSPS) (19H02637, 20H05670); Ministerio de Ciencia e Innovación y Universidades (FIS2016-75652-P, PID2019-106910GB-I00, RYC-2017-22745); Junta de Castilla y León FEDER (SA287P18); Ministerio de Educación, Cultura y Deporte (FPU16/02591); H2020 European Research Council (ERC) (851201).

Acknowledgment. We thank Prof. Luis Plaja and Prof. C. D. Lin for fruitful discussions. The experimental work was undertaken at the National Tsing Hua University, Institute of Photonic Technologies. M.-C. C. gratefully acknowledges a Taiwan MOST Young Scholar Fellowship. K. A. acknowledges support from the Y.-S. Liu Global Talent Scholarship. H. M. and K. O. acknowledge the JSPS.

Disclosures. The authors declare no conflict of interest.

Supplemental document. See Supplement 1 for supporting content.

REFERENCES

1. A. McPherson, G. Gibson, H. Jara, U. Johann, T. S. Luk, I. A. McIntyre, K. Boyer, and C. K. Rhodes, "Studies of multiphoton production of vacuum ultraviolet-radiation in the rare-gases," J. Opt. Soc. Am. B **4**, 595–601 (1987).
2. K. J. Schafer, B. Yang, L. F. DiMauro, and K. C. Kulander, "Above threshold ionization beyond the high harmonic cutoff," Phys. Rev. Lett. **70**, 1599–1602 (1993).
3. P. B. Corkum, "Plasma perspective on strong-field multiphoton ionization," Phys. Rev. Lett. **71**, 1994–1997 (1993).
4. R. Zerne, C. Altucci, M. Bellini, M. B. Gaarde, T. W. Hänsch, A. L'Huillier, C. Lynga, and C. G. Wahlström, "Phase-locked high-order harmonic sources," Phys. Rev. Lett. **79**, 1006–1009 (1997).
5. Y. Pertot, C. Schmidt, M. Matthews, A. Chauvet, M. Huppert, V. Svoboda, A. von Conta, A. Tehlar, D. Baykusheva, J.-P. Wolf, and H. J. Wörner, "Time-resolved x-ray absorption spectroscopy with a water window high-harmonic source," Science **355**, 264–267 (2017).
6. T. D. Frazer, J. L. Knobloch, K. M. Hoogeboom-Pot, D. Nardi, W. Chao, R. W. Falcone, M. M. Murnane, H. C. Kapteyn, and J. N. Hernandez-Charpak, "Engineering nanoscale thermal transport: size- and spacing-dependent cooling of nanostructures," Phys. Rev. Appl. **11**, 024042EP (2019).
7. C. La-O-Vorakiat, M. Siemens, M. M. Murnane, H. C. Kapteyn, S. Mathias, M. Aeschlimann, P. Grychtol, R. Adam, C. M. Schneider, J. M. Shaw, H. Nembach, and T. J. Silva, "Ultrafast demagnetization dynamics at the M edges of magnetic elements observed using a tabletop high-harmonic soft x-ray source," Phys. Rev. Lett. **103**, 257402 (2009).
8. F. Siegrist, J. A. Gessner, M. Ossiander, C. Denker, Y.-P. Chang, M. C. Schröder, A. Guggenmos, Y. Cui, J. Walowski, U. Martens, J. K. Dewhurst, U. Kleinberg, M. Münzenberg, S. Sharma, and M. Schultze, "Light-wave dynamic control of magnetism," Nature **571**, 240–244 (2019).
9. O. Kfir, S. Zayko, C. Nolte, M. Sivis, M. Möller, B. Hebler, S. S. P. K. Arekapudi, D. Steil, S. Schäfer, M. Albrecht, O. Cohen, S. Mathias, and C. Ropers, "Nanoscale magnetic imaging using circularly polarized high-harmonic radiation," Sci. Adv. **3**, eaao4641 (2017).
10. D. F. Gardner, M. Tanksalvala, E. R. Shanblatt, X. Zhang, B. R. Galloway, C. L. Porter, R. Karl, Jr., C. Bevis, D. E. Adams, H. C. Kapteyn, M. M. Murnane, and G. F. Mancini, "Subwavelength coherent imaging of periodic samples using a 13.5 nm tabletop high-harmonic light source," Nat. Photonics **11**, 259–263 (2017).
11. N. L. Wagner, A. Wüest, I. P. Christov, T. Popmintchev, X. Zhou, M. M. Murnane, and H. C. Kapteyn, "Monitoring molecular dynamics using coherent electrons from high harmonic generation," Proc. Natl. Acad. Sci. USA **103**, 13279 (2006).
12. J. Itatani, J. Levesque, D. Zeidler, H. Niikura, H. Pepin, J. C. Kieffer, P. B. Corkum, and D. M. Villeneuve, "Tomographic imaging of molecular orbitals," Nature **432**, 867–871 (2004).
13. S. Beaulieu, A. Comby, A. Clergerie, J. Caillat, D. Descamps, N. Dudovich, B. Fabre, R. Géneaux, F. Légaré, S. Petit, B. Pons, G. Porat, T. Ruchon, R. Taïeb, V. Blanchet, and Y. Mairesse, "Attosecond-resolved photoionization of chiral molecules," Science **358**, 1288–1294 (2017).
14. D. Baykusheva, D. Zindel, V. Svoboda, E. Bommeli, M. Ochsner, A. Tehlar, and H. J. Wörner, "Real-time probing of chirality during a chemical reaction," Proc. Natl. Acad. Sci. USA **116**, 23923 (2019).
15. O. Neufeld, D. Ayuso, P. Decleva, M. Y. Ivanov, O. Smirnova, and O. Cohen, "Ultrasensitive chiral spectroscopy by dynamical symmetry breaking in high harmonic generation," Phys. Rev. X **9**, 031002EP (2019).
16. A. A. Lanin, E. A. Stepanov, A. B. Fedotov, and A. M. Zheltikov, "Mapping the electron band structure by intraband high-harmonic generation in solids," Optica **4**, 516–519 (2017).
17. M. Lewenstein, P. Salières, and A. L'Huillier, "Phase of the atomic polarization in high-order harmonic generation," Phys. Rev. A **52**, 4747–4754 (1995).
18. H. Wikmark, C. Guo, J. Vogelsang, P. W. Smorenburg, H. Coudert-Alteirac, J. Lahl, J. Peschel, P. Rudawski, H. Dacasa, S. Carlström, S. Maclot, M. B. Gaarde, P. Johnsson, C. L. Arnold, and A. L'Huillier, "Spatiotemporal coupling of attosecond pulses," Proc. Natl. Acad. Sci. USA **116**, 4779–4787 (2019).
19. L. Quintard, V. Strelkov, J. Vabek, O. Hort, A. Dubrouil, D. Descamps, F. Burgy, C. Péjot, E. Mével, F. Catoire, and E. Constant, "Optics-less focusing of XUV high-order harmonics," Sci. Adv. **5**, eaau7175 (2019).
20. H. J. Shin, D. G. Lee, Y. H. Cha, K.-H. Hong, and C. H. Nam, "Generation of nonadiabatic blueshift of high harmonics in an intense femtosecond laser field," Phys. Rev. Lett. **83**, 2544–2547 (1999).
21. Y. Mairesse, A. De Bohan, L. J. Frasinski, H. Merdji, L. C. Dinu, P. Monchicourt, P. Breger, M. Kovacev, R. Taïeb, B. Carré, H. G. Muller, P. Agostini, and P. Salieres, "Attosecond synchronization of high-harmonic soft x-rays," Science **302**, 1540–1543 (2003).
22. K. T. Kim, C. Zhang, A. D. Shiner, B. E. Schmidt, F. Légaré, D. M. Villeneuve, and P. B. Corkum, "Petahertz optical oscilloscope," Nat. Photonics **7**, 958–962 (2013).
23. P. Carpeggiani, M. Reduzzi, A. Comby, H. Ahmadi, S. Kühn, F. Calegari, M. Nisoli, F. Frassetto, L. Poletto, D. Hoff, J. Ullrich, C. D. Schroter, R. Moshammer, G. G. Paulus, and G. Sansone, "Vectorial optical field reconstruction by attosecond spatial interferometry," Nat. Photonics **11**, 383–389 (2017).
24. H.-W. Sun, P.-C. Huang, Y.-H. Tzeng, J.-T. Huang, C. D. Lin, C. Jin, and M.-C. Chen, "Extended phase matching of high harmonic generation by plasma-induced defocusing," Optica **4**, 976–981 (2017).
25. L. Hareli, L. Lobachinsky, G. Shoulga, Y. Eliezer, L. Michaeli, and A. Bahabad, "On-the-fly control of high-harmonic generation using a structured pump beam," Phys. Rev. Lett. **120**, 183902 (2018).
26. A. Zaïr, M. Holler, A. Guandalini, F. Schapper, J. Biegert, L. Gallmann, U. Keller, A. S. Wyatt, A. Monmayrant, I. A. Walmsley, E. Cormier, T. Auguste, J.-P. Caumes, and P. Salieres, "Quantum path interferences in high-order harmonic generation," Phys. Rev. Lett. **100**, 143902 (2008).
27. J. E. Kruse, P. Tzallas, E. Skantzakis, and D. Charalambidis, "Persistent quantum interfering electron trajectories," Phys. Rev. A **82**, 033438 (2010).
28. G. Kolliopoulos, B. Bergues, H. Schröder, P. A. Carpeggiani, L. Veisz, G. D. Tsakiris, D. Charalambidis, and P. Tzallas, "Revealing quantum path details in high-field physics," Phys. Rev. A **90**, 013822 (2014).
29. P. Balcou, P. Salieres, A. L'Huillier, and M. Lewenstein, "Generalized phase-matching conditions for high harmonics: the role of field-gradient forces," Phys. Rev. A **55**, 3204–3210 (1997).
30. C. M. Heyl, J. Güdde, U. Höfer, and A. L'Huillier, "Spectrally resolved maker fringes in high-order harmonic generation," Phys. Rev. Lett. **107**, 033903 (2011).
31. C. Corsi, A. Pirri, E. Sali, A. Tortora, and M. Bellini, "Direct interferometric measurement of the atomic dipole phase in high-order harmonic generation," Phys. Rev. Lett. **97**, 023901 (2006).
32. J. Lu, E. F. Cunningham, Y. S. You, D. A. Reis, and S. Ghimire, "Interferometry of dipole phase in high harmonics from solids," Nat. Photonics **13**, 96–100 (2018).
33. P.-C. Huang, C. Hernández-García, J.-T. Huang, P.-Y. Huang, C.-H. Lu, L. Rego, D. D. Hickstein, J. L. Ellis, A. Jaron-Becker, A. Becker, S. D. Yang, C. G. Durfee, L. Plaja, H. C. Kapteyn, M. M. Murnane, A. H. Kung, and M.-C. Chen, "Polarization control of isolated high-harmonic pulses," Nat. Photonics **12**, 349–354 (2018).
34. R. M. A. Azzam and B. J. Thompson, *Selected Papers on Ellipsometry*, Vol. 27 of SPIE Milestone Series (SPIE, 1991).
35. H. Tompkins and E. A. Irene, *Handbook of Ellipsometry* (William Andrew, Elsevier, 2005).
36. T. Koide, T. Shidara, M. Yuri, N. Kandaka, K. Yamaguchi, and H. Fukutani, "Elliptical-polarization analyses of synchrotron radiation in the 5–80-eV region with a reflection polarimeter," Nucl. Instrum. Methods Phys. Res., Sect. A **308**, 635–644 (1991).
37. A. Ferré, C. Handschin, M. Dumergue, F. Burgy, A. Comby, D. Descamps, B. Fabre, G. A. Garcia, R. Géneaux, L. Merceron, E. Mével, L. Nahon, S. Petit, B. Pons, D. Staedter, S. Weber, T. Ruchon, V. Blanchet, and Y. Mairesse, "A table-top ultrashort light source in the extreme ultraviolet for circular dichroism experiments," Nat. Photonics **9**, 93–98 (2015).
38. T. Hahn, J. Bierbach, C. Rödel, D. Hemmers, M. Yeung, B. Dromey, S. Fuchs, A. Galestian, S. Kuschel, M. Zepf, G. G. Paulus, and G. Pretzler, "Broadband XUV polarimetry of high harmonics from plasma surfaces using multiple Fresnel reflections," Appl. Phys. B **118**, 241–245 (2015).
39. K. Veyrinas, C. Elkharrat, S. Marggi Poullain, N. Saquet, D. Dowek, R. R. Lucchese, G. A. Garcia, and L. Nahon, "Complete determination of the state of elliptically polarized light by electron-ion vector correlations," Phys. Rev. A **88**, 063411 (2013).

40. L. Barreau, K. Veyrinas, V. Gruson, S. J. Weber, T. Auguste, J.-F. Hergott, F. Lepetit, B. Carré, J.-C. Houver, D. Dowek, and P. Salières, "Evidence of depolarization and ellipticity of high harmonics driven by ultrashort bichromatic circularly polarized fields," Nat. Commun. **9**, 4727 (2018).
41. C. Hernández-García, J. S. Román, L. Plaja, and A. Picón, "Quantum-path signatures in attosecond helical beams driven by optical vortices," New J. Phys. **17**, 093029 (2015).
42. L. Rego, J. S. Román, A. Picón, L. Plaja, and C. Hernández-García, "Nonperturbative twist in the generation of extreme-ultraviolet vortex beams," Phys. Rev. Lett. **117**, 163202EP (2016).
43. L. Rego, K. M. Dorney, N. J. Brooks, Q. L. Nguyen, C.-T. Liao, J. San Román, D. E. Couch, A. Liu, E. Pisanty, M. Lewenstein, L. Plaja, H. C. Kapteyn, M. M. Murnane, and C. Hernández-García, "Generation of extreme-ultraviolet beams with time-varying orbital angular momentum," Science **364**, eaaw9486 (2019).
44. D. D. Hickstein, F. J. Dollar, P. Grychtol, J. L. Ellis, R. Knut, C. Hernández-García, D. Zusin, C. Gentry, J. M. Shaw, T. Fan, K. M. Dorney, A. Becker, A. Jaron-Becker, H. C. Kapteyn, M. M. Murnane, and C. G. Durfee, "Non-collinear generation of angularly isolated circularly polarized high harmonics," Nat. Photonics **9**, 743–750 (2015).
45. C. Hernández-García, C. G. Durfee, D. D. Hickstein, T. Popmintchev, A. Meier, M. M. Murnane, H. C. Kapteyn, I. J. Sola, A. Jaron-Becker, and A. Becker, "Schemes for generation of isolated attosecond pulses of pure circular polarization," Phys. Rev. A **93**, 043855 (2016).
46. M. B. Gaarde, J. L. Tate, and K. J. Schafer, "Macroscopic aspects of attosecond pulse generation," J. Phys. B **41**, 132001 (2016).
47. A. Fleischer, O. Kfir, T. Diskin, P. Sidorenko, and O. Cohen, "Spin angular momentum and tunable polarization in high-harmonic generation," Nat. Photonics **8**, 543–549 (2014).
48. J. L. Ellis, K. M. Dorney, D. D. Hickstein, N. J. Brooks, C. Gentry, C. Hernández-García, D. Zusin, J. M. Shaw, Q. L. Nguyen, C. A. Mancuso, G. S. M. Jansen, S. Witte, H. C. Kapteyn, and M. M. Murnane, "High harmonics with spatially varying ellipticity," Optica **5**, 479–485 (2018).
49. D. Azoury, O. Kneller, M. Krüger, B. D. Bruner, O. Cohen, Y. Mairesse, and N. Dudovich, "Interferometric attosecond lock-in measurement of extreme-ultraviolet circular dichroism," Nat. Photonics **13**, 198–204 (2019).
50. L. Rego, J. S. Román, L. Plaja, A. Picón, and C. Hernández-García, "Ultrashort extreme ultraviolet vortices," in *Vortex Dynamics and Optical Vortices*, H. Perez-de-Tejada, ed. (IntechOpen, 2017), Chapter 9.
51. T. Kanai, E. J. Takahashi, Y. Nabekawa, and K. Midorikawa, "Destructive interference during high harmonic generation in mixed gases," Phys. Rev. Lett. **98**, 153904 (2007).
52. D. Azoury, O. Kneller, S. Rozen, B. D. Bruner, A. Clergerie, Y. Mairesse, B. Fabre, B. Pons, N. Dudovich, and M. Krüger, "Electronic wavefunctions probed by all-optical attosecond interferometry," Nat. Photonics **13**, 54–61 (2018).
53. M. V. Ammosov, N. B. Delone, and V. P. Karinov, "Tunnel ionization of complex atoms and of atomic ions in an alternating electromagnetic field," Sov. Phys. JETP **64**, 1191 (1987).
54. E. Bordo, O. Neufeld, O. Kfir, A. Fleischer, and O. Cohen, "Spectroscopy of atomic orbital sizes using bi-elliptical high-order harmonic generation," Phys. Rev. A **100**, 043419EP (2019).
55. N. Klemke, N. Tancogne-Dejean, G. M. Rossi, Y. Yang, F. Scheiba, R. E. Mainz, G. Sciacca, A. Rubio, F. X. Kärtner, and O. D. Mücke, "Polarization-state-resolved high-harmonic spectroscopy of solids," Nat. Commun. **10**, 1–7 (2019).
56. D. Ayuso, O. Neufeld, A. F. Ordonez, P. Decleva, G. Lerner, O. Cohen, M. Ivanov, and O. Smirnova, "Synthetic chiral light for efficient control of chiral light–matter interaction," Nat. Photonics **13**, 866–871 (2019).

A.3 CONSERVATION OF TORUS-KNOT ANGULAR MOMENTUM IN HIGH-ORDER HARMONIC GENERATION

PHYSICAL REVIEW LETTERS **122,** 203201 (2019)

Conservation of Torus-knot Angular Momentum in High-order Harmonic Generation

Emilio Pisanty,[1,*] Laura Rego,[2] Julio San Román,[2] Antonio Picón,[1,3] Kevin M. Dorney,[4] Henry C. Kapteyn,[4] Margaret M. Murnane,[4] Luis Plaja,[2] Maciej Lewenstein,[1,5] and Carlos Hernández-García[2]

[1]*ICFO—Institut de Ciencies Fotoniques, The Barcelona Institute of Science and Technology, Av. Carl Friedrich Gauss 3, 08860 Castelldefels (Barcelona), Spain*

[2]*Grupo de Investigación en Aplicaciones del Láser y Fotónica, Departamento de Física Aplicada, University of Salamanca, E-37008, Salamanca, Spain*

[3]*Departamento de Química, Universidad Autónoma de Madrid, 28049, Madrid, Spain*

[4]*JILA, Department of Physics, University of Colorado Boulder, Boulder, Colorado, 80309, USA*

[5]*ICREA, Passeig de Lluís Companys, 23, 08010 Barcelona, Spain*

(Received 22 October 2018; published 22 May 2019; corrected 20 June 2019 and 25 July 2019)

High-order harmonic generation stands as a unique nonlinear optical up-conversion process, mediated by a laser-driven electron recollision mechanism, which has been shown to conserve energy, linear momentum, and spin and orbital angular momentum. Here, we present theoretical simulations that demonstrate that this process also conserves a mixture of the latter, the torus-knot angular momentum J_γ, by producing high-order harmonics with driving pulses that are invariant under coordinated rotations. We demonstrate that the charge J_γ of the emitted harmonics scales linearly with the harmonic order, and that this conservation law is imprinted onto the polarization distribution of the emitted spiral of attosecond pulses. We also demonstrate how the nonperturbative physics of high-order harmonic generation affect the torus-knot angular momentum of the harmonics, and we show that this configuration harnesses the spin selection rules to channel the full yield of each harmonic into a single mode of controllable orbital angular momentum.

DOI: 10.1103/PhysRevLett.122.203201

Nonlinear optical processes offer the unique possibility of mediating interactions and transferring energy between modes of the electromagnetic field at different frequencies [1]. When this transfer happens in a symmetric medium, the interaction will also carry the symmetry's conserved charge to the recipient mode [2,3], so one can, e.g., combine two photons with well-defined orbital angular momentum (OAM) [4] to make a single photon at twice the frequency and twice the angular momentum [5]. The few-photon exchanges of perturbative nonlinear optics, however, have a relatively limited scale and complexity in comparison to high-order harmonic generation (HHG) [6,7], where strong-field interactions can produce harmonics with photon energy hundreds or thousands of times larger than the driver [8]. HHG is a nonperturbative phenomenon which is best understood using a semiclassical picture: an ionized electron is accelerated back to its parent ion, emitting high-frequency light in the ensuing recollision [9–11]. Despite the lack of a photon-exchange model, HHG is often regarded as a parametric process, and its conservation properties have been explored extensively as regards energy [12], linear momentum [13], and orbital and spin angular momentum (SAM) [14–26].

The individual symmetries associated with these conservation laws of the electromagnetic field can be composed in nontrivial ways to make new ones. This is the case for *coordinated* rotations (CRs): symmetry transformations in which the spatial dependence of the field is rotated by an angle θ about the propagation axis, while the light's polarization is rotated by $\gamma\theta$ around the same axis, γ being a coordination parameter. CRs are generated by the linear combination $J_\gamma = L + \gamma S$ of the orbital and spin angular momenta, L and S, which are otherwise independently conserved in the paraxial regime [27]. For monochromatic light, γ is restricted to integer or half-integer values [28,29], with the latter case imparting on the field the topology of a Möbius strip [30–32]. However, when the monochromatic restriction is lifted, γ can take arbitrary values and still admit invariant states of the field [33], since polychromatic combinations can have polarization states with higher-order internal rotational symmetries.

One particularly relevant example is the threefold-symmetric trefoil field present in the "bicircular" HHG configurations [22–26,34–41] used to produce circularly-polarized harmonics. This field consists of two counter-rotating circularly-polarized drivers at different frequencies, and exhibits the same configuration after a polarization rotation by an angle $2\pi/n$, with $n \geq 3$. If we then add different OAM to the two drivers, this polarization rotation can be realized over a 2π rotation of the spatial dependence. The resulting field, which carries both SAM and OAM, but is not an eigenstate of either, has the topology of a torus

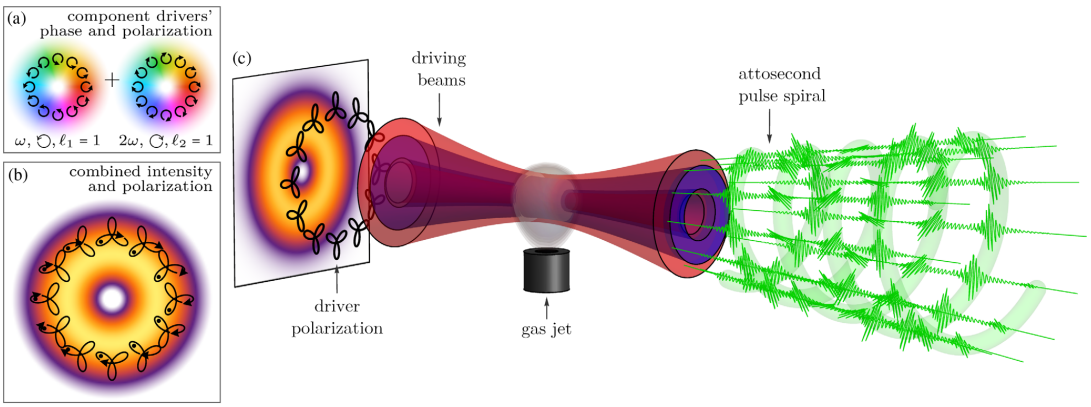

FIG. 1. High-harmonic generation driven by a torus-knot beam. The combination of counter-rotating circular beams at frequencies ω and 2ω with different OAM and therefore different azimuthal phase gradients [(a), with optical phase as the hue color scale] produces a bicircular trefoil polarization which rotates and acquires a delay over azimuthal displacements (b). Here, with $\ell_1 = \ell_2 = 1$, tracking one lobe over an azimuthal loop around the beam axis (black dots) produces a 120° rotation, which induces the topology of a torus knot [33], as well as a time delay within each trefoil (arrows). When this combination impinges on a gas jet at high intensity (c), the attosecond pulse trains produced share the coordinated-rotation invariance of the driver, so that the emission at different azimuthal points is related by a time delay and a rotation of the polarization.

knot: when the polarization and spatial dependences of the field are unfolded, the trefoil tips trace out a knotted curve embedded on the surface of a torus [33]. With suitable choices of the OAM and frequency of the two components, any arbitrary torus knot [42] can be achieved. Moreover, this topology mirrors the subgroup of the independent-rotations group $\mathrm{SO}(2) \times \mathrm{SO}(2)$ generated by the torus-knot angular momentum (TKAM) $J_\gamma = L + \gamma S$ [33].

In this Letter, we show that the topological charge J_γ is conserved in high-order harmonic generation for any arbitrary rational coordination parameter $\gamma \in \mathbb{Q}$ [43], providing an infinite family of topological charges (corresponding to an infinite family of dynamical symmetries) that are preserved by the nonperturbative nonlinear interaction. We show that this spin-orbit linking appears in the time domain as a structured spiral of attosecond pulses, that it opens a new window for the exploration of nonperturbative effects in harmonic generation, and that it provides an extreme ultraviolet (XUV) light source with controllable OAM.

To demonstrate this conservation property, we study HHG driven by TKAM beams that are invariant under coordinated rotations with a mixing parameter $\gamma \in \frac{1}{3}\mathbb{Z}$. This configuration corresponds, as we will show below, to a bicircular field consisting of two beams at frequencies ω and 2ω, with counter-rotating right- and left-handed circular polarizations, $\circlearrowleft$ and $\circlearrowright$, and carrying independent OAM, ℓ_1 and ℓ_2, respectively, as shown in Fig. 1. The OAM of the drivers determines the mixing parameter γ under which the bicircular beam is CR-invariant, so that the two components carry a TKAM of $j_\gamma^{(1)} = \ell_1 + \gamma$ and $j_\gamma^{(2)} = 2j_\gamma^{(1)} = \ell_2 - \gamma$, respectively [44]. (The drivers are required to carry different TKAM to have identical CR dynamical symmetries, since phase and time delays correspond differently at different frequencies.) Within that framework, then, the TKAM conservation is expressed as

$$j_\gamma^{(q)} = q j_\gamma^{(1)}, \tag{1}$$

i.e., in the linear scaling of the J_γ charge carried by the qth harmonic with the harmonic order q.

In this configuration, the local field at each point in the beam is the usual bicircular trefoil [22], so that each atom in the target emits harmonics in circularly-polarized doublets with opposite helicities: $\circlearrowleft$-polarized harmonics at frequencies $(3n+1)\omega$, and $\circlearrowright$-polarized harmonics at $(3n-1)\omega$; in the time domain, the emission forms a train of attosecond pulses with linear polarizations at 120° from each other [35,38]. The orientation of this local trefoil, given by the relative phase between the two components rotates around the beam, as shown in Fig. 1(b).

Thus, the dynamical symmetry of the driving field $\mathbf{F}$ is

$$R(\gamma\alpha)\mathbf{F}(R^{-1}(\alpha)\mathbf{r}, t) = \mathbf{F}(\mathbf{r}, t + \tau\alpha), \tag{2}$$

where τ is a time-delay constant and the angle α parametrizes the transformation. Here, the rotations act on the circular polarization basis $\hat{\mathbf{e}}_\pm = \frac{1}{\sqrt{2}}(\hat{\mathbf{e}}_x \pm i\hat{\mathbf{e}}_y)$ and on the spatial dependence via

$$R(\gamma\alpha)\hat{\mathbf{e}}_\pm = e^{\mp i\gamma\alpha}\hat{\mathbf{e}}_\pm \quad \text{and} \tag{3a}$$

$$R^{-1}(\alpha)(r, \theta, z) = (r, \theta - \alpha, z), \tag{3b}$$

i.e., as an active and a passive transformation, respectively, with the polarization rotation $R(\gamma\alpha)$ acting through a fraction $\gamma\alpha$ of the spatial rotation angle α.

Our driving field consists of two components with well-defined SAM and OAM,

$$\mathbf{F}_1(\mathbf{r},t) = \mathrm{Re}[F_1\hat{\mathbf{e}}_+ f_1(r,z)e^{i\ell_1\theta}e^{-i\omega t}] \tag{4a}$$

$$\mathbf{F}_2(\mathbf{r},t) = \mathrm{Re}[F_2\hat{\mathbf{e}}_- f_2(r,z)e^{i\ell_2\theta}e^{-2i\omega t}], \tag{4b}$$

each of which satisfies separate orbital and spin invariance properties

$$R(\gamma\alpha)\mathbf{F}_1(\mathbf{r},t) = \mathbf{F}_1(\mathbf{r},t+\gamma\alpha/\omega), \tag{5a}$$

$$\mathbf{F}_1(R^{-1}(\alpha)\mathbf{r},t) = \mathbf{F}_1(\mathbf{r},t+\ell_1\alpha/\omega), \tag{5b}$$

$$R(\gamma\alpha)\mathbf{F}_2(\mathbf{r},t) = \mathbf{F}_2(\mathbf{r},t-\gamma\alpha/2\omega), \tag{5c}$$

$$\mathbf{F}_2(R^{-1}(\alpha)\mathbf{r},t) = \mathbf{F}_2(\mathbf{r},t+\ell_2\alpha/2\omega). \tag{5d}$$

The correct CR invariance of the system can then be found by requiring that the combined time delay imposed by Eqs. (5a), (5b) matches that produced by the combination of Eqs. (5c), (5d), so that

$$\frac{\ell_1\alpha}{\omega}+\frac{\gamma\alpha}{\omega}=\frac{\ell_2\alpha}{2\omega}-\frac{\gamma\alpha}{2\omega} \quad\Rightarrow\quad \gamma=\frac{\ell_2-2\ell_1}{3}, \tag{6}$$

with a time-delay constant $\tau=(\ell_1+\ell_2)/3\omega$. This then sets the TKAM charge $j_\gamma^{(n)}$ for each driver, defined in analogy to the OAM charge in Eqs. (5b), (5d) by requiring that

$$R(\gamma\alpha)\mathbf{F}_n(R^{-1}(\alpha)\mathbf{r},t) = \mathbf{F}(\mathbf{r},t+j_\gamma^{(n)}\alpha/n\omega), \tag{7}$$

to be $j_\gamma^{(n)}=n\omega\tau=n(\ell_1+\ell_2)/3$ [45].

Turning to the HHG radiation, we can now see the conserved TKAM charge in action, via the standard correspondence between dynamical symmetries and conserved charges, and their associated selection rules [46,47]. Since in our configuration the application of a CR to the driving field is equivalent to a time delay, via Eq. (2), and the gaseous generating medium is unaffected by the transformation, the same must be true for the emitted HHG radiation. With the XUV emission's TKAM charge defined as in Eq. (7), the CR invariance then guarantees the conservation of the TKAM charge as expressed in Eq. (1).

To explore the conservation of TKAM in HHG, we perform numerical simulations of HHG by solving the Schrödinger-Maxwell equations for a sample of atoms in the interaction region within the SFA+ approximation and using the electromagnetic field propagator described in Ref. [48]; further details of our method can be found in Refs. [15,17,49].

We consider the harmonic emission driven by a bicircular field with $\ell_1=\ell_2=1$, as shown in Fig. 1, equal beam waists of 30 μm, and pulses of total intensity $I=2\times10^{14}$ W/cm^2. The ω and 2ω driving pulse envelopes are modelled as a trapezoidal function with 5.3 fs linear on- and off-ramps and 10.7 fs of constant amplitude. Harmonics are generated in a thin-slab argon gas jet and propagated to the far field (i.e., longitudinal phase-matching effects are neglected, since transverse phase-matching effects are dominant [17,49]).

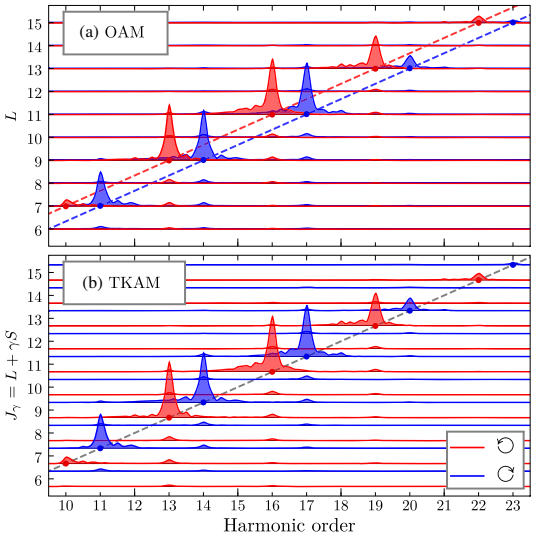

FIG. 2. Simulated HHG spectra of the right and left-polarized components (shown in red and blue, respectively) driven by a bicircular field with $\ell_1=\ell_2=1$. We compare the (a) OAM and (b) TKAM spectra, with $\gamma=-1/3$, as a function of the harmonic order. We calculate the OAM spectrum by taking a standard Fourier series over the azimuthal dependence and integrating over the radial dependence. For the TKAM spectrum, the OAM charge of the $\circlearrowleft$- and $\circlearrowright$-polarized components is shifted by γ times their SAM. The conservation of TKAM is clear in the linear trend shown in (b).

We present our results in Fig. 2, by comparing the (a) OAM and (b) TKAM spectra of the circularly polarized components of the HHG emission as a function of harmonic order. Since in this configuration $j_\gamma^{(1)}=2/3$, following Eq. (1) the qth harmonic exhibits a TKAM of $j_\gamma^{(q)}=\frac{2}{3}q$ (so, e.g., $j_\gamma^{(13)}=\frac{26}{3}$ and $j_\gamma^{(14)}=\frac{28}{3}$) and, following the definition of the TKAM, its OAM would be $\ell_q=j_\gamma^{(q)}-\gamma S_q=(2q\pm1)/3$ for right- (+) and left- (−) polarized harmonics (therefore giving $\ell_{13}=\ell_{14}=9$, in agreement with the results of Refs. [41,50]). Thus, while the OAM behaviour can be explained using photon-counting methods, the spectrum is much easier to understand via the TKAM conservation law, which is embodied in the linear trend observed in the TKAM spectrum, as in Eq. (1). A similar conservation law, with $\gamma=1/2$, can also be

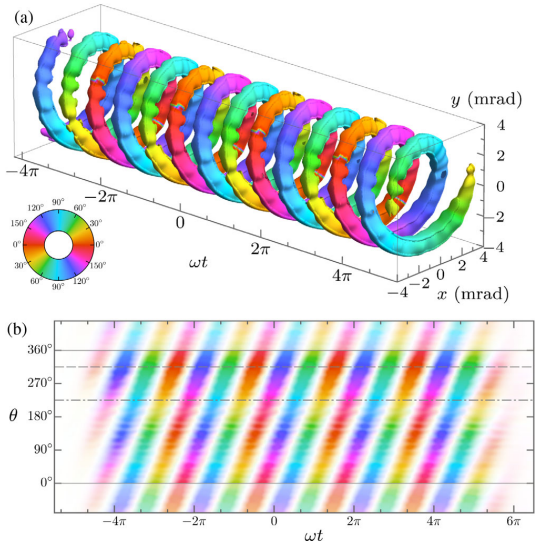

FIG. 3. Twisted-spiral structure of the attosecond pulse train emitted by CR-invariant bicircular drivers at $\ell_1 = \ell_2 = 1$, as in Fig. 2. (a) Iso-intensity surface of the HHG emission, filtered above harmonic order 10, over the far-field divergence Cartesian coordinates x and y, with the color denoting the local polarization direction as in (b). (b) Polarization angle of the attosecond pulses over azimuthal emission angle θ, obtained from the time-windowed $T_{22}(\mathbf{r}, t)$ field moment of Eq. (8) with $\sigma = 15°/\omega$ and integrated over angular divergence, with $\frac{1}{2}\arg\left(T_{22}(\mathbf{r}, t)\right)$ plotted as the hue and $|T_{22}(\mathbf{r}, t)|$ (which closely follows the XUV intensity) as the color saturation. The polarization angle rotates by $-120°$ over each turn of the spiral, directly confirming the $\gamma = -1/3$ rotation-coordination parameter of the beam. At each fixed θ, the polarization jumps over three complementary colors such as blue-green-red (dashed line) or cyan-yellow-magenta (dot-dashed line), showing the local polarization structure as a train of linear pulses at 120° from each other.

observed in HHG driven by monochromatic CR-invariant beams [51].

The CR invariance can also be seen in the time domain: similarly to OAM-beam HHG, where spatial rotations are equivalent to time delays and the attosecond pulse train (APT) forms a spiral [15,18,49], the addition of a polarization rotation means that here the spiral also has a twisted-polarization structure [51]. We present this in Fig. 3(a), using an isosurface plot for the XUV intensity and the color scale to represent the polarization direction, which twists smoothly along the attosecond pulse spiral.

To study this polarization structure quantitatively, we require a measure of the absolute orientation of the APT at different azimuthal points in the beam—and, ideally, one which is sensitive to the pulse train's structure as a sequence of linearly-polarized pulses at nontrivial angles [35,38]. For monochromatic radiation, the polarization ellipse orientation angle is obtained via the eigenvectors of the polarization matrix $\langle E_i E_j \rangle$ [52] or, equivalently, as the phase of the quadrupole component $T_{22} = \int_{-\infty}^{\infty} (E_x(t) + iE_y(t))^2 dt$ [33]. The symmetry of our APT means that the average orientation is undefined, so we use a time-windowed version [53],

$$T_{22}(\mathbf{r}, t) = \int_{-\infty}^{\infty} \left(E_x^{(\mathrm{XUV})}(\mathbf{r}, t') + iE_y^{(\mathrm{XUV})}(\mathbf{r}, t')\right)^2 \times e^{-(t'-t)^2/2\sigma^2} dt', \tag{8}$$

from which the local polarization orientation angle can be obtained as $\frac{1}{2}\arg\left(T_{22}(\mathbf{r}, t)\right)$ [54]. Thus, e.g., a linearly polarized pulse along $\hat{\mathbf{e}}_x$ produces a positive T_{22}, an $\hat{\mathbf{e}}_y$ polarization gives a negative moment, and there is a continuous passage between the two behaviors.

The time-windowed quadrupole moment, which we plot in Fig. 3(b), clearly shows the twisted-spiral structure of the XUV emission: the amplitude is constrained to two strips that wind around the azimuthal axis, acquiring a time delay of $4\pi/3\omega$ after one revolution, while the polarization direction, indicated by the hue color scale, turns by $-120°$ over that span, in an essentially linear progression. This directly confirms the CR invariance of the HHG emission, in the sense of Eq. (2), and, with that, its nontrivial torus-knot topology.

Here, it is also instructive to broaden our scope to consider what happens when the coordinated-rotation invariance gets broken, by perturbing the OAM of one or both of the drivers. For single-color driving fields, this fully brings into play the nonperturbative physics of HHG, through the intrinsic dipole phase of the harmonics, which is proportional to the field intensity [55–58]. In that case, an OAM perturbation imprints an azimuthal intensity gradient that, through the intrinsic phase, broadens the OAM content of each harmonic [17]. Bicircular drivers, on the other hand, allow us to perform a wider exploration of the nonperturbative physics of OAM-HHG, since we can now affect both the field intensity and its shape.

To impart an intensity gradient, as in the single-color case, we divert 10% of the intensity to a donutlike $\ell = 0$ mode (with an amplitude profile $\sim r^2 e^{-r^2/\sigma^2}$) on both modes; the results are displayed in Fig. 4(b) and, as in the one-color case [17], they display an OAM broadening on each harmonic. To impart a phase gradient, on the other hand, we switch the phase of one of the $\ell = 0$ modes, so that the intensity profiles are complementary, giving a constant total intensity but a varying $I_\omega/I_{2\omega}$ intensity ratio. This produces a smaller broadening, shown in Fig. 4(c), with a different origin: the intensity ratio affects the quantum-path dynamics [40], which alters both the action and the vector aspects of the recollision [39]. Note that similarly, even in the unperturbed case, quantum-path

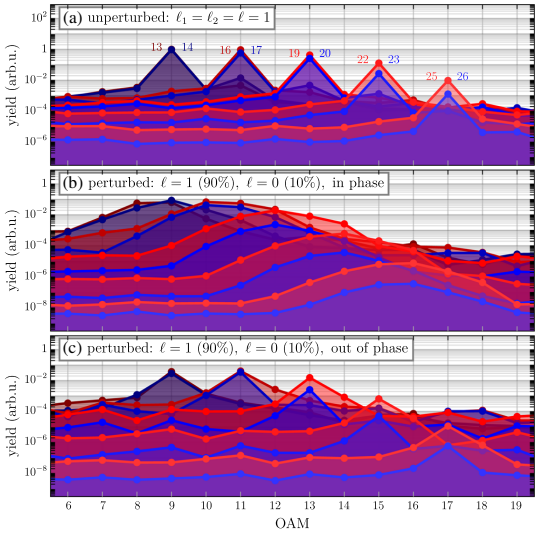

FIG. 4. OAM spectrum of the HHG radiation driven by a bicircular field with $\ell_1 = \ell_2 = 1$ (a), as in Fig. 2, as well as with a 10% intensity perturbation on a donutlike $\ell = 0$ mode on both drivers: (b) with both perturbations in phase, with matching intensity profiles, and (c) with the perturbations in opposite phase, with complementary intensity profiles. [The lines are color-coded by harmonic order, as in (a)].

dynamics and phase-matching effects should contribute to radial structures in the HHG emission [49,59].

Finally, it is important to note that this configuration also allows for the production of XUV radiation with controllable OAM, as recently pointed out in Refs. [41,50,60]. In single-color collinear experiments the OAM scales linearly [16–18], with the qth harmonic carrying OAM $\ell_q = q\ell$ [15,17]; for high q, this OAM is often too big to be useful, and it is challenging to detect and characterize it in the first place [16,61]. One solution is to use a noncollinear perturbing beam [16,19,20], but that spreads the harmonic yield over a range of different OAM modes.

Here, however, the use of CR-invariant drivers allows us to imprint the qth harmonic with an arbitrary OAM ℓ_q by leveraging the bicircular spin selection rules [22,24,46] to concentrate all of the harmonic yield at a given harmonic order into a single OAM mode. Moreover, the interaction region is no longer constrained to lie within the intersection of two noncollinear beams, allowing it to be substantially longer and therefore to support a stronger harmonic emission when properly phase matched.

The generation of structured high-frequency pulses through TKAM conservation provides a source of bright XUV radiation with customized polarization and OAM. For example, it opens a scenario to explore spin-orbit coupling at the nanoscale [62], and to study the modification of photoionization dynamics of single atoms and molecules [63,64]. Such XUV beams with controlled angular momenta can also be used to enhance light microscopy—through high-contrast high-resolution spiral-phase imaging [65] or XUV microscopy [16]—in lithography [66], and as tailored waveforms for developing and improving spectroscopic techniques [67,68]. Finally, we note that TKAM conservation in HHG provides a new tool to study ultrafast magnetism, in particular to image magnetic domains [69], to uncover spin or charge dynamics in magnetic materials [70], and to generate ultrafast magnetic fields [71].

We thank T. Ruchon for helpful observations. E. P. acknowledges Cellex-ICFO-MPQ fellowship funding; E. P. and M. L. acknowledge the Spanish Ministry MINECO (National Plan 15 Grants: FISICATEAMO No. FIS2016-79508-P, SEVERO OCHOA No. SEV-2015-0522, FPI), European Social Fund, Fundació Cellex, Generalitat de Catalunya (AGAUR Grant No. 2017 SGR 1341 and CERCA/Program), ERC AdG OSYRIS, EU FETPRO QUIC, and the National Science Centre, Poland-Symfonia Grant No. 2016/20/W/ST4/00314. A. P. acknowledges funding from Comunidad de Madrid through TALENTO Grant No. 2017-T1/IND-5432. J. S. R., L. P., and C. H.-G acknowledge support from Junta de Castilla y León (SA046U16) and Ministerio de Economía y Competitividad (FIS2013-44174-P, FIS2016-75652-P). C. H.-G. acknowledges support from a 2017 Leonardo Grant for Researchers and Cultural Creators, BBVA Foundation and Ministerio de Ciencia, Innovación y Universidades for a Ramón y Cajal contract (RYC-2017-22745), co-funded by the European Social Fund. L. R. acknowledges support from Ministerio de Educación, Cultura y Deporte (FPU16/02591). H. C. K. and M. M. M. acknowledge support from the Department of Energy BES Award No. DE-FG02–99ER14982, as well as a DARPA TEE Award No. D18AC00017. We thankfully acknowledge the computer resources at MareNostrum and the technical support provided by Barcelona Supercomputing Center (RES-AECT-2014-2-0085). This research made use of the high-performance computing resources of the Castilla y León Supercomputing Center (SCAYLE), financed by the European Regional Development Fund (ERDF).

*Corresponding author.
emilio.pisanty@icfo.eu

[1] R. Boyd, *Nonlinear Optics* (Academic Press, San Diego, 2003).
[2] D. E. Neuenschwander, *Emmy Noether's Wonderful Theorem* (John Hopkins University Press, Baltimore, 2011).
[3] N. Bloembergen, Conservation laws in nonlinear optics, J. Opt. Soc. Am. **70**, 1429 (1980).
[4] G. Molina-Terriza, J. P. Torres, and L. Torner, Twisted photons, Nat. Phys. **3**, 305 (2007).
[5] J. Courtial, K. Dholakia, L. Allen, and M. J. Padgett, Second-harmonic generation and the conservation of orbital

angular momentum with high-order Laguerre-Gaussian modes, Phys. Rev. A **56**, 4193 (1997).
[6] M. Ivanov and O. Smirnova, in *Attosecond and XUV Physics: Ultrafast Dynamics and Spectroscopy*, edited by T. Schultz and M. Vrakking (Wiley-VCH, Weinheim, 2014), pp. 201–256.
[7] F. Krausz and M. Ivanov, Attosecond physics, Rev. Mod. Phys. **81**, 163 (2009).
[8] T. Popmintchev, M.-C. Chen, D. Popmintchev, P. Arpin, S. Brown, S. Ališauskas, G. Andriukaitis, T. Balčiunas, O. D. Mücke, A. Pugzlys, A. Baltuška, B. Shim, S. E. Schrauth, A. Gaeta, C. Hernández-García, L. Plaja, A. Becker, A. Jaron-Becker, M. M. Murnane, and H. C. Kapteyn, Bright coherent ultrahigh harmonics in the keV X-ray regime from mid-infrared femtosecond lasers, Science **336**, 1287 (2012).
[9] M. Lewenstein, P. Balcou, M. Y. Ivanov, A. L'Huillier, and P. B. Corkum, Theory of high-harmonic generation by low-frequency laser fields, Phys. Rev. A **49**, 2117 (1994).
[10] P. B. Corkum, Plasma perspective on strong field multiphoton ionization, Phys. Rev. Lett. **71**, 1994 (1993).
[11] K. J. Schafer, B. Yang, L. F. DiMauro, and K. C. Kulander, Above threshold ionization beyond the high harmonic cutoff, Phys. Rev. Lett. **70**, 1599 (1993).
[12] M. D. Perry and J. K. Crane, High-order harmonic emission from mixed fields, Phys. Rev. A **48**, R4051 (1993).
[13] J. B. Bertrand, H. J. Wörner, H.-C. Bandulet, É. Bisson, M. Spanner, J.-C. Kieffer, D. M. Villeneuve, and P. B. Corkum, Ultrahigh-Order Wave Mixing in Noncollinear High Harmonic Generation, Phys. Rev. Lett. **106**, 023001 (2011).
[14] M. Zürch, C. Kern, P. Hansinger, A. Dreischuh, and C. Spielmann, Strong-field physics with singular light beams, Nat. Phys. **8**, 743 (2012).
[15] C. Hernández-García, A. Picón, J. San Román, and L. Plaja, Attosecond Extreme Ultraviolet Vortices from High-Order Harmonic Generation, Phys. Rev. Lett. **111**, 083602 (2013).
[16] G. Gariepy, J. Leach, K. T. Kim, T. J. Hammond, E. Frumker, R. W. Boyd, and P. B. Corkum, Creating High-Harmonic Beams with Controlled Orbital Angular Momentum, Phys. Rev. Lett. **113**, 153901 (2014).
[17] L. Rego, J. S. Román, A. Picón, L. Plaja, and C. Hernández-García, Nonperturbative Twist in the Generation of Extreme-Ultraviolet Vortex Beams, Phys. Rev. Lett. **117**, 163202 (2016).
[18] R. Géneaux, A. Camper, T. Auguste, O. Gobert, J. Caillat, R. Taïeb, and T. Ruchon, Synthesis and characterization of attosecond light vortices in the extreme ultraviolet, Nat. Commun. **7**, 12583 (2016).
[19] F. Kong, C. Zhang, F. Bouchard, Z. Li, G. G. Brown, D. H. Ko, T. Hammond, L. Arissian, R. W. Boyd, E. Karimi *et al.*, Controlling the orbital angular momentum of high harmonic vortices, Nat. Commun. **8**, 14970 (2017).
[20] D. Gauthier, P. R. Ribič, G. Adhikary, A. Camper, C. Chappuis, R. Cucini, L. DiMauro, G. Dovillaire, F. Frassetto, R. Géneaux *et al.*, Tunable orbital angular momentum in high-harmonic generation, Nat. Commun. **8**, 14971 (2017).
[21] C. Hernández-García, A twist in coherent X-rays, Nat. Phys. **13**, 327 (2017).
[22] A. Fleischer, O. Kfir, T. Diskin, P. Sidorenko, and O. Cohen, Spin angular momentum and tunable polarization in high-harmonic generation, Nat. Photonics **8**, 543 (2014).
[23] M. Ivanov and E. Pisanty, Taking control of polarization, Nat. Photonics **8**, 501 (2014).
[24] E. Pisanty, S. Sukiasyan, and M. Ivanov, Spin conservation in high-order-harmonic generation using bicircular fields, Phys. Rev. A **90**, 043829 (2014).
[25] D. D. Hickstein, F. J. Dollar, P. Grychtol, J. L. Ellis, R. Knut, C. Hernández-García, D. Zusin, C. Gentry, J. M. Shaw, K. M. D. Tingting Fan, A. Becker, A. Jaroń-Becker, H. C. Kapteyn, M. M. Murnane, and C. G. Durfee, Non-collinear generation of angularly isolated circularly polarized high harmonics, Nat. Photonics **9**, 743 (2015).
[26] P.-C. Huang, C. Hernández-García, J.-T. Huang, P.-Y. Huang, C.-H. Lu, L. Rego, D. D. Hickstein, J. L. Ellis, A. Jaron-Becker, A. Becker *et al.*, Polarization control of isolated high-harmonic pulses, Nat. Photonics **12**, 349 (2018).
[27] J. Leach, J. Courtial, K. Skeldon, S. M. Barnett, S. Franke-Arnold, and M. J. Padgett, Interferometric Methods to Measure Orbital and Spin, or the Total Angular Momentum of a Single Photon, Phys. Rev. Lett. **92**, 013601 (2004).
[28] K. E. Ballantine, J. F. Donegan, and P. R. Eastham, There are many ways to spin a photon: Half-quantization of a total optical angular momentum, Sci. Adv. **2**, e1501748 (2016).
[29] M. R. Dennis, Polarization singularities in paraxial vector fields: morphology and statistics, Opt. Commun. **213**, 201 (2002).
[30] I. Freund, Cones, spirals, and Möbius strips, in elliptically polarized light, Opt. Commun. **249**, 7 (2005).
[31] T. Bauer, P. Banzer, E. Karimi, S. Orlov, A. Rubano, L. Marrucci, E. Santamato, R. W. Boyd, and G. Leuchs, Observation of optical polarization Möbius strips, Science **347**, 964 (2015).
[32] T. Bauer, M. Neugebauer, G. Leuchs, and P. Banzer, Optical Polarization Möbius Strips and Points of Purely Transverse Spin Density, Phys. Rev. Lett. **117**, 013601 (2016).
[33] E. Pisanty, G. J. Machado, V. Vicuña-Hernández, A. Picón, A. Celi, J. P. Torres, and M. Lewenstein, Knotting fractional-order knots with the polarization state of light, Nat. Photonics, https://doi.org/10.1038/s41566-019-0450-2.
[34] H. Eichmann, A. Egbert, S. Nolte, C. Momma, B. Wellegehausen, W. Becker, S. Long, and J. K. McIver, Polarization-dependent high-order two-color mixing, Phys. Rev. A **51**, R3414 (1995).
[35] D. B. Milošević and W. Becker, Attosecond pulse trains with unusual nonlinear polarization, Phys. Rev. A **62**, 011403 (2000).
[36] O. Kfir, P. Grychtol, E. Turgut, R. Knut, D. Zusin, D. Popmintchev, T. Popmintchev, H. Nembach, J. M. Shaw, A. Fleischer *et al.*, Generation of bright phase-matched circularly-polarized extreme ultraviolet high harmonics, Nat. Photonics **9**, 99 (2015).
[37] T. Fan *et al.*, Bright circularly polarized soft X-ray high harmonics for X-ray magnetic circular dichroism, Proc. Natl. Acad. Sci. U.S.A. **112**, 14206 (2015).
[38] C. Chen, Z. Tao1, C. Hernández-García, P. Matyba, A. Carr, R. Knut, O. Kfir, D. Zusin, C. Gentry, P. Grychtol, O. Cohen, L. Plaja, A. Becker, A. Jaron-Becker, H. Kapteyn, and M. Murnane, Tomographic reconstruction of circularly polarized high-harmonic fields: 3D attosecond metrology, Sci. Adv. **2**, e1501333 (2016).

[39] E. Pisanty and A. Jiménez-Galán, Strong-field approximation in a rotating frame: High-order harmonic emission from p states in bicircular fields, Phys. Rev. A **96**, 063401 (2017).

[40] A. Jiménez-Galán, N. Zhavoronkov, D. Ayuso, F. Morales, S. Patchkovskii, M. Schloz, E. Pisanty, O. Smirnova, and M. Ivanov, Control of attosecond light polarization in two-color bicircular fields, Phys. Rev. A **97**, 023409 (2018).

[41] K. M. Dorney, L. Rego, N. J. Brooks, J. S. Román, C.-T. Liao, J. L. Ellis, D. Zusin, C. Gentry, Q. L. Nguyen, J. M. Shaw, A. Picón, L. Plaja, H. C. Kapteyn, M. M. Murnane, and C. Hernández-García, Controlling the polarization and vortex charge of attosecond high-harmonic beams via simultaneous spin-orbit momentum conservation, Nat. Photonics **13**, 123 (2019).

[42] C. C. Adams, *The Knot Book: An Elementary Introduction to the Mathematical Theory of Knots* (American Mathematical Society, Providence, Rhode Island, 2004).

[43] Irrational coordination parameters are also achievable, using combinations of non-commensurate bichromatic drivers and, thus, a quasi-periodic driving field. While possible, quasi-periodic fields require infinite time and infinitely small bandwidth to distinguish from nearby commensurate frequency pairs, a requirement that is generally at odds with physical experiments and particularly so with the short pulses required by HHG.

[44] Note that if one works with dimensionful angular momenta, with OAM and SAM defined as $\hbar\ell$ and $\pm\hbar$, respectively, then TKAM is given by $\hbar j_\gamma$. For simplicity, we factor out $\hbar$, and work with the dimensionless TKAM j_γ.

[45] This formalism extends naturally to bicircular combinations of frequencies $p\omega$ and $q\omega$, with p, q coprime integers, for which $\gamma = \frac{p\ell_1 - q\ell_2}{p+q}$ and $\tau = \frac{\ell_1+\ell_2}{(p+q)\omega}$.

[46] O. E. Alon, V. Averbukh, and N. Moiseyev, Selection Rules for the High Harmonic Generation Spectra, Phys. Rev. Lett. **80**, 3743 (1998).

[47] V. Averbukh, O. E. Alon, and N. Moiseyev, Stability and instability of dipole selection rules for atomic high-order-harmonic-generation spectra in two-beam setups, Phys. Rev. A **65**, 063402 (2002).

[48] C. Hernández-García, J. A. Pérez-Hernández, J. Ramos, E. C. Jarque, L. Roso, and L. Plaja, High-order harmonic propagation in gases within the discrete dipole approximation, Phys. Rev. A **82**, 033432 (2010).

[49] C. Hernández-García, J. S. Román, L. Plaja, and A. Picón, Quantum-path signatures in attosecond helical beams driven by optical vortices, New J. Phys. **17**, 093029 (2015).

[50] W. Paufler, B. Böning, and S. Fritzsche, Tailored orbital angular momentum in high-order harmonic generation with bicircular Laguerre-Gaussian beams, Phys. Rev. A **98**, 011401 (2018).

[51] A. Turpin, L. Rego, A. Picón, J. S. Román, and C. Hernández-García, Extreme ultraviolet fractional orbital angular momentum beams from high harmonic generation, Sci. Rep. **7**, 43888 (2017).

[52] I. Freund, Coherency matrix description of optical polarization singularities, J. Opt. A **6**, S229 (2004).

[53] P. Antoine, B. Piraux, and A. Maquet, Time profile of harmonics generated by a single atom in a strong electromagnetic field, Phys. Rev. A **51**, R1750(R) (1995).

[54] For the TKAM beams we use to drive the emission, the knotted structure of the beam is best explored through the third field moment $\langle E_i E_j E_k \rangle$, and more specifically its hexapolar component $T_{33}(\mathbf{r}) = \int_{-\infty}^{\infty} (E_x(\mathbf{r},t) + iE_y(\mathbf{r},t))^3 \mathrm{d}t$, which intrinsically respects the threefold rotational symmetry of the polarization [33]. For a broadband APT, however, this is not a suitable measure, since its spectral characteristics favour contributions from low-order harmonics, so that it acquires an unphysical dependence on the filter used to isolate the pulse train from the perturbative response at low harmonic orders.

[55] A. L'Huillier, P. Balcou, S. Candel, K. J. Schafer, and K. C. Kulander, Calculations of high-order harmonic-generation processes in xenon at 1064 nm, Phys. Rev. A **46**, 2778 (1992).

[56] M. Lewenstein, P. Salières, and A. L'Huillier, Phase of the atomic polarization in high-order harmonic generation, Phys. Rev. A **52**, 4747 (1995).

[57] A. Zaïr, M. Holler, A. Guandalini, F. Schapper, J. Biegert, L. Gallmann, U. Keller, A. S. Wyatt, A. Monmayrant, I. A. Walmsley, E. Cormier, T. Auguste, J. P. Caumes, and P. Salières, Quantum Path Interferences in High-Order Harmonic Generation, Phys. Rev. Lett. **100**, 143902 (2008).

[58] C. Hernández-García and L. Plaja, Off-axis compensation of attosecond pulse chirp, J. Phys. B **45**, 074021 (2012).

[59] R. Géneaux, C. Chappuis, T. Auguste, S. Beaulieu, T. T. Gorman, F. Lepetit, L. F. DiMauro, and T. Ruchon, Radial index of Laguerre-Gaussian modes in high-order-harmonic generation, Phys. Rev. A **95**, 051801 (2017).

[60] F. Kong, C. Zhang, H. Larocque, F. Bouchard, Z. Li, M. Taucer, G. Brown, T. J. Hammond, E. Karimi, and P. B. Corkum, Spin constrained orbital angular momentum control in high-harmonic generation, arXiv:1810.05894.

[61] F. Sanson, A. Pandey, F. Harms, G. Dovillaire, E. Baynard, J. Demailly, O. Guilbaud, B. Lucas, O. Neveu, M. Pittman *et al.*, Hartmann wavefront sensor characterization of a high charge vortex beam in the extreme ultraviolet spectral range, Opt. Lett. **43**, 2780 (2018).

[62] F. Cardano and L. Marrucci, Spin-orbit photonics, Nat. Photonics **9**, 776 (2015).

[63] A. Picón, A. Benseny, J. Mompart, J. V. de Aldana, L. Plaja, G. F. Calvo, and L. Roso, Transferring orbital and spin angular momenta of light to atoms, New J. Phys. **12**, 083053 (2010).

[64] S. Eckart, M. Kunitski, M. Richter, A. Hartung, J. Rist, F. Trinter, K. Fehre, N. Schlott, K. Henrichs, L. P. H. Schmidt *et al.*, Ultrafast preparation and detection of ring currents in single atoms, Nat. Phys. **14**, 701 (2018).

[65] S. Fürhapter, A. Jesacher, S. Bernet, and M. Ritsch-Marte, Spiral phase contrast imaging in microscopy, Opt. Express **13**, 689 (2005).

[66] T. F. Scott, B. A. Kowalski, A. C. Sullivan, C. N. Bowman, and R. R. McLeod, Two-color single-photon photoinitiation and photoinhibition for subdiffraction photolithography, Science **324**, 913 (2009).

[67] P. Rebernik Ribič, B. Rösner, D. Gauthier, E. Allaria, F. Döring, L. Foglia, L. Giannessi, N. Mahne, M. Manfredda, C. Masciovecchio, R. Mincigrucci, N. Mirian, E. Principi, E. Roussel, A. Simoncig, S. Spampinati, C. David, and G. De Ninno, Extreme-Ultraviolet Vortices from a Free-Electron Laser, Phys. Rev. X **7**, 031036 (2017).

[68] C. Hernández-García, J. Vieira, J. T. Mendonça, L. Rego, J. S. Román, L. Plaja, P. R. Ribic, D. Gauthier, and A. Picón, Generation and applications of extreme-ultraviolet vortices, Photonics **4**, 28 (2017).

[69] O. Kfir, S. Zayko, C. Nolte, M. Sivis, M. Möller, B. Hebler, S. S. P. K. Arekapudi, D. Steil, S. Schäfer, M. Albrecht, O. Cohen, S. Mathias, and C. Ropers, Nanoscale magnetic imaging using circularly polarized high-harmonic radiation, Sci. Adv. **3**, eaao4641 (2017).

[70] P. Tengdin, W. You, C. Chen, X. Shi, D. Zusin, Y. Zhang, C. Gentry, A. Blonsky, M. Keller, P. M. Oppeneer *et al.*, Critical behavior within 20 fs drives the out-of-equilibrium laser-induced magnetic phase transition in nickel, Sci. Adv. **4**, eaap9744 (2018).

[71] M. Blanco, F. Cambronero, M. T. Flores-Arias, E. Conejero Jarque, L. Plaja, and C. Hernández-García, Ultraintense femtosecond magnetic nanoprobes induced by azimuthally polarized laser beams, ACS Photonics **6**, 38 (2019).

Correction: Extra characters were inserted inadvertently in the DOI string for Ref. [33] during the final production stage and have been removed, enabling proper access.

Second Correction: The previously published Figure 4 was processed improperly during the production cycle for the PDF version and its rendition has been corrected.

BIBLIOGRAPHY

1. Schafer, K. J., Yang, B., DiMauro, L. F. & Kulander, K. C. Above threshold ionization beyond the high harmonic cutoff. *Physical Review Letters* **70,** 1599–1602. doi:10.1103/physrevlett.70.1599 (1993) (cit. on pp. 1, 10, 20).
2. Corkum, P. B. Plasma perspective on strong field multiphoton ionization. *Physical Review Letters* **71,** 1994–1997. doi:10.1103/physrevlett.71.1994 (1993) (cit. on pp. 1, 10, 20, 22, 25).
3. Lebedew, P. Untersuchungen über die Druckkräfte des Lichtes. *Annalen der Physik* **311,** 433–458. doi:10.1002/andp.19013111102 (1901) (cit. on pp. 2, 10).
4. Nichols, E. F. & Hull, G. F. The Pressure Due to Radiation. (Second Paper.) *Physical Review (Series I)* **17,** 26–50. doi:10.1103/physrevseriesi.17.26 (1903) (cit. on pp. 2, 10).
5. Poynting, J. H. The wave motion of a revolving shaft, and a suggestion as to the angular momentum in a beam of circularly polarised light. *Proceedings of the Royal Society of London. Series A, Containing Papers of a Mathematical and Physical Character* **82,** 560–567. doi:10.1098/rspa.1909.0060 (1909) (cit. on pp. 3, 10).
6. Beth, R. A. Mechanical Detection and Measurement of the Angular Momentum of Light. *Physical Review* **50,** 115–125. doi:10.1103/physrev.50.115 (1936) (cit. on pp. 3, 10, 154).
7. Allen, L., Beijersbergen, M. W., Spreeuw, R. J. C. & Woerdman, J. P. Orbital angular momentum of light and the transformation of Laguerre-Gaussian laser modes. *Physical Review A* **45,** 8185–8189. doi:10.1103/physreva.45.8185 (1992) (cit. on pp. 3, 11, 92, 154).
8. Grier, D. G. A revolution in optical manipulation. *Nature* **424,** 810–816. doi:10.1038/nature01935 (2003) (cit. on pp. 3, 11).
9. Simpson, N. B., Allen, L. & Padgett, M. J. Optical tweezers and optical spanners with Laguerre–Gaussian modes. *Journal of Modern Optics* **43,** 2485–2491. doi:10.1080/09500349608230675 (1996) (cit. on pp. 3, 11).
10. Wang, J., Yang, J.-Y., Fazal, I. M., Ahmed, N., Yan, Y., Huang, H., Ren, Y., Yue, Y., Dolinar, S., Tur, M. & Willner, A. E. Terabit free-space data transmission employing orbital angular momentum multiplexing. *Nature Photonics* **6,** 488–496. doi:10.1038/nphoton.2012.138 (2012) (cit. on pp. 3, 11).

11. Fürhapter, S., Jesacher, A., Bernet, S. & Ritsch-Marte, M. Spiral interferometry. *Optics Letters* **30,** 1953. doi:10.1364/ol.30.001953 (2005) (cit. on pp. 3, 11).

12. Vicidomini, G., Bianchini, P. & Diaspro, A. STED super-resolved microscopy. *Nature Methods* **15,** 173–182. doi:10.1038/nmeth.4593 (2018) (cit. on pp. 3, 11).

13. Mair, A., Vaziri, A., Weihs, G. & Zeilinger, A. Entanglement of the orbital angular momentum states of photons. *Nature* **412,** 313–316. doi:10.1038/35085529 (2001) (cit. on pp. 3, 11).

14. Torres, J. *Twisted photons : applications of light with orbital angular momentum* ISBN: 9783527409075. doi:10.1002/9783527635368 (Wiley-VCH Verlag, Weinheim, 2011) (cit. on pp. 3, 11).

15. Rego, L., Hernández-García, C., Picón, A. & Plaja, L. Site-specific tunnel-ionization in high harmonic generation in molecules. *New Journal of Physics* **22,** 043012. doi:10.1088/1367-2630/ab7dde (2020) (cit. on pp. 4, 6, 12, 14, 17, 46, 52–54).

16. Rego, L., Dorney, K. M., Brooks, N. J., Nguyen, Q. L., Liao, C.-T., Román, J. S., Couch, D. E., Liu, A., Pisanty, E., Lewenstein, M., Plaja, L., Kapteyn, H. C., Murnane, M. M. & Hernández-García, C. Generation of extreme-ultraviolet beams with time-varying orbital angular momentum. *Science* **364,** eaaw9486. doi:10.1126/science.aaw9486 (2019) (cit. on pp. 4, 6, 12, 14, 46, 71, 83, 85, 90, 92, 149, 152, 164).

17. Rego, L., Brooks, N. J., Nguyen, Q. L. D., Román, J. S., Binnie, I., Plaja, L., Kapteyn, H. C., Murnane, M. M. & Hernández-García, C. Necklace-structured high harmonic generation for low-divergence, soft X-ray harmonic combs with tunable line spacing. Submitted to Science Advances. arXiv: 2107.12669 [physics.optics] (2021) (cit. on pp. 4, 6, 13, 14, 71, 86, 90, 103).

18. Dorney, K. M., Rego, L., Brooks, N. J., Román, J. S., Liao, C.-T., Ellis, J. L., Zusin, D., Gentry, C., Nguyen, Q. L., Shaw, J. M., Picón, A., Plaja, L., Kapteyn, H. C., Murnane, M. M. & Hernández-García, C. Controlling the polarization and vortex charge of attosecond high-harmonic beams via simultaneous spin–orbit momentum conservation. *Nature Photonics* **13,** 123–130. doi:10.1038/s41566-018-0304-3 (2019) (cit. on pp. 4–6, 13, 14, 132, 141, 144, 149, 153, 154, 164).

19. Rego, L., Román, J. S., Plaja, L. & Hernández-García, C. Trains of attosecond pulses structured with time-ordered polarization states. *Optics Letters* **45,** 5636. doi:10.1364/ol.404402 (2020) (cit. on pp. 5, 6, 13, 14, 132, 153, 164).

20. Huang, P.-C., Hernández-García, C., Huang, J.-T., Huang, P.-Y., Lu, C.-H., Rego, L., Hickstein, D. D., Ellis, J. L., Jaron-Becker, A., Becker, A., Yang, S.-D., Durfee, C. G., Plaja, L., Kapteyn, H. C., Murnane, M. M., Kung, A. H. & Chen, M.-C. Polarization control of isolated high-harmonic pulses. *Nature Photonics* **12,** 349–354. doi:10.1038/s41566-018-0145-0 (2018) (cit. on pp. 5, 6, 13, 14, 46, 133, 135, 177).

21. Chang, K.-Y., Huang, L.-C., Asaga, K., Tsai, M.-S., Rego, L., Huang, P.-C., Mashiko, H., Oguri, K., Hernández-García, C. & Chen, M.-C. High-order nonlinear dipole response characterized by extreme ultraviolet ellipsometry. *Optica* **8,** 484. doi:10.1364/optica.413531 (2021) (cit. on pp. 5, 6, 13, 14, 46, 137, 177).

22. Pisanty, E., Rego, L., Román, J. S., Picón, A., Dorney, K. M., Kapteyn, H. C., Murnane, M. M., Plaja, L., Lewenstein, M. & Hernández-García, C. Conservation of Torus-knot Angular Momentum in High-order Harmonic Generation. *Physical Review Letters* **122,** 203201. doi:10.1103/physrevlett.122.203201 (2019) (cit. on pp. 5, 6, 13, 14, 147–149, 177).

23. Corkum, P. B. & Krausz, F. Attosecond science. *Nature Physics* **3,** 381–387. doi:10.1038/nphys620 (2007) (cit. on p. 17).

24. Salières, P., Maquet, A., Haessler, S., Caillat, J. & Taïeb, R. Imaging orbitals with attosecond and Ångström resolutions: toward attochemistry? *Reports on Progress in Physics* **75,** 062401. doi:10.1088/0034-4885/75/6/062401 (2012) (cit. on p. 17).

25. Baker, S., Robinson, J. S., Haworth, C. A., Teng, H., Smith, R. A., Chirilă, C. C., Lein, M., Tisch, J. W. G. & Marangos, J. P. Probing Proton Dynamics in Molecules on an Attosecond Time Scale. *Science* **312,** 424–427. doi:10.1126/science.1123904 (2006) (cit. on pp. 17, 30, 46, 54).

26. Lein, M., Hay, N., Velotta, R., Marangos, J. P. & Knight, P. L. Interference effects in high-order harmonic generation with molecules. *Physical Review A* **66,** 023805. doi:10.1103/physreva.66.023805 (2002) (cit. on pp. 18, 30, 46, 47, 51, 54).

27. Baker, S., Robinson, J. S., Lein, M., Chirilă, C. C., Torres, R., Bandulet, H. C., Comtois, D., Kieffer, J. C., Villeneuve, D. M., Tisch, J. W. G. & Marangos, J. P. Dynamic Two-Center Interference in High-Order Harmonic Generation from Molecules with Attosecond Nuclear Motion. *Physical Review Letters* **101,** 053901. doi:10.1103/physrevlett.101.053901 (2008) (cit. on pp. 18, 30).

28. Luu, T. T., Garg, M., Kruchinin, S. Y., Moulet, A., Hassan, M. T. & Goulielmakis, E. Extreme ultraviolet high-harmonic spectroscopy of solids. *Nature* **521,** 498–502. doi:10.1038/nature14456 (2015) (cit. on p. 18).

29. Silva, R. E. F., Blinov, I. V., Rubtsov, A. N., Smirnova, O. & Ivanov, M. High-harmonic spectroscopy of ultrafast many-body dynamics in strongly correlated systems. *Nature Photonics* **12,** 266–270. doi:10.1038/s41566-018-0129-0 (2018) (cit. on p. 18).

30. Itatani, J., Levesque, J., Zeidler, D., Niikura, H., Pépin, H., Kieffer, J. C., Corkum, P. B. & Villeneuve, D. M. Tomographic imaging of molecular orbitals. *Nature* **432,** 867–871. doi:10.1038/nature03183 (2004) (cit. on pp. 18, 46).

31. Vampa, G., McDonald, C., Orlando, G., Klug, D., Corkum, P. & Brabec, T. Theoretical Analysis of High-Harmonic Generation in Solids. *Physical Review Letters* **113,** 073901. doi:10.1103/physrevlett.113.073901 (2014) (cit. on p. 18).

32. Ghimire, S., Ndabashimiye, G., DiChiara, A. D., Sistrunk, E., Stockman, M. I., Agostini, P., DiMauro, L. F. & Reis, D. A. Strong-field and attosecond physics in solids. *Journal of Physics B: Atomic, Molecular and Optical Physics* **47,** 204030. doi:10.1088/0953-4075/47/20/204030 (2014) (cit. on p. 18).

33. Zurrón-Cifuentes, Ó., Boyero-García, R., Hernández-García, C., Picón, A. & Plaja, L. Optical anisotropy of non-perturbative high-order harmonic generation in gapless graphene. *Optics Express* **27,** 7776. doi:10.1364/oe.27.007776 (2019) (cit. on pp. 18, 52, 132).

34. Luu, T. T., Yin, Z., Jain, A., Gaumnitz, T., Pertot, Y., Ma, J. & Wörner, H. J. Extreme–ultraviolet high–harmonic generation in liquids. *Nature Communications* **9.** doi:10.1038/s41467-018-06040-4 (2018) (cit. on p. 18).

35. Yoshikawa, N., Tamaya, T. & Tanaka, K. High-harmonic generation in graphene enhanced by elliptically polarized light excitation. *Science* **356,** 736–738. doi:10.1126/science.aam8861 (2017) (cit. on p. 18).

36. Sutherland, J. R., Christensen, E. L., Powers, N. D., Rhynard, S. E., Painter, J. C. & Peatross, J. High harmonic generation in a semi-infinite gas cell. *Optics Express* **12,** 4430. doi:10.1364/opex.12.004430 (2004) (cit. on p. 18).

37. Göppert-Mayer, M. Über Elementarakte mit zwei Quantensprüngen. *Annalen der Physik* **401,** 273–294. doi:10.1002/andp.19314010303 (1931) (cit. on p. 18).

38. Kaiser, W. & Garrett, C. G. B. Two-Photon Excitation in $CaF_2 : Eu^{2+}$. *Physical Review Letters* **7,** 229–231. doi:10.1103/physrevlett.7.229 (1961) (cit. on p. 18).

39. Franken, P. A., Hill, A. E., Peters, C. W. & Weinreich, G. Generation of Optical Harmonics. *Physical Review Letters* **7,** 118–119. doi:10.1103/physrevlett.7.118 (1961) (cit. on p. 18).

40. Lompré, L. A., L'Huillier, A., Ferray, M., Monot, P., Mainfray, G. & Manus, C. High-order harmonic generation in xenon: intensity and propagation effects. *Journal of the Optical Society of America B* **7,** 754. doi:10.1364/josab.7.000754 (1990) (cit. on p. 18).

41. McPherson, A., Gibson, G., Jara, H., Johann, U., Luk, T. S., McIntyre, I. A., Boyer, K. & Rhodes, C. K. Studies of multiphoton production of vacuum-ultraviolet radiation in the rare gases. *Journal of the Optical Society of America B* **4,** 595. doi:10.1364/josab.4.000595 (1987) (cit. on p. 19).

42. Ferray, M., L'Huillier, A., Li, X. F., Lompre, L. A., Mainfray, G. & Manus, C. Multiple-harmonic conversion of 1064 nm radiation in rare gases. *Journal of Physics B: Atomic, Molecular and Optical Physics* **21,** L31–L35. doi:10.1088/0953-4075/21/3/001 (1988) (cit. on pp. 19, 24).

43. Li, X. F., L'Huillier, A., Ferray, M., Lompré, L. A. & Mainfray, G. Multiple-harmonic generation in rare gases at high laser intensity. *Physical Review A* **39,** 5751–5761. doi:10.1103/physreva.39.5751 (1989) (cit. on p. 19).

44. Popmintchev, T., Chen, M.-C., Popmintchev, D., Arpin, P., Brown, S., Ališauskas, S., Andriukaitis, G., Balčiunas, T., M¨˜cke, O. D., Pugzlys, A., Baltuška, A., Shim, B., Schrauth, S. E., Gaeta, A., Hernández-García, C., Plaja, L., Becker, A., Jaron-Becker, A., Murnane, M. M. & Kapteyn, H. C. Bright Coherent Ultrahigh Harmonics in the keV X-ray Regime from Mid-Infrared Femtosecond Lasers. *Science* **336,** 1287–1291. doi:10.1126/science.1218497 (2012) (cit. on pp. 19, 25).

45. Popmintchev, D., Hernández-García, C., Dollar, F., Mancuso, C., Pérez-Hernández, J. A., Chen, M.-C., Hankla, A., Gao, X., Shim, B., Gaeta, A. L., Tarazkar, M., Romanov, D. A., Levis, R. J., Gaffney, J. A., Foord, M., Libby, S. B., Jaron-Becker, A., Becker, A., Plaja, L., Murnane, M. M., Kapteyn, H. C. & Popmintchev, T. Ultraviolet surprise: Efficient soft x-ray high-harmonic generation in multiply ionized plasmas. *Science* **350,** 1225–1231. doi:10.1126/science.aac9755 (2015) (cit. on p. 19).

46. Farkas, G. & Tóth, C. Proposal for attosecond light pulse generation using laser induced multiple-harmonic conversion processes in rare gases. *Physics Letters A* **168,** 447–450. doi:10.1016/0375-9601(92)90534-s (1992) (cit. on p. 19).

47. Paul, P. M. Observation of a Train of Attosecond Pulses from High Harmonic Generation. *Science* **292,** 1689–1692. doi:10.1126/science.1059413 (2001) (cit. on pp. 19, 40).

48. Guo, C., Harth, A., Carlström, S., Cheng, Y.-C., Mikaelsson, S., Mårsell, E., Heyl, C., Miranda, M., Gisselbrecht, M., Gaarde, M. B., Schafer, K. J., Mikkelsen, A., Mauritsson, J., Arnold, C. L.

& L'Huillier, A. Phase control of attosecond pulses in a train. *Journal of Physics B: Atomic, Molecular and Optical Physics* **51,** 034006. doi:10.1088/1361-6455/aa9953 (2018) (cit. on pp. 19, 37).

49. Sansone, G., Benedetti, E., Calegari, F., Vozzi, C., Avaldi, L., Flammini, R., Poletto, L., Villoresi, P., Altucci, C., Velotta, R., Stagira, S., Silvestri, S. D. & Nisoli, M. Isolated Single-Cycle Attosecond Pulses. *Science* **314,** 443–446. doi:10.1126/science.1132838 (2006) (cit. on pp. 19, 25).

50. Chini, M., Zhao, K. & Chang, Z. The generation, characterization and applications of broadband isolated attosecond pulses. *Nature Photonics* **8,** 178–186. doi:10.1038/nphoton.2013.362 (2014) (cit. on p. 19).

51. Sansone, G., Kelkensberg, F., Pérez-Torres, J. F., Morales, F., Kling, M. F., Siu, W., Ghafur, O., Johnsson, P., Swoboda, M., Benedetti, E., Ferrari, F., Lépine, F., Sanz-Vicario, J. L., Zherebtsov, S., Znakovskaya, I., L'Huillier, A., Ivanov, M. Y., Nisoli, M., Martín, F. & Vrakking, M. J. J. Electron localization following attosecond molecular photoionization. *Nature* **465,** 763–766. doi:10.1038/nature09084 (2010) (cit. on p. 20).

52. Calegari, F., Ayuso, D., Trabattoni, A., Belshaw, L., Camillis, S. D., Anumula, S., Frassetto, F., Poletto, L., Palacios, A., Decleva, P., Greenwood, J. B., Martín, F. & Nisoli, M. Ultrafast electron dynamics in phenylalanine initiated by attosecond pulses. *Science* **346,** 336–339. doi:10.1126/science.1254061 (2014) (cit. on p. 20).

53. Nisoli, M., Decleva, P., Calegari, F., Palacios, A. & Martín, F. Attosecond Electron Dynamics in Molecules. *Chemical Reviews* **117,** 10760–10825. doi:10.1021/acs.chemrev.6b00453 (2017) (cit. on p. 20).

54. Kern, C., Zürch, M. & Spielmann, C. Limitations of Extreme Nonlinear Ultrafast Nanophotonics. *Nanophotonics* **4,** 303–323. doi:10.1515/nanoph-2015-0013 (2015) (cit. on p. 20).

55. Keldysh, L. V. Ionization in the field of a strong electromagnetic wave. *Journal of Experimental and Theoretical Physics* **20,** 1307 (1964) (cit. on pp. 21, 30).

56. Augst, S., Meyerhofer, D. D., Strickland, D. & Chint, S. L. Laser ionization of noble gases by Coulomb-barrier suppression. *Journal of the Optical Society of America B* **8,** 858. doi:10.1364/josab.8.000858 (1991) (cit. on p. 22).

57. Becker, A., Plaja, L., Moreno, P., Nurhuda, M. & Faisal, F. H. M. Total ionization rates and ion yields of atoms at nonperturbative laser intensities. *Physical Review A* **64,** 023408. doi:10.1103/physreva.64.023408 (2001) (cit. on pp. 22, 30).

58. *Proceedings of the Workshop, Super Intense Loser Atom Physics (SILAP) III* (eds Piraux, B., L'Huillier, A. & Rzążewski, K.) doi:10.1007/978-1-4615-7963-2 (1993) (cit. on pp. 22, 25).

59. Hernández-García, C. *Coherent attosecond light sources based on high-order harmonic generation: influence of the propagation effects* (University of Salamanca, 2013). doi:10.14201/gredos.121369 (cit. on pp. 23, 41, 42, 44).

60. Kulander, K. C. & Shore, B. W. Calculations of Multiple-Harmonic Conversion of 1064-nm Radiation in Xe. *Physical Review Letters* **62,** 524–526. doi:10.1103/physrevlett.62.524 (1989) (cit. on p. 24).

61. Tate, J., Auguste, T., Muller, H. G., Salières, P., Agostini, P. & DiMauro, L. F. Scaling of Wave-Packet Dynamics in an Intense Midinfrared Field. *Physical Review Letters* **98,** 013901. doi:10.1103/physrevlett.98.013901 (2007) (cit. on p. 25).

62. Pérez-Hernández, J. A., Roso, L. & Plaja, L. Harmonic generation beyond the Strong-Field Approximation: the physics behind the short-wave-infrared scaling laws. *Optics Express* **17,** 9891. doi:10.1364/oe.17.009891 (2009) (cit. on pp. 25, 30, 33, 34).

63. Sola, I. J., Mével, E., Elouga, L., Constant, E., Strelkov, V., Poletto, L., Villoresi, P., Benedetti, E., Caumes, J.-P., Stagira, S., Vozzi, C., Sansone, G. & Nisoli, M. Controlling attosecond electron dynamics by phase-stabilized polarization gating. *Nature Physics* **2,** 319–322. doi:10.1038/nphys281 (2006) (cit. on p. 25).

64. Christov, I. P., Murnane, M. M. & Kapteyn, H. C. High-Harmonic Generation of Attosecond Pulses in the "Single-Cycle" Regime10.1126/science.1059413. *Phys. Rev. Lett.* **78,** 1251–1254. doi:10.1103/PhysRevLett.78.1251. https://link.aps.org/doi/10.1103/PhysRevLett.78.1251 (7 1997) (cit. on p. 25).

65. Mairesse, Y., de Bohan, A., Frasinski, L. J., Merdji, H., Dinu, L. C., Monchicourt, P., Breger, P., Kovačev, M., Taïeb, R., Carré, B., Muller, H. G., Agostini, P. & Salières, P. Attosecond Synchronization of High-Harmonic Soft X-rays. *Science* **302,** 1540–1543. doi:10.1126/science.1090277 (2003) (cit. on pp. 26, 39).

66. Crank, J. & Nicolson, P. A practical method for numerical evaluation of solutions of partial differential equations of the heat-conduction type. *Mathematical Proceedings of the Cambridge Philosophical Society* **43,** 50–67. doi:10.1017/s0305004100023197 (1947) (cit. on p. 27).

67. Jackson, J. D. *Classical Electrodynamics* (John Wiley & Sons, 1999) (cit. on pp. 28, 44).

68. Faisal, F. H. M. Multiple absorption of laser photons by atoms. *Journal of Physics B: Atomic and Molecular Physics* **6,** L89–L92. doi:10.1088/0022-3700/6/4/011 (1973) (cit. on p. 30).

69. Reiss, H. R. Effect of an intense electromagnetic field on a weakly bound system. *Physical Review A* **22,** 1786–1813. doi:10.1103/physreva.22.1786 (1980) (cit. on p. 30).

70. Lewenstein, M., Balcou, P., Ivanov, M. Y., L'Huillier, A. & Corkum, P. B. Theory of high-harmonic generation by low-frequency laser fields. *Physical Review A* **49,** 2117–2132. doi:10.1103/physreva.49.2117 (1994) (cit. on pp. 30, 35).

71. Lewenstein, M., Salières, P. & L'Huillier, A. Phase of the atomic polarization in high-order harmonic generation. *Physical Review A* **52,** 4747–4754. doi:10.1103/physreva.52.4747 (1995) (cit. on pp. 30, 35, 36).

72. Salières, P., Carré, B., Déroff, L. L., Grasbon, F., Paulus, G. G., Walther, H., R. Kopold, W. B., Milošević, D. B., Sanpera, A. & Lewenstein, M. Feynman's Path-Integral Approach for Intense-Laser-Atom Interactions. *Science* **292,** 902–905. doi:10.1126/science.108836 (2001) (cit. on p. 30).

73. Chirilă, C. C. & Lein, M. Strong-field approximation for harmonic generation in diatomic molecules. *Physical Review A* **73,** 023410. doi:10.1103/physreva.73.023410 (2006) (cit. on pp. 30, 46).

74. Zhou, X., Tong, X. M., Zhao, Z. X. & Lin, C. D. Alignment dependence of high-order harmonic generation from N_2 and O_2 molecules in intense laser fields. *Physical Review A* **72,** 033412. doi:10.1103/physreva.72.033412 (2005) (cit. on p. 30).

75. Zimmermann, B., Lein, M. & Rost, J. M. Analysis of recombination in high-order harmonic generation in molecules. *Physical Review A* **71,** 033401. doi:10.1103/physreva.71.033401 (2005) (cit. on p. 30).

76. Vozzi, C., Negro, M., Calegari, F., Sansone, G., Nisoli, M., Silvestri, S. D. & Stagira, S. Generalized molecular orbital tomography. *Nature Physics* **7,** 822–826. doi:10.1038/nphys2029 (2011) (cit. on pp. 30, 46).

77. Kamta, G. L. & Bandrauk, A. D. Three-dimensional time-profile analysis of high-order harmonic generation in molecules: Nuclear interferences in H_2^+. *Physical Review A* **71,** 053407. doi:10.1103/physreva.71.053407 (2005) (cit. on p. 30).

78. Miller, M. R., Jaroń-Becker, A. & Becker, A. High-harmonic spectroscopy of laser-driven nonadiabatic electron dynamics in the hydrogen molecular ion. *Physical Review A* **93,** 013406. doi:10.1103/physreva.93.013406 (2016) (cit. on pp. 30, 46, 54).

79. Smirnova, O., Mairesse, Y., Patchkovskii, S., Dudovich, N., Villeneuve, D., Corkum, P. & Ivanov, M. Y. High harmonic interferometry of multi-electron dynamics in molecules. *Nature* **460,** 972–977. doi:10.1038/nature08253 (2009) (cit. on p. 30).

80. Blaga, C. I., Xu, J., DiChiara, A. D., Sistrunk, E., Zhang, K., Agostini, P., Miller, T. A., DiMauro, L. F. & Lin, C. D. Imaging ultrafast molecular dynamics with laser-induced electron diffraction. *Nature* **483,** 194–197. doi:10.1038/nature10820 (2012) (cit. on p. 30).

81. Volkov, D. M. Über eine Klasse von Lösungen der Diracschen Gleichung. *Zeitschrift für Physik* **94,** 250–260. doi:10.1007/bf01331022 (1935) (cit. on p. 31).

82. Krainov, V. P. Ionization rates and energy and angular distributions at the barrier-suppression ionization of complex atoms and atomic ions. *Journal of the Optical Society of America B* **14,** 425. doi:10.1364/josab.14.000425 (1997) (cit. on p. 32).

83. Ciappina, M. F., Chirilă, C. C. & Lein, M. Influence of Coulomb continuum wave functions in the description of high-order harmonic generation with H_2^+. *Physical Review A* **75,** 043405. doi:10.1103/physreva.75.043405 (2007) (cit. on p. 32).

84. Pérez-Hernández, J. A. *Intense-field high-order harmonic generation: beyond the standard picture* (University of Salamanca, 2015) (cit. on p. 33).

85. Ammosov, M. V., Delone, N. B. & Krainov, V. P. Tunnel ionization of complex atoms and of atomic ions in an alternating electromagnetic field. *Sov. Phys. JETP* **64,** 1191. doi:10.1117/12.938695 (1987) (cit. on pp. 35, 48).

86. Pfeiffer, A. N., Cirelli, C., Smolarski, M., Dimitrovski, D., Abusamha, M., Madsen, L. B. & Keller, U. Attoclock reveals natural coordinates of the laser-induced tunnelling current flow in atoms. *Nature Physics* **8,** 76–80. doi:10.1038/nphys2125 (2011) (cit. on p. 36).

87. Landsman, A. S., Weger, M., Maurer, J., Boge, R., Ludwig, A., Heuser, S., Cirelli, C., Gallmann, L. & Keller, U. Ultrafast resolution of tunneling delay time. *Optica* **1,** 343. doi:10.1364/optica.1.000343 (2014) (cit. on p. 36).

88. Torlina, L., Morales, F., Kaushal, J., Ivanov, I., Kheifets, A., Zielinski, A., Scrinzi, A., Muller, H. G., Sukiasyan, S., Ivanov, M. & Smirnova, O. Interpreting attoclock measurements of tunnelling times. *Nature Physics* **11,** 503–508. doi:10.1038/nphys3340 (2015) (cit. on p. 36).

89. Balcou, P., Salières, P., L'Huillier, A. & Lewenstein, M. Generalized phase-matching conditions for high harmonics: The role of field-gradient forces. *Physical Review A* **55,** 3204–3210. doi:10.1103/physreva.55.3204 (1997) (cit. on p. 36).

90. Corsi, C., Pirri, A., Sali, E., Tortora, A. & Bellini, M. Direct Interferometric Measurement of the Atomic Dipole Phase in High-Order Harmonic Generation. *Physical Review Letters* **97,** 023901. doi:10.1103/physrevlett.97.023901 (2006) (cit. on p. 36).

91. Wikmark, H., Guo, C., Vogelsang, J., Smorenburg, P. W., Coudert-Alteirac, H., Lahl, J., Peschel, J., Rudawski, P., Dacasa, H., Carlström, S., Maclot, S., Gaarde, M. B., Johnsson, P., Arnold, C. L. & L'Huillier, A. Spatiotemporal coupling of attosecond pulses. *Proceedings of the National Academy of Sciences* **116,** 4779–4787. doi:10.1073/pnas.1817626116 (2019) (cit. on pp. 38, 39, 42, 43, 89).

92. Shin, H. J., Lee, D. G., Cha, Y. H., Hong, K. H. & Nam, C. H. Generation of Nonadiabatic Blueshift of High Harmonics in an Intense Femtosecond Laser Field. *Physical Review Letters* **83,** 2544–2547. doi:10.1103/physrevlett.83.2544 (1999) (cit. on p. 39).

93. Quintard, L., Strelkov, V., Vabek, J., Hort, O., Dubrouil, A., Descamps, D., Burgy, F., Péjot, C., Mével, E., Catoire, F. & Constant, E. Optics-less focusing of XUV high-order harmonics. *Science Advances* **5,** eaau7175. doi:10.1126/sciadv.aau7175 (2019) (cit. on pp. 39, 89).

94. Varjú, K., Mairesse, Y., Carré, B., Gaarde, M. B., Johnsson, P., Kazamias, S., López-Martens, R., Mauritsson, J., Schafer, K. J., Balcou, P., L'Huillier, A. & Salières, P. Frequency chirp of harmonic and attosecond pulses. *Journal of Modern Optics* **52,** 379–394. doi:10.1080/09500340412331301542 (2005) (cit. on p. 39).

95. Zaïr, A., Holler, M., Guandalini, A., Schapper, F., Biegert, J., Gallmann, L., Keller, U., Wyatt, A. S., Monmayrant, A., Walmsley, I. A., Cormier, E., Auguste, T., Caumes, J. P. & Salières, P. Quantum Path Interferences in High-Order Harmonic Generation. *Physical Review Letters* **100,** 143902. doi:10.1103/physrevlett.100.143902 (2008) (cit. on pp. 39, 40).

96. He, X., Miranda, M., Schwenke, J., Guilbaud, O., Ruchon, T., Heyl, C., Georgadiou, E., Rakowski, R., Persson, A., Gaarde, M. B. & L'Huillier, A. Spatial and spectral properties of the high-order harmonic emission in argon for seeding applications. *Physical Review A* **79,** 063829. doi:10.1103/physreva.79.063829 (2009) (cit. on p. 40).

97. Lu, J., Cunningham, E. F., You, Y. S., Reis, D. A. & Ghimire, S. Interferometry of dipole phase in high harmonics from solids. *Nature Photonics* **13,** 96–100. doi:10.1038/s41566-018-0326-x (2018) (cit. on p. 40).

98. Gaarde, M. B., Tate, J. L. & Schafer, K. J. Macroscopic aspects of attosecond pulse generation. *Journal of Physics B: Atomic, Molecular and Optical Physics* **41,** 132001. doi:10.1088/0953-4075/41/13/132001 (2008) (cit. on pp. 40, 137).

99. Popmintchev, T., Chen, M.-C., Arpin, P., Murnane, M. M. & Kapteyn, H. C. The attosecond nonlinear optics of bright coherent X-ray generation. *Nature Photonics* **4,** 822–832. doi:10.1038/nphoton.2010.256 (2010) (cit. on p. 40).

100. Hernández-García, C., Sola, I. J. & Plaja, L. Signature of the transversal coherence length in high-order harmonic generation. *Physical Review A* **88,** 043848. doi:10.1103/physreva.88.043848 (2013) (cit. on p. 42).

101. Salières, P., L'Huillier, A. & Lewenstein, M. Coherence Control of High-Order Harmonics. *Physical Review Letters* **74,** 3776–3779. doi:10.1103/physrevlett.74.3776 (1995) (cit. on p. 43).

102. Antoine, P., L'Huillier, A. & Lewenstein, M. Attosecond Pulse Trains Using High–Order Harmonics. *Physical Review Letters* **77,** 1234–1237. doi:10.1103/physrevlett.77.1234 (1996) (cit. on p. 43).

103. Gaarde, M. B. & Schafer, K. J. Space-Time Considerations in the Phase Locking of High Harmonics. *Physical Review Letters* **89,** 213901. doi:10.1103/physrevlett.89.213901 (2002) (cit. on p. 43).

104. Hernández-García, C., Pérez-Hernández, J. A., Ramos, J., Jarque, E. C., Roso, L. & Plaja, L. High-order harmonic propagation in gases within the discrete dipole approximation. *Physical Review A* **82,** 033432. doi:10.1103/physreva.82.033432 (2010) (cit. on p. 43).

105. Hernández-García, C, Román, J. S., Plaja, L & Picón, A. Quantum-path signatures in attosecond helical beams driven by optical vortices. *New Journal of Physics* **17,** 093029. doi:10.1088/1367-2630/17/9/093029 (2015) (cit. on pp. 44, 46, 74).

106. Rego, L., Román, J. S., Picón, A., Plaja, L. & Hernández-García, C. Nonperturbative Twist in the Generation of Extreme-Ultraviolet Vortex Beams. *Phys. Rev. Lett.* **117,** 163202. doi:10.1103/PhysRevLett.117.163202 (16 2016) (cit. on pp. 44, 46, 74, 76, 80).

107. Hernández-García, C., Rego, L., Román, J. S., Picón, A. & Plaja, L. Attosecond twisted beams from high-order harmonic generation driven by optical vortices. *High Power Laser Science and Engineering* **5.** doi:10.1017/hpl.2017.1 (2017) (cit. on pp. 44, 74).

108. L'Huillier, A., Balcou, P., Candel, S., Schafer, K. J. & Kulander, K. C. Calculations of high-order harmonic-generation processes in xenon at 1064 nm. *Physical Review A* **46,** 2778–2790. doi:10.1103/physreva.46.2778 (1992) (cit. on p. 45).

109. Hehre, W. J., Stewart, R. F. & Pople, J. A. Self-Consistent Molecular-Orbital Methods. I. Use of Gaussian Expansions of Slater-Type Atomic Orbitals. *The Journal of Chemical Physics* **51,** 2657–2664. doi:10.1063/1.1672392 (1969) (cit. on p. 47).

110. Smirnova, O., Spanner, M. & Ivanov, M. Anatomy of strong field ionization II: to dress or not to dress? *Journal of Modern Optics* **54,** 1019–1038. doi:10.1080/09500340701234656 (2007) (cit. on p. 47).

111. Schiff, L. I. *Quantum Mechanics* (McGraw-Hill, 1949) (cit. on p. 49).

112. Lein, M., Corso, P. P., Marangos, J. P. & Knight, P. L. Orientation dependence of high-order harmonic generation in molecules. *Physical Review A* **67,** 023819. doi:10.1103/physreva.67.023819 (2003) (cit. on p. 51).

113. Le, A.-T., Picca, R. D., Fainstein, P. D., Telnov, D. A., Lein, M & Lin, C. D. Theory of high-order harmonic generation from molecules by intense laser pulses. *Journal of Physics B: Atomic, Molecular and Optical Physics* **41,** 081002. doi:10.1088/0953-4075/41/8/081002 (2008) (cit. on p. 51).

114. Zhou, X., Lock, R., Wagner, N., Li, W., Kapteyn, H. C. & Murnane, M. M. Elliptically Polarized High-Order Harmonic Emission from Molecules in Linearly Polarized Laser Fields. *Physical Review Letters* **102,** 073902. doi:10.1103/physrevlett.102.073902 (2009) (cit. on pp. 52, 132).

115. Sakdinawat, A. & Liu, Y. Soft-x-ray microscopy using spiral zone plates. *Optics Letters* **32,** 2635. doi:10.1364/ol.32.002635 (2007) (cit. on p. 71).

116. Van Veenendaal, M. & McNulty, I. Prediction of Strong Dichroism Induced by X Rays Carrying Orbital Momentum. *Physical Review Letters* **98,** 157401. doi:10.1103/physrevlett.98.157401 (2007) (cit. on p. 71).

117. Picón, A., Mompart, J., de Aldana, J. R. V., Plaja, L., Calvo, G. F. & Roso, L. Photoionization with orbital angular momentum beams. *Optics Express* **18,** 3660. doi:10.1364/oe.18.003660 (2010) (cit. on p. 71).

118. Hernández-García, C., Vieira, J., Mendonça, J., Rego, L., Román, J. S., Plaja, L., Ribic, P., Gauthier, D. & Picón, A. Generation and Applications of Extreme-Ultraviolet Vortices. *Photonics* **4,** 28. doi:10.3390/photonics4020028 (2017) (cit. on p. 71).

119. Baghdasaryan, B., Böning, B., Paufler, W. & Fritzsche, S. Dichroism in two-color above-threshold ionization with twisted XUV beams and intense infrared laser fields. *Physical Review A* **99,** 023403. doi:10.1103/physreva.99.023403 (2019) (cit. on p. 71).

120. Beijersbergen, M., Coerwinkel, R., Kristensen, M. & Woerdman, J. Helical-wavefront laser beams produced with a spiral phaseplate. *Optics Communications* **112,** 321–327. doi:10.1016/0030-4018(94)90638-6 (1994) (cit. on p. 71).

121. Marrucci, L., Manzo, C. & Paparo, D. Optical Spin-to-Orbital Angular Momentum Conversion in Inhomogeneous Anisotropic Media. *Physical Review Letters* **96,** 163905. doi:10.1103/physrevlett.96.163905 (2006) (cit. on p. 71).

122. Atencia, J., Collados, M.-V., Quintanilla, M., Marín-Sáez, J. & Sola, Í. J. Holographic optical element to generate achromatic vortices. *Optics Express* **21,** 21056. doi:10.1364/oe.21.021056 (2013) (cit. on p. 71).

123. Berkhout, G. C. G., Lavery, M. P. J., Courtial, J., Beijersbergen, M. W. & Padgett, M. J. Efficient Sorting of Orbital Angular Momentum States of Light. *Physical Review Letters* **105,** 153601. doi:10.1103/physrevlett.105.153601 (2010) (cit. on p. 71).

124. Mirhosseini, M., Malik, M., Shi, Z. & Boyd, R. W. Efficient separation of the orbital angular momentum eigenstates of light. *Nature Communications* **4.** doi:10.1038/ncomms3781 (2013) (cit. on p. 71).

125. Peele, A. G., McMahon, P. J., Paterson, D., Tran, C. Q., Mancuso, A. P., Nugent, K. A., Hayes, J. P., Harvey, E., Lai, B. & McNulty, I. Observation of an x-ray vortex. *Optics Letters* **27,** 1752. doi:10.1364/ol.27.001752 (2002) (cit. on p. 71).

126. Woods, J. S., Chen, X. M., Chopdekar, R. V., Farmer, B., Mazzoli, C., Koch, R., Tremsin, A. S., Hu, W., Scholl, A., Kevan, S., Wilkins, S., Kwok, W.-K., Long, L. E. D., Roy, S. & Hastings, J. T. Switchable X-Ray Orbital Angular Momentum from an Artificial Spin Ice. *Physical Review Letters* **126,** 117201. doi:10.1103/physrevlett.126.117201 (2021) (cit. on p. 71).

127. Saleh, B. E. A. & Teich, M. C. *Fundamentals of Photonics* doi:10.1002/0471213748 (John Wiley & Sons, Inc., 1991) (cit. on p. 71).

128. Zürch, M., Kern, C., Hansinger, P., Dreischuh, A. & Spielmann, C. Strong-field physics with singular light beams. *Nature Physics* **8,** 743–746. doi:10.1038/nphys2397 (2012) (cit. on p. 73).

129. Hernández-García, C., Picón, A., San Román, J. & Plaja, L. Attosecond Extreme Ultraviolet Vortices from High-Order Harmonic Generation. *Phys. Rev. Lett.* **111,** 083602. doi:10.1103/PhysRevLett.111.083602 (2013) (cit. on pp. 73, 74, 144).

130. Gariepy, G., Leach, J., Kim, K. T., Hammond, T. J., Frumker, E., Boyd, R. W. & Corkum, P. B. Creating High-Harmonic Beams with Controlled Orbital Angular Momentum. *Phys. Rev. Lett.* **113,** 153901. doi:10.1103/PhysRevLett.113.153901 (2014) (cit. on p. 73).

131. Géneaux, R., Camper, A., Auguste, T., Gobert, O., Caillat, J., Taïeb, R. & Ruchon, T. Synthesis and characterization of attosecond light vortices in the extreme ultraviolet. *Nature Communications* **7.** doi:10.1038/ncomms12583 (2016) (cit. on pp. 73, 144).

132. Gauthier, D., Ribič, P. R., Adhikary, G., Camper, A., Chappuis, C., Cucini, R., DiMauro, L. F., Dovillaire, G., Frassetto, F., Géneaux, R., Miotti, P., Poletto, L., Ressel, B., Spezzani, C., Stupar, M., Ruchon, T. & Ninno, G. D. Tunable orbital angular momentum in high-harmonic generation. *Nature Communications* **8.** doi:10.1038/ncomms14971 (2017) (cit. on pp. 75, 144).

133. Kong, F., Zhang, C., Bouchard, F., Li, Z., Brown, G. G., Ko, D. H., Hammond, T. J., Arissian, L., Boyd, R. W., Karimi, E. & Corkum, P. B. Controlling the orbital angular momentum of high harmonic vortices. *Nature Communications* **8.** doi:10.1038/ncomms14970 (2017) (cit. on pp. 75, 144).

134. Turpin, A., Rego, L., Picón, A., Román, J. S. & Hernández-García, C. Extreme Ultraviolet Fractional Orbital Angular Momentum Beams from High Harmonic Generation. *Scientific Reports* **7.** doi:10.1038/srep43888 (2017) (cit. on p. 75).

135. Géneaux, R., Chappuis, C., Auguste, T., Beaulieu, S., Gorman, T. T., Lepetit, F., DiMauro, L. F. & Ruchon, T. Radial index of Laguerre-Gaussian modes in high-order-harmonic generation. *Physical Review A* **95,** 051801. doi:10.1103/physreva.95.051801 (2017) (cit. on p. 75).

136. Zhang, X., Shen, B., Shi, Y., Wang, X., Zhang, L., Wang, W., Xu, J., Yi, L. & Xu, Z. Generation of Intense High-Order Vortex Harmonics. *Physical Review Letters* **114,** 173901. doi:10.1103/physrevlett.114.173901 (2015) (cit. on p. 75).

137. Mendonça, J. T. & Vieira, J. High harmonic generation in underdense plasmas by intense laser pulses with orbital angular momentum. *Physics of Plasmas* **22,** 123106. doi:10.1063/1.4936824 (2015) (cit. on p. 75).

138. Babiker, M., Power, W. L. & Allen, L. Light-induced Torque on Moving Atoms. *Physical Review Letters* **73,** 1239–1242. doi:10.1103/physrevlett.73.1239 (1994) (cit. on p. 80).

139. Padgett, M. & Bowman, R. Tweezers with a twist. *Nature Photonics* **5,** 343–348. doi:10.1038/nphoton.2011.81 (2011) (cit. on p. 80).

140. Karimi, E., Marrucci, L., de Lisio, C. & Santamato, E. Time-division multiplexing of the orbital angular momentum of light. *Optics Letters* **37,** 127. doi:10.1364/ol.37.000127 (2012) (cit. on p. 81).

141. Sedeh, H. B., Salary, M. M. & Mosallaei, H. Time-varying optical vortices enabled by time-modulated metasurfaces. *Nanophotonics* **9,** 2957–2976. doi:10.1515/nanoph-2020-0202 (2020) (cit. on p. 85).

142. Liebmann, M., Treffer, A., Bock, M., Wallrabe, U. & Grunwald, R. Ultrashort Vortex Pulses with Controlled Spectral Gouy Rotation. *Applied Sciences* **10,** 4288. doi:10.3390/app10124288 (2020) (cit. on p. 85).

143. Xue, J., Liu, C., Zhou, C. & Ruan, S. Generation of necklace-shaped high harmonics in a two-color vortex field. *Optics Express* **29,** 17831. doi:10.1364/oe.427595 (2021) (cit. on p. 88).

144. Yao, A. M. & Padgett, M. J. Orbital angular momentum: origins, behavior and applications. *Advances in Optics and Photonics* **3,** 161. doi:10.1364/aop.3.000161 (2011) (cit. on p. 92).

145. Cireasa, R., Boguslavskiy, A. E., Pons, B., Wong, M. C. H., Descamps, D., Petit, S., Ruf, H., Thiré, N., Ferré, A., Suarez, J., Higuet, J., Schmidt, B. E., Alharbi, A. F., Légaré, F., Blanchet, V., Fabre, B., Patchkovskii, S., Smirnova, O., Mairesse, Y. & Bhardwaj, V. R. Probing molecular chirality on a sub-femtosecond timescale. *Nature Physics* **11,** 654–658. doi:10.1038/nphys3369 (2015) (cit. on p. 131).

146. Smirnova, O., Mairesse, Y. & Patchkovskii, S. Opportunities for chiral discrimination using high harmonic generation in tailored laser fields. *Journal of Physics B: Atomic, Molecular and Optical Physics* **48,** 234005. doi:10.1088/0953-4075/48/23/234005 (2015) (cit. on p. 131).

147. Ayuso, D., Neufeld, O., Ordonez, A. F., Decleva, P., Lerner, G., Cohen, O., Ivanov, M. & Smirnova, O. Synthetic chiral light for efficient control of chiral light–matter interaction. *Nature Photonics* **13,** 866–871. doi:10.1038/s41566-019-0531-2 (2019) (cit. on p. 131).

148. Allaria, E., Diviacco, B., Callegari, C., Finetti, P., Mahieu, B., Viefhaus, J., Zangrando, M., Ninno, G. D., Lambert, G., Ferrari, E., Buck, J., Ilchen, M., Vodungbo, B., Mahne, N., Svetina, C., Spezzani, C., Mitri, S. D., Penco, G., Trovó, M., Fawley, W. M., Rebernik, P. R., Gauthier, D., Grazioli, C., Coreno, M., Ressel, B., Kivimäki, A., Mazza, T., Glaser, L., Scholz, F., Seltmann, J., Gessler, P., Grünert, J., Fanis, A. D., Meyer, M., Knie, A., Moeller, S. P., Raimondi, L., Capotondi, F., Pedersoli, E., Plekan, O., Danailov, M. B., Demidovich, A., Nikolov, I., Abrami, A.,

Gautier, J., Lüning, J., Zeitoun, P. & Giannessi, L. Control of the Polarization of a Vacuum-Ultraviolet, High-Gain, Free-Electron Laser. *Physical Review X* **4,** 041040. doi:10.1103/physrevx.4.041040 (2014) (cit. on p. 131).

149. Lutman, A. A., MacArthur, J. P., Ilchen, M., Lindahl, A. O., Buck, J., Coffee, R. N., Dakovski, G. L., Dammann, L., Ding, Y., Dürr, H. A., Glaser, L., Grünert, J., Hartmann, G., Hartmann, N., Higley, D., Hirsch, K., Levashov, Y. I., Marinelli, A., Maxwell, T., Mitra, A., Moeller, S., Osipov, T., Peters, F., Planas, M., Shevchuk, I., Schlotter, W. F., Scholz, F., Seltmann, J., Viefhaus, J., Walter, P., Wolf, Z. R., Huang, Z. & Nuhn, H.-D. Polarization control in an X-ray free-electron laser. *Nature Photonics* **10,** 468–472. doi:10.1038/nphoton.2016.79 (2016) (cit. on p. 131).

150. Budil, K. S., Salières, P., L'Huillier, A., Ditmire, T. & Perry, M. D. Influence of ellipticity on harmonic generation. *Physical Review A* **48,** R3437–R3440. doi:10.1103/physreva.48.r3437 (1993) (cit. on p. 132).

151. Dietrich, P., Burnett, N. H., Ivanov, M. & Corkum, P. B. High-harmonic generation and correlated two-electron multiphoton ionization with elliptically polarized light. *Physical Review A* **50,** R3585–R3588. doi:10.1103/physreva.50.r3585 (1994) (cit. on p. 132).

152. Antoine, P., L'Huillier, A., Lewenstein, M., Salières, P. & Carré, B. Theory of high-order harmonic generation by an elliptically polarized laser field. *Physical Review A* **53,** 1725–1745. doi:10.1103/physreva.53.1725 (1996) (cit. on p. 132).

153. Vodungbo, B., Sardinha, A. B., Gautier, J., Lambert, G., Valentin, C., Lozano, M., Iaquaniello, G., Delmotte, F., Sebban, S., Lüning, J. & Zeitoun, P. Polarization control of high order harmonics in the EUV photon energy range. *Optics Express* **19,** 4346. doi:10.1364/oe.19.004346 (2011) (cit. on p. 132).

154. Tancogne-Dejean, N., Mücke, O. D., Kärtner, F. X. & Rubio, A. Ellipticity dependence of high-harmonic generation in solids originating from coupled intraband and interband dynamics. *Nature Communications* **8.** doi:10.1038/s41467-017-00764-5 (2017) (cit. on p. 132).

155. Ferré, A., Handschin, C., Dumergue, M., Burgy, F., Comby, A., Descamps, D., Fabre, B., Garcia, G. A., Géneaux, R., Merceron, L., Mével, E., Nahon, L., Petit, S., Pons, B., Staedter, D., Weber, S., Ruchon, T., Blanchet, V. & Mairesse, Y. A table-top ultrashort light source in the extreme ultraviolet for circular dichroism experiments. *Nature Photonics* **9,** 93–98. doi:10.1038/nphoton.2014.314 (2014) (cit. on p. 132).

156. Lambert, G., Vodungbo, B., Gautier, J., Mahieu, B., Malka, V., Sebban, S., Zeitoun, P., Luning, J., Perron, J., Andreev, A., Stremoukhov, S., Ardana-Lamas, F., Dax, A., Hauri, C. P., Sardinha, A. & Fajardo, M. Towards enabling femtosecond helicity-dependent spectroscopy with high-harmonic sources. *Nature Communications* **6.** doi:10.1038/ncomms7167 (2015) (cit. on p. 132).

157. Mahieu, B., Stremoukhov, S., Gauthier, D., Spezzani, C., Alves, C., Vodungbo, B., Zeitoun, P., Malka, V., Ninno, G. D. & Lambert, G. Control of ellipticity in high-order harmonic generation driven by two linearly polarized fields. *Physical Review A* **97,** 043857. doi:10.1103/physreva.97.043857 (2018) (cit. on p. 132).

158. Ellis, J. L., Dorney, K. M., Hickstein, D. D., Brooks, N. J., Gentry, C., Hernández-García, C., Zusin, D., Shaw, J. M., Nguyen, Q. L., Mancuso, C. A., Jansen, G. S. M., Witte, S., Kapteyn, H. C. & Murnane, M. M. High harmonics with spatially varying ellipticity. *Optica* **5,** 479. doi:10.1364/optica.5.000479 (2018) (cit. on p. 133).

159. Azoury, D., Kneller, O., Krüger, M., Bruner, B. D., Cohen, O., Mairesse, Y. & Dudovich, N. Interferometric attosecond lock-in measurement of extreme-ultraviolet circular dichroism. *Nature Photonics* **13,** 198–204. doi:10.1038/s41566-019-0350-5 (2019) (cit. on p. 133).

160. Hickstein, D. D., Dollar, F. J., Grychtol, P., Ellis, J. L., Knut, R., Hernández-García, C., Zusin, D., Gentry, C., Shaw, J. M., Fan, T., Dorney, K. M., Becker, A., Jaroń-Becker, A., Kapteyn, H. C., Murnane, M. M. & Durfee, C. G. Non-collinear generation of angularly isolated circularly polarized high harmonics. *Nature Photonics* **9,** 743–750. doi:10.1038/nphoton.2015.181 (2015) (cit. on pp. 133, 134).

161. Hernández-García, C., Durfee, C. G., Hickstein, D. D., Popmintchev, T., Meier, A., Murnane, M. M., Kapteyn, H. C., Sola, I. J., Jaron-Becker, A. & Becker, A. Schemes for generation of isolated attosecond pulses of pure circular polarization. *Physical Review A* **93,** 043855. doi:10.1103/physreva.93.043855 (2016) (cit. on pp. 133–135).

162. Eichmann, H., Egbert, A., Nolte, S., Momma, C., Wellegehausen, B., Becker, W., Long, S. & McIver, J. K. Polarization-dependent high-order two-color mixing. *Physical Review A* **51,** R3414–R3417. doi:10.1103/physreva.51.r3414 (1995) (cit. on pp. 133, 138).

163. Long, S., Becker, W. & McIver, J. K. Model calculations of polarization-dependent two-color high-harmonic generation. *Physical Review A* **52,** 2262–2278. doi:10.1103/physreva.52.2262 (1995) (cit. on pp. 133, 138).

164. Milošević, D. B., Becker, W. & Kopold, R. Generation of circularly polarized high-order harmonics by two-color coplanar field mixing. *Physical Review A* **61,** 063403. doi:10.1103/physreva.61.063403 (2000) (cit. on pp. 133, 138).

165. Fleischer, A., Kfir, O., Diskin, T., Sidorenko, P. & Cohen, O. Spin angular momentum and tunable polarization in high-harmonic generation. *Nature Photonics* **8,** 543–549. doi:10.1038/nphoton.2014.108 (2014) (cit. on pp. 133, 138, 140, 164).

166. Kfir, O., Grychtol, P., Turgut, E., Knut, R., Zusin, D., Popmintchev, D., Popmintchev, T., Nembach, H., Shaw, J. M., Fleischer, A., Kapteyn, H., Murnane, M. & Cohen, O. Generation of bright phase-matched circularly-polarized extreme ultraviolet high harmonics. *Nature Photonics* **9,** 99–105. doi:10.1038/nphoton.2014.293 (2014) (cit. on pp. 133, 138, 141, 164).

167. Jiménez-Galán, Á., Zhavoronkov, N., Ayuso, D., Morales, F., Patchkovskii, S., Schloz, M., Pisanty, E., Smirnova, O. & Ivanov, M. Control of attosecond light polarization in two-color bicircular fields. *Physical Review A* **97,** 023409. doi:10.1103/physreva.97.023409 (2018) (cit. on p. 133).

168. Ivanov, M. & Pisanty, E. Taking control of polarization. *Nature Photonics* **8,** 501–503. doi:10.1038/nphoton.2014.141 (2014) (cit. on p. 139).

169. Dorney, K. M., Ellis, J. L., Hernández-García, C., Hickstein, D. D., Mancuso, C. A., Brooks, N., Fan, T., Fan, G., Zusin, D., Gentry, C., Grychtol, P., Kapteyn, H. C. & Murnane, M. M. Helicity-Selective Enhancement and Polarization Control of Attosecond High Harmonic Waveforms Driven by Bichromatic Circularly Polarized Laser Fields. *Physical Review Letters* **119,** 063201. doi:10.1103/physrevlett.119.063201 (2017) (cit. on p. 140).

170. Chen, C., Tao, Z., Hernández-García, C., Matyba, P., Carr, A., Knut, R., Kfir, O., Zusin, D., Gentry, C., Grychtol, P., Cohen, O., Plaja, L., Becker, A., Jaron-Becker, A., Kapteyn, H. & Murnane, M. Tomographic reconstruction of circularly polarized high-harmonic fields: 3D attosecond metrology. *Science Advances* **2,** e1501333. doi:10.1126/sciadv.1501333 (2016) (cit. on p. 141).

171. Pisanty, E., Machado, G. J., Vicuña-Hernández, V., Picón, A., Celi, A., Torres, J. P. & Lewenstein, M. Knotting fractional-order knots with the polarization state of light. *Nature Photonics* **13,** 569–574. doi:10.1038/s41566-019-0450-2 (2019) (cit. on p. 147).

172. Barreau, L., Veyrinas, K., Gruson, V., Weber, S. J., Auguste, T., Hergott, J.-F., Lepetit, F., Carré, B., Houver, J.-C., Dowek, D. & Salières, P. Evidence of depolarization and ellipticity of high harmonics driven by ultrashort bichromatic circularly polar-

ized fields. *Nature Communications* **9.** doi:10.1038/s41467-018-07151-8 (2018) (cit. on p. 150).

173. McMaster, W. H. Polarization and the Stokes Parameters. *American Journal of Physics* **22,** 351–362. doi:10.1119/1.1933744 (1954) (cit. on p. 152).

COLOPHON

This thesis have been funded by the Ministerio de Educación, Cultura y Deporte (FPU16/02591).

This document was typeset using the typographical look-and-feel `classicthesis` developed by André Miede. The style was inspired by Robert Bringhurst's seminal book on typography "*The Elements of Typographic Style*". `classicthesis` is available for both LaTeX and LyX:

https://bitbucket.org/amiede/classicthesis/

Ultrashort laser pulses are a unique tool to explore the fastest dynamics in matter. Remarkably, the shortest laser pulses to date are produced from the non-linear phenomenon of high-order harmonic generation, which results in the emission of extreme-ultraviolet/X-ray attosecond pulses. Importantly, such attosecond pulses can exhibit a very exciting property, the angular momentum, in two different forms: the spin angular momentum and the orbital angular momentum.

In this thesis, we develop a compilation of schemes for the creation of ultrashort pulses with novel spin and orbital angular momentum properties. To this end, we structure the process of high-order harmonic generation through the characteristics of the driving beams. As one of our main results, we demonstrate the generation of high-frequency beams with time-varying angular momentum, a new degree of freedom that opens new routes for the study of light-matter interactions.

ALF USAL